1997-96 Dup

TÜBİTAK

TÜRKİYE BİLİMSEL VE
TEKNİK ARAŞTIRMA KURUMU

THE SCIENTIFIC AND TECHNICAL
RESEARCH COUNCIL OF TURKEY

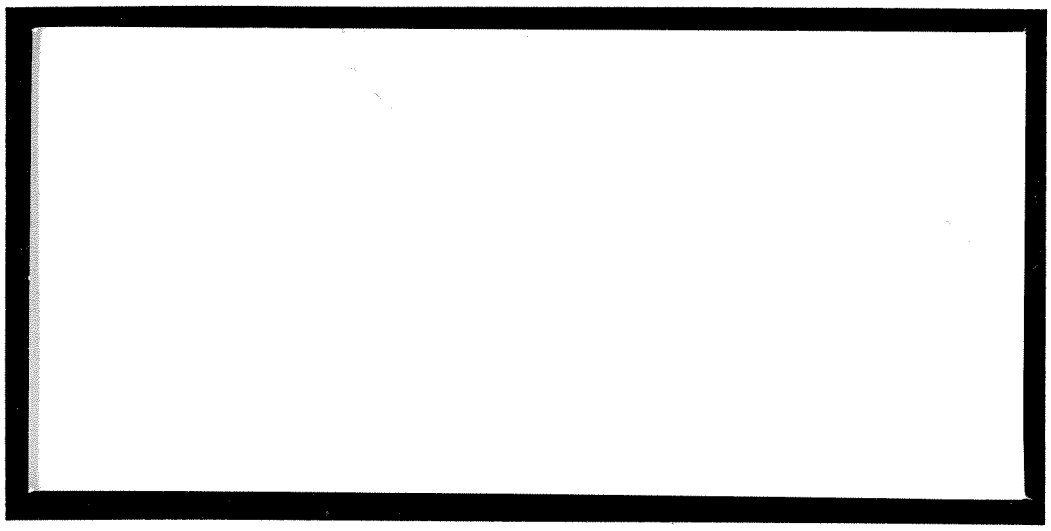

Elektrik, Elektronik ve Enformatik Araştırma Grubu

Electric, Electronics and Informatics Research Grant Committee

ACTIVE PHASED ARRAYS AND ARRAY FED ANTENNAS

AKTİF FAZ TARAMALI DİZİLER VE DİZİ BESLEMELİ ANTENLER

Proje No: COST 245

Prof. Dr. Tuncay Birand
Prof. Dr. Canan Toker
Prof. Dr. Altunkan Hızal
Prof. Dr. Nilgün Günalp
Prof. Dr. Merih Büyükdura
Doç. Dr. Gülbin Dural
Öğr. Gör. Dr. Ceyhun Bulutay
Öğr. Gör. Dr. Özlem Aydın Çivi
Öğr. Gör. Dr. Lale Hayırlıoğlu Alatan
Öğr. Gör. Şimşek Demir

Ekim 1997
Ankara

ÖNSÖZ

Aktif Faz Taramalı Diziler ve Dizi Beslemeli Antenler (Active Phased Arrays and Array Fed Antennas) adlı COST 245 projesinde faz taramalı anten dizileri, monolitik mikrodalga entegre devreler (MMIC), geniş bantlı antenler ve bu tür yapıların nümerik metotlarla analizi konuları yer almıştır. Avrupa Ekonomik Topluluğu üye ülkeleriyle işbirliği içerisinde yürütülen bu proje, Orta Doğu Teknik Üniversitesi, Elektrik ve Elektronik Mihendisliği Bölümü' nde bir ekip tarafından gerçekleştirilmiş ve 1 Ocak 1994 - 1 Temmuz 1997 tarihleri arasıda TÜBİTAK tarafından desteklenmiştir.

İÇİNDEKİLER

sayfa

ÖNSÖZ ii

ŞEKİL LİSTESİ v

TABLO LİSTESİ xi

ÖZ 1

ABSTRACT 2

I. GİRİŞ 3

II. TEKNİK ÇALIŞMALAR 6

A. Research On Phased Array Antennas 7

A.1 TVRO and Related Phased Arrays 7

A.1.1 Introduction and preliminary studies 7
A.1.2 Theoretical material 17
A.1.3 Test fixture (jig) design and patch antenna measurements 30
A.1.4 Antenna array designs 44

A.2. Smart Antennas 57

B. Monolithic Microwave Integrated Circuit Designs 82

B.1 Narrow and wideband amplifiers 84

B.2 Voltage controlled oscillator 90

B.3 Mixer 96

B.4 Low noise amplifier 103

B.5 Transmit / Receive switch 108

B.6 Power amplifier 113

B.7 Wideband voltage variable attenuator 115

B.8 Phase shifter 122

C. Geniş Bantlı Antenler ve Nümerik Metotlarla ilgili Araştırmalar..... 130

C.1 Milimetrik dalga bandında iki ve üç katmanlı (ferit-dielektrik) antenlerle elektronik demet taraması..... 130

C.2 2-18 GHz ve 6-18 GHz frekans bantlı Vivaldi antenler ile 6-18 GHz frekans bantlı Vivaldi anten dairesel dizisi..... 134

C.3 Düzlemsel mikroşerit yapıların incelenmesinde kullanılan MoM metodunun nümerik integrasyondan arındırılması..... 145

C.4 Sonlu dizi antenlerin integral danklem sistemi ile sistematik çözümü..... 151

III. SONUÇ 156

EK I: YAYINLAR 159

EK II: COST-245 PROJESİNİN ULUSLARARASI ORGANİZASYONU

ŞEKİL LİSTESİ

sayfa

A.1.1 Dual beam TVRO antenna illustration 7

A.1.2 Dual beam generation using end-fed topology. 8

A.1.3 Positions of the two satellites and Ankara. 9

A.1.4 The beam angles in the azimuth plane with the ground base chosen as Ankara. 9

A.1.5 First preliminary design a) having series fed topology b) individual arrays. 11

A.1.6 Second preliminary topology having a parallel fed array A. 12

A.1.7 The variation of the input impedance within the array B. 12

A.1.8 The third preliminary antenna with center-fed topology. 13

A.1.9 The fourth preliminary center-fed topology. 14

A.1.10 The radiation pattern of array A. 14

A.1.11 The radiation pattern of array B. 14

A.1.12 The input VSWR versus frequency of the fourth preliminary design. 16

A.1.13 Microstrip patch arrays: Array A and Array B 17

A.1.14 Active antenna array structures: a) passive sub-array b) active array..... 21

A.1.15 Receiving antenna array and the conjugate matched termination..... 24

A.1.16 Parallel fed linear microstrip patch array and the transmission line equivalent model corresponding to this array..... 25

A.1.17 Series fed linear microstrip patch array and the transmission line equivalent model corresponding to this array..... 26

A.1.18 The variation of output equivalent noise temperature by the number of antenna elements in the array for both parallel and series fed geometries. 28

A.1.19 The dependence of output noise temperature on the losses in the transmission lines..... 29

A.1.20 Insertion loss of the microstrip line..... 31

A.1.21 Return loss of the microstrip line. 32
A.1.22 Single patch antenna with 50 Ohm microstrip line..... 33
A.1.23 Return loss curve of the patch antenna..... 34
A.1.24 Return loss curve of the patch antenna..... 35
A.1.25 3 GHz patch antenna with matching section..... 33
A.1.26 Return loss curve of the patch antenna with jig #2..... 36
A.1.27 Return loss curve of the patch antenna with MTF 26..... 37
A.1.28 Return loss curve of the patch antenna with jig #1..... 38
A.1.29 10 GHz microstrip patch antenna 39
A.1.30 Return loss curve of the patch antenna with MTF 26..... 40
A.1.31 10 GHz square patch antenna with matching section..... 41
A.1.32 Return loss curve of the patch antenna with MTF 26..... 42
A.1.33 Return loss curve of the patch antenna with jig #1..... 43
A.1.34 8x4 microstrip patch antenna array for design 1..... 44
A.1.35 Array B..... 44
A.1.36 Return loss of the overall array..... 45
A.1.37 E-plane radiation pattern of the array..... 46
A.1.38 H-plane radiation pattern of the array..... 47
A.1.39 12x32 array..... 49
A.1.40 Microstrip patch antenna and equivalent circuit..... 49
A.1.41 Array B of microstrip patch antenna array..... 50
A.1.42 Array A of microstrip patch antenna array..... 50
A.1.43 Active array, s= 18.957mm, d=15.726mm, l_o=31.56mm, w_p=l_p=8.189mm..... 52
A.1.44 Array B of microstrip patch antenna array..... 53
A.1.45 Rectangular microstrip patch antenna array on cylindirical substrate..... 54
A.1.46 Radiation pattterns in q=p/2 plane of patch antenna on a cylindirical substrate..... 55
A.1.47 Radiation pattterns in f=0 plane of patch antenna on a cylindirical substrate..... 55
A.2.1 Layout and dimensions of the smart antenna array..... 58

A.2.2 Dimensions of single element of antenna array..... 57
A.2.3 a) Block diagram and b) a photograph of the smart antenna system..... 59
A.2.6 Measured S-parameters: Q1 port..... 62
A.2.7 Measured S-parameters: I1 port..... 63
A.2.8 Measured S-parameters: Q2 port..... 64
A.2.9 Measured S-parameters: I2 port..... 65
A.2.10 Measured S-parameters: Q3 port..... 66
A.2.11 Measured S-parameters: I3 port..... 67
A.2.12 Measured S-parameters: Q4 port..... 68
A.2.13 Measured S-parameters: I4 port..... 69
A.2.14 Measured S-parameters: Q5 port..... 70
A.2.15 Measured S-parameters: I5 port..... 71
A.2.16 Measured S-parameters: Q6 port..... 72
A.2.17 Measured S-parameters: I6 port..... 73
A.2.18 Measured S-parameters: A7..... 74
A.2.19 Measured S-parameters: B7..... 75
A.2.20 Calibration accuracy..... 76
A.2.21 Spherical wave model of the incident wave..... 77
B.1.1 Circuit diagrams of the amplifiers and component values..... 86
B.1.2 MMIC layout of the three amplifiers..... 87
B.1.3 Simulation and measurement results of the one-stage amplifier..... 88
B.1.4 Simulation and measurement results of the two-stage amplifier..... 89
B.2.1 Circuit diagram of the VCO..... 92
B.2.2 MMIC layout of the VCO..... 92
B.2.3 Oscillation frequency versus tuning voltage (measurement)..... 94
B.2.4 Output power versus tuning voltage (measurement)..... 94
B.2.5 Spectrum analyzer output at the 'Hold Maximum' mode..... 95
B.3.1 Circuit diagram of the mixer..... 98
B.3.2 Conversion loss characteristics..... 98
B.3.3 Isolation properties..... 99
B.3.4 Mixer layout..... 99

B.3.5 Measured conversion loss..... 100
B.3.6 Measured RF to LO isolation..... 101
B.3.7 Measured LO to IF isolation..... 102
B.4.1 Circuit diagram of the LNA..... 105
B.4.2 MMIC layout of the LNA..... 106
B.4.3 Simulation and measurement results..... 107
B.5.1 (a) Circuit topology of a general purpose SPDT RF switch
(b) Circuit topology of the proposed asymmetric T/R switch..... 110
B.5.2 MMIC layout of the T/R switch..... 111
B.5.3 Simulation and measurement results..... 112
B.6.1 Amplifier circuit diagram..... 114
B.6.2 Layout of the amplifier..... 114
B.6.3 Simulation results of the amplifier..... 114
B.7.1 Network configurations for (a) T-type attenuator (b) PI-type attenuator
(c) Bridged T-type attenuator..... 117
B.7.2 Parallel combination of several FETs with a resistive voltage divider..... 118
B.7.3 Schematic diagram of the complete attenuator..... 118
B.7.4 MMIC layout of the attenuator..... 119
B.7.5 Attenuation as a function of the control voltage..... 120
B.7.6 Input and output return loss as a function of the control voltage..... 120
B.7.7 Phase shift through the attenuator as a function of attenuation..... 121
B.8.1 Schematics of T-type low pass/high pass sections and SPDT switches..... 124
B.8.2 Block diagram of the three bit phase shifter..... 124
B.8.3 Layout of 90° phase bit with SPDT switches..... 125
B.8.4 Insertion loss of the 90° phase bit when high pass and low pass paths are selected..... 125
B.8.5 Return loss of the 90° phase bit when high pass and low pass paths are selected..... 126
B.8.6 Differential phase shift and the insertion phases of the 90° phase bit when high pass and low pass paths are selected..... 126

B.8.7 Amplitude difference between the two paths of the 90° phase bit when high pass and low pass paths are selected 127
B.8.8 Insertion loss of the reference state (State I) 127
B.8.9 Input and output return losses of the reference state 128
B.8.10 Differential phases of the seven phase states 128
C.1.1 İki katmanlı yapı 132
C.1.2 İki katmanlı yapı için ışıma örüntüleri, f=26.5 GHz, d=6mm a) h=2mm, b) h=2.3mm, c) h=2.7mm 132
C.1.3 Üç katmanlı yapı için ışıma örüntüleri, f=26.5 GHz, d=4.1mm, h=3mm, l=1mm 132
C.1.4 Bo'ya karşılık ışın demetinin yönü, f=26.5 GHz, d=6mm, h=2mm, l=3mm 133
C.1.5 Farklı frekanslar için Bo'ya karşılık ışın demetinin yönü, f=26.5 Ghz, d=6mm, h=2mm, l=3mm 133
C.2.1 Vivaldi antenin açılım eğrisi 136
C.2.2 Vivaldi anten 136
C.2.3 2-18 GHz frekans bantlı Vivaldi antenin giriş yansıma katsayısı 137
C.2.4 2-18 GHz frekans bantlı Vivaldi antenin 3 dB hüzme genişliği 137
C.2.5 2-18 GHz frekans bantlı Vivaldi antenin kazancı 138
C.2.6 2-18 GHz frekans bantlı Vivaldi antenin 13 GHz deki ışıma örüntüsü 138
C.2.7 2-18 GHz frekans bantlı Vivaldi antenin 13 GHz deki ışıma örüntüsü 139
C.2.8 6-18 GHz frekans bantlı Vivaldi antenin giriş yansıma katsayısı 139
C.2.9 6-18 GHz frekans bantlı Vivaldi antenin 3 dB hüzme genişliği 140
C.2.10 6-18 GHz frekans bantlı Vivaldi antenin kazancı 140
C.2.11 6-18 GHz frekans bantlı Vivaldi antenin 13 GHz deki ışıma örüntüsü 141
C.2.12 6-18 GHz frekans bantlı Vivaldi antenin 13 GHz deki ışıma örüntüsü 141
C.2.13 Bir dizi elemanının giriş yansıma katsayısı 142
C.2.14 Bir dizi elemanının 3 dB hüzme genişliği 142
C.2.15 Bir dizi elemanının kazancı 143
C.2.16 Bir dizi elemanının 13 GHz deki ışıma örüntüsü 143

C.2.17 Bir dizi elemanının 13 GHz deki ışıma örüntüsü..... 144
C.3.1 Formülasyonun uygulandığı mikroşerit hat geometrisi..... 146
C.3.2 Elde edilen akım dağılımları..... 149
C4.1 MxN dizi anten..... 151

TABLO LİSTESİ

sayfa

A.1.1 Voltage ratios and synthesized characteristic admittances for array B..... 15

A.1.2 Voltage ratios and synthesized characteristic admittances for array A..... 16

A.1.3 Element values for transmission line equivalent model 27

A.1.4 Characteristics of RT-DUROID 5880..... 30

A.1.5 $|S_{11}|$ values for various C_d , ε_r , L_p values..... 33

A.1.6 $|S_{11}|$ values for various C_d , ε_r , L_p values..... 39

A.1.7 $|S_{11}|$ values for various C_d , ε_r , L_p values..... 41

A.1.8 $|S_{11}|$ values for various C_d , ε_r , L_p values..... 41

A.1.9 Lengths and widths of lines in the array, for t=0.0175 mm..... 48

A.1.10 Comparison of results..... 48

A.1.11 Grace Electronic Materials ECCOFOAM PP-4 specifications..... 48

A.1.12 Parameters of microstrip lines..... 48

A.1.13 Microstrip patch antenna parameters..... 49

A.1.14 Impedances, lengths and widths of the transmission lines used in the array B..... 50

A.1.15 Impedances, lengths and widths of the transmission lines used in the array A..... 50

A.1.16 Radiation pattern characteristics of array A (E-plane pattern)..... 51

A.1.17 Radiation pattern characteristics of array B (H-plane pattern)..... 51

A.1.18 Rogers RT-DUROID 6002 substrate specifications..... 51

A.1.19 Parameters of microstrip lines..... 51

A.1.20 Microstrip patch antenna parameters..... 51

A.1.21 Impedances, lengths and widths of the transmission lines used in Section II of the array B..... 52

A.1.22 Impedances, lengths and widths of the transmission lines used in Section I of the array B..... 52

A.1.23 Radiation characteristics of the antenna array..... 53

A.1.24 Radiation pattern characteristics of array A (H-plane pattern)..... 53

A.1.25 Radiation pattern characteristics of array B (E-plane pattern)..... 53
A.1.26 Resonance dimensions of a planar patch antenna of square shape at 2.21 GHz..... 54
B.2.1 Simulation results for the VCO..... 93
B.2.2 Measurement results for the VCO..... 93
B.8.1 Amplitude difference and phase error for each state..... 129
C.3.1 İki ayrı yöntem ile elde edilen CPU zamanları..... 149

ÖZ

COST 245 "Aktif Faz Taramalı Diziler ve Dizi Beslemeli Antenler" (Active Phased Arrays and Array Fed Antennas) Projesinin Ortak Niyet Beyanı ülkemiz adına imzalanarak, çalışmaları ODTÜ Elektrik ve Elektronik Mühendisliği Bölümünde görevli ekip tarafından yürütülmüştür. AT ülkeleriyle bilimsel işbirliği içerisinde yürütülen bu proje sonucu, diğer üye ülkelerin araştırma ve endüstriyel kuruluşlarında yapılan çalışmaları yakından izlemek ve bu üyelerin konuyla ilgili problemleri çözüm yollarını ele alış biçimleri hakkında fikir sahibi olmak imkanı elde edilmiştir.

Proje kapsamında yapılan çalışmalar A. Faz taramalı anten dizileri konusundaki çalışmalar, B. Monolitik mikrodalga entegre devrelerle (MMIC) ile ilgili çalışmalar ve C. Geniş bantlı antenler ve nümerik metotlar olarak üç ana grupta toplanmıştır. Birinci bölümde düzlemsel bir çift hüzmeli (dual beam) TVRO anteni gerçekleştirmek üzere mikroşerit faz taramalı anten dizileri üzerinde kapsamlı bir çalışma yapılmıştır. Uydu alıcı antenlerinde ortaya çıkan termal gürültünün analizi ve yüksek G/T (kazanç/eşdeğer gürültü derecesi) oranlı mikroşerit anten dizileri besleme yapıları tasarımı için özgün bir yöntem geliştirilmiştir. Bu çalışmalar sonucunda, 8x4 elemanlı (10 GHz), 32x12 elemanlı (11.3 GHz), 24x32 elemanlı aktif (9.5 GHz) ve silindirik yüzey üzerine yerleştirilmiş mikroşerit yama anten dizileri tasarımlanıp üretilmiş ve ölçümleri yapılmıştır.

İkinci bölümde faz taramalı anten dizilerinde kullanımı büyük avantaj sağlayan monolitik mikrodalga entegre devrelerinden, dar ve geniş bantlı yükselteçler, voltaj kontrollu osilatör, karıştırıcı, düşük gürültülü yükselteç, alıcı/verici anahtar, güç yükselteci, geniş bantlı voltaj kontrollu zayıflatıcı ve faz kaydırıcı devrelerinin tasarımı yapılmış ve bunlardan ilk beş tanesi üretilerek performansları ölçülmüştür.

Üçüncü bölümde ise geniş bantlı Vivaldi antenler ve dairesel Vivaldi anten dizileri gerçekleştirilmiş, ayrıca, dielektrik ve ferit katmanlar içeren antenlerle elektronik hüzme taraması elde edilebileceği gösterilmiştir. Bunlara ilaveten, düzlemsel mikroşerit yapıların incelenmesinde kullanılan moment yöntemi entegrasyondan arındırılarak hızlı analiz yapılabilmesi sağlanmıştır. Bir başka uygulama olarak da sonlu dizi antenler için, integral denklem sistemi ile sistematik bir çözüm yöntemi geliştirilmiştir.

Anahtar sözcükler: Faz taramalı diziler, aktif anten dizileri, mikroşerit antenler, monolitik mikrodalga entegre devreler, moment metodu.

ABSTRACT

The project COST 245 "Active Phased Arrays and Array Fed Antennas" is carried out by a team of researchers at the Department of Electrical and Electronics Engineering, Middle East Technical University, after the signatures on behalf of our country were put on the memorandum of understanding. The project is conducted with the participation of member countries of EC and the coordination of the efforts is achieved through project management committee meetings held in various countries.

Within the framework of the project, the research activities are carried out in three main groups: A. Research on phased array antennas, B. Monolithic microwave integrated circuit (MMIC) designs and C. Research on wide band antennas and numerical methods. In the first group, a detailed study is carried out on microstrip phased antenna arrays in order to realize a planar dual beam TVRO antenna. An original method is developed for the analysis of the thermal noise in the satellite receiving antennas and for the design of the feeding networks for antennas with low G/T (gain/equivalent noise temperature) ratio. As a result of these studies, microstrip patch antenna arrays (8x4 element 10 GHz, 32x12 element 11.3 GHz, 24x32 element active 9.5 GHz and one placed on cylindrical surface) are designed, implemented and measured.

In the second group a number of monolithic microwave integrated circuits which offer great advantages in phased arrays are designed. These are narrow and wide band amplifiers, voltage controlled oscillator, mixer, low noise amplifier, transmit/receive switch, power amplifier, wide band voltage variable attenuator and phase shifter. First five of the circuits are manufactured and their performances are measured.

In the third group wide band Vivaldi antennas and circular Vivaldi arrays are realized and also electronic beam scanning is achieved using antennas with dielectric and ferrite layers. In addition, the numerical integration is eliminated in the method of moments whereby a fast numerical algorithm is developed for the analysis of planar microstrip structures. A systematic solution technique is also obtained for the integral equation set corresponding to planar antenna arrays.

Key words: Phased arrays, active antenna arrays, microstrip antennas, monolithic microwave integrated circuits, method of moments.

I GİRİŞ :

COST 245 Projesi, Ortak Niyet Beyanı ülkemiz adına daha önce imzalanarak çalışmaları ODTÜ Elektrik ve Elektronik Mühendisliği Bölümünde görevli ekip tarafından yürütülen "Antennas in the 1990's: Active Array Antennas for future Satellite and Terrestrial Communications" adlı ve COST 223 No.lu projenin devamı niteliğindedir. COST 245 kapsamında AT ülkeleriyle bilimsel işbirliği içerisinde yürütülen bu proje sonucu, diğer üye ülkelerin araştırma ve endüstriyel kuruluşlarında yapılan çalışmaları yakından izlemek, bu üyelerin konuyla ilgili problemleri ve çözüm yollarını ele alış biçimleri hakkında fikir sahibi olmak imkanı elde edilmiştir. COST-245 Projesine aşağıda belirtilen 18 Avrupa ülkesi katılmıştır:

Belçika, Bulgaristan, İsviçre, Almanya, Danimarka, İspanya, Hollanda, Fransa, Yunanistan, İtalya, Norveç, Portekiz, Polonya, İsveç, Finlandiya, Türkiye, İngiltere.

Yakın geleceğin önemli teknolojilerine sahip olmak, ilgili iletişim sistemleri üzerinde çalışmalar yaparak bu konuda gelişmiş ülkelere yetişmek, en azından bu ülkelerden geri kalmamak projenin ana hedefi olmuştur. İletişim uydularında, uçaklarda veya yer yüzündeki platformlarda kullanılmaları öngörülen aktif dizi anten sistemlerinin geliştirilmesi amaçlanmıştır. Aktif anten dizileri, anten elemanlarının ve bu elemanlara bağlanacak kazancı ayarlanabilir yükselteç ve faz kaydırıcı birimlerinin aynı yüzey üzerinde gerçekleştirildiği sistemlerdir. Dizi elemanlarının, daha karmaşık yapıda çoklu hüzme oluşturucu devrelerle de beslenebilmeleri öngörülmüştür. Aktif dizi sistemlerinin kullanılmasındaki amaç, verici ve alıcı modlarında çalışırken ortaya çıkan kayıpların yükselteçler vasıtasıyla uygun şekilde telafi edilmesiyle, çakışan (overlapping) ve yeniden şekillendirilebilen (reconfigurable) hüzmelerin oluşturulmasıdır. Dizideki anten elemanlarının karakteristikleri, diziden genel olarak istenen düşük yan hüzme, tarama genişliği v.b. gibi özelliklerle uyuşum içinde olması öngörülmüştür.

COST 245 projesinin amacı, yukarıda tanımlanan özelliklere sahip bir prototipin gerçeleştirilebilmesine yönelik teorik ve pratik çalışmaların yapılması, bu doğrultudaki çeşitli araştırma-geliştirme çabalarının COST 245 çatısı altında, COST kuruluşunun ilkelerine uygun olarak, koordinasyonunun sağlanması olmuştur. Bu amaçla başlıca üç araştırma grubu oluşturulmuştur:

WG 1 - Modelleme ve Analiz (Modelling and Analysis),
WG II - Işıma Elemanları (Radiating Elements),
WG III - Tasarım, Devreler, Elemanlar ve Ölçme (Architecture, Circuits, Components and Measurements).

Türkiye, projeye katılan ülkelerden biri olarak, projenin genel amaçlarına koordineli bir biçimde katkıda bulunmuş, aynı zamanda bağımsız, ama amaca uygun olarak ürettiği bilgileri projenin yukarıda adı geçen çalışma gruplarında tartışmıştır.

COST 245 projesinin amaçlarına uygun olarak yapılan çalışmalar üç ana grupta toplanmıştır:

A. Faz taramalı anten dizileri konusundaki çalışmalar,

B. Monolitik mikrodalga entegre devrelerle (MMIC) ilgili çalışmalar,

C. Geniş bantlı antenler ve nümerik metotlarla ilgili çalışmalar.

Faz taramalı anten dizileri konusundaki çalışmalar ayrıca kendi içerisinde iki ayrı grup halinde ele alınmıştır:

A.1 TVRO (TV Receive Only) ve ilgili faz taramalı anten dizileri,

A.2 Akıllı Antenler (Smart Antennas).

COST 245 projesinin genel amacına uygun olarak düzlemsel bir çift hüzmeli (dual beam) TVRO anteni gerçekleştirmek üzere mikroşerit faz taramalı anten dizileri üzerinde kapsamlı bir çalışma yapılmıştır. Önce çeşitli konfigürasyonlar teorik olarak incelenmiş ve bilgisayar analiz programları geliştirilmiştir.

Uydu alıcı antenlerinde yüksek G/T (kazanç/eşdeğer gürültü derecesi) oranı istendiğinden mikroşerit anten dizilerinde ortaya çıkan termal gürültünün analizi ve yüksek G/T oranlı anten dizisi besleme yapısı tasarımı için özgün bir yöntem geliştirilmiştir.

Bir sonraki aşamada, bir mikroşerit ölçme sistemi hazırlanarak mikroşerit hatların ve çeşitli mikroşerit yama antenlerin karakteristikleri ölçülmüştür.

Son aşamada ise aşağıda sıralanan mikroşerit yama anten dizileri tasarımlanıp üretilmiş ve ölçümleri yapılmıştır.

i - 8x4 elemanlı mikroşerit yama anten dizisi (10 GHz),
ii - 32x12 elemanlı mikroşerit yama anten dizisi (11.3 GHz, COST 245 TVRO spesifikasyonlarına uygun),
iii - 24x32 elemanlı aktif mikroşerit anten dizisi (9.5 GHz),
iv - Silindirik yüzey üzerinde mikroşerit anten dizisi.

Akıllı antenler konusunda ise 7 GHz de çalışan, yön bulma ve sayısal hüzme oluşturma kapasitesine sahip doğrusal bir mikroşerit anten dizisi tasarımlanıp üretilmiş ve ölçümleri yapılmıştır.

Düşük maliyet, tasarım esnekliği, yüksek güvenilirlik, üretimde tekrarlanabilirlik, küçük boyutlar ve hafiflik gibi avantajlar nedeni ile MMIC (Monolithic Microwave Integrated Circuit - tek parça mikrodalga tümleşik devre) teknolojisi ileri sanayi ülkelerinde yaygın olarak kullanılmaktadır. Monolitik sözcüğü bir mikrodalga devresindeki bütün aktif ve pasif devre elemanlarının ve bağlantılarının tek bir yarıiletken katman üzerinde gerçekleştirilmesi anlamına gelmektedir. Bu teknik, daha düşük frekanslarda kullanılan VLSI teknolojisinin mikrodalga frekanslarındaki benzer uygulaması olarak görülebilir. Yukarıda bahsedilen özellikleri nedeniyle MMIC devreleri, özellikle düzlemsel yapıdaki aktif anten dizilerinde kullanılan çok sayıdaki RF modülleri için uygun bir çözüm olmaktadır. Bu amaca yönelik olarak sekiz değişik MMIC devresinin tasarım ve ölçümleri gerçekleştirilmiştir. Bütün devrelerin tasarım ve optimizasyonları, LIBRA ve ACADEMY yazılım paketleri kullanılarak ve GEC-Marconi firmasının F20 yapım kurallarına uygun olarak yapılmıştır. Tasarımlanan bu devreler Eurochip kanalıyla üretilmiş ve karakteristikleri ölçülmüştür. Ölçüm sonuçlarıyla bilgisayar simülasyon sonuçlarının iyi bir uyum içinde oldukları görülmüştür.

Üçüncü bölümdeki çalışmalar ise projenin genel amaçlarına uygun olarak düzlemsel mikroşerit yapıların incelenmesinde kullanılan MoM metodunun nümerik entegrasyondan arındırılması, sonlu dizi antenlerin integral denklem sistemi ile sistematik çözümü, geniş bantlı dairesel Vivaldi anten dizisi tasarımı ve milimetrik dalga bandında iki ve üç katmanlı (ferit-dielektrik) antenlerle elektronik demet taraması gibi araştırmaları kapsamaktadır.

Bütün bu konularda yapılan çalışmaların tanıtımı, literatür taraması ve sonuçları Teknik Çalışmalar Bölümünde yer almıştır. Proje kapsamında ortaya çıkan yurt içi ve yurt dışı yayınlar da raporun sonunda EK I'de sunulmuştur. EK II de ise projenin uluslararası organizasyonu hakkında bilgiler verilmiştir.

II TEKNİK ÇALIŞMALAR

A- RESEARCH ON PHASED ARRAY ANTENNAS

Being the central theme of the COST 245 project, phased array antennas are thoroughly investigated by our METU-ASELSAN COST 245 team. These studies can be grouped under two subheadings: TVRO and related phased arrays, and the smart antennas having digital beamforming capabilities. In both of these fields, final theoretical designs are manufactured and measured using the facilities of METU and ASELSAN.

A.1 TVRO and Related Phased Arrays

A.1.1 Introduction and Preliminary Studies

For the coherency of the international efforts, the idea of "coordinated outputs" was put forward in the COST 245 meeting held in Ankara in October 1994. The originator of this idea was A. Roederer from ESA-ESTEC, who also offered a number of concrete problems to be worked upon. Our group showed interest particularly on the "dual beam TVRO- TV Receive Only" project (see the illustration in Fig. A.1.1) that would offer us the opportunity to get into the receiving microstrip phased arrays.

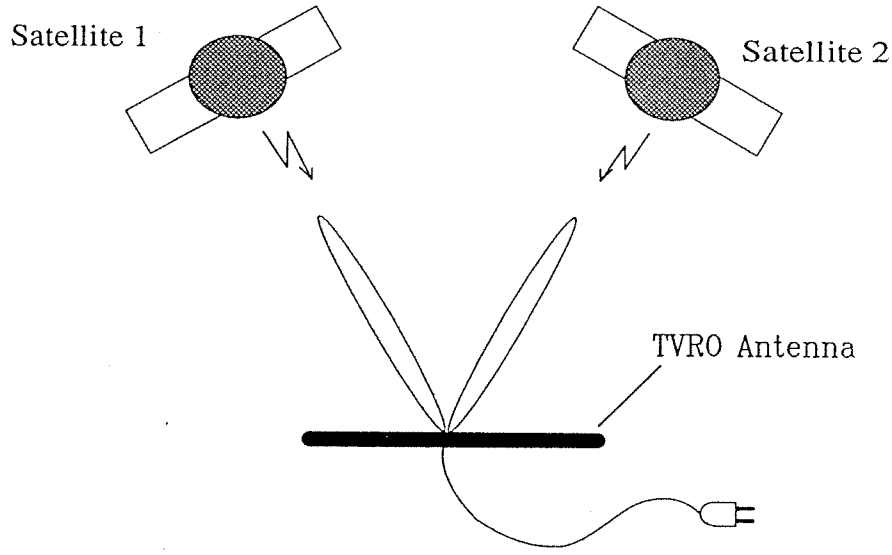

Figure A.1.1 Dual beam TVRO antenna illustration

TVRO Technical Specifications

The technical specifications of the planar dual beam TVRO antenna are listed below. Our weekly meetings were devoted to TVRO discussions for a better comprehension of the problem as well as the technical specifications; further clarifications were also requested from A. Roederer. A possible dual beam operation is illustrated in Fig. A.1.2, using a one-dimensional array for simplicity and the dots resemble the individual radiators. The basic mechanism of dual beam generation relies on the end-fed topology. In the following sections we investigate this idea more deeply. Before we embark on phased-array topologies, it is timely to explore the satellite positions as seen from Ankara.

Frequency: 10.9 - 11.7 GHz

Beam Numbers: 2 (42° East - Turksat** and 19.2° East Eutelsat 2)

Side Lobe Level: < -25 dB for $\theta \geq 3.0°$ in plane of geostationary orbit

Polarization: Switchable two linear polarizations
with 1° polarization alignment accuracy
-20 dB cross-polarization level (within 1 dB contour)

G/T (Gain/Noise Temperature): 12.5 dB/°K =10log(G/T)

Pointing Error: < 0.4°

**In the original specs distributed by A. Roederer, Eutelsat 1 at 13° East was actually given instead of the Turksat satellite, however, this modification was made by our group based on our particular interest.

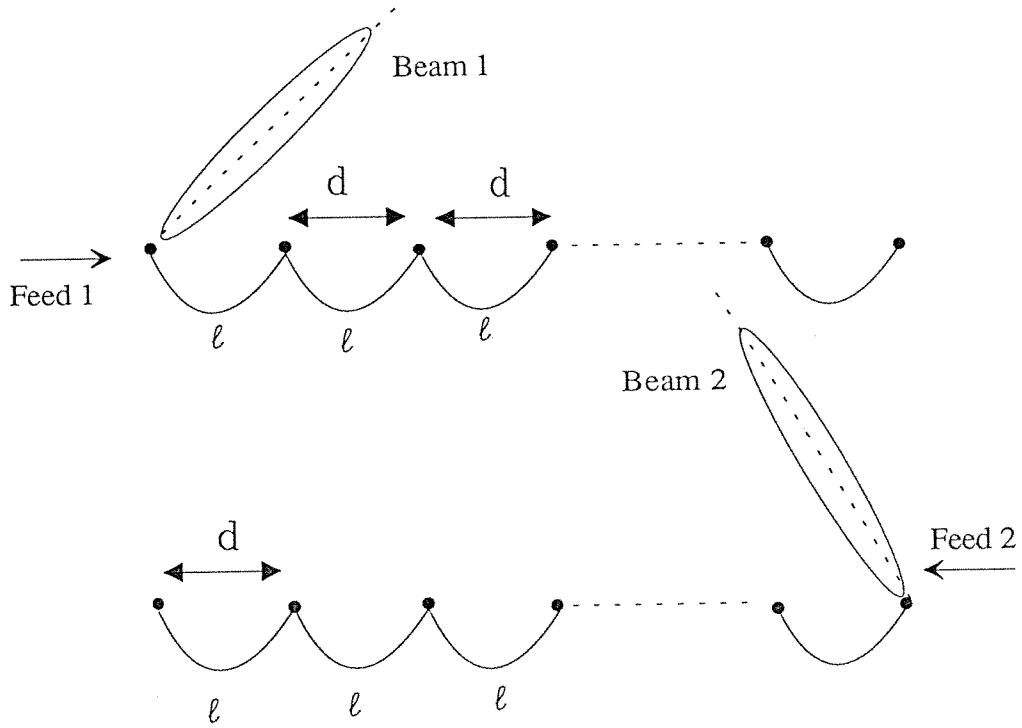

Figure A.1.2 Dual beam generation using end-fed topology

Satellite Positions

The specific radiation pattern of the dual beam TVRO antenna depends on the relative positions of the receiver and the two satellites. First we display the absolute positions of these three objects; see Fig. A.1.3 and the following illustrations.

Receiver: 32.875° East, 39.9375° North (Ankara)
Turksat: 42° East, 0° North (Equatorial plane)
Eutelsat 2: 19.2° East, 0° North (Equatorial plane)

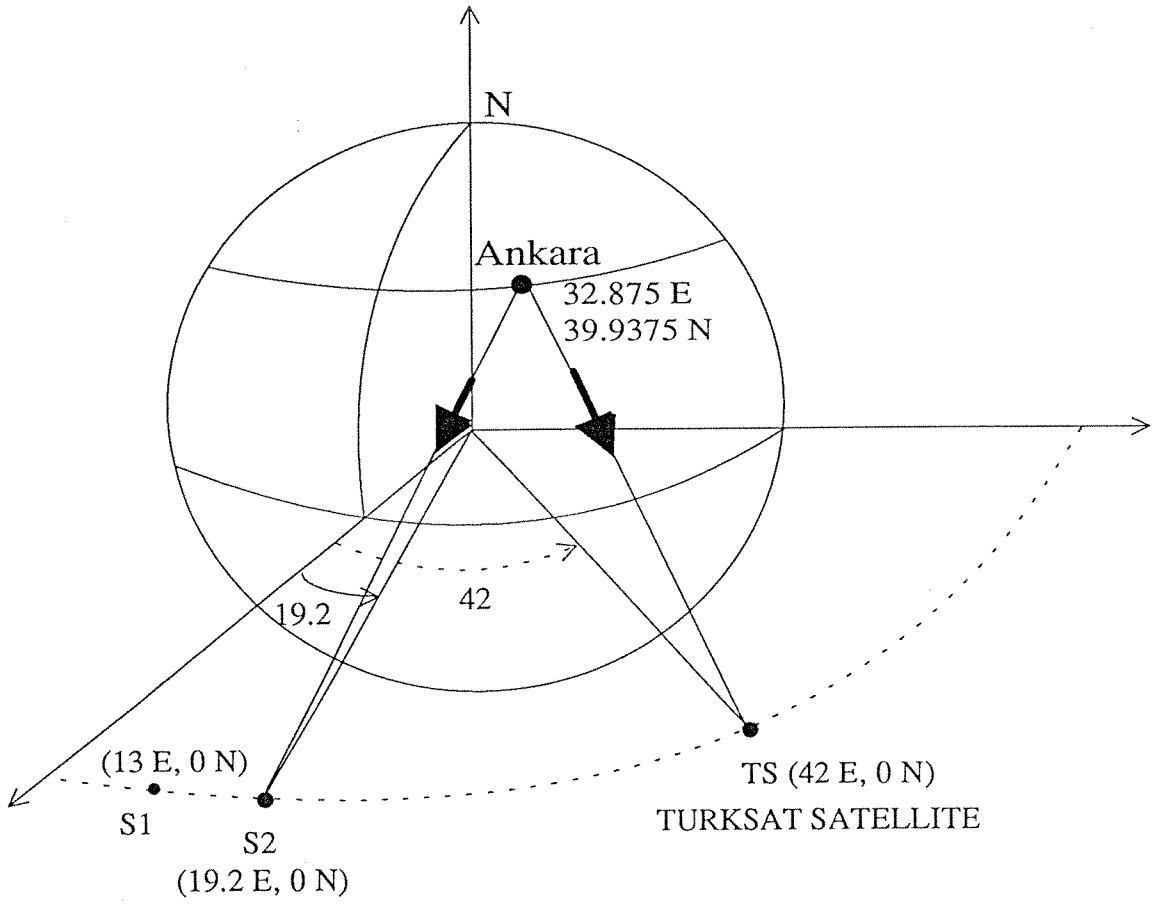

Figure A.1.3 Positions of the two satellites and Ankara

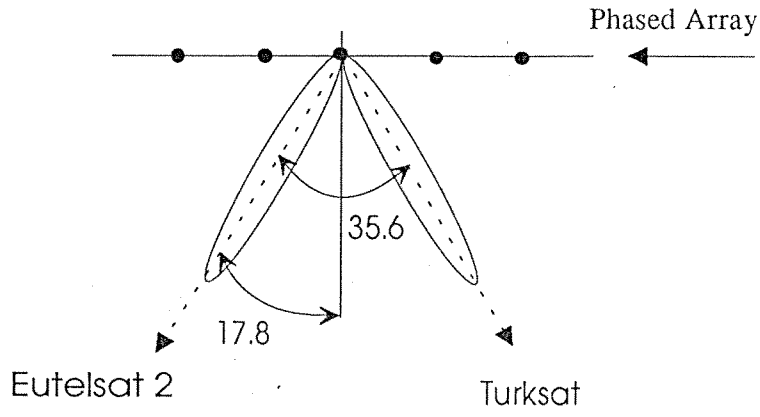

Figure A.1.4 The beam angles in the azimuth plane with the ground base chosen as Ankara

Unit Vectors:

$\mathbf{r}_1$=0.7179 $\mathbf{a}_X$ + 0.68385 $\mathbf{a}_Y$ - 0.13025 $\mathbf{a}_Z$ (Ankara → Turksat)

$\mathbf{r}_2$=0.95008 $\mathbf{a}_X$ + 0.28334 $\mathbf{a}_Y$ - 0.13064 $\mathbf{a}_Z$ (Ankara → Eutelsat 2)

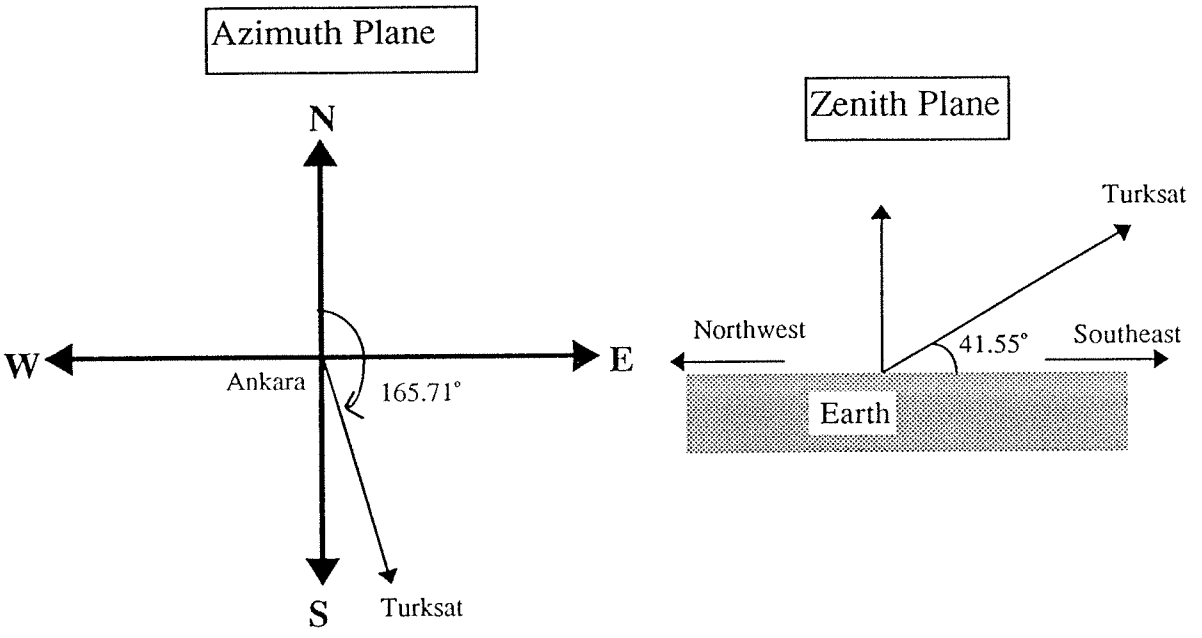

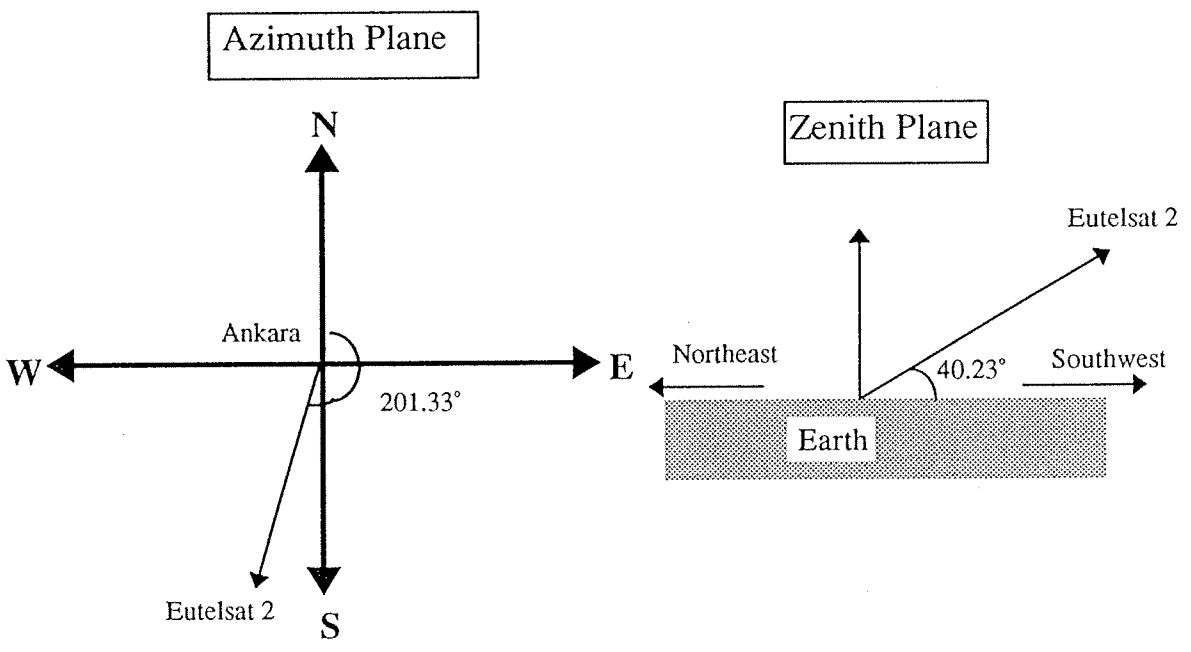

According to the calculated satellite poistions with respect to Ankara, the angle between the two beams becomes 35.6° in the azimuth plane (see Fig. A.1.4).

Preliminary Studies

After examining several types of configurations, it is decided that a microstrip patch antenna array with microstrip line feeds is feasible for the required design. A planar array with 39 elements in one direction and 18 elements in the other direction is designed to meet the high gain specifications. To provide low side lobe level, a Gaussian tapered excitation is found to be appropriate in both directions. The amount of tapering (the ratio of the largest to the lowest excitation coefficient) is dictated by the beamwidth specification. Tapering is achieved by using transmission-line transformers between the patches.

Several feeding configurations are examined, such as series and parallel; the advantages and disadvantages of each topology are summarized below.

Our first trial design is shown in Fig. A.1.5. In this array, series feeding is used in both directions.

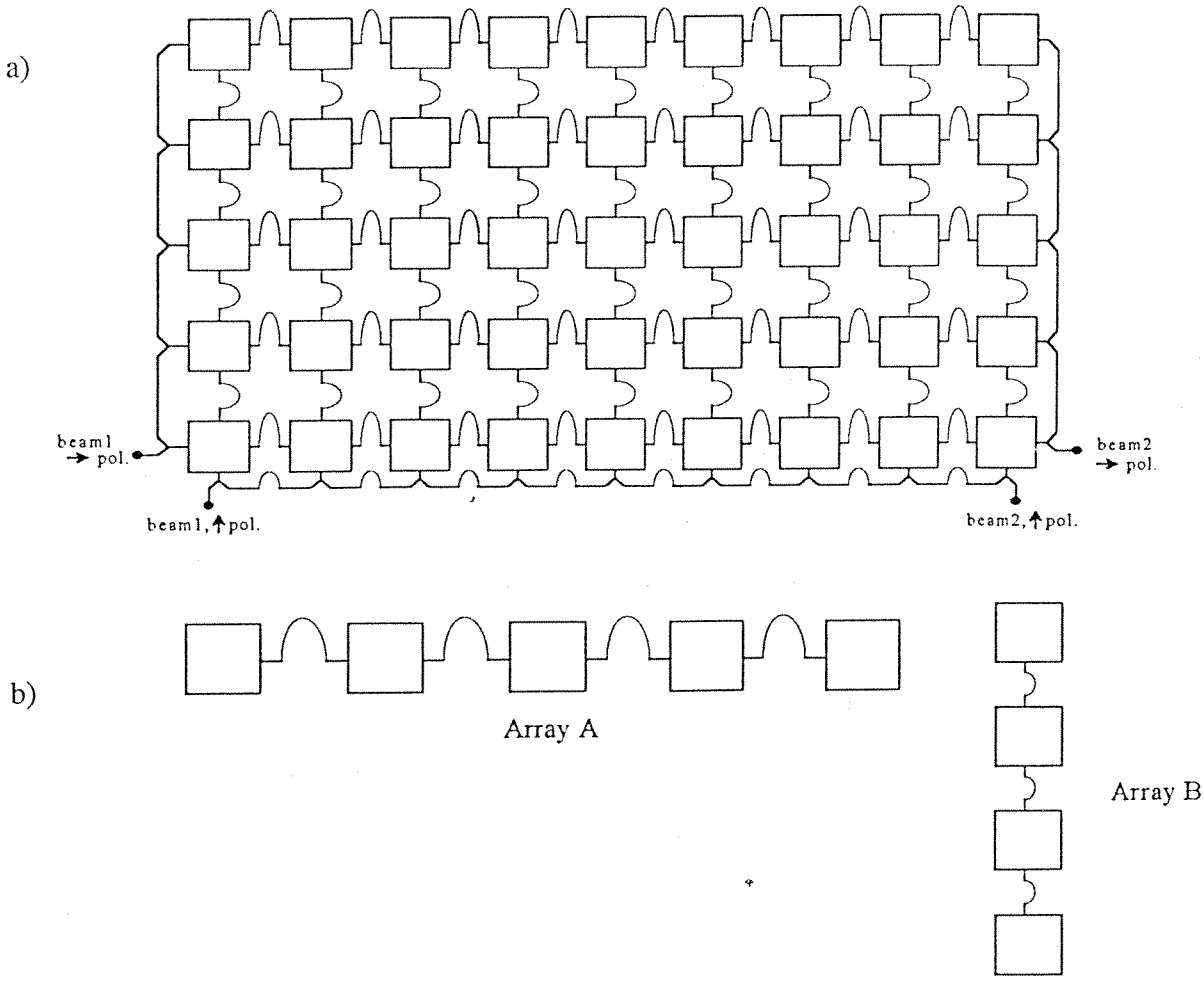

Figure A.1.5 First preliminary design a) having series fed topology, and b) individual arrays

In this design, horizontally polarized beam 1 is excited from the upper left port, whereas vertically polarized beam 1 is excited from the lower port. With this topology it is not possible to make the ends of the one-dimensional arrays open. This causes some problems in impedance calculations, since it is required to feed both of

the ends to obtain a dual beam. For this reason a new array with the same number of elements but a different feeding structure for array A is designed. As shown in Fig. A.1.6, for this case the feeding of array A is chosen to be parallel whereas the feeding of array B is kept series. For the required excitation coefficients, two-step transformers are designed between the patches. However, it is observed that when the one-dimensional array is fed from one end, the input impedances seen from the input of each patch becomes smaller and smaller as one proceeds to the input of the array. In Fig. A.1.7, the input impedances seen from the input of each patch is plotted for array B.

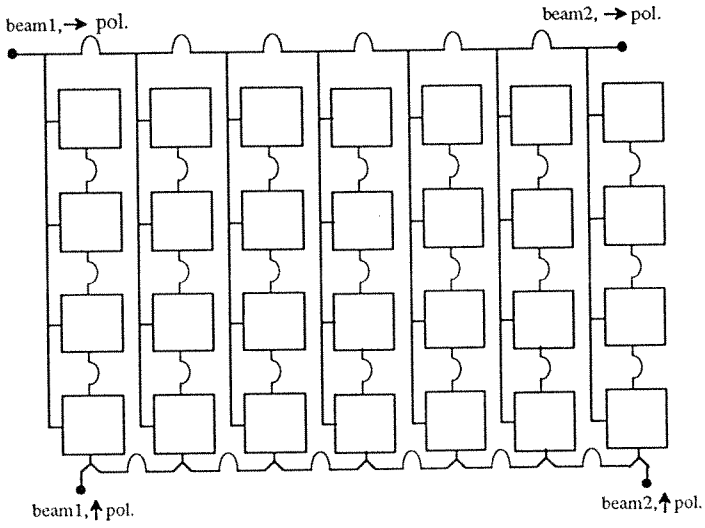

Figure A.1.6 Second preliminary topology having a parallel fed array A

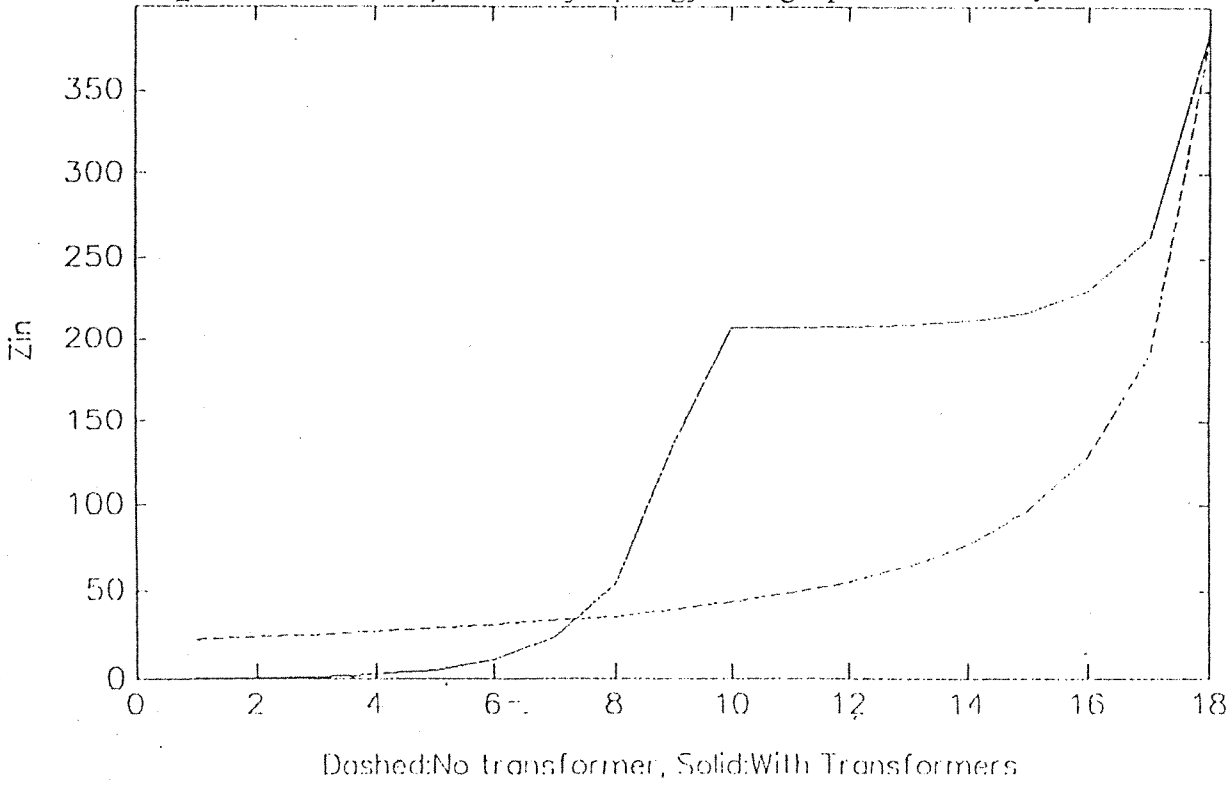

Figure A.1.7 The variation of the input impedance within the array B

As can be observed from Fig. A.1.7, the input impedance decreases drastically after the midpoint of the array since the Gaussian tapering changes direction after this point. In other words, the coefficients begin to decrease after the midpoint, whereas they increase before the midpoint. In order to eliminate this problem, it is decided to switch to a center-fed topology. Dual beam operation is not possible by using a center-fed topology. However, dual beam satellite antenna has an important drawback: the angle between the two beams depends highly on the local position of the antenna. Thus, different antennas need to be designed for different cities. In this case, a dual beam can be achieved by just adjusting the orientation of two separate antenna arrays.

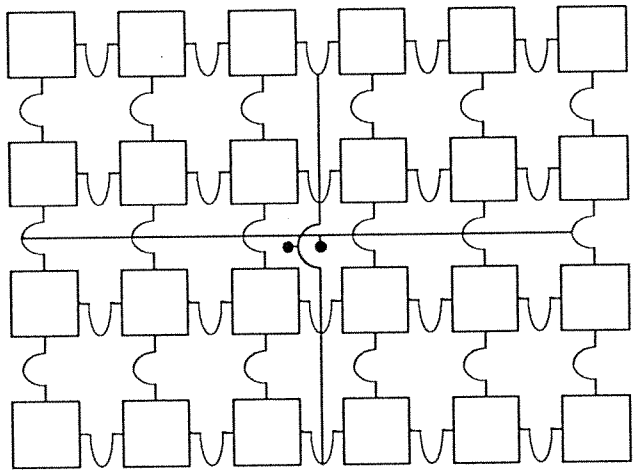

Figure A.1.8 The third preliminary antenna with center-fed topology

In Fig. A.1.8, the center-fed topology is shown. To satisfy symmetry, an even number of elements is used. Due to the symmetry of this configuration, in addition to the transmission-line transformers, losses along these lines are utilized to achieve tapering. In this way losses are used in a beneficial manner, and this advantage results in a low noise temperature. The decrease in noise temperature enables one to decrease the gain in order to meet the same G/T requirement. Consequently array dimensions are decreased from 39x18 to 32x12.

A more detailed investigation of the last topology reveals that series feed leads to a tuning problem. The physical length of a microstrip patch antenna is generally chosen to be slightly smaller than the half of the guided wavelength for resonance. In other words, the physical resonance length of a patch is calculated by equating the imaginary part of the input impedance to zero. However, in the series feeding case, each patch is loaded by the remaining ones. Consequently, the length of each patch should be adjusted to a different value due to the different loading. On the other hand, the patches should be square in order to obtain dual polarization. Hence when the resonance is obtained for one polarization, it cannot be satisfied for the other polarization. In order to eliminate the tuning problem, a parallel feeding structure is preferred. When both array A and array B are fed in parallel, the feeding lines will cross each other. Thus, a two-layered structure must be considered to obtain dual polarization. As an initial step, we decided to complete all the calculations and analysis of an array with one polarization (see Fig. A.1.9).

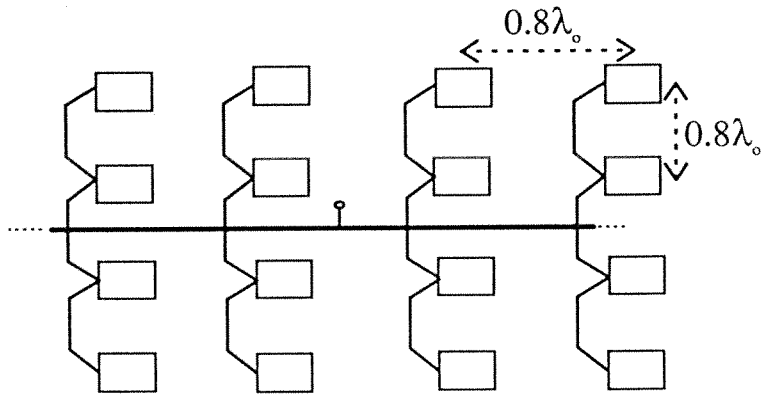

Figure A.1.9 The fourth preliminary center-fed topology (only a portion is shown)

For both array A and B, Gaussian tapering is used, and the spacing between the array elements are chosen to 0.8 of the wavelength. The associated radiation patterns are supplied in Figs. A.1.10 and A.1.11.

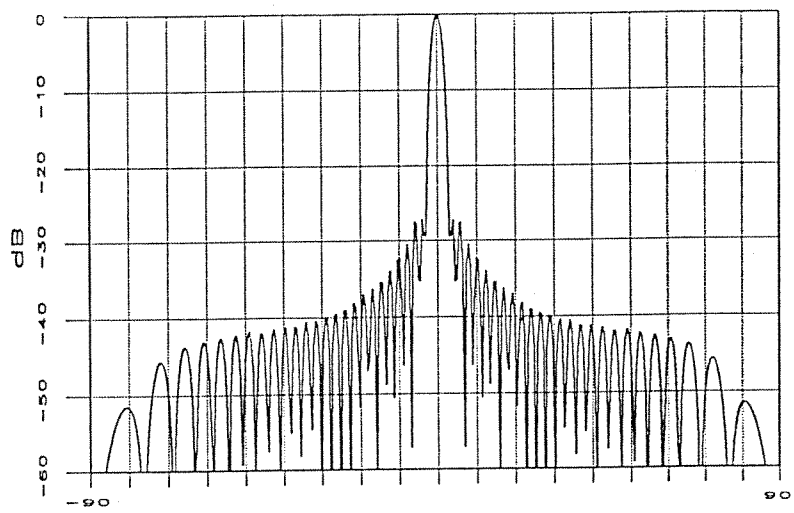

Figure A.1.10 The radiation pattern of array A

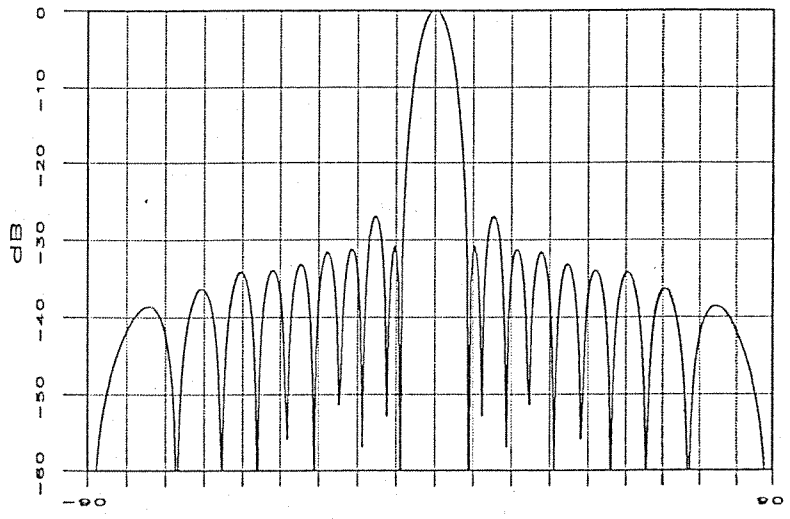

Figure A.1.11 The radiation pattern of array B

A software is developed to analyze the performance of the designed array. Patch antennas are substituted by their transmission-line equivalent models. The radiation conductance, effective permittivity, and the slot capacitance of the patch are evaluated by using the more recently developed formulas. The losses in the transmission-lines are computed by using the empirical formulas of the transmission-line model and the losses in the patch antennas are evaluated by using the cavity model. The analysis is carried out by using the ABCD matrix method. In order to obtain wideband operation, two-step transmission-line transformers are used between the array elements to achieve Gaussian tapering. A transmission-line transformer is a combination of two transmission-lines with different characteristic admittances. A two-step transformer is obtained by using two single transformers successively. Consequently, between each element, there are four pieces of transmission-lines, each having a length of quarter-wavelength. The characteristic admittance of the first and the third section (Y_s) of the transformer are chosen to be equal between each antenna and the width of this transmission-line section is fixed to 1 mm (Y_s=0.0061 mho). The characteristic admittance of the second and the forth sections (Y_{sn}) are chosen to be equal and they are synthesized for each element to achieve tapering. By using Gaussian distribution, the required voltage ratio (V_m) of two adjacent array elements are calculated. Starting from the last element of the array, the initial guess of the characteristic is made by equating the ratio Y_s/Y_{Sn} to the square root of the desired voltage ratio. Then the voltage ratio is calculated due to this characteristic admittance. The characteristic admittance is updated by using the error between the desired and the calculated voltage ratios and the same procedure is iterated until an acceptable error is attained. After the synthesis of the last element is finished, the same procedure is applied to the proceeding element. For array B, as there was not enough space, a single step transformer is designed at the input of the first element. By the first element it is meant the first element with respect to the symmetry axis of the array. If the input admittance seen from the first element of array B is Y_B then the elements of array A have input admittance values of $2Y_B$. Due to this fact, the transformer at the input of array B is synthesized in such a way that Y_B is equated to the half of Y_s in order to minimize the mismatches. The desired voltage ratios and the synthesized characteristic admittances for array B and A are given in Tables A.1.1 and A.1.2, respectively.

n	voltage ratio(V_{rn})	Y_{cn} of the line
1	0.442387	1.37766E-02
2	0.890899	6.44989E-03
3	0.824861	6.70618E-03
4	0.763712	6.97185E-03
5	0.707104	7.24762E-03
6	0.654691	7.53462E-03

Table A.1.1 Voltage ratios and synthesized characteristic admittances for array B

n	voltage ratio(V_{rn})	Y_{cn} of the line
1	0.994589	6.05976E-03
2	0.983879	6.09936E-03
3	0.973283	6.13807E-03
4	0.962800	6.17613E-03
5	0.952429	6.21372E-03
6	0.942170	6.25099E-03
7	0.932022	6.28803E-03
8	0.921982	6.32497E-03
9	0.912051	6.36186E-03
10	0.902227	6.39880E-03
11	0.892508	6.43588E-03
12	0.882894	6.47319E-03
13	0.873384	6.51086E-03
14	0.863976	6.54906E-03
15	0.854669	6.58806E-03
16	0.845459	6.62826E-03

Table A.1.2 Voltage ratios and synthesized characteristic admittances for array A

Input impedance of the overall antenna array is calculated for different frequencies and the obtained VSWR versus frequency curve is given in Fig. A.1.12. It can be observed from the figure that the required frequency bandwidth is achieved as far as the input impedance is concerned (in finding the bandwidth, VSWR values under 2 are considered).

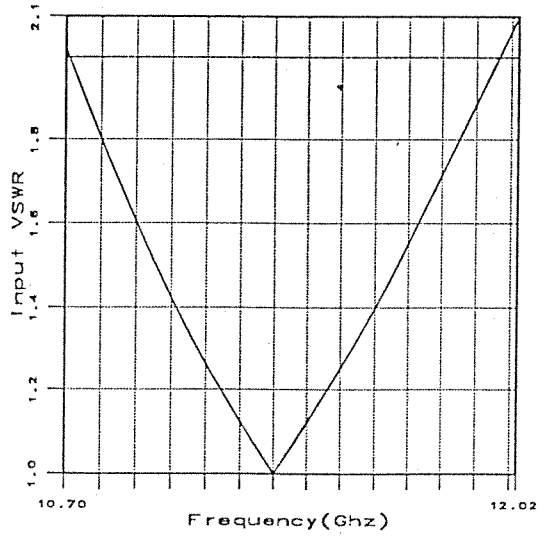

Figure A.1.12 The input VSWR versus frequency of the fourth preliminary design

A.1.2 Theoretical Material

In this section we would like to gather some of the theoretical material that we developed and/or used for the comprehension and the design of the phased array antennas.

Directivity Calculations

In computing the overall directivity of the planar array the formula given in the "Antenna Handbook", written by J.R. James is used [1]. The planar array consists of two orthogonal linear arrays, array A and array B as shown in Fig. A.1.13.

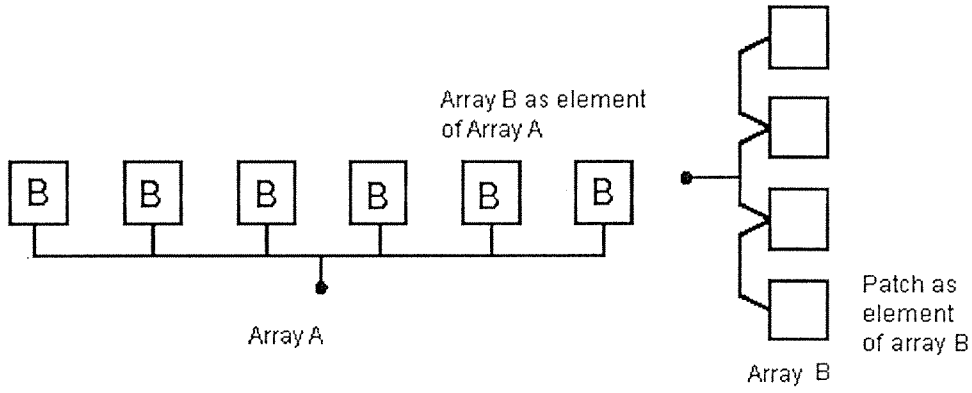

Figure A.1.13 Microstrip patch arrays: Array A and Array B

If D_A and D_B are directivities of these two arrays and D_e is the directivity of the patch element, then the directivity of the overall array according to the book by R.S. James, [1], is given as

$$D = \pi D_A D_B D_e ,$$

where

Directivity of array A, $$D_A = \frac{\left[\sum_{m=1}^{N_A} \alpha_A(m)\right]^2}{\sum_{m=}^{N_A}\sum_{n=1}^{N_A} \alpha_A(m)\alpha_A(n)\frac{\sin[k_o(d_m - d_n)]}{k_o(d_m - d_n)}}$$

Directivity of array B, $$D_A = \frac{\left[\sum_{m=1}^{N_B} \alpha_B(m)\right]^2}{\sum_{m=}^{N_B}\sum_{n=1}^{N_B} \alpha_B(m)\alpha_B(n)\frac{\sin[k_o(d_m - d_n)]}{k_o(s_m - s_n)}}$$

$d_m=(m-1)d$, $s_m=(m-1)s$

α_A , α_B: excitation coefficients of array A and array B, respectively:

$$\alpha_A(n) = \exp\left[\left(\frac{n}{N_A}\right)^2 \ln P_A\right], \quad \alpha_B(n) = \exp\left[\left(\frac{n}{N_B}\right)^2 \ln P_B\right]$$

N_A, N_B: number of elements in array A and B respectively

d: spacing between centers of adjacent two element in array A
s: spacing between centers of adjacent two element in array B

By making use of this formula the overall directivity for P_A=P=0.25, N_A=38, N_B=16, s=d=0.85l_o, and f=11.3 GHz (l_o=26.53 mm) is calculated as 41.75 dB, (D_A=44.75, D_B=16.39, D_e = 6.5, D = 14,979.25 (41.75 dB)). On the other hand, the directivity can also be computed approximately by using a modified version of the Kraus formula which is widely used for the analysis of arrays. If θ_E θ_H and are the half power beamwidths (in degrees) in the E-plane and H-plane, respectively, then the directivity of the overall array can be approximated as:

$$D = \frac{32400}{\theta_E \theta_H}$$

This approximate formula is valid as long as the beamwidths are narrow and sidelobe levels are low. In the designed TVRO antenna array, both of these conditions are satisfied so Kraus' formula can be used to calculate the directivity of the array. The field pattern of the array is computed by including the element pattern and the half power beamwidths are found to be 2° in the E-plane and 5° in the H-plane. Consequently, the directivity is computed to be 35.1 dB. The big discrepancy between the two directivity values lead us to question whether there is a mistake in the formula given by the handbook. Pattern multiplication rule is a well known theorem in the array analysis, but this directivity formula makes use of directivity multiplication which is not an admissible approach. In the pattern multiplication, field patterns are multiplied but directivity multiplication requires the multiplication of powers that is not permitted. In order to remove any doubts about the calculation of the directivity, a rigorous approach which makes use of the definition of directivity is used. If U is the radiation intensity (Watts/steradian) and U_0 is radiation intensity of isotropic source, then the directivity is defined as:

$$D = \frac{U_{\max}}{U_o} = \frac{4\pi U_{\max}}{P_{rad}}$$

where P_{rad} is the total radiated power.

The field pattern has already been computed, so only the integration of the power intensity over the whole space is required. The integration is performed by two different methods. In the first approach, the integration with respect to ϕ is performed analytically and the integration with respect to θ is performed numerically. The ϕ integration results in Bessel functions which can be computed numerically by using some approximations. In the other approach the double integration is performed numerically. In both methods, Gauss' Quadrature procedure is used for numerical integrations. To test the convergence of the integrals, the integration interval is divided into subintervals and the number of Gauss' Quadrature points are increased. As a result, the two different approaches gave the same result which is 35.7 dB. This result is very close to the directivity of an array with isotropic sources, D=35.4 dB. This result is not surprising as the array is so directive that the directivity of the element does not contribute to the overall antenna performance. This would not be the case if the array involves grating lobes, fan beams or main beam in any other direction rather than the broadside. As a result, the formula given in the handbook is

basically wrong and not applicable to all types of array configurations and the rigorous calculation of the directivity can be found only by computing the total radiated power.

Linearity Considerations for an Active Phased Array Antenna

Active receive arrays operate in a medium where the frequencies of the signals are closely distributed as in the case of satellite communication. In the framework of COST 245 we deal with passive and active antenna arrays. Linearity is not an important issue for passive arrays because there is no nonlinear element in the structures. However, active antennas and antenna arrays include transistors as the active elements and due to nonlinear structure of these devices, linearity becomes an issue to be considered. Linearity of an active array is of ultimate importance from point of view of intermodulation distortion. Linearity of systems like amplifiers, mixers, have been widely studied by several authors and fast analysis methods are also proposed [2,3], but linearity of an active antenna array is not considered so far.

Such antenna arrays include a number of active elements in their structure and this number increases as the size of the array increases. Active antenna arrays are analysed and designed using microwave circuit simulators [4]. However, a nonlinear analysis for determining linearity of an active array using nonlinear analysis tools of such simulators (e.g harmonic balance) will require a considerable computing time.

Linearity Calculation of an Active Array

We describe a method to calculate the linearity of an active antenna array without using such time consuming simulation tools. Moreover, we present an accurate nonlinear analysis tool which is faster than any previously reported methods [2]. We used this tool for linearity analysis of a 4x8 active antenna array. We show that the linearity of such an array increases as the number of distinct amplifier per antenna element increases, and it is also shown that linearity and noise performance of distributed amplification, as in the case of an active antenna, is superior to amplification with a single amplifier placed at the output of the array.

It is well-known that nonlinear behaviour of the active devices result in intermodulation (IM) products. Nonlinear parameters of the active element and the input and the output impedances connected to the active element at the fundamental and the IM frequencies determine the nonlinear operation.

In the case of an active array, the input signal entering from an antenna element mix with the other frequency components received by the same antenna, at the active device and continue its way to the output together with the generated IM products. All these signals are sum up at the output of the array and yield the distorted received signal. Analysis of the complete active array using a harmonic balance simulation costs a high computation time because of the multiple nonlinear elements in the system.

An active antenna array differs from structures like amplifiers and mixers, being a multiple input, single output system. Therefore, usual nonlinear analysis treatments can not be applied directly [2,3,5].

We treat the active devices as if they are distinct amplifiers operating in a system having the identical connections as in the array. By this way, we come over complicated nonlinear analysis of multiple active devices placed in the same structure. Using our nonlinear analysis tool, the IM products generated by these active devices are calculated considering the nonlinear behaviour and the termination impedances. Then, it is assumed that signals equivalent to these IM products in magnitude are received by antenna elements from outside the antenna. In the next step, active elements are assumed to be linear and the contribution of IM products which are referred to the antenna side are summed up at the antenna output to find the IM product and this cumulative signal is compared with the power of the signal at the fundamental frequency in order to determine the linearity.

Active Antenna Array Structure

A 4x8 active antenna array, which is shown in Fig. A.1.14, is designed and analysed for its linearity. The feed system of the array is designed for a specific feed taper which is required for a given side lobe level. Because of this, other than the symmetry in the feed system, each antenna group which is connected to an active circuit sees a different impedance. Moreover, the impedance matching considerations are taken into account at the fundamental frequency only, but, for IM products the impedance levels at the intermediate frequencies are also of prime importance. Due to these facts the IM products generated by these active circuits will generally be of different phase and amplitude. Therefore nonlinear analysis are carried out for each of them seperately.

We have developed a power series based nonlinear analysis of HEMT and MESFET transistors which yields results that are consistent with harmonic balance simulations but at much lower computational cost. This method is capable of calculating IM products for all active devices simultaneously. IM products of the above array is calculated within seconds and written to a data file.

The active array is constructed on the microwave circuit simulator LIBRA, using the transmission line model of the patch antennas and the feed coefficients of the active array, which represent the received power of individual antenna elements through two current sources, are loaded from a data file as described in [4]. In our method, active array is simulated twice by the linear simulation tool of LIBRA. In the first one, the feed coefficients have progressive phase shifts which stands for a received signal at an incident angle. In the next simulation, the data file generated by our nonlinear analysis is used, which stands for the IM products generated by the active elements. The results of these two simulations are processed to obtain the linearity of the active antenna array. This completes the simple and fast nonlinear analysis of active array for its linearity.

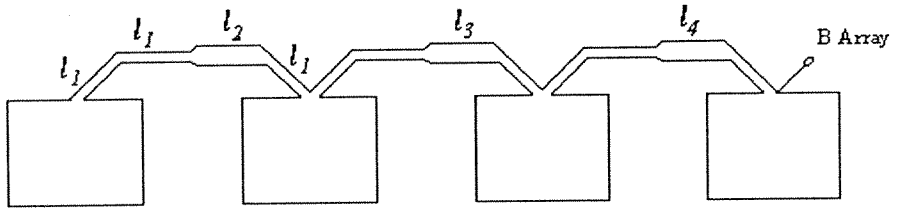

Line		
#	Width	Length
1	0.150	5.82
2	0.429	5.72
3	0.326	5.75
4	0.240	5.79

Patch Length : 9.5 mm
Width :10.0mm

(a)

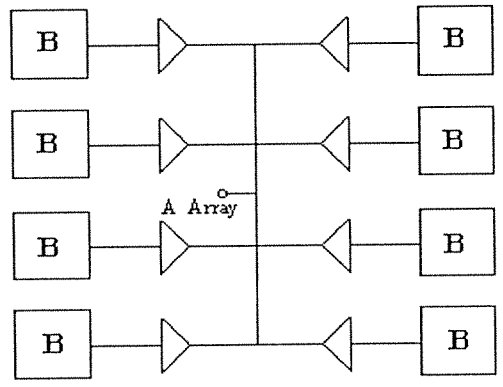

(b)

Figure A.1.14 Active antenna array structures: (a) passive sub-array (b) active array

Comment on Linearity of Passive and Active Antenna Arrays

A passive antenna arrays by itself is a highly linear element. However, a low noise amplifier (LNA) should be connected to this passive array for a proper receive operation. The combination of these two structures will be a nonlinear structure due to the nonlinearity of the LNA.

IM products are proportional to the third power of the input signal. In a distributed amplification system like an active antenna array, IM products will be generated for a lower input signal and then, will be added at the output. However, in a passive array and LNA combination, the signal will first be added at the output of the passive array and then, will be amplified and distorted by the LNA, which, obviously, creates more distortion compared to the distributed amplification case under the assumption that active circuits have similiar linearity performance in both cases.

This simple comparison shows that active antenna arrays have better linearity compared to passive antenna array systems.

References

[1] J. R. James and P. S. Hall, "Handbook of Microstrip Antennas", IEE EMT Series 28, vol.2, 1989, p.831.

[2] J. C. Pedro, J. Perez, 'Accurate Simulation of GaAs MESFET's Intermodulation Distortion Using a New Drain Current Model', IEEE Transactions on MTT, vol. 42, Jan. 1994, pp 25-33.

[3] S. A. Maas, D. Neilson, 'Modeling MESFETs for Intermodulation Analysis of Mixers and Amplifiers', IEEE Transactions on MTT, vol. 38, Dec. 1990, pp 1964-1971.

[4] S. Demir, C. Toker, A.Hizal, "Design of Active Microstrip Array Using a Microwave Circuit Simulator", in 1997 IEEE MTT-S International Topical Symp. on Technologies for Wireless Applications, Vancouver.

[5] A. M. Crosmun, S. A. Maas, 'Minimization of Intermodulation Distortion in GaAs MESFET Small Signal Amplifiers' IEEE Transactions on MTT, vol. 37, Sep. 1989, pp 1411-1417.

Thermal Noise Analysis in Antenna Arrays

Introduction

For satellite receiving antennas, a high value of G/T ratio (the so-called figure of merit of the antenna) is desired. G is the power gain of the antenna system and T characterizes the output noise power of an antenna system in terms of an equivalent temperature [1]. Accordingly, antenna design must also assess the noise performance of the system as well as its gain. The output noise is due to noise sources in space and the sources within the receiving array. Especially for printed antenna arrays that can contain as much as, some few hundred antenna elements, the noise generated within the antenna array can reach quite high levels. In this work we do not consider the space generated noise and present a simple methodology for the analysis of thermal noise generated by receiving arrays, based on Nyquist's formula and basic thermal equilibrium concepts. In other words, the only source of noise is considered to be the thermal noise (Johnson noise) due to lossy elements within the receiving antenna.

Thermal Noise

Thermal noise, which is essentially a *fluctuating* electrical signal, has intimate connection with the losses (i.e., *dissipation*) within the system. This relation was uncovered by the fluctuation-dissipation theorem due to Callen and Welton in 1951 [2]. However, the theoretical basis of thermal noise in electrical circuits was established long time ago by Nyquist taking into account full quantum mechanical effects [3,4]. The expression simplifies for frequencies less than 10 THz and the associated rms noise voltage across a resistor R having a physical temperature T (°K) becomes $\upsilon_n = \sqrt{4kTBR}$ where k is Boltzmann's constant and B is an arbitrary bandwidth. For antenna arrays the thermal noise generation is due to interconnecting transmission lines and conductor and dielectric losses within the radiating array elements. In contrast to this, the radiation resistance of the antenna elements do not take part in thermal noise generation and their role is to represent the radiation mechanism. As a matter of fact, the presence of radiation resistances reduces the noise power at the output of the antenna array as the generated thermal noise is *radiated* to outer space through these antenna elements. At this point we assume that the radiated thermal noise from an array element is not picked up by an other member of the array (no mutual coupling), that is to say that part of the noise is completely lost. In summary, from a circuit analysis point of view we consider the radiation resistances to be noiseless (or equivalently at 0 °K). Then for an antenna array that is terminated by a conjugate matched load Z_L (Fig. A.1.15), the thermal noise power delivered to Z_L can be determined with the following equations

$$P_{net} = P_{tot} - \sum_i P_{ni}$$

where P_{net} is the net thermal noise power delivered to load Z_L generated by lossy elements within the receiving array, P_{tot} is the noise power delivered to Z_L as if the radiation

resistances are also noisy and P_{ni} is the noise power contribution of the i'th radiation resistance (assuming it to be at T degrees) at Z_L. P_{tot} is given by

$$P_{tot} = \frac{4kTB\,\mathrm{Re}\{Z_{ant}\}\,\mathrm{Re}\{Z_L\}}{\left|Z_{ant} + Z_L\right|^2},$$

and for a conjugate matched load this reduces to the well-known case $P_{tot}=kTB$. Having calculated P_{net} we can characterize this power by an equivalent temperature as $T_{eql}=P_{net}/kB$.

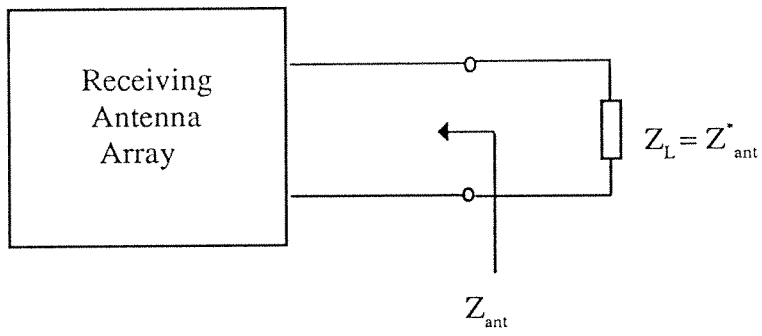

Figure A.1.15 Receiving antenna array and the conjugate matched termination.

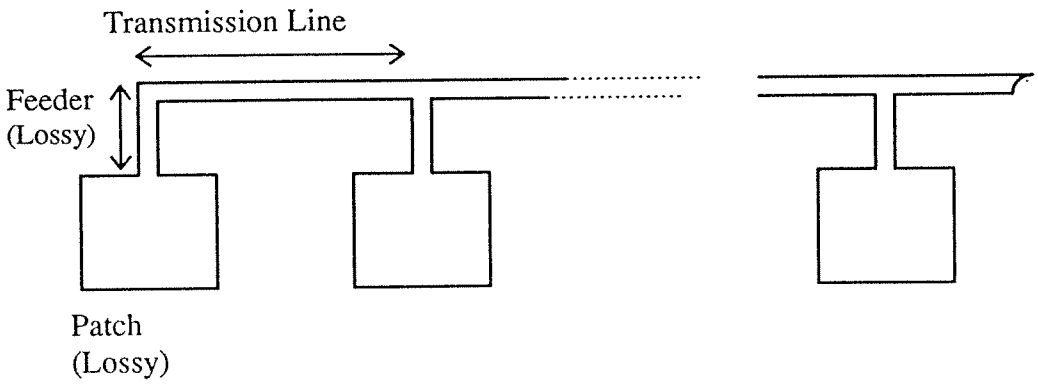

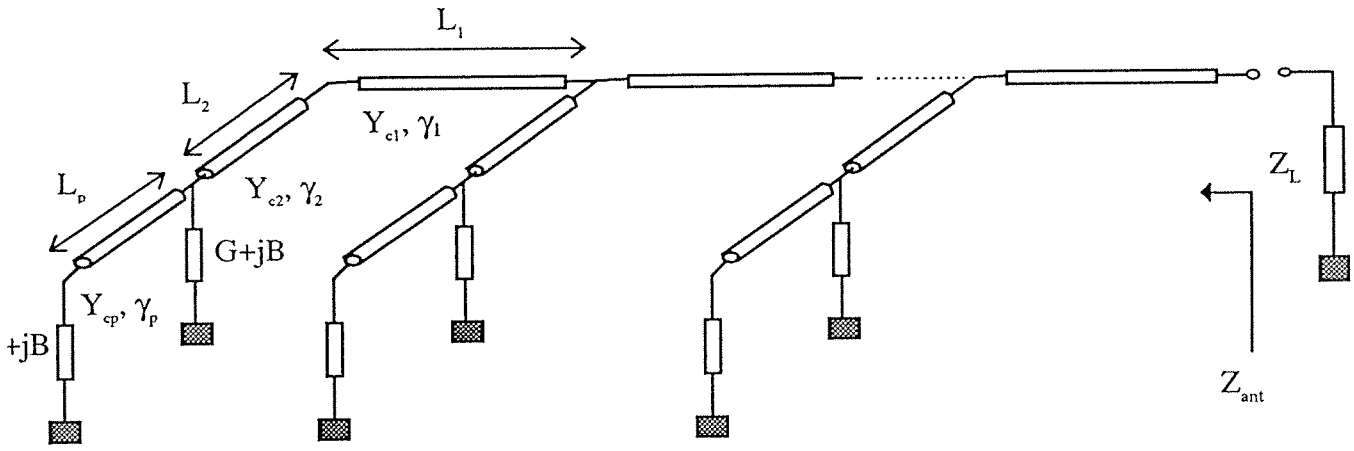

Figure A.1.16 Parallel fed linear microstrip patch array (top) and the transmission-line equivalent model corresponding to this array (bottom).

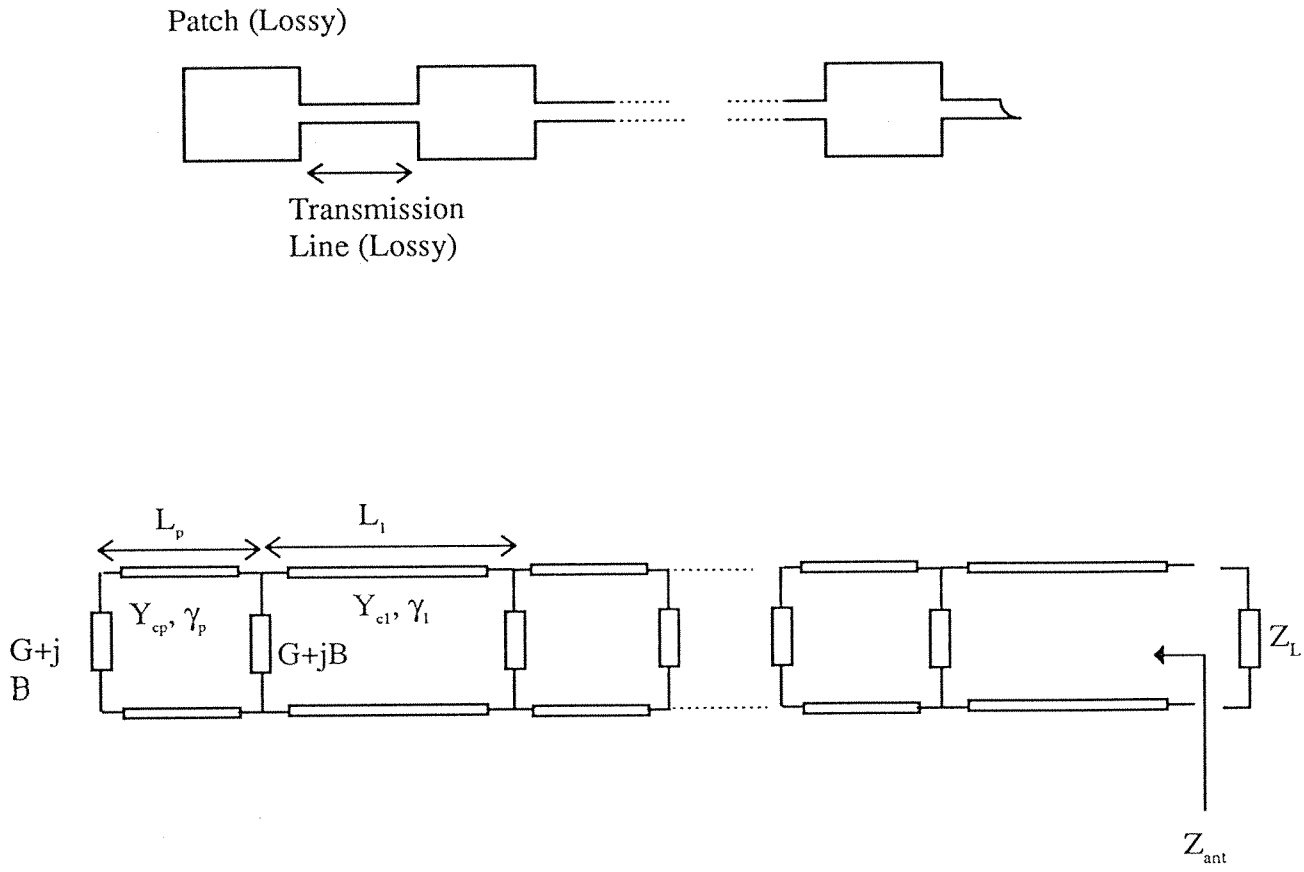

Figure A.1.17 Series fed linear microstrip patch array (top) and the transmission-line equivalent model corresponding to this array (bottom).

Results and Conclusions

The thermal noise output characteristics of linear parallel and series fed microstrip patch arrays are considered in this section. These arrays are analysed by using their equivalent transmission line models [5] shown in Figs. A.1.16 and A.1.17. The variation of equivalent output noise temperature T_{eql} with respect to the number of array elements (N) is illustrated in Fig. A.1.18 for both parallel and series fed arrays. The element values for the equivalent transmission line model is listed in Table A.1.3. For each new value of N, the array is terminated with a conjugate matched load corresponding to the maximum power transfer condition. For a parallel fed array T_{eql} initially increases proportionally with N even though the series fed one virtually does not depend on the number of stages and shows a much smaller value. In Fig. A.1.19, the dependence of T_{eql} on the losses of transmission lines is illustrated for parallel and series fed arrays. The values in Table

.3 are used with N=20. If every resistive element in the array were noisy T_{eql} would be °K. However, due to dominating contribution of radiation resistances this value is :h lower (loss multiplication factor equal to unity case). But as the losses of ismission lines are increased, asymptotically the 290 °K value is reached. From Fig. .19, it is seen that the parallel fed geometry is initially more susceptible to loss iations than the series fed case. As far as thermal noise performance is concerned es fed microstrip arrays seem to be superior to parallel fed linear arrays.

	Characteristic Admittance (mho)	Propagation Constant (mm^{-1})	Length (mm)	Radiation Admittance (mho)
Patch	Y_{cn}= 0.019804	γ_n= 4.916 .10^{-5} + j0.235884	L_n= 9.248384	G+jB=0.00265+ j0.010162
ınsmission Line	Y_{c1}= 0.00610	γ_1= 8.278 .10^{-5}+ j0.2346	L_1= 26.78179	Not Applicable
:eder Line parallel fed)	Y_{c2}= 0.00610	γ_2= 8.278 .10^{-5}+ j0.2346	L_2= 3.3477	Not Applicable

ıble A.1.3 Element values for transmission-line equivalent model (see Figs. A.1.16 d A.1.17 for the elements).

nally, the same thermal noise analysis methodology is applied to the *planar* microstrip ometry mentioned in the previous section (A.1.1) shown in Fig. A.1.9. For this pology the equivalent noise temperature is calculated as T_{eql}=26.1 °K.

eferences

] K. Feher, 'Digital communications', 1983, pp. 29-44

] E. M. Lifshitz and L. P. Pitaevskii, 'Statistical physics', Part 1, (Pergamon Press,)80), pp. 384-389

] M. Schwartz, 'Information transmission, modulation, and noise' (McGraw-Hill,)70), pp. 541-555

] R. E. Collin, 'Antennas and radio wave propagation' (McGraw-Hill, 1985), pp. 312-25

] K. C. Gupta, in 'Handbook of microstrip antennas' edited by James, J.R. and Hall, .S., (Peter Peregrinus Ltd., 1989), pp. 455-460.

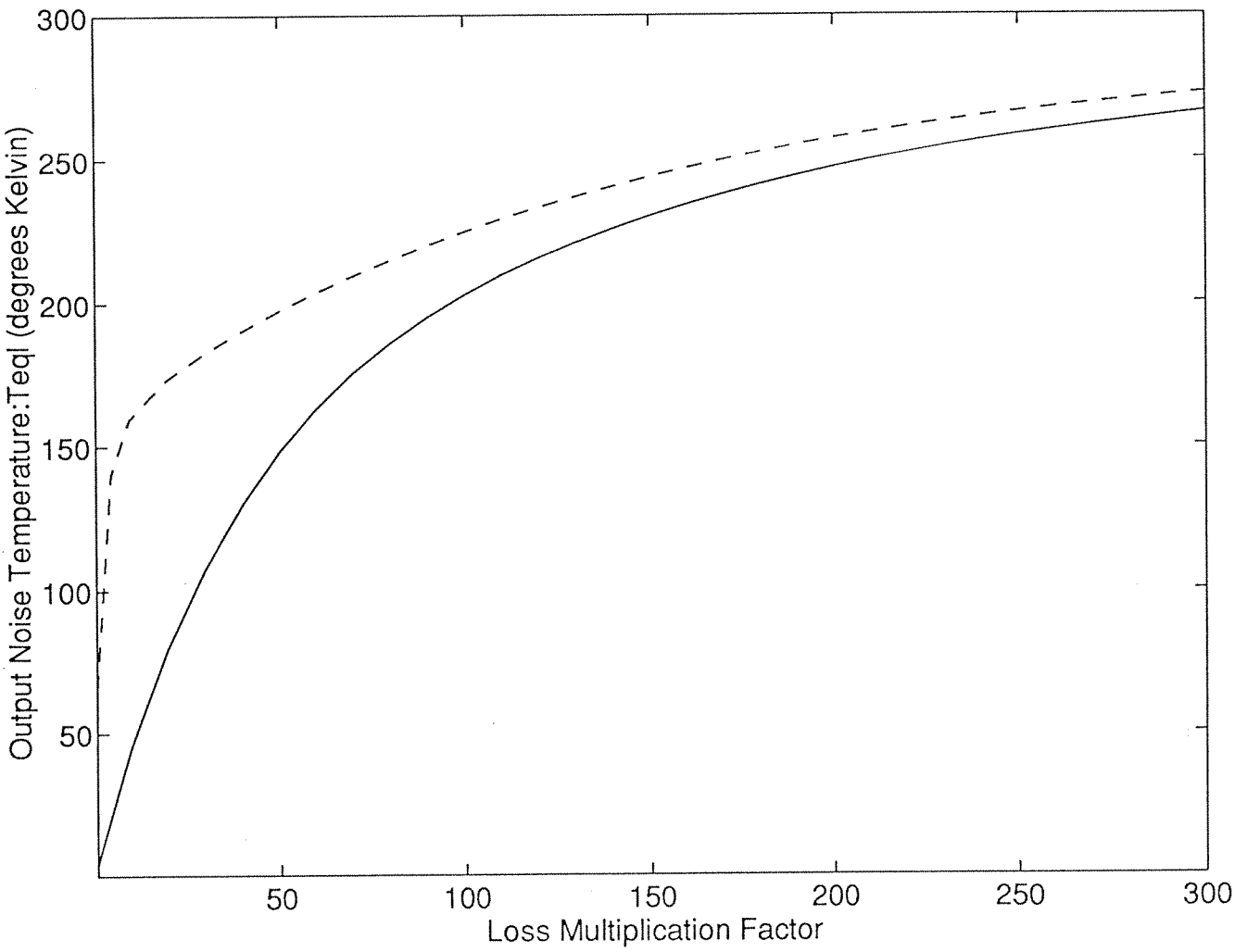

Figure A.1.19 The dependence of output noise temperature on the losses in the transmission lines

A.1.3 Test Fixture (Jig) Design and Patch Antenna Measurements

A microstrip measurement setup is prepared and microstip lines and patch antennas have been designed for testing purposes. Four different patch antennas which are resonant at 3 and 10 GHz have been manufactured by ASELSAN and measured at METU by using various jigs and HP 8757D Scalar Network Analyzer. RT Duroid 5880 has been used as the substrate of all prototypes, Table A.1.4.

Table A.1.4 Characteristics of RT-DUROID 5880

Dielectric constant, ε_r	2.2+0.015
Loss tangent, tan δ	0.0009
Conductivity, σ	0.556×10^5 S/mm
Cladding, t	0.035 mm

Jig Design

For measurement purposes of microstrip patch antennas, a microstrip to coaxial transition, which would be realized on a jig is necessary. A number of commercial transitions and jigs are available in the market. In order to measure the microstrip patch antennas and antenna arrays of COST 245, two types of transitions and jigs are manufactured in our department.

The first jig is a two-piece structure. Transition from coaxial to microstrip is realized by an SMA connector which is properly fit into the jig and the inner conductor of this connector is further machined to have a smooth tab. The elimination of the sharp corners by smoothing the tab is necessary to reduce the parasitic capacitance which probably will degrade the performance of the jig. This tapered tab provides the transition from coaxial to microstrip line. The two pieces are connected to by means of two screws which are also used as thickness adjustment screws. This thickness adjustment ability enables us to measure antennas which are produced on different thickness substrates.

The second jig is primarily constituted of a coaxial to microstrip SMA connector. The 2052-1618-02 SMA connector for microstrip circuits is a specially designed and produced connector. The inner conductor of the coaxial structure extends as a short strip on the other side. This wide enough strip serves as the launcher to the microstrip structure. A suitable construction which can hold this connector and the microstrip structure together is produced to form the second jig.

Microstrip Line Design

50 ohm microstrip line has been designed and manufactured. Insertion and return loss measurements are shown in Fig. A.1.20 and A.1.21, respectively.

Figure A.1.20 Insertion loss of the microstrip line.

Figure A.1.21 Return loss of the microstrip line.

Patch Antenna Design and Measurements

DESIGN 1: Single rectangular patch antenna with 50 Ω microstrip line has been designed to operate at 3 GHz. Dimensions of the patch and the line are given in Fig. A.1.22.

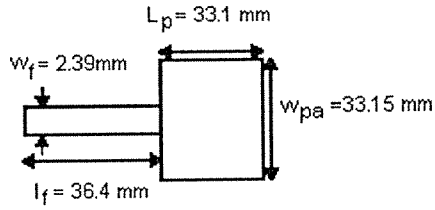

Figure A.1.22 Single patch antenna with 50 Ω microstrip line

Measured return loss curves are shown in Fig. A.1.23 and A.1.24. In Fig. A.1.23, measurement has been performed by using MTF/26 microwave test fixture, while jig #2 has been used in measurement shown in Fig. A.1.24. In both measurements, 50 Ω line was tapered for better transition to the connector. Resonance frequency of patch is measured to be 3.001 GHz. There is a discontinuity capacitance, C_d, between the jig and the microstrip line. Return loss is calculated and presented in Table A.1.5 for different values of C_d, ε_r, L_p, and frequency.

Table A.1.5 $|S_{11}|$ values for various C_d, ε_r, L_p values

	L_p=33.10mm				L_p=33.15mm
f (GHz)	C_d=0 ε_r=2.2	C_d=0.2 ε_r=2.2	C_d=0.2 ε_r=2.185	C_d=0.1 ε_r=2.215	C_d=0.1 ε_r=2.215
2.9800		-3.1830	-3.1460	-3.1600	-3.1620
2.9888		-3.1750	-3.1830	-3.1610	-3.1430
3.0000	-3.1590	-3.1040	-3.1720	-3.1030	
3.0200	-3.1200				

DESIGN 2: 3 GHz microstrip patch antenna with matching section has been designed. As shown in Fig. A.1.25, patch is matched to 50 Ω with quarter-wavelength matching line sections.

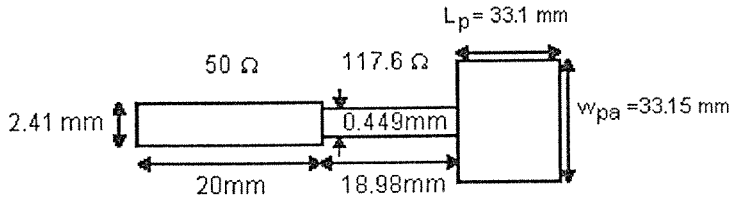

Figure A.1.25 3 GHz patch antenna with matching section

Measurement results of this antenna are shown in Fig. A.1.26-28. In Fig. A.1.26, jig #2 is used in the measurement. The resonance frequency has been measured as 2.966 GHz. In Fig. A.1.27, the end of 50 Ω line has been tapered and measurement has been performed by MTF/26 test fixture. The resonance frequency has been maesured as 2.973 GHz, in this case. In Fig. A.1.28, jig #1 with thin strip has been used for measurement. The resonance

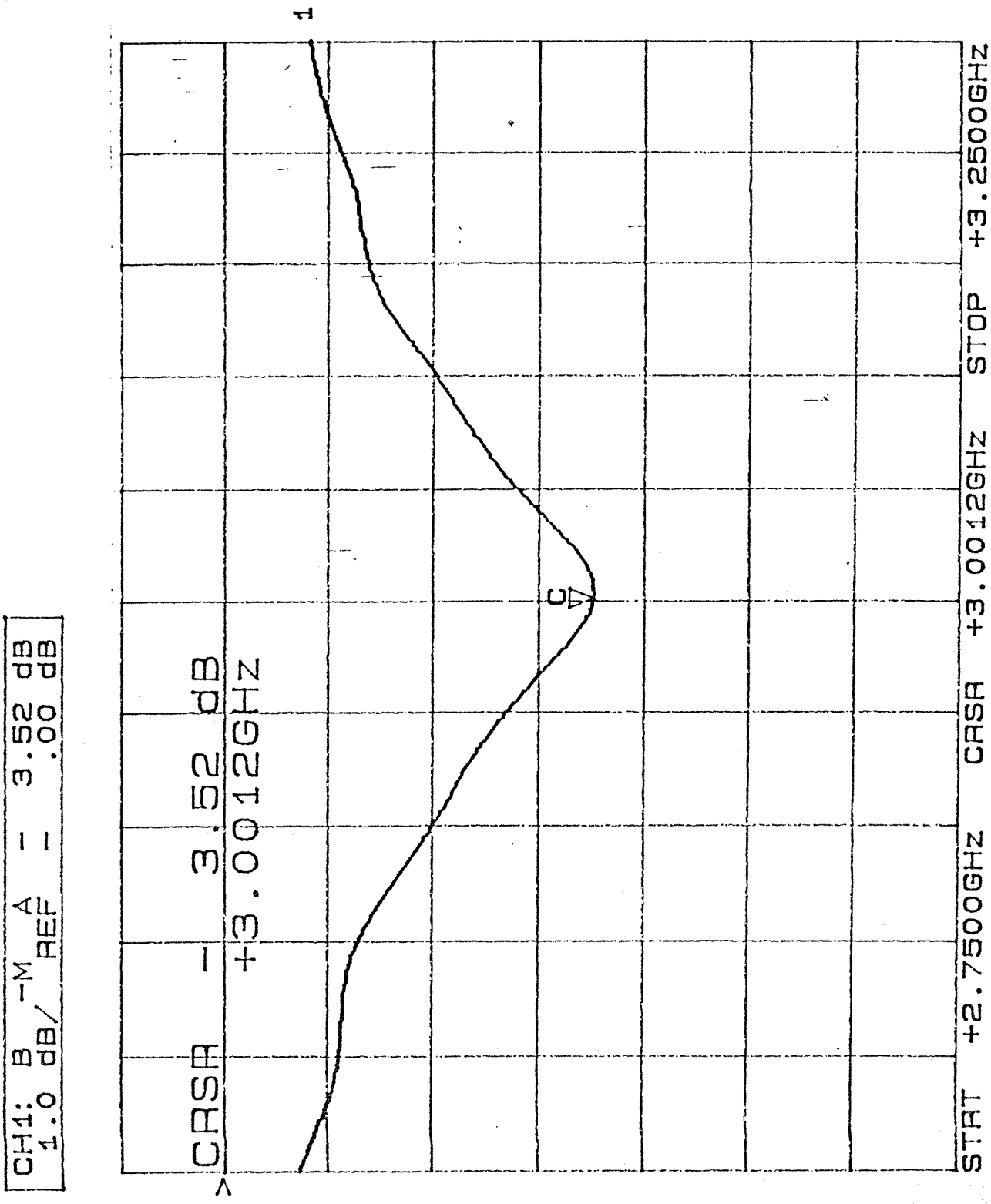

Figure A.1.23 Return loss curve of the patch antenna.

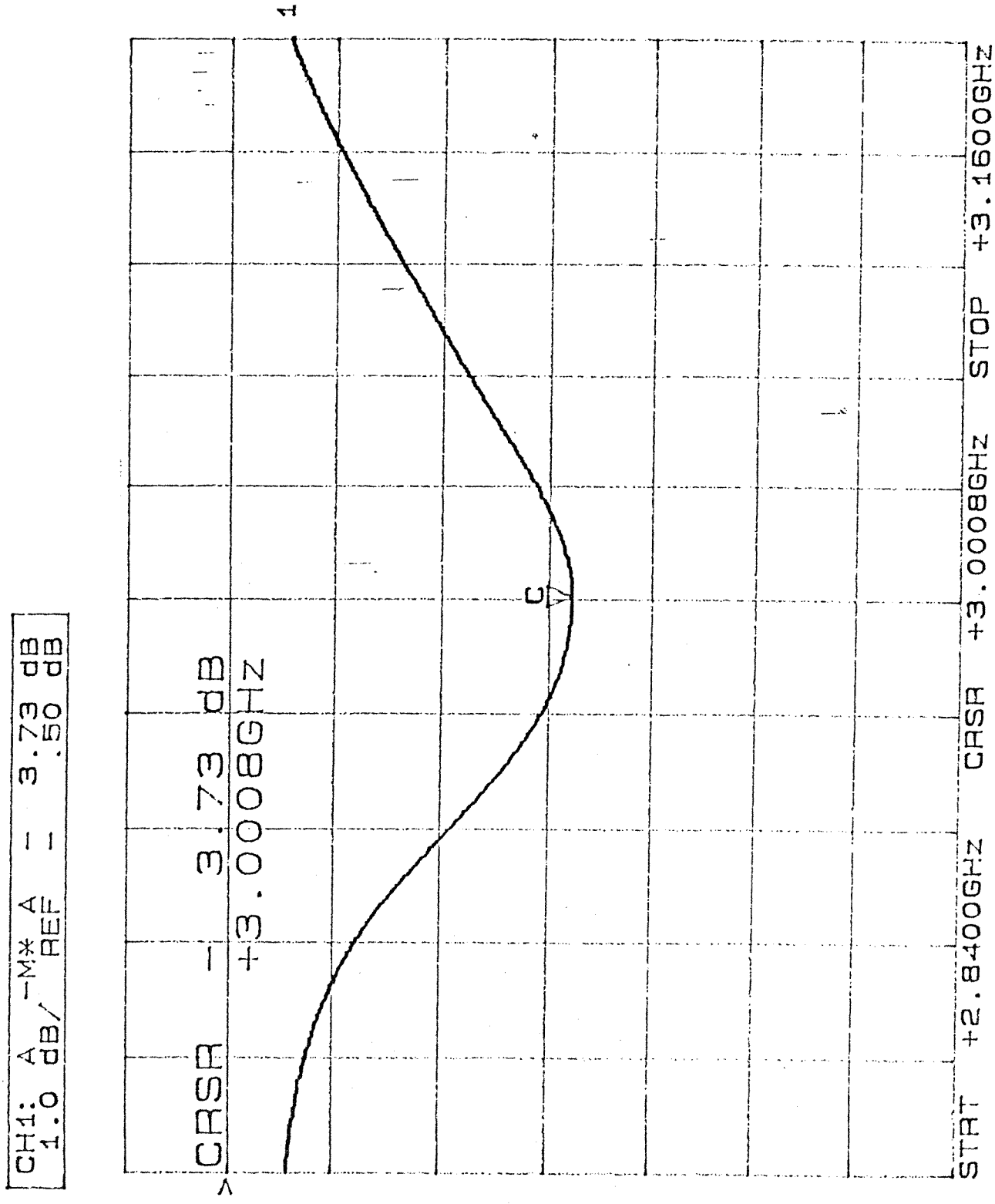

Figure A.1.24 Return loss curve of the patch antenna. .

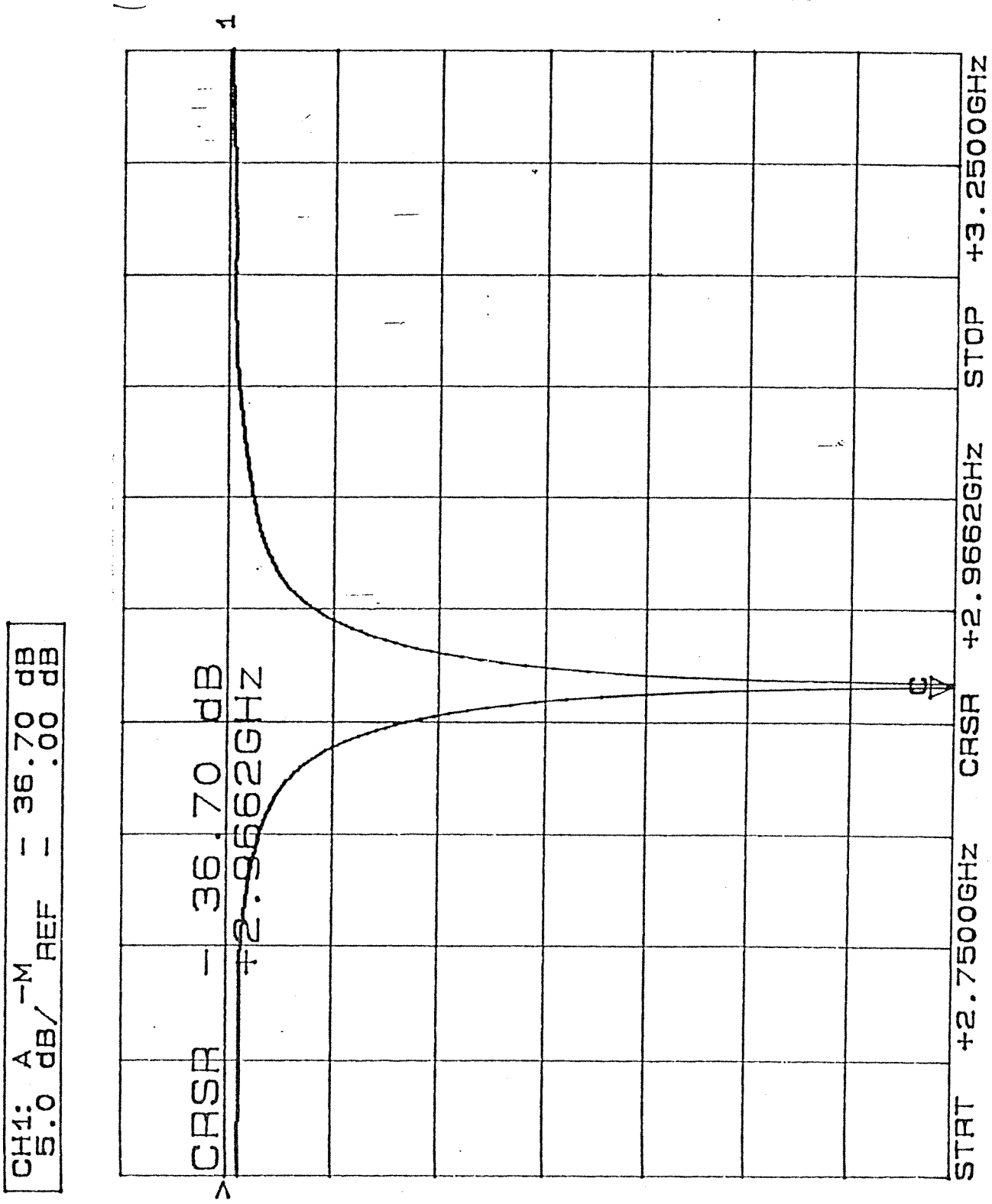

Figure A.1.26 Return loss curve of the patch antenna with jig #2.

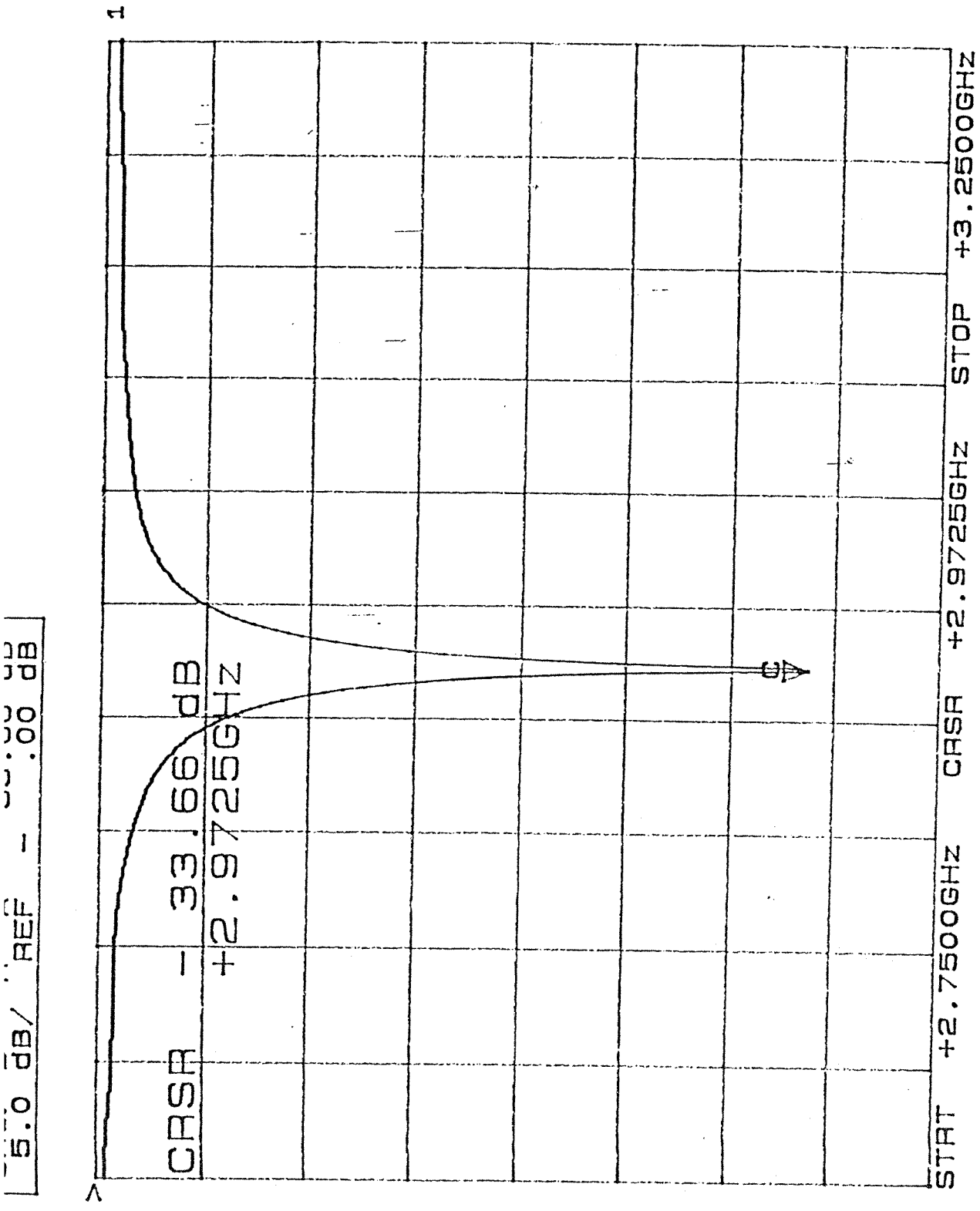

Figure A.1.27 Return loss curve of the patch antenna with MTF 26.

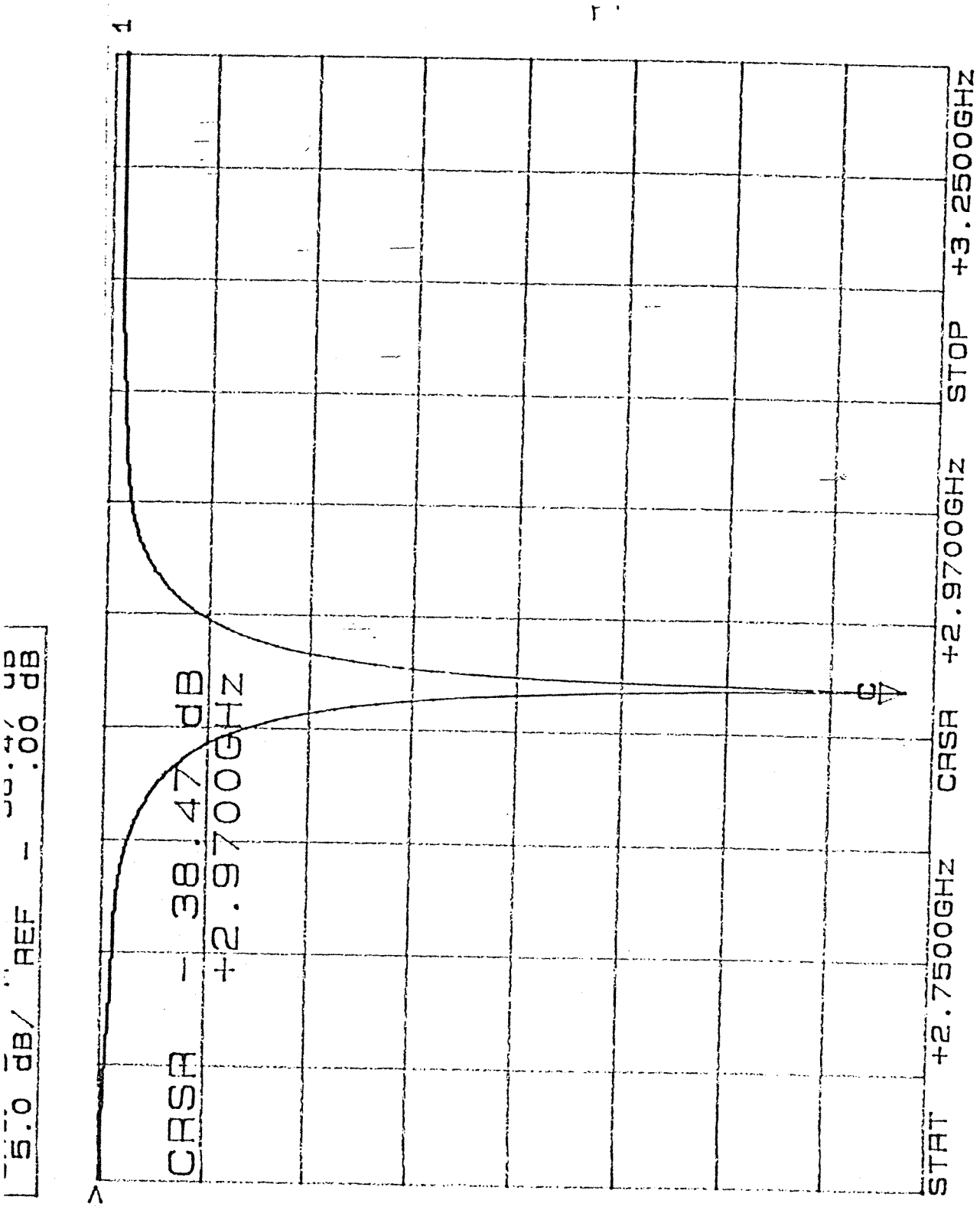

Figure A.1.28 Return loss curve of the patch antenna with jig #1.

frequency is 2.97 GHz. There is a step discontinuity capacitance, C_f, at the transition from quarter-wave transformer to 50 Ω line. This capacitance can be calculated as, [1]

$$C_f = \sqrt{w_1 w_2}\left(10.1 \log\varepsilon_r + 2.33\right)\frac{w_2}{w_1} - 12.6 \log\varepsilon_r - 3.17 \text{ pF/m} \quad (1)$$

w_1 and w_2 are in mm, range of validity $w_2/w_1 < 3.5$, $\varepsilon_r < 10$ with 10% accuracy.

Step discontinuity capacitance is calculated by using (1), C_f is 0.025 pF. $|S_{11}|$ calculations have been made and tabulated in Table A.1.6 for different values of C_d, ε_r, L_p, and frequency.

Table A.1.6 $|S_{11}|$ values for various C_d, ε_r, L_p values

	L_p=33.175 mm				L_p=33.15 mm	L_p=33.20 mm
f (GHz)	C_d=0.0 ε_r=2.2	C_d=0.8 ε_r=2.2	C_d=1.2 ε_r=2.2	C_d=0.05 ε_r=2.2	C_d=0.2 ε_r=2.215	C_d=0.2 ε_r=2.215
2.965			-12.990			
2.970			-14.760		-9.921	-11.270
2.980		-18.000	-11.916		-20.912	-26.970
2.988	-13.335	-13.925	-8.590	-14.280	-18.510	-15.434
3.000	-21.288	-7.776		-19.360		
3.010	-9.182			-9.390		

DESIGN 3: 10 GHz single square patch antenna has been designed and produced. The antenna and the dimensions are shown in Fig. A.1.29.

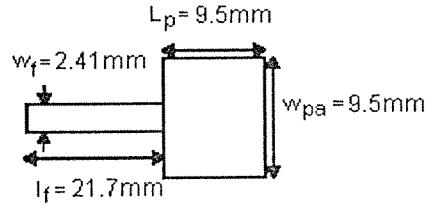

Figure A.1.29 10 GHz microstrip patch antenna

In measurements, tip of the 50 Ω line has been tapered. $|S_{11}|$ has been measured by using MTF/26 and plotted on Fig. A.1.30. The resonance frequency is 10.025 GHz. To observe the effect of variation in length of patch, discontinuity capacitance and ε_r on resonance frequency, some calculations have been made and given in Table A.1.7.

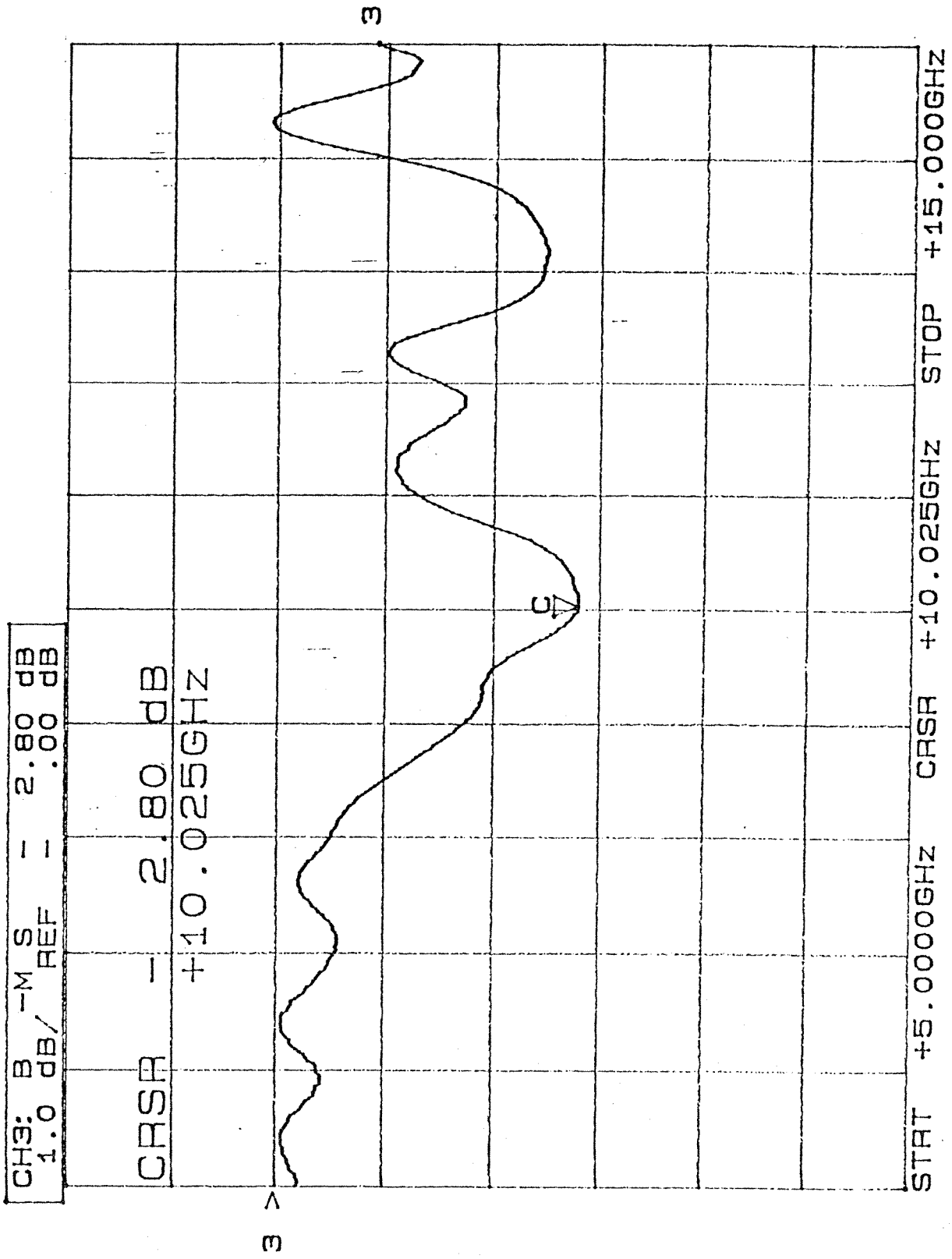

Figure A.1.30 Return loss curve of the patch antenna with MTF 26.

Table A.1.7 $|S_{11}|$ values for various C_d, ε_r, L_p values

	L_p=9.5 mm			L_p=9.47 mm	L_p=9.47 mm
f (GHz)	C_d=0.0 ε_r=2.2	C_d=0.05 ε_r=2.2	C_d=0.05 ε_r=2.185	C_d=0.01 ε_r=2.185	C_d=0.05 ε_r=2.185
9.800		-2.196	-2.926	-2.923	
9.850		-2.902	-2.920	-2.924	
9.900	-2.760	-2.874	-2.899	-2.910	
9.950	-2.780	-2.835			-2.807
10.000	-2.804	-2.786			-2.812
10.092	-2.815				

DESIGN 4: 10 GHz square patch antenna with matching section has been designed and shown in Fig. A.1.31.

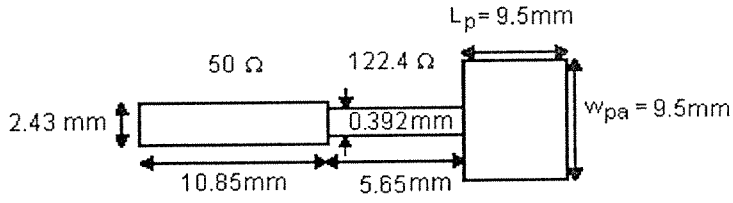

Figure A.1.31 10 GHz Square patch antenna with matching section

Step discontinuity capacitance has been calculated as 0.028 pF, using (1). $|S_{11}|$ measurements by MTF/26 and jig #1 are shown in Fig. A.1.32 and A.1.33 respectively. The resonance frequency of the antenna has been measured as 9.94 GHz by MTF/26 and 9.93 GHz by jig #1. In Table A.1.8, calculated $|S_{11}|$ values for different discontinuity capacitance, ε_r values are tabulated.

Table A.1.8 $|S_{11}|$ values for various C_d, ε_r, L_p values

f (GHz)	C_d=0.00 ε_r=2.2	C_d=0.05 ε_r=2.2	C_d=0.2 ε_r=2.2	C_d=0.05 ε_r=2.185	C_d=0.05 ε_r=2.215
9.980	-26.551	-18.107	-9.402		-27.030
10.000	-42.920	-22.880	-10.620	-16.330	-30.704
10.020	-24.290	-30.690	-11.877	-19.986	-22.246
10.040		-25.600	-12.960	-25.880	
10.060			-13.496	-29.187	
10.100			-12.260		

Reference

[1] T. C. Edwards, 'Foundations for Microstrip Circuit Design', p113, John Wiley&Sons.

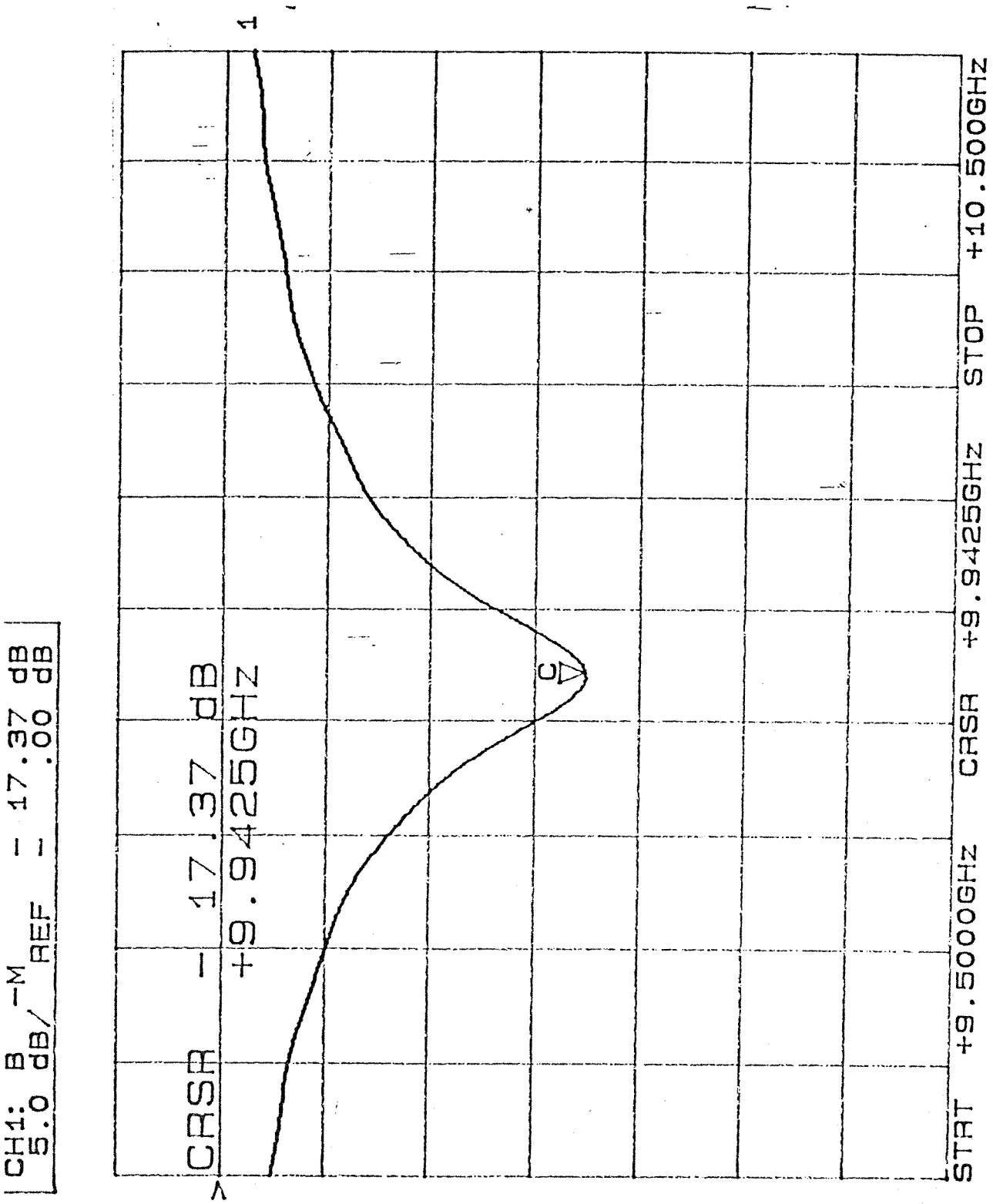

Figure A.1.32 Return loss curve of the patch antenna with MTF 26.

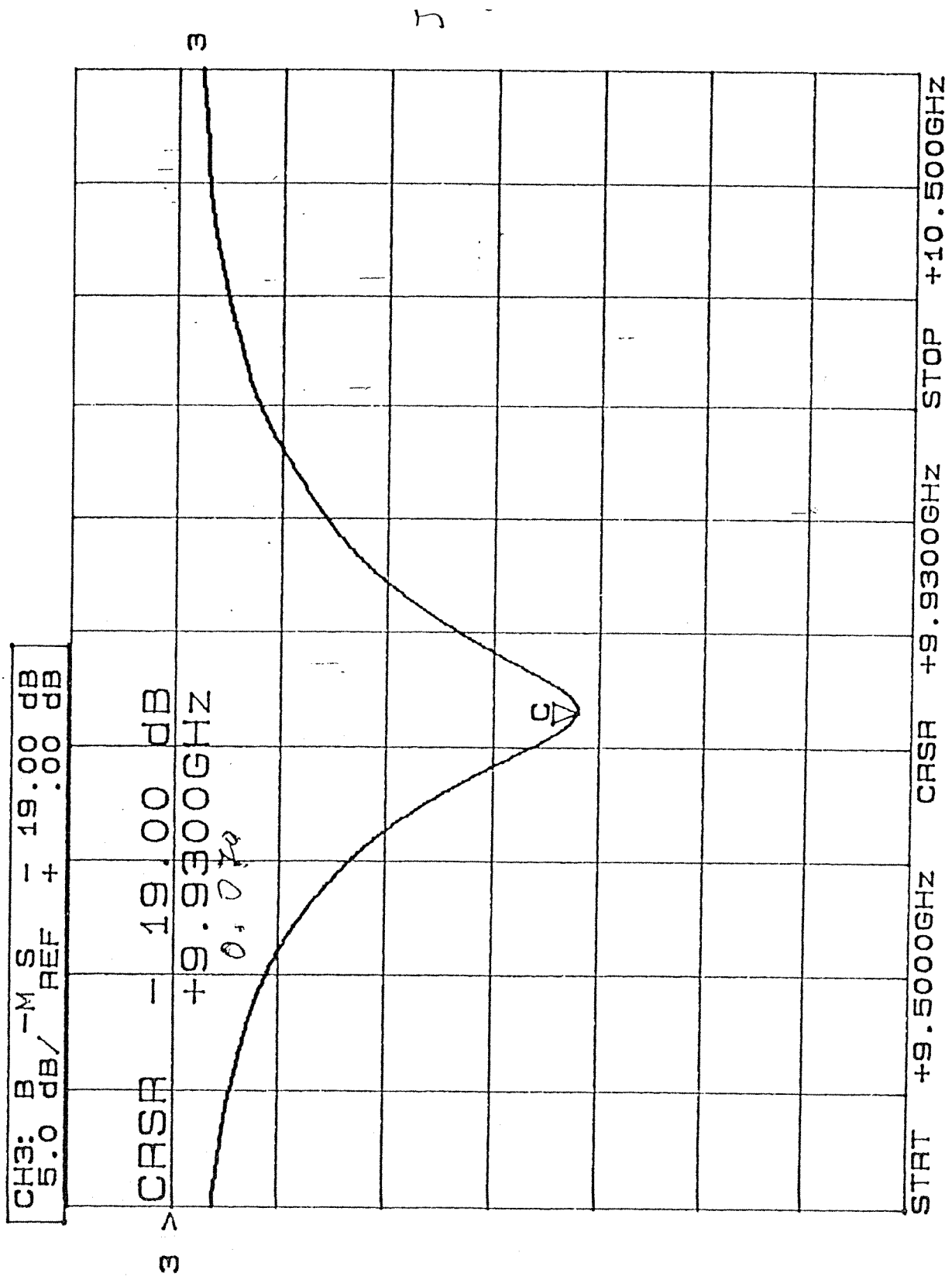

Figure A.1.33 Return loss curve of the patch antenna with jig #1.

A.1.4 Antenna Array Designs

In the following parts, various rectangular microstrip patch antenna array design and measurement studies are presented.

DESIGN 1: *8x4 Microstrip Patch Antenna Array*

A 8x4 microstrip patch antenna array has been designed at 10 GHz, Fig. A.1.34 Lengths and widths of the feed lines are given in Table A.1.9. Patches are square with $w_p=L_p=9.488$ mm. Calculations showed that the frequency bandwidth of the input impedance of a single patch and the array are the same, 257 MHz. It is also shown that upto 30 microns variation in widths of lines does not change the resonance frequency.

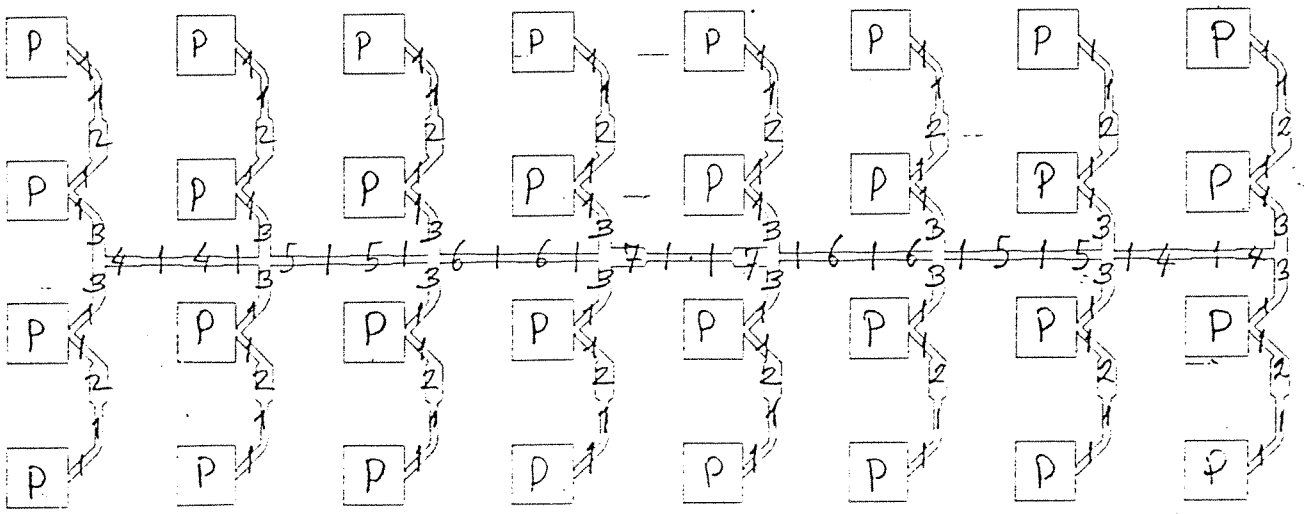

Figure A.1.34 8x4 Microstrip patch array for design 1

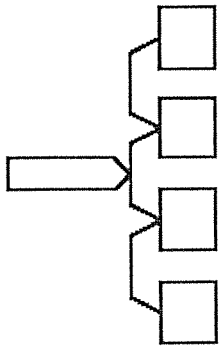

Figure A.1.35 Array B

Array B (Fig. A.1.35) of this planar array has been manufactured and measured. Return loss of array B is measured at ASELSAN and in METU (jig #2). The resonance frequency

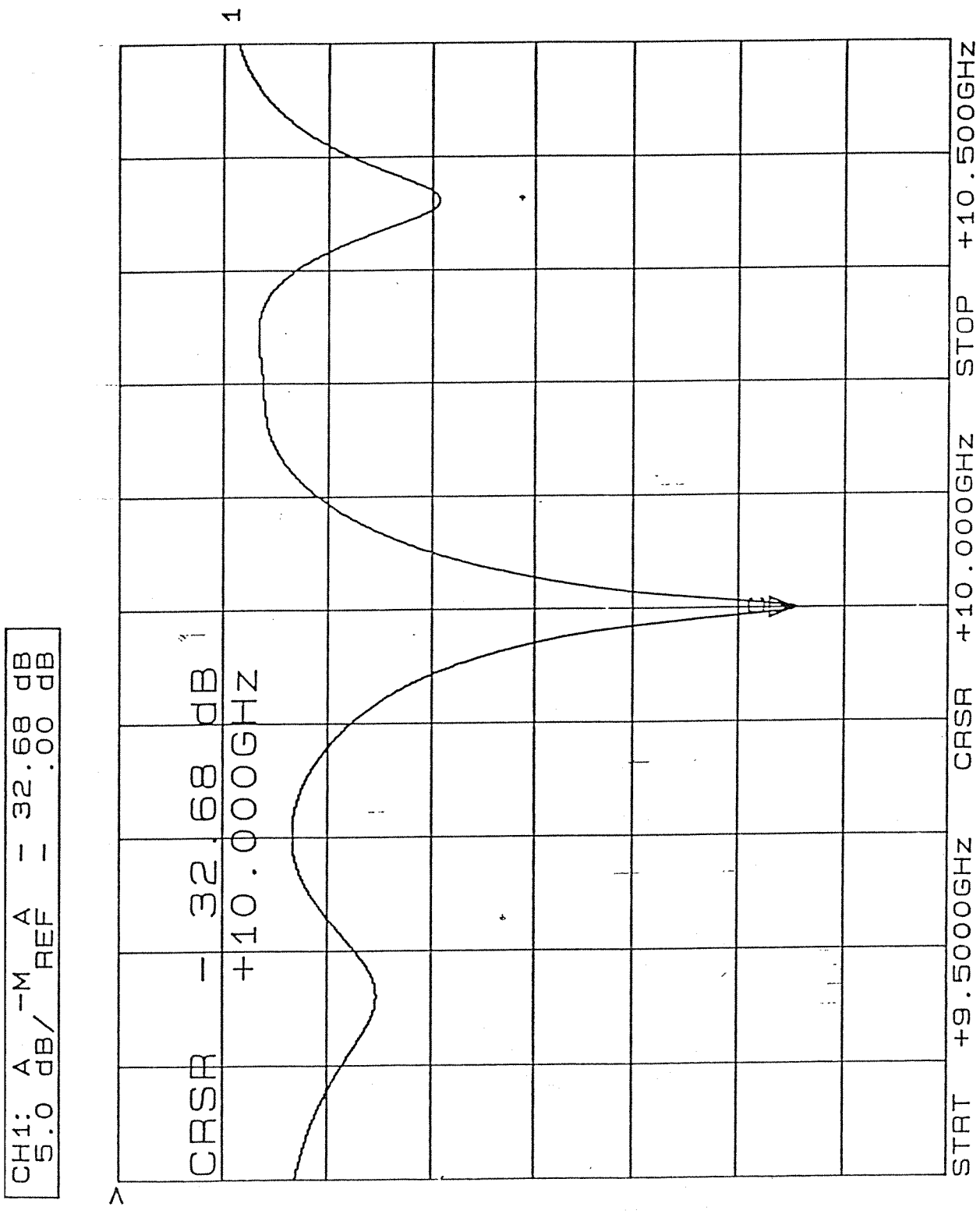

Figure A.1.36 Return loss of the overall array.

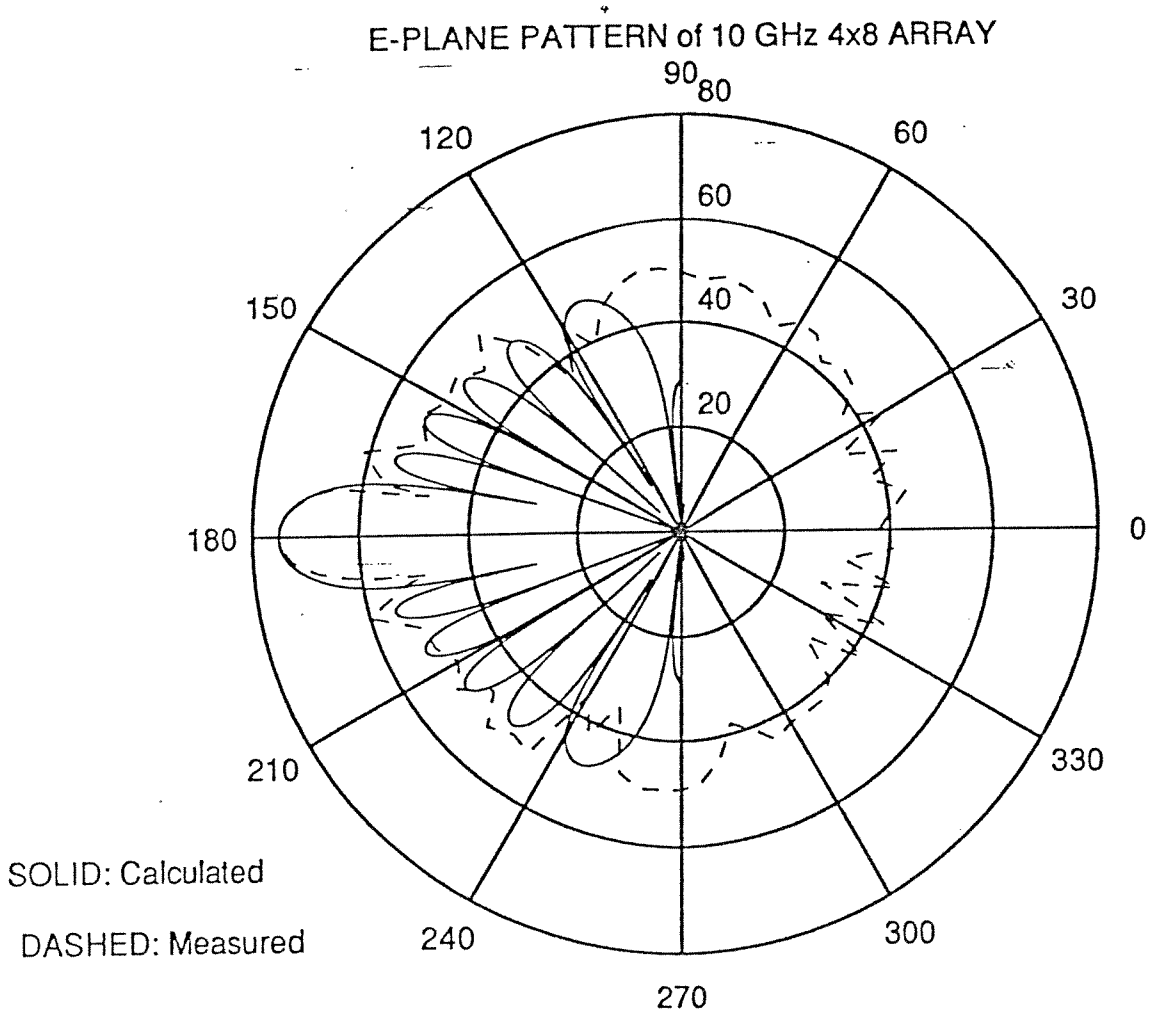

Figure A.1.37 E-plane radiation pattern of the array.

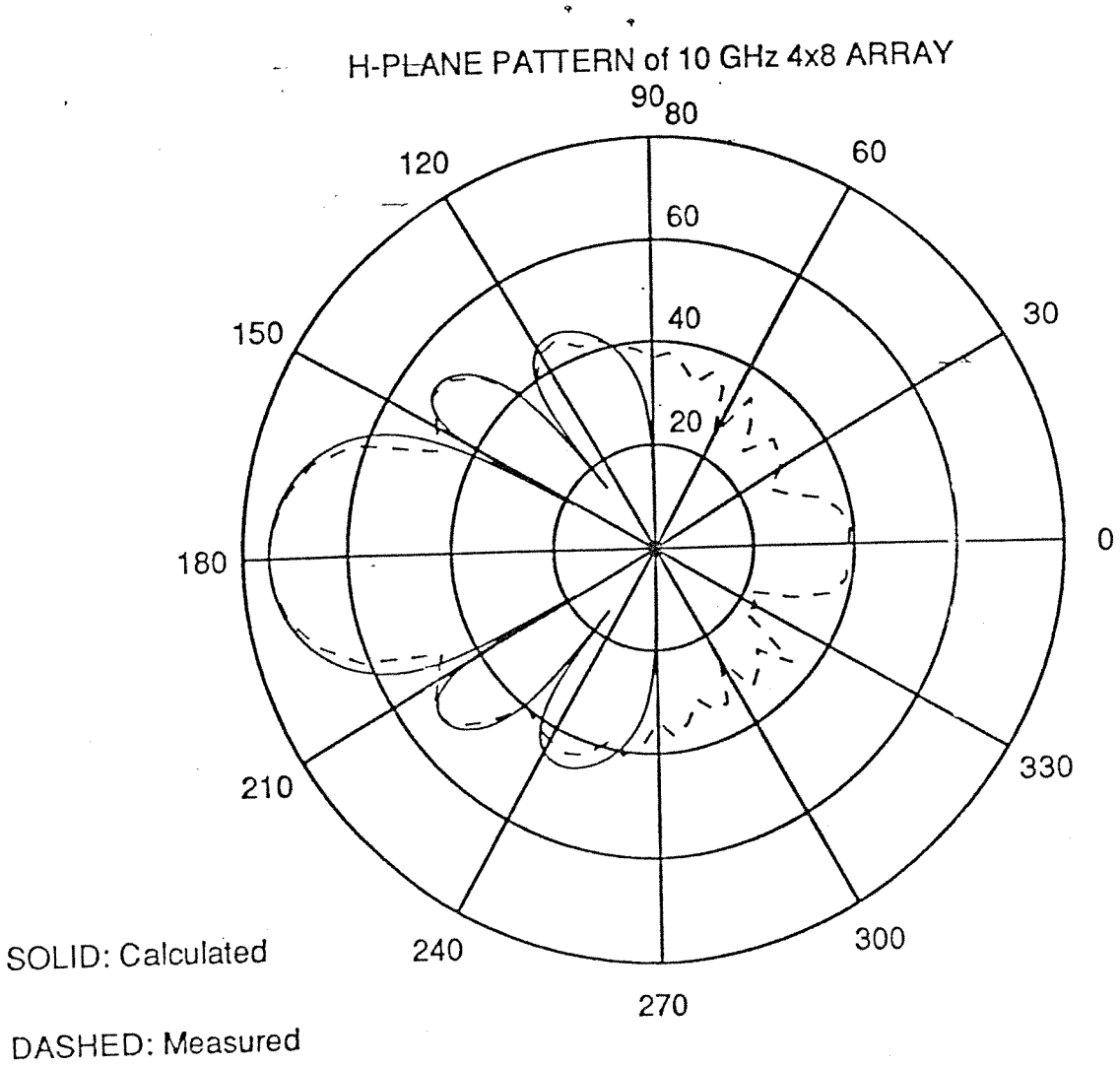

Figure A.1.38 H-plane radiation pattern of the array.

is 10.098 GHz. A small coper patch has been placed on tapered intersection point and the resonance frequency is shifted to 10 GHz. The return loss of the overall array is measured, Fig. A.1.36. It is seen that the resonance frequency is 10 GHz. The E and H-plane radiation patterns are measured and compared with theoretical results, Figs. A.1.37 and A.1.38. Summary of this comparison is given in Table A.1.10 Directivity and efficiency of the array are calculated to be 22.25 dB and 91%, respectively whereas measured gain is 21.5 dB. Array noise temperature due to losses is calculated to be 26°K. Cross polarization level is measured to be -35 dB.

Table A.1.9 Lengths and widths of lines in the array, for t=0.0175 mm

Line #	width (mm)	length (mm)	Line #	width (mm)	length (mm)
1	0.5	5.664	5	0.647	5.635
2	1.504	5.508	6	0.579	5.648
3	0.481	5.668	7	1.239	5.54
4	0.719	5.621			

Table A.1.10 Comparison of results

	Radiation pattern in E-plane		Radiation pattern in H-plane	
	-3 dB beamwidth	Side lobe level	-3 dB beamwidth	Side lobe level
Calculated	22.5°	-21.96 dB at 38.4°	9.5°	-19.75dB at 25.2°
Measured	22.3°	-21.33 dB at 36°	9.3°	-16dB at 15°

DESIGN 2: *11.3 GHz TVRO Antenna*

A 32x12 element microstrip patch antenna array which satisfies the COST 245 TVRO requirements is designed at 11.3 GHz; see Fig. A.1.39. Eccofoam PP-4 is used as the substrate, Table A.1.11. Microstrip line parameters and microstrip patch antenna parameters are given in Tables A.1.12 and A.1.13, respectively. Characteristic impedances of the lines, line lengths and widths which satify the required phase and amplitude distributions in the antenna elements are given in Tables A.1.14 and A.1.15. In this design, antenna elements are excited according to Gaussian distribution coefficients.

Table A.1.11 Grace Electronic Materials, Eccofoam PP-4 specifications

ε_r	1.06	cladding, t	0.075 mm
tan δ	0.0001	surface roughness, Δ	0.0005 mm
h	1.6 mm	surface conductivity, σ	0.556x105 s/mm

Table A.1.12 Parameters of microstrip lines

w	1 mm	λ_g	26.03624 mm
ε_{reff}	1.038312	α	0.001119 dB/mm
Z_{line}	144.3239 Ω	l	6.509060 mm

Table A.1.13 Microstrip patch antenna parameters

w_m	1.414214 mm	G_m	-0.00061 mho
w_n ,L_n	10.814879 mm	B_n	0.008083 mho
e_{cn}	1.051991	B_m	-0.000994 mho
l_n	25.8666417 mm	G_m	0.004371 mho
D_l	1.254681 mm	h_n	0.994374
G_n	0.002950 mho	Z_{in}	227.497131 ohm

Microstrip patch antenna element and its equivalent circuit are shown in Fig. A.1.40. Array B is shown in Fig. A.1.41. Impedances, lengths, and widths of the transmission lines used in the input of array B are Z_{sBe} =192.769 Ω, w_{sbe}=0.37075 mm, l_{sbe}=6.5183 mm, respectively. Impedances, lengths, and widths of the transmission lines used in array B are Z_{sae}=88.651 Ω, w_{sae} =3.0116 mm, l_{sae} =6.4920 mm, respectively. Array A is given in Fig. A.1.42.

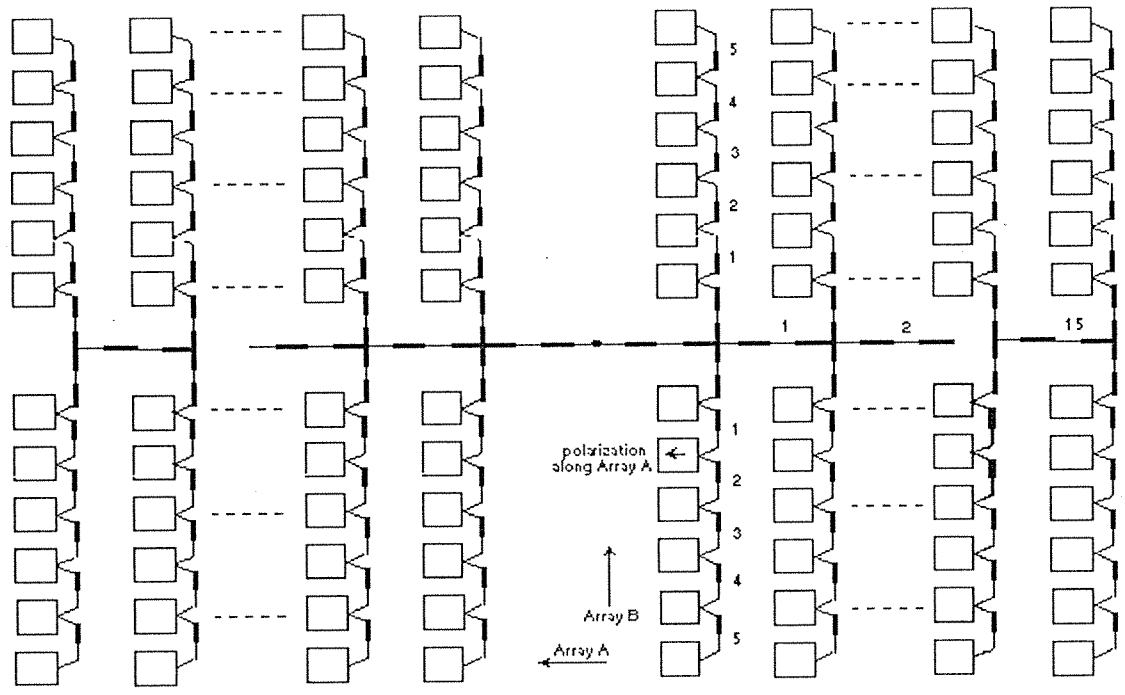

Figure A.1.39 12x32 Array

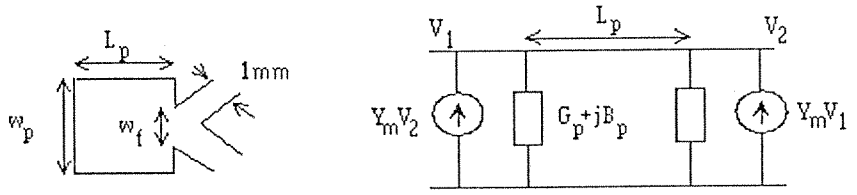

Figure A.1.40 Microstrip patch antenna and equivalent circuit

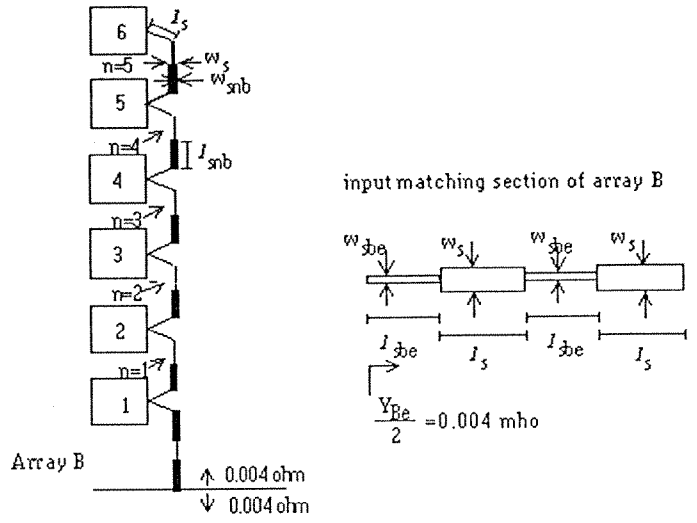

Figure A.1.41 Array B of microstrip patch antenna array

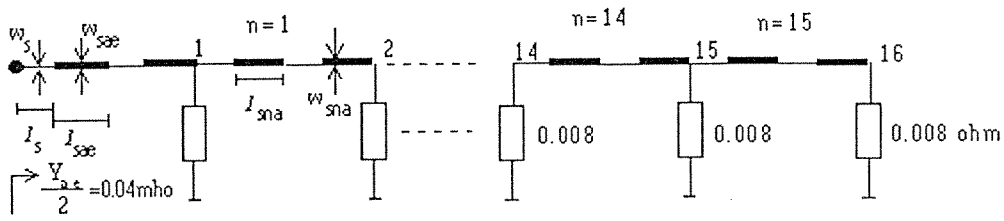

Figure A.1.42 Array A of microstrip patch antenna array

Table A.1.14 Impedances, lengths, and widths of the transmission lines used in array B (see Fig.A.1.35)

n	Z_{snb} (ohm)	w_{snb} (mm)	l_{snb} (mm)
5	94.63515	2.659888	6.4943
4	102.29014	2.277496	6.4970
3	110.54589	1.932812	6.4998
2	119.47627	1.622389	6.5025
1	129.165	1.343555	6.5053

Table A.1.15 Impedances, lengths, and widths of the transmission lines used in array A

n	Z_{sna} (ohm)	w_{sna} (mm)	l_{sna} (mm)	n	Z_{sna} (ohm)	w_{sna} (mm)	l_{sna} (mm)
15	132.9067	1.2493	6.5063	7	139.66	1.095	6.508
14	133.7808	1.228	6.5065	6	140.538	1.0768	6.5082
13	134.469	1.2082	6.5067	5	141.436	1.0581	6.5084
12	135.4638	1.1887	6.5069	4	142.359	1.0392	6.5086
11	136.2934	1.1697	6.5072	3	143.315	1.0199	6.5088
10	137.123	1.1509	6.5074	2	144.314	1.0002	6.5091
9	137.95	1.1323	6.5076	1	145.367	0.9798	6.5093
8	138.8	1.1138	6.5078				

Table A.1.16 Radiation pattern characteristics of array A (E-plane pattern):

-3 dB Beamwidth	2.451156°	Side lobe level	-26.47 dB, at 3.92°
Normalized field at 2.27°	-20 dB	Other side lobe levels	< -26.47 dB
First null	3.23°		

Table A.1.17 Radiation pattern characteristics of array B (H-plane pattern):

-3 dB Beamwidth	6.660424°	First Side lobe level	-31.47 dB at 10.4°
Normalized field at 7.61°	-20dB	Second Side lobe level	-27.5 dB at 15.5°
First null	9°	Other side lobe levels	< -31.47 dB
Second null	12.5°		

Radiation pattern calculations are given in Table A.1.16 and A.1.17. Array directivity, D_{array}, is 33.62577 dB (directivity of the element with low directivity can be neglected in the directivity calculation of highly directive antenna arrays) and overall antenna efficiency, η_A, is 0.869802. Overall noise temperature, T, is 30°K. G/T ratio of the antenna is calculated as 18.25 dB/°K and the required minumum G/T is 12.5 dB/K. Hence, our design satisfies this requirement.

DESIGN 3: *Active Phased Array Antenna*

A 24x32 active microstrip patch antenna array is designed at 9.5 GHz, Fig. A.1.43. Array B is composed of symmetrically placed 24 patch antenna elements. There is one amplifier for a group of 6 elements. Dimensions of the array are 50x40 cm^2. RT/Duroid 6002 is used as the substrate, Table A.1.18. Microstrip line parameters and microstrip patch antenna parameters are given in Table A.1.19 and Table A.1.20, respectively. Characteristic impedances of the lines, line lengths and widths which satify the equi-phase and tapered excitation distributions are given in Tables A.1.21 and A.1.22.

Table A.1.18 Rogers, RT/Duroid 6002 substrate specificatons

ε_r	2.94	surface roughness, Δ	0.0004 mm
$\tan\delta_i$	0.0012	surface conductivity, σ_c	0.556x105 s/mm
h	1.52 mm	Thermal coefficient	0 (0°C - 100°C)
cladding, t	70 μm		

Table A.1.19 Parameters of microstrip lines

w_s	0.5 mm	λ_s	21.4152 mm
ε_{ces}	2.17144	α_s	0.00288077 dB/mm
Z_s	126.0461Ω	l_s	5.3538 mm

Table A.1.20 Microstrip patch antenna parameters

w_f	0.5 mm	G_m	0.0030603065 mho
w_p , L_p	8.18884 mm	η_p	0.9764
ε_{cp}	2.6699717	Z_{in}	319.059 Ω
Δ_l	0.81072 mm		

Array B is shown in Fig. A.1.44. Inputs of Sections I and II will be fed separately to form a phased array such that each element in the array satisfies the phase shift and amplitude-tapering requirements. There are 4 inputs for array B and then there are 4x32=128 inputs to the whole array. The array is capable of scanning the beam ± 45° from the boresight by adjusting the phases of the 128 inputs. In transmit mode the array will be fed by solid state power amplifiers with a maximum power output of one watt to the element m=±1, $P_{i,B(I)}(I)=1$ W.

Table A.1.21 Impedances, lengths, and widths of the lines used in Section II of array B.

n	Z_{snh} (Ω)	w_{snh} (mm)	l_{snh} (mm)	n	Z_{snh} (Ω)	w_{snh} (mm)	l_{snh} (mm)
12	*	*	*	9	105.400	0.88797	5.27843
11	101.197	0.99568	5.260976	8	107.531	0.83770	5.28695
10	103.294	0.94046	5.269797	7	109.700	0.78935	5.29542

Table A.1.22 Impedances, lengths, and widths of the lines used in Section I of array B.

n	Z_{snh} (Ω)	w_{snh} (mm)	l_{snh} (mm)	n	Z_{snh} (Ω)	w_{snh} (mm)	l_{snh} (mm)
6	*	*	*	3	118.460	0.61936	5.32774
5	113.609	0.70874	5.310184	2	120.954	0.57754	5.33648
4	116.016	0.66299	5.318993	1	123.516	0.53726	5.34528

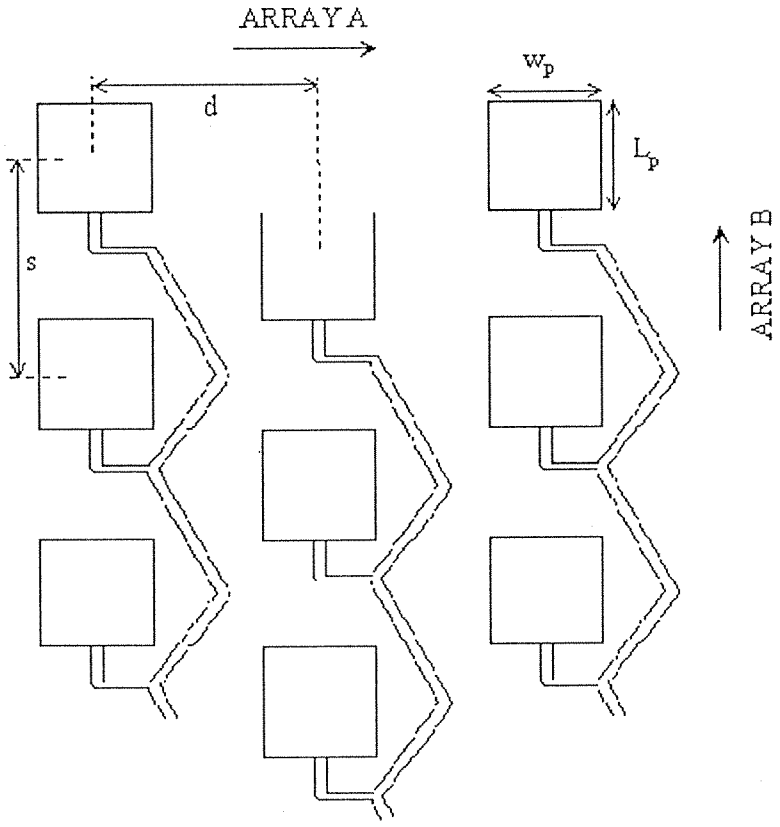

Figure A.1.43 Active array, s=18.957 mm, d=15.726 mm, λ_0=31.56 mm, w_p=L_p=8.189 mm

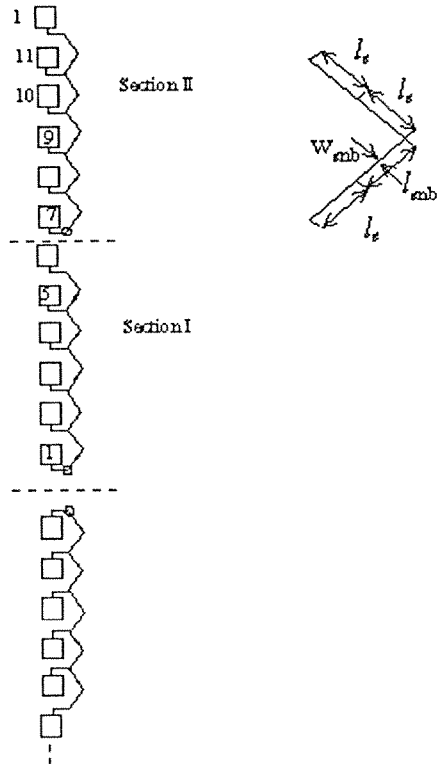

Figure A.1.44 Array B of microstrip patch antenna array

Input admittance seen from element 7 is $Y_{ib}(7)=0.0076974$ mho and the impedance is $Z_{ib}(7)=129.914\ \Omega$. Input admittance seen from element 1 is Yib(1)=0.011839 mho and the impedance is Zib(1)=84.464 Ω. Radiation characteristics of the overall array, together with array A and B are given in Tables A.1.23, A.1.24 and A.1.25, respectively.

Table A.1.23 Radiation characteristics of the antenna array

D_{array}	33.43 dB at 0° scan angle,	P_{inout}	40.12 Watt
D_{array}	31.92 dB at 45° scan angle	$P_{radiated}$	37.53 Watt
$\eta_{antenna}$	% 93.549	P_{loss}	2.586 Watt

Table A.1.24 Radiation pattern characteristics of array A (H-plane pattern)

Main beam direction	-3 dB beamwidth	-10 dB beamwidth	Nulls	Side lobe levels
0°	3. 9345°	6.787°	5.1°, 7.6°, 11.2°	< -25 dB
20°	4.18559°	7.2215o	8.31°, 12°, 14.5°, 25.5°, 28.3°, 32.6°	< -25 dB
45°	5.54168°	9.58°	38.1°, 52.8°	< -25 dB

Table A.1.25 Radiation pattern characteristics of array B (E-plane pattern)

-3 dB Beamwidth	4.36711°	1st side lobe level at 6.92°	-27.6 dB
-10 dB Beamwidth	7.5416°	2nd side lobe level at 10.3°	-27.6 dB
Nulls	5.69°, 8.46°, 512.5°, 16.3°	Other side lobe levels	< -31.4 dB

DESIGN 4: *Array On Cylindirical Surfaces*

Microstrip antennas on cylindrical substrates have found many applications in aircrafts, spacecrafts, missiles, and boosters. We have used our experience and accumulation of know-how in the design of microstrip patch array on cylindrical dielectric substrate. The geometry of a single patch on a cylindrical substrate is shown in Fig. A.1.45.

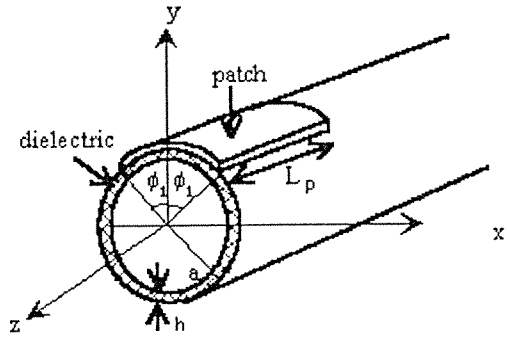

Figure A.1.45 Rectangular microstrip patch antenna on cylindrical substrate

The radius of the cylinder is a=113.5 mm and the thickness of the substrate, h, is 1.52 mm. Operating frequency is 2210 MHz (λ=135.6527 mm). RT/Duroid 6002 is chosen as the substrate, Table A.1.18. Resonance dimensions of a planar microstrip patch antenna of square shape at 2.21 GHz are calculated and tabulated in Table A.1.26.

Table A.1.26 Resonance dimensions of a planar patch antenna of square shape at 2.21 GHz.

w_p , L_p	38.7029252 mm	Δ_l	0.9270432 mm
w_s	1 mm	Z_{in}	331.8529501
l_s	91.522795 mm		

Integral equation formulation using the pertinent Green's function can be used for the exact formulation of the curved patch antenna and MoM gives the current distribution [1]. Alternatively, cavity model can be used for thin substrates (h<<a) [2,3] which gives the resonant frequencies and the electric field under the patch. Then the problem is simplified to the radiation of magnetic currents of the length w_p and separated by $L'=L_p+\Delta_l$ for the TM_{011} mode in the presence of dielectric coated conducting cylinder. Far fields are evaluated using the numerically computed Green's function by method developed in [4].

The resonance frequency of a planar patch antenna and the cylindrically curved patch antenna are approximately equal for a>>h and h<<λ_0, [3]. For the given patch dimensions the radiation patterns are given in Fig. A.1.46 and Fig. A.1.47. Piecewise parabolic functions are fitted to these patterns and the input impedance and directivity of the antenna are calculated. For this design, f=2.21 GHz, a=113.58 mm, b-a=1.52 mm, $w_p=L_p$=38.7 mm, ε_r=2.94.

The input impedance of a curved microstrip rectangular patch antenna on a cylindrical body has been considered in [2] for the TM_{01} and TM_{10} modes. Also an expression is given for input impedance for the coaxial fed patch antennas. In the graphs presented in [2,5], it

is seen that the resonance frequency is effected negligibaly while the radiation resistance decreases by a factor of 1.1-1.3. We shall estimate the ratio of the input conductance G_p of the curved patch. The ratio of directivities $D_{e,p}/D_{e,c}$ should be the same as the ratio of input conductances, G_c/G_p. The directivity of planar patch antenna, $D_{e,p}$, is 4.793 (6.806 dB). Hence G_c/G_p=1.0862 and the input impedance $Z_{i,c}=Z_{i,p}/1.0862$, and the directivity, $D_{e,c}$,of curved patch antenna are 4.413 (6.447 dB) and 305.512 Ω respectively. The ratio of $R_{i,p}/R_{i,c}$ is around 1.05-1.2 according to [2,5]. We shall take this ratio as 1.106, so that $Z_{i,c}$=331.85/1.10616=300 Ω.

The microstrip patch array which wraps around the cylinder with the given radius is designed. The mutual coupling between the patches is calculated as, [6], $|S_{12}|$ = -25 dB. Mutual coupling in the E-plane is about -20 dB [6,7].

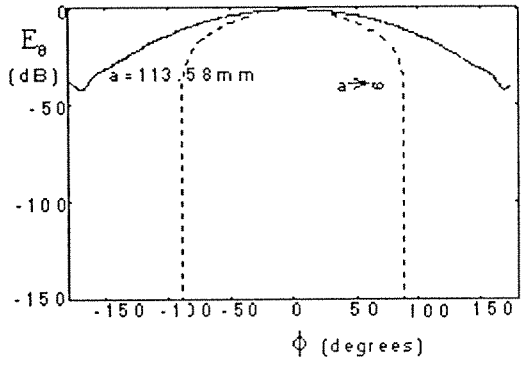

Figure A.1.46 Radiation patterns in θ=π/2 plane of patch antenna on a cylindrical substrate

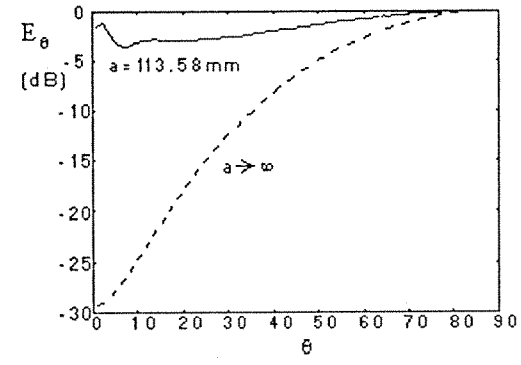

Figure A.1.47 Radiation patterns in ϕ=0 plane of patch antenna on a cylindrical substrate

References

[1] S. M. Ali, T. M. Habashy, J. F. Kiang, and J. A. Kong, "Resonance in cylindrical-rectangular and wraparound miscrostrip structures", IEEE Trans. Microwave Theory Tech., vol.37, pp.1773-1783, Nov. 1989.

[2] K. Luk, K. Lee, and J. Dahele, "Analysis of the cylindrical-rectangular patch antenna", IEEE Trans. Antennas Propagat., vol. AP-37, pp.143-147, Feb. 1989.

[3] C. M. Krowne, "Cylindrical-rectangular microstrip antenna", IEEE Trans. Antennas Propagat., vol. AP-31, no.1, pp.194-199, Jan. 1983.

[4] Ö. Aydin Çivi, "Effects of anisotropy of ferrite coating on the radiation characteristics of a cylindrical conductor excited by elementary sources", Ph. D. Thesis, METU, 1996.

[5] J. S. Dahele, R. J. Mitchell, K. M. Lak, and K. F. Lee, "Effect of curvature on charectristics of rectangular patch antenna", Electronics Letter, vol.23, no.14, pp.1258, July 1987.

[6] A. Van de Capella, Microstrip Antenna Handbook, Chap.10, vol.1, (by J.R. James and D.S.Hall)

[7] W. Y. Tam, A. K. Y. Lai, and K. M. Luk, "Mutual coupling between cylindrical rectangular microstrip antennas", IEEE Trans. Antennas Propagat., vol. AP-43, no.8, p.897, August 1995.

A.2 SMART ANTENNAS

With more sophisticated operations required from today's telecomunications and radar systems, techniques for improving the antenna performance are in constant demand. Recently, there is considerable interest in digital beam forming, *smart antennas*. High speed computing developments and advances in hardware technology have made digital beam forming feasible for many applications.

Beamforming methods are used to improve the reception and/or transmission performance of the antenna according to the type of application. For instance, these methods are used to maximize the received signal from the desired source and eliminate unwanted signals; to direct the transmitted signal to the optimum path to reach the target when physical rotation of the antenna is impractical; to scan a wide area in surveillance applications; to shift the main beam to receive data from multiple sources. The methods are based on changing the magnitude and the phase of the signal transmitted/received from each element of an antenna array to collectively change the radiation characteristics of the overall array. Furthermore, maxima or nulls can be created in some directions by changing the array factor both in transmission and reception.

A smart antenna which is capable of direction finding and digital beam forming has been designed and manufactured. Six element linear microstrip patch array with a reference patch antenna has been designed to operate at 7 GHz as the receiving antenna. Antenna has been manufactured by ASELSAN. Designed antenna is shown in Fig. A.2.1. Single patch and its dimensions are shown in Fig. A.2.2. Distance between the patches in linear 6 element array is $d=0.75\lambda_0$. Distance between the reference antenna and the first patch of the array is $2\lambda_0$. RT-Duroid 5880 with thickness 35mm is used as substrate.

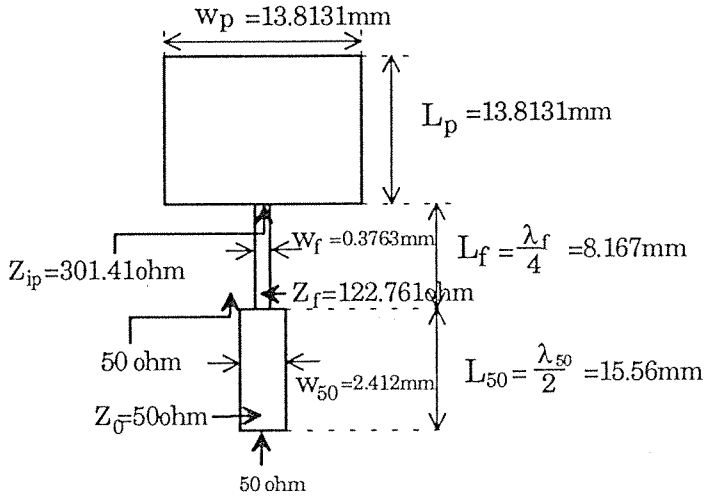

Figure A.2.2 Dimensions of single element of antenna array

In Fig. A.2.3, designed system for direction finding and for the emulation of some beamforming techniques is shown. Signal levels at each antenna terminal are considered seperately by means of a switch. Before the received signal data is sent to a digital device, a 90° hybrid and two mixers are used to obtain two uncorrelated signals. These signals are digitally processed to find the direction of the incoming signal.

6.6.1996

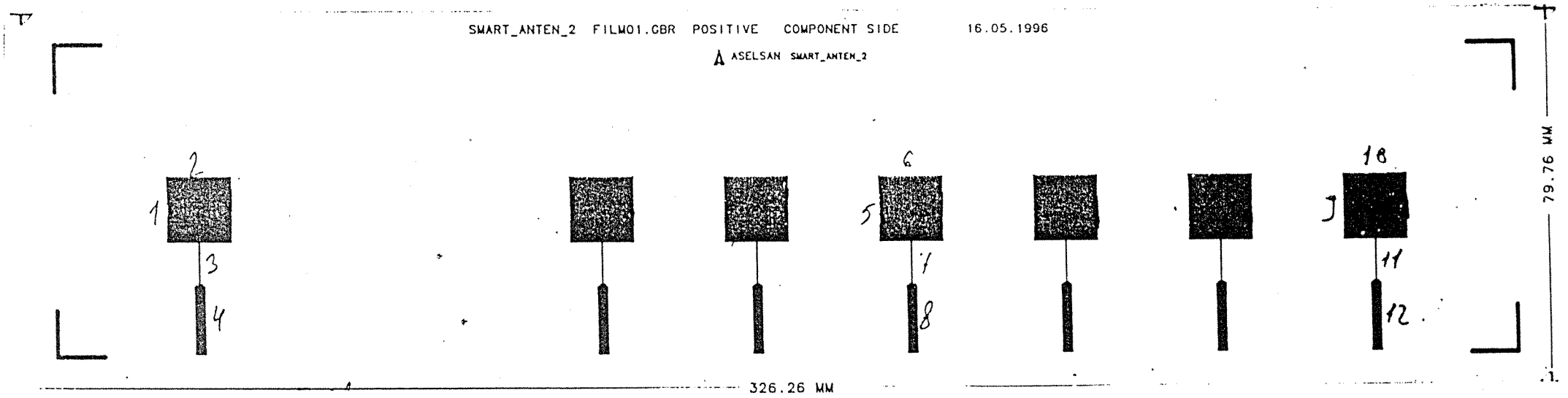

	1	2	3	4	5	6	7	8	9	10	11	12
Film (in μm)	13640	13845	413	2442	13655	13845	415	2448	13650	13841	408	2454
Card(in μm)	13643	13860	404	2445	13686	13838	400	2435	13655	13832	398	2445

Figure A.2.1 Layout and dimensions of the smart antenna

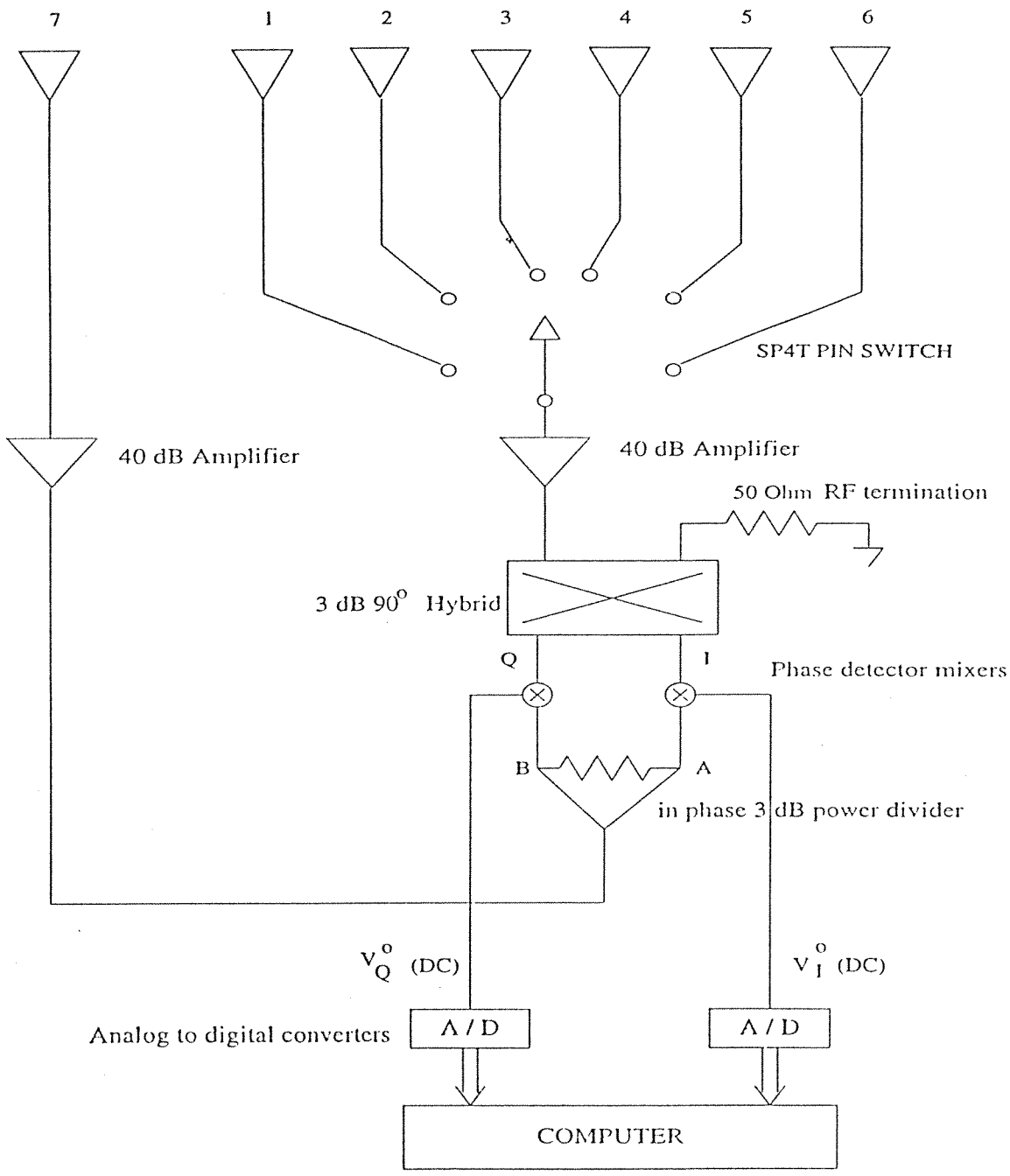

Figure A.2.3a Block diagram of the smart antenna system

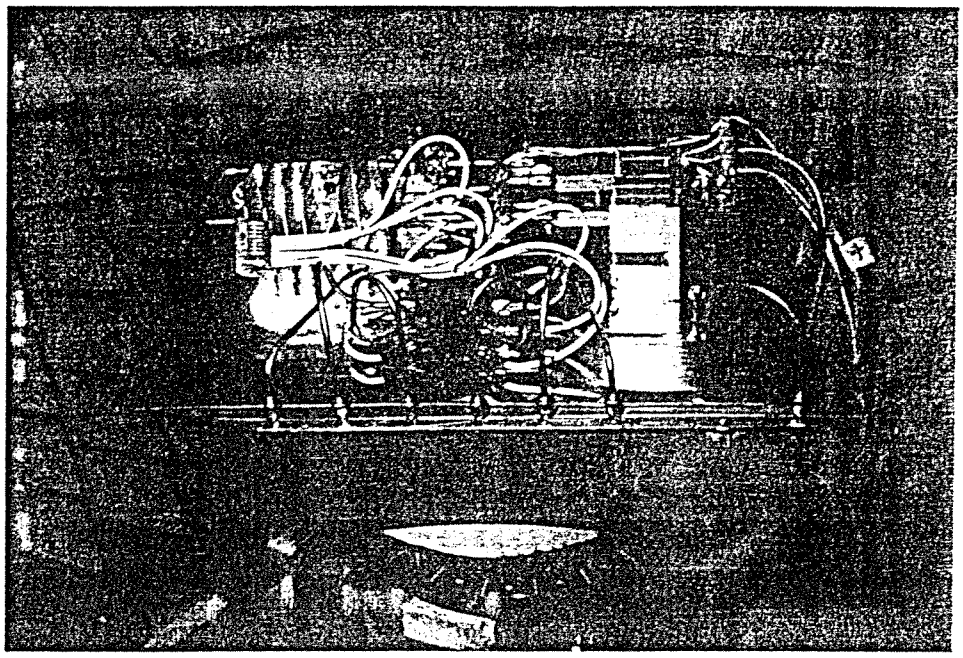

Figure A.2.3b Photograph

Two amplifiers of approximately 35 dB gain, two identical mixers, a 90° hybrid and a Wilkinson power divider are used between antenna elements and digital processing unit. The 90° hybrid supplies the in-phase component of the received signal to one of the mixer and the quadrature component to the other mixer. The mixers yield a DC voltage which is proportional to the phases of the received signals at each element of the array. The signal received from the reference antenna is fed into the inputs of each mixer and the signal received from the other elements is fed into the other inputs of the mixer. The reference signal is used to eliminate the frequency terms and to obtain the phase terms only at the outputs of the mixers. The single pole six throw switch is used rather than using the same set of mixer systems for each of the elements of the antenna array. This switch is to be controlled by the digital circuitry.

Calibration Procedures

In order to model the circuit correctly, a calibration procedure is necessary. Two types of calibration processes are proposed:

1. Method

S-parameters of the parts from each patch to the I and Q ports shown in Fig. A.2.3, are measured in ASELSAN and given in Fig. A.2.6 to Fig. A.2.20. Also, S-parameters S_{A7} and S_{B7} are defined as the S-parameters of the part from reference antenna to ports A and B, shown in Fig. A.2.3, respectively. All the S-parameters are defined with respect to 50 ohm reference.

Then, the voltage at port I, when switch is connected to the i'th element is given by

$$V_{Ii} = Re\{V_i S_{Ii} e^{j\omega t}\} = |V_i||S_{Ii}|\cos(\omega t + \phi_i + \psi_{Ii})$$

where

$$V_i = |V_i|e^{j\phi_i},\ S_{Ii} = |S_{Ii}|e^{j\psi_{Ii}}$$

V_i is the voltage received by the i'th element, ϕ_i is the random phase of the received signal at the i'th element, ψ_{Ii} is the phase factor introduced by the system on the i'th signal in-phase component.

Similarly, we define

$$V_{Qi} = Re\{V_i S_{Qi} e^{j\omega t}\} = |V_i||S_{Qi}|\cos(\omega t + \phi_i + \psi_{Qi})$$

where

$$S_{Qi} = |S_{Qi}|e^{j\psi_{Qi}} \quad .$$

The voltages at ports A and B are defined as

$$V_A = |V_7||S_{A7}|\cos(\omega t + \phi_7 + \psi_{A7})$$

$$V_B = |V_7||S_{B7}|\cos(\omega t + \phi_7 + \psi_{B7}) \quad .$$

The outputs of the mixers for DC component are expressed by

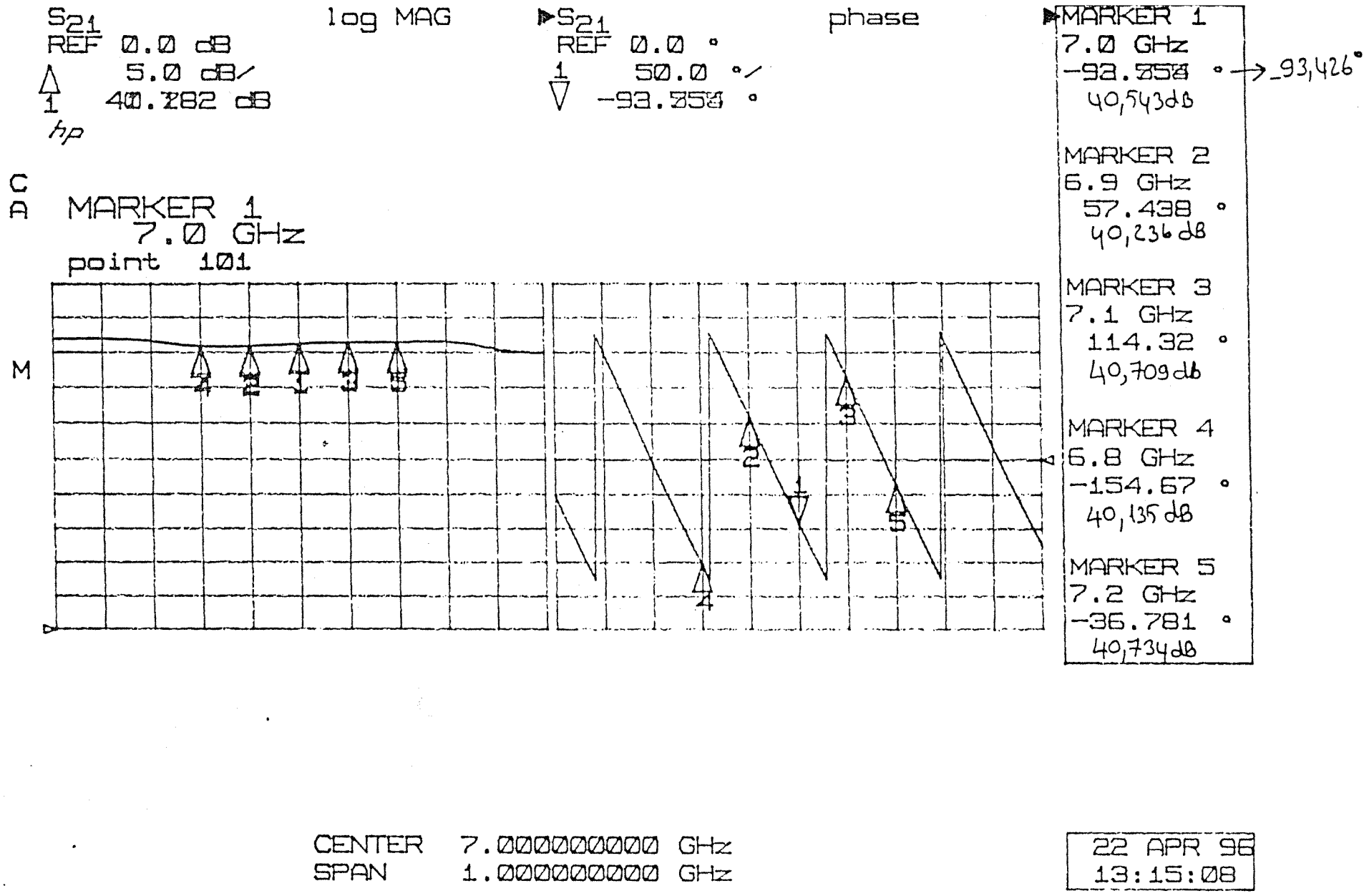

Figure A.2.6 Measured S-parameters: Q1 port

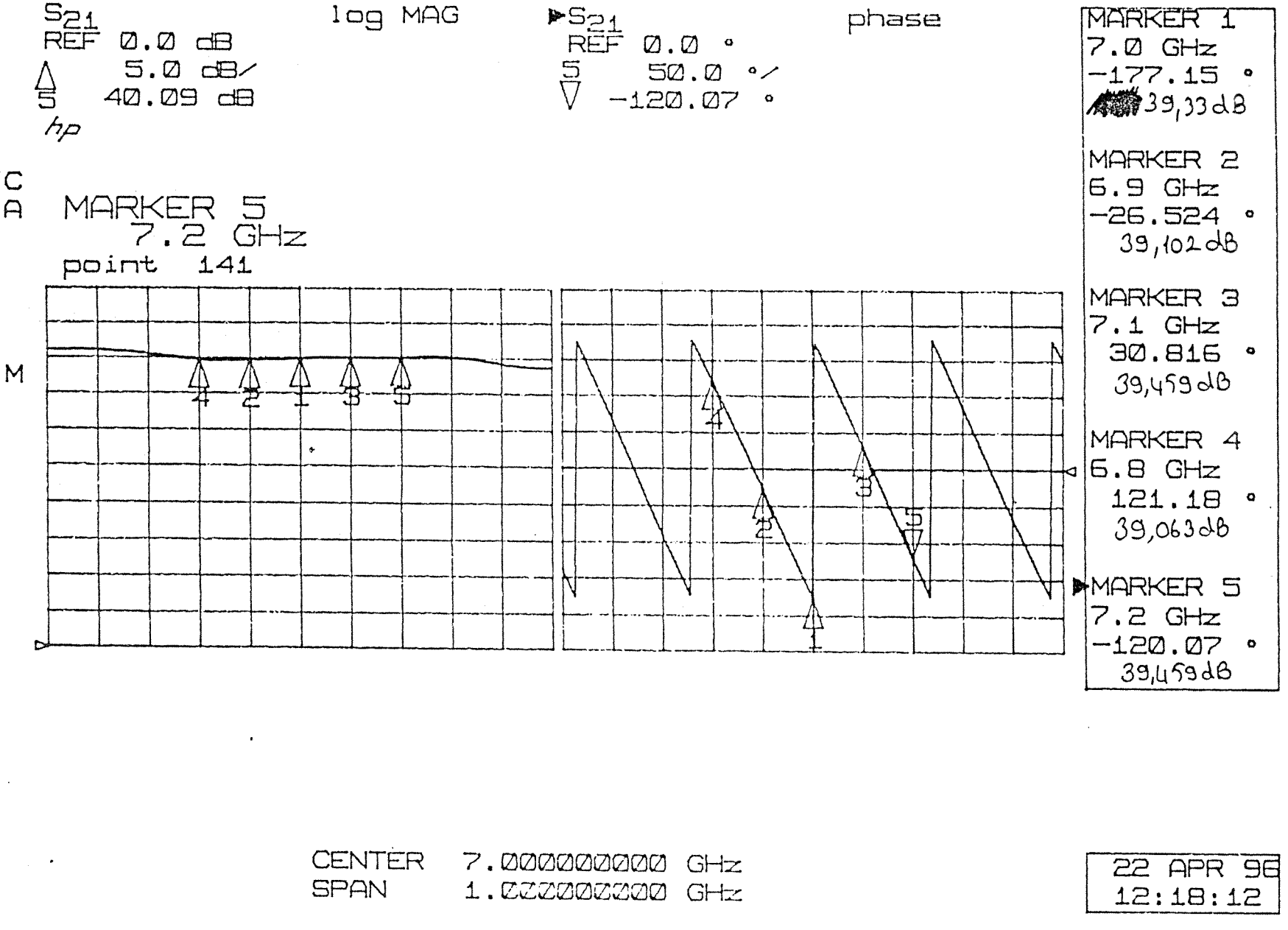

Figure A.2.7 Measured S-parameters: I1 port

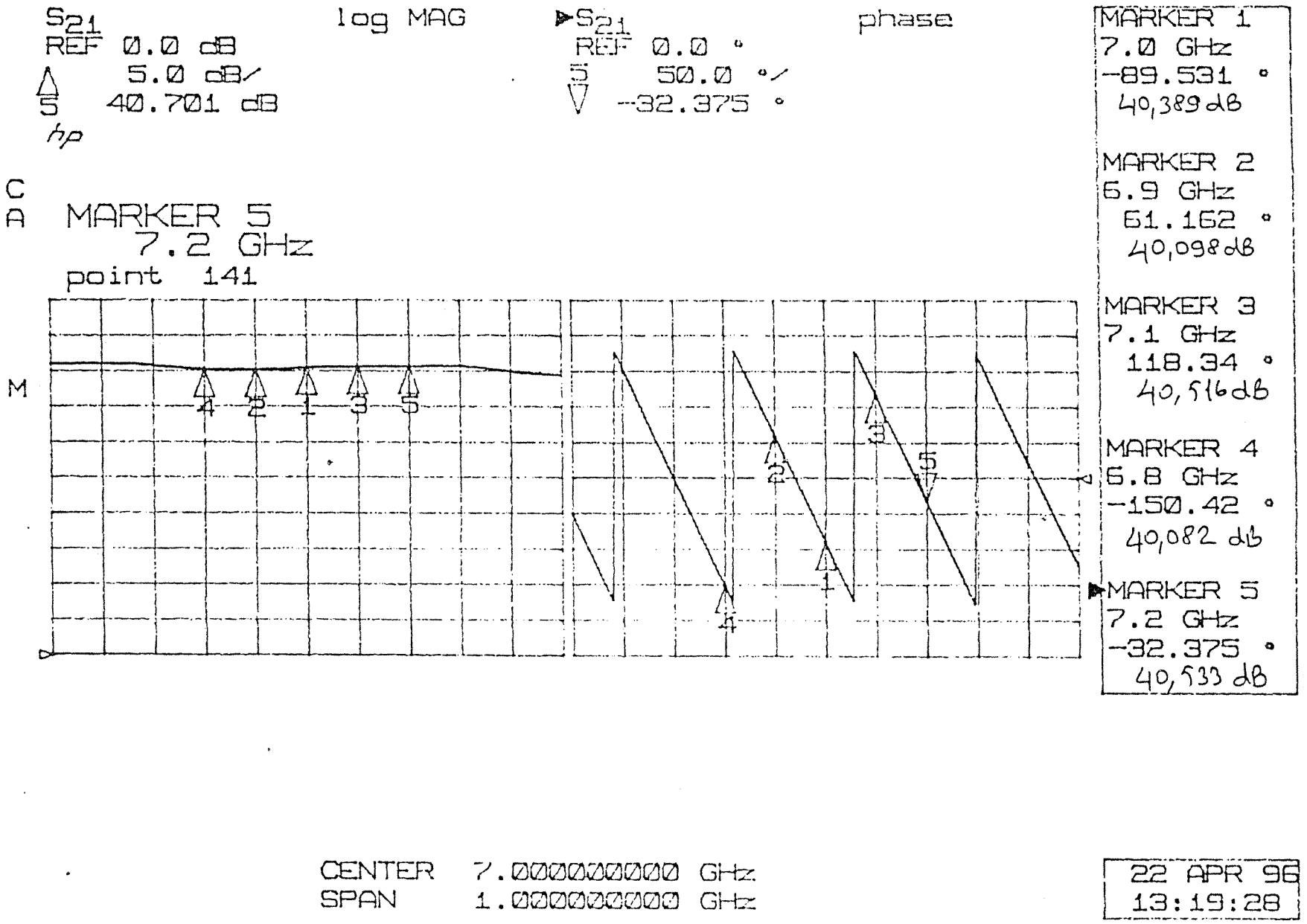

Figure A.2.8 Measured S-parameters: Q2 port

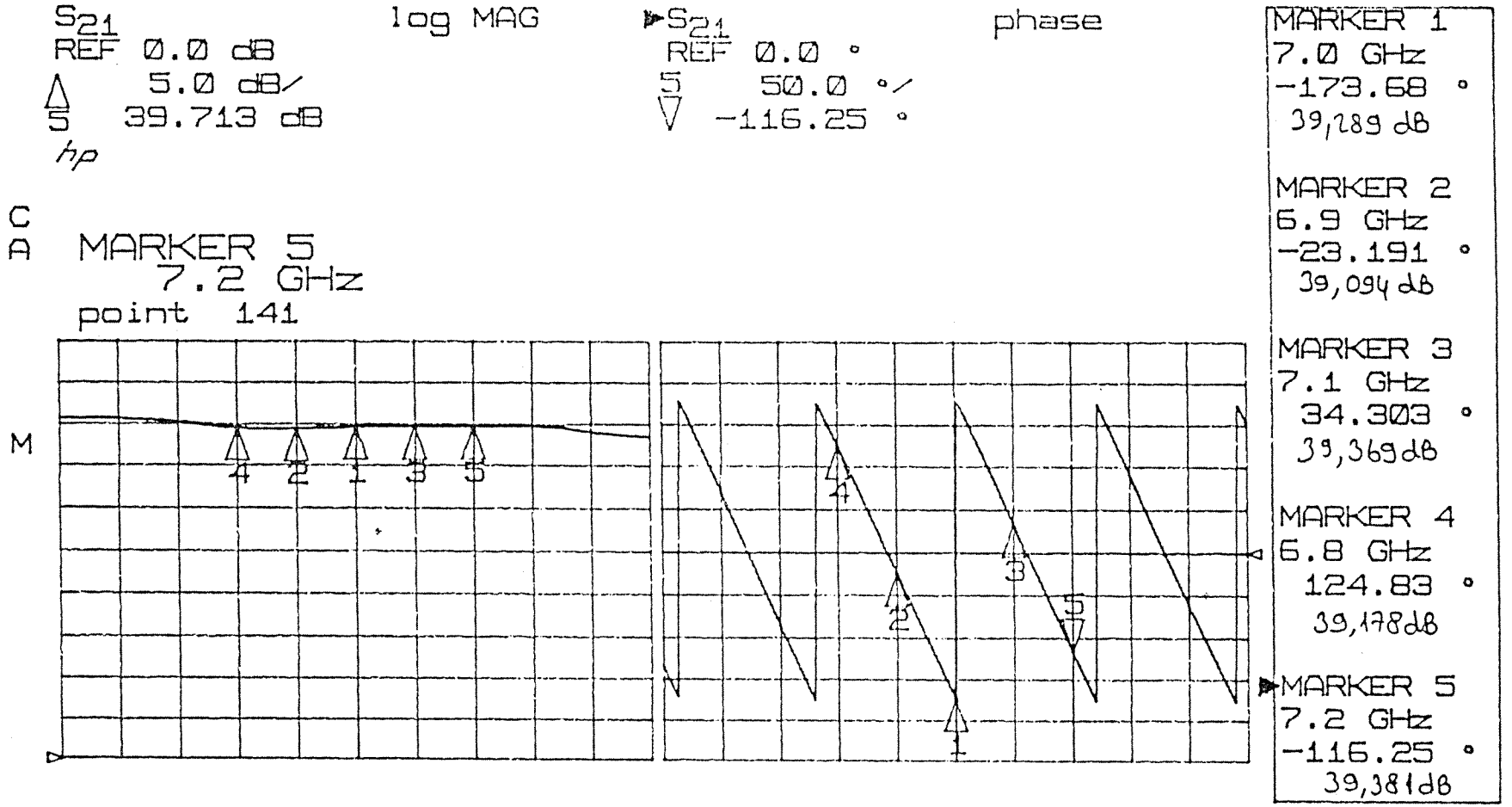

Figure A.2.9 Measured S-parameters: I2 port

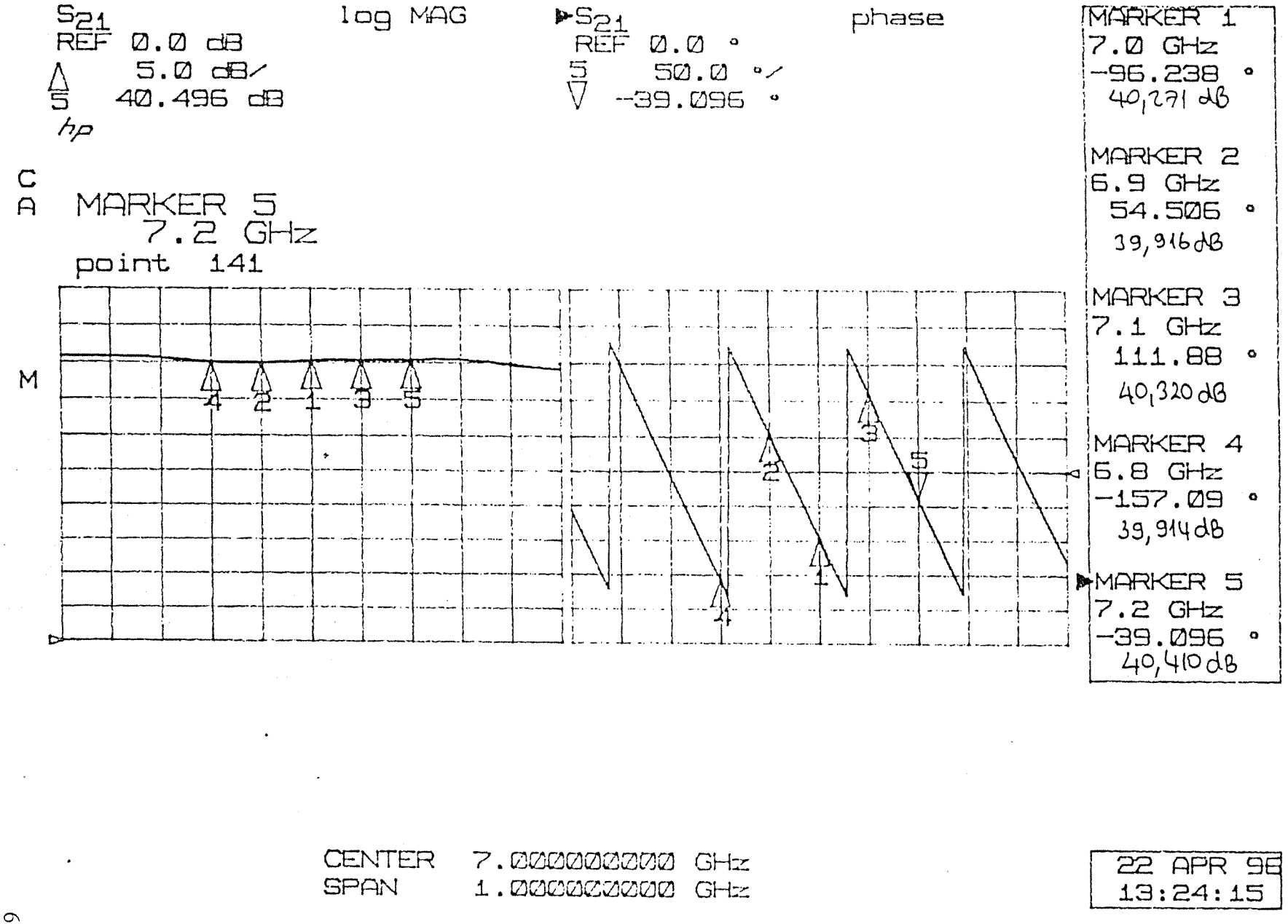

Figure A.2.10 Measured S-parameters: Q3 port

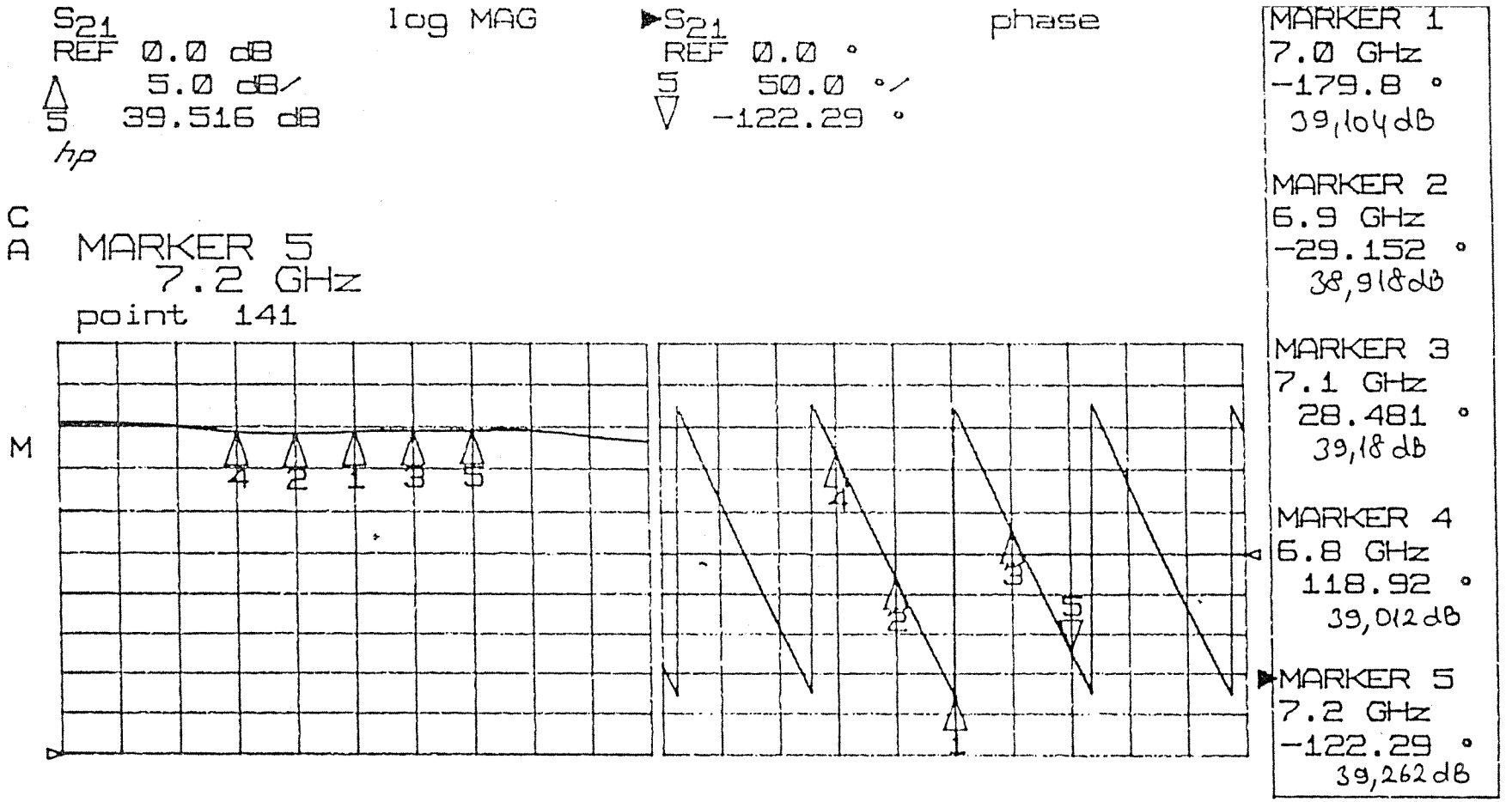

Figure A.2.11 Measured S-parameters: I3 port

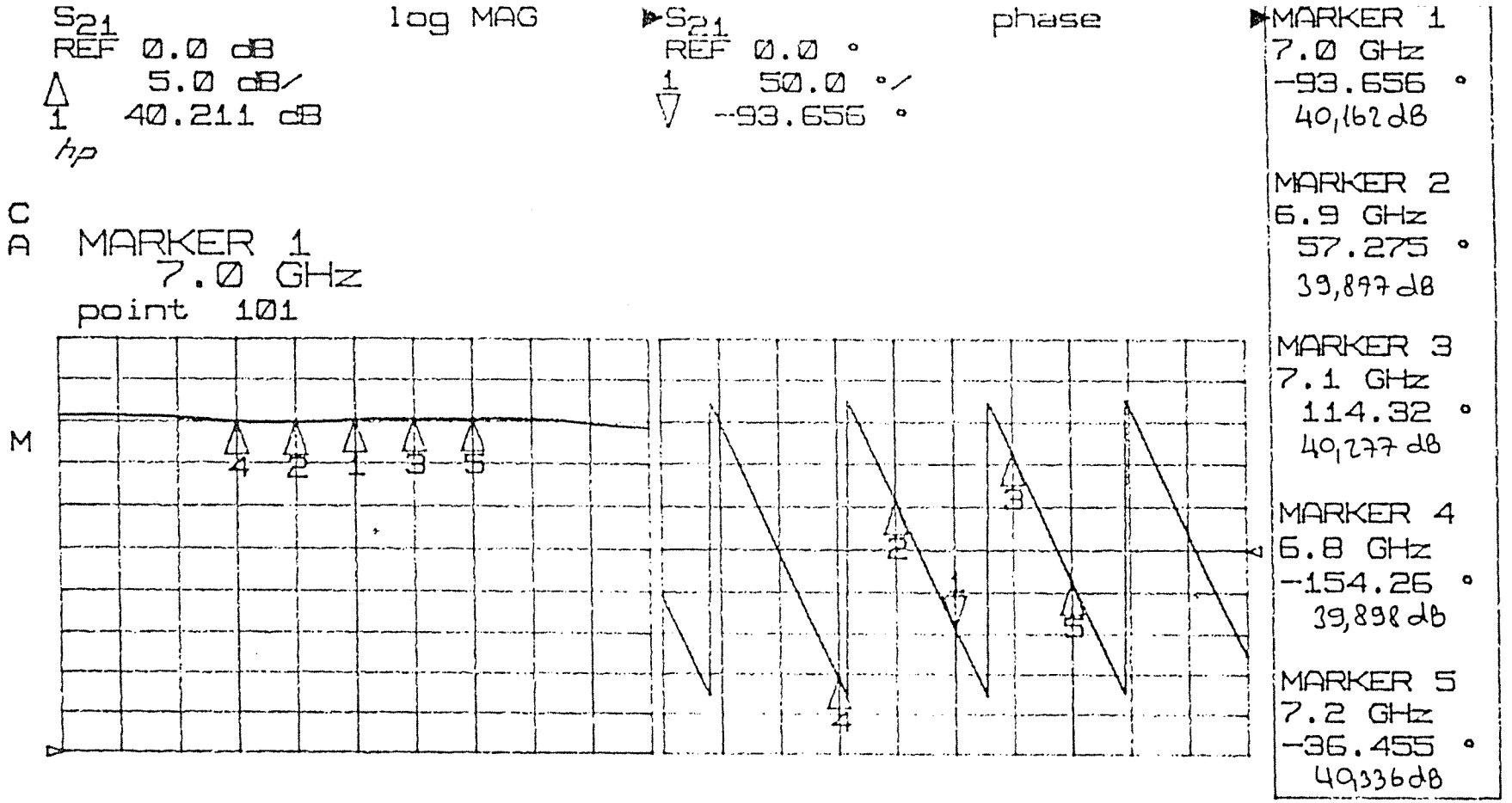

Figure A.2.12 Measured S-parameters: Q4 port

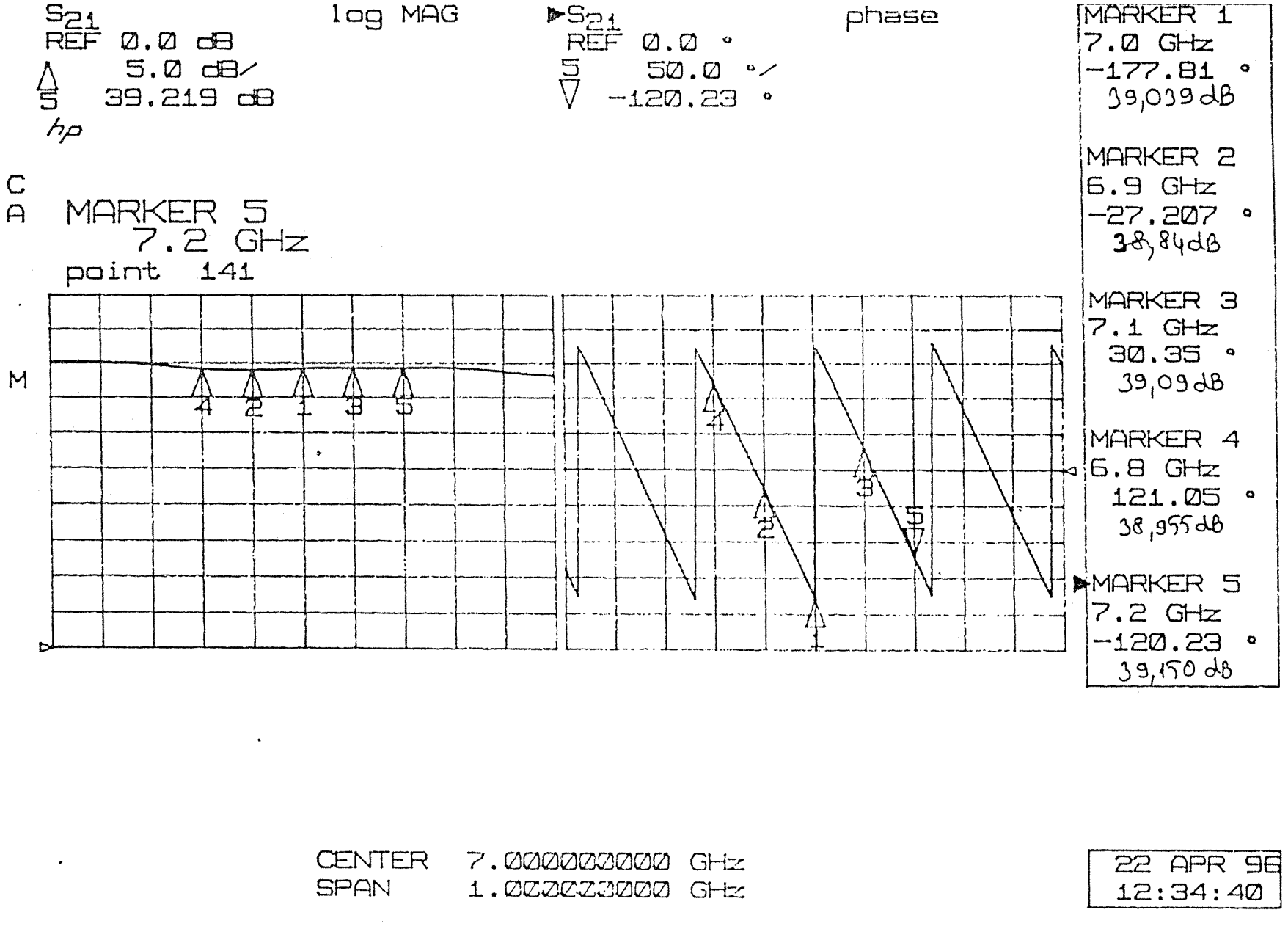

Figure A.2.13 Measured S-parameters: I4 port

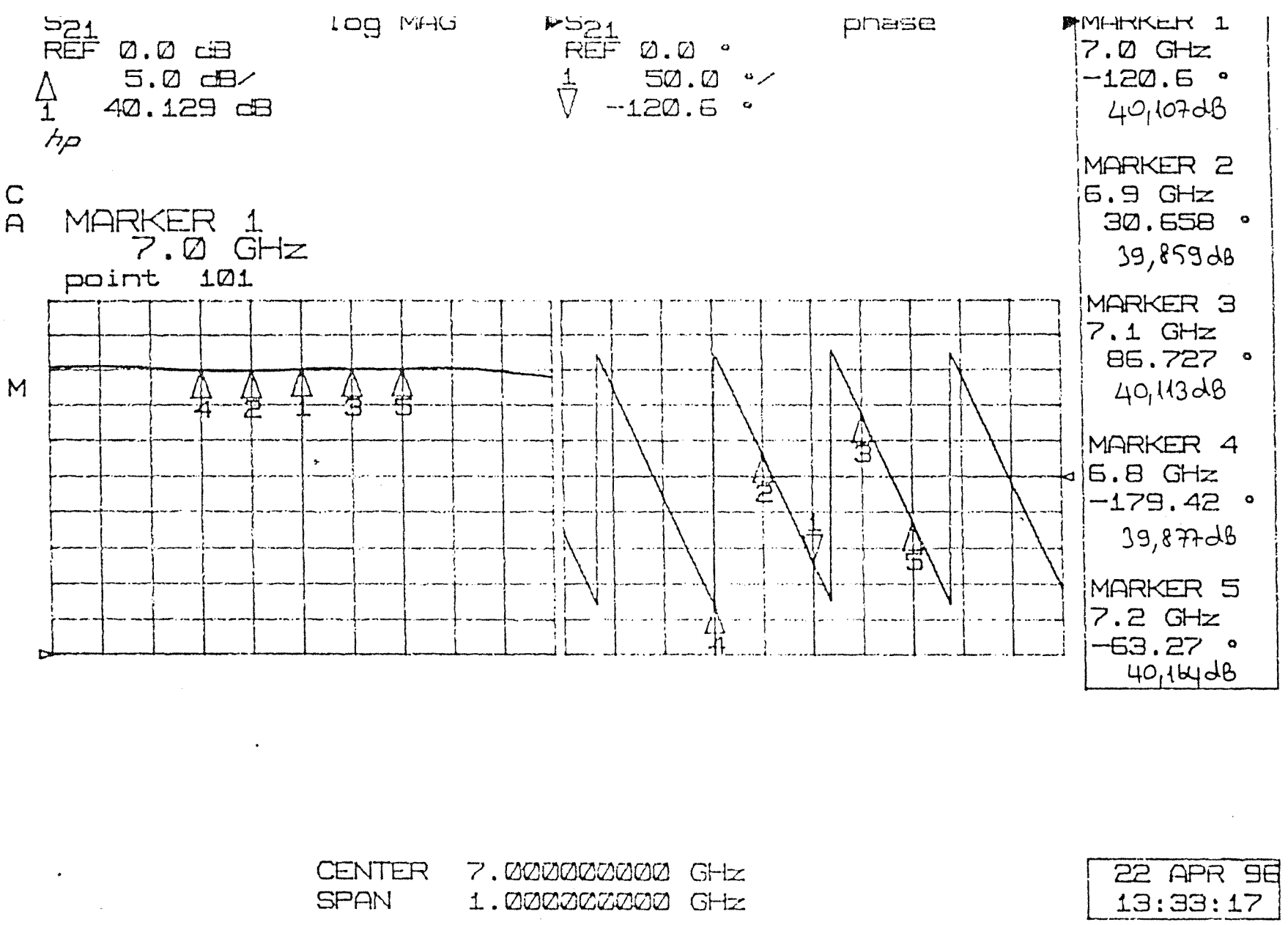

Figure A.2.14 Measured S-parameters: Q5 port

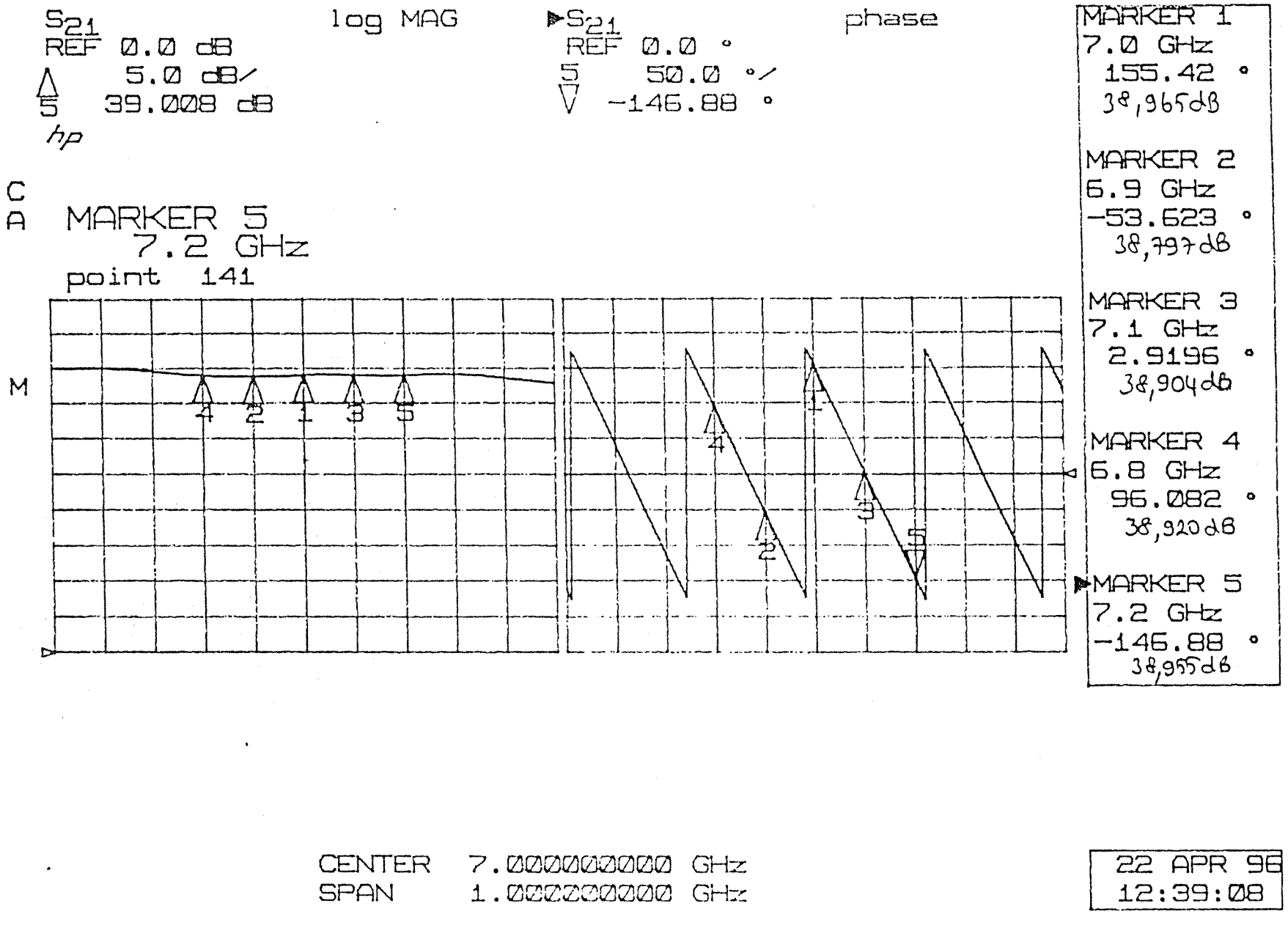

Figure A.2.15 Measured S-parameters: I5 port

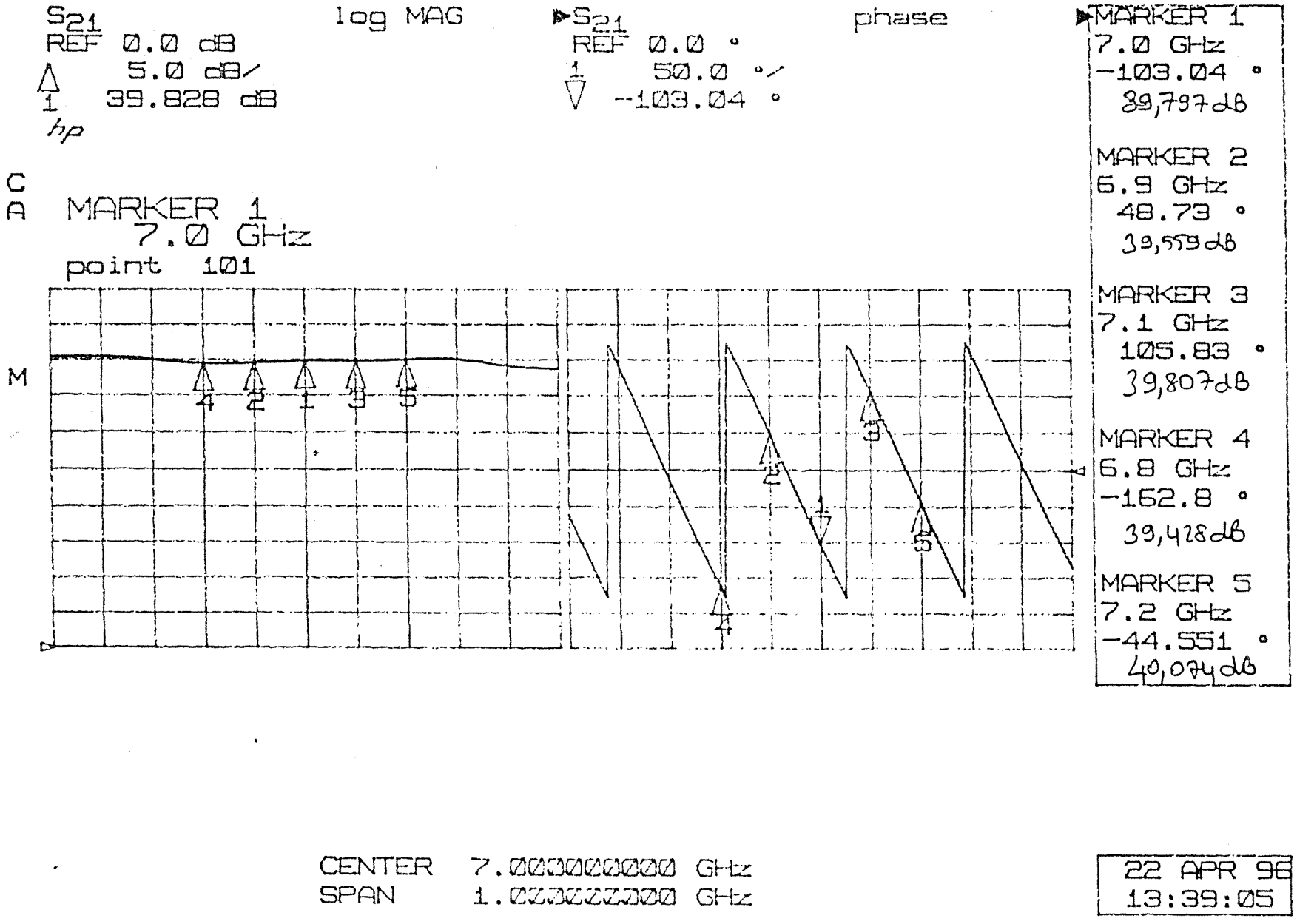

Figure A.2.16 Measured S-parameters: Q6 port

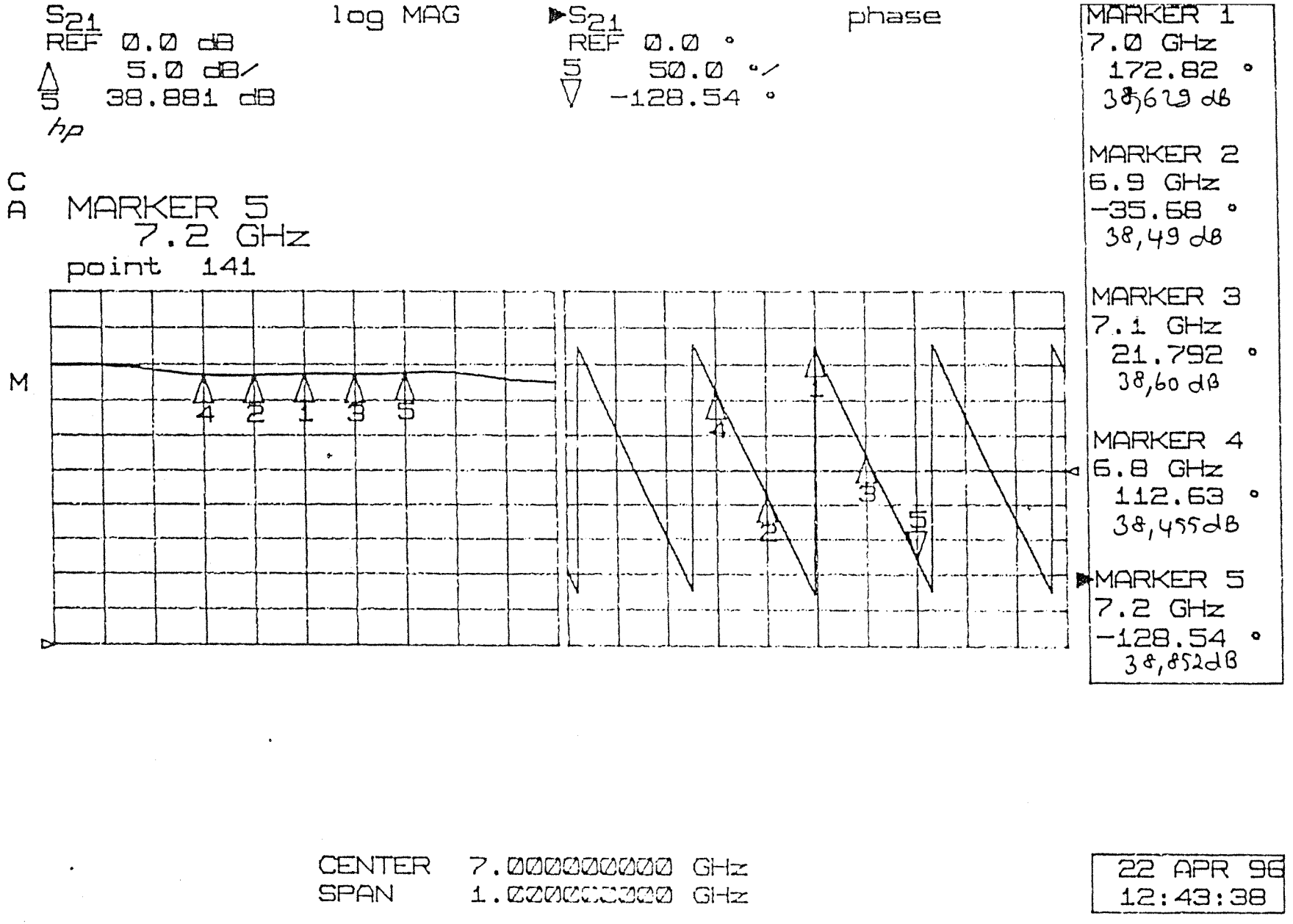

Figure A.2.17 Measured S-parameters: I6 port

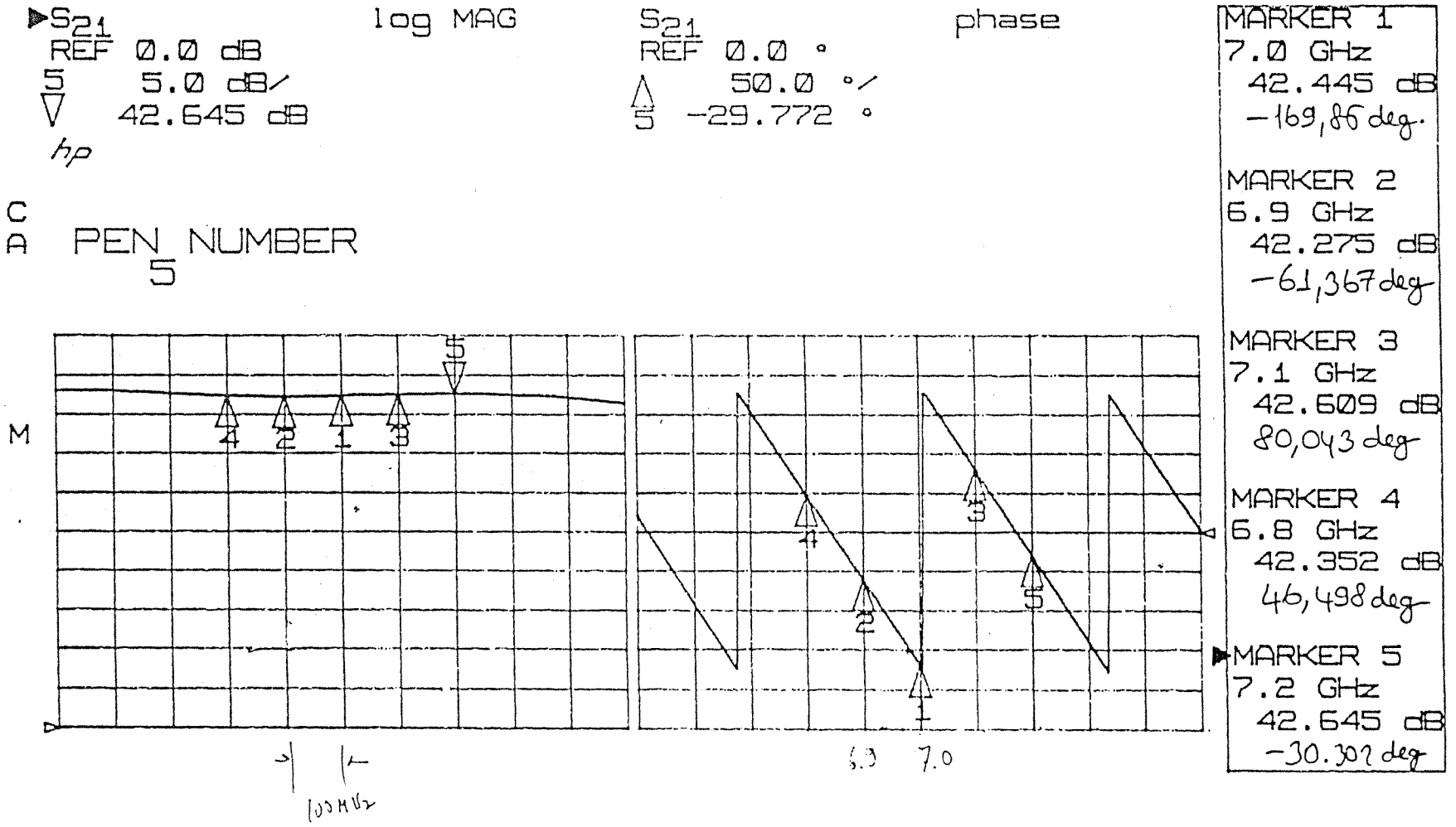

Figure A.2.18 Measured S-parameters: A7

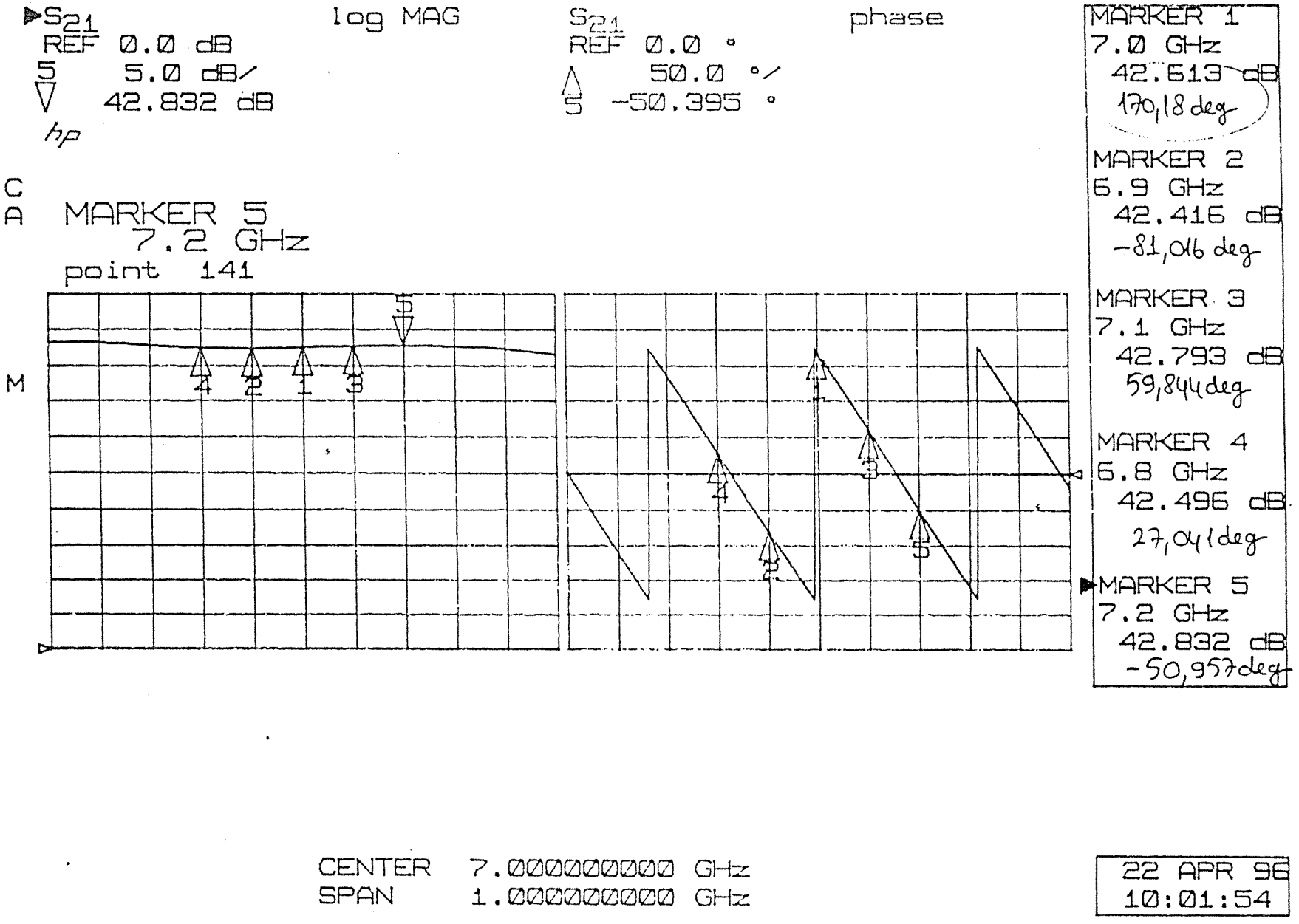

Figure A.2.19 Measured S-parameters: B7

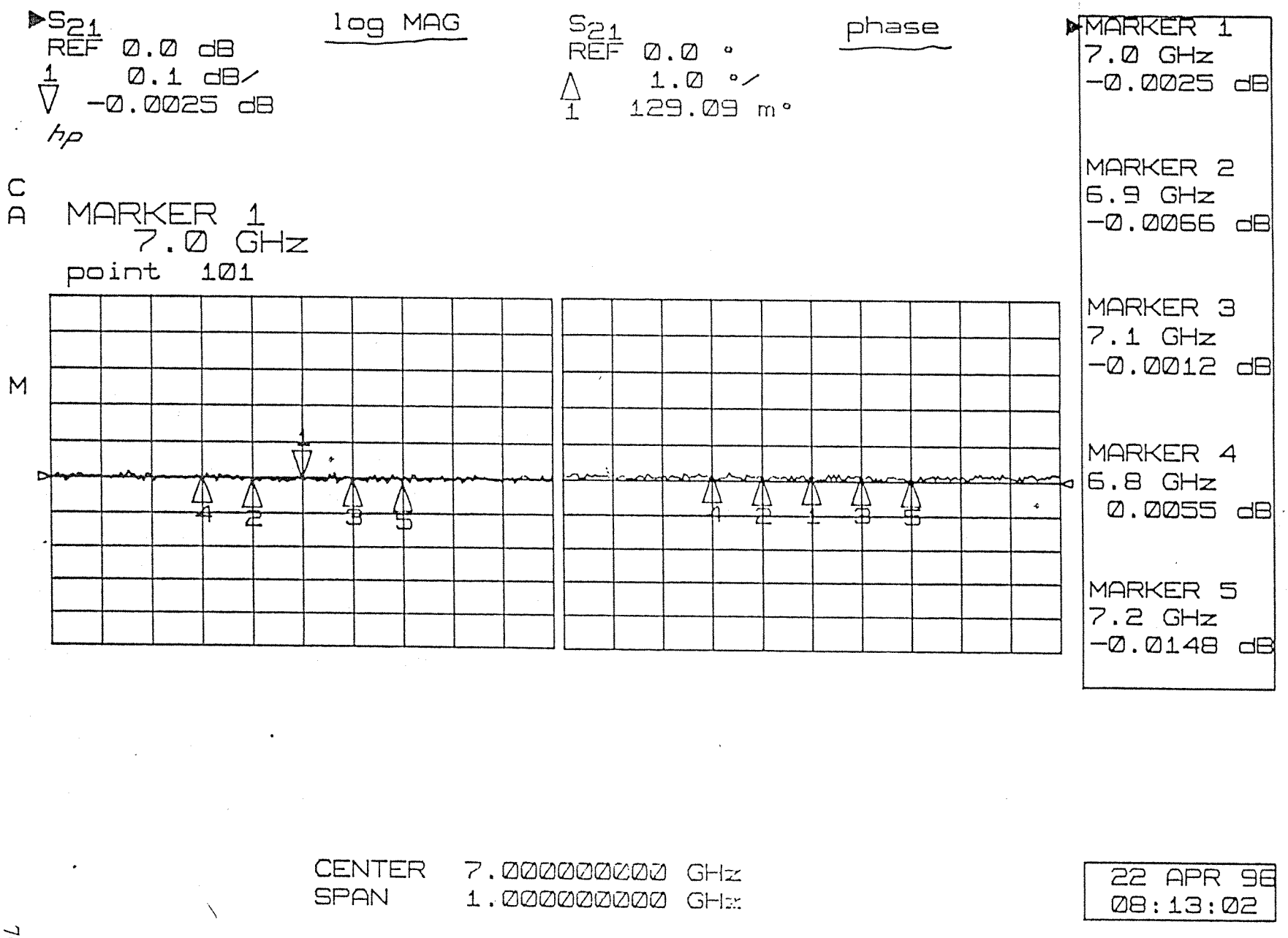

Figure A.2.20 Calibration accuracy.

$$V_{Ii}^{o} = \underbrace{k_I |V_7||S_{A7}||V_i||S_{Ii}|}_{|V_{Ii}^{o}|} \cos\left(\underbrace{\phi_i + \psi_{Ii} - \phi_7 - \psi_{A7}}_{\upsilon_{Ii}}\right)$$

$$V_{Qi}^{o} = \underbrace{k_Q |V_7||S_{B7}||V_i||S_{Qi}|}_{|V_{Qi}^{o}|} \cos\left(\underbrace{\phi_i + \psi_{Qi} - \phi_7 - \psi_{B7}}_{\upsilon_{Qi}}\right).$$

In our laboratory conditions, the incoming wave is assumed as a spherical wave. Spherical wave model and the receiving array is shown in Fig. A.2.21. The 3rd element of the array is assumed at the origin. Distance from 3rd element to the phase center of the transmitting antenna is h and the angle between y-axis and R_3 =h is θ.

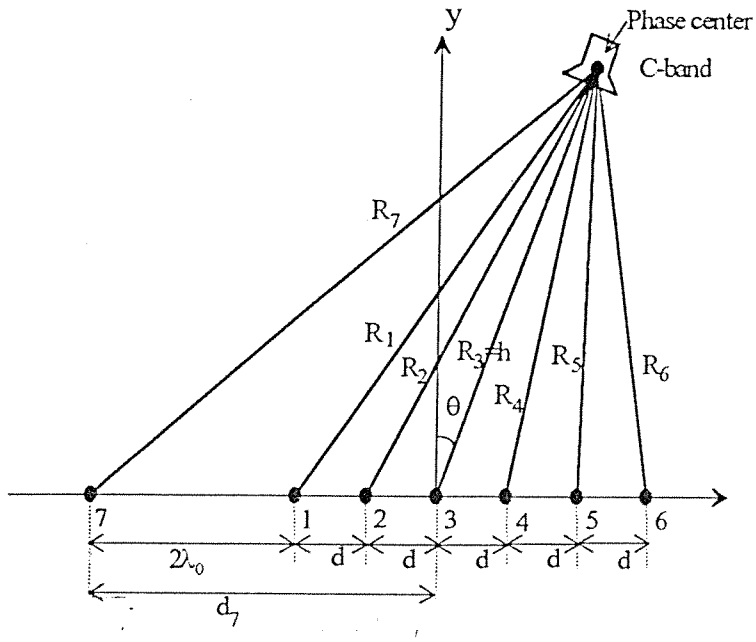

Figure A.2.21 Spherical wave model of the incident wave

Distance from the reference antenna to the phase center of the transmitting antenna is given by

$$R_7 = \left(d_7^2 + h^2 + 2d_7 h \sin\theta\right)^{1/2}.$$

Distance of the i'th element to the phase center is given by

$$R_i = \left[(3-i)^2 d^2 + h^2 + 2(3-i) d h \sin\theta\right]^{1/2}, \qquad \forall i.$$

$$\cos\upsilon_I(i) = \cos\left(\phi_i - \phi_7 + \psi_I(i) - \psi_{A7}\right)$$

$$\cos\upsilon_Q(i) = \cos\left(\phi_i - \phi_7 + \psi_Q(i) - \psi_{B7}\right)$$

Let

$$\gamma_i = \phi_i - \phi_7 = -k_0(R_i - R_7)$$

Since $d_7 << h$, then

$$R_7 \approx \left(d_7^2 + h^2\right)^{1/2} + \frac{d_7 h}{\sqrt{d_7^2 + h^2}} \sin\theta.$$

Similarly $|3-i|d << h$, then d_7 can be replaced by $|3-i|d$, and R_i becomes

$$R_i = \left[(3-i)^2 d^2 + h^2\right]^{1/2} + \frac{(3-i)dh}{\sqrt{(3-i)^2 d^2 + h^2}} \sin\theta \quad .$$

Then

$$R_i - R_7 \cong P_i + S_i \sin\theta$$

and

$$\gamma_i = -k_0 P_i - k_0 S_i \sin\theta$$

where

$$P_i = \sqrt{(3-i)^2 d^2 + h^2} - \sqrt{d_7^2 + h^2}$$

$$S_i = \frac{(3-i)\,d\,h}{\sqrt{(3-i)^2 d^2 + h^2}} - \frac{d_7 h}{\sqrt{d_7^2 + h^2}} \quad .$$

Then following manipulations are made to find θ_i

$$\gamma_i(\theta) = -k_0(R_i - R_7)$$

$$N_i(\theta) = \tan\gamma_i(\theta) = \tan[\gamma_i(\theta) - n\pi] \qquad , n = 0,\ \pm 1,\ \pm 2, ..$$

$$\gamma_i(\theta) = \tan^{-1}[N_i(\theta)] + n\pi$$

$$\theta_i = \sin^{-1}\left[\frac{\tan^{-1}N_i(\theta) + n\pi + k_0 P_i}{-k_0 S_i}\right],\ n = 0,\ \pm 1,\ \pm 2, ..$$

The above equation will be different for each element of the antenna array and hence six different equations will be obtained. Each equation will yield many solutions for θ and only one of them will be correct. Comparing all of the six set of solutions, one should be able to determine the actual solution, since only the actual solution will exist in all of the solution sets. This can be done by a computer program.

Mixer Characterization

To characterize mixers, nonlinear model is used.

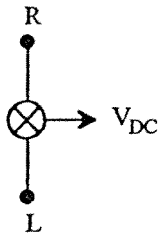

$$V_{DC} = k\,V_L\,V_R\,\cos(\phi_L - \phi_R) + \alpha|V_L|^2 + \beta|V_R|^2 \quad ,$$

k, α, β for I and Q components are the unknowns to be determined. Then V_{Ii} and V_{Qi} are expressed by

$$V_{Ii} = k_I V_0^2 |S_{A7}||S_{Ii}|\cos\upsilon_{Ii} + \alpha_I V_0^2 |S_{A7}|^2 + \beta_I V_0^2 |S_{Ii}|^2$$

$$V_{Qi} = k_Q V_0^2 |S_{B7}||S_{Qi}|\cos\upsilon_{Qi} + \alpha_Q V_0^2 |S_{B7}|^2 + \beta_Q V_0^2 |S_{Qi}|^2 \quad .$$

We define M_i as the ratio of V_{Ii} and V_{Qi} as

$$M_i = \frac{p\cos\upsilon_{Ii} + s}{\cos\upsilon_{Qi} + q}$$

where

$$p = \frac{k_I}{k_Q}\frac{|S_{A7}||S_{Ii}|}{|S_{B7}||S_{Qi}|},\quad s = \frac{\alpha_I|S_{A7}|^2 + \beta_I|S_{Ii}|^2}{k_Q|S_{B7}||S_{Qi}|},\quad q = \frac{\alpha_Q|S_{B7}|^2 + \beta_Q|S_{Qi}|^2}{k_Q|S_{B7}||S_{Qi}|}.$$

Then,

$$M = \frac{p\cos(\gamma + a) + s}{\cos(\gamma + b) + q} \quad .$$

After some algebraic manipulations and rearragenements s/p and q/p ratios are found as

$$\frac{s}{p} = \frac{\alpha_I}{k_I}\frac{|S_{A7}|}{|S_{Ii}|} + \frac{\beta_I}{k_I}\frac{|S_{Ii}|}{|S_{A7}|} \quad ,$$

$$\frac{q}{p} = \frac{\alpha_Q}{k_I}\frac{|S_{B7}|^2}{|S_{A7}||S_{Ii}|} + \frac{\beta_Q}{k_I}\frac{|S_{Qi}|^2}{|S_{A7}||S_{Ii}|}.$$

To find θ_i, following steps must be followed beginning from the equation of M:

$$\underbrace{\frac{\frac{M}{p}\cos b - \cos a}{\frac{M}{p}\sin b - \sin a}}_{K}\cos\gamma = \sin\gamma + \underbrace{\frac{\frac{s}{p} - M\frac{q}{p}}{\frac{M}{p}\sin b - \sin a}}_{T}$$

$$\tan\gamma = \frac{K \pm T\sqrt{1 + K^2 - T^2}}{1 - T^2}$$

$$W = T\sqrt{1 + K^2 - T^2}$$

$$\tan\gamma = \frac{K \pm W}{1-T^2},\ \gamma = -k_0 P_i - k_0 S_i \sin\theta \quad .$$

Both signs are considered in the solution. Hence, solution for θ_i is given by

$$\theta_i = \sin^{-1}\left\{\frac{1}{-k_0 S_i}\left[\tan^{-1}\left(\frac{K \pm W}{1-T^2}\right) + n\pi + k_0 P_i\right]\right\},\ n = 0,\ \pm 1,\ \pm 2, ..$$

The precision in the calculation of the angle of arrival of the incoming signal is highly dependent on phase variations. Therefore, it is very important that the phase quantities are taken into account correctly.

2. Method

The other proposed calibration procedure is to calibrate the whole system at certain levels of signal strengths. In this procedure, V_{Ii} and V_{Qi} voltages for six antenna elements are measured for incoming signals coming from 0, $\pm 1^o$, $\pm 2^o$,.. at specific signal levels. Then, look-up table is formed from these data. Hence, for unknown incoming signal, the measured V_{Ii} and V_{Qi} values are compared with values in lokk-up table and the direction of arrival can be found. To make this calibration procedure independent from the strength of the incoing signal, limiting amplifiers can be used in this system.

Beamforming

By using the knowledge of the direction of the incoming signal we can apply a beamforming algorithm and steer either the null or the maximum to the desired direction.
Receiving array pattern in xz plane, including the y-polarized element pattern, can be written as

$$f(\theta) = f_e(\theta) \sum_{n=1}^{6} \alpha_n e^{jkd(n-3)\sin\theta} \quad .$$

Measured response of the array in I and Q channels are $V_{In}(\theta)$ and $V_{Qn}(\theta)$. We shall combine these voltages as

$$\sum_{n=1}^{6} a_n V_{In}(\theta) + jb_n V_{Qn}(\theta) = f_b,\ -\frac{\pi}{2} \le \theta \le \frac{\pi}{2}$$

$f_b(\theta)$ is the synthesized pattern.
Fourier series expansion of $f_b(\theta)$ is given by

$$f_b(\theta) = \sum_{n=-\infty}^{\infty} c_m e^{j},\ c_m = \frac{1}{2\pi}\int_0^{2\pi} f_b(\theta) e^{-jm\theta}\, d\theta$$

Then

$$c_m = \sum_{n=1}^{6} a_n \underbrace{\left[\frac{1}{2\pi}\int_o^{2\pi} V_{In}(\theta) e^{-jm\theta}\, d\theta\right]}_{I_{mn}} + \sum_{n=1}^{6} b_n \underbrace{\left[\frac{j}{2\pi}\int_o^{2\pi} V_{Qn}(\theta) e^{-jm\theta}\, d\theta\right]}_{Q_{mn}}$$

$$c_m = \sum_{n=1}^{6} I_{mn} a_n + \sum_{n=1}^{6} Q_n$$

$$\begin{bmatrix} c_1 \\ \cdot \\ \cdot \\ c_{12} \end{bmatrix} = \begin{bmatrix} I_{1,1} & \cdot & \cdot & I_{1,6} \\ \cdot & \cdot & \cdot & \cdot \\ \cdot & \cdot & \cdot & \cdot \\ I_{12,1} & \cdot & \cdot & I_{12,6} \end{bmatrix} \begin{bmatrix} a_1 \\ \cdot \\ \cdot \\ a_6 \end{bmatrix} + \begin{bmatrix} Q_{1,1} & \cdot & \cdot & Q_{1,6} \\ \cdot & \cdot & \cdot & \cdot \\ \cdot & \cdot & \cdot & \cdot \\ Q_{12,1} & \cdot & \cdot & Q_{12,6} \end{bmatrix} \begin{bmatrix} b_1 \\ \cdot \\ \cdot \\ b_6 \end{bmatrix}$$

$$[C] = \underbrace{\begin{bmatrix} I & Q \end{bmatrix}}_{[S]} [x]$$

$[x] = [S]^{-1}[C]$ gives the required coefficient (weigths) for the synthesized pattern.

Finding c_m 's

For an equispaced linear array, let $f_b(\theta) = \sum_{n=1}^{6} \alpha_n e^{jk_0(n-3)\epsilon}$ be the given synthesized pattern. Then c_m's can be found by

$$c_m = \frac{1}{2\pi} \sum_{n=1}^{6} \alpha_n \int_0^{2\pi} e^{jk_0(n-3)d \sin\theta - jm\theta} d\theta \quad .$$

Conclusion

The smart antenna system is in line with the COST 245 activity, as well as with the follow-up COST project, due to its capability of forming adaptive beams by digital electronics and computer software. A prototype is built and tested in the microwave research laboratory of our Department; the early results are promising, however, much more work remains to be done in this prosperous field.

B- MONOLITHIC MICROWAVE INTEGRATED CIRCUIT DESIGNS

Introduction

"Monolithic Microwave Integrated Circuit", MMIC, can be defined as the implementation of a microwave circuit using a single semi-insulating substrate on which all active and passive circuit elements or components and interconnections are formed by some deposition scheme such as epitaxy, ion implantation, evaporation, diffusion or a combination of these processes and others. The MMIC technology can be considered roughly the microwave equivalent of the low frequency integrated circuit technology which has a direct effect on the development of the low cost, efficient, reliable and compact electronic equipment.

In the last 20 years there has been a tremendous work for the monolithic integration of microwave circuits because of the following inherent advantages:

- Low cost,
- Small size and light weight,
- Design flexibility,
- High reliability,
- Reproducibility,
- Broadband performance.

MMIC's find many applications in various microwave systems. The concept of active microwave antenna array is particularly attractive for radar and satellite applications. Such an array involves the use of active devices combined with each array element, or with each small subarray, for the purpose of microwave power generation, phase shifting or receiving. In a large active antenna array the use of MMIC elements will certainly introduce additional advantages due to their small size, low cost, repeatability and easy integration with the radiating and feed elements.

With the above advantages in mind, various MMIC's have been designed, implemented and tested within the framework of this project. Designs and optimizations of all the circuits are achieved using CAD tools of LIBRA and ACADEMY software packages. The designs are carried out according to GEC-Marconi F20 process rules with an objective of minimizing the chip area. The chips were manufactured through EUROCHIP. The measurements on the manufactured chips were carried out using probe stations and network analysers at Bilkent University Physics Department; Aselsan; GEC Marconi, England and University of Massachuttes at Amherst, USA.

The MMIC chips that are designed in various functional areas are as follows:

1- Narrow and Wideband Amplifiers
2- Voltage Controlled Oscillator
3- Mixer
4- Low Noise Amplifier
5- Transmit/Receive Switch
6- Power Amplifier
7- Wideband Voltage Variable Attenuator
8- Phase Shifter

In the following sections these circuits will be briefly explained. For more detailed information, the previous progress reports may be resorted.

B1. NARROW AND WIDEBAND AMPLIFIERS

In the design of these amplifiers, the following criteria are considered:

a) The input and output return losses,
b) The gain,
c) The bandwidth.

The choice of the transistors for MMIC applications up to 20 GHz is the MESFET. All the circuit components including MESFET's are the F20 Marconi Plessy Foundry elements. The transistor employed in the amplifiers is a MESFET with 0.5μm gate length and 6x50μm gate width. The quiescent current is %100 I_{DSS}.

Three amplifier topologies are used: i) one-stage and ii) two-stage 3-8 GHz wideband, iii) 10% bandwidth around 10.5 GHz. For the wide band amplifiers negative feedback is incorporated. The DC biasing circuits are R-C type. To obtain high gain, wide bandwidth and low return loss, optimization methods, which are available in LIBRA, are employed. The circuit diagrams of these amplifiers with the component values obtained after optimization are shown in Fig. B1.1. The narrowband amplifier is designed with the aim of obtaining highest gain from the smallest chip area.

After obtaining the satisfactory results from simulation of schematic circuits, layout of the amplifiers are prepared using ACADEMY. While doing so, maximum care is taken to avoid coupling between the adjacent lines and to occupy the minimum possible chip area. Fig. B1.2 shows the layouts of the three amplifiers placed on the same chip. The overall chip area is about 1.4x1.8mm^2.

The design objectives of the single-stage amplifier were:

- 6dB gain in 0.1-8 GHz band,
- Minimum -10dB return loss for both input and output ports in 3-8 GHz.
- %100 I_{DSS} for the transistor is 45 mA. However, the manufacturer states that this value could be anywhere between 30-60 mA. The measured value of the current under 5V drain to source voltage was 50 mA.

About ten identical chips were supplied by the foundry. These were labeled as C1, C2,....etc. Measurements were carried out on many of these chips. The results showed that repeatability was excellent. Fig. B1.3 shows the simulation and measurement results for chip number 1 under 5 V drain to source voltage (i.e., C1/5V). As is seen from the figure the agreement between the simulation and measurement results is very good, especially in the band 0.5-6 GHz.

The design objectives of the two-stage amplifier were:

- 14dB gain in 3-8 GHz band,
- Minimum -12dB return loss for both input and output ports in 3-8 GHz.- Total measured current for the two transistors under 5V drain to source voltage was 100mA as expected.

Fig. B1.4 shows The simulation and measurement results of two-stage amplifier. The agreement, again, is very good except for output return loss, S_{22}, at frequencies greater than 6 GHz.

As a final conclusion it can be said that the agreement between the simulation and measurement results is good for both amplifiers. The discrepancy for return losses were attributed to the compact placements of components which might have caused coupling between the adjacent components. These coupling effects are not taken into account during simulation.

REFERENCES

[1] R. Soares, "GaAs MESFET Circuit Design", Artech House, Boston & London, 1988.

[2] T.T. Ha, "Solid State Microwave Amplifier Design", Wiley & Son, New York, 1981.

[3] GaAs IC Foundry Design Process F20/F14 GEC Marconi, 1993.

[4] K. B. Niclas, "Multioctave Performance of Single Ended Microwave Solid State Amplifiers", IEEE Transactions on Microwave Theory and Techniques, vol. MTT-32, p. 896, 1984.

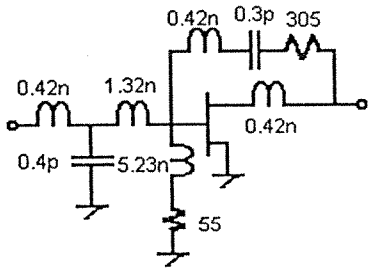

One-Stage Amplifier

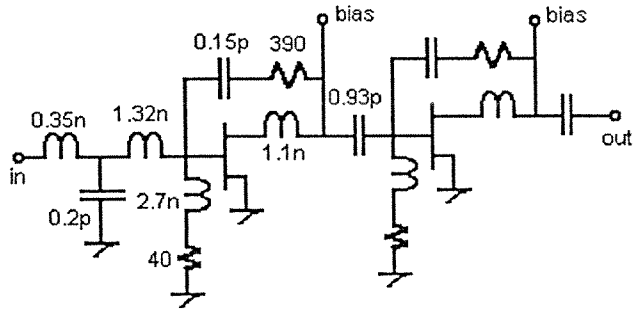

Two-Stage Amplifier

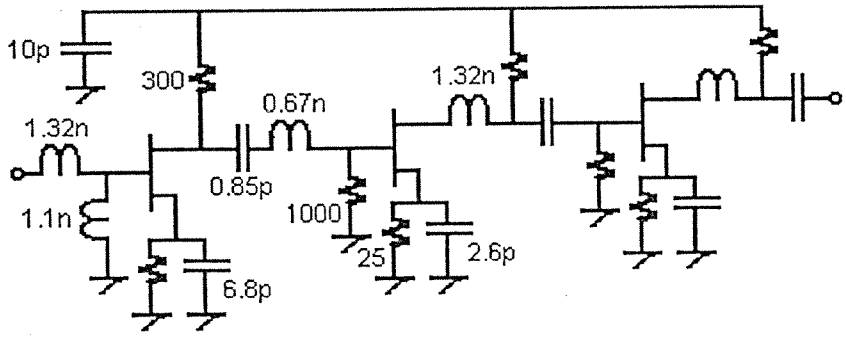

Narrowband Amplifier

Figure B1.1 Circuit Diagrams of the Amplifiers and Component Values

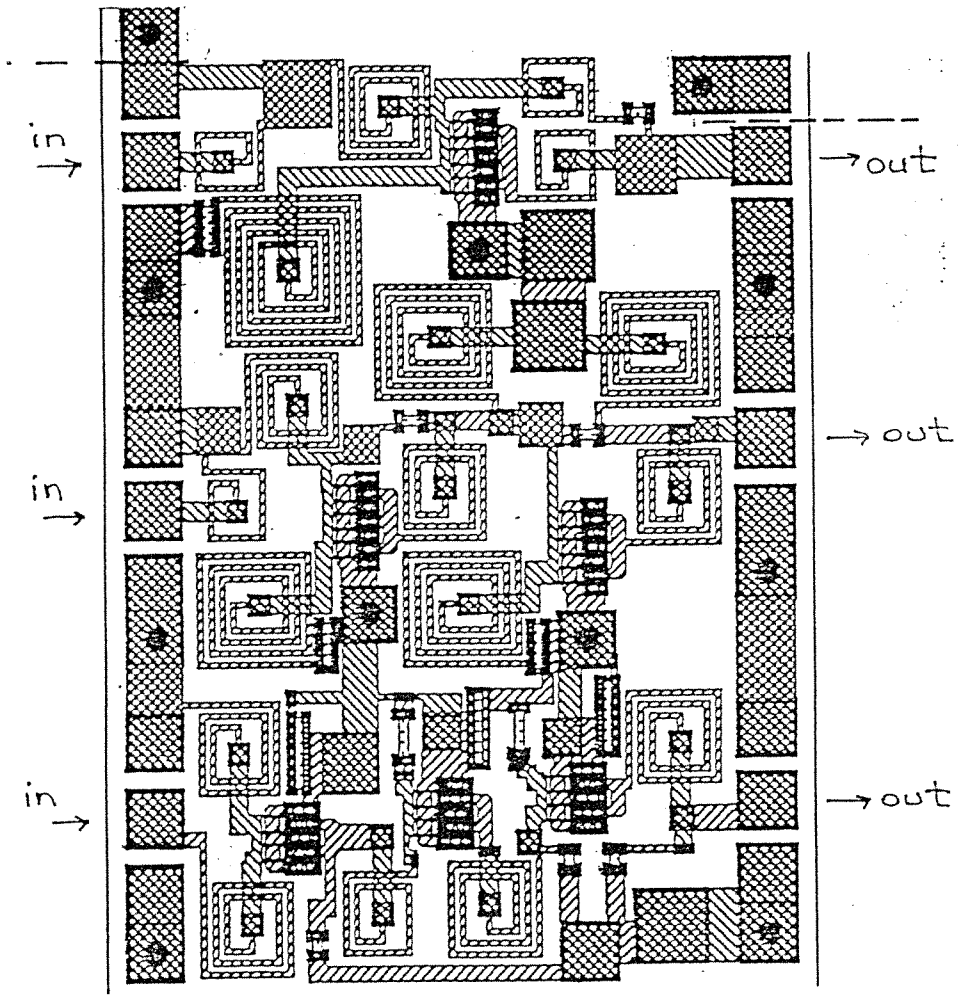

Figure B1.2 MMIC Layout of the Three Amplifiers

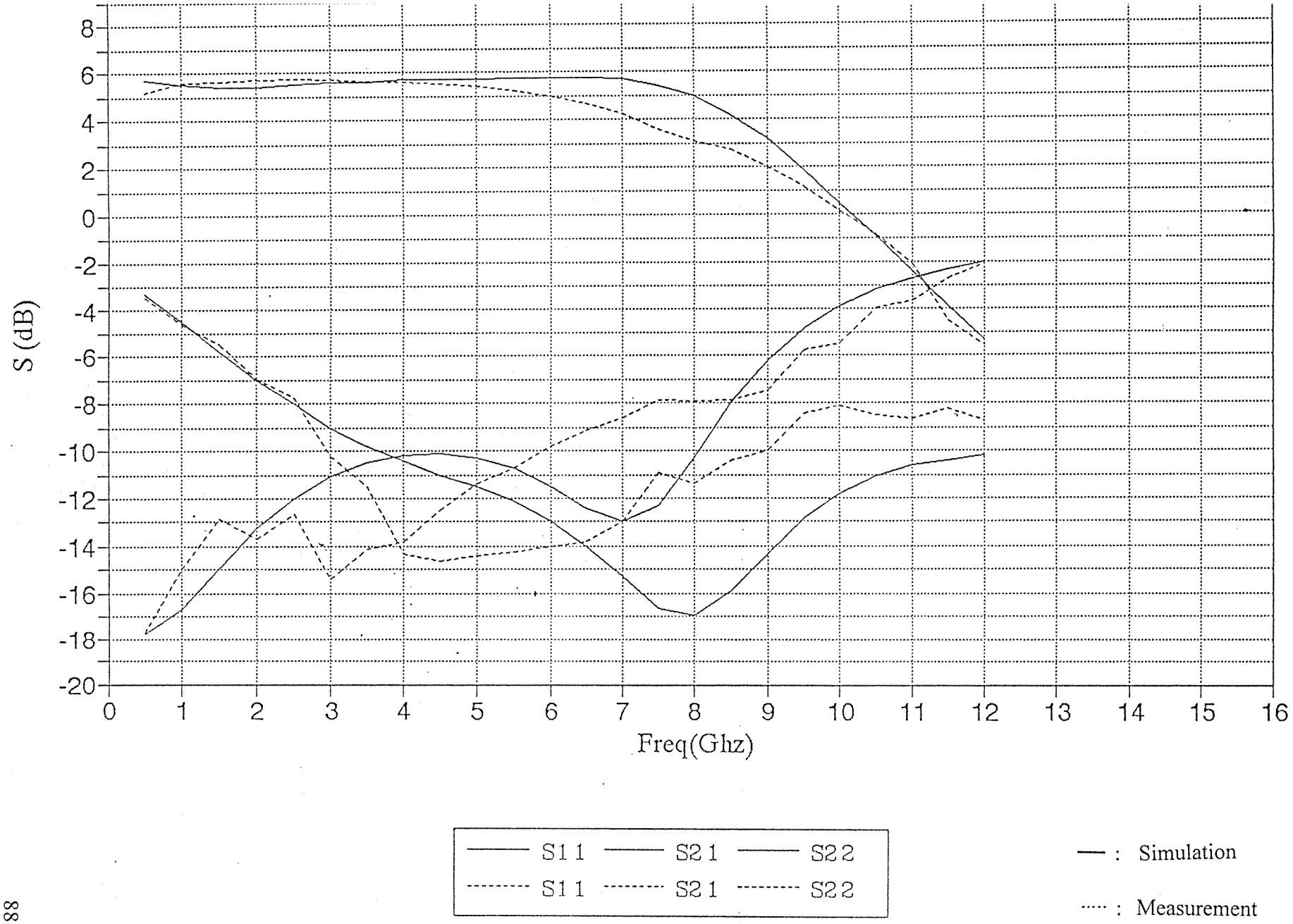

Figure B1.3 Simulation and Measurement Results of the One-Stage Amplifier

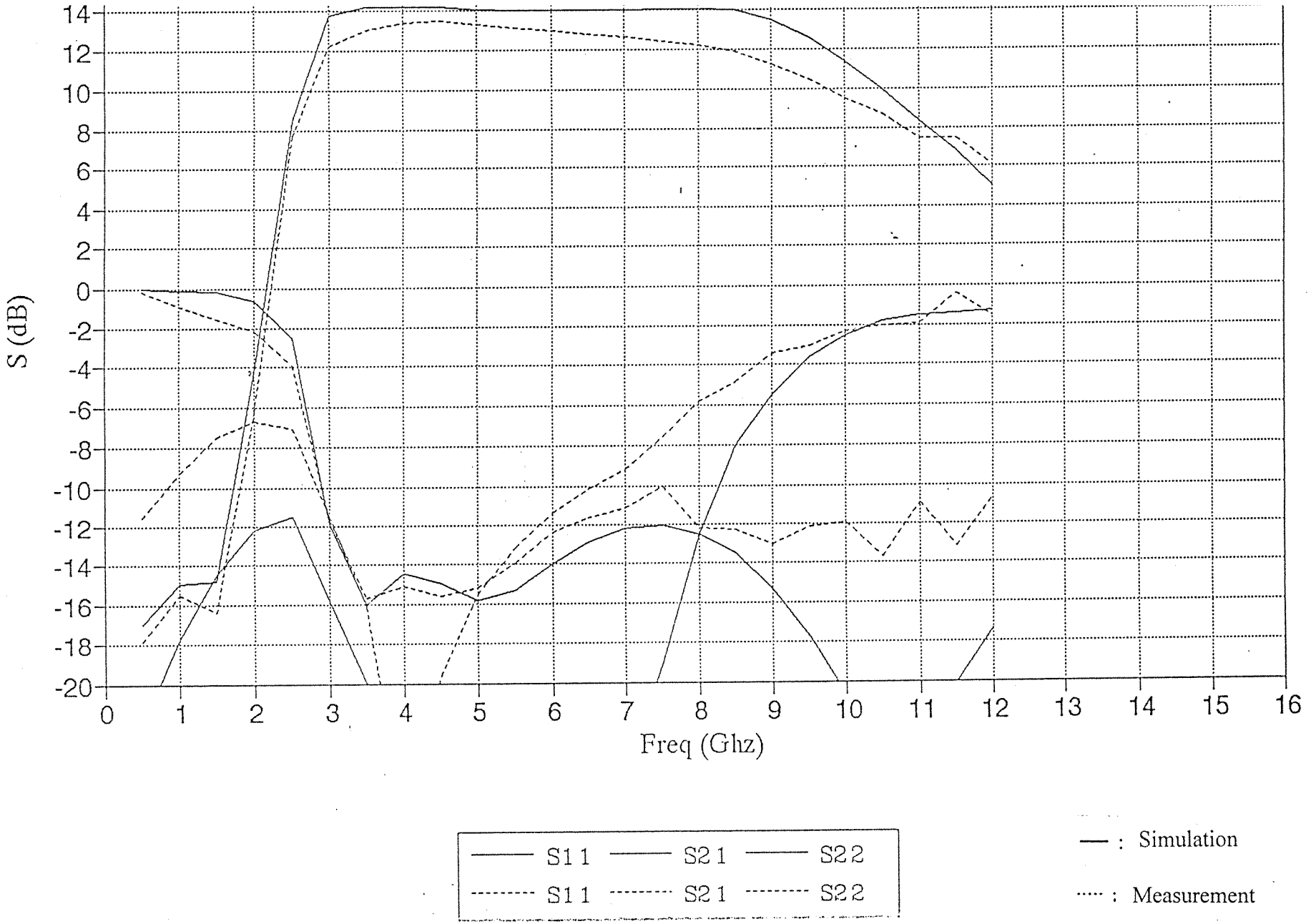

Figure B1.4 Simulation and Measurement Results of the Two-Stage Amplifier

B2. VOLTAGE CONTROLLED OSCILLATOR

A voltage controlled oscillator (VCO) is designed using negative resistance approach [1], and implemented with MMIC technology. In the design stage, the 'harmonic balance analysis' and optimization tools of LIBRA software are used. The circuit schematic and the MMIC layout of the VCO are given in Figs. B2.1 and B2.2, respectively.

In the circuit, a 4 finger MESFET of a total gate width of 300 μm (4x75) is used as the active device. The negative resistance at the gate input of the FET is obtained by means of a capacitive feedback at the source. The variable capacitance (varactor) which is necessary to change the oscillation frequency is also realized by a 4x75 MESFET, since varactor diodes are not available in the GEC Marconi process [2]. For this purpose, the drain and source of the transistor are grounded, and a bias (tuning) voltage is applied at the gate. This creates a variable gate-to-source capacitance. By connecting another capacitance in parallel with this, an equivalent voltage variable capacitor is obtained with a suitable capacitance range. This variable capacitor, together with the inductors connected next to it (see Fig B2.1), forms a resonator, and determines the oscillation frequency of the VCO.

The bias circuit is designed so that the drain current equals $I_{DSS}/2$. The capacitance in the feedback circuit is realized by two polyimide capacitors in parallel to reduce parasitic effects and to use the chip area more efficiently. A band pass filter is also included at the output to suppress the harmonics.

In evaluating the design in LIBRA, the OSCTEST [3] tool is used. This tool allows the user to inject an AC voltage, at the fundamental frequency, into the feedback loop of the oscillator, and determine the oscillation frequency and the output power. Table B2.1 gives the computer simulation results of the VCO. The tuning voltage is varied from 0.5 v down to -10 v, and the corresponding oscillation frequency (both start-up and the steady-state values) and the output power are tabulated.

Measurements are carried out on the fabricated chip, and the results given in Table B2.2 are obtained. A comparison of the two tables reveals that there are some discrepancies between the estimated and measured circuit characteristics:

i) According to the computer simulations, the circuit was expected to oscillate in the frequency range 8.79 to 10.15 Ghz as the tuning voltage is varied from 0.5 to -10 volts. The actual oscillation range turned out to be 9.29 to 11.03 Ghz for tuning voltages between 1 and -8 volts. So there is an upward shift in the oscillation band. The estimated bandwidth was around 14%, whereas the measured bandwidth is 17%.

ii) The output power level was expected to take values between 12.7 and 11 dBm, but the measured power is less (between 8 and 5 dBm for frequencies 9.29 upto 11.01 Ghz,

and even less in the rest of the band). Around 1 dB of this difference is due to the cable losses in the measurement system.

Above discrepancies are thougth to be mainly due to the insufficient accuracy of the circuit model which is used for the characterization of the large signal behaviour of the MESFETs.

Figures B2.3 and B2.4 show the variation of the oscillation frequency and the output power, respectively, versus the tuning voltage. Finally, in Fig. B2.5 the spectrum analyzer output at the Hold Maximum Mode is given. In obtaining this characteristic, the tuning voltage is swept from 1v to -10 v in 0.25 v steps.

As a conclusion, it can be said that although there are some differences between the estimated and measured performance, the VCO circuit has satisfactory operation.

REFERENCES

[1] K. Kurokawa, "Some Basic Characteristics of Broadband Negative Resistance Oscillator Circuits", The Bell System Technical Journal, p.1937, July-August 1969.

[2] GaAs IC Foundry Design Guide- Process F20/F14, GEC Marconi, 1993.

[3] EESOF Element Catalog, Version 3.5, November 1982.

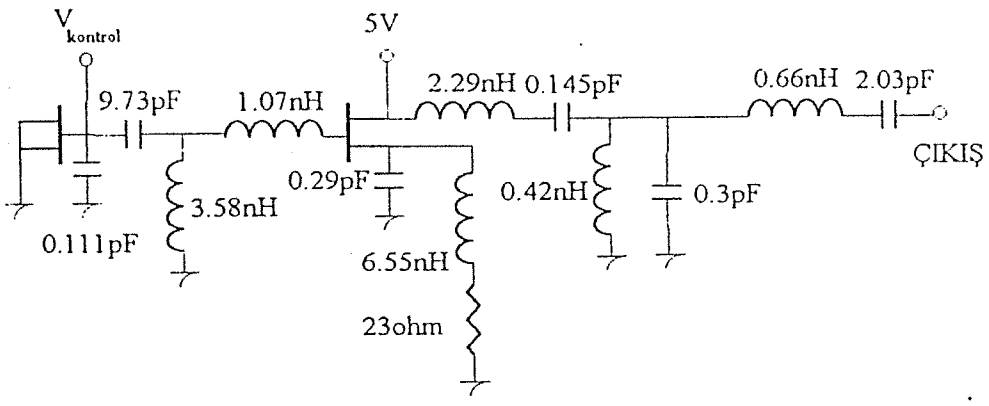

Figure B2.1 Circuit Diagram of the VCO

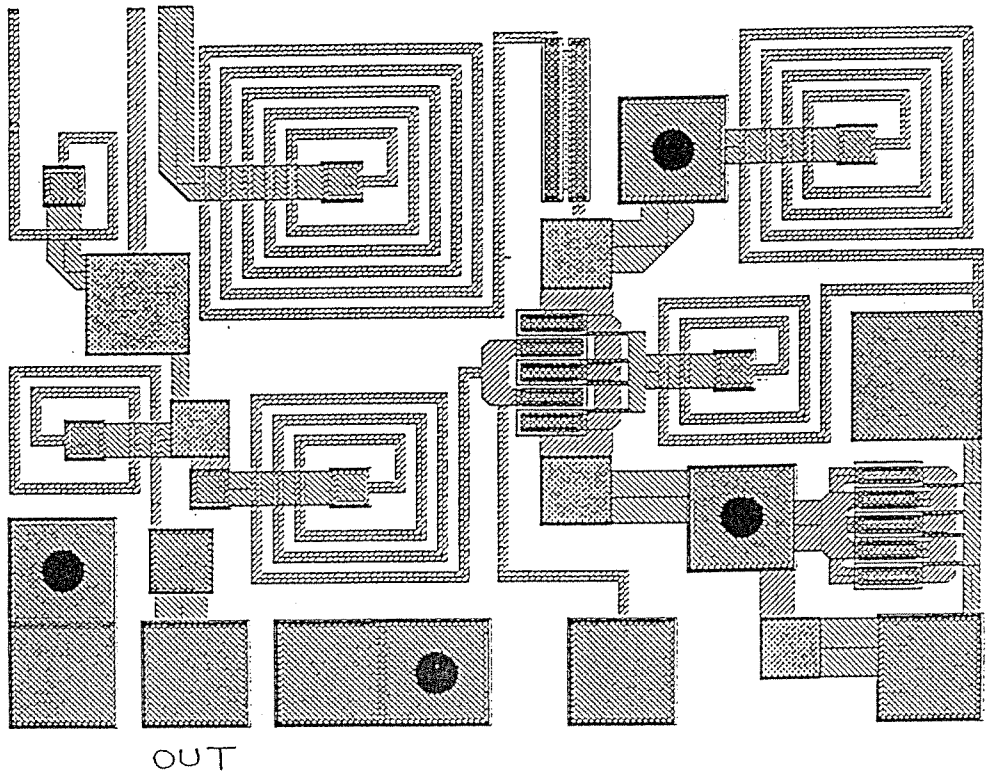

Figure B2.2 MMIC Layout of the VCO

Table B2.1 Simulation Results for the VCO

V_{tune}	$f_{start\text{-}up}$(GHz)	$f_{oscillation}$(GHz)	Output Power (dBm)
0.5	9.46	8.79	12.54
0	9.62	9.27	13.14
-0.5	9.72	9.60	12.70
-1	9.80	9.71	12.45
-1.5	9.83	9.82	12.18
-2	9.88	9.88	12.06
-2.5	9.90	9.92	11.90
-10	10.15	10.15	10.95

Table B2.2 Measurement Results for the VCO

V_{tune}(v)	f_{osc}(GHz)	P_{out}(dBm)	I_{bias}(mA)
1.0	9.295	6.33	32.7
0.5	9.592	7.67	31.3
0.0	10.040	7.67	29.3
-0.5	10.311	8.00	27.7
-1.0	10.488	8.00	26.6
-1.5	10.674	7.50	25.9
-2.0	10.928	5.50	25.9
-3.0	11.010	5.17	25.9
-4.0	11.016	4.83	25.9
-5.0	11.019	4.50	25.9
-6.0	11.022	4.33	25.85
-8.0	11.028	3.67	25.8

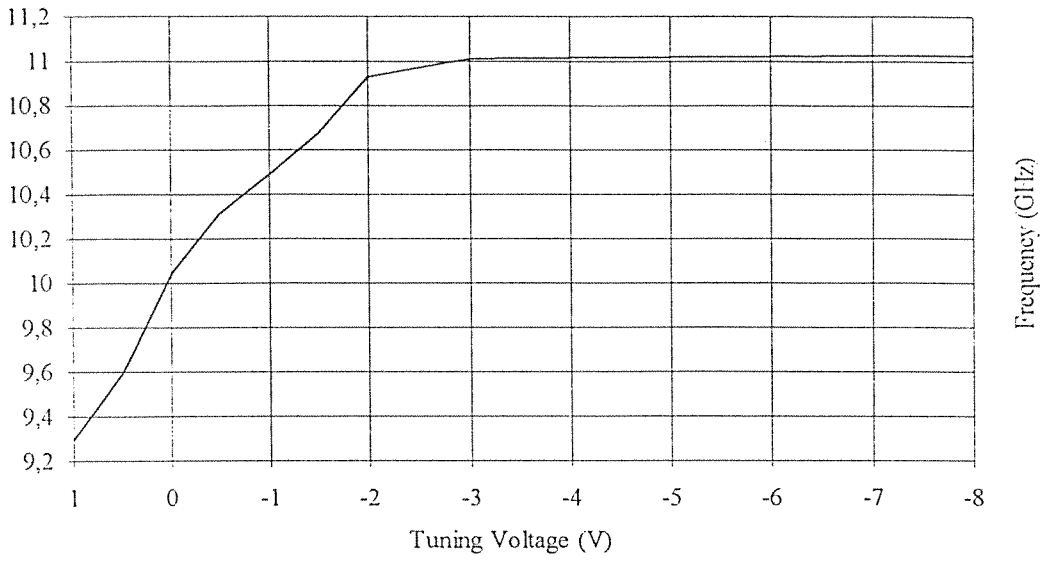

Figure B2.3 Oscillation Frequency versus Tuning Voltage (Measurement)

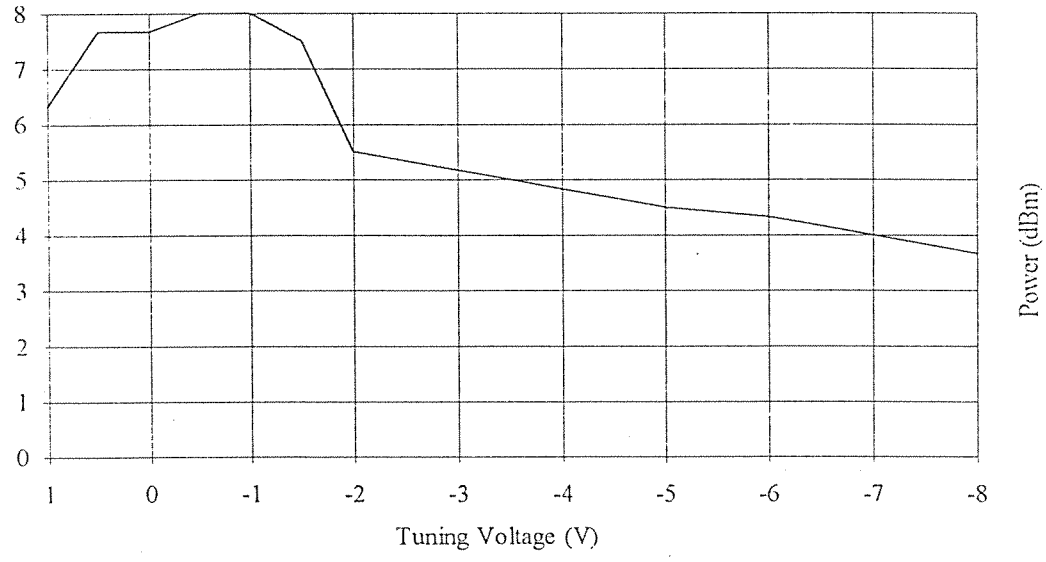

Figure B2.4 Output Power versus Tuning Voltage (Measurement)

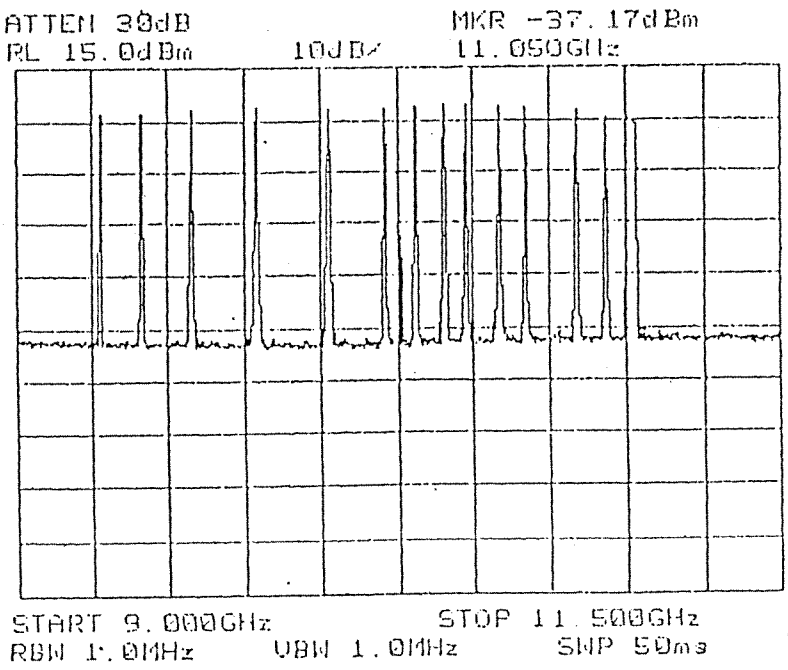

Figure B2.5 Spectrum Analyzer Output at the 'Hold Maximum' Mode

B3. MIXER

Various mixer designs and their simulations are carried out in this project. The nonlinear elements employed are either planar Schottky diodes or FET's. Balance mixer configurations are selected because of their inherent properties of rejection of spurious responses and intermodulation products and good isolation without the need for filters over a broad bandwidth. There are some disadvantages, as well, such as high LO (Local Oscillator) power requirements, higher conversion loss and noise figure. With double balanced mixers it is a common practice to use balun circuits including hybrids, phase shifters and power dividers. However, it is difficult to realize a conventional balun design in monolithic form. The balun and hybrid circuits used in descrete mixers are generally not compatible with MMIC technology. Some passive balun designs are impractical since they occupy large chip area. Therefore, the use of active baluns employing transistors are favored. Most of the MMIC mixers use FET's as nonlinear elements, instead of diodes, because of their high conversion gain, low noise and good intermodulation performance.

The simulation results of various MMIC mixers designed that employ baluns, power dividers and phase shifters will not be given here but can be found in [1]. These designs were not sent for implementation because of their large chip areas, hence, for financial reasons. A simple two-transistor mixer circuit that employs neither baluns, power dividers nor phase shifters, was designed and sent for realization.

The schematic of the designed mixer is shown in Fig. B3.1. Two single gate MESFET's are connected in cascode configuration to simulate a dual-gate FET. From one of the FET gates LO signal and from the other FET gate RF signal are applied. The signal excitations from different gates provide good isolation property especially from LO to RF port as in a mixer using dual-gate FET's. The given LO signal changes the transconductance of the lower FET and achieves the mixing phenomena. LO and RF matching circuits are LC networks between FET gates and LO and RF input ports. At the IF port there is no matching circuit nor an IF amplifier. To suppress LO frequency at the output and improve the LO to IF isolation, a shunt capacitor of value 5 pF is used. Lower FET is biased to operate in its linear region and the upper one works in its saturation mode. A self-biasing scheme is used by incorporating an active load. By connecting gate and source of the FET together, DC wise, creates an active load. From the drain of the upper FET, a DC voltage of 3.5V is applied. With this bias scheme, drain current becomes 21 mA.

Curtice and Ettenberg nonlinear GaAs FET model with cubic dependency is used for the 4x75μm MESFET's in GEC-Marconi F20 process. For the nonlinear simulation of the mixer, Harmonic Balance method in Libra software is used. All the simulations were made at an LO power of 8 dBm. The mixer has an RF bandwidth between 10-11 GHz. At these frequencies RF signal from the RF input port is down converted into the

intermediate frequency signal at 70 MHz. At IF frequency, conversion loss performance is given in Fig. B3.2. Conversion loss has maximum value of 5.95 dB and minimum value of 3.29 dB in the RF band. LO to RF isolation and RF to LO isolations are shown in Fig. B3.3. LO to IF isolation is found to be better than 15 dB over the band. These isolation properties should be evaluated bearing the fact in mind that this is not a balanced mixer. 1 dB compression point is found at -5 dBm RF power. The layout of the final circuit is shown in Fig. B3.4. The total chip area is 1.2 x 0.8 mm^2.

Measurements were carried out on the two fabricated chips in Hittite Electronics Inc., USA. This was necessary since three-probe probe-station was not available, then, anywhere in Turkey. Due to the non-availability of required instruments, the measurements were carried out at an IF frequency of 10 MHz, instead of the design frequency of 70 MHz. Although the simulations were made for a LO power of 8 dBm, two different LO power levels namely 10 dBm and 15 dBm were used at two bias voltages 3.5 V and 5 V. Fig. B3.5 shows the measured conversion loss characteristics. The legend items for this figure are as follows: CL 1(103.5V) means "conversion loss for chip number 1, at LO power of 10 dBm and bias voltage of 3.5 V". Similarly CL 2(155V) means "conversion loss for chip number 2, at LOA power of 15 db and bias voltage of 5 V". The others follow in this logical sequence. Fig. B3.6 shows LOA to FR isolation. The legend follows the same pattern as to the previous figure except L-R, this time, means isolation from LO to RF. Fig. B3.7 shows isolation LO to IF.

From the measurements of conversion loss characteristics, the RF band seems to be shifted to about 11.5-12 GHz. The discrepancies between the simulated and measured results can be explained as follows: The use of 10 MHz as IF frequency instead of 70 MHz brings the RF and LO frequencies very near to each other. This, in turns, affects the isolation levels. The use of 10 or 15 dBm LO power levels instead of 8 dBm also changes the conversion characteristics. Another factor which is not taken into account during simulations is the effect of bias tee that is used during measurements. Its characteristics is altogether unknown. If one accept the shift in frequency band due to the above reasons, the simulation and measurement results can be considered to be in agreement.

REFERENCES

[1] S. Baskan, "Design of Microwave Mixers Using MAC Technology", MS Thesis, Department of Electrical and Electronic Engineering, MEET, 1994.

[2] Y. Imai, M. Tokumitsu and A. Minakawa, "Design and Performance of Low Current GaAs MMIC's for L-Band Front-End Applications", IEEE Trans. onMTT, Vol. 39, Feb. 1991, p.209.

[3] T. Sugiura, K. Honjo and T. Tsuji, "12 GHz-Band GaAs Dual Gate MESFET Monolithic Mixers", IEEE Trans. on MTT, Vol. 33, Feb. 1985, p. 105.

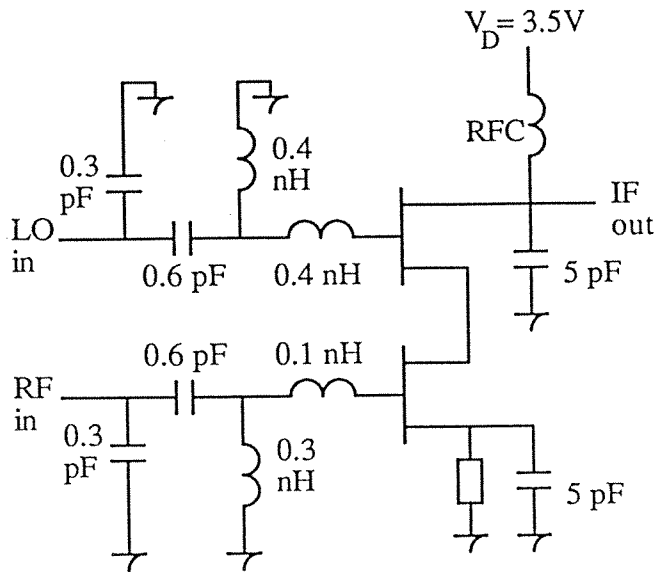

Figure B3.1 Circuit Diagram of the Mixer

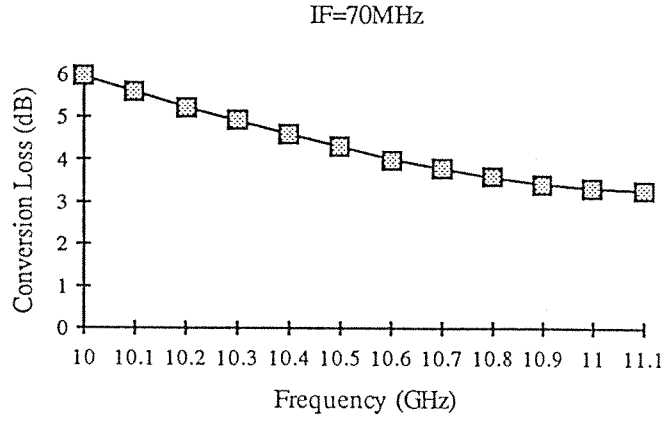

Figure B3.2 Conversion Loss Characteristics

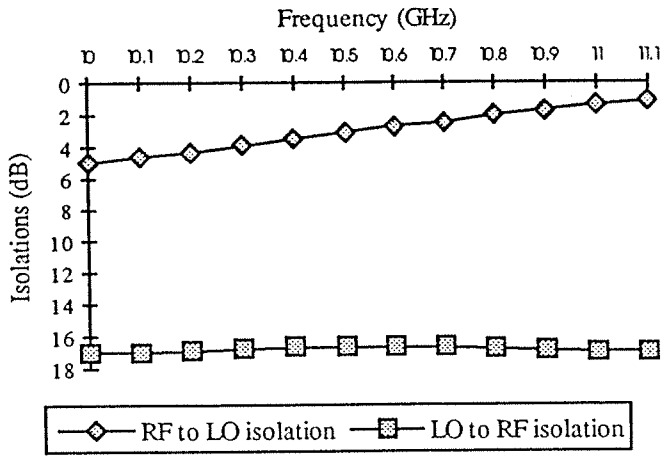

Figure B3.3 Isolation Properties

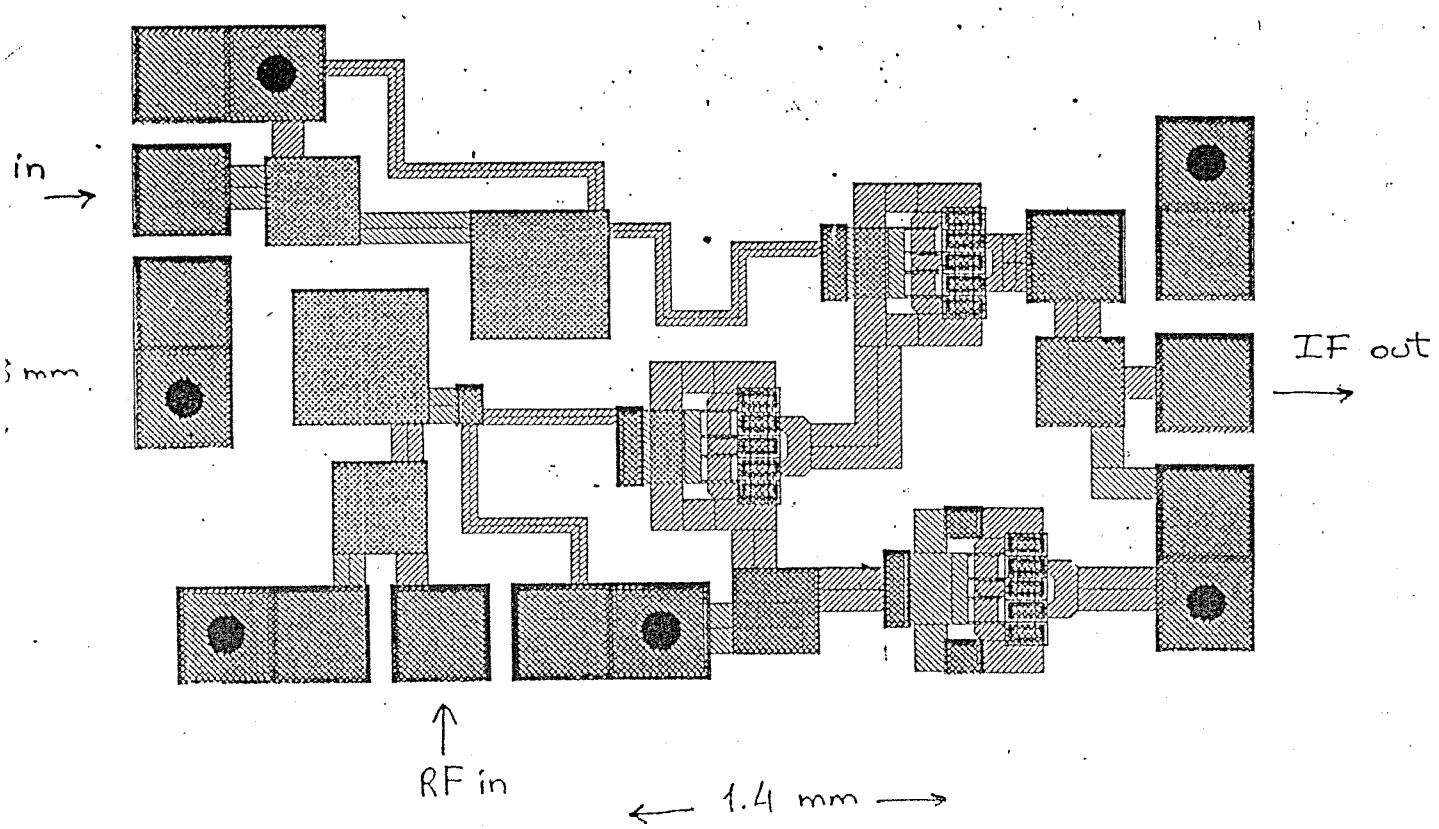

Figure B3.4 Mixer Layout

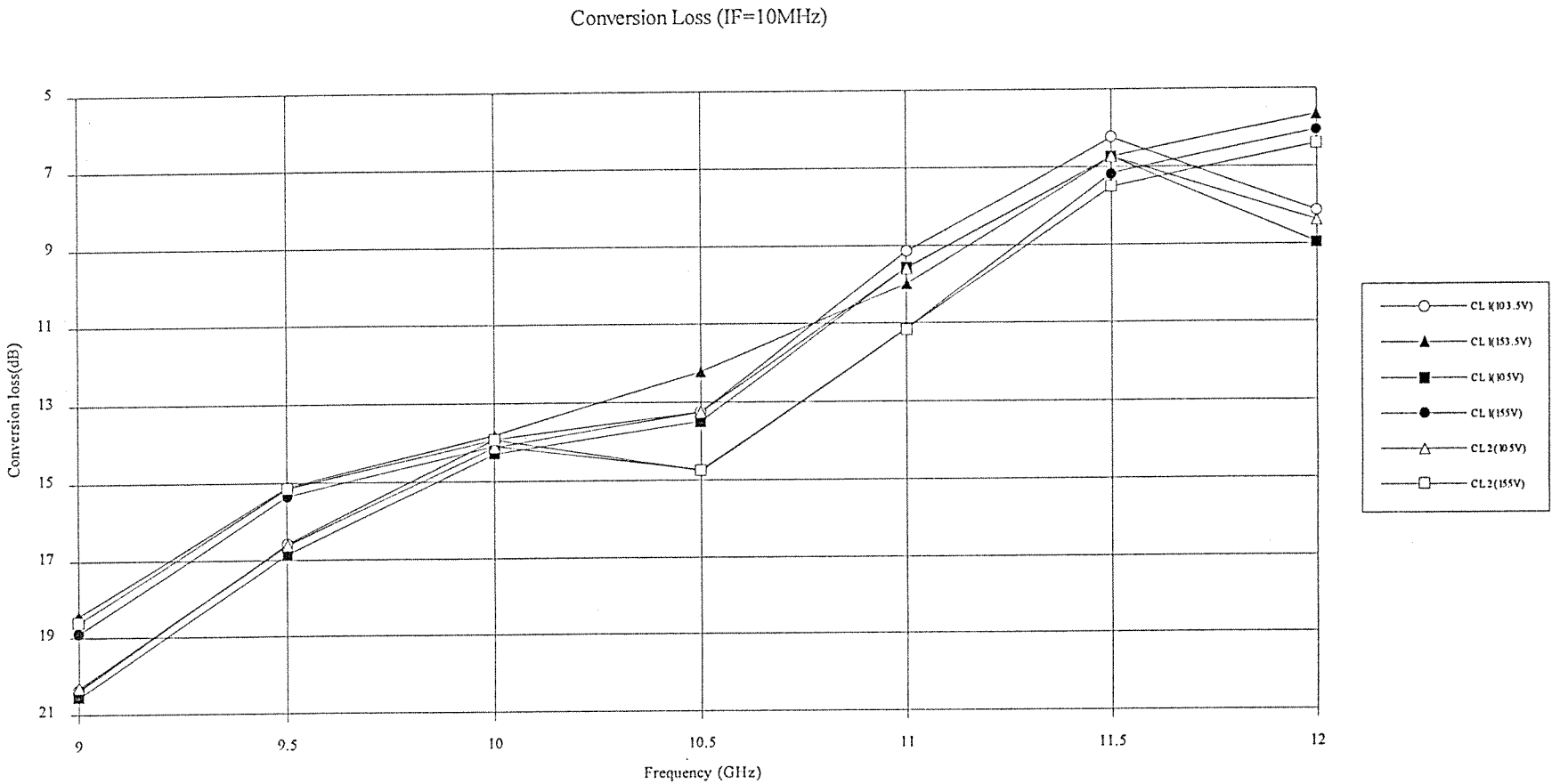

Figure B3.5 Measured Conversion Loss

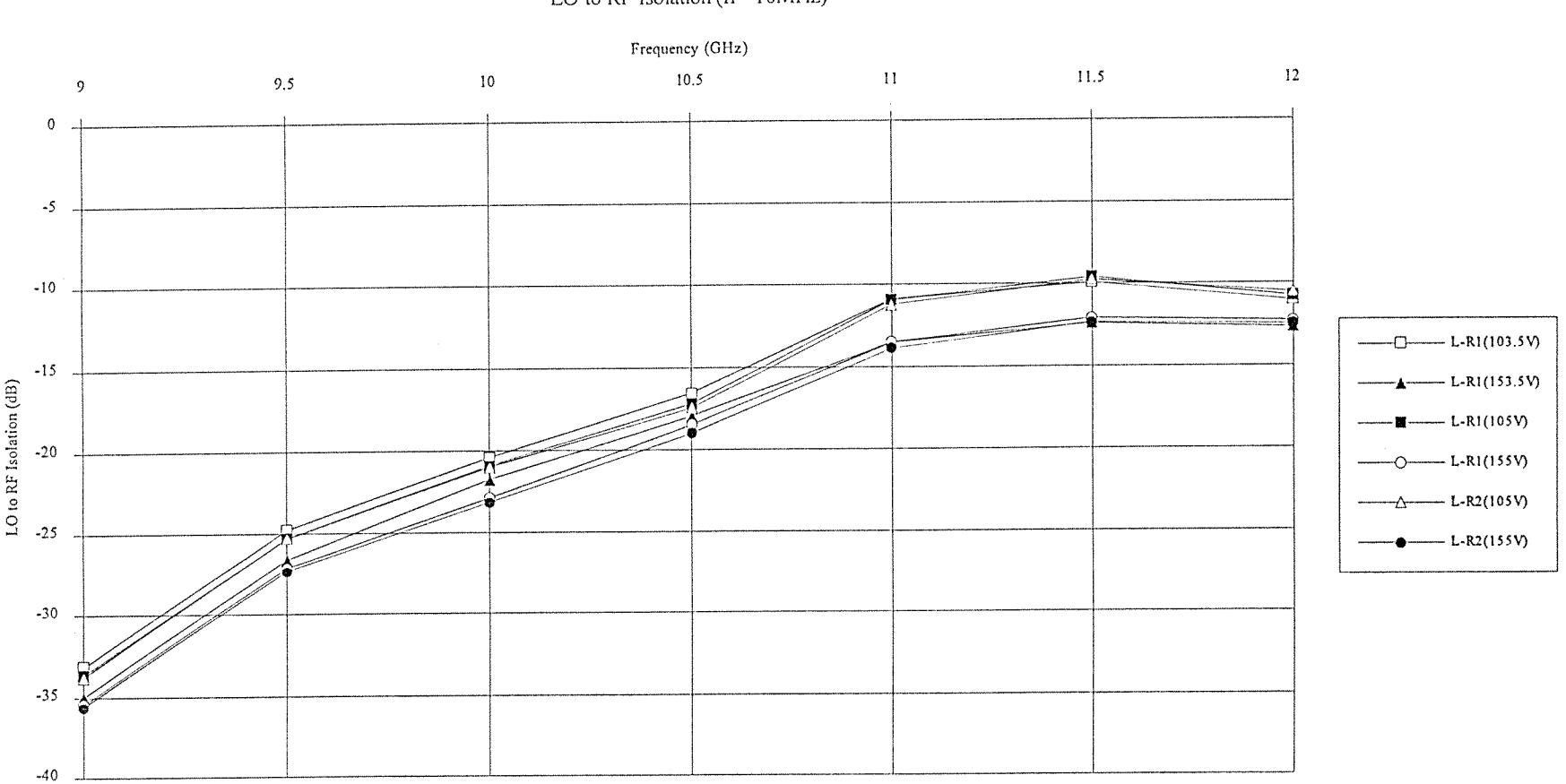

Figure B3.6 Measured LO to RF Isolation

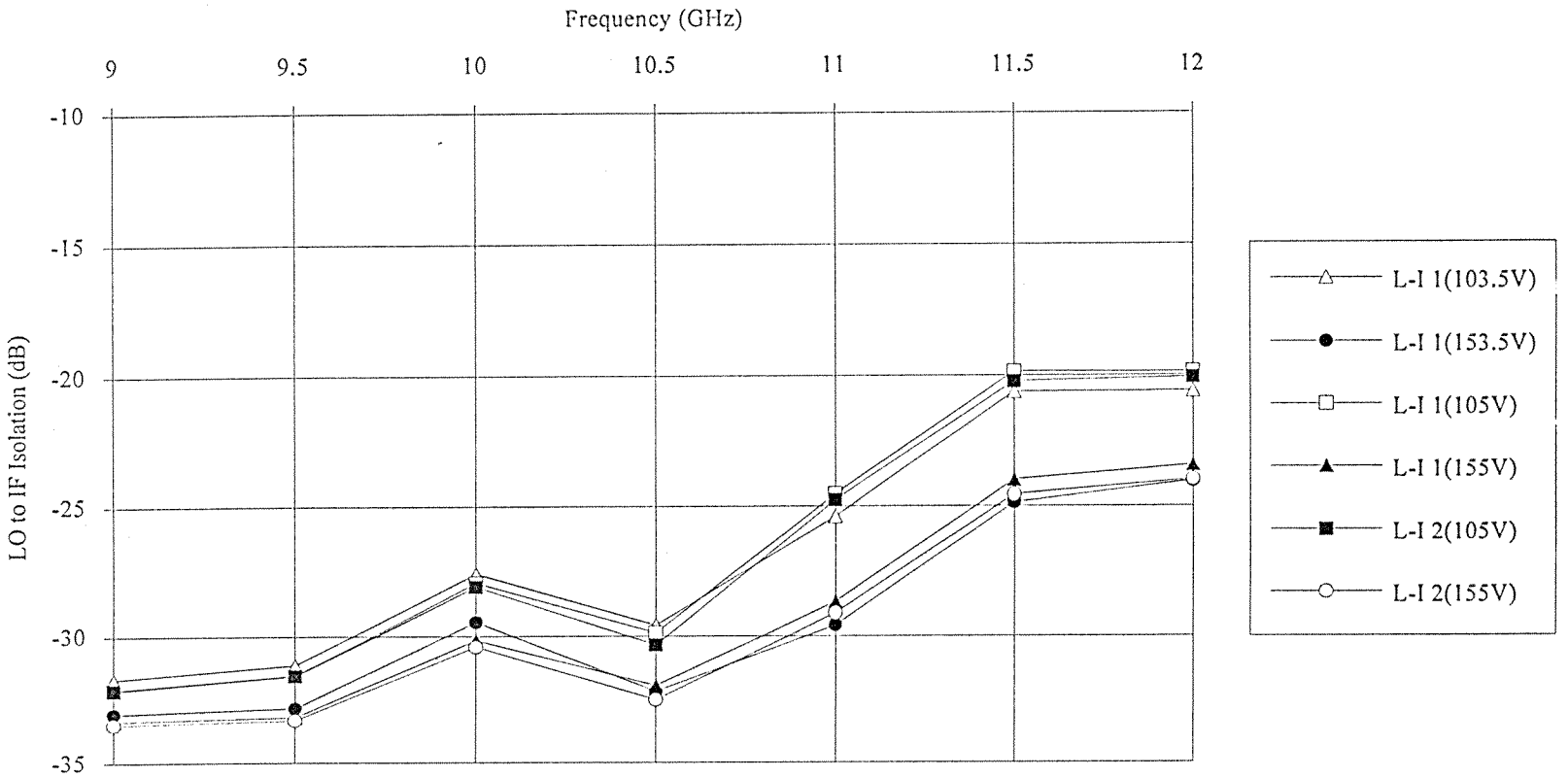

Figure B3.7 Measured LO to IF Isolation

B4. LOW NOISE AMPLIFIER

The MMIC technology is originally addressed for the implementation of microwave circuits around X-band and at higher frequencies by exploiting the excellent high frequency properties of the GaAs material. However, in recent years, there is a tremendous demand on monolithic RF products in the newly emerging wireless communication market. Although these new wireless communication systems use the lower part of the microwave frequencies, the MMIC technology provides efficient, low cost and monolithic solutions. By the motivation of this fact, an LNA is designed in MMIC form according to the specifications of the DECT wireless communication system operating at 1.9 Ghz. Since the cost of a MMIC circuit is inversely proportional with its active chip area, the key objective in this design was to minimize the chip area while achieving satisfactory electrical performance. The design and the optimization of the circuit are achieved using CAD tools LIBRA and ACADEMY.

The design goals were put as follows: An active chip area not exceeding 1 mm2, a gain around 13 dB, and a noise figure less than 3 dB while keeping the return losses at the input and the output better than 14 dB. Although the amplifier is designed for a narrowband system, it is desired to have a 400 Mhz bandwidth around 1.9 Ghz (or a 20% bandwidth) with a 1 dB gain margin to compensate for any possible shift in the peak of the gain. Finally, the amplifier should be unconditionally stable at all frequencies.

The amplifier designed (see Fig. B4.1) consists of two stages: The first stage is a common-gate stage used to match the input of the next stage. This active matching technique exploits the low input reflection coefficient property exhibited by the common-gate configuration of the FET. (While the GaAs MESFET shows high gain and low noise in the common-source configuration, it has good input match property in the common-gate configuration.This property is used to achieve high return losses at the input of the amplifiers [1])

The next stage is the main amplifying stage of the LNA, and consists of a common-source FET. Since the second stage also affects the noise (due to the low gain of the first stage) some precautions are taken. In order to bring the optimum noise match impedance to the conjugate input match impedance, a series inductive feedback is used at the source of the FET [2,3]. In order to stabilize the common-source stage, a shunt resistive feedback is also applied. The common-gate FET is stabilized with a resistor connected to its drain. The common-gate simultaneous match output impedance is brought to the conjugate of the simultaneous input impedance of the common-source stage through the use of an inductor. (A piece of a transmission line could also be used here if its length is sufficiently small). The otput of the common-source stage is matched through the use of conventional narrowband matching techniques by an L-type high pass section. The introduction of real MMIC elements is then made. The matching inductors are chosen to be of the stacked spiral type. These inductors have the advantage that they offer high

inductance per unit area as compared to the standard spiral inductors, though they are lossy [4]. By this choice a large chip area is saved at the expense of a few dB gain loss.

The MMIC layout of the LNA is shown in Fig.B4.2. The gate of the common-gate is tried to be perfectly grounded to avoid any inductance path which can cause instability problems at higher frequencies. The input and output RF ports are located at the opposite sides of the chip to avoid any positive feedback. Since the operation frequency is low, the packaging density of the elements is kept high. The active chip area of the circuit is about 0.9 mm2 (1.18x 0.74 mm). The FETs are biased by using a self bias scheme at 20% Idss, where the FETs have their optimum noise figures. The choke inductors and a bias resistor are connected off chip. The amplifier can be operated from a 6 VDC drawing 36 mA current.

According to the computer simulations, the bandwith of the LNA is about 600 Mhz with a +/-0.5 dB gain flatness. The expected gain is 14 dB at the middle of the band, and the return losses are better than 14 dB. The noise figure is better than 3 dB with a value of 2.7 dB at the middle of the band. The stability analysis of the overall amplifier reveals that the circuit is stable for all frequencies upto 20 Ghz to which the FETs are defined. Fig.B4.3 shows the simulation results and the measurement results together.

The circuit responses are measured at the Bilkent University by an HP8510C network analyzer. Measurements are done on three LNA chips fabricated on the same wafer, and almost identical responses are obtained. The gain is around 12.5 dB in a frequency band of 1.5 Ghz width about the design frequency. Considering the probe losses, this corresponds to a value which is only 0.5 dB below the expected gain. However, the bandwidth turned out to be greater than the estimated one which was 600 Mhz. The input return loss, S11, follows the simulation results quite closely, and it is in fact better than the expectations. Similar arguments hold for S22 as well. S12, which is an indication of the circuit isolation, is measured to be better than 30 dB.

REFERENCES

[1] Niclas, "Active Matching with Common-Gate MESFETs", IEEE MTT-33, No.6, June 1985, pp. 492-499.
[2] Engberg, "Simultaneous Input Power Match and Noise Optimization Using Feedback", IV. European Microwave Conf., 1974, pp. 385-389.
[3] Besser, "Stability Considerations of Low Noise Transistor Amplifiers with Simultaneous Noise and Power Match", IEEE Microwave Symp., 1975, pp. 327-329.
[4] GEC-Marconi F20 Process Foundry Design Rule Guide, 1991.

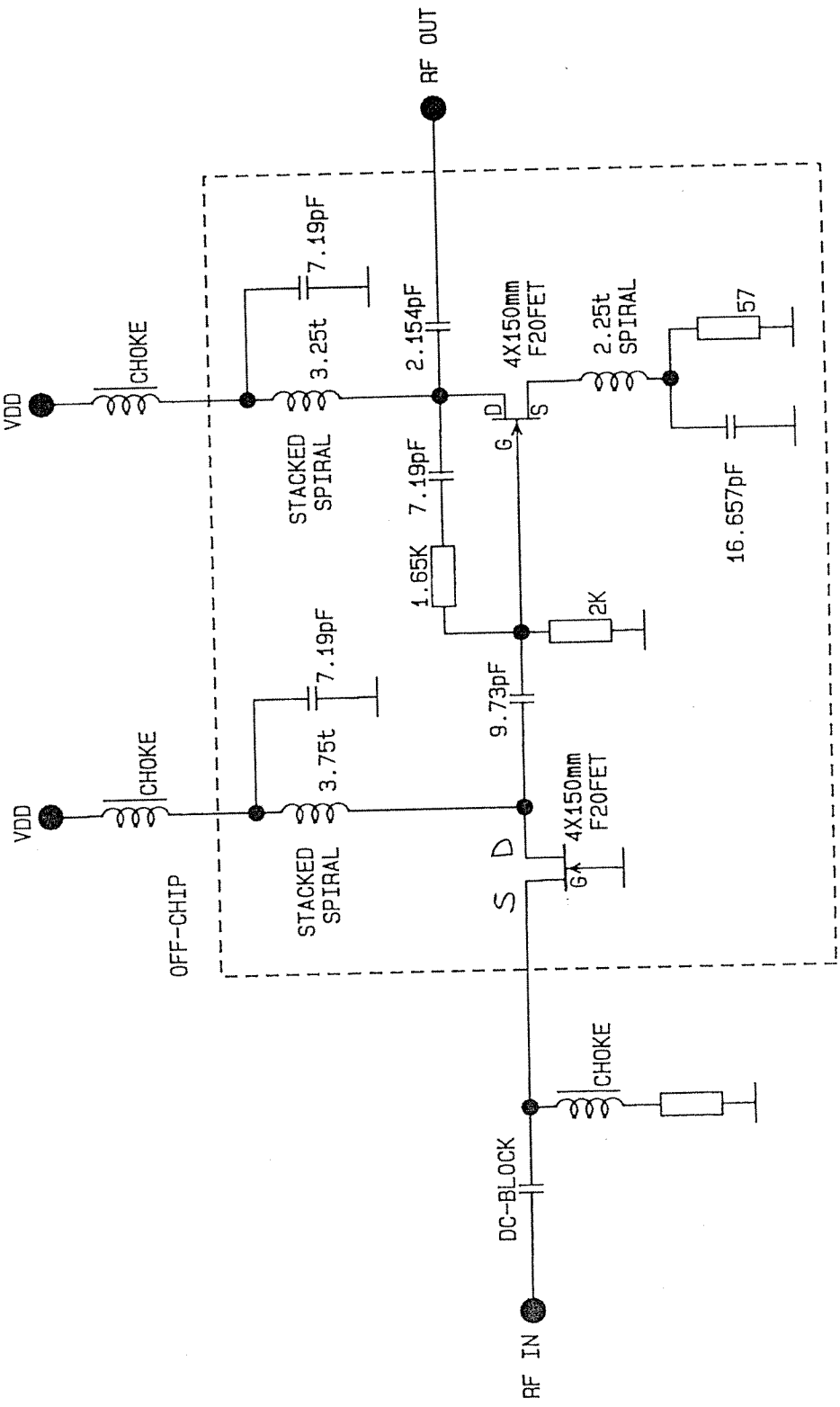

Figure B4.1 Circuit Diagram of the LNA

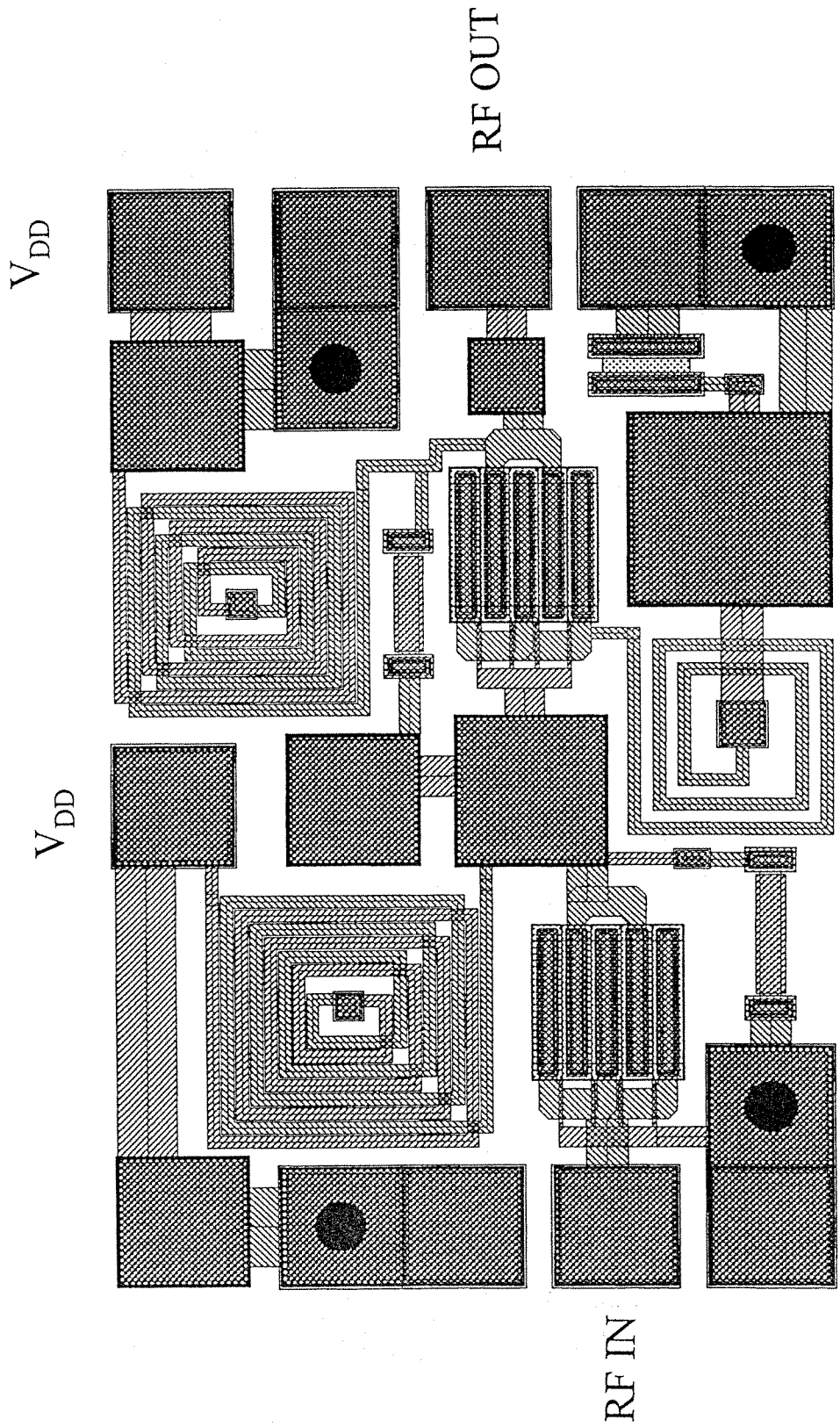

Figure B4.2 MMIC Layout of the LNA

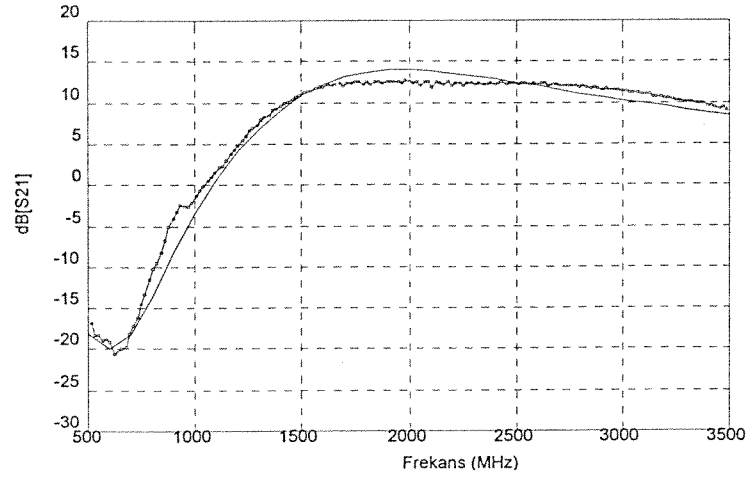

(a)

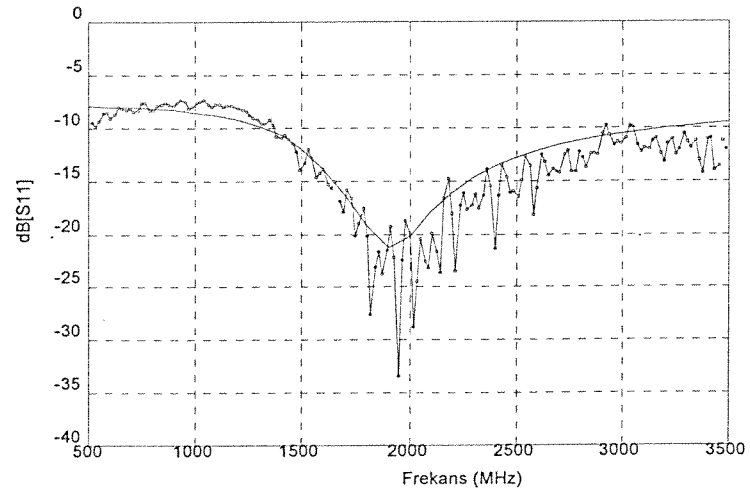

(b)

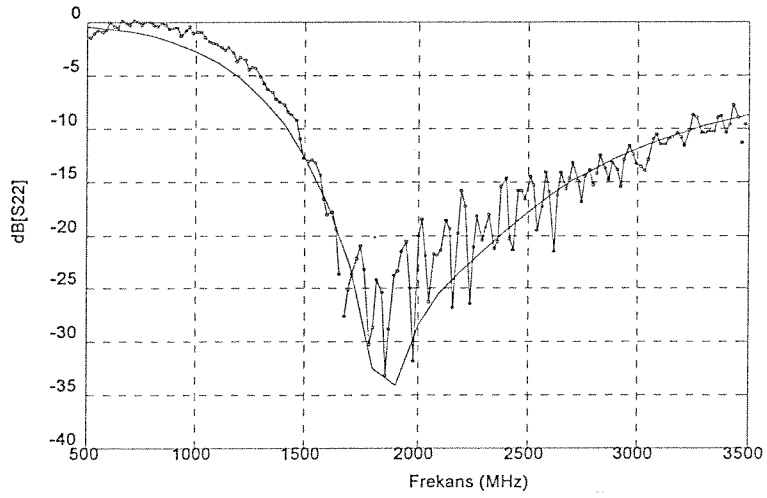

(c)

Figure B4.3 Simulation (-----) and Measurement (--o--) Results
(a) Gain (S_{12}) (b) Input Return Loss (S_{11})
(c) Output Return Loss (S_{22})

B5. TRANSMIT / RECEIVE SWITCH

An asymmetric Transmit / Receive (T/R) switch is designed and implemented in MMIC form for the RF section of a 1.9 Ghz wireless communication system. The key objective in this design was to minimize the chip area while achieving satisfactory electrical performance. The design goals for the switch were put as follows: An insertion loss in the TX-ANT (transmitter-antenna) path less than 0.3 dB, an insertion loss in the ANT-RX (antenna-receiver) path less than 1 dB, a TR-RX isolation better than 20 dB. The switch should handle a power of 400 mW.

In conventional T/R switches for radio applications, discrete solutions using PIN diodes have been popular until recently. However, in monolithic form, the FET as a switch element offers more cost effective solutions. A T/R switch is actually a single pole double throw (SPDT) switch. The SPDT switches, and in general all RF switches made up of FETs, have standard topologies using series and shunt connected FETs like the one shown in Fig. B5.1a. In this symmetric structure, the series FETs are used to effectively break the RF path between the RF common port and the other RF ports. On the other hand, the shunt FETs provide the required isolation between the isolated ports. In radio applications it is desirable to have lower insertion loss in the TX-ANT path than that in the ANT-RX path while preserving the required isolation between the TX and RX in the TX-ANT "ON" mode. For this purpose, the shunt FET in the TX-ANT path can be removed. In this way, the extra insertion loss which would be introduced by the shunt FET is avoided and the chip area is reduced. Another advantage of this structure is that the power handling capacity of the TX-ANT path is no longer limited by the breakdown of the shunt FET. The only disadvantage brougt by the removal of the shunt FET is a decrease in the isolation, but this can be tolerable in our case. Fig.B5.1b shows the circuit schematic of the asymmetric T/R switch.

The next stage of the design is to obtain the conducting and non-conducting state equivalent circuits of the FET as a switch element. The equivalent circuits of the switch FET are well established by several workers [1], [2]. In this work we adopt the models proposed by Ayasli. The conducting state model of the FET consists of a simple resistor R_{ON} whose value can be determined from the FET DC Ids-Vds characteristics. The slope of the curve at the ohmic region gives this resistance value. To obtain the non-conducting model elements is more difficult, because some of them are directly related with the physical parameters of the FET such as the doping level, channel thickness etc. which are not always available to circuit designers. However, in the non-conducting model, there is an element which is dominant to the electrical performance, and its value can be accurately predicted using the geometrical information of the FET such as the gate length, drain-source width, etc. This element is the drain to source capacitance, C_{ds}, which describes physically the electrostatic capacitance between the drain and source both via the GaAs substrate and the air. The other elements which have considerable effect on the electrical performance are the gate to source and gate to drain capacitances whose values

are predicted using the standard formulas for FETs [3]. The gate resistances are taken one half of the conducting state resistance as suggested in [1].

Then the gate widths of the three FETs are optimized according to the predetermined design goals, and the MMIC layout is prepared as shown in Fig.B5.2. The active chip area is around 0.5 mm^2 (0.86x0.59 mm).

The designed T/R switch has been fabricated in the GEC Marconi MMIC foundry in England, where they have also carried out several measurements on five chips fabricated on the same wafer. The five switches tested show almost identical responses indicating that the yield would be high on a mass production. The results of these measurements are given in Fig.B5.3 together with the computer simulation results. As can be seen, there is a good agreement between the simulation and measurement results. At 1.9 Ghz, the ANT-RX insertion loss is around 0.6 dB, whereas the TX-ANT insertion loss is around 0.3 dB. The isolation is measured to be 30 dB. Althoug the switch will be used at 1.9 Ghz, the FET switches can be operated down to DC as the results also indicate.

REFERENCES

[1] Ayasli, "Microwave Switching with GaAs FETs", Microwave Journal, Vol.25, No.11, 1982, pp.61-74.
[2] Jain and Gutman, "Modeling and Design of GaAs MESFET Control Devices for Broadband Applications", IEEE MTT-38, No.2, 1990, pp.109-117.
[3] GEC-Marconi F20 Process Foundry Design Rule Guide F14/F20, 1991.

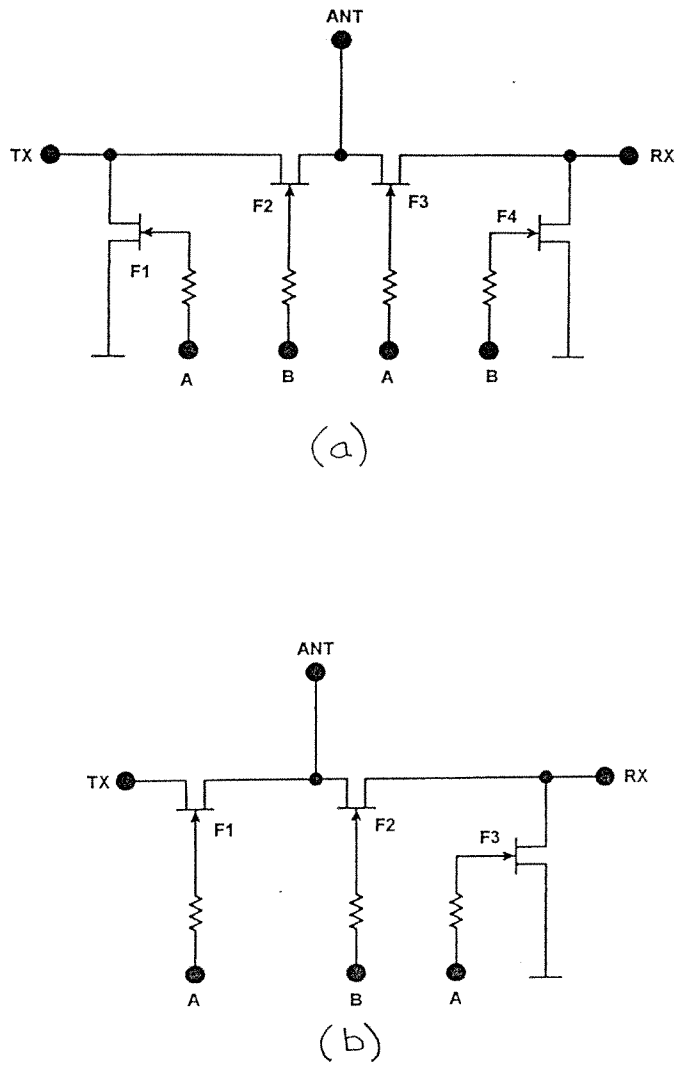

Figure B5.1 a) Circuit Topology of a General Purpose SPDT RF Switch.
b) Circuit Topology of the Proposed Asymmetric T/R Switch.

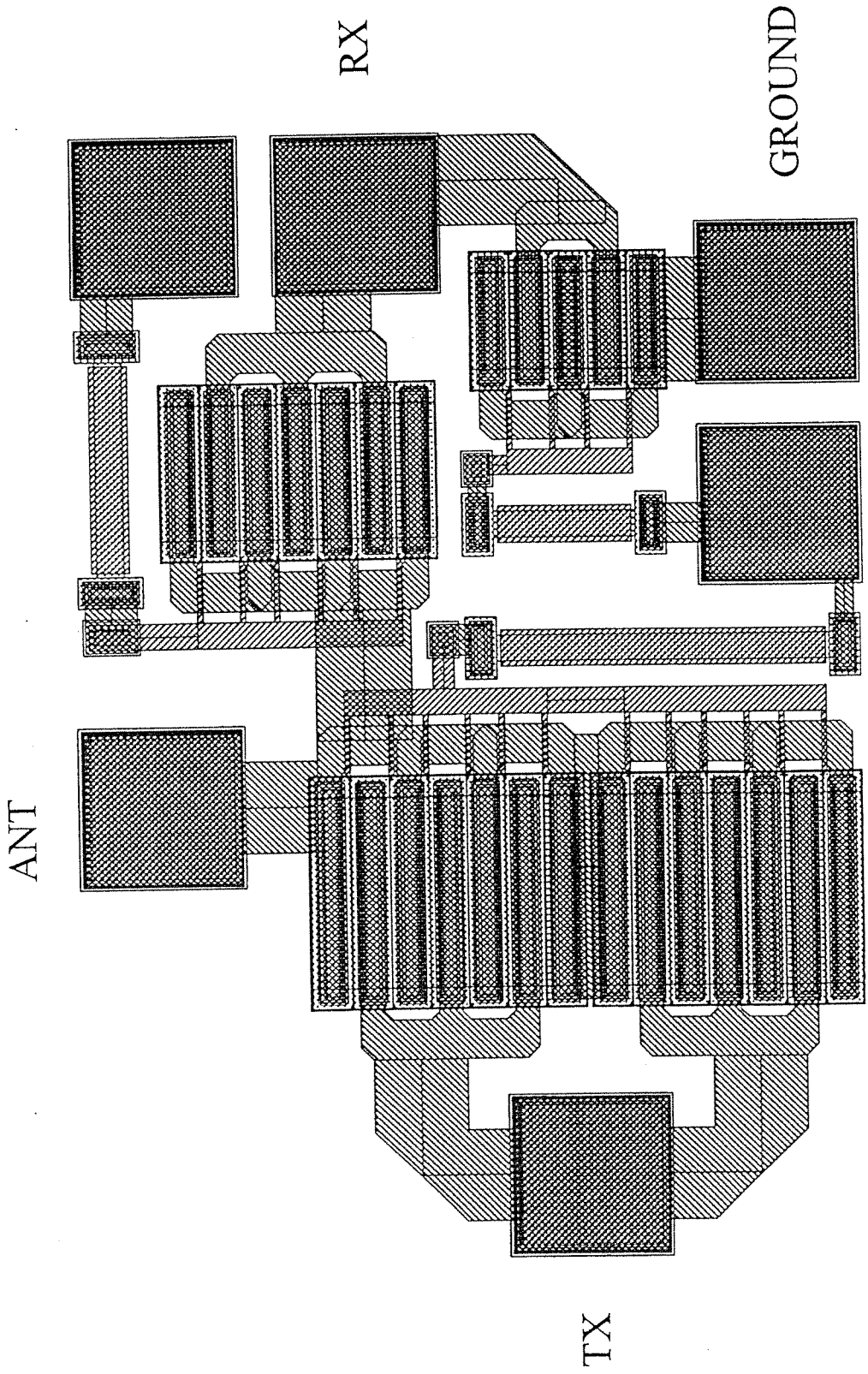

Figure B5.2 MMIC Layout of the T/R Switch.

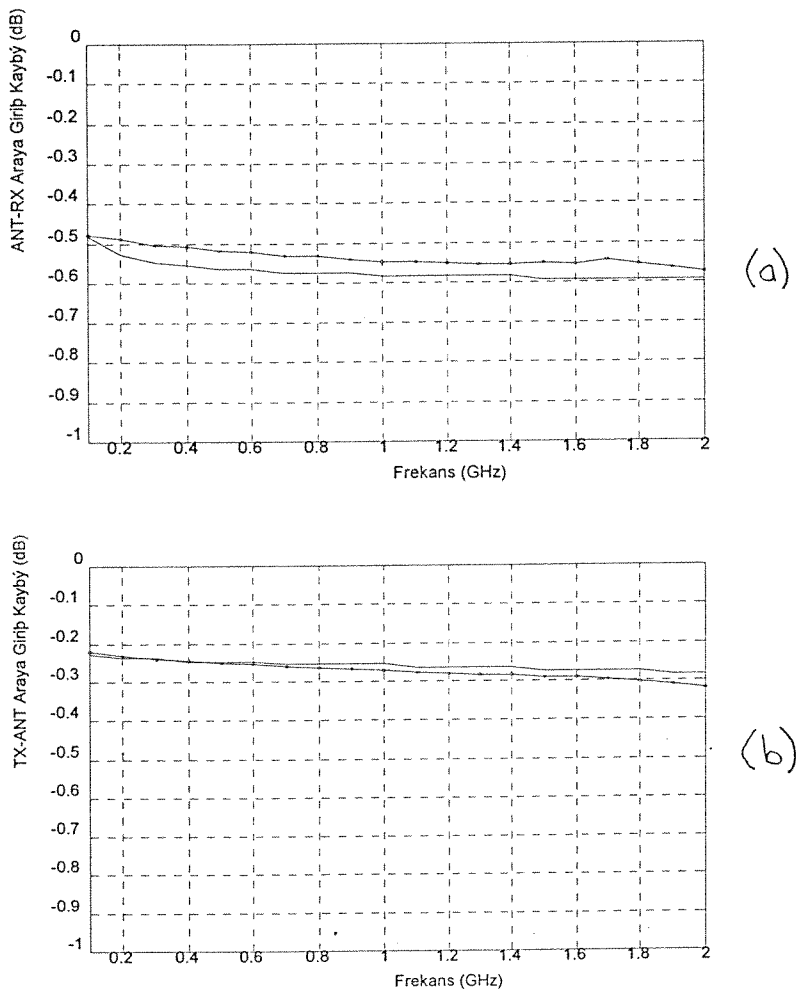

Figure B5.3 Computer Simulation (-----) and Measurement (--o--) Results
a) ANT-RX Insertion Loss
b) TX-ANT Insertion Loss

B6. POWER AMPLIFIER

A Power Amplifier is designed using MMIC Technology. The specifications of the design are as follows:

Frequency range: 12.5 GHz - 13.5 GHz
Bandwidth : At least 1 GHz
Output power : 200 mW minimum
Gain : 14 dB minimum
Gain flatness : 0.2 dB
Input and Output return losses < 10 dB
Bias voltage : 5 V.

The circuit topology of the amplifier is shown in Fig. B6.1. Two cascaded stages are used to guarantee the specifications. The types of the GaAs MESFET which are employed in the design is determined according to their drain currents. In GEC-MARCONI F20 foundry process, the current carrying capacity of the metal layer is 5 A/mm. Also the maximum width of the lines of the inductors is 24 μm which corresponds 120 mA maximum. Bearing in mind the circuit topology, the drain current must be less than 120 mA. at V_{gs}=0. To fulfill these requirements 4x150 μm FET is selected.

The first stage is designed separately from 50 Ω input to 50 Ω output and 15 dbm output is obtained for 0 dbm input at 13 GHz. To achieve a stable operation throughout the frequency band, RLC feedback is employed at this stage. The feedback is selected such that gain and bandwidth are not affected duly. The best results are obtained with series capacitors having values 5-6 pF. The second stage is also separately designed from 50 Ω input to 50 Ω output and to have at least 200 mW output power. Finally the two stages are combined and optimized. After the final values of the components are determined, the stability check is accomplished. It is shown that the amplifier is stable for all frequencies.

The layout of the amplifier is shown in Fig. B6.2. The chip size is 0.8x1.4 mm. Due to the financial reasons this amplifier is not sent for implementation.

Fig. B6.3 shows the large signal scattering parameters of the simulation results. The gain, bandwidth and output return loss have been achieved with regard to the specifications. However, input return loss is only below 10 dB between 13.7 GHz -16 GHz. Also the simulation results show that 1 dB compression point occurs at 5 dbm input. The corresponding output is 20 dbm or 100mW which is lower than the specified value. It is concluded that FET's having larger gate widths than the ones used would give higher output powers. Still higher output power can be obtained using hybrid divider-combiner techniques, but these require much more chip area than the present one. Simulation results also show that at 100 mW output level, the second harmonic is 40 dB below; and third harmonic is 65 dB below the fundamental.

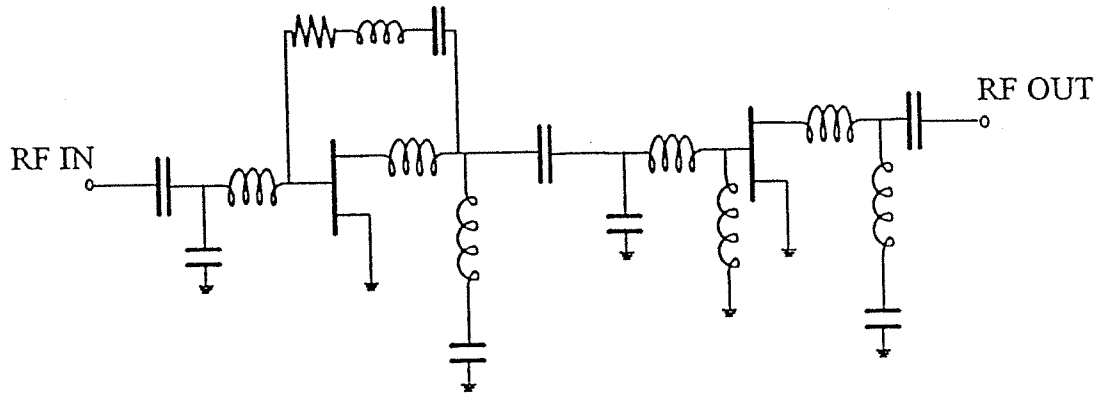

Figure B6.1 Amplifier Circuit Diagram

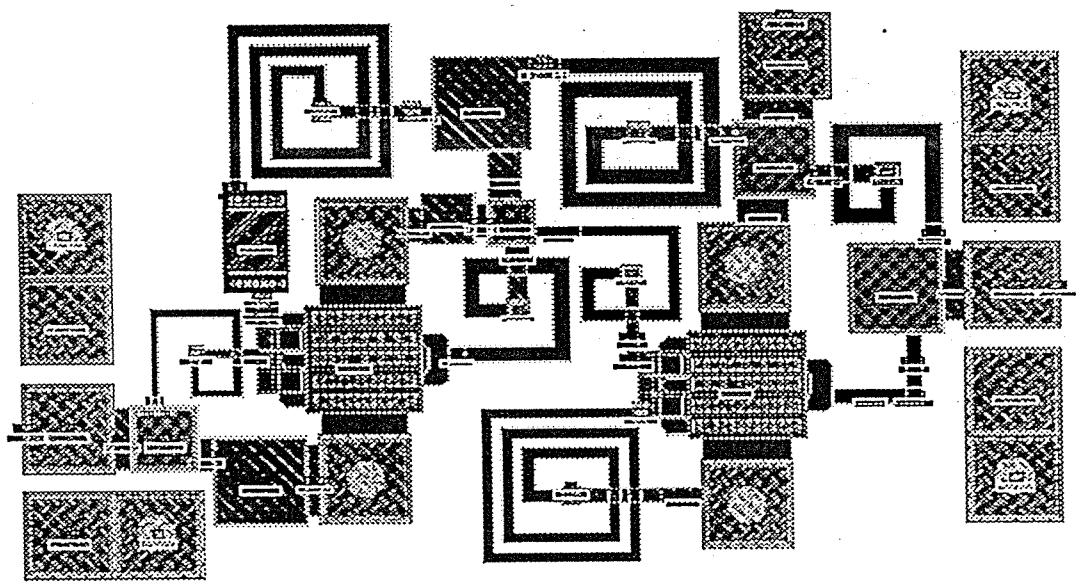

Figure B6.2 Layout of the Amplifier

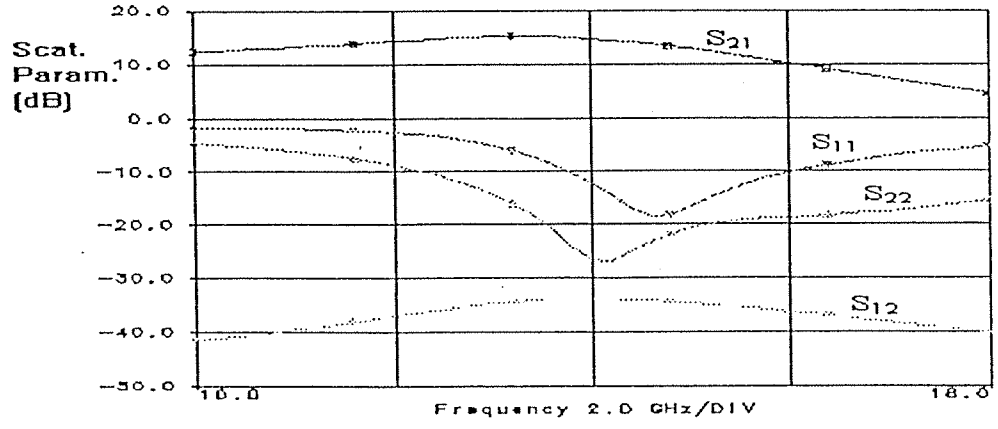

Figure B6.3 Simulation Results of the Amplifier

B7. WIDEBAND VOLTAGE VARIABLE ATTENUATOR

A linear, wideband (1-20 Ghz) voltage variable attenuator (VVA) is designed in MMIC form for the high frequency operating communication systems. An attenuator is a network that reduces the input power by a predetermined ratio. To achieve a linear relationship between the attenuetion measured in dB and the control voltage, most of the existing attenuator circuits employ externel active linearization circuitry which complicates the component and reduces reliability. In this work, linearization is achieved by connecting a number of field effect transistors in a special fashion to form a composite FET whose channel resistance is a prescribed function of its gate-to-source voltage, as suggested in [1].

There are three forms of resistive networks that lend themselves conveniently to realization of microwave attenuators. These are the T, PI, and bridged-T configurations shown in Fig.B7.1. Each configuration can be used to implement a variable attenuator by replacing the fixed value resistors R_1 and R_2 with variable resistors. Variable resistors are three-terminal components where the resistance measured between two terminals is controlled by a signal (a voltage in the case of a VVA) applied to the third terminal. In MMIC technology, variable resistors are realized by using MESFETs. The channel resistance of the MESFET is varied by a control voltage applied between the gate and the source.

In the present design, the bridged-T configuration shown in Fig.B7.1c) is used, and in order to achieve a linear operation, the variable resistors are realized by 'composite' FETs which are formed by the parallel combination of several FETs with a resistive voltage divider as shown in Fig.B7.2. The number of the FETs, and the resistors in the voltage divider are optimized for linear operation of the attenuator in the 1-20 Ghz band. A schematic diagram of the complete attenuator is given in Fig.B7.3. Four FETs are used for the series resistor, while two FETs were sufficient to realize the shunt resistor. The circuit is arranged so that the two control voltages V_{c1} and V_{c2} constitute a complementary pair in the form V_{c2}= -6-V_{c1}. Since it is relatively easy to generate complementary voltages from a single control voltage, this would be desirable in applications where only one control signal is available.

The MMIC layout of the VVA is prepared as shown in Fig.B7.4 using the elements of the GEC Marconi F20 process [2]. All transistors are 4x75 micrometer MESFETs. The active chip area is approximately 1.6 mm^2.

Since the circuit has not been fabricated yet, only the computer simulation results are available to predict the performance of the attenuator. According to these results (see Figs. B7.5-B7.7), the attenuator has the following characteristics:

i) Through a wide frequency range (1-20 Ghz), a highly linear relationship between the attenuation and the control voltage is obtained.

ii) Attenuator has a dynamic range of 10 dB through the frequency band, with a minimum attenuation value of -2 dB and a maximum attenuation value of -12 dB.

iii) Attenuation flatness at all states of the control voltage is always better than 0.5 dB.

iv) The return loss both at the input and the output is better than 15 dB.

v) At low frequencies, the phase shift through the attenuator remains almost constant for all attenuation values (an overall change of 2.3 degrees at 1 Ghz), whereas at the high frequency end of the band, the phase change shows a large variation with the attenuation level (about 19 degrees at 20 Ghz).

REFERENCES

[1] Barak Maoz, "A Novel, Linear Voltage Variable MMIC Attenuator", IEEE Trans. on MTT, Vol.38, No.11, Nov. 1990, pp.1675-1683.

[2] GaAs IC Foundry Design Guide- Process F20/F14, GEC Marconi, 1993.

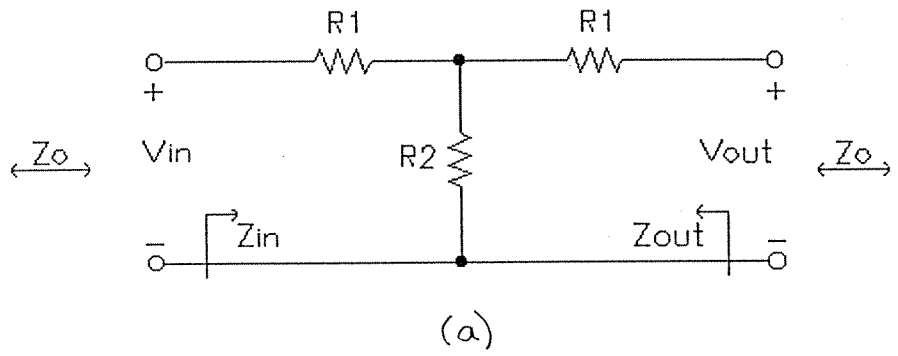

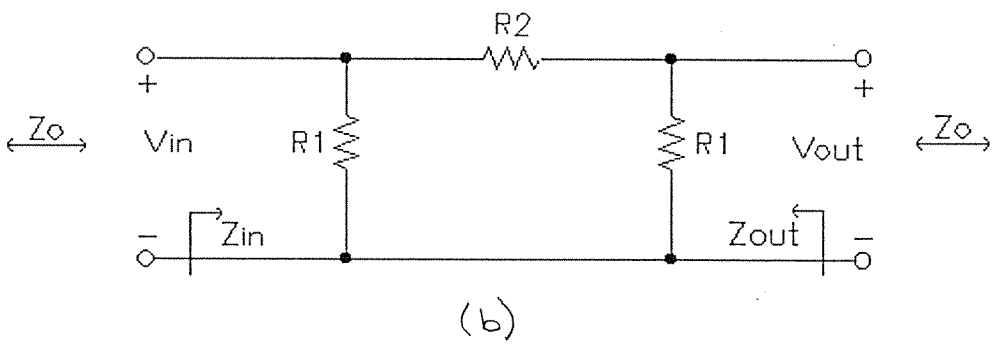

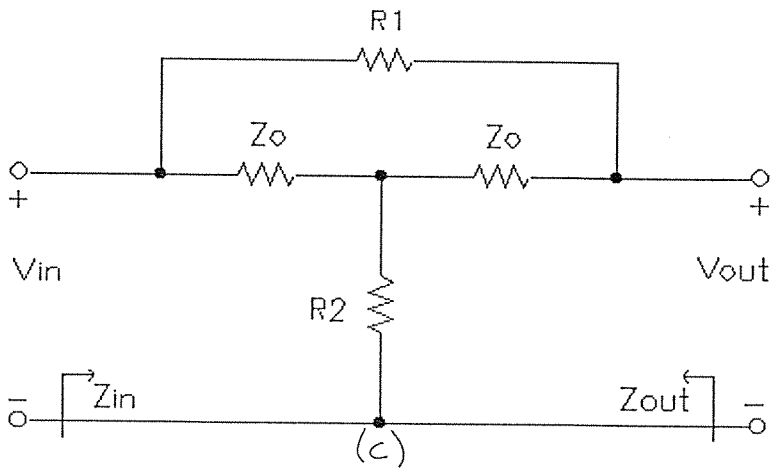

Figure B7.1 Network Configuration for
a) T-Type Attenuator
b) PI-Type Attenuator
c) Bridged T-Type Attenuator

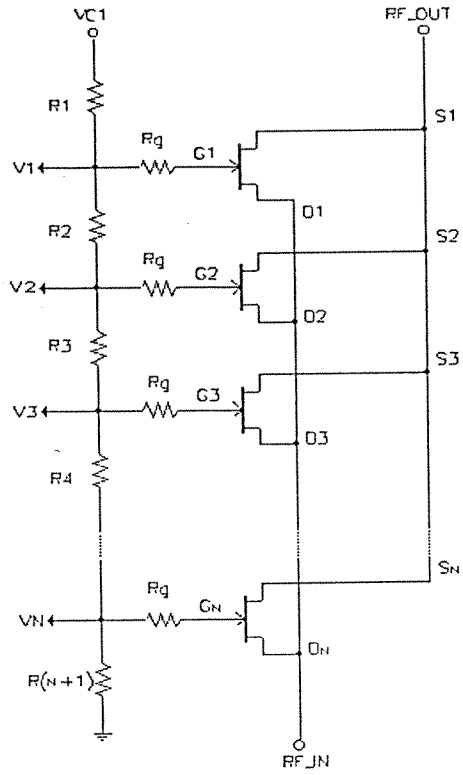

Figure B7.2 Parallel Combination of Several FETs with a Resistive Voltage Divider

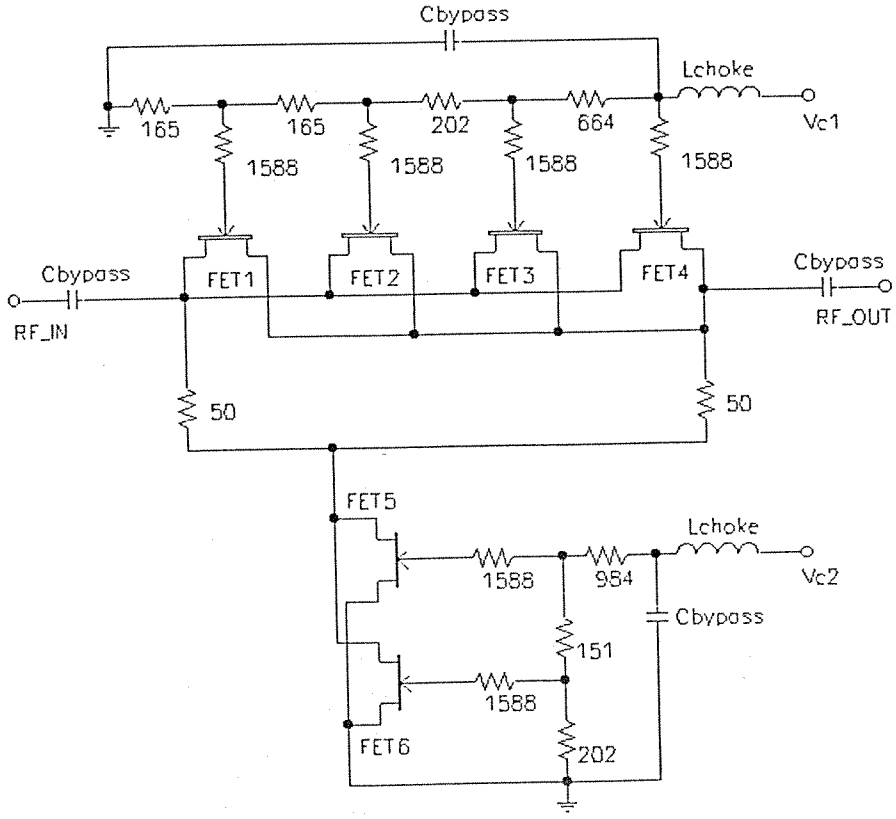

Figure B7.3 Schematic Diagram of the Complete Attenuator

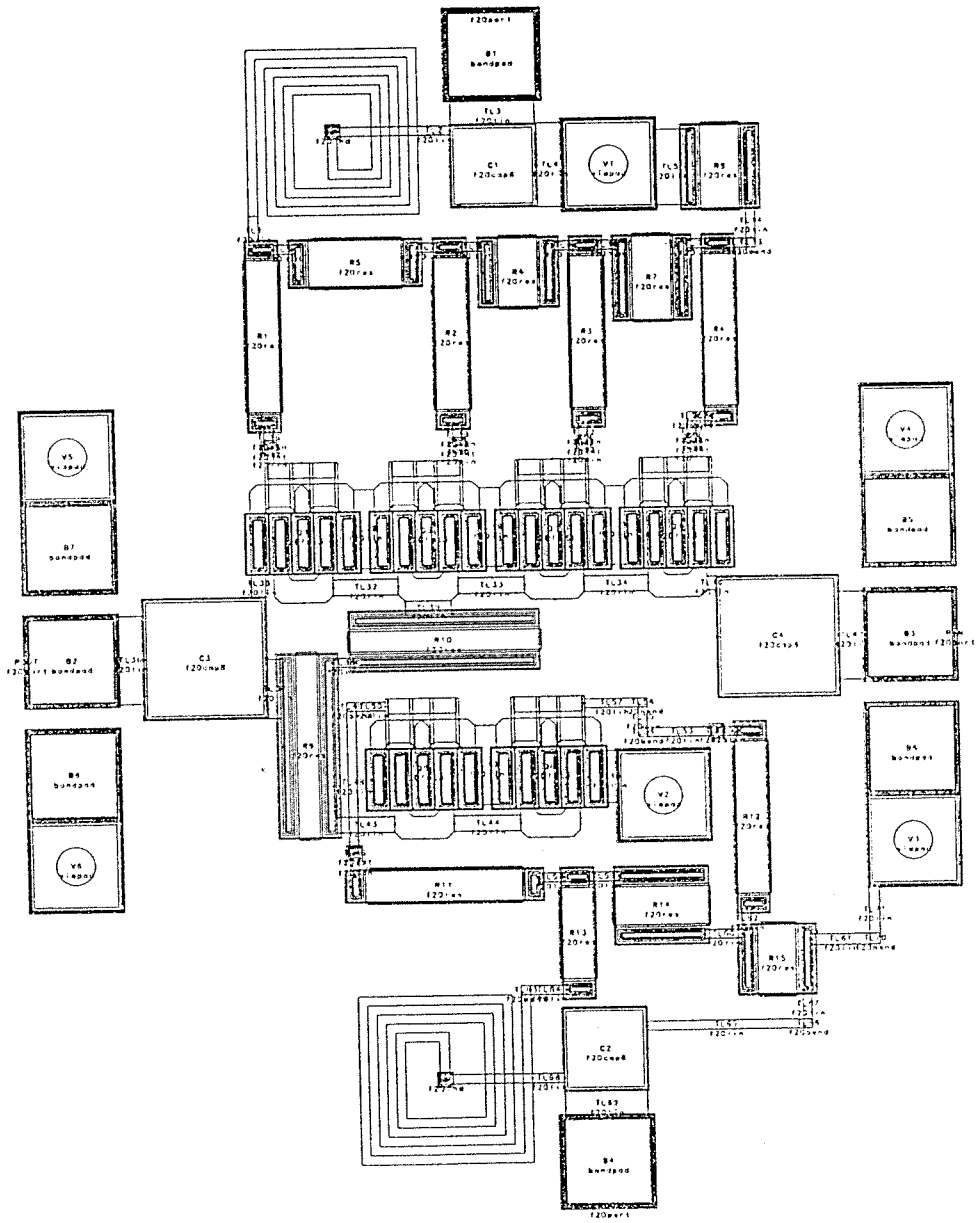

Figure B7.4 MMIC Layout of the Attenuator

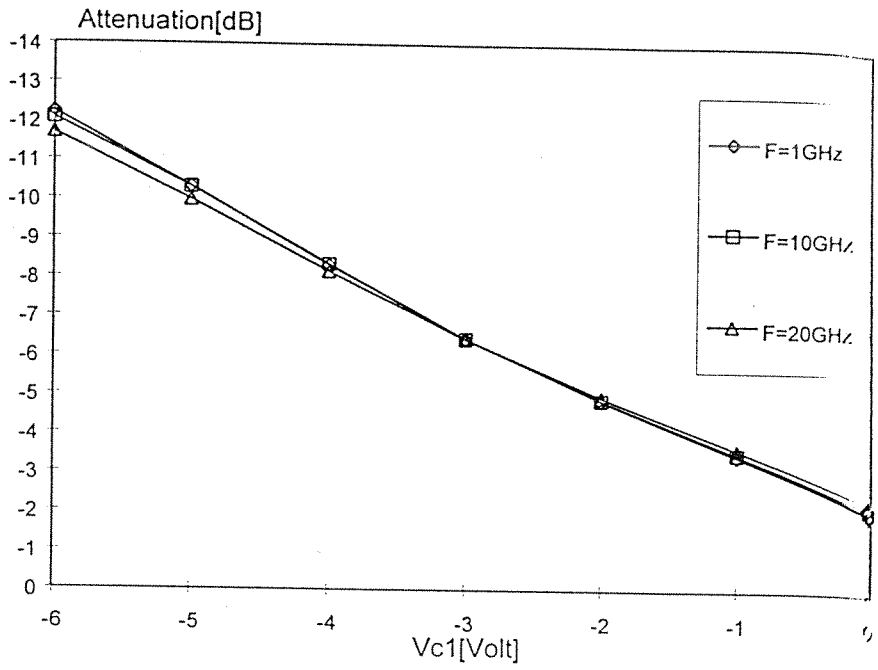

Figure B7.5 Attenuation as a Function of the Control Voltage

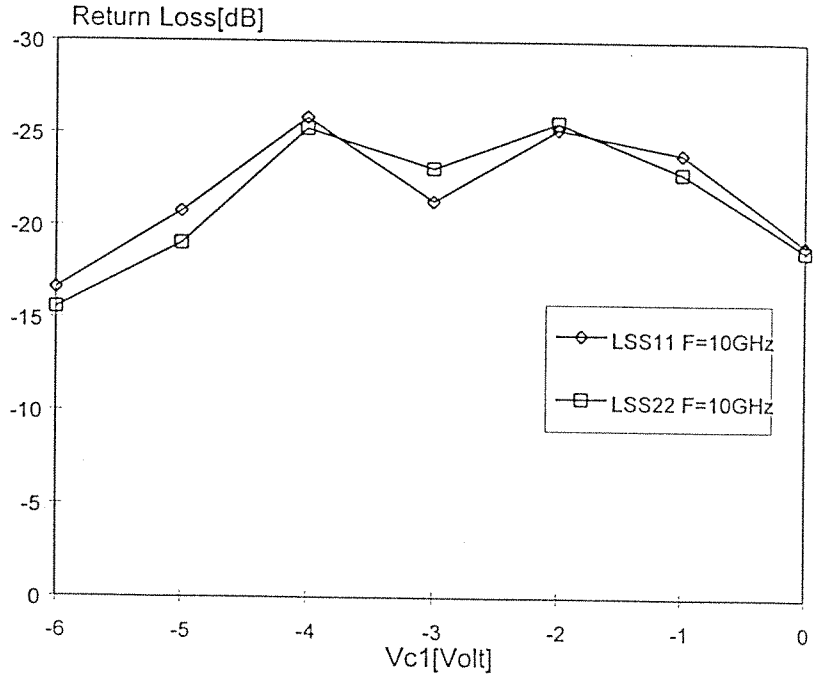

Figure B7.6 Input and Output Return Loss as a Function of the Control Voltage

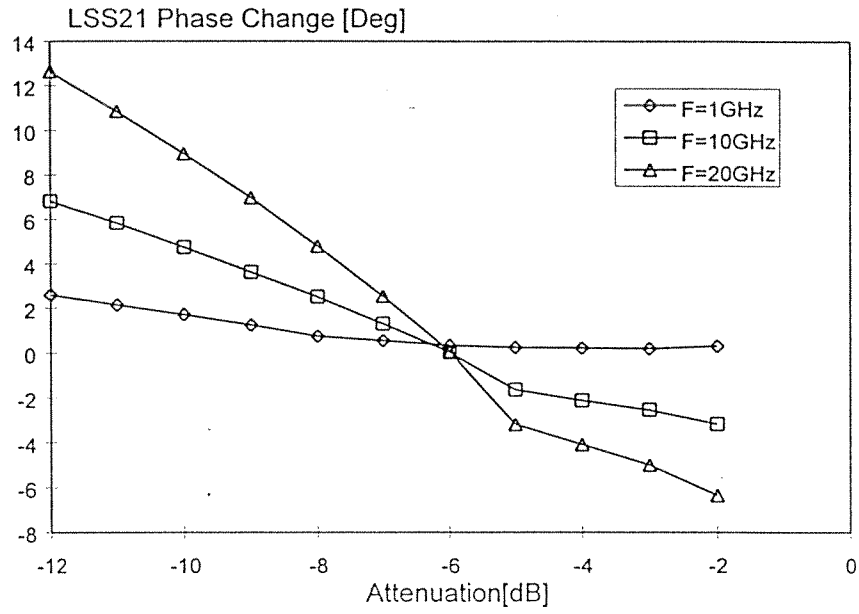

Figure B7.7 Phase Shift through the Attenuator as a Function of Attenuation

B8. PHASE SHIFTER

An extensive study on a variety of phase shifters is made and their principles of operation, tuning mechanisms and circuit topologies are investigated. Phase shifter circuits using switching devices such as "switched line phase shifters", "loaded line phase shifters" and "high-pass/low-pass phase shifters" are analyzed and their characteristics are noted. Reflective type phase shifters are also examined. A vector modulator topology employing bi-phase modulators, in particular, is simulated and its wide band operation is compared to the performance of other types of phase shifters.

Operation principles of a FET as a switching element in phase shifters are studied in detail. A single pole double throw, SPDT, using GEC-Marconi F20 process MMIC technology is designed and simulated. Also a three phase-bits are designed using GEC-Marconi foundry elements and HP's Libra 5.0 simulation software. In this design lumped element high-pass/low-pass type phase bits are employed. After the integration of SPDT switches with the high-pass/low-pass sections to form a "three-bit phase shifter", the simulation results are obtained. Due to the financial reasons, this design is not sent for implementation.

Schematics of a T-type high-pass/low-pass section is shown in Fig. B8.1 together with switches. Block diagram of the three-bit phase shifter is shown in Fig. B8.2 with 90^0, 45^0 and 180^0 phase bits, but without switches. The three possible combination for cascading scheme are worked out and it is found that, the optimum configuration for good input and output return losses, for less phase error and for less amplitude unbalance, is achieved when 45 degrees phase bit is placed in the middle as shown in Fig.B8.2.

As the first step in the design, ideal normalized reactance and susceptance values are computed for the T-type high-pass/low-pass sections for the given degree of the phase bit and for the reference termination of 50Ω at the center frequency of 10 GHz. These values are compared with the minimum and maximum realizable lumped inductance and capacitance values available in the GEC-Marconi F20 process. Certain microstrip lines are added wherever necessary to obtain the required phase shift. Using the models for the lumped elements of F20 process, appropriate elements are selected to construct the filter sections. Due to the parasitic capacitances, lead inductances, connecting microstrip lines and losses of the lumped elements, more than 1 degree shift in the differential phase from the theoretical values is encountered. Therefore, effects of all the elements on the ultimate results are analyzed and circuit element parameters are optimized towards obtaining the design specifications.

All the 45^0, 90^0 and 180^0 phase bit circuits are designed and optimized separately first without the switches and then with the switches. Only the 90^0 phase bit circuit will be

given here in some detail since the others follow similar pattern. Full detail can be found in [1].

Fig. B8.3 shows the layout of the 90^0 phase bit with the SPDT switches. The overall dimensions of the chip are 1770μm by 1160μm. Simulation results of insertion loss, return loss, differential phase shift together with the insertion phases and amplitude difference characteristics in 6-14 GHz band are shown in Figures B8.4, B8.5, B8.6 and B8.7 respectively. After the integration with the SPDT switches, it is observed that return loss of the high-pass section is degraded. In order to reduce the reflections, a 0.15nH inductance is connected in series with the capacitance of the high-pass section. Deviation in the differential phase shift is readjusted by increasing the length of the microstrip line in the low-pass section. The overall insertion loss increases to 5.5 dB (for low-pass path) at 10 GHz. Return loss is better than 11 dB in the overall frequency band for both paths. Frequency band for $\pm 2^0$ phase error is 8 GHz to 12.7 GHz. Since the two paths of the SPDT switch have identical insertion phase characteristics, the differential phase shift remains the same. There exits a maximum amplitude unbalance of 0.8 dB.

After the design of each phase shifter bit, they are cascaded to form a three-bit digital phase shifter. The reference state is specified as high-pass path of 90^0 phase bit, low-pass path of 45^0 phase bit and high-pass path of 180^0 phase bit. Table B8.1 gives the state combinations and the corresponding amplitude difference and differential phase shift at 10 GHz. After examining this table , one sees that an overall phase error of $+6^0$ occurs. Figures B8.8 and Fig. B8.9 show the insertion loss and the input/output return losses of the reference state respectively. Insertion loss at 10 GHz is 15.2 dB, where as input and output return losses are better than 10 dB in the operating band. Fig. B8.10 shows the differential phase shifts of the states from 2 to 8 in the frequency band 6-14 GHz. State 1 which is the reference state, has 0^0 phase shift and hence is not shown.

The excessive insertion loss originates from the individual losses of the SPDT switches. GEC-Marconi F20 process, implant IG has a relatively high resistivity. The other implant offered by GEC-Marconi F20 process, implant IS has half the resistivity of implant IG. The circuit models of implant IS, although not available, should be used in the design procedure. Bandwidth of the phase shifter is 7.8-11.7 GHz (1:1.5). Bandwidth can be widened by using the parasitic reactances of the switches as the elements of the filter sections.

REFERENCE

[1] M. E. Inal, "Monolithic Microwave Integrated Circuit Phase Shifters", M.S. Thesis, Department of Electrical and Electronic Engineering, Middle East Technical University, April 1997.

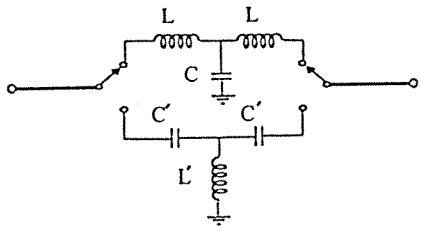

Figure B8.1 Schematics of T-Type Low-Pass/High-Pass Sections and SPDT Switches

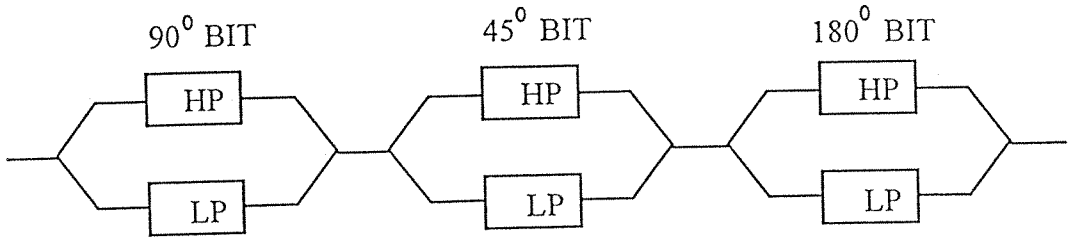

Figure B8.2 Block Diagram of the Three-Bit Phase Shifter

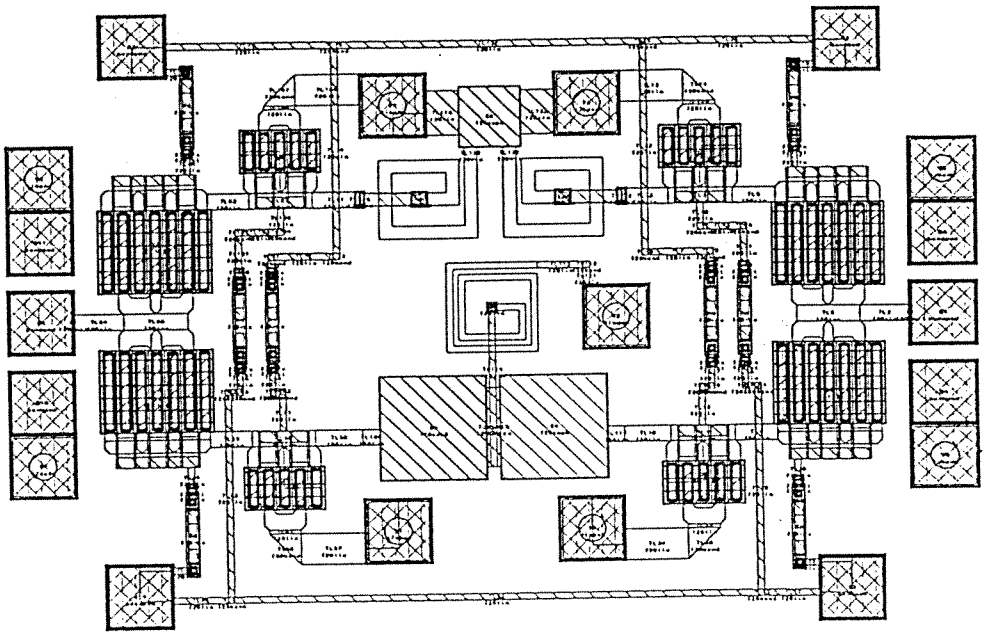

Figure B8.3 Layout of 90^0 Bhase Bit with SPDT Switches

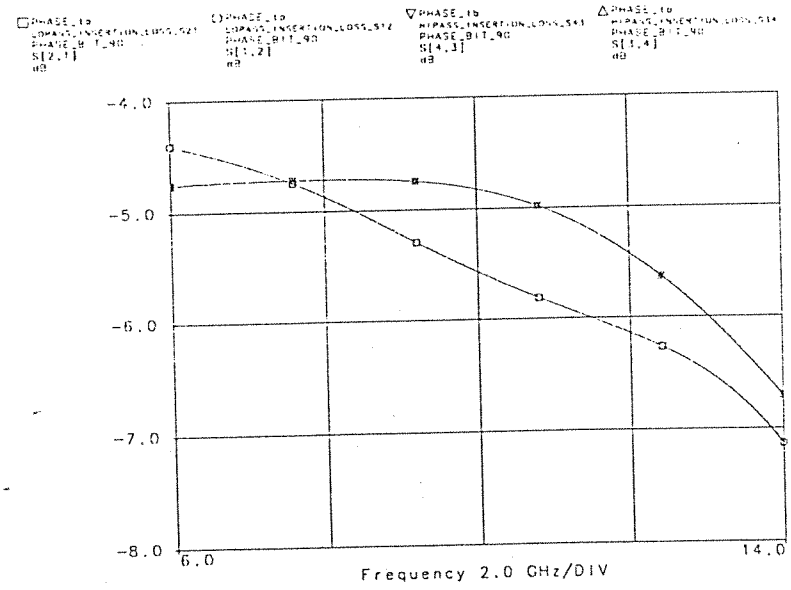

Figure B8.4 Insertion Loss of the 90^0 Phase Bit when High-Pass and Low-Pass Paths are Selected

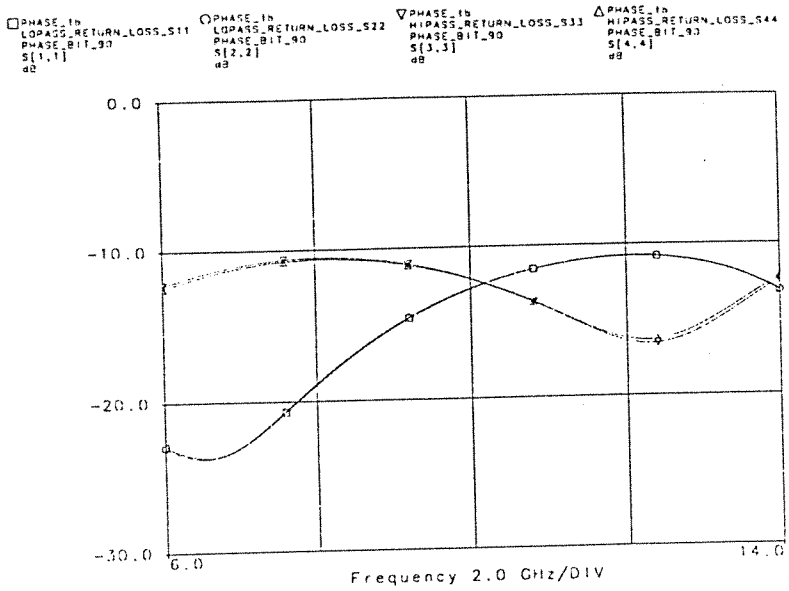

Figure B8.5 Return Loss of the 90^0 Phase Bit when High-Pass and Low-Pass Paths are Selected

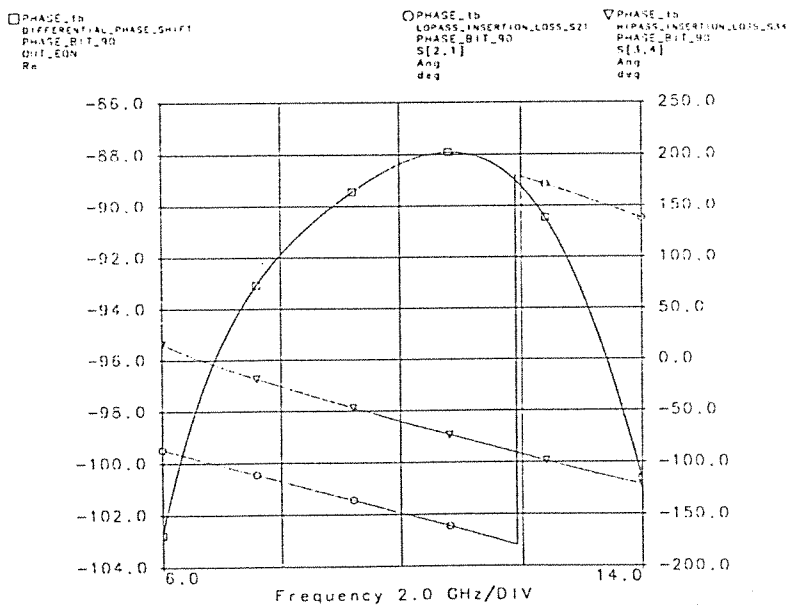

Figure B8.6 Differential Phase Shift and the Insertion Phases of the 90^0 Phase Bit when High-Pass and Low-Pass Paths are Selected

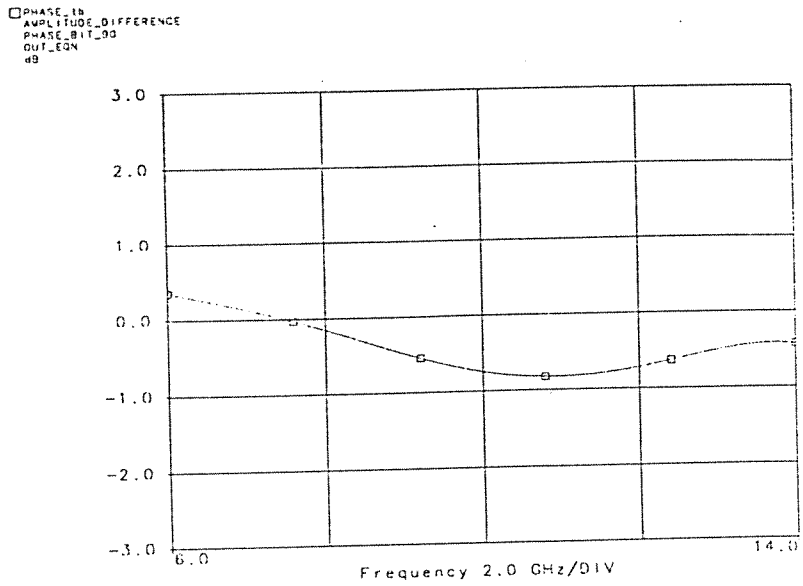

Figure B8.7 Amplitude Difference Between the Two Paths of the 90^0 Phase Bit when High-Pass and Low-Pass Paths are Selected

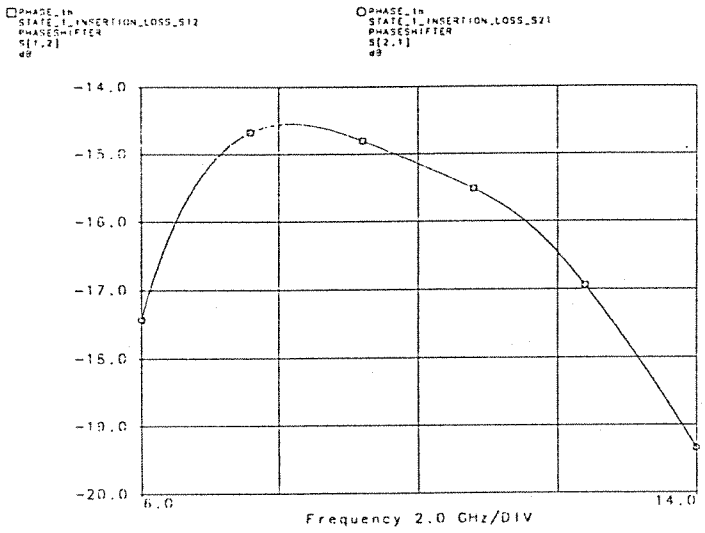

Figure B8.8 Insertion loss of the Reference State (State 1)

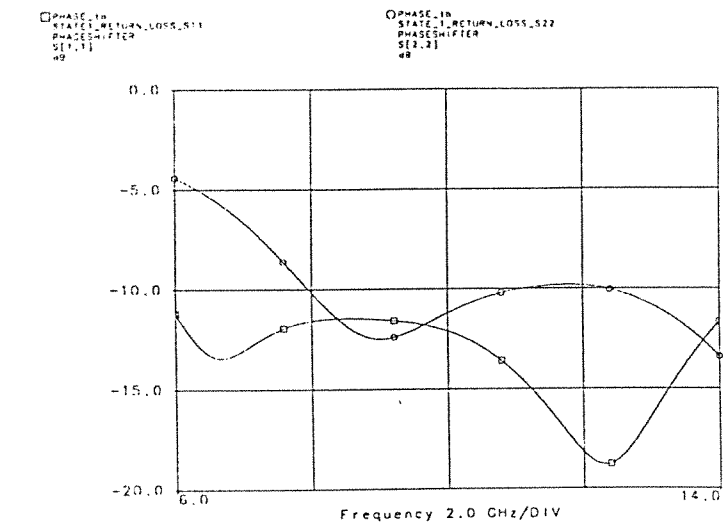

Figure B8.9 Input and Output Return Losses of the Reference State

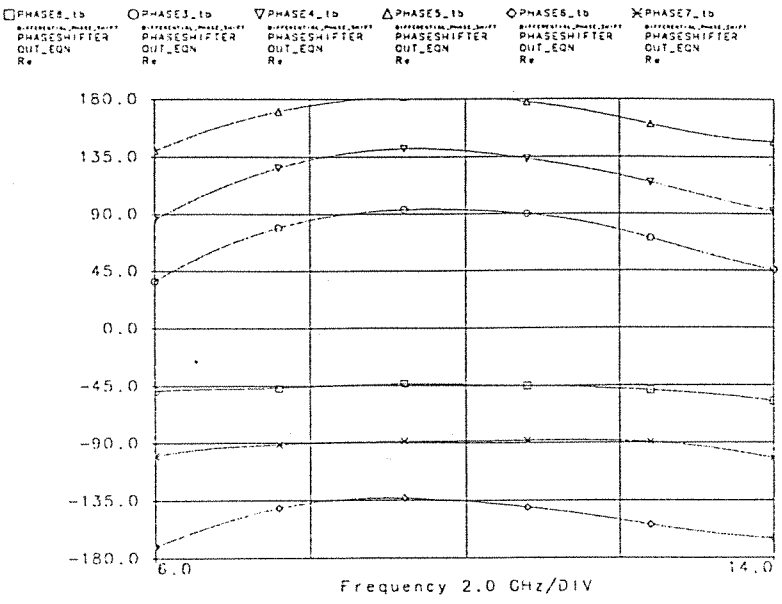

Figure B8.10 Differential Phases of the Seven Phase States

Table B8.1 Amplitude Difference and Phase Error for each State

STATE	90° BIT	45° BIT	180° BIT	ΔIL (dB)	$\Delta\phi_{theoretical}$ (°)	$\Delta\phi_{act}$ (°)	$\Delta\phi_{err}$ (°)
1	HP	LP	HP	0.0	0	0	0
2	HP	HP	HP	+1.7	45	40	-5
3	LP	LP	LP	-1.3	90	94	+4
4	LP	HP	LP	+0.6	135	141	+6
5	HP	LP	LP	-0.8	180	182	+2
6	HP	HP	LP	+0.8	225	226	+1
7	LP	LP	HP	-0.7	270	272	+2
8	LP	HP	HP	+1.0	315	316	+1

C- GENİŞ BANTLI ANTENLER ve NÜMERİK METOTLARLA İLGİLİ ARAŞTIRMALAR

C1. MİLİMETRİK DALGA BANDINDA İKİ VE ÜÇ KATMANLI (FERİT-DİELEKTRİK) ANTENLERLE ELEKTRONİK DEMET TARAMASI

Üzerine ferit dilim konulmuş tam iletken tabaka içindeki yarık antenin ışınım özellikleri daha önce incelenmiştir [1-2]. Bu yapı ile, ferit dilime uygulanan DC manyetik alanı değiştirerek, milimetrik dalga frekanslarında sürekli bir tarama elde edilebileceği gösterilmiştir. Ayrıca, bu çalışmalarda [1-2], izotropik olmayan maddeler de içeren çok katmanlı düzlemsel sistemler için, belirlenen sınır koşullarını da kapsayan basit bir ağ modeli geliştirilmiştir. Bu yöntem, Şekil-1'de görülen iki katmanlı (ferite-dielektrik) ve üç katmanlı (dielektrik-ferite-dielektrik) yapılara uygulanmış ve çeşitli madde parametrelerinin ve frekansın ışıma örüntüsüne etkisi incelenmiştir [2-3]. Verilen sayısal örneklerde DC manyetik alanın ferit dilime dik olacak şekilde uygulandığı ve ferit dilimin doygunluğa eriştiği varsayılmıştır. Ferit dik olarak manyetize edildiği için ışıma örüntüleri z eksenine göre simetriktir. DC manyetik alan farklı yönlerde uygulanırsa, ışıma örüntüsünün simetrisi bozulur. Bu durumda, problemin çözümünde, geliştirilen ağ modeli kullanılamaz. Kaynak olarak Hertz manyetik dipolü kullanılmıştır. Örneklerdeki dielektriklerin dielektrik sabitleri 2.4, feritinki ise 14'tür. Feritin doygunluk manyetik katsayısı 0.3 T'dır.

Şekil-2'de, ışıma örüntüsü, değişik Bo (DC manyetik alan) değerleri için çizilmiştir. Görüldüğü gibi, manyetik alan değiştikçe, ışıma demeti de hareket etmektedir. Ayrıca, Şekil-2'de dielektrik kalınlığının değişiminin ışıma örüntüsüne etkisi de gözlenmektedir. Aynı Bo değerleri için, dielektriğin kalınlığı 2 mm iken, ışın demeti 30 dereceden 15 dereceye kadar, kalınlık 2.3 mm iken 45 dereceden 35 dereceye kadar, kalınlık 2.7 mm iken ise 55 dereceden 50 dereceye kadar taramaktadır. Dielektriğin kalınlığı, ışın demetinin şeklini değiştirmemekte yalnızca farklı açısal alanlarda tarama yapılmasını sağlamaktadır.

Üç katmanlı (dielektrik-ferit-dielektrik) bir yapıda, ışıma örüntüsünün Bo ile değişimi Şekil-3'de çizilmiştir. Üstteki dielektriğin kalınlığı "l" dir. Grafikten görüldüğü gibi Bo=0.24 T iken tek bir ışın demeti olmasına karşın, Bo arttırıldığında demet önce ikiye sonra üçe bölünmüştür. Bo=0.28 T iken ise yine iki ışın demeti vardır.

Şekil-4'de iki katmanlı ve üç katmanlı yapılar için, ışın demetinin yönü manyetik alanın fonksiyonu olarak çizilmiştir. Bu ve bundan sonraki örneklerde, üstteki dielektriğin dielektrik sabiti 2'dir. Grafikten de görüldüğü gibi üç katmanlı bir yapı ile daha geniş bir alan taranabilmektedir.

Üç katmanlı yapı için, ışın demeti yönünün frekansla değişimi incelenmiş ve Şekil-5'de gösterilmiştir. Şekilden görüldüğü gibi 25 GHz'de tarama olmamaktadır. Buna karşın 25.5 GHz'de Bo 0.05T ile 0.15 T arasında değişirken 65 derecelik, 26 GHz'de Bo 0.05 T ile 0.2 T arasında değişirken 65 derecelik, 27 GHz'de Bo 0.05 ile 0.31 T arasında değişirken 70 derecelik tarama gerçekleşebilmektedir. Buradan, Bo'daki küçük değişikliklerin frekans 25.5 GHz veya 26 GHz' olduğunda, 27 GHz durumuna göre, ışın demetinin yönünde daha büyük sapmalar sağladığı sonucunu çıkarabiliriz.

Burada incelenen anten yapısı ile, milimetrik dalga frekanslarında, uygun madde seçimiyle, DC manyetik alanı değiştirerek, ışın demetinin şekli değiştirilebilmekte ve elektronik demet taraması elde edilebilmektedir.

REFERANSLAR:

[1] Ö. Aydın ve A. Hızal, "Electronic beam scanning by a vertically magnetized ferrite slab", COST224 Final Report, Ağustos 1992.

[2] Ö. Aydın ve A. Hızal, "Dielectric coated vertically magnetized ferrite slab for electronically scanning mm-wave antennas", Elektrik (Turkish Journal of Electrical Engineering and Computer Sciences), s. 206, Ekim 1993.

[3] Ö. Aydın ve A. Hızal, "Electronic beam scanning in millimeter-wave band with dielectric-ferrite loaded antennas", Antalya'da yapılan MELECON Konferansı bildiriler kitabı, Nisan 1994.

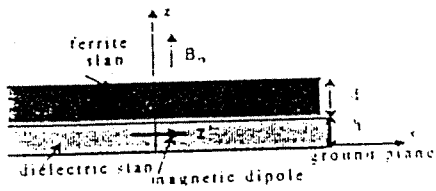

Şekil 1. İki katmanlı yapı

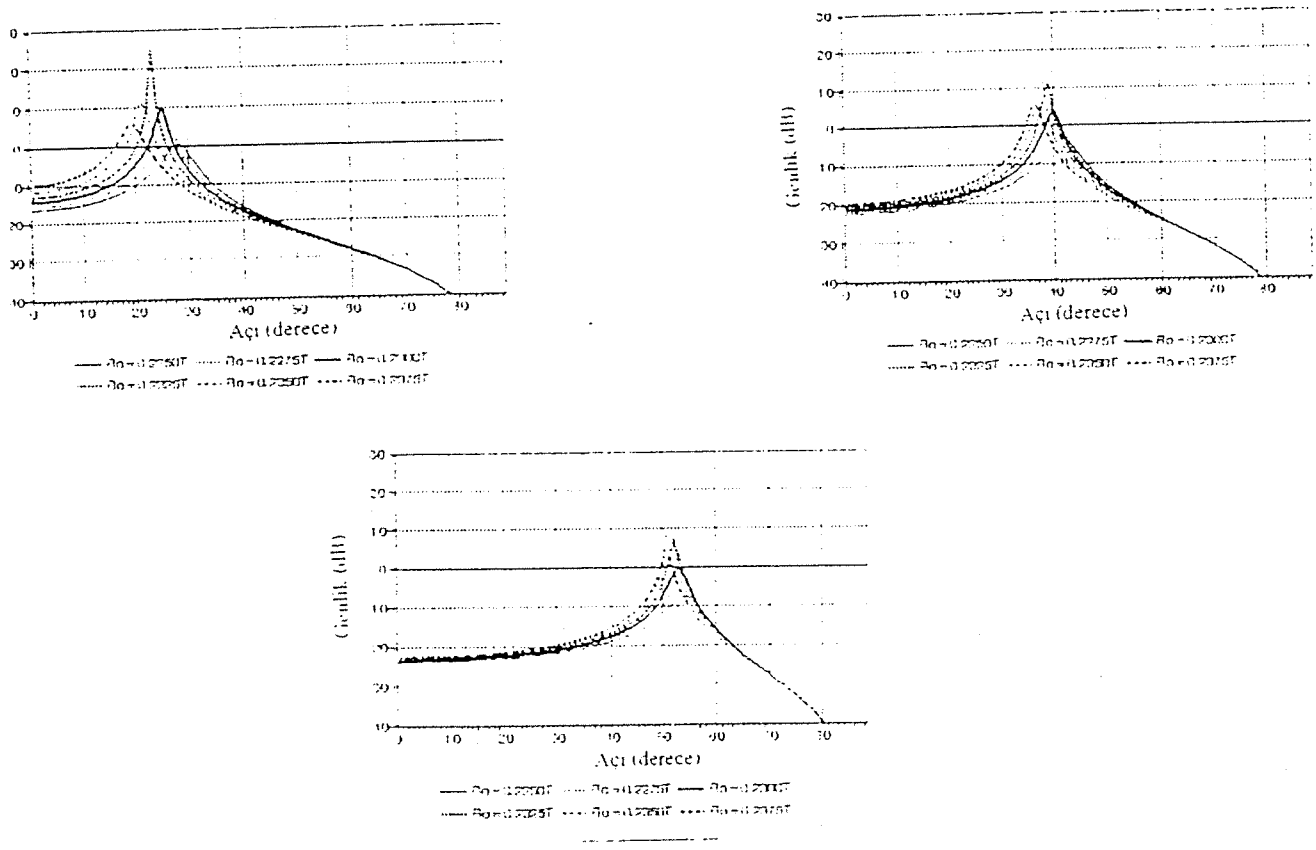

Şekil 2. İki katmanlı yapı için ışıma örüntüleri. f=26.5 GHz. d=6mm
a) h=2mm. b)2.3mm. c)h=2.7mm

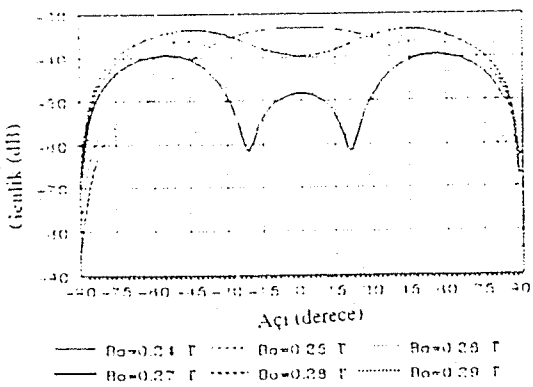

Şekil 3. Üç katmanlı yapı için ışıma örüntüleri. f=26.5 GHz. d=4.1mm. h=3mm. l=1mm

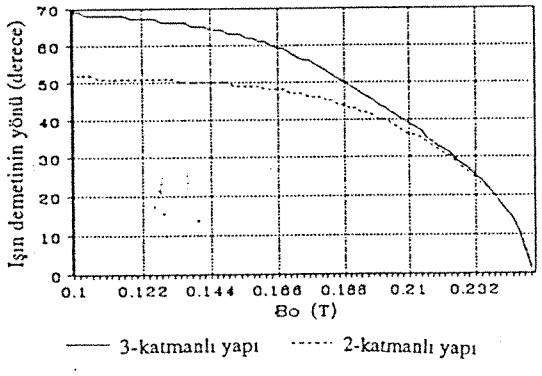

Şekil 4. Bo'ya karşılık ışın demetinin yönü, f=26.5 GHz, d=6mm, h=2mm, l=3mm

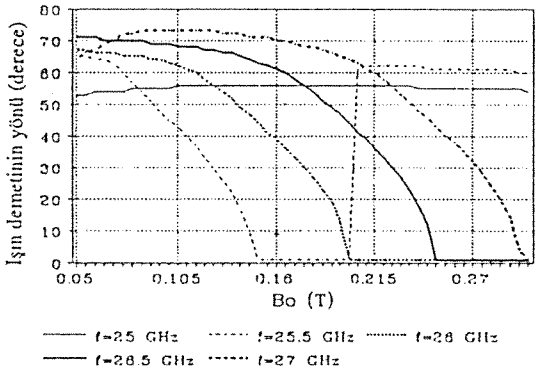

Şekil 5. Farklı frekanslar için Bo'ya karşılık ışın demetinin yönü, d=6mm, h=2mm, l=3mm

C2. 2-18 GHz VE 6-18 GHz FREKANS BANTLI VİVALDİ ANTENLER İLE 6-18 GHz FREKANS BANTLI VİVALDİ ANTEN DAİRESEL DİZİSİ TASARIMI

Mikrodalga ve milimetre-dalga teknolojilerindeki en son gelişmeler, küçük, ucuz, kolay üretilebilen, düzlemsel ve almaç ön devreleriyle aynı taban malzemesi üzerinde kolayca birleştirilebilen antenlere gereksinim duymaktadır. Vivaldi anten frekansa göre sürekli kendini tekrar eden, yürüyen dalga tipi antenler sınıfındandır. Teorik olarak sonsuz frekans bandına sahiptir (1:20). Yüksek bir kazancı, düşük yan lob seviyesi ve simetrik end-fire hüzmesi vardır. Düzlemsel, küçük, düşük profilli ve ucuz maliyetli bir antendir. Eksponensiyel olarak açılan yarık hat anten yapısına sahiptir. Yarık hat çift yüzlü ve dengelidir. Antenin girişinde mikroşerit hattan dengeli hatta geçişi sağlayan bir balun bulunmaktadır.

Vivaldi anten yavaş yürüyen galga antenleri grubundadır. Bu tip yapılar için ışıma sadece düzgün olmayan dağılıma sahip yerlerde, eğriliklerde ve süreksizliklerde oluşur. Yayılmış ya da ayrı olabilen süreksizlikler, anten yüzeyinde hareket eden dalgayı etkiler ve ışımaya sebep olurlar. Vivaldi antende ışıma; yarık genişliği dalga boyunun yarısına eşit olduğunda gerçekleşir. Bu durumda yürüyen dalganın anten üzerindeki faz hızı, uzaydakine eşit olur. Vivaldi antenin geometrik yapısı, frekansa göre kendini tekrarlayan bir yapıdadır. Bu sebeple ışıma özellikleri de teorik olarak frekansdan bağımsızdır. Ancak pratikte antenin fiziksel yapısı belli bir yerden kesildiği için bir alt kesim frekansı bulunmaktadır.

Antenin besleme bölümü bir dengelenmemiş mikroşerit hat, ardından mikroşerit daralan balun, onun ardından da eşit genişlikteki dengeli hat kısımlarından oluşmaktadır. Bütün bu kısımların karakteristik empedansı 50 Ohm dur. Besleme bölümünün ardından ışımayı yapan çift yüzlü yarık hat kısım gelir.

Bu çalışmada ilk olarak 2-18 GHz frekans bandında çalışan tek bir anten tasarlanmış ve RT/duroid® taban malzemesi kullanılarak üretilmiştir. Antenin besleme bölümündeki balun kısmı O.D.T.Ü. de geliştirilen sonlu eleman analiz programı kullanılarak tasarlanmıştır. Antenin giriş yansıma katsayısı (s11), ışıma örüntüsü ve kazancı gibi parametreleri ölçülmüş ve aşağıdaki şekillerde verilmiştir. Daha sonra 6-18 GHz frekans bandında çalışan bir Vivaldi anten tasarlanmış ve aynı taban malzemesi kullanılarak üretilmiştir. Bu tasarımda besleme bölümünün boyu kısaltılmış, antenin elektriksel performansı ölçülmüş ve bu kısalmadan dolayı bir performans kaybı gözlenmemiştir, ölçüm sonuçları aşağıdaki şekillerde sunulmuştur. Antenin mekanik

yapısı üzerinde yapılan deneyler sonucunda, ışımayı yapan bölümün boyunun uzatılması durumunda, giriş yansıma katsayısının azalacağı anlaşılmıştır. Bunun üzerine daha uzun bir ışıma bölgesine sahip 6-18 GHz frekans bantlı Vivaldi anten tasarlanmış ve bu antenden 8 adedi aynı taban malzemesi üzerine dairesel bir geometri içinde basılarak bir anten dizisi üretilmiştir. Dizi elemanlarının elektriksel performans özelikleri ölçülmüş ve aşağıda sunulmuştur. Elemanların giriş yansıma katsayısı, tekli 6-18 GHz Vivaldi anteninkine göre daha düşüktür. Ayrıca ışıma yapan bölgenin daha uzun olması sebebiyle kazancı daha yüksek ve komşu dizi elemanların blokaj etkisiyle yan lob ve arka lob seviyleri de tekli antene göre daha düşüktür.

Tasarlanan ve üretilen antenlerin elektriksel performans özellikleri tatmin edicidir. Dairesel anten dizisi, monopals genlik ya da faz karşılaştırmalı yön bulma sistemlerinde kullanılabilir. Diğer bir uygulama da dizi elemanlarını uygun faz ve genliklerde sürerek, hüzme tarayan anten şeklinde kullanmaktır.

Referanslar:

[1] Gibson, P.J., " The Vivaldi Aerial ".
9 th European Microwave Conference Proceedings,1979,pp.101-105.

[2] Gazit, E., " Improved Design of The Vivaldi Antenna".
IEE Proceedings Vol.-135, 1988 pp.89-92.

[3] Günalp N., Birand T., Hızal A., "Design of Tapered Slot Antennas with Broadband Feeds".
Contribution by the Turkish COST-223 Working Group METU (Turkey): Cost 223 Final Report.

[4] Birant T., et al., "Antennas in 1990`s: Active Antenna Array for Future Satellite and Terrestrial Communication".
Project Final Report for TUBITAK within the Frame Work of the COST-223 Project. January 1993 Ankara.

[5] Gvozdev, V.I., "Use of The Unbalanced Slotted Line in SHF Microcircuits".

Radio Eng. & Electron Phys., Vol.-27, 1982, pp. 42-47.

[6] Schiek, B., Köhler, J., " An Improved Microstrip-to-Microslot Transition."

IEEE Trans. Vol. MTT-24, 1976, pp. 231-233.

[7] Kuzuoğlu, M., " A New Finite Element Method for Electromagnetic Boundary Value Problems in Combined Exterior and Interior Regions".

Ph. D. Thesis in Elec. and Electron. Eng. METU., 1986.

[8] Akdeniz, T. " Analysis of Microstrip and Microstrip-like Structures by the Finite Element Method ".

A Master's Thesis in Elec. and Electron. Eng. METU., 1989.

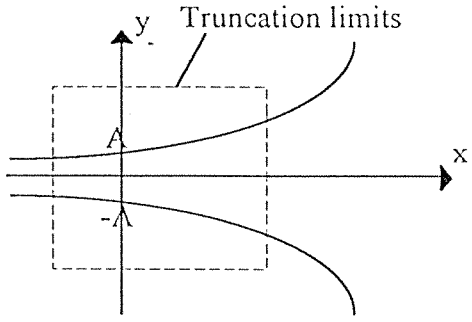

Şekil 1 Vivaldi Antenin Açılım Eğrisi

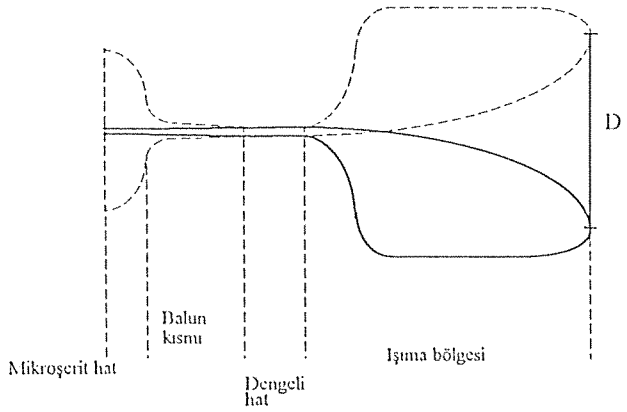

Şekil 2 Vivaldi Anten

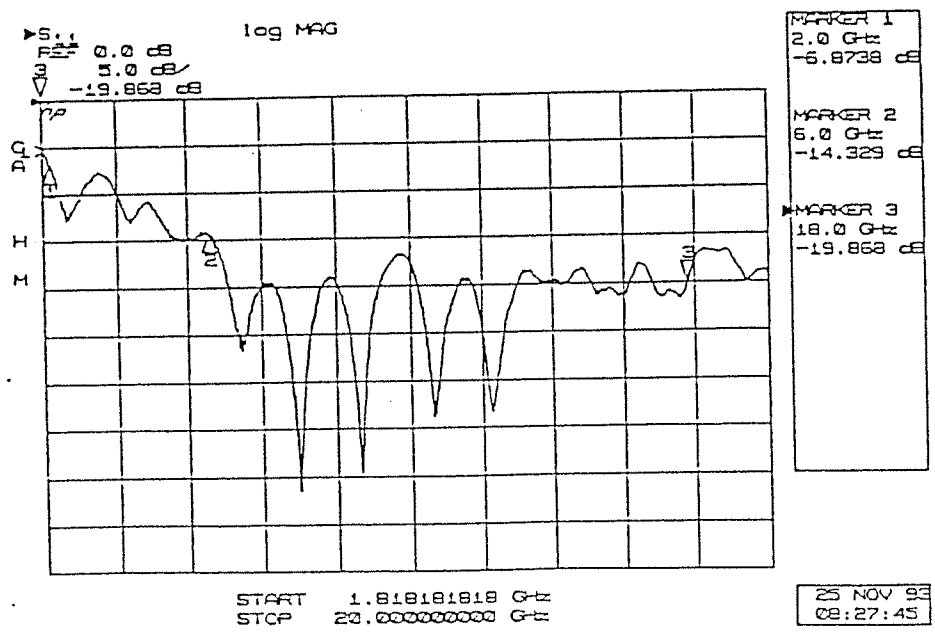

Şekil 3 2-18 GHz Frekans Bantlı Vivaldi Antenin Giriş Yansıma Katsayısı

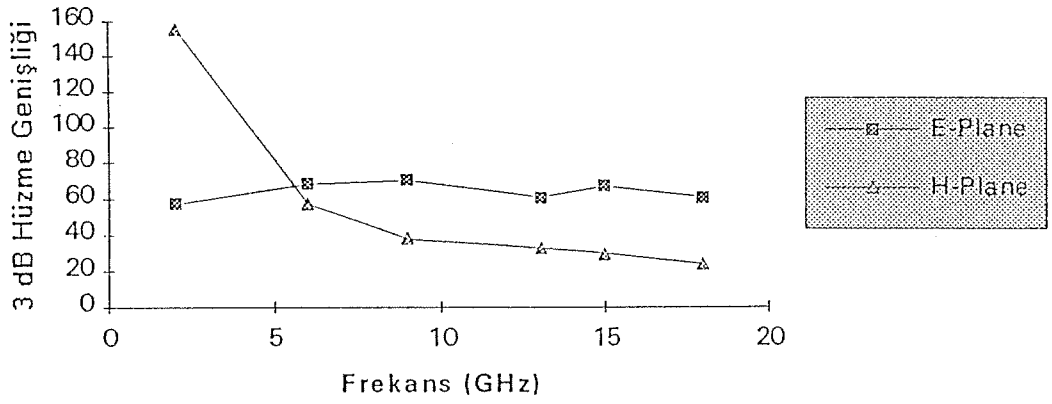

Şekil 4 2-18 GHz Frekans Bantlı Vivaldi Antenin 3 dB Hüzme Genişliği

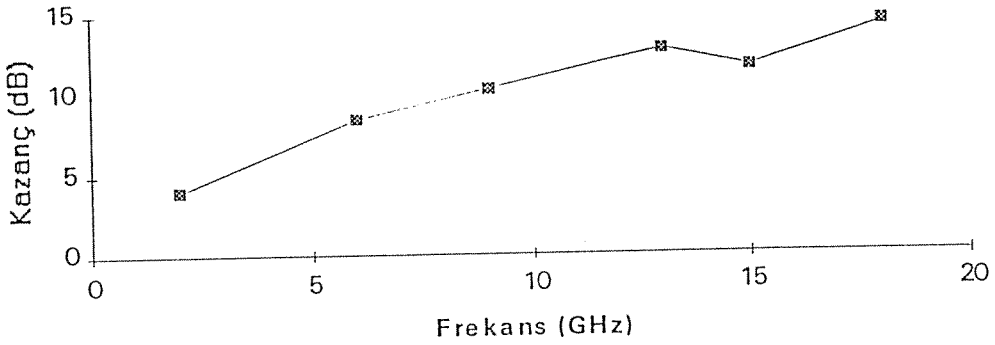

Şekil 5 2-18 GHz Frekans Bantlı Vivaldi Antenin Kazancı

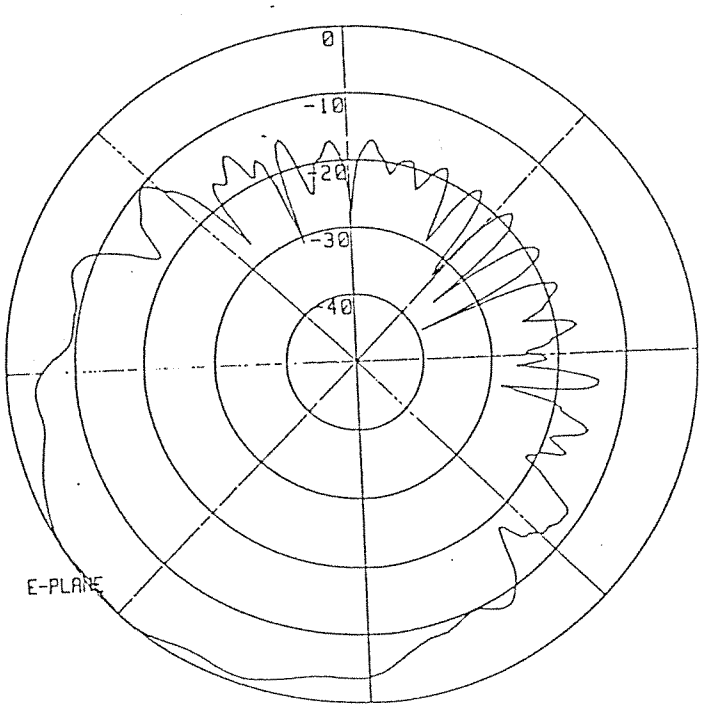

Şekil 6 2-18 GHz Frekans Bantlı Vivaldi Antenin 13 GHz deki Işıma Örüntüsü

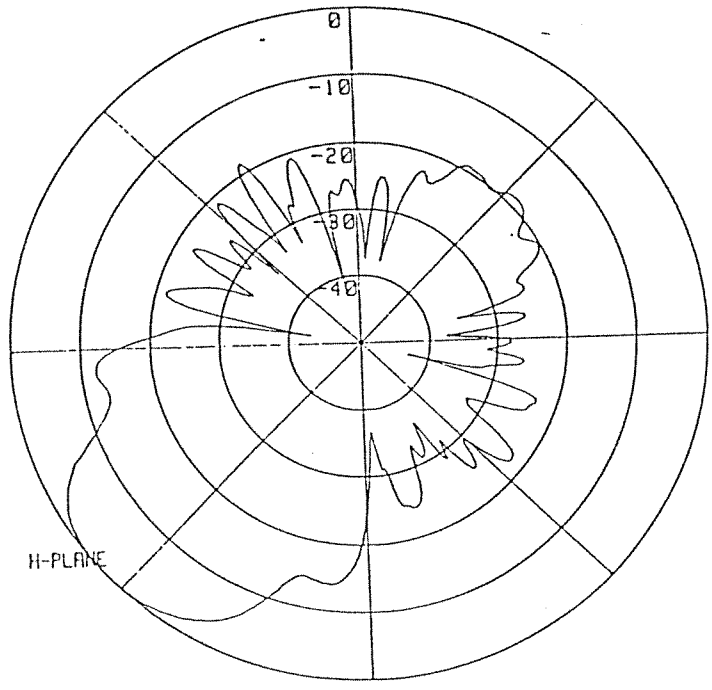

Şekil 7 2-18 GHz Frekans Bantlı Vivaldi Antenin 13 GHz deki Işıma Örüntüsü

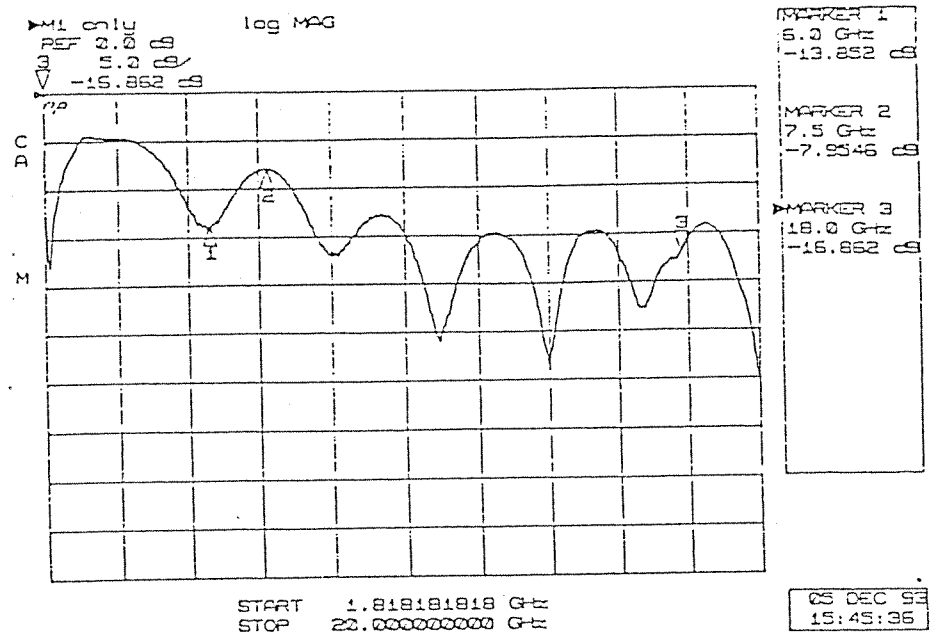

Şekil 8 6-18 GHz Frekans Bantlı Vivaldi Antenin Giriş Yansıma Katsayısı

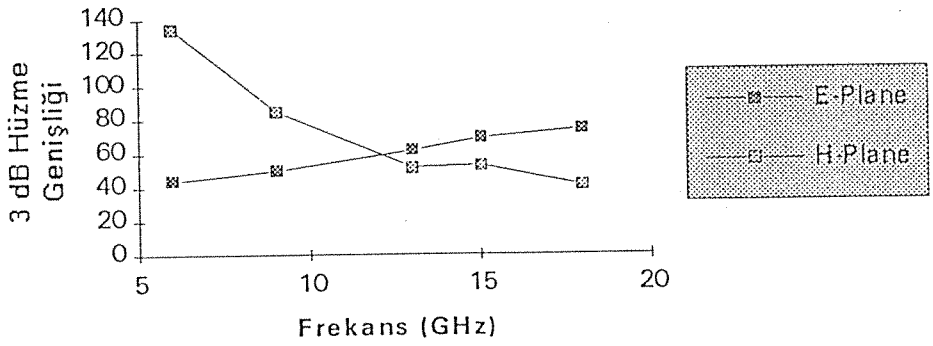

Şekil 9 6-18 GHz Frekans Bantlı Vivaldi Antenin 3 dB Hüzme Genişliği

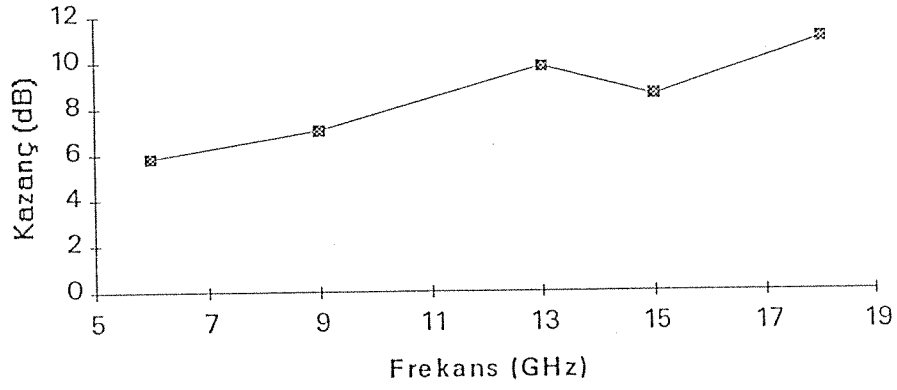

Şekil 10 6-18 GHz Frekans Bantlı Vivaldi Antenin Kazancı

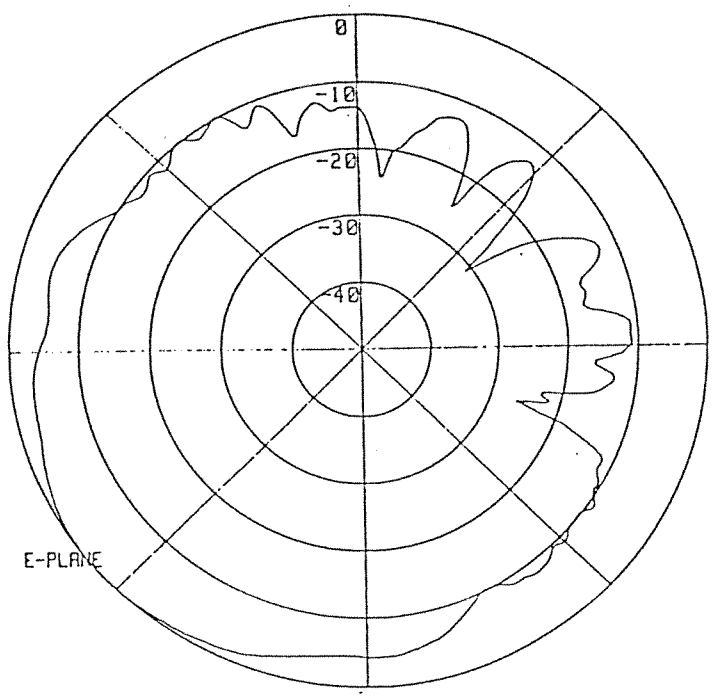

Şekil 11 6-18 GHz Frekans Bantlı Vivaldi Antenin 13 GHz deki Işıma Örüntüsü

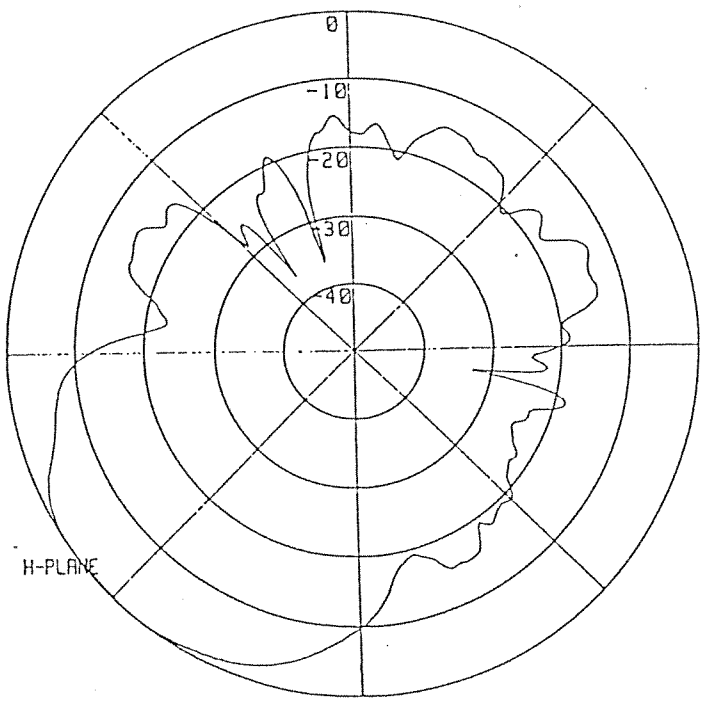

Şekil 12 6-18 GHz Frekans Bantlı Vivaldi Antenin 13 GHz deki Işıma Örüntüsü

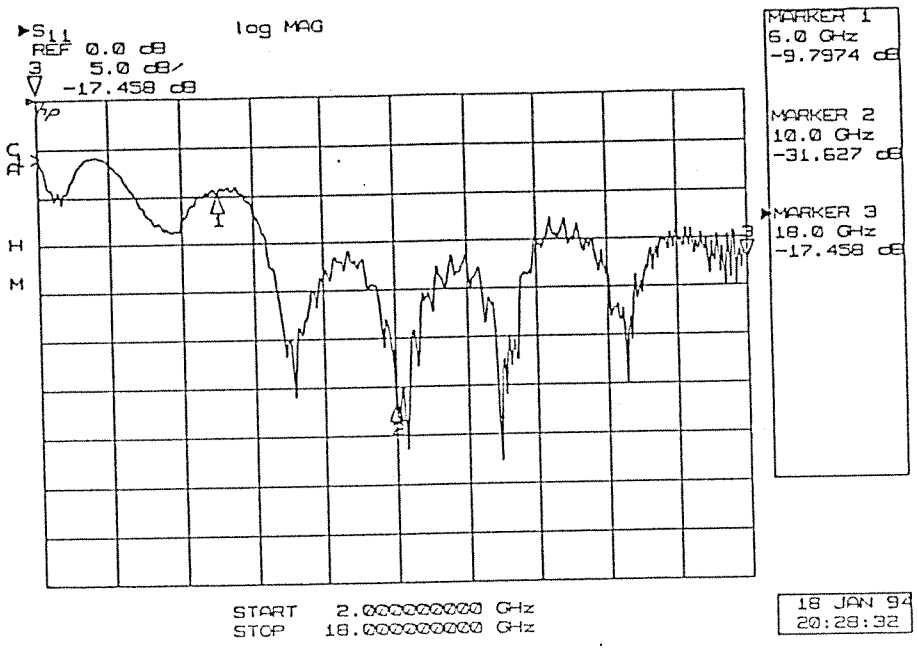

Şekil 13 Bir Dizi Elemanının Giriş Yansıma Katsayısı

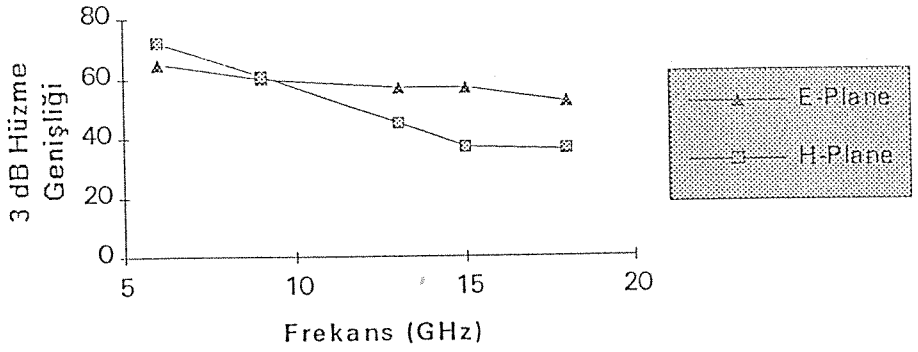

Şekil 14 Bir Dizi Elemanının 3 dB Hüzme Genişliği

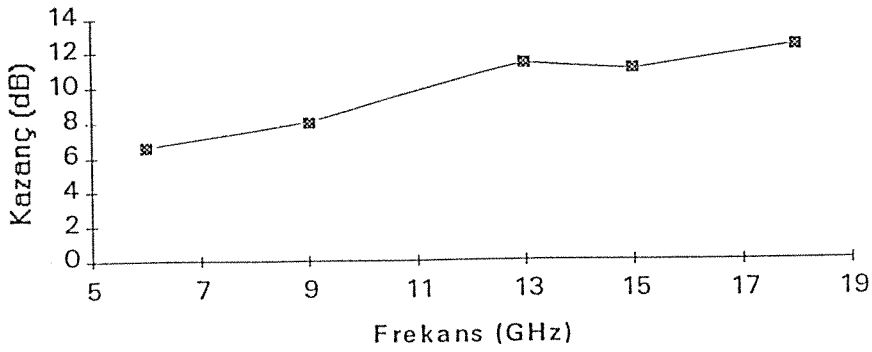

Şekil 15 Bir Dizi Elemanının Kazancı

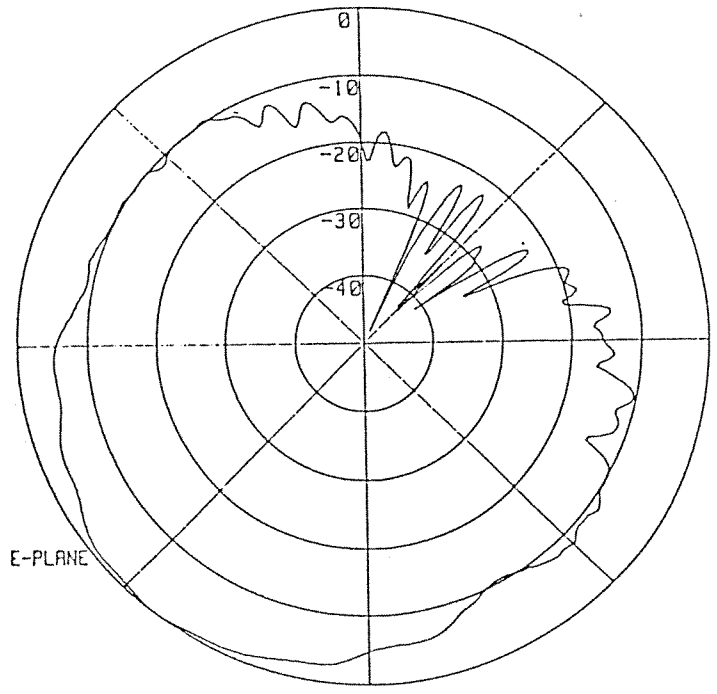

Şekil 16 Bir Dizi Elemanının 13 GHz deki Işıma Örüntüsü

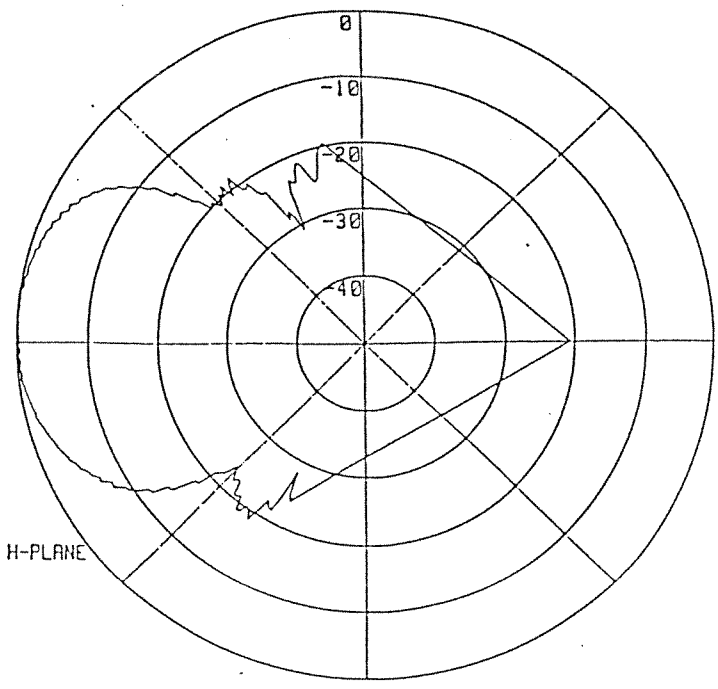

Şekil 17 Bir Dizi Elemanının 13 GHz deki Işıma Örüntüsü

C3. DÜZLEMSEL MİKROŞERİT YAPILARIN İNCELENMESİNDE KULLANILAN MOM METODUNUN NÜMERİK İNTEGRASYONDAN ARINDIRILMASI

GİRİŞ

Anten dizilerinin ve monolitik mikrodalga entegre devrelerin (MMIC) tasarımında tüm dalga analizi yapan metodların gelişmesi büyük önem taşımaktadır. Anten dizilerinde ya da mikrodalga devrelerde birbirlerine yakın elemanların etkileşimi, sistemin performansı üzerinde büyük etki yaratmaktadır. Bu nedenle bu tür devrelerin analizinde nümerik bir metod olan Moment Metod (MoM) sık olarak kullanılmaktadır [1],[2].Bu metod için hem izgesel uzayda hem de gerçek uzayda formülasyonlar mevcuttur. Ancak izgesel uzay formülasyonu çok hızlı salınan ve yavaş yakınsayan fonksiyonların sonsuz limitli ve iki-boyutlu integrallerinin nümerik olarak hesaplanmasını gerektirmektedir. Bu nedenle izgesel uzay uygulamalarında MoM matrisini doldurmak çok uzun zaman almaktadır. Bu metodu hızlandırmak için bazı yöntemler kullanılmasına rağmen, gerçek uzay formülasyonunda elde edilen gelişmelerden sonra izgesel uzay formülasyonu daha az tercih edilir olmuştur.

Gerçek uzay formülasyonundaki sorun ise yavaş yakınsayan izgesel uzay Green Fonksiyonunun Sommerfeld integrali (ya da Hankel Dönüşümü) adı verilen yüksek salınımlı bir integral aracılığı ile gerçek uzay Green Fonksioyununa dönüştürülmesidir [3]. Bu sorun izgesel uzay Green Fonksiyonunun kompleks üsteller ile yakınlaştırılması ile çözülmüştür [4],[5]. Bu yöntem kullanıldığında gercek uzay MoM matris elemanlarının hesaplanması, sınırlı bir aralıkta iki-boyutlu integrallerin nümerik olarak alınmasını gerektirmektedir. Bu çalışmada, bahsedilen iki-boyutlu integrallerin integral terimleri (integrand) Taylor Açılımı ile yakınlaştırılarak integraller analitik olarak hesaplanmıştır. Böylelikle gerçek uzay MoM formülasyonu hem nümerik integrasyondan kurtulmakta hem de hesaplama süresinde belirgin azalmalar elde edilmektedir.

Konu ile ilgili formülasyon ikinci bölümünde, mikroşerit bir hat üzerindeki uygulamada elde edilen sonuçlar ve karşılaştırmalar ise üçüncü bölümde sunulmaktadır.

FORMÜLASYON

Bu bölümde sunulan formülasyon, çok katmanlı ortamlardaki [6] üç boyutlu düzlemsel mikroşerit geometrilerine uygulanabilmektedir. Formülasyonun karmaşıklığına girmeden, sunulan metodun ana fikrini verebilmek amacı ile metod Şekil 1'de gösterilen tek katmanlı bir ortamdaki mikroşerit hat için uygulanmıştır.

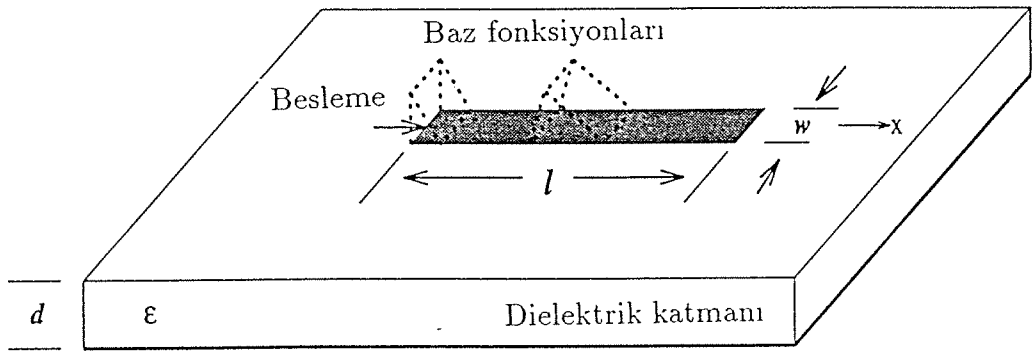

Şekil 1 : Formülasyonun uygulandığı mikroşerit hat geometrisi

Mikroşerit hat için elde edilen karışık potansiyel integral denklemi, MoM kullanılarak matris denklemine dönüştürüldüğünde matris elemanları aşağıdaki iç çarpım kullanılarak hesaplanır [7]:

$$< T_{xm}, G^A_{xx} * B_{xn} > + \frac{1}{\omega^2} < T_{xm}, \frac{\partial}{\partial x}\left(G_q * \frac{\partial}{\partial x} B_{xn} \right) > \qquad (1)$$

Bu denklemde B_{xm} baz fonksiyonu (basis function), T_{xm} test fonksiyonu, G^A vektör potansiyelin Green fonksiyonu ve G_q skalar potansiyelin Green fonksiyonu için kullanılmıştır.

Türev içermeyen terimde geliştirilen metod türevli terim için de aynı şekilde kullanılabileceği için formülasyon yalnızca ilk terim üzerinde gösterilecektir. İlk iç çarpımdaki integrasyonun sırası değiştirildiğinde aşağıdaki ifade elde edilmektedir:

$$< T_{xm}, G^A_{xx} * B_{xn} > = \int_{D_T}\int dx dy T_{xm}(x,y) \int_{D_B}\int dx' dy' G^A_{xx}(x-x', y-y') B_{xn}(x',y')$$
$$\int\int du\, dv\; G^A_{xx}(u,v) \underbrace{\int\int dx\, dy\; T_{xm}(x,y)\, B_{xn}(x-u, y-v)}_{\text{korelasyon fonksiyonu } (T_{xm} \otimes B_{xn})} \qquad (2)$$

Test ve baz fonksiyonları olarak akım yönünde üçgen, akıma dik yönde ise sabit olan çatı (rooftop) fonksiyonları seçildiğinde korelasyon fonksiyonu aşağıdaki şekilde ifade edilmektedir:

$$T_{xm} \otimes B_{xn} = f(u)g(v) \tag{3}$$

bu denklemde

$$\begin{aligned} f(u) &= \gamma_3 u^3 + \gamma_2 u^2 + \gamma_1 u + \gamma_0 \qquad (m-n-2)h_x < u < (m-n+2)h_x \\ g(v) &= \frac{1}{h_y^2} \begin{cases} v + h_y & -h_y \le v \le 0 \\ -v + h_y & 0 \le v \le h_y \end{cases} \end{aligned} \tag{4}$$

Kompleks üsteller ile yakınlaştırma metodu kullanılarak gerçek uzay Green Fonksiyonu aşağıdaki formda elde edilmektedir.

$$G(x, y, z = 0) \cong \sum_{n=1}^{N} a_n \frac{e^{-jkr_n}}{r_n} \tag{5}$$

bu denklemde $r_n = \sqrt{x^2 + y^2 - \alpha_n^2}$ kompleks uzaklık ve k ise kaynak ortamındaki dalga numarasıdır.

Denklem (4)'de gösterilen korelasyon fonksiyonu ve (5)'de verilen Green fonksiyonu (2)'ye yerleştirildiğinde aşağıdaki integraller elde edilir.

$$\begin{aligned} \frac{1}{h_y^2} \sum_{n=1}^{N} a_n \Bigg[& \gamma_0 \left(h_y \int\int \frac{e^{-jk_s r_n}}{r_n} dv\, du - \int\int \frac{e^{-jk_s r_n}}{r_n} v\, dv\, du \right) \\ & + \gamma_1 \left(h_y \int\int \frac{e^{-jk_s r_n}}{r_n} u\, dv\, du - \int\int \frac{e^{-jk_s r_n}}{r_n} u\, v\, dv\, du \right) \\ & + \gamma_2 \left(h_y \int\int \frac{e^{-jk_s r_n}}{r_n} u^2\, dv\, du - \int\int \frac{e^{-jk_s r_n}}{r_n} u^2\, v\, dv\, du \right) \\ & + \gamma_3 \left(h_y \int\int \frac{e^{-jk_s r_n}}{r_n} u^3\, dv\, du - \int\int \frac{e^{-jk_s r_n}}{r_n} u^3\, v\, dv\, du \right) \Bigg] \end{aligned} \tag{6}$$

MoM uygulamalarında bu integraller nümerik olarak hesaplanmakta, bu da matris doldurma süresini çok arttırmaktadır. (6)'da verilen ilk integral terimindeki üstelin Taylor açılımı kullanılarak iki boyutlu integralin analitik olarak alınabileceği gösterilmiştir [8]. Bu bilgi ve bazı integral özellikleri [9] kullanılarak (6)'da verilen tüm integraller analitik olarak hesaplanmıştır.

e^{-jkr_n} teriminin, R_c merkez noktası etrafında açılan m'inci derecedeki Taylor açılımı için hata aşağıdaki denklem ile sınırlanmıştır.

$$hata \le \frac{|k_s(r_n - R_c)|^{m+1}}{(m+1)!}$$

Taylor açılımı nedeniyle gelen hataya bir sınır koyabilmek amacıyla her integral için R_c, o integral aralığının orta noktası olarak seçilmiştir. Integral aralığı x yönünde $4h_x$, y yönünde $2h_y$ olduğu için $|r_n - R_c| \leq \sqrt{(2h_x)^2 + h_y^2}$. Bir dalga boyu için yirmi baz fonksiyonu seçildiğinde beşinci derecedeki Taylor açılımındaki hata 10^{-4} ile sınırlandırılmıştır. Bu hata sınırının sonuçta elde edilen akım dağılımını etkilemediği gözlenerek Taylor açılımındaki terim sayısı daha da arttırılmamıştır.

R_c etrafındaki beşinci dereceden Taylor açılımı kullanılarak $e^{-jk_s r_n}$ aşağıdaki şekilde yakınlaştırılmaktadır.

$$e^{-jk_s r_n} \approx \beta_0 + \beta_1 r_n + \beta_2 r_n^2 + \beta_3 r_n^3 + \beta_4 r_n^4 + \beta_5 r_n^5 \tag{7}$$

(6)'deki $e^{-jk_s r_n}$, (7)'deki Taylor açılımıyla yakınlaştırıldığında aşağıdaki integrallerin analitik olarak hesaplanması gerekmektedir.

$$\int\int r_n^j u^k v^l \, du \, dv \qquad \text{for j=-1,0,...,4, k=0,...,3, l=0,1} \tag{8}$$

Bu integraller kapalı formda elde edilmiştir. Böylelikle MoM nümerik integrallerden tam olarak arındırılmıştır. Önerilen metod test ve baz fonksiyonları polinom benzeri fonksiyonlar olduğu sürece uygulanabilmektedir.

SONUÇLAR

Bir önceki bölümde anlatılan yöntem mikroşerit bir hattın analizi için uygulanmıştır. Ortamın dielektrik sabiti $\epsilon_r = 4$, hattın genişliğinin katman kalınlığına olan oranı 4, katmanın kalınlığı 0.02032 cm, frekans 1 GHz ve hattın uzunluğu 10 cm'dir. CPU zamanları SUN Sparc 10 iş istasyonu kullanılarak elde edilmiştir.

Hat üzerindeki akım dağılımı önce nümerik integrasyon (1. durum), daha sonra da analitik integrasyon yöntemi (2. durum) kullanılarak hesaplanmıştır. Nümerik integrasyon için, mevcut algoritmalar arasında en hızlılarından kabul edilen 16 noktalı Gauss integrasyon algoritması kullanılmıştır. İntegralin yakınsamasını garantilemek için integral aralığı alt aralıklara ayrılmıştır. Değişik sayıdaki baz fonksiyonları için CPU zamanlarının karşılaştırılması Tablo 1'de verilmştir. 40 baz fonksiyonu kullanılarak ve iki ayri yöntem ile elde edilen akım dağılımları Şekil 2 'de verilmiştir.

baz fonks. sayısı	CPU zamanı(saniye)(1.Durum)	CPU zamanı(saniye)(2.Durum)
10	13.3	0.36
20	27.0	0.65
30	39.0	0.98
40	52.95	1.33

Tablo 1 : İki ayrı yöntem ile elde edilen CPU zamanları

Tablo 1 incelendiğinde, analitik integrasyonun hesaplama süresinde 40 katlık bir hızlanma sağladığı gözlenmektedir. Nümerik integrasyonun kaldırılması ile MoM nümerik integrasyondan gelen hatalardan ve problemin yapısına uygun nümerik integrasyon algoritması bulmak için harcanan zamandan arındırılmıştır. Matris elemanları kapalı formda ifade edilebildiği için mikroşerit hattın genişliği, uzunluğu gibi parametrelerin akım dağılımı üzerindeki etkileri gerekli değişkenlere göre türev alarak gözlenebilmektedir.

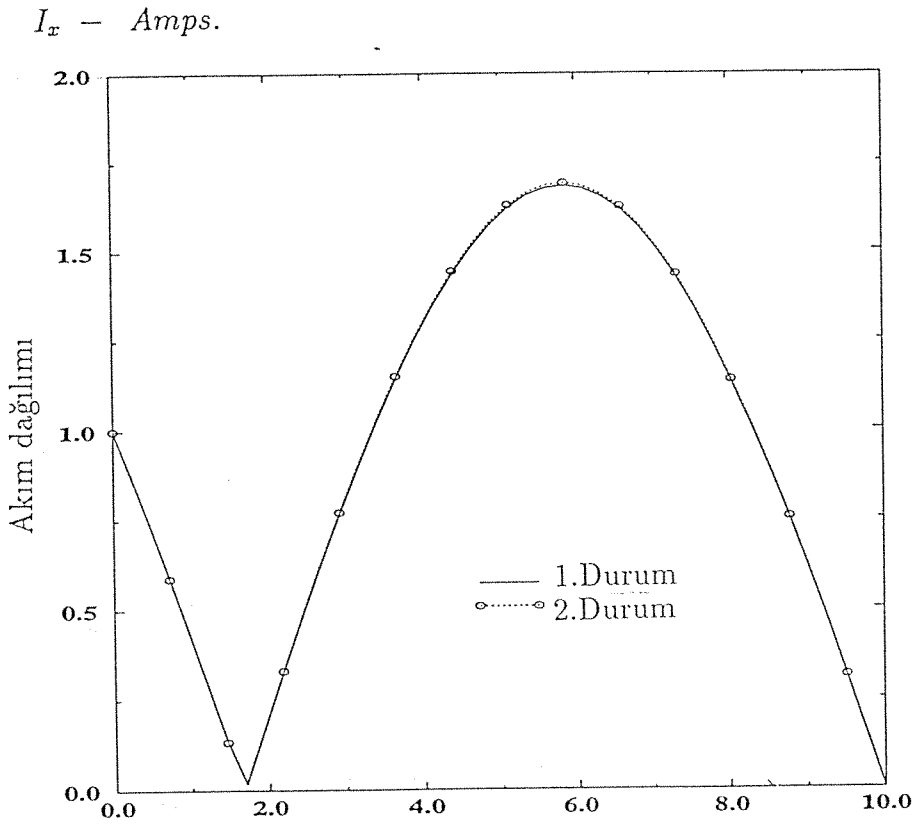

Şekil 2 : Elde edilen akım dağılımları

Bir tam dalga analiz yöntemi olan MoM, bu çalışmada önerilen yöntem ile hızlandırılarak herhangi bir düzlemsel mikroşerit yapısının (anten dizisi ya da MMIC devre) tasarımında uygun bir optimizasyon programı ile verimli olarak çalışabilecek bir metoda dönüştürülmüştür.

Kaynakça

[1] R. F. Harrington, *Field Computation by Moment Methods.* New York: MacMillan; Florida; Krieger Publishing, 1983.

[2] D. M. Pozar, " Input Impedance and Mutual Coupling of Rectangular Microstrip Antennas,"it IEEE Trans. Antennas Propagat., vol. AP-30, pp. 1191-1196, Nov. 1982.

[3] A. Sommerfeld, *Partial Differential Equations in Physics.* New York: Academic Press Inc., 1949.

[4] Y. L. Chow, J. J. Yang, and D. F. Fang and G. E. Howard, "Closed form spatial Green's function for the thick substrate," *IEEE Trans. Microwave Theory Tech.*, vol. MTT-39, pp. 588-592, Mar. 1991.

[5] M. I. Aksun and R. Mittra, "Derivation of closed-form Green's functions for a general microstrip geometries," *IEEE Trans. Microwave Theory Tech.*, vol. MTT-40, pp. 2055-2062, Nov., 1992.

[6] G. Dural and M. I. Aksun, "Closed-form Green's functions for general sources and stratified media," submitted for publication.

[7] J. R. Mosig and F. E. Gardiol, "General Integral Equation Formulation for Microstrip Antennas and Scatterers,"*IEE Proc.*, pt. H, no. 7, vol. 132, pp. 424-432, 1985.

[8] R. F. Harrington, " Matrix metods for field problems,"*Proc. IEEE*, vol. 55, pp. 136-149, Feb. 1967.

[9] K. Mahadevan and H. A. Auda, " Electromagnetic field of a rectangular patch of uniform and linear distributions of current,"*IEEE Trans. Antennas Propagat.*, vol. AP-37, pp. 1503-1509, Dec. 1989.

C4. SONLU DİZİ ANTENLERİN İNTEGRAL DENKLEM SİSTEMİ İLE SİSTEMATİK ÇÖZÜMÜ

GİRİŞ

Bu çalışmada mükemmel iletken bir toprak yüzeye açılan dikdörtgen dalga kılavuzlarının oluşturduğu sonlu dizi antenler incelenmiştir. Dalga kılavuzları sadece temel kipi (TE_{10}) destekleyen eşit boyutlardadır. Dalga kılavuzları toprak yüzey üzerine istenildiği gibi (konum kiplenimli dizi elde edebilmek için) yerleştirilebilir. Şekil 1'de, hesaplamaları kolaylaştırmak için sonsuz yüzey üzerine eşit aralıklarla yerleştirilmiş bir dizi anten gösterilmiştir.

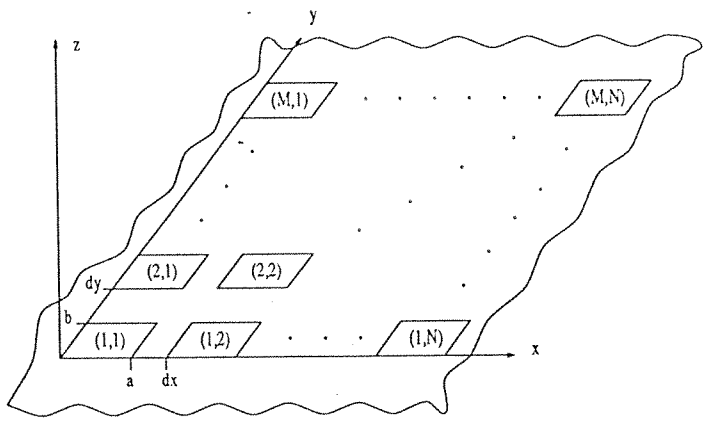

Şekil 1: $M \times N$ dizi anten.

Fenn v.d. [1] Şekil.1'de gösterilen dizi anteni moment metod tekniği kullanarak ve temel kipe dik olarak oluşan kipleri ihmal ederek küçük dizi eleman boyutları için çözmüştür. Aynı problemi Sharma v.d. [2] birbirlerinden uzak elemanlardan oluşan dizi antenler için sonuşur (asimtotik) yöntemlerle çözmüştür. Bu çalışmada, sonsuz bir yüzeye açılan dikdörtgen dalga kılavuzunun çözümü (H. Yavuz ve O.M. Büyükdura [3],[4]) dizi antenlere uyarlanmıştır.

Dalga kılavuzlarındaki ve yarı-uzaydaki alanlar uygun 'dyadic Green' işlevleri ve açıklıklar üzerindeki bilinmeyen alan dağılımları cinsinden yazılmış ve bütün açıklıklar üzerinde manyetik alanın yatay bileşeninin sürekliliği kullanılarak bir integral denklem sistemi

elde edilmiştir. Dalga kılavuzu kiplerinin dikgenlik (orthogonality) özelliği kullanılarak açıklıklar üzerindeki bilinmeyen alan dağılımının katsayıları için bir matris eşitliği elde edilmiştir. Bu hesaplamalarda dizi elemanlarının karşılıklı bağlaşımları da gözönüne alınmıştır.

Elde edilen matrisin en önemli özelliği dizi anten elemanlarının beslemesinden bağımsız olmasıdır. Matris, bir dizi anten için bir kere hesaplanıp tersi alındıktan sonra o dizi anten elemanlarının (ışıyan açıklıkların) alan dağılımlarını ve besleme noktasından görünen admitanslarını değişik besleme birleşimleri için bulunmasında kullanılabilecektir. Anten elemanları dikdörtgen ızgara biçiminde yerleştirilirse elde edilen matris blok 'Toeplitz' özelliğine sahip olacak ve matrisin hesaplama zamanı, saklama alanı büyük ölçüde azalacaktır.

FORMÜLASYON

Alan eşitlik prensibi kullanılarak Şekil.1'de verilen problem iki bölgeye ayrılmıştır, yani dalga kılavuzlarının ağız açıklıkları mükemmel bir elektriksel iletken ile örtülmüştür. Daha sonra bilinmeyen manyetik akımlar $-\vec{M}_p$ ve $\vec{M}_p$ p'inci eleman ağzının sırasıyla yarı-uzay ve dalga kılavuzu tarafına yerleştirilmiştir; bu seçimle elektrik alanının enine bileşeninin p'inci elemanın ağız açıklığı boyunca devamlılığı sağlanmıştır. Bütün elemanlar istenen tarama açısında ışınım yapması için uygun biçimde evrelendirilmiş temel TE_{10} kipi ile beslenmiştir.

$$\vec{M}_p = \hat{z} \times \vec{E}_p \qquad p = 1,2,...,M \times N \tag{1}$$

burada $M \times N$ dizi anten elemanlarının sayısıdır.

Yarı-uzaydaki ve p'inci dalga kılavuzundaki elektrik alanları dizi elemanlarının ağız açıklıklarındaki bilinmeyen manyetik akımlar cinsinden yazılabilirler:

$$\vec{E}^{hs}(\vec{R}) = -\sum_{p=1}^{M\times N} \int_{S_p} [\nabla \times \overline{\overline{\Gamma}}_2^{hs}(\vec{R},\vec{R}')][\hat{z} \times \vec{E}_p(\vec{R}')]ds' \tag{2}$$

$$\vec{E}_p(\vec{R}) = \hat{y} A_p \sin\frac{\pi}{a}x(e^{-jk_{z10}z} - e^{jk_{z10}z}) - \int_{S_p} [\nabla \times \overline{\overline{\Gamma}}_2^{wg}(\vec{R},\vec{R}')] \cdot [-\hat{z} \times \vec{E}_p(\vec{R}')]ds' \tag{3}$$

burada

$$k_{z10} = \sqrt{k^2 - (\frac{\pi}{a})^2} \tag{4}$$

A_p p'inci dalga kılavuzunun beslemesinin büyüklüğünü ve evresini, s_p p'inci dalga kılavuzunun ağız açıklığını, $\vec{R}'$ s_p üzerindeki bir noktayı, $\overline{\overline{\Gamma}}_2^{hs}$ yarı-uzay 'dyadic Green' işlevini, $\overline{\overline{\Gamma}}_2^{wg}$ ağız açıklığı mükemmel bir elektriksel iletken ile örtülmüş yarı-sonsuz dalga kılavuzunun 'dyadic Green' işlevini gösterir. Bu 'dyadic Green' işlevleri aşağıdaki gibi bulunmuştur:

$$\overline{\overline{\Gamma}}_2^{hs}(\vec{R},\vec{R}') = -2(\overline{\overline{I}} + \frac{\nabla\nabla}{k^2})G_0(\vec{R},\vec{R}') \tag{5}$$

$$\overline{\overline{\Gamma}}_2^{wg}(\vec{R},\vec{R}') = \sum_{m=0}^{\infty}\sum_{n=0}^{\infty}\frac{2(2-\delta_0)}{abk_{zmn}k_c^2}[j\vec{M}^{<}_{omn}(\vec{R})\vec{M}^{>}_{omn}(\vec{R}') + \vec{N}^{<}_{emn}(\vec{R})\vec{N}^{>}_{emn}(\vec{R}')] \tag{6}$$

burada

$$G_0(\vec{R},\vec{R}') = \frac{e^{jk|\vec{R}-\vec{R}'|}}{4\pi\mid\vec{R}-\vec{R}'\mid} \quad , \quad \overline{\overline{I}} = \hat{x}\hat{x} + \hat{y}\hat{y} + \hat{z}\hat{z} \tag{7}$$

$\overline{\overline{I}}$ birim 'dyad' ı, G_0 serbest-uzay sayıl Green işlevini, $\vec{M}$ ve $\vec{N}$ ise dikdörtgen dalga kılavuzu geometrisine uygun vektörel Hansen dalga işlevlerini göstermektedir.

Elektrik alanının enine bileşenleri dalga kılavuzlarının ağız açıklıklarında ($z = 0$) bilinmeyen katsayılarla çarpılmış dalga kılavuzu kiplerinin toplamı halinde yazılarak çözüme ulaşılmıştır:

$$\vec{E}_p(\vec{R}')\mid_{z'=0} = \sum_m\sum_n c^p_{mn}\vec{n}_{omn}(x',y') + d^p_{mn}\vec{m}_{emn}(x,y) \tag{8}$$

burada $\vec{m}$, $\vec{n}$ dalga kılavuzu kiplerini ve d_{mn}, c_{mn} sırasıyla TE ve TM kiplerinin bilinmeyen katsayılarını göstermektedir. Daha sonra bütün elemanların ağız açıklıkları boyunca manyetik alanın enine bileşeninin sürekliliği uygulanmıştır.

$$\nabla\times\vec{E}^{hs}(\vec{R})\mid_{R\ s_p\ uzerinde} = \nabla\times\vec{E}^{wg}_p(\vec{R})\mid_{R\ s_p\ uzerinde} \qquad p = 1,2,..,M\times N \tag{9}$$

Elde edilen eşitliklerin test işlevleriyle (dalga kılavuzu kipleri) sayıl çarpımları alınıp (Galerkin yöntemi) bütün elemanların ağız açıklığı boyunca manyetik alanın x ve y bileşenlerinin sürekliliği için iki eşitlik sistemi elde edilmiştir. Bu eşitlikler aşağıdaki gibi yazılabilir.

$$\sum_{k=1}^{N}(\sum_m\sum_n X^{pk}_{mn,li}d^k_{mn} + Y^{pk}_{mn,li}c^k_{mn}) = T^p_{li} \tag{10}$$

$$\sum_{k=1}^{N}(\sum_m\sum_n Z^{pk}_{mn,li}d^k_{mn} + W^{pk}_{mn,li}c^k_{mn}) = 0 \tag{11}$$

burada p = 1,2, ... ,$M \times N$. Eşitlik (10) ve (11) deki X, Y, Z ve W iki boyutlu integrallerdir ve integral sınırları içinde tekil noktalar vardır. İntegrallerdeki tekilliklerle

şedebilmek için serbest-uzay sayıl Green işlevi G_0 bir düzlem dalgası izgesi (spektrumu) iminde yazılmıştır.

$$G_0(\vec{R},\vec{R}') = -\frac{j}{8\pi^2}\int_{-\infty}^{\infty}\int_{-\infty}^{\infty}\frac{e^{-j[\beta_x(x-x')+\beta_y(y-y')+\beta_z|z-z'|]}}{\beta_z}d\beta_x d\beta_y \tag{12}$$

rmülasyonun bakışımlılık (simetri) özellikleri kullanılarak eşitlik (10) ve (11) daki ğişkenler aşağıdaki gibi 0 dan ∞ a iki boyutlu integraller olarak yazılabilir:

$$\begin{aligned} X^{jk}_{mn,lp} &= -\frac{32}{\pi^2}\int_0^{\infty}\int_0^{\infty}\frac{d\beta_x d\beta_y}{\beta_z}A(\beta_x,\beta_y)B(\beta_x,\beta_y)\beta_y^2(\frac{l\pi}{a}) \\ &\quad \{\beta_x^2\left[(\frac{m\pi}{a})^2+(\frac{n\pi}{b})^2\right]-k^2(\frac{m\pi}{a})^2\Big]\}\cos(\beta_x(x_k-x_j))\cos(\beta_y(y_k-y_j)) \\ &+ \quad k_{zlp}(\frac{l\pi}{a})(\frac{ab}{4})S_{lp}\delta(l-m,p-n)\delta(k-j) \end{aligned} \tag{13}$$

$$\begin{aligned} Y^{jk}_{mn,lp} &= -\frac{32}{\pi^2}\int_0^{\infty}\int_0^{\infty}\frac{d\beta_x d\beta_y}{\beta_z}A(\beta_x,\beta_y)B(\beta_x,\beta_y)\beta_y^2(\frac{l\pi}{a}) \\ &\quad \Big[-k^2(\frac{m\pi}{a})(\frac{n\pi}{b})\Big]\cos(\beta_x(x_k-x_j))\cos(\beta_y(y_k-y_j)) \\ &+ \quad \frac{k^2}{k_{zlp}}\varepsilon_{lp}(\frac{p\pi}{b})(\frac{ab}{4})S_{lp}\delta(l-m,p-n)\delta(k-j) \end{aligned} \tag{14}$$

$$\begin{aligned} Z^{jk}_{mn,lp} &= -\frac{4}{\pi^2}\int_0^{\infty}\int_0^{\infty}\frac{d\beta_x d\beta_y}{\beta_z}A(\beta_x,\beta_y)B(\beta_x,\beta_y)\beta_x^2(\frac{p\pi}{b}) \\ &\quad \{\beta_y^2\left[(\frac{m\pi}{a})^2+(\frac{n\pi}{b})^2\right]-k^2(\frac{n\pi}{b})^2\}\cos(\beta_x(x_k-x_j))\cos(\beta_y(y_k-y_j)) \\ &+ \quad k_{zlp}(\frac{p\pi}{b})(\frac{ab}{4})U_{lp}\delta(l-m,p-n)\delta(k-j) \end{aligned} \tag{15}$$

$$\begin{aligned} W^{jk}_{mn,lp} &= -\frac{4}{\pi^2}\int_0^{\infty}\int_0^{\infty}\frac{d\beta_x d\beta_y}{\beta_z}A(\beta_x,\beta_y)B(\beta_x,\beta_y)\beta_x^2(\frac{p\pi}{b}) \\ &\quad k^2(\frac{m\pi}{a})(\frac{n\pi}{b})\cos(\beta_x(x_k-x_j))\cos(\beta_y(y_k-y_j)) \\ &- \quad \frac{k^2}{k_{zlp}}\varepsilon_{lp}(\frac{l\pi}{a})(\frac{ab}{4})U_{lp}\delta(l-m,p-n)\delta(k-j) \end{aligned} \tag{16}$$

$$T^j_{lp} = k_{z10}V_j\sqrt{2ab}\,\delta(l-1,p) \tag{17}$$

$$A(\beta_x,\beta_y) = e^{j(\frac{\beta_x a+m\pi}{2})}\frac{\sin(\frac{\beta_x a+m\pi}{2})}{\beta_x^2-(\frac{m\pi}{a})^2}e^{j(\frac{\beta_y b+n\pi}{2})}\frac{\sin(\frac{\beta_y b+n\pi}{2})}{\beta_y^2-(\frac{n\pi}{b})^2} \tag{18}$$

$$B(\beta_x,\beta_y) = e^{-j(\frac{\beta_x a+l\pi}{2})}\frac{\sin(\frac{\beta_x a+l\pi}{2})}{\beta_x^2-(\frac{l\pi}{a})^2}e^{-j(\frac{\beta_y b+p\pi}{2})}\frac{\sin(\frac{\beta_y b+p\pi}{2})}{\beta_y^2-(\frac{p\pi}{b})^2} \tag{19}$$

ları gelişigüzel yerleştirilebilir, yani konum kiplenimli dizi antenler de verilen yöntemle çözülebilir. Bağlaşım matrisi C dizi elemanlarının beslemelerinden bağımsız olduğu için verilen anten geometrisi için bir kez hesaplanıp tersi alınacaktır. Daha sonra herhangi bir besleme için aynı matris dizinin çözümünde kullanılabilecektir.

Şekil.1 de verilen dikdörtgen ızgara şeklinde bir dizi için bağlaşım matrisi C block-Toeplitz biçimindedir ve C nin her Toeplitz bloğu yine Toeplitz biçimindedir. C nin bu özellikleri kullanıldığında problemin çözümü için kullanılan bilgisayar zamanı ve saklama alanı azalacaktır.

KAYNAKÇA

[1] A.J.Fenn, v.d., "Moment Method Analysis of Finite Rectangular Waveguide Phased Arrays", *IEEE Trans. Antennas Propagat.*,vol. AP-30, No. 4, July 1982.

[2] M. G. Sharma v.d., "Admittance Analysis of Nonuniformly Spaced Phased Arrays of Waveguide Apertures in a Ground Plane", *IEEE Trans. AP*,vol. AP-30, No. 5, pp. 432-437, Mayıs, 1982.

[3] H.Yavuz, Full-Mode Analysis of Finite Rectangular Phased Arrays, Doktora Tezi (basılacak), Orta Doğu Teknik Universitesi Elektrik Elektronik Mühendisliği Bölümü.

[4] O.M. Büyükdura ve H. Yavuz, "Sonlu bir İletken Yüzey Üzerindeki Anten Dizi Elemanlarının Karşılıklı ve Öz Admitansları", Elektrik Mühendisliği 5. Ulusal Kongresi, Eylül 1993.

[5] R. Piessens, v.d., *Quadpack a Subroutine Package for Automatic Integration*, Berlin: Springer-Verlag, 1980.

III SONUÇ :

Türkiye, COST 245 projesinde oluşturulan üç çalışma grubunda da projenin genel amaçlarına uygun olarak katkıda bulunmuş, proje faaliyetlerinin eşgüdümünün amaçlandığı yönetim kurulu toplantılarına katılmış, ürettiği bilgileri projenin çeşitli toplantılarında tartışmış ve diğer ülke ekiplerinin çalışmalarını izlemiştir.

COST 245 projesi çerçevesinde üzerinde çalışılması planlanan konular kapsamında ekibimiz çalışmalarını başlıca üç ana bölümde yürütmüştür: A. Faz taramalı anten dizileri, B. Monolitik mikrodalga entegre devreleri (MMIC), C. Geniş bantlı antenler ve nümerik metotlar.

İlk bölümde, uydu yayınlarını televizyon alıcıları ile alabilmeye uygun düzlemsel anten dizisi tasarım ve analizine yönelik çalışmalar yapılmıştır. Tasarlanacak anten dizisinin hem Avrupa hem de Türkiye'den izlenebilen TV yayını verici uydularına uygun olması ön planda tutulmuş ve bu uydulara ilişkin spesifikasyonların belirlenmesi için bir ön çalışma yapılmıştır. Daha sonra mikroşerit yapılarla yapılması öngörülen anten dizilerinin pratik kısıtlamaları incelenmiştir. Ön çalışmalarda iki kutuplu (dual polarization) ve iki hüzmeli anten dizisinin pratik olmadığının görülmesi üzerine, çalışmalar tek kutuplu ve tek hüzmeli alıcı antenler üzerinde yoğunlaştırılmıştır. Bu amaca en uygun anten dizisi yapısının iki seviyeli paralel kol besleme yapısı olduğu görülerek tasarım aşamasına geçilmiştir.

Anten dizisi tasarım çalışmasına paralel olarak anten dizilerinin, yönlülük (directivity), gürültü sıcaklığı gibi performans kriterleri üzerinde analitik çalışmalar sürdürülmüştür. Yüksek kazanç ve düşük gürültü performasına sahip bir anten dizisinin aktif anten dizileri ile gerçekleştirilebileceğinin belirlenmesi üzerine aktif anten dizilerinin gürültü performansının belirlenmesi yanında doğrusallık kriteri de gözönüne alınmış ve aktif anten dizilerine yerleştirilebilecek yükselteçler üzerine analiz, tasarım ve benzetim çalışmaları yapılmıştır.

Tasarım çalışmalarının ardından üretim ve ölçüm çalışmalarına geçilmiş ve mikroşerit yapılarının ölçümlerinin yapılmasına uygun ölçüm düzenekleri geliştirilmiştir. Mikroşerit hatlar ve yama antenler tasarlanarak üretilmiş ve ölçülerek simülasyon sonuçları ile karşılaştırılmıştır. Ölçüm sonuçlarının tasarım değerleri ile uygun olmasının belirlenmesinin ardından anten alt dizileri ve ardından anten dizileri üretilerek ölçümleri yapılmıştır.

Alternatif anten dizi çalışması olarak silindirik yüzeylerde mikroşerit anten dizileri de incelenmiştir.

Akıllı anten özellikleri taşıyan doğrusal bir alıcı anten dizisi tasarımı ve üretimi yapılmıştır. Bu dizi yön bulma ve sayısal hüzme oluşturma yeteneklerine sahip olacak biçimde tasarlanmış ve bu özellikleri ölçümler yoluyla sınanmıştır.

Çalışmaların ikinci bölümü MMIC çalışmalarına ayrılmıştır. Radar ve uydu uygulamalarında, aktif anten kavramı giderek önemini arttırmaktadır. Bu tür antenlerde aktif elemanlar anten dizisi elemanlarıyla birleştirirlerek anten performansında belirgin iyileştirmeler elde edilebilmektedir. Büyük ölçekli anten dizilerinde çok sayıda aktif eleman kullanılması gerektiğinden, gerek küçük boyutlar ve hafiflik ve gerekse ucuzluk açısından MMIC uygulamalarına gereksinim duyulmaktadır. Bu avantajları göz önünde bulundurularak, proje kapsamında bir aktif anten dizisinde yer alması sözkonusu devrelerden aşağıda belirtilenler üzerinde çalışmalar yürütülmüştür:

1- Dar ve geniş bantlı yükselteçler,
2- Voltaj kontrollu osilatör,
3- Karıştırıcı,
4- Düşük gürültülü yükselteç,
5- Alıcı/verici anahtar,
6- Güç yükselteci,
7- Geniş bantlı voltaj kontrollu zayıflatıcı,
8- Faz kaydırıcı.

Tüm devrelerin tasarım ve optimizasyonu, LIBRA ve ACADEMY yazılım paketleri kullanılarak ve GEC-MARCONI firmasının F-20 proses kurallarına göre yapılmıştır. Bu devrelerin tasarımı, üretim aşamasında maliyeti düşürmek için elektriksel performansdan ödün vermeksizin en az yonga alanı kapsayacak şekilde yapılmıştır. Şu ana kadar bunlardan ilk beş maddede belirtilen devreler üretilmiş ve performansları ölçülmüştür. Ölçüm sonuçlarıyla daha önce elde edilen bilgisayar simülasyon sonuçlarının çok iyi uyum içinde oldukları görülmüştür. Bu sonuç, tasarım aşamasında kullanılan aktif ve pasif eleman modellerinin gerçekçi ve yeterince doğru olduğunu göstermektedir. MMIC devreleri üzerinde tasarımdan sonra herhangi bir değişiklik veya düzeltme yapılması mümkün olmadığından, tasarım aşamasında modelleme açısından çok titiz davranılması önemli olmaktadır.

Üretilen MMIC devrelerinin diğer devreler ve anten elemanları ile birlikte kullanılabilmesi için özel bağlantı tekniklerinin (bonding) uygulanması gereklidir. Bu bağlantılar sonucunda devrelerin performansında, az da olsa, bir takım değişikliklerin olması doğaldır.

Çaşılmaların üçüncü bölümünde milimetrik dalga bandında iki ve üç ferit-dielektrik katmanlı antenlerle elektronik hüzme taraması konusu incelenmiş ve uygun madde seçimiyle, D.C. manyetik alanı değiştirerek ışın demetinin şeklinin değiştirilebileceği ve elektronik hüzme taraması elde edilebileceği görülmüştür. Geniş bantlı Vivaldi

antenlerle ilgili çalışmalarda ise tasarlanan ve üretilen antenlerin elektriksel performans özellikleri tatmin edicidir. Dairesel Vivaldi anten dizisi, monopals genlik ya da faz karşılaştırılmaı yön bulma sistemlerinde kullanılabilir. Bu bölümde ayrıca, bir tam dalga nümerik analiz yöntemi olan MoM (Method of Moments) nümerik entegrasyondan arındırılarak hızlandırılmış ve herhangi bir düzlemsel mikroşerit yapısının (anten dizisi veya MMIC devre) tasarımında uygun bir optimizasyon programı ile verimli olarak çalışabilecek bir metoda dönüştürülmüştür. Son olarak mükemmel iletken bir toprak yüzeye açılan dikdörtgen dalga kılavuzlarının oluşturduğu dizi antenler incelenmiş ve bu yapıların bir integral denklem sistemi ile sistematik çözümü yapılmıştır.

Bütün bu çalışmalarla ilgili teknik bilgiler ve varılan sonuçlar, her çalışmanın anlatıldığı bölümde ayrıntılı bir biçimde yer almıştır.

Proje kapsamında ortaya çıkan 16 adet yurt içi ve yurt dışı yayın da ekte sunulmuştur.

İleriye dönük başlıca araştırma önerileri:

Yeni oluşturulmakta olan COST 260 Adaptif Anten Dizileri projesi konularının bir kısmi, COST 245 projesinde ekibimiz tarafından gerçekleştirilen çalışmaların devamı niteliğindedir. Bu yeni projede yine aktif anten sistemleri konu alınmakta, ancak anten dizilerine, sinyal işleme teknikleri kullanmak suretiyle adaptif bir özellik kazandırarak, programlanabilir "akıllı anten dizileri" (smart antenna arrays) elde edilmesi amaçlanmaktadır. Akıllı antenlerin en önemli özelliği adaptif olmasıdır. Bu antenlerde hüzme kontrolu, hüzme formasyonu, çıkış gücü kontrolü, sayısal teknikler ve bilgisayar yardımı ile yapılmaktadır. Bu tür anten dizilerinde, anten elemanları ayrı ayrı kontrol edilebilmektedir. Kullanılan teknoloji, MMIC, VLSI ve mikroşerit anten dizileri ile ilgili teknolojilerdir.

Bu hususlar gözönünde bulundurularak, aşağıda belirtilen konularda çalışmalar yapılması önerilmektedir:

1- Mikroşerit antenler ve özellikle de çok katlı ve yarık-kuplajlı (aperture/slot coupled) antenler üzerindeki çalışmaların devam etmesi,
2- Antenlerdeki, genlik ve faz kontrolu için MMIC çalışmalarının devam etmesi,
3- Adaptif antenlerde hüzme formasyonu için algoritma geliştirilmesi,
4- Prototip bir adaptif anten tasarlanarak laboratuar koşullarında denenmesi.

EK I:

YAYINLAR

YAYINLAR

1) Kınayman, G. Dural, M. I. Aksun, " A Numerically Efficient Technique for the Analysis of Slots in Multilayer Media", *IEEE Trans. MTT* de yayınlanmak üzere kabul edildi.
2) L. Alatan, M. I. Aksun, K. Mahadevan, M. T. Birand, "Analytical Evaluation of MoM Matrix Elements", *IEEE Trans. MTT*, Vol. 44, No. 4, Nisan 1996, sf. 519-525
3) G. Dural, M. I. Aksun, "Closed form Green's Functions for General Sources and Stratified Media", *IEEE Trans. MTT*, Vol. 43, No. 7, Temmuz 1995, sf. 1545-1552.
4) M. I. Aksun, G. Dural, "Comparative Evaluation of Absorbing Boundary Conditions Using Green's Functions for Layered Media", *IEEE Trans. AP*, Vol. 44, No. 2, Şubat 1996, sf. 152-156.
5) Ş. Demir, C. Toker, A. Hızal, " Design of a Active Microstrip Array Using Microwave Simulator", *IEEE MTT-S Top. Symp. on Tech. for Wireless Appl.*, Vancouver, Kanada, Şubat 1997, sf. 103-106.
6) Ş. Demir, C. Toker, A. Hızal, " A Novel Low Noise Active circuit Replacement Criteria for Parallel Fed Large Scale Active Antenna Arrays", *27th European Microwave Conference*, Kudüs, İsrail, Ekim 1997, sf. 56-61.
7) L. Alatan, M. I. Aksun, M. T. Birand, "Use of Computationally Efficient Spatial-Domain Method of Moments in CAD of Microstrip Antennas", *COST 245 ESA Workshop on Active Antennas*, ESTEC, Noordwijk, Hollanda, 27-28 Haziran 1996, sf. 13-15.
8) A. Hızal, Ş. Demir, L. Alatan, C. Bulutay, H. Yıldız, "Performance of a 10 Ghz, 32 Elements Receiving Planar Microstrip Antenna Array", *COST 245 ESA Workshop on Active Antennas*, ESTEC, Noordwijk, Hollanda, 27-28 Haziran 1996, sf. 205-209.
9) L. Alatan, M. I. Aksun, M. T. Birand, "Computationally Efficient Analysis and Design of Printed Structures", *IEEE AP International Symposium*, Baltimore, MD, 1996, sf. 276-279.
10) Ö. Aydın, A. Hızal, "Radiation of Dipoles in Multilayered Cylinder with Ferrite Layer", *IEEE AP International Symposium*, Baltimore, MD, 1996, sf. 1836-1939.
11) H. Yavuz, M. Büyükdura, "Mutual Coupling Effects of Finite Rectangular Phased Arrays", *IEEE AP international Symposium*, Saettle, WA,1996, sf. 418-421.
12) C. Birdir, N. Günalp, "MMIC Teknolojisi Kullanılarak Tasarımlanmış Voltaj Kontrollü Osilatör", *Elektrik Mühendisliği 6. Ulusal Kongresi*, Bursa, Eylül 1995 sf. 684-687.
13) F. Üstüner, N. Günalp, "MMIC Teknolojisiyle Düşük Gürültülü Yükselteç ve Anten Anahtarı Tasarımı", *Elektrik Mühendisliği 7. Ulusal Kongresi*, Ankara, 1997 sf. 244-247.
14) Ç. Tokgöz, G. Dural, "Çok Katmanlı Silindirik Yapılardaki Genel Akım Kaynakları için Gerçek Uzayda Kapalı Formda Green Fonksiyonlarının Çıkarılması", *Elektrik Mühendisliği 7. Ulusal Kongresi*, Ankara, 1997 sf. 280-283.
15) Ş. Demir, C. Toker, A. Hızal, "Özgün Düşük Gürültülü Aktif Anten Dizisi Analiz ve Tasarım Yöntemi", *Elektrik Mühendisliği 7. Ulusal Kongresi*, Ankara, 1997 sf. 319-322.

A Numerically Efficient Technique for the Analysis of Slots in Multilayer Media

Noyan Kınayman[1], *Member, IEEE*, Gülbin Dural[2], *Member, IEEE*,
and M. I. Aksun[1], *Member, IEEE*

1: Bilkent University, Dept. of Electrical and Electronics Eng.
06533, Ankara, Turkey

2: Middle East Technical University, Dept. of Electrical and Electronics Eng.
06531, Ankara, Turkey

Abstract— A numerically efficient technique for the analysis of slot geometries in multilayer media is presented using closed-form Green's functions in spatial domain in conjunction with the Method of Moments. The slot is represented by an equivalent magnetic current distribution which is then used to determine the total power crossing through the slot and the input impedance. In order to calculate power and current distribution, spatial-domain closed-form Green's functions are expanded as power series of the radial distance, ρ, which makes the analytical evaluation of the spatial-domain integrals possible saving considerable amount of computation time.

I. Introduction

Slot geometries have broad spectrum of applications either as transmission lines or radiating elements and have been examined extensively in the literature [1;2;3;4]. The most commonly used numerical technique for analyzing the slot geometries is the Method of Moments (MoM) which can be applied either in spatial domain or

in spectral domain. Although the MoM is preferred over the differential equation methods because it is relatively efficient in terms of the computation time, it is still time consuming because of the slow convergence and the oscillatory nature of the integrals involved. One approach to overcome these difficulties is to employ the closed-form Green's functions in the spatial domain that can speed up the computation of the MoM matrix elements by several orders of magnitude as compared to the numerical evaluation of the Sommerfeld integral [5;6;7;8].

In this paper, the Galerkin's MoM analysis of the slot geometries in multilayer media has been developed by employing the closed-form Green's functions for the vector and scalar potentials of a horizontal magnetic dipole (HMD) in the spatial domain [9]. The formulation is presented for narrow slot geometries excited with coaxial-line feed, however it can be applied to slot geometries of any kind of excitation without any major modification. The equivalent magnetic current distribution of the slot is computed and used for the computation of power crossing the slot and the input impedance. Numerical calculation of the power crossing the slot and equivalent magnetic slot current are computationally very demanding procedure because the numerical evaluation of the integrals involved is very time consuming either in the spatial domain or in the spectral domain. Here, the spatial-domain Green's functions are approximated as power series of radial distance, ρ, and integrals involving the Green's functions are carried out analytically saving considerable amount of computational time both in current and power calculations [10].

II. Formulation

An example of a narrow slot placed in a multilayer medium is shown in Fig. 1. It is assumed that the layers extend to infinity in the transverse direction and the slot is excited with a coaxial-line of current I_{in} amperes at the feeding point. It is also assumed that there is no conducting or dielectric losses, therefore the only loss

mechanism is the radiation.

The tangential component of the magnetic field on the slot can be expressed in terms of an equivalent magnetic current density, $\vec{J}^m$, using the MPIE formulation [11] as follows:

$$H_x = -j\omega G_{xx}^F * J_x^m + \frac{1}{j\omega}\frac{\partial}{\partial x}\left(G_x^{q_m} * \nabla \cdot \vec{J}^m\right) \tag{1}$$

where J_x^m is the longitudinal component of the current density $\vec{J}^m$, G_{xx}^F and $G_x^{q_m}$ are the spatial-domain Green's functions for the vector and scalar magnetic potentials for an HMD, respectively. To solve the equivalent magnetic current density J_x^m using the MoM, the current density is expressed as a linear combination of suitable sub-domain basis functions in the following form:

$$J_x^m = \sum_{n=1}^{N} I_{xn} B_{xn}(x, y) \tag{2}$$

where B_{xn}'s are the basis functions which are chosen in this work to be the rooftops. Since a narrow slot is assumed, the current variation in the $\hat{y}$ direction is considered to be constant. Enforcing the boundary conditions for the tangential fields, the following equation is obtained:

$$\begin{aligned} \langle T_{xm},\ J_s\delta(x-d)\rangle &= \left\langle T_{xm},\ \left(G_{xx}^F\big|_{z<0} + G_{xx}^F\big|_{z>0}\right) * J_{xn}^m \right\rangle \\ &+ \frac{1}{w^2}\left\langle T_{xm},\ \frac{\partial}{\partial x}\left[\left(G_x^{q_m}\big|_{z<0} + G_x^{q_m}\big|_{z>0}\right) * \frac{\partial J_{xn}^m}{\partial x}\right]\right\rangle \end{aligned} \tag{3}$$

where T_{xm} denotes the testing functions expressed by sub-domain basis functions, $\langle\ ,\ \rangle$ designates the inner product, and $*$ designates the convolution between the basis and the Green's functions. Note that the Green's functions appearing in Eq. (3) are the spatial-domain closed-form Green's functions which can be obtained through the closed-form spectral-domain Green's functions [9] by numerically evaluating the Sommerfeld integral [6;12]. The spatial-domain closed-form Green's functions are expressed in the following form:

$$G_{xx,x}^{F,q_m} \cong \sum_{m=1}^{N} a_m \frac{e^{-jk_i r_m}}{r_m} \tag{4}$$

where $r_m = \sqrt{\rho^2 - b_m^2}$, and $k_i^2 = k_{z_i}^2 + k_\rho^2$. Here, a_m's and b_m's are the complex constants in general. Consequently, for the slot geometry given in Fig. 1, the spatial-domain Green's functions encountered in Eq. (3) can be written as follows:

$$G_{xx}^F = \begin{cases} 2\dfrac{\varepsilon_0}{4\pi}\dfrac{e^{-jk_0 r}}{r} & : \quad z > 0 \qquad (5a) \\ \displaystyle\sum_{m=1}^{M} a_m \frac{e^{-jkr_m}}{r_m} & : \quad z < 0 \qquad (5b) \end{cases}$$

$$G_x^{q_m} = \begin{cases} 2\dfrac{1}{4\pi\mu_0}\dfrac{e^{-jk_0 r}}{r} & : \quad z > 0 \qquad (6a) \\ \displaystyle\sum_{n=1}^{N} a_n \frac{e^{-jkr_n}}{r_n} & : \quad z < 0 \qquad (6b) \end{cases}$$

After evaluating the closed-form Green's functions, the remaining job is to evaluate the related integrals. In this work, each exponential term in the above Green's functions is expanded as a power series of ρ which makes the analytical evaluation of the inner products in Eq. (3) possible saving considerable amount of computational time [10]. Also note that since the spatial-domain Green's functions have a surface integrable singularity at the origin, analytical evaluation of these integrals does not need the extraction of singularity.

2.1. Calculation of the Total Power and Input Impedance

Once the equivalent magnetic current density on the slot is obtained, then the power crossing through the slot can be calculated by using the following integral:

$$-P_c = \iint_{slot} \vec{E} \times \vec{H}^* \cdot d\vec{s} \qquad (7)$$

where

$$\left(\vec{E} \times \vec{H}^*\right)_z = E_x H_y^* - E_y H_x^* \qquad (8)$$

$$E_y = J_x^m \qquad (9)$$

$$E_x = 0 \qquad (10)$$

here H_x and J_x^m are given by Eqs. (1) and (2), respectively, and $(\ )^*$ denotes the complex conjugate. It should be noted that since the geometry is physically separated into two half spaces by replacing the slot with a perfect electric conductor, which carries an equivalent magnetic current density instead of slot, the power should be computed for each region separately and then should be combined to get the total power. Hence,

$$P_c^{total} = P_c\Big|_{z>0} + P_c\Big|_{z<0} \tag{11}$$

Note that $P_c\Big|_{z>0}$ and $P_c\Big|_{z<0}$ are evaluated on the slot surface at $z = 0^+$ and $z = 0^-$ but with different sets of Green's functions given in Eqs. (9) and (10), respectively. By substituting Eqs. (1), (9) and (10) into Eq. (7) and taking the complex conjugate of both sides, one can obtain the following expression

$$P_c^*\Big|_{z\lesseqgtr 0} = \iint_{slot} J_x^{m^*} \left\{ -jwG_{xx}^F * J_x^m + \frac{1}{jw}\frac{\partial}{\partial x}\left[G_x^{qm} * \frac{\partial}{\partial x} J_x^m \right] \right\} dx\, dy \tag{12}$$

and expanding the convolution integrals the following expression is obtained

$$\begin{aligned} P_c^*\Big|_{z\lesseqgtr 0} &= -jw \iint_{slot} dx\, dy J_x^{m^*} \iint dx'\, dy' G_{xx}^F (x-x', y-y')\, J_x^m \\ &+ \frac{1}{jw} \iint_{slot} dx\, dy J_x^{m^*} \frac{\partial}{\partial x} \iint dx'\, dy' G_x^{qm} (x-x', y-y') \frac{\partial}{\partial x'} J_x^m \end{aligned} \tag{13}$$

Note that Eq. (13) contains quadruple integrals in spatial domain, therefore numerical methods to evaluate Eq. (13) would be very inefficient. On the other hand, it is also possible to carry the convolution in Eq. (12) to the spectral-domain thus eliminating one of the double integrals. In that case, although the spectral-domain Green's functions are in closed form, they are still oscillatory functions and the limits of the integrals extend to infinity yielding computationally expensive numerical integrals. To overcome these difficulties, Eq. (13) can be written in matrix form as

follows:

$$P_c^*\Big|_{z\lessgtr 0} = \begin{bmatrix} I_{x1} & I_{x2} & \cdots & I_{xn} \end{bmatrix}^* [A_{nn'}] \begin{bmatrix} I_{x1} \\ I_{x2} \\ \vdots \\ I_{xn'} \end{bmatrix} \tag{14}$$

where

$$\begin{aligned} A_{nn'} &= -jw \iint_{slot} dx\, dy B_{xn}(x,y) \iint dx'\, dy' G_{xx}^F (x-x', y-y')\, B_{xn'}(x',y') \\ &- \frac{1}{jw} \iint_{slot} dx\, dy \frac{\partial}{\partial x} B_{xn}(x,y) \iint dx'\, dy' G_x^{qm} (x-x', y-y') \frac{\partial}{\partial x'} B_{xn'}(x',y') \end{aligned} \tag{15}$$

Now, one can notice that the matrix entry which appears in Eq. (15) is similar with the MoM impedance matrix entries. Hence, the Green's functions in Eq. (15) can be also approximated by power series of ρ yielding analytical integration possible. Finally, the input impedance seen from the feed point is obtained by

$$Z_{in} = \frac{P_c^{total}}{I_{in}^2} \tag{16}$$

III. Results and Conclusions

The first investigated geometry consists of an infinitely large ground plane with narrow rectangular center-fed slot which separates the geometry two infinite half-spaces. This can be achieved by setting $h_2 = h_1 = 0$ in the geometry shown in Fig. 1. The input impedance of the slot is calculated and it is compared with the results presented in literature [2], and as it can be seen in Figs. 2 and 3, there is a good agreement between the results. The difference between the results near resonance could be due to the fact that Kominami et. al. uses a different set of basis functions which forces the edge singularity, and they obtain the results for a lossy dielectric, whereas in our case, the dielectric is assumed to be lossless. As a second example,

a multilayer geometry is selected by setting $h_2 \neq 0$ and $h_1 \neq 0$, and both center-fed and offset-fed configurations are analyzed. The input impedances of the slot for both cases are given in Fig. 4. It should be noted that offset-feeding has not changed the resonance frequency of the structure.

As a conclusion, it can be stated that the use of closed-form spatial-domain Green's functions increases the computational efficiency in the analysis of slot geometries in multilayer media. Although the formulation is presented for narrow slot geometries with coaxial feeding, it can be applied to general slot geometries placed in a multilayer geometry, such as slot-coupled microstrip patch antennas, as well.

ACKNOWLEDGMENT

This work was supported in part by NATO's Scientific Affairs Division in the framework of the Science for Stability programme.

REFERENCES

[1] K. C. Gupta, Ramesh Garg and I. J. Bahl. *Microstrip Lines and Slotlines.* Artech House, Inc., 1979.

[2] Masanobu Kominami, David M. Pozar and Daniel H. Schaubert "Dipole and Slot Elements and Arrays on Semi-Infinite Substrates," *IEEE Trans. on Antennas and Propagation*, vol. 33, pp. 600–607, June 1985.

[3] Masoud Kahrizi, Tapan K. Sarkar, and Zoran A. Maricevic "Analysis of a Wide Radiating Slot in the Ground Plane of a Microstrip Line," *IEEE Trans. on Microwave Theory Tech.*, vol. 41, pp. 29–37, Jan. 1993.

[4] Richard C. Hall, and Juan R. Mosig "The Analysis of Arbitrarily Shaped Aperture-Coupled Patch Antennas Via a Mixed-Potential Integral Equation," *IEEE Trans. on Antennas and Propagation*, vol. 44, pp. 608–614, May 1996.

[5] Noyan Kınayman and M. I. Aksun "Comparative Study of Acceleration Techniques for Integrals and Series in Electromagnetic Problems," *Radio Science*, vol. 30, pp. 1713–1722, Nov.-Dec. 1995.

[6] Y. L. Chow, J. J. Yang, D. G. Fang and G. E. Howard "A Closed-Form Spatial Green's Function for the Thick Microstrip Substrate," *IEEE Trans. on Microwave Theory Tech.*, vol. 39, pp. 588–592, Mar. 1991.

[7] Miguel Marin, Sina Barkeshli and Prabhakar H. Pathak "Efficient Analysis of Planar Microstrip Geometries Using a Closed-Form Asymptotic Representation of the Grounded Dielectric Slab Green's Function," *IEEE Trans. on Microwave Theory Tech.*, vol. MTT-37, pp. 669–679, Apr. 1989.

[8] Miguel Marin, and Prabhakar H. Pathak "An Asymptotic Closed-Form Representation for the Grounded Double-Layer Surface Green's Function," *IEEE Trans. on Microwave Theory Tech.*, vol. AP-40, pp. 1357–1366, Nov. 1992.

[9] G. Dural, and M. I. Aksun "Closed-Form Green's Functions For General Sources and Stratified Media," *IEEE Trans. on Microwave Theory Tech.*, vol. 43, pp. 1545–1552, July 1995.

[10] Lale Alatan, M. I. Aksun, Karthikeyan Mahadevan, and Tuncay Birand "Analytical Evaluation of the MoM Matrix Elements," *IEEE Trans. on Microwave Theory Tech.*, vol. 44, pp. 519–525, Apr. 1996.

[11] Juan R. Mosig "Arbitrarily Shaped Microstrip Structures and Their Analysis with a Mixed Potential Integral Equation," *IEEE Trans. on Microwave Theory Tech.*, vol. MTT-36, pp. 314–323, Feb. 1988.

[12] M. I. Aksun "A Robust Approach for the Derivation of Closed-Form Green's Functions," *IEEE Trans. on Microwave Theory Tech.*, vol. 44, pp. 651–658, May 1996.

List of Figures

1 A slot structure on a multilayer medium. The region above the slot is free space. 9

2 Input impedance vs. normalized length (l/λ_0) for the slot given in Fig. 1 (w/l=0.02 cm, h_1=h_2=0.0 cm, ε_{r3}=2.55, and d=5.0 cm). . . . 10

3 Input impedance vs. normalized length (l/λ_0) for the slot given in Fig. 1 (w/l=0.02 cm, h_1=h_2=0.0 cm, ε_{r3}=12.8, and d=5.0 cm). . . . 11

4 Input impedance vs. normalized length (l/λ_0) for the slot given in Fig. 1 (w/l=0.02 cm, h_1=0.2 cm, h_2=0.05 cm, ε_{r1}=2.55, ε_{r2}=12.8, ε_{r3}=1.0). 12

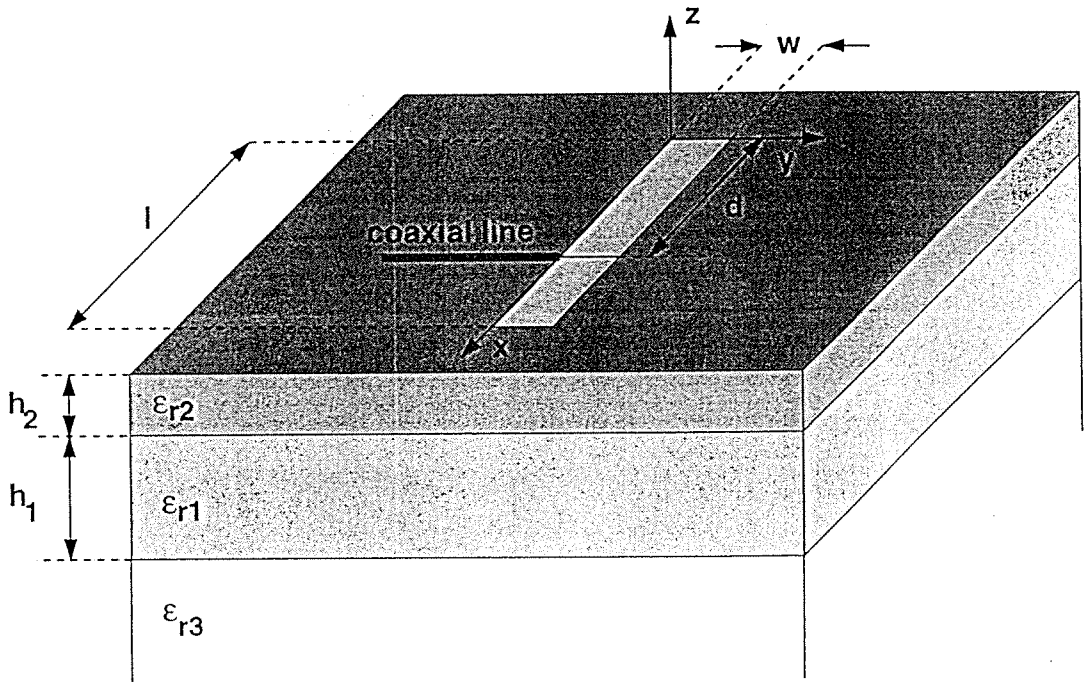

Fig. 1.

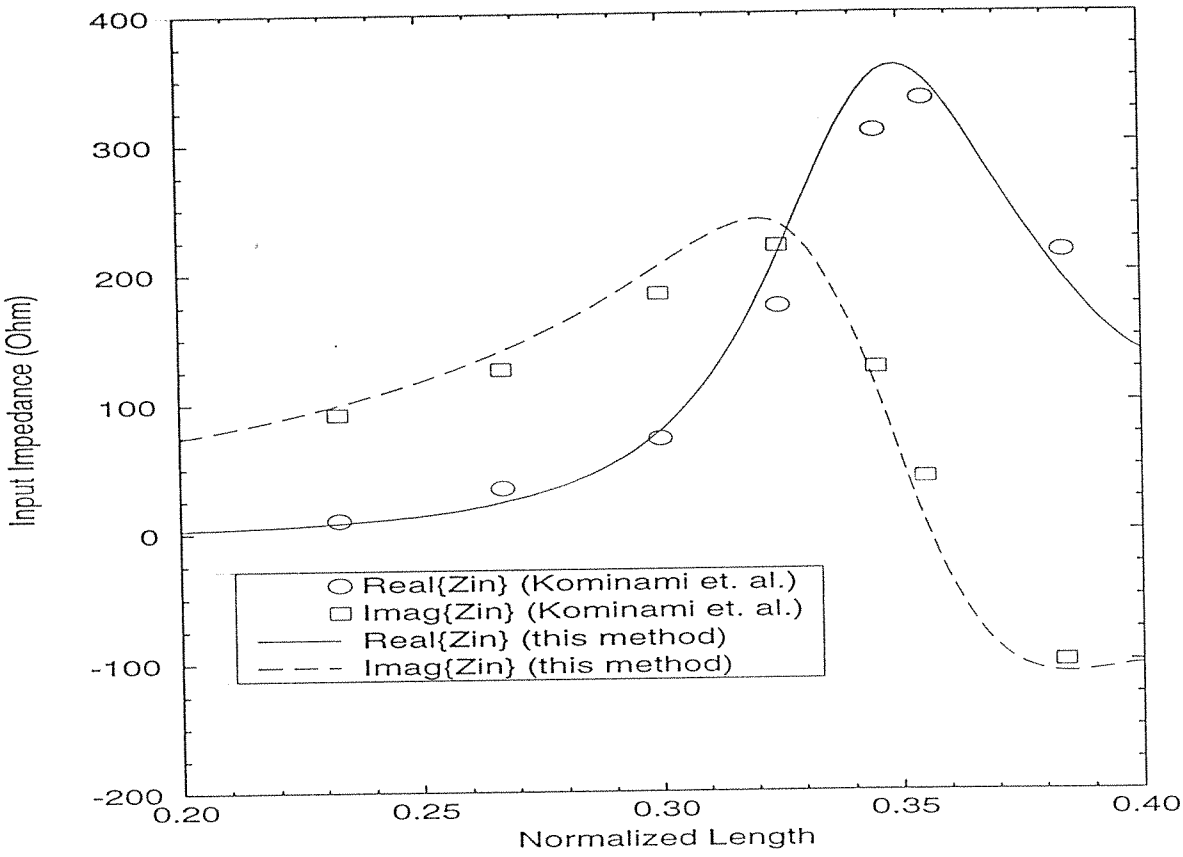
400
300
200
100
0
-100
-200
0.20
0.25
0.30
0.35
0.40
Input Impedance (Ohm)
Normalized Length
Real{Zin} (Kominami et. al.)
Imag{Zin} (Kominami et. al.)
Real{Zin} (this method)
Imag{Zin} (this method)

Fig. 2.

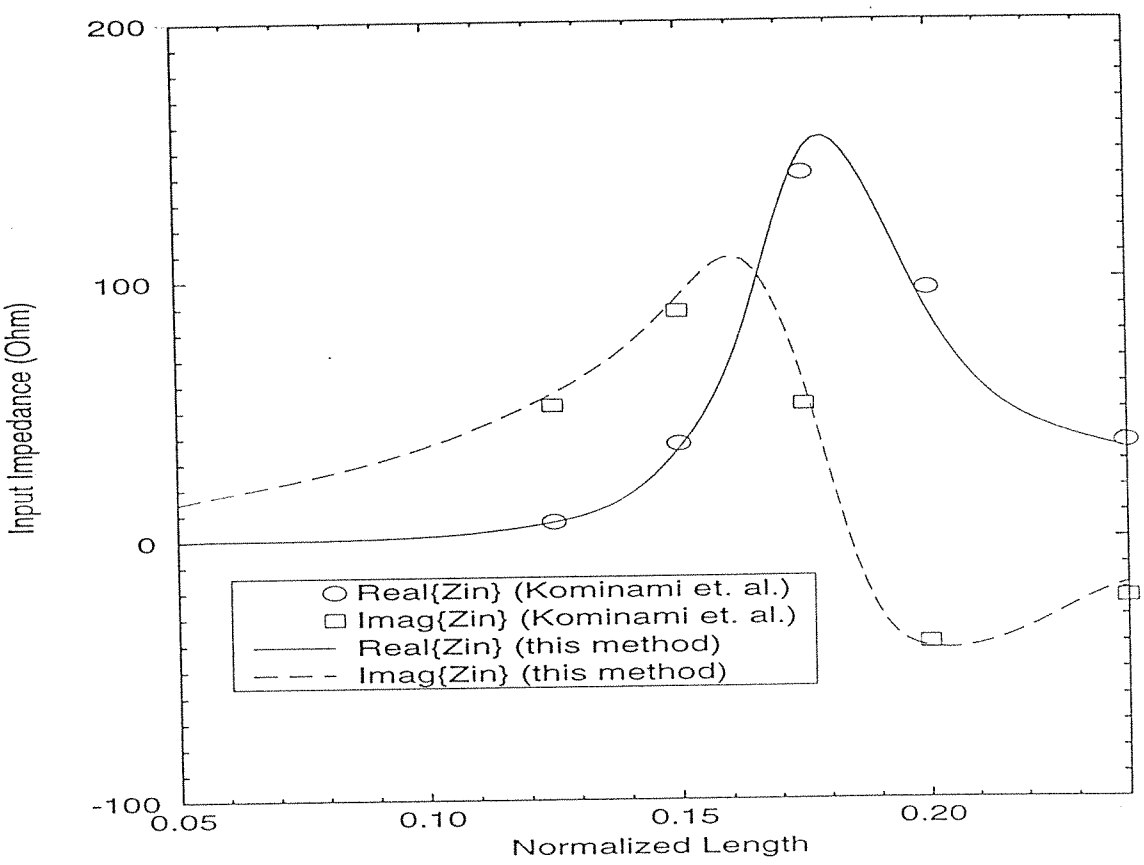
200
100
0
-100
0.05
0.10
0.15
0.20
Normalized Length
Input Impedance (Ohm)
Real{Zin} (Kominami et. al.)
Imag{Zin} (Kominami et. al.)
Real{Zin} (this method)
Imag{Zin} (this method)

Fig. 3.

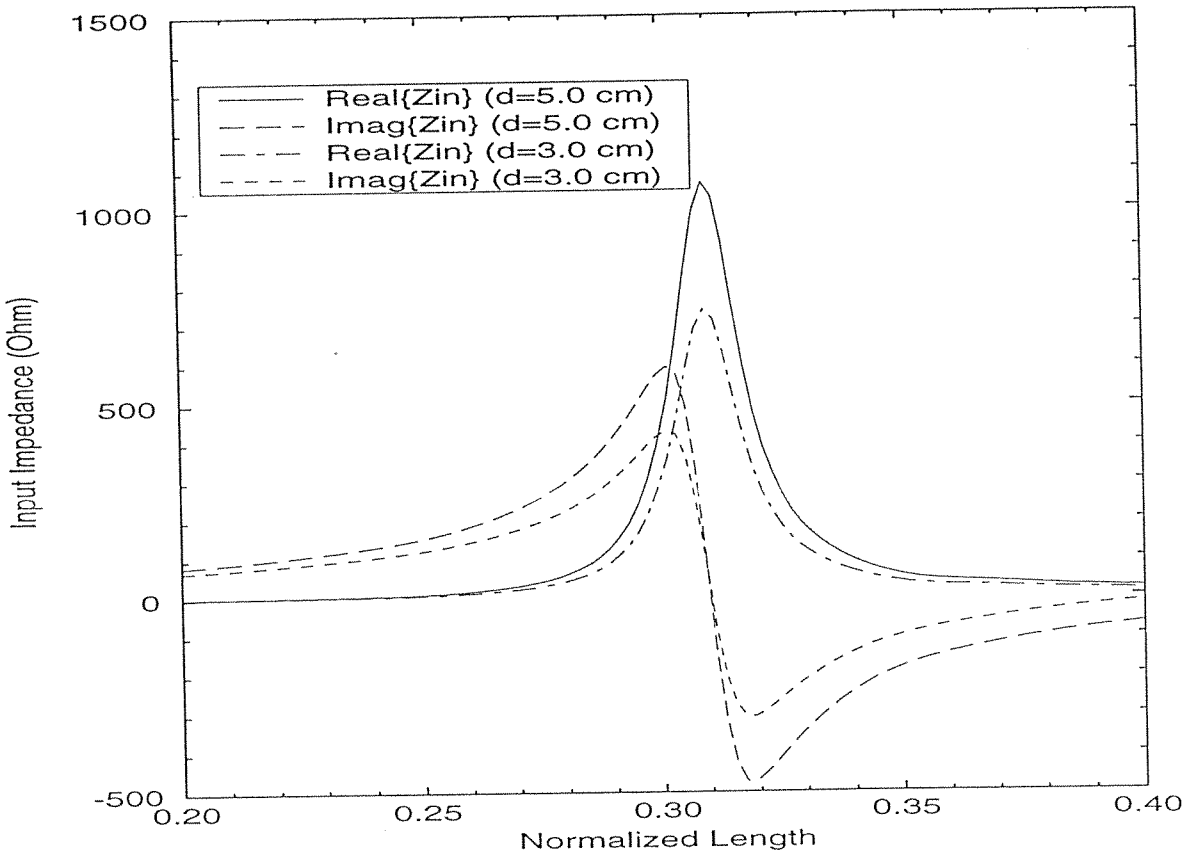
Real{Zin} (d=5.0 cm)
Imag{Zin} (d=5.0 cm)
Real{Zin} (d=3.0 cm)
Imag{Zin} (d=3.0 cm)
Input Impedance (Ohm)
1500
1000
500
0
-500
0.20
0.25
0.30
0.35
0.40
Normalized Length

Fig. 4.

Analytical Evaluation of the MoM Matrix Elements

Lale Alatan, *Student Member, IEEE*, M. I. Aksun, *Member, IEEE*, Karthikeyan Mahadevan, and M. Tuncay Birand, *Member, IEEE*

Abstract—**Derivation of the closed-form Green's functions has minated the computationally expensive evaluation of the Som-rfeld integrals to obtain the Green's functions in the spatial main. Therefore, using the closed-form Green's functions in njunction with the method of moments (MoM) has improved e computational efficiency of the technique significantly. Fur-er improvement can be achieved on the calculation of the atrix elements involved in the MoM, usually double integrals for anar geometries, by eliminating the numerical integration. The ntribution of this paper is to present the analytical evaluation the matrix elements when the closed-form Green's functions e used, and to demonstrate the amount of improvement in mputation time.**

I. Introduction

ELECTROMAGNETIC modeling plays an important role in the analysis and the design of electronic packages, igh-speed digital circuits, and microwave integrated cir-uits, most of which are fabricated in a planar environment. herefore, a variety of numerical techniques for accurately odeling and simulating the electrical performances of such ircuits have been proposed and studied extensively. These nclude the method of moments (MoM) [1], the finite el-ment method (FEM) [2], the finite-difference time-domain nethod (FDTD) [3], and quasi-static methods like conformal napping [4]. Among these approaches, the MoM in the patial and the spectral domains are the most commonly sed numerical techniques in the rigorous analysis of printed eometries in multilayer planar media. As these structures re generally used in the design of monolithic microwave ntegrated circuits (MMIC) and printed antennas, improving he numerical efficiency of the MoM has been a major research opic in computational electromagnetics. In the analysis of electrically small geometries (spanning a few wavelengths in two dimensions), the efficiency can be improved by reducing the computation time used to evaluate the matrix elements, since the significant part of the overall solution time is the calculation of the matrix elements, also called matrix-fill time.

Manuscript received November 10, 1994; revised December 18, 1995. This work was supported in part by NATO's Scientific Affairs Division in the framework of the Science for Stability Programme, and by TUBITAK (The Scientific and Technical Research Council of Turkey) within the scope of COST 245 (European Cooperation in the Field of Scientific and Technical Research) project.

L. Alatan and T. Birand are with the Department of Electrical and Electronics Engineering, Middle East Technical University, 06531 Ankara, Turkey.

M. I. Aksun is with the Department of Electrical and Electronics Engineering, Bilkent University, 06533

Ankara, Turkey.

K. Mahadevan is with the SG Microwaves Inc., Kitchener, Ontario N2G 2N3 Canada.

Publisher Item Identifier S 0018-9480(96)02347-2.

In the spectral domain formulation, the MoM matrix elements involve two-dimensional (2-D) integrals of complex, oscillatory, and slow-converging functions over an infinite domain [5]. Therefore, the numerical evaluation of these elements is quite time consuming, rendering the technique computationally inefficient. Although acceleration techniques and approximations can improve the computational efficiency of the spectral-domain MoM, they are more likely to impose some restrictions.

On the other hand, the application of the spatial-domain MoM to the mixed-potential integral equation (MPIE) requires the necessary Green's functions in the spatial domain [6]. The spatial-domain Green's functions can be obtained from their spectral domain counterparts, which can be derived analytically for planar multilayer media, via Hankel transformation, also called Sommerfeld integral [7], [8]. Because the kernel of the transformation is the Bessel function of the first kind and because the function to be transformed is the spectral-domain Green's function, the integrand is an oscillatory and slow-converging function. Therefore, the calculation of the spatial-domain Green's function, i.e., numerical implementation of the Hankel transformation, is the computational bottleneck of the spatial-domain MoM.

An approach has recently been proposed to accelerate the calculation of the spatial-domain Green's functions [9]. In its original form, the spectral-domain Green's function to be transformed is approximated by complex exponentials via the original Prony method, and the Hankel transformation can be performed analytically with the use of the Sommerfeld identity. Although the original approach was restricted for a single, thick substrate and for an horizontal electric dipole source, it was improved first to cover geometries with a substrate and a superstrate of arbitrary thicknesses [10], then to cover for multilayer geometries with arbitrary thicknesses and for arbitrary source types, horizontal electric dipole (HED), vertical electric dipole (VED), horizontal magnetic dipole (HMD), and vertical magnetic dipole (VMD) [11]. A deficiency of this approach is its being not robust, that is, one needs to examine the function to be approximated prior to the application of an exponential approximation method in order to decide on the approximation parameters, like the range of the approximation and the number of samples in this range. With a recent improvement on the approximation scheme, the calculation of the spatial-domain Green's functions has become robust and extremely efficient [12]. The use of the closed-form Green's functions in conjunction with the MoM results in 2-D integrals over finite domains, and consequently the computational efficiency of the spatial-domain MoM has

ı improved significantly, about two order of magnitudes , compared to the spectral domain approach. In this paper, demonstrate that the use of the complex exponentials ılace of the spatial-domain Green's functions facilitates ytical evaluation of the double integrals. Therefore, a ıtantial improvement in the matrix-fill time is achieved.

ince the use of the closed-form Green's functions is ial for the formulation proposed in this paper, we review ed-form Green's functions in Section II. Section III gives evaluation of the double integrals and necessary integral ıtities. Section IV describes application of the formulation microstrip geometry and computational efficiency. Section resents the conclusion.

II. Closed-Form Green's Functions

is well known that the spectral-domain Green's functions the vector and scalar potentials are represented analytically multilayer medium, [11], [14]. Hence, the spatial-domain en's functions are simply the Hankel transform of the ctral-domain Green's functions as defined

$$G = \frac{1}{4\pi}\int_{SIP} dk_\rho k_\rho H_o^{(2)}(k_\rho\rho)\tilde{G}(k_\rho) \qquad (1)$$

ere $k_\rho^2 = k_x^2 + k_y^2$, ρ is the variable in cylindrical coordinate tem, G and $\tilde{G}$ are the Green's functions in the spatial and ctral domains, respectively, $H_o^{(2)}$ is the Hankel function of second kind and SIP is the Sommerfeld integration path. te that this integral, also called the Sommerfeld integral, can be evaluated analytically for the spectral-domain Green's ctions $\tilde{G}$. Chow *et al.* [9] recognized that if the spectral-nain Green's function $\tilde{G}$ is approximated by exponentials, Sommerfeld integral (1) can be evaluated analytically using well-known Sommerfeld identity

$$\frac{e^{-jk_s r}}{r} = -\frac{j}{2}\int_{SIP} dk_\rho k_\rho H_o^{(2)}(k_\rho\rho)\frac{e^{-jk_z|z|}}{k_z}. \qquad (2)$$

e approximation of the spectral-domain Green's functions complex exponentials is the heart of this technique, and described in [12] the two-level approximation scheme in ıjunction with the generalized pencil of function (GPOF) thod, [15], results in a robust and computationally efficient proach, whose details are given in [12]. Following the two-el approach, the spectral-domain Green's function can be itten as

$$\tilde{G} \cong \frac{1}{j2k_{z_s}}\left[\sum_{n=1}^{N_1} a_{1n}e^{-\alpha_{1n}k_{z_s}} + \sum_{n=1}^{N_2} a_{2n}e^{-\alpha_{2n}k_{z_s}}\right] \qquad (3)$$

ıere a_{1n}, α_{1n} and a_{2n}, α_{2n} are the coefficients and exponents tained from the application of the GPOF method in the first d second parts of the two-level approximation, respectively, d the subscript "s" denotes the layer number of the source lo-tion. Once this representation of the spectral-domain Green's nction is substituted into (1) and the Sommerfeld identity (2) employed, the spatial-domain Green's function can be cast to a form of

$$G \cong \sum_{n=1}^{N_1} a_{1n}\frac{e^{-jk_s r_{1n}}}{r_{1n}} + \sum_{n=1}^{N_2} a_{2n}\frac{e^{-jk_s r_{2n}}}{r_{2n}} \qquad (4)$$

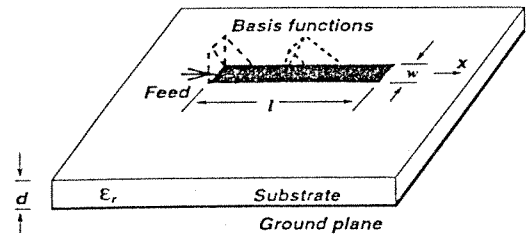

Fig. 1. A typical microstrip geometry. $\epsilon_r = 4.0, d = 0.02032$ cm, $f = 1.0$ GHz.

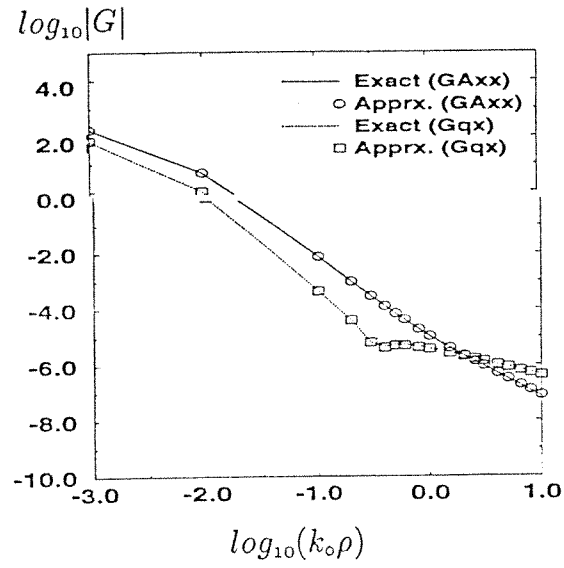

Fig. 2. The magnitude of the normalized Green's functions $4\pi G_{xx}^A/\mu_o, 4\pi\epsilon_o G_q$. $\epsilon_r = 4.0, d = 0.02032$ cm, $f = 1.0$ GHz.

where $r_{1n} = \sqrt{x^2+y^2-\alpha_{1n}^2}$ and $r_{2n} = \sqrt{x^2+y^2-\alpha_{2n}^2}$ are the complex distances and k_s is the wave number in the source medium.

As an example, consider the following parameters for the geometry of a substrate backed by a ground plane as in Fig. 1 which shows the dielectric constant of the substrate $\epsilon_r = 4$; the thickness of the substrate $d = 0.020\,32$ cm; and the frequency of operation $f = 1.0$ GHz. The Green's functions of the vector and scalar potentials due to a HED at the air-substrate interface are obtained in closed forms via two-level approximation scheme, and the coefficients a_{1n}, a_{2n} and the exponents α_{1n}, α_{2n} are given in Table I along with the normalized Green's functions for vector and scalar potentials, $4\pi G_{xx}^A/\mu_o$ and $4\pi\epsilon_o G_q$, respectively, in Fig. 2.

III. Formulation

This formulation is applicable to general microstrip geometries in a multilayer medium where it is assumed that the layers extend to infinity in the transverse directions. However, to avoid complexity and to emphasize the main idea of the proposed method, the formulation is presented, without loss of generality, for a microstrip line on a substrate for which only the longitudinal current is assumed to exist.

The mixed-potential integral equation for the microstrip line can be transformed into the matrix equation with the use of

TABLE I
DEFFICIENTS AND EXPONENTS FOR THE CLOSED-FORM GREEN'S FUNCTIONS

$4\pi G_{xx}^A/\mu_0 = \sum_{n=1}^{N_1=4} a_n e^{-jk_s r_n}/r_n$

a_n	α_n
-1.0000+j0.0000	0.000+j0.0406
0.495e-6-j0.123e-5	-0.0512+j0.0505
0.498e-6+j0.123e-5	0.0511+j0.0506
1.0+j0.0	0.0+j0.0

$4\pi\epsilon_0 G_q = \sum_{n=1}^{N_2=8} a_n e^{-jk_s r_n}/r_n$

a_n	α_n
-0.590623+j0.0	0.0-j0.103e-3
0.0196+j0.0374	0.0390+j0.0598
-0.4485+j0.0	0.0+j0.0345
0.0196-j0.0374	-0.0390+j0.0598
-0.260e-10+j0.771e-11	-53.33+j439.67
0.279e-5-j0.245e-6	-0.3396+j0.9239
0.204e-6+j0.328e-6	1.0270-j0.2907
1.0+j0.0	0.0+j0.0

e well-known MoM procedure, and a typical matrix element given below to help demonstrate the use of the formulation

$$\langle T_{xm}, G_{xx}^A * B_{xn}\rangle + \frac{1}{\omega^2}\left\langle T_{xm}, \frac{\partial}{\partial x}\left(G_q * \frac{\partial}{\partial x} B_{xn}\right)\right\rangle \quad (5)$$

here $\langle\ ,\ \rangle$ and $*$ denote inner product and convolution, spectively, and T_{xm}, B_{xn} are the testing and basis functions, spectively. The first inner product of (5) is written explicitly

$$\langle T_{xm}, G_{xx}^A * B_{xn}\rangle = \iint_{D_T} dx\,dy T_{xm}(x,y) \cdot \iint_{D_B} dx'\,dy' G_{xx}^A(x-x', y-y') B_{xn}(x',y') \quad (6)$$

here D_T and D_B denote the domains of the testing and asis functions, respectively, and the closed-form Green's unction G_{xx}^A is expressed as in (4). By changing the order f integration, the inner product takes the form of

$$\iint du\,dv G_{xx}^A(u,v) \iint dx\,dy T_{xm}(x,y) \cdot B_{xn}(x-u, y-v) \quad (7)$$

where the inner double integral is a correlation function epresented as $T_{xm} \otimes B_{xn}$. As is well known, the choice of the basis and testing functions are of great importance or the accuracy of the results and for the convergence of he matrix elements involved in the MoM [16]. Since the ormulation presented here requires the correlation function o be polynomial function, the choice of testing and basis functions is restricted to polynomial like functions. Therefore, we choose the rooftop functions, which are triangular functions in the longitudinal direction and uniform in the transverse direction, as the basis and testing functions. Half rooftop functions are also used to model the current density at the load and source terminals [13].

For the above choice of the basis and testing functions, the correlation function becomes

$$T_{xm} \otimes B_{xn} = f(u)g(v) \quad (8)$$

where

$$f(u) = \gamma_3 u^3 + \gamma_2 u^2 + \gamma_1 u + \gamma_0 \qquad (m-n-2)h_x < u < (m-n+2)h_x$$
$$g(v) = \frac{1}{h_y^2}\begin{cases} v + h_y & -h_y \le v \le 0 \\ -v + h_y & 0 \le v \le h_y \end{cases} \quad (9)$$

and $\gamma_0, \gamma_1, \gamma_2, \gamma_3$ are constants determined by m, n, and h_x (the half-span of the basis functions in x-direction); and the length of the unit cell in y-direction, h_y, is chosen to be equal to the width of the microstrip line for the specific geometry considered herein. It should be noted that the formulation given here is also valid for a 2-D patch since the order of the polynomials in (9) is the highest that can be encountered in the analysis. By substituting the correlation function (8) and the Green's function (4) into (7), the inner-product term can be written as

$$\frac{1}{h_y^2}\sum_{n=1}^{N} a_n \left[\gamma_0\left(h_y \iint \frac{e^{-jk_s r_n}}{r_n} dv\,du - \iint \frac{e^{-jk_s r_n}}{r_n} v\,dv\,du\right) + \gamma_1\left(h_y \iint \frac{e^{-jk_s r_n}}{r_n} u\,dv\,du - \iint \frac{e^{-jk_s r_n}}{r_n} uv\,dv\,du\right) + \gamma_2\left(h_y \iint \frac{e^{-jk_s r_n}}{r_n} u^2\,dv\,du - \iint \frac{e^{-jk_s r_n}}{r_n} u^2 v\,dv\,du\right) + \gamma_3\left(h_y \iint \frac{e^{-jk_s r_n}}{r_n} u^3\,dv\,du - \iint \frac{e^{-jk_s r_n}}{r_n} u^3 v\,dv\,du\right)\right] \quad (10)$$

where r_n is either r_{1n} or r_{2n} as defined in (4).

Because the integrals in (10) occur in the calculation of matrix elements, and because they cannot be evaluated analytically, their numerical evaluations constitute almost the entire fill time of the MoM matrix. Although the use of the closed-form Green's functions in conjunction with the MoM improves the matrix fill time significantly [13], it could be further improved if the integrals involved (10) can be evaluated analytically. It has been shown that the Taylor's series expansion of the exponential term in the integrand of the first integral in (10) results in an analytically integrable function over a surface [17]. Using this fact, and some of the integral identities given in [18], we can evaluate the integrals in (10) analytically. The case of the Taylor's series expansion requires examining its convergence for all r_n values

h the same number of terms; therefore, the expansion performed around different center points R_c for different ions corresponding to different basis and testing function rs. The mth order Taylor series expansion of $f(z)$ around involves an error term of

$$\text{error} = \left| \frac{f^{m+1}(c)}{(m+1)!}(z - z_o)^{m+1} \right|$$

ere c is a point in the region of convergence. As the mth ivative of $e^{-jk_s r_n}$ is bounded by k_s^m, the error introduced using the mth order expansion is

$$\text{error} \leq \frac{|k_s(r_n - R_c)|^{m+1}}{(m+1)!}.$$

can be observed that the distance to the center point ectly determines the error. Hence, to minimize the error, locations of the center points are chosen to be the mid-int of the each integration region for which the integration ervals are $2h_y$ and $4h_x$ for v and u integrations, respectively, d consequently, $r_n - R_c \leq \sqrt{(2h_x)^2 + h_y^2}$. For the choice 20 basis functions for each wavelength, $r_n - R_c$ is bounded 0.11λ and the error is obtained in the following form

$$\text{error} \leq \frac{(2\pi \times 0.11)^{m+1}}{(m+1)!} = \frac{(0.7)^{m+1}}{(m+1)!} \tag{11}$$

om which it is easily shown that an error bounded by 10^{-4} n be obtained with the use of at least five terms of the Taylor ries. The results presented in Section IV demonstrate that amount of error of 10^{-4} or smaller does not affect the end sult as the current distributions obtained by using analytic d numeric integrations are in good agreement. Hence, it is t worthwhile to increase the number of terms any further.

Using the fifth-order Taylor series expansion around $e^{-jk_s r_n}$ can be approximated as

$$e^{-jk_s r_n} \approx e^{-jk_s R_c}(\beta_0 + \beta_1 r_n + \beta_2 r_n^2 + \beta_3 r_n^3 + \beta_4 r_n^4 + \beta_5 r_n^5) \tag{12}$$

here

$$\beta_0 = \left(1 + jk_s R_c - \frac{k_s^2 R_c^2}{2} - j\frac{k_s^3 R_c^3}{6} + \frac{k_s^4 R_c^4}{24} + j\frac{k_s^5 R_c^5}{120}\right)$$

$$\beta_1 = \left(-jk_s + k_s^2 R_c + j\frac{k_s^3 R_c^2}{2} - \frac{k_s^4 R_c^3}{6} - j\frac{k_s^5 R_c^4}{24}\right)$$

$$\beta_2 = \left(-\frac{k_s^2}{2} - j\frac{k_s^3 R_c}{2} + \frac{k_s^4 R_c^2}{4} + j\frac{k_s^5 R_c^3}{12}\right)$$

$$\beta_3 = \left(j\frac{k_s^3}{6} - \frac{k_s^4 R_c}{6} - j\frac{k_s^5 R_c^2}{12}\right)$$

$$\beta_4 = \left(\frac{k_s^4}{24} + j\frac{k_s^5 R_c}{24}\right)$$

$$\beta_5 = -j\frac{k_s^5}{120}.$$

eplacing the exponential term $e^{-jk_s r_n}$ in (10) by its Taylor eries expansion given in (12) results in the integrals of the type

$$\iint r_n^j u^k v^l \, du \, dv \quad \text{for } j = -1, 0, \cdots, 4, \quad k = 0, \cdots, 3, \quad l = 0, 1. \tag{13}$$

These integrals are analytically integrable and their results are given in the Appendix. Note that the same procedure presented above can be applied to the second inner-product term of (5) in which G_q has the same functional form as G_{xx}^A given in (4).

IV. Results and Discussions

In this part of the study, the formulation described above is applied to a microstrip line to evaluate computational efficiency. The dielectric constant of the medium is $\epsilon_r = 4.0$, the ratio of line width w to substrate thickness d is 4.0. The thickness of the substrate is 0.02032 cm (= 8.0 mils.), the frequency is 1 GHz, and the length of the line is 10 cm. Computational efficiency of the proposed method is assessed in terms of the CPU (central processing unit) time obtained from a SUNsparc-10 workstation.

The current distribution on the microstrip line is obtained by numerically integrating the double integrals (7) (Case 1) involved in the MoM matrix elements, and then by using the analytic integration formulation presented in Section III (Case 2). The current distributions obtained via the use of the numerical integration (Case 1) have been verified by comparing it with the results obtained via the transmission line method described in [13]; therefore, Case 1 serves here as a reference for the accuracy of the current distribution as well. In the numerical integration, 16-point Gauss quadrature integration algorithm, which is considered to be one of the fastest numerical integration algorithms, is employed for the double integrals for which the range of the integration is divided into subregions to guarantee the convergence of the numerical integration. For both cases, the CPU times are obtained for different numbers of basis functions and are listed in Table II. The current distributions obtained via numerical and analytical evaluations of the integrals for 40 basis functions are shown in Fig. 3. It can be observed from Table II that the elimination of the numerical integrals reduces the computation time approximately by a factor of 40. Besides the improvement in computational efficiency, the formulation based on the analytical integration also provides a number of other advantages. First, as the MoM becomes a technique free from any numerical integrations, the numerical errors due to integration and the time used to find an appropriate numerical integration algorithm are eliminated. Second, as the matrix entries are expressed in closed-forms, the effect of changes in geometrical parameters, such as length and width of the microstrip line, onto the output parameters like, current distribution, input impedance or spurious radiation, can be studied analytically by taking a derivative with respect to the desired parameter. Finally, if a method uses numerical integrations, it is necessary to extract the singularity at the source point, while in the analytic integration formulation this problem is completely eliminated because the singularities involved are integrable over a surface. It should be noted that

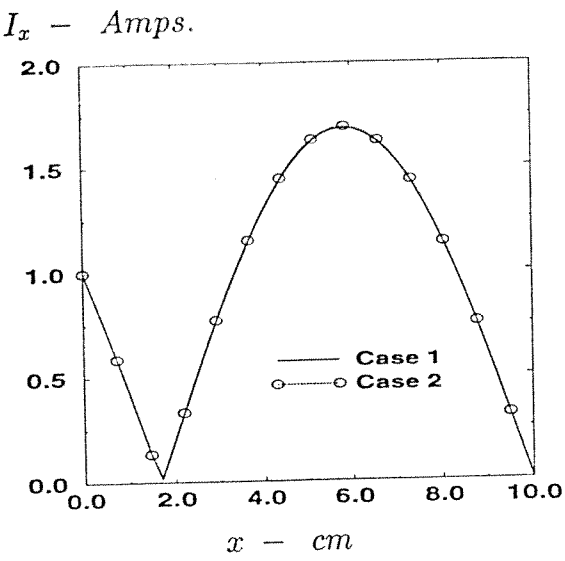

g. 3. Current distributions obtained by using 40 basis functions. = 4.0, d = 0.02032 cm, f = 1.0 GHz, w = 0.08128 cm, l = 10 cm.

TABLE II
CPU TIMES FOR DIFFERENT NUMBER OF BASIS FUNCTIONS

number of basis func.	CPU time in sec. (Case 1)	CPU time in sec. (Case 2)
10	13.3	0.36
20	27.0	0.65
30	39.0	0.98
40	52.95	1.33

he application of the proposed approach here has no restriction or the size of the geometry, provided the closed-form Green's unctions are valid for the distance as far as the maximum listance of the geometry.

V. CONCLUSION

When the spatial-domain MoM is used in conjunction with the closed-form Green's functions for the solution of the mixed-potential integral equation, the MoM matrix elements involve 2-D integrals whose numerical evaluations increase the matrix fill-time. In order to improve the numerical efficiency of the method, the integrand is approximated by its Taylor series and each term of the expansion is integrated analytically. By eliminating the numerical integration from the MoM, the matrix fill-time is decreased drastically, which is a significant improvement in the matrix-fill time of the MoM. This acceleration in the matrix fill time makes the MoM a fast full-wave analysis technique which can be utilized in an optimization algorithm for the solution of a design problem. Besides, the proposed method offers other advantages such as expressing the matrix entries in closed-forms, which opens up the possibility of investigating the effect of some parameters on the end result by examining the matrix entries analytically.

APPENDIX
THE ANALYTIC EVALUATION OF THE INTEGRALS GIVEN IN (13)

$$R = \sqrt{u^2 + v^2 + c^2}$$

where c is any of the complex exponents. Some special integrals are defined in order to simplify the formulation

$$J_0 = \int R\,du = \frac{1}{2}(Ru + (v^2 + c^2) \cdot \log(u + R))$$

$$J_1 = \int uR\,du = \frac{R^3}{3}$$

$$J_2 = \int u^2 R\,du = \frac{u(v^2 + c^2 + 2u^2)R}{8} - \frac{(v^2 + c^2)^2}{8} \cdot \log(u + R)$$

$$J_3 = \int u^3 R\,du = \frac{R^5}{5} - (v^2 + c^2)\frac{R^3}{3}$$

$$J_4 = \int u^4 R\,du = \left(-\frac{3}{2}(v^2 + c^2)^2 + (v^2 + c^2)u^2 + 4u^4\right)\left(\frac{uR}{24}\right) + \frac{1}{16}(v^2 + c^2)^3 \log(u + R)$$

$$J_5 = \int u^5 R\,du = \frac{R^7}{7} - \frac{2}{5}R^5(v^2 + c^2) + \frac{R^3}{3}(v^2 + c^2)^2$$

$$J_6 = \int u^6 R\,du = \frac{7u}{8}J_5 - \frac{(v^2 + c^2)}{40}J_4 + \frac{(v^2 + c^2)^2}{30}J_2 - \frac{(v^2 + c^2)^3}{15}J_0$$

$$J_7 = \int u^7 R\,du = \frac{R^9}{9} - 3(v^2 + c^2)\frac{R^7}{7} + 3(v^2 + c^2)^2\frac{R^5}{5} - (v^2 + c^2)^3\frac{R^3}{3}$$

$$K_0 = \int \frac{1}{R}\,du = \log(u + R)$$

$$K_1 = \int \frac{u}{R}\,du = R$$

$$K_n = \int \frac{u^n}{R}\,du = J_{n-2} - (v^2 + c^2) \cdot K_{n-2}$$

$$J_0 = \int \frac{1}{(u^2 + c^2)R}\,du = \frac{1}{vc}\arctan\left(\frac{uv}{cR}\right)$$

$$I_1 = \int \frac{u}{(u^2+c^2)R}\,du = \frac{\log(R-v)-\log(R+v)}{2v}$$

$$I_n = \int \frac{u^n}{(u^2+c^2)R}\,du = K_{n-2} - c^2 I_{n-2}$$

$$L_0 = \int \frac{1}{(u^2+c^2)}\,du = \frac{1}{c}\arctan\left(\frac{u}{c}\right)$$

$$L_1 = \int \frac{u}{(u^2+c^2)}\,du = \frac{\log(u^2+c^2)}{2}$$

$$L_n = \int \frac{u^n}{(u^2+c^2)}\,du = \frac{u^{n-1}}{n-1} - c^2 L_{n-2}$$

$$M_n = \iint \frac{u^n}{R}\,dv\,du = (u^{n+1}\log(v+R) - L_{n+2} + vI_{n+2})/(n+1)$$

$$\iint u^n R\,dv\,du = \frac{1}{2}(vJ_n + M_{n+2} + c^2 M_n)$$

$$\iint u^n R^2\,dv\,du = \frac{u^{n+1}}{n+1}\left(\frac{v^3}{3}+vc^2\right) + \frac{u^{n+3}}{n+3}v$$

$$\iint u^n R^3\,dv\,du = \frac{5}{8}vJ_{n+2} + \frac{v}{4}\left(\frac{5c^2}{2}+v^2\right)J_n + \frac{3}{8}(M_{n+4} + 2c^2 M_{n+2} + c^4 M_n)$$

$$\iint u^n R^4\,dv\,du = \frac{u^{n+1}}{n+1}\left(c^4 v + \frac{v^5}{5} + \frac{2c^2v^3}{3}\right) + \frac{2u^{n+3}}{n+3}\left(\frac{v^3}{3}+c^2 v\right) + \frac{vu^{n+5}}{n+5}$$

$$\iint \frac{u^n v}{R}\,dv\,du = J_n$$

$$\iint u^n vR\,dv\,du = \frac{J_{n+2}}{3} + \frac{(v^2+c^2)J_n}{3}$$

$$\iint u^n vR^2\,dv\,du = \frac{u^{n+3}v^2}{2(n+3)} + \frac{v^2}{2}\left(c^2+\frac{v^2}{2}\right)\frac{u^{n+1}}{n+1}$$

$$\iint u^n vR^3\,dv\,du = \frac{J_{n+4}}{5} + \frac{2(v^2+c^2)}{5}J_{n+2} + \frac{(v^2+c^2)^2}{5}J_n$$

$$\iint u^n vR^4\,dv\,du = \frac{u^{n+5}v^2}{2(n+5)} + \frac{u^{n+3}}{n+3}\left(c^2v^2+\frac{v^4}{2}\right) + \frac{u^{n+1}}{n+1}\left(\frac{c^4v^2}{2}+\frac{v^6}{6}+\frac{c^2v^4}{2}\right).$$

REFERENCES

[1] R. F. Harrington, *Field Computation by Moment Methods*. New York: MacMillan; FL: Krieger, 1983.

[2] J. Jin, *The Finite Element Method in Electromagnetics*. New York: Wiley, 1993.

[3] K. Kunz and R. Luebber, *The Finite Difference Time Domain Method for Electromagnetics*. Boca Raton, FL: CRC, 1993.

[4] R. Schinzinger and P. Laura, *Conformal Mapping: Methods and Applications*. New York: Elsevier, 1991.

[5] D. M. Pozar, "Input impedance and mutual coupling of rectangular microstrip antennas," *IEEE Trans. Antennas Propagat.*, vol. AP-30, pp. 1191–1196, Nov. 1982.

[6] J. R. Mosig and F. E. Gardiol, "General integral equation formulation for microstrip antennas and scatterers," *IEE Proc.*, pt. H, vol. 132, no. 7, pp. 424–432, 1985.

[7] A. Sommerfeld, *Partial Differential Equations in Physics*. New York: Academic, 1949.

[8] W. C. Chew, *Waves and Fields in Inhomogeneous Media*. New York: Van Nostrand, 1990.

[9] Y. L. Chow, J. J. Yang, D. F. Fang and G. E. Howard, "Closed form spatial Green's function for the thick substrate," *IEEE Trans. Microwave Theory Tech.*, vol. 39, pp. 588–592, Mar. 1991.

[10] M. I. Aksun and R. Mittra, "Derivation of closed-form Green's functions for a general microstrip geometries," *IEEE Trans. Microwave Theory Tech.*, vol. 40, pp. 2055–2062, Nov. 1992.

[11] G. Dural and M. I. Aksun, "Closed-form Green's functions for general sources and stratified media," *IEEE Trans. Microwave Theory Tech.*, vol. 43, no. 7, pp. 1545–1552, Jul. 1995.

[12] M. I. Aksun, "A robust approach for the derivation of the closed-form Green's functions," *IEEE Trans. Microwave Theory Tech.*, in press.

[13] M. I. Aksun and R. Mittra, "Estimation of spurious radiation from microstrip etches using closed-form Green's functions," *IEEE Trans. Microwave Theory Tech.*, vol. 40, pp. 2063–2069, Nov. 1992.

[14] N. K. Das and D. M. Pozar, "A spectral-domain Green's function for multilayer dielectric substrates with application to multilayer transmission lines," *IEEE Trans. Microwave Theory Tech.*, vol. MTT-35, pp. 326–335, Mar. 1987.

[15] Y. Hua and T. K. Sarkar, "Generalized pencil-of-function method for extracting poles of an EM system from its transient response," *IEEE Trans. Antennas Propagat.*, vol. 37, pp. 229–234, Feb. 1989.

[16] M. I. Aksun and R. Mittra, "Choices of expansion and testing functions for the method of moments applied to a class of electromagnetic problems," *IEEE Trans. Microwave Theory Tech.*, vol. 41, pp. 503–509, Mar. 1993.

[17] R. F. Harrington, "Matrix methods for field problems," *Proc. IEEE*, vol. 55, pp. 136–149, Feb. 1967.

[18] K. Mahadevan and H. A. Auda, "Electromagnetic field of a rectangular patch of uniform and linear distributions of current," *IEEE Trans. Antennas Propagat.*, vol. 37, pp. 1503–1509, Dec. 1989.

Lale Alatan (S'91) received the B.S. and M.S. degrees in electrical and electronics engineering from Middle East Technical University (METU), Ankara, Turkey, in 1990 and 1993, respectively. Currently, she is working toward the Ph.D. degree at METU.

Her research area includes numerical analysis of printed structures, microstrip antennas, and microwave and millimeter-wave circuits.

M. I. Aksun (M'92) received the B.S. and M.S. degrees in electrical and electronics engineering from the Middle East Technical University, Ankara, Turkey, in 1981 and 1983, respectively, and the Ph.D. degree in electrical and computer engineering from the University of Illinois at Urbana-Champaign in 1990. From 1990 to 1992, he was a Post Doctoral Fellow at the Electromagnetic Communication Laboratory, University of Illinois at Urbana-Champaign.

Since 1992, he has been on the Faculty of the Department of Electrical and Electronics Engineering at Bilkent University, Ankara, Turkey, where he is currently an Associate Professor. His research interests include the numerical methods for electromagnetics, microstrip antennas, and microwave and millimeter-wave integrated circuits.

Karthikeyan Mahadevan was born in Thanjavur, India, on December 1, 1957. He received the B.E. degree with honors in electronics and communication engineering from the Regional Engineering College, Tiruchirappalli, India in 1980; the M.S. degree in electrical engineering from the Indian Institute of Technology (IIT), Madras, India, in 1983; and the Ph.D. degree in engineering science from the University of Mississippi, University, in 1991.

From 1980 to 1986, he was with the Center for ystems and Devices, IIT, working on a development project in electromag- tics and antennas sponsored by the Defense Research and Development rganization of the Government of India. In 1986, he joined the Department Electrical Engineering of the University of Mississippi as a Graduate esearch Assistant. From 1991 to 1993, he worked in the Electromagnetic ommunication Laboratory of the University of Illinois as a Post Doctoral ellow. In 1994, he joined SG Microwaves Inc., Kitchener, Ontario, Canada as n Advanced Technical Member. His areas of interest include electromagnetic eld theory and computation.

M. Tuncay Birand (S'67–M'72) received the B.S., M.S., and Ph.D. degrees from Middle East Technical University (METU), Ankara, Turkey, in 1966, 1967, and 1971, respectively.

He was a Visiting Professor at the Queen Mary College, England, from 1978 to 1979, and at the University of Illinois, Department of ECE on a Fullbright program from 1988 to 1989. He was a Consultant with the ERA Tech. Ltd., Radio Frequency Technical Division, Leatherhead, England, from 1979 to 1981. He was Chairman of the EE Department, Gazi University, Turkey, from 1982 to 1983, and from 1984 to 1988, and the Chairman of the EE Department of METU from 1991 to 1992. He is the National Representative in the Senior Officials Committee of the European Cooperation in the Field of Scientific and Technical Research. Currently, he is the Dean of the Faculty of Engineering, METU, Ankara, Turkey. His research interests are antenna near-field and far-field transformations, printed antennas and computational electromagnetics.

Dr. Birand won the Promotion Award of the Turkish Scientific and Research Council in 1983. He is a member of the Chamber of Electrical Engineers of Turkey and the New York Academy of Sciences.

Closed-Form Green's Functions for General Sources and Stratified Media

Gülbin Dural, *Member, IEEE*, and M. I. Aksun, *Member, IEEE*

stract—The closed-form Green's functions of the vector and ır potentials in the spatial domain are presented for the ces of horizontal electric, magnetic, and vertical electric, netic dipoles embedded in general, multilayer, planar media. t, the spectral domain Green's functions in an arbitrary layer derived analytically from the Green's functions in the source r by using a recursive algorithm. Then, the spatial domain en's functions are obtained by adding the contributions of the ct terms, surface waves, and complex images approximated the Generalized Pencil of Functions Method (GPOF). In derivations, the main emphasis is to put these closed-form resentations in a suitable form for the solution of the mixed ential integral equation (MPIE) by the method of moments in eneral three-dimensional geometry. The contributions of this er are: 1) providing the complete set of closed-form Green's ctions in spectral and spatial domains for general stratified dia; 2) using the GPOF method, which is more robust and ; noise sensitive, in the derivation of the closed-form spatial nain Green's functions; and 3) casting the closed-form Green's ıctions in a form to provide efficient applications of the method moments.

I. Introduction

DUE to the increased use of multilayer microstrip geometries in the application of microstrip antennas [1]–[6] d monolithic microwave integrated circuits [7]–[11], the layed geometries have recently attracted widespread attention. ıerefore, a considerable amount of interest has been focused ı the development of a rigorous and yet computationally ficient computer-aided design tools for microstrip geometries a layered medium.

The rigorous analysis of layered microstrip structures reıires the computation of the Green's functions for multilayer ıedia, which are traditionally represented by the Sommerfeld ıtegrals in the spatial domain, and by closed-form expressions ı the spectral domain. When these traditional expressions for ıe Green's functions are employed in the method of moments MoM), the numerical evaluation of the MoM matrix elements ecomes very time consuming in either domain, because the ıtegrals involved are oscillatory and slow decaying functions 12]. To alleviate this problem, the spatial domain Green's unctions for the vector and scalar potentials, represented by he Sommerfeld integrals, are approximated by closed-form expressions and used in the solution of the mixed potential integral equation (MPIE) by the MoM. This approach of approximating the spectral domain Green's functions was first proposed in [13] for a horizontal electric dipole (HED) over a thick substrate backed by a ground plane and extended to a geometry with a substrate and a superstrate with arbitrary thicknesses [14], using the original and least-square Prony's methods [16], respectively. It was demonstrated that the use of the closed-form Green's functions in the analysis of a microstrip geometry via the MoM improves the computational efficiency significantly [15].

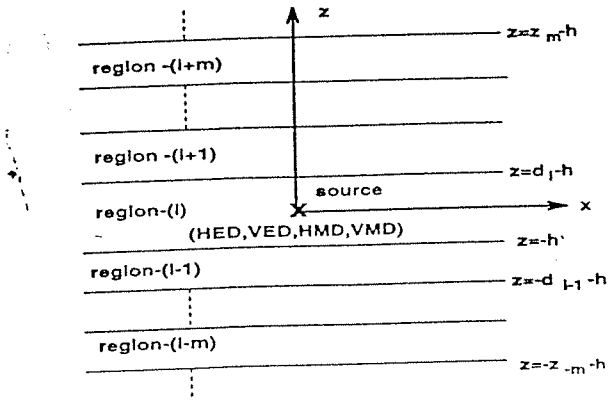

Fig. 1. Sources embedded in a multilayer medium.

In this paper, the closed-form Green's functions of the vector and scalar potentials of a Horizontal Electric Dipole (HED), Horizontal Magnetic Dipole (HMD), Vertical Electric Dipole (VED), and a Vertical Magnetic Dipole (VMD) located in an arbitrary layer of a planar-layered medium are presented. The layers are considered to have different dielectric and magnetic properties (ϵ_r, μ_r) or are made of perfect electric or magnetic conductors (PEC, PMC), as shown in Fig. 1. The Green's functions are first obtained in the spectral domain, which can be represented in closed-form, in the source layer and these expressions are extended to an arbitrary layer using an iterative algorithm [8] for TE and TM components individually. Then, the spatial domain closed-form Green's functions are obtained by adding the contributions of the direct terms and surface waves to the complex images approximated by the Generalized Pencil of Functions (GPOF) method [17], which is less noise sensitive and more efficient than the Prony's methods. Since the spectral domain Green's functions, excluding the direct term and the surface wave components, are approximated by the GPOF method, their dependence on z must be kept in

Manuscript received December 9, 1993; revised December 31, 1994. This work was supported in part by NATO's Scientific Affairs Division in the framework of the Science for Stability Programme and Cost 223 and Cost 245 projects.

G. Dural is with the Department of Electrical and Electronics Engineering, Middle East Technical University, 06531 Ankara, Turkey.

M. I. Aksun is with the Department of Electrical and Electronics Engineering, Bilkent University, 06533 Ankara, Turkey.

IEEE Log Number 9412042.

form to avoid the repeated use of GPOF approximation
ıcrease the computational efficiency in cases of vertical
ıons. Since the Green's functions for the vector and
otentials are not uniquely defined in stratified media
9], the closed-form representations of an alternative
tion of the Green's functions are also provided, which
ɔe used in cases where the vertical and horizontal
are present at the same point [20].
/ation of the closed-form Green's functions are given
ion II and the numerical considerations associated
ıeir evaluation are discussed. In Section III, some
ɔal examples of the closed-form Green's functions are
ed for two different multilayer geometries and the
imate Green's functions are compared with the exact
s functions obtained by the numerical evaluation of the
ɔonding Sommerfeld integrals.

II. Formulation

eneral planar-layered medium is shown in Fig. 1. The
, (HED, HMD, VED or VMD) is embedded in region i
e observation point can be located in an arbitrary layer.
ayer can have different electric and magnetic properties
.) and thickness (d_i). The perfect electric or magnetic
cting planes and half space are also considered as layers
e formulation. The procedure for deriving the closed-
Green's functions can be summarized as the following

Derivation of the Green's functions in the spectral domain.

a) Green's functions are derived in the source layer.
b) Green's functions in the observation layer are obtained using an iterative algorithm applied to each TE and TM component of the Green's functions in the source layer.

Derivation of the spatial domain, closed-form Green's functions.

a) Spectral Domain Green's functions, after having the surface wave poles and the direct terms extracted, are approximated in terms of complex exponentials obtained from the GPOF method.
b) Closed-form Green's functions are obtained analytically using the Sommerfeld identity for each complex exponential.

ıe derivation of the Green's functions for the vector and
ır potentials in the spectral domain follows the similar
edure given in [8], where the Green's functions for the
tric and magnetic fields are obtained. Thus, the derived
ɔn's functions, without giving the details of the derivation,
given in Section II-A with all the necessary definitions
he reflection coefficients and amplitudes for the sake of
ıpleteness and for later references.
ıll of the Green's functions presented here are for the vector
scalar potentials that are indeed not uniquely defined in
tified media [18], [19]. Therefore, different sets of Green's
ctions for the vector and scalar potentials can be chosen
ıatisfy the same boundary conditions. The following form of the Green's function is commonly used and referred as the traditional form for the vector potentials

$$\bar{\bar{G}}_{A,F} = (\hat{x}\hat{x} + \hat{y}\hat{y})G_{xx} + \hat{z}\hat{x}G_{zx} + \hat{z}\hat{y}G_{zy} + \hat{z}\hat{z}G_{zz} \quad (1)$$

and for the scalar potentials, $G_{x,y}^{q_e,m}$ and $G_z^{q_e,m}$ [20]. Note that in this representation, the scalar potentials of the point charges associated with the horizontal and vertical dipoles are not identical. This results in some difficulties in the solution of the mixed potential integral equation for a geometry where both the horizontal and vertical sources (HED and VED or HMD and VMD) are present at the same point, as in the case of a microstrip etch fed by a vertical probe. To overcome this difficulty, an alternative formulation is proposed in [19] and adopted in this paper to the procedure described above. The alternative representations of the Green's functions are given in the Appendix.

A. Green's Functions in the Spectral Domain

To derive the spectral domain Green's function for the source layer (layer i), the z dependence of the fields in the source region is written as the sum of the direct term and up- and down-going waves due to the reflections from the boundaries at $z = -h$ and $z = d_i - h$, respectively. The coefficients of the up- and down-going waves can be obtained in terms of the generalized reflection coefficients by applying the appropriate boundary conditions. The spectral domain Green's functions (traditional form) in the source layer are obtained for the sources of HED, HMD, VED, and VMD as

HED

$$\tilde{G}_{xx}^{A} = \frac{\mu_i}{2jk_{z_i}}[e^{-jk_{z_i}|z|} + A_h^e e^{jk_{z_i}z} + C_h^e e^{-jk_{z_i}z}] \quad (2)$$

$$\tilde{G}_{zx}^{A} = \frac{-\mu_i}{2jk_{z_i}}\left[\frac{k_x k_{z_i}}{k_\rho^2}(A_h^e + B_h^e)e^{jk_{z_i}z} + \frac{k_x k_{z_i}}{k_\rho^2}(D_h^e - C_h^e)e^{-jk_{z_i}z}\right] \quad (3)$$

$$\tilde{G}_{x}^{q_e} = \frac{1}{j2\epsilon_i k_{z_i}}\left[e^{-jk_{z_i}|z|} + \frac{k_{z_i}^2 B_h^e + k_i^2 A_h^e}{k_\rho^2}e^{jk_{z_i}z} + \frac{k_i^2 C_h^e - k_{z_i}^2 D_h^e}{k_\rho^2}e^{-jk_{z_i}z}\right] \quad (4)$$

HMD

$$\tilde{G}_{xx}^{F} = \frac{\epsilon_i}{2jk_{z_i}}[e^{-jk_{z_i}|z|} + A_h^m e^{jk_{z_i}z} + C_h^m e^{-jk_{z_i}z}] \quad (5)$$

$$\tilde{G}_{zx}^{F} = \frac{-\epsilon_i}{2jk_{z_i}}\left[\frac{k_x k_{z_i}}{k_\rho^2}(A_h^m + B_h^m)e^{jk_{z_i}z} + \frac{k_x k_{z_i}}{k_\rho^2}(D_h^m - C_h^m)e^{-jk_{z_i}z}\right] \quad (6)$$

$$\tilde{G}_{x}^{q_m} = \frac{1}{j2\mu_i k_{z_i}}\left[e^{-jk_{z_i}|z|} + \frac{k_{z_i}^2 B_h^m + k_i^2 A_h^m}{k_\rho^2}e^{jk_{z_i}z} + \frac{k_i^2 C_h^m - k_{z_i}^2 D_h^m}{k_\rho^2}e^{-jk_{z_i}z}\right] \quad (7)$$

VED

$$\tilde{G}_{zz}^{A} = \frac{\mu_i}{j2k_{z_i}}[e^{-jk_{z_i}|z|} + A_v^e e^{-jk_{z_i}z} + B_v^e e^{jk_{z_i}z}] \quad (8)$$

$$\tilde{G}_z^{q_e} = \frac{1}{j2k_{z_i}\epsilon_i}[e^{-jk_{z_i}|z|} + C_v^e e^{-jk_{z_i}z} + D_v^e e^{jk_{z_i}z}] \quad (9)$$

MD:

$$\tilde{G}_{zz}^{F} = \frac{\epsilon_i}{j2k_{z_i}}[e^{-jk_{z_i}|z|} + A_v^m e^{-jk_{z_i}z} + B_v^m e^{jk_{z_i}z}] \quad (10)$$

$$\tilde{G}_z^{q_m} = \frac{1}{j2k_{z_i}\mu_i}[e^{-jk_{z_i}|z|} + C_v^m e^{-jk_{z_i}z} + D_v^m e^{jk_{z_i}z}] \quad (11)$$

ere $\tilde{G}_{ij}^{A,F}$ denotes the spectral domain Green's functions the vector potentials in direction-i due to a unit j-directed rent element, $\tilde{G}_i^{q_e,m}$ represents the Green's function of the lar potential in the spectral domain due to a unit i-directed tric or magnetic current element, $k_i^2 = k_\rho^2 + k_{z_i}^2$, the erscripts A and F represent the magnetic and the electric tor potentials, respectively, q_e and q_m represent electric l magnetic scalar potentials, respectively. The coefficients, $_{,v}^{m}, B_{h,v}^{e,m}, C_{h,v}^{e,m}, D_{h,v}^{e,m}$ are functions of the generalized re- tion coefficients $\tilde{R}_{\mathrm{TE,TM}}$ [8], and are given by

$$A_h^{e,m} = e^{-jk_{z_i}(d_i-h)}\tilde{R}_{\mathrm{TE,TM}}^{i,i+1}[e^{-jk_{z_i}(d_i-h)} + \tilde{R}_{\mathrm{TE,TM}}^{i,i-1}e^{-jk_{z_i}(d_i+h)}]M_i^{\mathrm{TE,TM}} \quad (12)$$

$$B_h^{e,m} = e^{-jk_{z_i}(d_i-h)}\tilde{R}_{\mathrm{TM,TE}}^{i,i+1}[e^{-jk_{z_i}(d_i-h)} - \tilde{R}_{\mathrm{TM,TE}}^{i,i-1}e^{-jk_{z_i}(d_i+h)}]M_i^{\mathrm{TM,TE}} \quad (13)$$

$$C_h^{e,m} = e^{-jk_{z_i}h}\tilde{R}_{\mathrm{TE,TM}}^{i,i-1}[e^{-jk_{z_i}h} + \tilde{R}_{\mathrm{TE,TM}}^{i,i+1}e^{-jk_{z_i}(2d_i-h)}]M_i^{\mathrm{TE,TM}} \quad (14)$$

$$D_h^{e,m} = e^{-jk_{z_i}h}\tilde{R}_{\mathrm{TM,TE}}^{i,i-1}[-e^{-jk_{z_i}h} + \tilde{R}_{\mathrm{TM,TE}}^{i,i+1}e^{-jk_{z_i}(2d_i-h)}]M_i^{\mathrm{TM,TE}} \quad (15)$$

$$A_v^{e,m} = e^{-jk_{z_i}h}\tilde{R}_{\mathrm{TM,TE}}^{i,i-1}[e^{-jk_{z_i}h} + \tilde{R}_{\mathrm{TM,TE}}^{i,i+1}e^{-jk_{z_i}(2d_i-h)}]M_i^{\mathrm{TM,TE}} \quad (16)$$

$$B_v^{e,m} = e^{-jk_{z_i}(d_i-h)}\tilde{R}_{\mathrm{TM,TE}}^{i,i+1}[e^{-jk_{z_i}(d_i-h)} + \tilde{R}_{\mathrm{TM,TE}}^{i,i-1}e^{-jk_{z_i}(d_i+h)}]M_i^{\mathrm{TM,TE}} \quad (17)$$

$$C_v^{e,m} = e^{-jk_{z_i}h}\tilde{R}_{\mathrm{TM,TE}}^{i,i-1}[-e^{-jk_{z_i}h} + \tilde{R}_{\mathrm{TM,TE}}^{i,i+1}e^{-jk_{z_i}(2d_i-h)}]M_i^{\mathrm{TM,TE}} \quad (18)$$

$$D_v^{e,m} = e^{-jk_{z_i}(d_i-h)}\tilde{R}_{\mathrm{TM,TE}}^{i,i+1}[-e^{-jk_{z_i}(d_i-h)} + \tilde{R}_{\mathrm{TM,TE}}^{i,i-1}e^{-jk_{z_i}(d_i+h)}]M_i^{\mathrm{TM,TE}} \quad (19)$$

here

$$M_i^{\mathrm{TE,TM}} = [1 - \tilde{R}_{\mathrm{TE,TM}}^{i,i+1}\tilde{R}_{\mathrm{TE,TM}}^{i,i-1}e^{-jk_{z_i}2d_i}]^{-1} \quad (20)$$

$$\tilde{R}_{\mathrm{TE,TM}}^{j+1,j} = \frac{R_{\mathrm{TE,TM}}^{j+1,j} + \tilde{R}_{\mathrm{TE,TM}}^{j,j-1}e^{-jk_{z_j}2d_j}}{1 - R_{j,j+1}\tilde{R}_{\mathrm{TE,TM}}^{j,j-1}e^{-jk_{z_j}2d_j}} \quad (21)$$

nd R and $\tilde{R}$ are the Fresnel and generalized reflection oefficients [8] for which the subscripts TE and TM represent ne polarization of the wave, and the superscripts $(i, i-1)$ r $(i, i+1)$ show the layer numbers. The subscripts h and used in the coefficients (12)–(17) represent the orientation f the source, horizontal and vertical, respectively, while the uperscripts e and m denote the type of the source, electric and nagnetic, respectively. It should be noted that the horizontal Green's functions for the y-oriented dipoles can be obtained simply by setting $\tilde{G}_{yy}^{A,F} = \tilde{G}_{xx}^{A,F}, \tilde{G}_{xy}^{A,F}/k_y = \tilde{G}_{xx}^{A,F}/k_x$, and $\tilde{G}_y^{q_e,m} = \tilde{G}_x^{q_e,m}$.

The amplitudes of the up- and down-going waves in a layer different from the source layer are related to those in the adjacent layers by

$$A_j^- = A_{j+1}^- \frac{T_{j+1,j}e^{-j(k_{z_{j+1}}-k_{z_j})(h+z_{-m+1})}}{1 - R_{j,j+1}\tilde{R}_{j,j-1}e^{-jk_{z_j}2d_j}} \quad (22)$$

where A_j^- and A_{j+}^- 1 are the amplitudes of the down-going waves in layers j and $j+1$, respectively, $(j = i-m), T$ is the transmission coefficient, and z_m is the distance between the lower boundary of the source layer i and the lower boundary of layer j (see Fig. 1). Similarly, the amplitudes of the up-going waves in layer $j = i+m$ can be written as

$$A_j^+ = A_{j-1}^+ \frac{T_{j-1,j}e^{-j(k_{z_{j-1}}-k_{z_j})(z_{m-1}+d_i-h)}}{1 - R_{j,j-1}\tilde{R}_{j,j+1}e^{-jk_{z_j}2d_j}}. \quad (23)$$

Therefore, starting from the source layer, the field expressions for any layer can be obtained iteratively [8].

B. Closed-form Green's Functions in the Spatial Domain

The spatial domain Green's functions are represented by the Sommerfeld integral [21] as

$$G^{A,F,q_e,q_m} = \frac{1}{4\pi}\int_{\mathrm{SIP}} dk_\rho k_\rho H_o^{(2)}(k_\rho\rho)\tilde{G}^{A,F,q_e,q_m}(k_\rho) \quad (24)$$

where G and $\tilde{G}$ are the Green's functions in the spatial and spectral domains, respectively, $H_o^{(2)}$ is the Hankel function of the second kind, and SIP is the Sommerfeld integration path. The Sommerfeld integral given in (24) cannot be integrated analytically, except for a few special cases. On the other hand, if the spectral domain representation of the Green's function, $\tilde{G}$, in the integrand can be approximated in terms of complex exponentials, then the analytical evaluation of the integral (24) becomes possible via the Sommerfeld identity. Since the contributions of the direct terms, $e^{-jk_{z_i}|z|}/k_{z_i}$, and the surface waves can be calculated analytically, they are excluded from the expressions to be approximated, [13], [14].

In approximating the spectral domain Green's functions, the GPOF method, which is based on solving a generalized eigenvalue problem, is used [17]. The spectral domain Green's functions, $\tilde{G}$, are uniformly sampled along an integration path, $k_z = k[-jt + (1 - t/T_o)]$ deformed from SIP [13] and approximated by complex exponentials as

$$\tilde{G} \cong \sum_{m=1}^{N} a_m e^{-b_m k_{z_i}} \quad (25)$$

where N is the number of exponentials used in the approximation. Then, the Sommerfeld identity

$$\frac{e^{-jkr}}{r} = -\frac{j}{2}\int_{\mathrm{SIP}} dk_\rho k_\rho H_o^{(2)}(k_\rho\rho)\frac{e^{-jk_z|z|}}{k_z} \quad (26)$$

is employed to obtain the Green's functions in the following form, referred as the closed-form

$$G \cong \sum_{m=1}^{N} a_m \frac{e^{-jk_i r_m}}{r_m} + \text{direct term} + \text{surface waves} \quad (27)$$

$r_m = \sqrt{\rho^2 - b_m^2}$ represents a complex distance. Since
rface wave contributions for thin-layered structures are
the exclusion of the surface wave contributions is
itical for such geometries; meanwhile, the extraction
surface wave poles could improve the approximation
ometries with thick layers. Note that the approximation
: spectral domain Green's functions (2)–(11) must be
med for the terms in the square brackets, i.e., the
are apart from $1/k_{zi}$ after extracting the direct term
urface wave poles, to be able to use the Sommerfeld
ty. In addition, k_x and k_y parameters in $\tilde{G}_{xx}^{A,F}$ and $\tilde{G}_{xy}^{A,F}$,
ctively, are excluded in the approximation and their
ibutions are added in the spatial domain (after having
ned the spatial domain representations of $\tilde{G}_{xx}^{A,F}/k_x$ and
$/k_y$) by differentiating analytically with respect to x and
spectively.

losed-Form Green's Functions for MoM Applications

far, a general procedure to obtain the closed-form
n's functions for the vector and scalar potentials has been
ained, but nothing has been done yet to make these closed-
expressions numerically efficient when they are used
onjunction with the method of moments. As mentioned
e, the terms in the square brackets in (2)–(11) are to be
pled uniformly along k_{zi} and approximated by complex
onentials. To do so, one needs to fix the vertical coordinate
able z; that is, the approximation technique GPOF has
e applied for each z value involved in the analysis.
cases of horizontal conductors only, this wouldn't cause
putational inefficiency because the conductors must be
ed at constant z-planes, resulting in the following MoM
rix element:

$$\langle T_{xm}, G_{xx}^A * B_{xn}\rangle + \frac{1}{\omega^2}\left\langle T_{xm}, \frac{\partial}{\partial x}\left[G_x^{q_e} * \frac{\partial B_{xn}}{\partial x}\right]\right\rangle \quad (28)$$

ere T_{xm} and B_{xn} are testing and basis functions, respec-
ly. G_{xx}^A and $G_x^{q_e}$ used in this formulation are approximated
GPOF for constant z's corresponding to the planes of the
ductors in the geometry. However, in geometries with both
tical and horizontal conductors with z and x-directed cur-
t components, respectively, typical MoM matrix elements
have the terms of

$$\langle T_{zm}, G_{zx}^A * B_{xn}\rangle, \quad \left\langle T_{zm}, \frac{\partial}{\partial z}\left[G_x^{q_e} * \frac{\partial B_{xn}}{\partial x}\right]\right\rangle$$
$$\langle T_{zm}, G_{zz}^A * B_{zn}\rangle, \quad \left\langle T_{zm}, \frac{\partial}{\partial z}\left[G_z^{q_e} * \frac{\partial B_{zn}}{\partial z}\right]\right\rangle \quad (29)$$

ere $G_{zx}^A, G_{zz}^A, G_x^{q_e}$ and $G_z^{q_e}$ need to be approximated at
ery observation point z and/or source point z' values (as-
ming the origin is at the bottom of the source layer for the
plication of the MoM, the coordinates used in the derivation
the Green's functions here can be transformed by $z \leftarrow z -$
$, h \leftarrow z'$) in the integration due to the testing and expansion
ocesses along a vertical conductor. This would defeat the
rpose of using the closed-form Green's functions in a MoM
plication. To circumvent the problem associated with the
sting process, which corresponds to integration along z, the

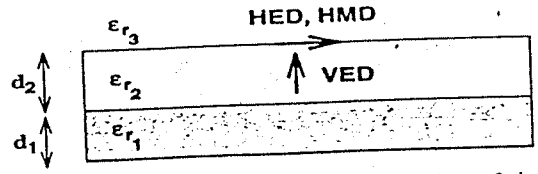

Fig. 2. Geometry of a 4-layer structure. Layer-0: PEC, Layer-3: half space, $\epsilon_{r_1} = 10, d_1 = 0.075$ cm, $\epsilon_{r_2} = 2, d_2 = 0.15$ cm, $\epsilon_{r_3} = 1, h = d_2$ for HED and HMD, $h = d_2/2$ for VED, $z = 0.0$ cm.

GPOF method can be applied to the complex coefficients of $e^{\pm jk_{zi}z}$ in all the Green's functions except $\tilde{G}_{xx}^{A,F}$. Hence, the z-dependence in the closed-form Green's functions becomes explicit and the testing procedure along the z-direction can be performed analytically for some testing functions like uniform and roof-top functions, which further improves the computational efficiency of using the closed-form Green's functions in conjunction with the method of moments. Another technique, proposed here, to overcome the above mentioned difficulties is to interchange the order of integration (29), provided that the basis and testing functions are so chosen that the involved integrals are uniformly convergent [12], and carrying out integration over z analytically for spectral domain representation of the Green's function multiplied with the testing function. Next, the approximation method, GPOF, is applied to the resulting spectral domain function. For the inner product terms involving both the z and z' integrations, these integrals can be performed analytically by using the procedure described above and subsequently applying the GPOF algorithm. Note that the spectral representations of the Green's functions are exponential functions of z and z', and this permits us to carry out z and z' integrations analytically.

III. Numerical Results and Discussions

The closed-form Green's functions presented in Section II can be used for planar-layered geometries having an arbitrary number of layers with arbitrary layer parameters and general sources. In this section, a multilayer geometry is investigated for different types of sources and the Green's functions obtained using the closed-forms (approximate) are compared with the exact Green's functions, calculated by evaluating the corresponding Sommerfeld integrals numerically.

The geometry investigated in this paper consists of a substrate and a superstrate with three different dipoles (HED, HMD, and VED) and modeled as a 4-layer structure with the following parameters—layer-0: PEC, layer-3: half-space, $\epsilon_{r_1} = 10$, $\epsilon_{r_2} = 2$, $\epsilon_{r_3} = 1$, $d_1 = 0.075$ cm, $d_2 = 0.15$ cm, as shown in Fig. 2. The horizontal dipoles (HED and HMD) are located at the air-dielectric interface ($h = d_2$) and the vertical dipole is located in the middle of the top layer ($h = d_2/2$). In all three cases, the observation points are chosen at the source plane ($z = z' = 0.0$ cm), which is the worst case as far as the convergence of the Green's functions are concerned. Figs. 3–9 show the magnitude of $G_{xx}^A, \int G_{zx}^A dx, G_x^{q_e}, G_{xx}^F, G_x^{q_e}, G_{zz}^A$ and $G_z^{q_m}$ with respect to the distance $k_o\rho$, which are obtained using both the closed-form representations and numerically evaluating the

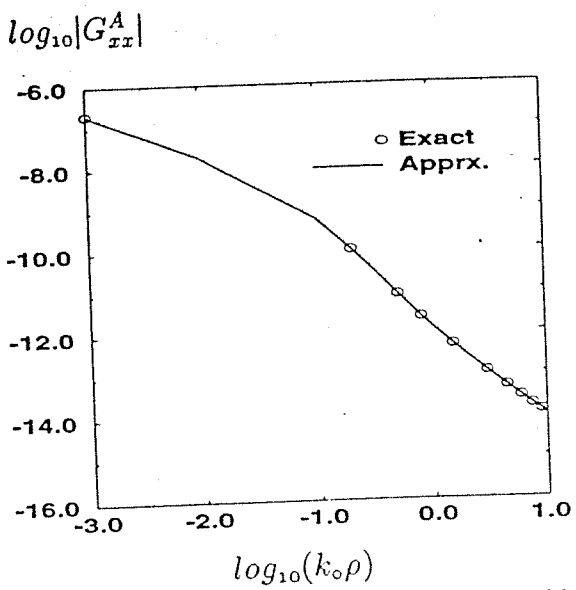

Fig. 3. Magnitude of the Green's function for the vector potential, G^A_{xx}, for an HED. Layer-0: PEC, Layer-3: half space, $\epsilon_{r_1} = 10, d_1 = 0.075$ cm, $\epsilon_{r_2} = 2, d_2 = 0.15$ cm, $\epsilon_{r_3} = 1, h = d_2, z = 0.0$ cm, $f = 1$ GHz.

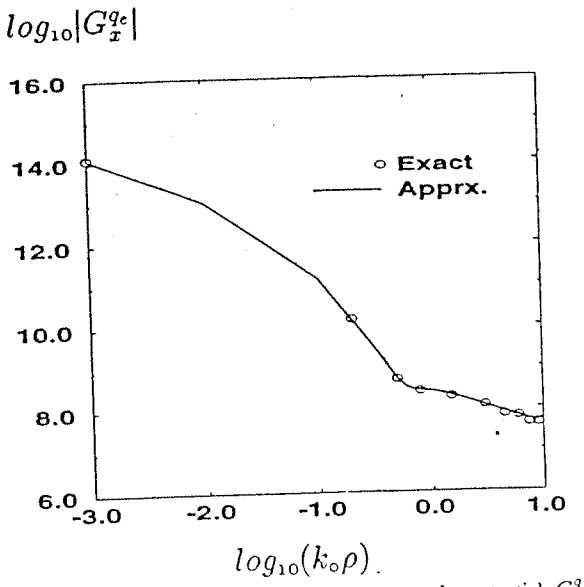

Fig. 5. Magnitude of the Green's function for the scalar potential, $G^{q_e}_x$, for an HED. Layer-0: PEC, Layer-3: half space, $\epsilon_{r_1} = 10, d_1 = 0.075$ cm, $\epsilon_{r_2} = 2, d_2 = 0.15$ cm, $\epsilon_{r_3} = 1, h = d_2, z = 0.0$ cm, $f = 1$ GHz.

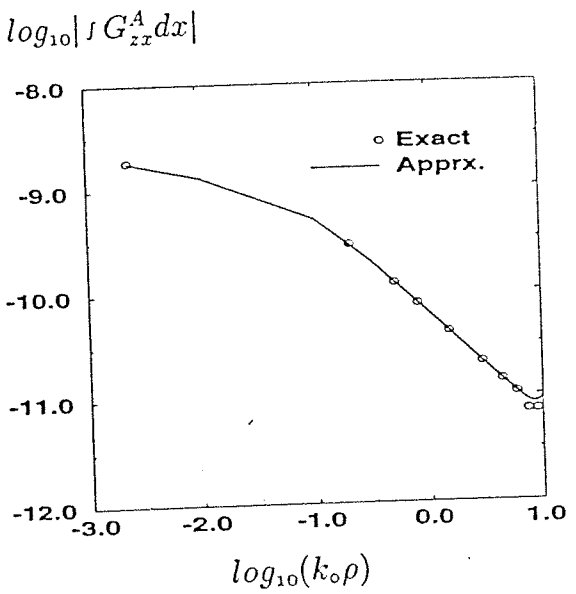

Fig. 4. Magnitude of the Green's function for the vector potential, $\int G^A_{zx}\,dx$, for an HED. Layer-0: PEC, Layer-3: half space, $\epsilon_{r_1} = 10, d_1 = 0.075$ cm, $\epsilon_{r_2} = 2, d_2 = 0.15$ cm, $\epsilon_{r_3} = 1, h = d_2, z = 0.0$ cm, $f = 1$ GHz.

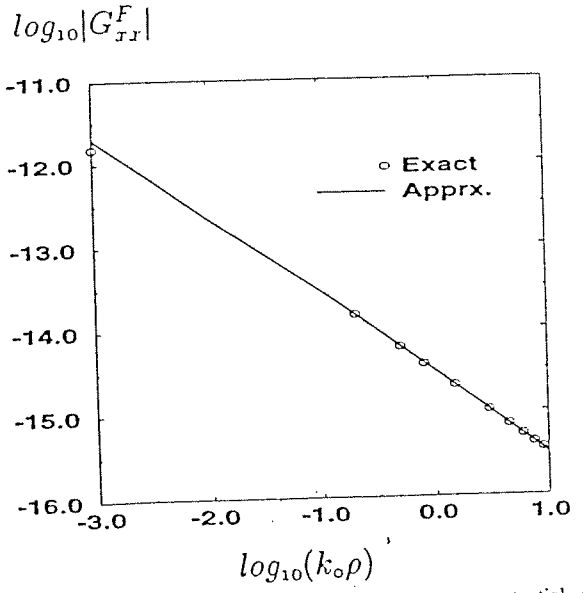

Fig. 6. Magnitude of the Green's function for the vector potential, G^F_{xx}, for an HMD. Layer-0: PEC, Layer-3: half space, $\epsilon_{r_1} = 10, d_1 = 0.075$ cm, $\epsilon_{r_2} = 2, d_2 = 0.15$ cm, $\epsilon_{r_3} = 1, h = d_2, z = 0.0$ cm, $f = 1$ GHz.

corresponding Sommerfeld integrals at a frequency of 1 GHz. In Fig. 4 $|\int G^A_{zx}\,dx|$ is given, instead of $|G^A_{zx}|$, because the approximation is performed on $\tilde{G}^A_{zx}/k_x$. Fig. 10 shows the approximate and the exact Green's functions, G^A_{zz}, calculated using the alternative form.

In approximating the spectral domain Green's functions using the GPOF, the choice of the number of samples used to represent a Green's function in the spectral domain, the maximum sampled value of k_z, and the number of exponentials used to approximate the spectral domain Green's functions depend on the parameters of the multilayer geometry, the type and the orientation of the dipole, and the Green's function to be approximated. For example, it is observed that fewer sampling points, a fewer number of exponentials, and a smaller value of T_o are required for G^A_{xx} than those required for $G^{q_e}_x$. This is because the vector potential contributes to the far field in the spatial domain; the major contributions in the spectral domain come from the region close to the origin. On the other hand, the scalar potential, which contributes to the near field dominantly, extends to larger values of k_ρ in the spectral domain. As one of the contributions of this paper, the

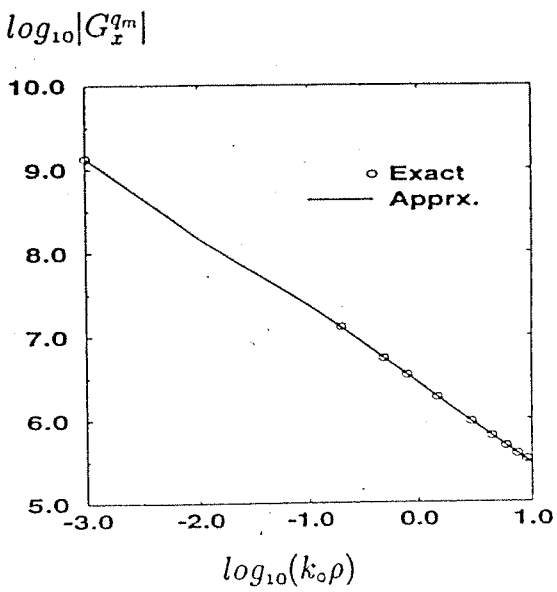

7. Magnitude of the Green's function for the scalar potential, $G_x^{q_m}$, n HMD. Layer-0: PEC, Layer-3: half space, $\epsilon_{r_1} = 10, d_1 = 0.075$ cm, $= 2, d_2 = 0.15$ cm, $\epsilon_{r_3} = 1, h = d_2, z = 0.0$ cm, $f = 1$ GHz.

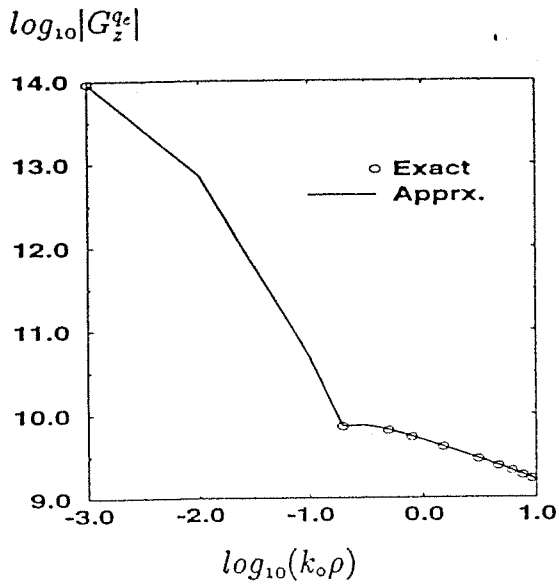

Fig. 9. Magnitude of the Green's function for the scalar potential, $G_z^{q_e}$, for a VED, traditional representation. Layer-0: PEC, Layer-3: half space, $\epsilon_{r_1} = 10, d_1 = 0.075$ cm, $\epsilon_{r_2} = 2, d_2 = 0.15$ cm, $\epsilon_{r_3} = 1, h = d_2/2, z = 0.0$ cm, $f = 1$ GHz.

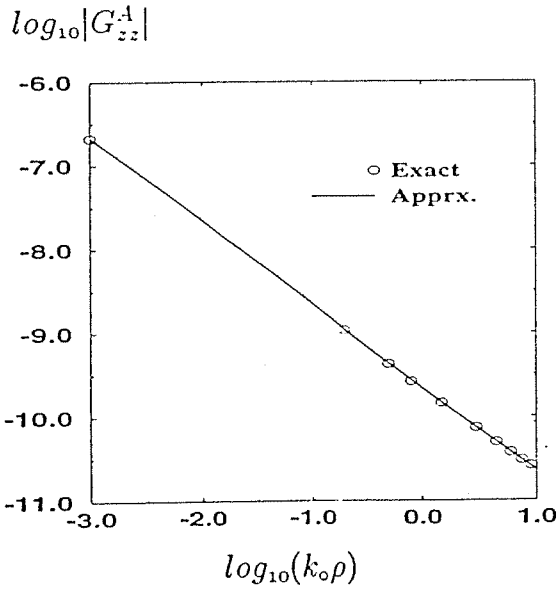

8. Magnitude of the Green's function for the vector potential, G_{zz}^A, a VED, traditional representation. Layer-0: PEC, Layer-3: half space, $= 10, d_1 = 0.075$ cm, $\epsilon_{r_2} = 2, d_2 = 0.15$ cm, $\epsilon_{r_3} = 1, h = d_2/2, z =$ cm, $f = 1$ GHz.

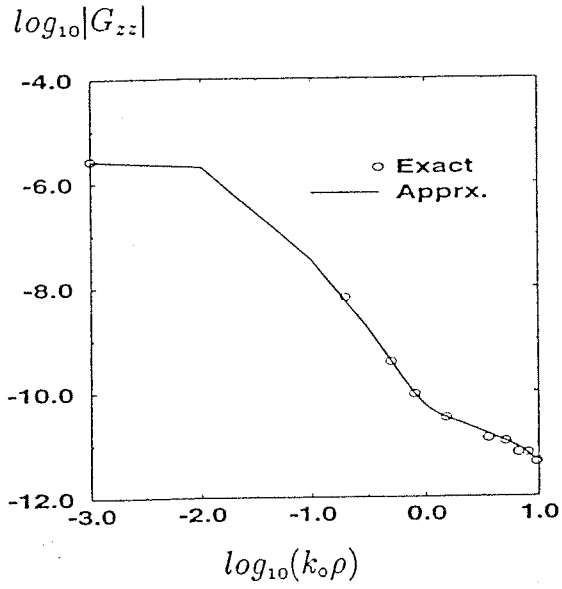

Fig. 10. Magnitude of the Green's function for the vector potential, G_{zz}^A, for a VED, alternative representation. Layer-0: PEC, Layer-3: half space, $\epsilon_{r_1} = 10, d_1 = 0.075$ cm, $\epsilon_{r_2} = 2, d_2 = 0.15$ cm, $\epsilon_{r_3} = 1, h = d_2/2, z = 0.0$ cm, $f = 1$ GHz.

roximation of the spectral domain Green's functions by nplex exponentials is performed by using the GPOF [17]. s technique is more robust and less noise sensitive [22] n the original and the least-square Prony's methods. The ustness of the technique comes from the fact that it utilizes singular value decomposition technique as an intermediate o to extract the complex exponentials, through which the nber of exponentials used in the approximation can be osen as the number of the most significant singular values ier automatically or interactively. Consequently, the number of exponentials chosen for each Green's function in the examples given in this paper is different. For example, in the approximation of G_{xx}^A of Fig. 3, the number of exponentials, the number of samples, and the maximum sampled value T_o are chosen as 4 (including the direct term), 201, and 100, respectively, while the same parameters are chosen as 10 (including the direct term with no surface wave extraction), 401, and 100 for $G_x^{q_e}$ of Fig. 5. It should be noted that the numbers given above are strongly dependent on the parameters of the geometry and the source.

IV. Conclusion

In this work, a complete set of closed-form, spatial domain reen's functions are provided in stratified media for general urces. The closed-form Green's functions are obtained using e GPOF method, which is more robust and less noise nsitive than the original Prony's and the least-square Prony's ethods. In addition, the Green's functions are cast into a form increase the numerical efficiency in the MoM applications. umerical examples of the closed-form Green's functions are ven for a multilayer medium. The approximate Green's nctions are compared with the exact ones and very good greement is observed.

Appendix
Alternative Form of Green's Function

Since the vector and scalar potentials are not uniquely de-ned in stratified media, different sets of Green's functions for e vector and scalar potentials are possible giving rise to many fferent MPIE formulations [18], [19]. Among these Green's nctions, three useful choices referred as formulations A, B, d C, are given in [20]. In this paper, the formulation C is osen as the alternative form of the Green's function and ven here as

$$\bar{\bar{G}}_{A,F} = (\hat{x}\hat{x} + \hat{y}\hat{y})G_{xx} + \hat{z}\hat{x}G_{zx} + \hat{z}\hat{y}G_{zy} + \hat{x}\hat{z}G_{xz} + \hat{y}\hat{z}G_{yz} + \hat{z}\hat{z}G_{zz} \quad (30)$$

d $G^{q_{e,m}}$ as the Green's function for the scalar potential r both horizontal and vertical dipoles, Fig. 1. Note that the fficulties encountered in the traditional formulation due to e difference between the scalar potentials of HED (HMD) d VED (VMD) are alleviated in this formulation. In the ove form of the Green's function, the terms associated with e horizontal dipoles ($G_{xx}^{A,F}, G_{yy}^{A,F}, G_{zx}^{A,F}, G_{zy}^{A,F}, G_x^{q_{e,m}}$, and $G_y^{q_{e,m}}$) remain the same as in the traditional form (2)–(7); vo new entries, $G_{xz}^{A,F}$ and $G_{yz}^{A,F}$, are introduced and $G_{zz}^{A,F}$ modified for the vertical dipoles. For an x-oriented HED d a z-oriented VED, the Green's function components used ith the alternative form are adopted to the formulation given Section II-A as

$$\tilde{G}_{zz}^{A} = \frac{1}{jk_{z_i}}\left[\frac{\mu_i}{2}e^{-jk_{z_i}|z|} + e^{-jk_{z_i}z}\left[\frac{\mu_i}{2}A_v^e - \frac{k_{z_i}^2}{2\omega^2\epsilon_i}\cdot\left[A_v^e - \frac{k_i^2C_h^e - k_{z_i}^2D_h^e}{k_\rho^2}\right]\right] + e^{jk_{z_i}z}\left[\frac{\mu_i}{2}B_v^e + \frac{k_{z_i}^2}{2\omega^2\epsilon_i}\cdot\left[-B_v^e + \frac{k_{z_i}^2B_h^e + k_i^2A_h^e}{k_\rho^2}\right]\right]\right] \quad (31)$$

$$\tilde{G}_{xz}^{A} = \frac{-j}{k_{z_i}}\frac{-k_xk_{z_i}}{2\omega^2\epsilon_i}\left[e^{-jk_{z_i}z}\left[A_v^e - \frac{k_i^2C_h^e - k_{z_i}^2D_h^e}{k_\rho^2}\right] + e^{jk_{z_i}}\left[-B_v^e + \frac{k_{z_i}^2B_h^e + k_i^2A_h^e}{k_\rho^2}\right]\right] \quad (32)$$

here $\tilde{G}_{zz}^{A}, \tilde{G}_{xz}^{A}$ are the alternative Green's function compo-ents in the source layer and $A_{h,v}^e, B_{h,v}^e, C_h^e, D_h^e$ are given in e (12)–(17).

Acknowledgment

Useful comments from Dr. E. Michielssen and D. Webb are gratefully acknowledged.

References

[1] N. K. Das and D. M. Pozar, "A spectral-domain Green's function for multilayer dielectric substrates with application to multilayer transmission lines," *IEEE Trans. Microwave Theory Tech.*, vol. MTT-35, pp. 326–335, Mar. 1987.

[2] F. Crog and D. M. Pozar, "Multifrequency operation of microstrip antennas using aperture coupled parallel resonators,"*IEEE Trans. Antennas Propagat.*, vol. 40, pp. 1367–1374, Nov. 1992.

[3] L. Barlatey, J. R. Mosig, and T. Sphicopoulos, "Analysis of stacked microstrip patches with mixed potential integral equation," *IEEE Trans. Antennas Propagat.*, vol. 18, pp. 608–615, May 1990.

[4] A. N. Tulintseff, S. M. Ali, and J. A. Kong, "Input impedance of a probe fed stacked circular microstrip antenna," *IEEE Trans. Antennas Propagat.*, vol. 39, pp. 381–390, Mar. 1991.

[5] K. R. Carver and J. W. Mink, "Microstrip antenna technology," *IEEE Trans. Antennas Propagat.*, vol. AP-29, pp. 2–24, Jan. 1981.

[6] D. R. Jackson and N. G. Alexopoulos,"Gain enhancement methods for printed antennas," *IEEE Trans. Antennas Propagat.*, vol. AP-33, pp. 976–987, Sept. 1985.

[7] C. I. G. Hsu, R. F. Harrington, K. A. Michalski, and D. Zheng,"Analysis of multiconductor transmission lines of arbitrary cross section in multilayered uniaxial media," *IEEE Trans. Microwave Theory Tech.*, vol. 41, pp. 70–78, Jan. 1993

[8] W. C. Chew, *Waves and Fields in Inhomogeneous Media.* New York: Van Nostrand Reinhold, 1990.

[9] M. Gillick, I. D. Robertson, and J. S. Joshi,"Design analysis of novel coupling structures for multilayer MMIC's," *IEEE Trans. Microwave Theory Tech.*, vol. 41, pp. 346–349, Feb. 1993.

[10] T. Tokumitsu, H. Hiraota, H. Makamoto, and T. Takenaka,"Multilayer MMIC using a 3 μm× 3-layer dielectric film structure," in *IEEE MTT-S Int. Microwave Symp. Dig.*, 1990, pp. 831–834.

[11] T. Hasegawa, S. Banba, H. Ogawa, and H. Nakamoto,"Characteristics of valley microstrip lines for use in multilayer MMIC's," *IEEE Microwave Guided Wave Lett.*, vol. 1, Oct. 1991.

[12] M. I. Aksun and R. Mittra, "Choices of expansion and testing functions for the method of moments applied to a class of electromagnetic problems," *IEEE Trans. Microwave Theory Tech.*, vol. 41, pp. 503–509, Mar. 1993.

[13] Y. L. Chow, J. J. Yang, and D. F. Fang, and G. E. Howard, "Closed form spatial Green's function for the thick substrate," *IEEE Trans. Microwave Theory Tech.*, vol. 39, pp. 588–592, Mar. 1991.

[14] M. I. Aksun and R. Mittra, "Derivation of closed-form Green's functions for a general microstrip geometry," *IEEE Trans. Microwave Theory Tech.*, vol. 40, pp. 2055–2062, Nov. 1992.

[15] ——, "Spurious radiation from microstrip interconnects," *IEEE Trans. Electromagn. Compat.*, vol. 35, pp. 148–158, May 1993.

[16] S. L. Marple, *Digital Spectral Analysis with Applications.* Englewood Cliffs, NJ: Prentice Hall, 1987.

[17] Y. Hua and T. K. Sarkar, "Generalized pencil-of-function method for extracting poles of an EM system from its transient response," *IEEE Trans. Antennas Propagat.*, vol. 37, pp. 229–234, Feb. 1989.

[18] A. Erteza and B. K. Park,"Nonuniqueness of resolution of Hertz vector in presence of a boundary, and a horizontal dipole problem," *IEEE Trans. Antennas Propagat.*, vol. AP-17, pp. 376–378, May 1969.

[19] K. A. Michalski, "On the scalar potential of a point charge associated with a time-harmonic dipole in a layered medium," *IEEE Trans. Antennas Propagat.*, vol. AP-35, pp. 1299–1301, Nov. 1987.

[20] K. A. Michalski and D. Zheng, "Electromagnetic scattering and radiation by surfaces of arbitrary shape in layered media, Part I: Theory," *IEEE Trans. Antennas Propagat.*, vol. 38, pp. 335–344, Mar. 1990.

[21] A. Sommerfeld, *Partial Differential Equations in Physics.* New York: Academic, 1949.

[22] A. J. Mackay and A. McCowen, "An improved pecil-of-functions method and comparisons with traditional methods of pole extraction," *IEEE Trans. Antennas Propagat.*, vol. AP-35, pp. 435–441, Apr. 1987.

Gülbin Dural (S'84–M'89) received the B.S. and M.S. degrees in electrical and electronics engineering from the Middle East Technical University, Ankara, Turkey, in 1981 and 1983, respectively, and the Ph.D. degree in electrical engineering from the Ohio State University, Columbus, OH, in 1988.

From 1981–1983, she was with the Middle East Technical University as a graduate assistant, and from 1984–1988 she was with the Ohio State University ElectroScience Laboratory as a graduate research associate. Since 1989, she has been on the ty of the department of electrical and electronics engineering at the lle East Technical University, Ankara, Turkey, where she is currently sociate professor. Her research interests include the numerical methods lectromagnetics, microstrip antennas, microwave and millimeter-wave rated circuits, and SAR and ISAR imaging techniques.

M. I. Aksun (M'92) received the B.S. and M.S. degrees in electrical and electronics engineering from the Middle East Technical University, Ankara, Turkey, in 1981 and 1983, respectively, and the Ph.D. degree in electrical and computer engineering from the University of Illinois at Urbana-Champaign in 1990.

From 1990–1992, he was a postdoctoral fellow at the Electromagnetic Communication Laboratory, University of Illinois at Urbana-Champaign. Since 1992, he has been on the faculty of the department of electrical and electronics engineering at Bilkent University, Ankara, Turkey, where he is currently an associate professor. His research interests include the numerical methods for electromagnetics, microstrip antennas and microwave and millimeter-wave integrated circuits.

Comparative Evaluation of Absorbing Boundary Conditions Using Green's Functions for Layered Media

M. I. Aksun, *Member, IEEE*, and Gülbin Dural, *Member, IEEE*

Abstract—Absorbing boundary conditions are comparatively studied using the Green's functions of the vector and scalar potentials for multilayer geometries and general sources. Since the absorbing boundaries are introduced as additional layers with predefined reflection coefficients into the calculation of the Green's functions, this approach provides an absolute measure of the effectiveness of different absorbing boundaries. The Green's functions are calculated using different reflection coefficients corresponding to different absorbing boundaries and compared to those obtained with no absorbing boundary. It is observed that the perfectly matched layer (PML) is by far the best among the other absorbing boundary conditions whose reflection coefficients are available.

I. Introduction

Application of the numerical techniques based on differential equations in unbounded regions, such as the finite-difference time-domain (FDTD) and the finite-element methods (FEM), requires the truncation of the solution domain with artificial boundaries. Ideally, these boundaries are supposed to absorb all the incident waves, that is, there should be no reflected waves, so they are called absorbing or radiation boundaries [1]–[7]. However, there is always some reflected waves due to imperfect cancelation of the impinging waves on these artificial boundaries. The level of the reflection depends upon the absorbing boundaries used and the order of the approximation.

Since different absorbing boundaries give rise to different level of reflected waves, one needs to examine these boundary conditions comparatively to decide on the type and the order of the absorbing boundary condition (ABC) to be used, to improve the accuracy of results. For the purpose of comparison, numerical experiments can be performed [8], [9] on the geometry of interest, but here, we propose the use of Green's functions to assess the level of imperfections of the ABC's for planar geometries. The Green's functions used in the comparative evaluation of ABC's are provided for general sources and planar stratified media by including the reflections from each boundary [10]. The absorbing boundaries are considered as additional layers, for which the reflection coefficients can be derived explicitly, above the original structure forming a multilayer geometry. The Green's functions of the vector and scalar potentials are then calculated and compared with those obtained for the original geometry (no absorbing boundary) to observe the effect of the ABC's on the Green's functions, providing an absolute measure of merit of the ABC's. The Green's functions used in this approach are calculated in the spatial domain via either numerically integrating the Sommerfeld-type integrals or approximating the integrals in closed form [10]. The technique proposed here eliminates extraneous problems caused by the discretizations required by the techniques used in conjunction with the ABC's and, therefore, gives a true comparison of different types and orders of the ABC's.

In this paper, the Green's function-based comparison of the ABC's is given for the sources of a horizontal electric dipole and a horizontal magnetic dipole in multilayer media. The comparison is based on the absorbing boundaries formulated by [3] for normal incidence, by [4], [5] for arbitrary angle of incidence, and by Berenger [11] as the perfectly matched layer (PML). The main goal of this approach is to compare the ABC's for planar geometries for the purpose of finding an ABC that can be used accurately. Even though the conclusion drawn here may not be directly extended to other geometries (nonplanar), the technique can be applied to any geometry provided that corresponding Green's functions are available.

The Green's functions used in the evaluation of the ABC's are discussed in Section II, including how these Green's functions in the spatial domain are obtained and how the absorbing boundaries are accounted for in the calculation. The reflection coefficients for the absorbing boundaries studied in this paper are presented in Section III, and discussion on the numerical results is given in Section IV.

II. Green's Functions for Multilayer Media

The Green's functions of the vector and scalar potentials used for the evaluation of the ABC's are given in [10] for the multilayer geometry, shown in Fig. 1, and for the sources of horizontal electric dipole (HED), horizontal magnetic dipole (HMD), vertical electric dipole (VED), and vertical magnetic dipole (VMD). Therefore, only a brief outline of the formulation is provided here, and, in addition, the spectral-domain Green's functions of HED and HMD, which are used in the applications presented in this paper, are given in the Appendix.

Manuscript received August 5, 1994; revised May 11, 1995.

M. I. Aksun is with the Department of Electrical and Electronics Engineering, Bilkent University, 06533 Ankara, Turkey.

G. Dural is with the Department of Electrical and Electronics Engineering, Middle East Technical University, 06531 Ankara, Turkey.

Publisher Item Identifier S 0018-926X(96)01195-7.

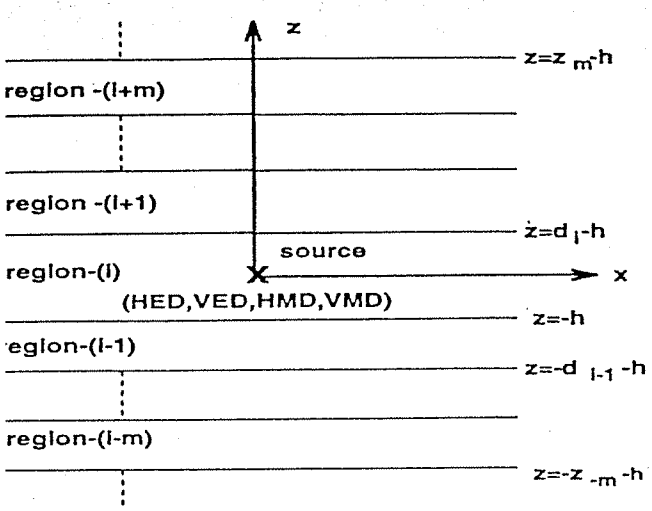

. 1. General multilayer geometry.

The multilayer geometry used in the formulation of the reen's functions (Fig. 1) consists of arbitrary number of anar layers with different electric and magnetic properties $_{r_i}, \mu_{r_i}$) and thicknesses (d_i). The perfect electric and mag-tic conducting planes (PEC and PMC) and half-space are so considered as layers for the formulation. The Green's nctions are first obtained in the spectral domain, as given in e Appendix, including the reflections from each boundary, en the spatial-domain Green's functions are calculated either ith the numerical evaluation of Sommerfeld's integral [1] xact) or in closed forms (approximate) using the generalized ncil of functions (GPOF) method [10], [13]. Both exact id approximate forms of the Green's functions are used for e purpose of comparison, but the numerical evaluation of e Sommerfeld integral is prefered for the results presented re, in this paper, to eliminate any question regarding to e possibility of error in the approximation. The numerical aluation of the Sommerfeld integral is performed with the ethod of averages [14], which is considered to be the fastest gorithm available.

These Green's functions can be utilized in the comparative aluation of the ABC's by introducing the absorbing bound-y as an additional layer above the original structure (Fig. 2), rming a multilayer geometry. Since the reflection coefficients sociated with different ABC's are available, the Green's nctions for the geometry with an absorbing boundary can be tained by including the reflection coefficients of the ABC's the formulation. To examine the effect of ABC's, these reen's functions are compared with the Green's functions tained for the ideal case which corresponds to the original eometry with no absorbing boundary.

III. Absorbing Boundaries

Various absorbing boundaries have been developed for the rpose of simulating an unbounded region for the solution f differential-equation-based numerical techniques. These ab-rbing boundaries can be formed as mode annihilating opera-rs, one-way wave equations, numerical approximations, and rfectly matched layers. Although the recent trend was toward

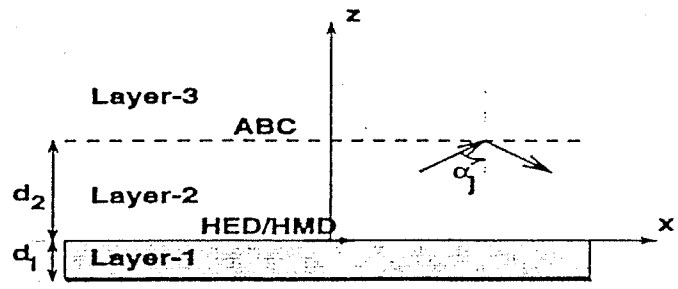

Fig. 2. A typical planar geometry.

numerical simulations of the absorbing boundaries, with the recent introduction of a novel boundary condition by Berenger, PML [11], this approach has gained a flurry of interest. It was numerically demonstrated that the PML absorbing boundary is more accurate than the second-order Mur [3] for 2-D and 3-D geometries [9]. In this paper, the PML absorbing boundary is compared to the other absorbing boundaries given by [3]–[7] for planar geometries. Since comparison given in this paper is based on the Green's functions it has the advantage of being immune to the error introduced by the numerical techniques due to discretizations.

The analytical absorbing boundary conditions discussed in this study are based on one-way wave equations and the corresponding reflection coefficients can be obtained as described in [3], [6]. Expressions for the reflection coefficients are given here for the second- and third-order ABC's as

$$R = \frac{-\frac{k_{z_i}}{k_i} + p_0 + p_2 \frac{k_\rho^2}{k_i^2}}{\frac{k_{z_i}}{k_i} + p_0 + p_2 \frac{k_\rho^2}{k_i^2}} \quad \text{(second order)} \tag{1}$$

$$R = \frac{-q_0 \frac{k_{z_i}}{k_i} - q_2 \frac{k_{z_i} k_\rho^2}{k_i^3} + p_0 + p_2 \frac{k_\rho^2}{k_i^2}}{q_0 \frac{k_{z_i}}{k_i} + q_2 \frac{k_{z_i} k_\rho^2}{k_i^3} + p_0 + p_2 \frac{k_\rho^2}{k_i^2}} \quad \text{(third order)} \tag{2}$$

where the subscript i stands for the layer number, k_ρ is the wave number in the transverse direction, and p's and q's depend upon the type of the approximation used in the derivation of the ABC and are given in [6]. A more general absorbing boundary, which is designed to absorb the plane waves incident at arbitrary angles, can be represented by the following reflection coefficient [4], [5]

$$R = -\prod_{j=1}^{\text{order}} \frac{\cos\alpha_j - \frac{k_{z_i}}{k_i}}{\cos\alpha_j + \frac{k_{z_i}}{k_i}} \tag{3}$$

where the perfect absorption occurs at the angles of α_j's.

The PML absorbing boundary is based on the absorption of electromagnetic waves by creating a nonphysical absorbing layer, or perfectly matched layer, that has a wave impedance independent of the angle of incidence and frequency [11]. The PML absorbing boundary consists of a normal free-space computational zone and a PML outer boundary layer backed by a perfectly conducting (PEC) wall. In this approach it is suggested that the loss associated with PML should increase gradually with depth, ρ, within the layer as $\sigma(\delta) =$

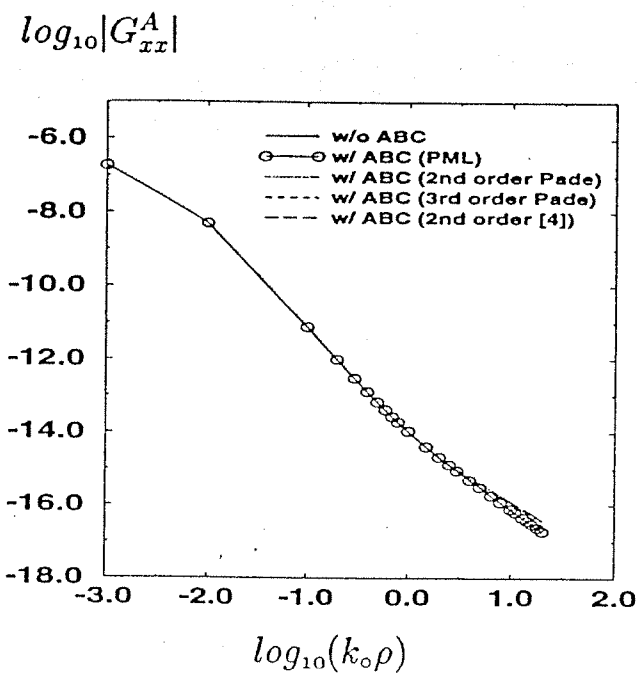

Fig. 3. Magnitude of the Green's function of the vector potential, G^A_{xx} for an HED. Layer-1: $\epsilon_{r_1} = 4.0$, $d_1 = 0.020\,32$ cm; layer-2: air, $d_2 = 10.0$ cm; layer-3: absorbing boundary, $f = 1.0$ GHz.

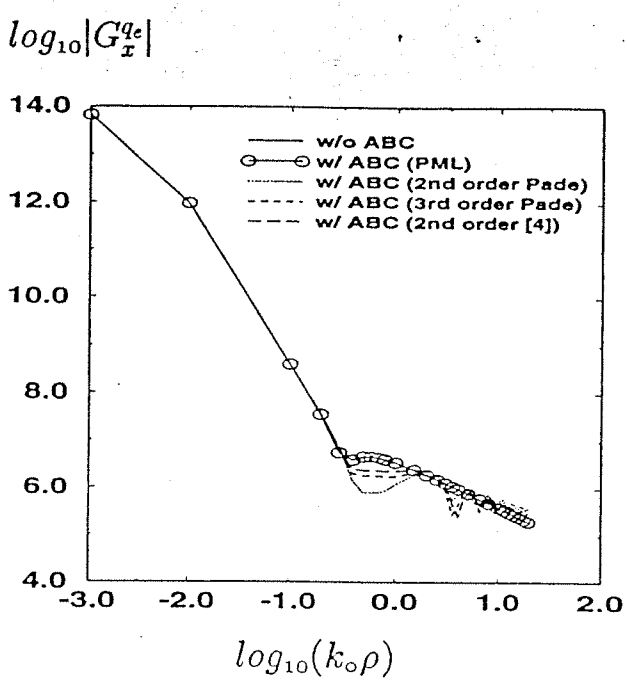

Fig. 4. Magnitude of the Green's function of the scalar potential, $G^{q_e}_x$ for an HED. Layer-1: $\epsilon_{r_1} = 4.0$, $d_1 = 0.020\,32$ cm; layer-2: air, $d_2 = 10.0$ cm; layer-3: absorbing boundary, $f = 1.0$ GHz.

$\sigma_{\max}(\rho/\delta)^n$. Hence, it yields a PML reflection factor of

$$R(\theta) = e^{-2\sigma_{\max}\delta\cos\theta/(n+1)\epsilon_0 c} \tag{4}$$

where δ is the PML thickness, σ is the loss associated with the layer, and c is the velocity of light. With the proper choice of δ, σ, and n, the reflection coefficient as low as 1/3000th those of standard second- and third-order ABC's, such as [3], has been reported [11].

IV. Results and Discussion

The approach discussed in Section II can be applied to any multilayer geometry with arbitrary layer parameters, such as thicknesses, permittivities, and permeabilities. For the sake of illustration, the following parameters have been chosen for the geometry shown in Fig. 2. The dielectric constant of the substrate $\epsilon_{r_1} = 4.0$; the thickness of the substrate $d_1 = 0.020\,32$ cm (8.0 mils); the frequency of operation $f = 1.0$ GHz; the distance of the ABC from the air-dielectric interface $d_2 = 10.0$ cm; layer-0 PEC.

Ideally, absorbing boundaries are supposed to absorb all the waves impinging upon them, but since the ABC's are approximations to the ideal case, inevitably there may be some reflections. Therefore, the ideal absorbing boundary corresponds to, in the case presented here, no absorbing boundary at all. To study the effect of the absorbing boundaries, the vector and scalar potentials at the air-dielectric interface in the presence of the absorbing boundaries are calculated and compared to those obtained with no absorbing boundary. The following Green's functions are employed to study the ABC's: $G^{A,F}_{xx}$—Green's function of the vector potential for an x oriented HED, HMD, respectively; $G^{q_e,m}_x$—Green's function of the scalar potential for an x oriented HED and HMD, respectively.

Figs. 3 and 4 show the magnitudes of the Green's functions of the vector and scalar potentials, G^A_{xx} and $G^{q_e}_x$, respectively, with and without the absorbing boundaries. It is observed that the second-order Padè approximation for the ABC, which only absorbs exactly the normal-incident plane waves, yields sufficiently good results for the vector potential (Fig. 3) as compared to those obtained with the ideal ABC (no ABC). On the other hand, the scalar potential shows some deviation from the ideal case, Fig. 4. Although it is not necessary to use the third-order Padè approximation for the ABC for the vector potential case, significant improvement is observed for the scalar potential which is more evident from the phase information of the scalar potential, as shown in Fig. 5. It might be claimed that if the absorbing boundary annihilates the incoming waves at different angles of incidence, it would improve the overall performance of the ABC without increasing the order of approximation. As a matter of fact, an improvement is observed in the magnitude of the scalar potential, Fig. 4 where the angles of exact absorption are set to 0° and 60° in (3) for the second-order approximation, but the improvement in the phase is not significant. On the other hand, the use of PML absorbing boundary results in perfect agreement with the ideal case in both magnitude and phase, see Figs. 3–5. To assess the level of error introduced by the absorbing boundaries, the plots of percentage error versus distance, corresponding to the above mentioned absorbing boundaries, are given in Fig. 6. As it is observed, the PML absorbing boundary is far superior than the other absorbing boundaries, which is due to very low sensitivity of the reflection coefficient (4) to the incidence angle θ. Furthermore, the performance of the

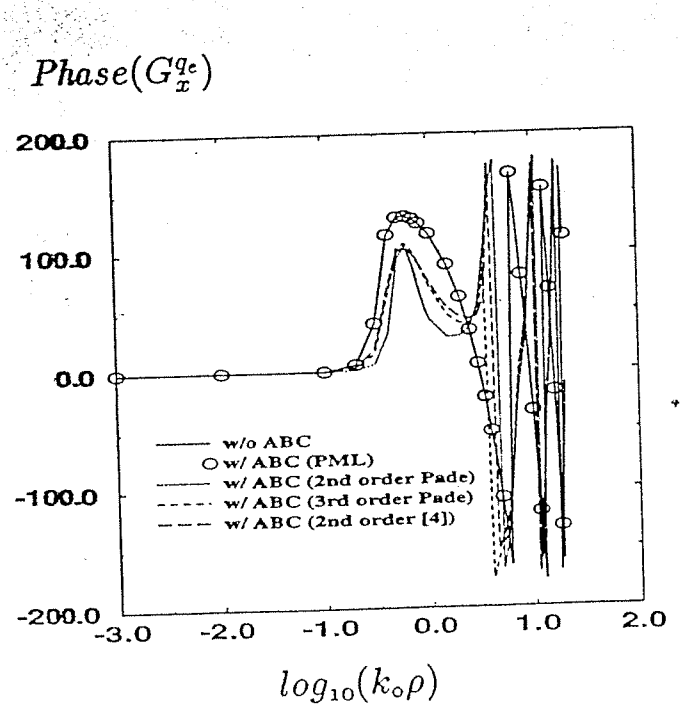

Fig. 5. Phase of the Green's function of the scalar potential, $G_x^{q_e}$ for an HED. Layer-1: $\epsilon_{r_1} = 4.0$, $d_1 = 0.020\,32$ cm; layer-2: air, $d_2 = 10.0$ cm; layer-3: absorbing boundary, $f = 1.0$ GHz.

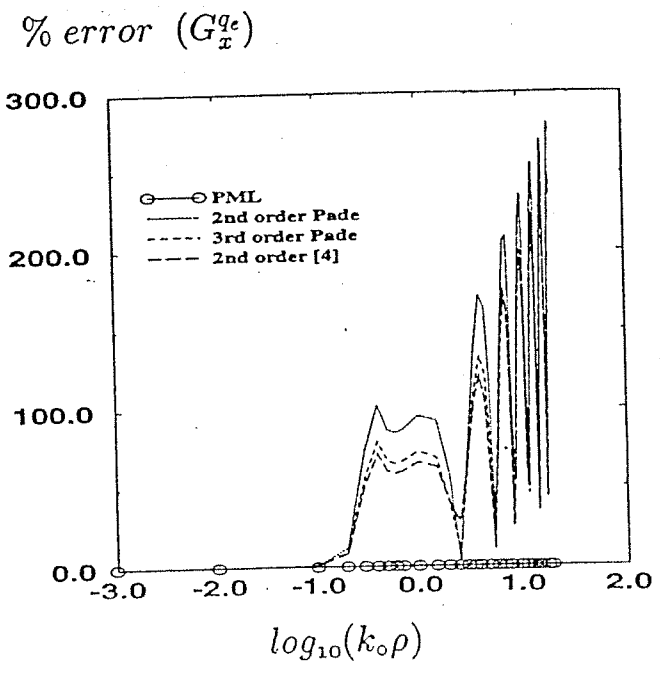

Fig. 6. Percentage error for $G_x^{q_e}$. Layer-1: $\epsilon_{r_1} = 4.0$, $d_1 = 0.020\,32$ cm; layer-2: air, $d_2 = 10.0$ cm; layer-3: absorbing boundary, $f = 1.0$ GHz.

PML can be easily improved by varying the depth, δ, and the conductivity, $\sigma(\rho)$ of the PML. It should be noted that the starting edge of the PML is positioned where the other absorbing boundaries are placed. Due to the finite thickness of the PML, this positioning might be considered as giving an unfair advantage to the PML over other ABC's. However, since the thickness of the PML is usually much smaller, or can be made smaller with the proper choice of the conductivity, than the distance where the PML is located, this positioning can have only a slight effect on the results presented here.

In practice, it is desirable to bring the outer boundary as close to the original geometry as possible to reduce the number of mesh points, and hence the computation time. On the other hand, when the distance of the absorbing boundary is reduced, the error introduced by the reflections from the absorbing boundary becomes significant. To demonstrate the effect of the distance of the PML, the percentage error of $|G_x^{q_e}|$ is given for the PML distances of $d_2 = 10$ cm and $d_2 = 1$ cm in Fig. 7. It is observed that when the PML distance is as low as 1 cm ($1/30\lambda$) the maximum error is less than 3%, which could even be reduced by adjusting the parameters of the PML.

The HMD is also studied as for the horizontal electric source case given above, and it is observed that the same arguments are valid for the HMD source as well.

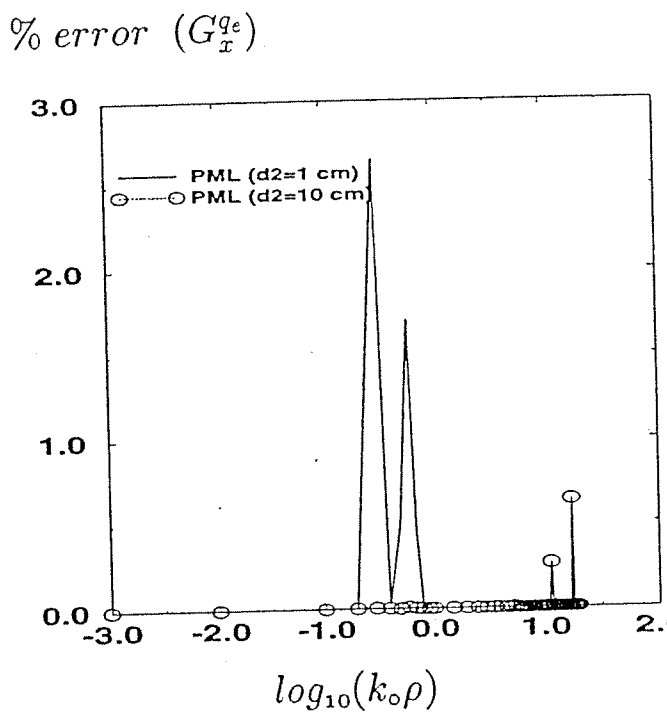

Fig. 7. Percentage error for $G_x^{q_e}$ for two different PML distances: $d_2 = 10$ cm and $d_2 = 1$ cm. Layer-1: $\epsilon_{r_1} = 4.0$, $d_1 = 0.020\,32$ cm; layer-2: air; layer-3: PML, $f = 1.0$ GHz.

V. Conclusion

The use of the Green's functions for the study of the ABC's have been demonstrated for planar media. Two different analytical ABC's and PML absorbing boundary have been compared with each other and with the ideal case, but this approach can also be applied to other ABC's provided that the associated reflection coefficients are available. The strength of this approach over the numerical comparison of the ABC's is the analytical nature of the comparison, which does not depend on the numerical technique used, and is to provide an absolute comparison between different ABC's. Among the compared absorbing boundaries, the error introduced by the PML absorbing boundary is much less than those of the others.

APPENDIX A

Green's functions of the vector and scalar potentials for the planar multilayer media shown in Fig. 1 are first derived in the spectral domain then transformed in to the spatial domain either in closed forms using an approximation technique such as GPOF [13], or with the numerical evaluation of Sommerfeld's integral. The spectral-domain Green's functions are first obtained in the source layer by including the reflections at each interface [12], then the Green's functions of the observation layer are obtained using an iterative algorithm applied to each TE and TM component of the Green's functions in the source layer. The spectral-domain Green's functions in the source layer are given for the sources of an HED and an HMD as [10], HED

$$\tilde{G}^A_{xx} = \frac{\mu_i}{2jk_{z_i}}\left[e^{-jk_{z_i}|z|} + A^e_h e^{jk_{z_i}z} + C^e_h e^{-jk_{z_i}z}\right] \quad (5)$$

$$\tilde{G}^A_{zx} = \frac{-\mu_i}{2jk_{z_i}}\left[\frac{k_x k_{z_i}}{k_\rho^2}(A^e_h + B^e_h)e^{jk_{z_i}z} + \frac{k_x k_{z_i}}{k_\rho^2}(D^e_h - C^e_h)e^{-jk_{z_i}z}\right] \quad (6)$$

$$\tilde{G}^{q_e}_x = \frac{1}{j2\epsilon_i k_{z_i}}\left[e^{-jk_{z_i}|z|} + \frac{k_{z_i}^2 B^e_h + k_i^2 A^e_h}{k_\rho^2}e^{jk_{z_i}z} + \frac{k_i^2 C^e_h - k_{z_i}^2 D^e_h}{k_\rho^2}e^{-jk_{z_i}z}\right] \quad (7)$$

HMD:

$$\tilde{G}^F_{xx} = \frac{\epsilon_i}{2jk_{z_i}}\left[e^{-jk_{z_i}|z|} + A^m_h e^{jk_{z_i}z} + C^m_h e^{-jk_{z_i}z}\right] \quad (8)$$

$$\tilde{G}^F_{zx} = \frac{-\epsilon_i}{2jk_{z_i}}\left[\frac{k_x k_{z_i}}{k_\rho^2}(A^m_h + B^m_h)e^{jk_{z_i}z} + \frac{k_x k_{z_i}}{k_\rho^2}(D^m_h - C^m_h)e^{-jk_{z_i}z}\right] \quad (9)$$

$$\tilde{G}^{q_m}_x = \frac{1}{j2\mu_i k_{z_i}}\left[e^{-jk_{z_i}|z|} + \frac{k_{z_i}^2 B^m_h + k_i^2 A^m_h}{k_\rho^2}e^{jk_{z_i}z} + \frac{k_i^2 C^m_h - k_{z_i}^2 D^m_h}{k_\rho^2}e^{-jk_{z_i}z}\right] \quad (10)$$

where the coefficients A, B, C, D, are functions of the generalized reflection coefficients, parameters of the geometry, and the source point, z'.

REFERENCES

[1] A. Sommerfeld, *Partial Differential Equations in Physics*. New York: Academic, 1949.

[2] B. Engquist and A. Majda, "Absorbing boundary conditions for the numerical simulation of waves," *Math. Comput.*, vol. 31, pp. 629–651, July 1977.

[3] G. Mur, "Absorbing boundary conditions for the finite difference approximation of time-domain electromagnetic field equations," *IEEE Trans. Electromag. Compat.*, vol. EMC-23, pp. 377–382, Nov. 1981.

[4] R. L. Higdon, "Absorbing boundary conditions for difference approximations to the multidimensional wave equation," *Math. Comput.*, vol. 47, pp. 437–459, Oct. 1986.

[5] R. Mittra and J.-F. Lee, "Direct Maxwell's equation solvers in time and frequency domains—A review," in *Directions in Electromagnetic Wave Modeling*, H. L. Bertoni and L. B. Felsen, Eds. New York: Plenum, 1991.

[6] T. G. Moore, J. G. Blashchak, A. Taflove, and G. A. Kriegsmann, "Theory and application of radiation boundary operators," *IEEE Trans. Antennas Propagat.*, vol. 36, pp. 1797–1812, Dec. 1988.

[7] R. Mittra and O. Ramahi, "Absorbing boundary conditions for the direct solution of partial differential equations arising in electromagnetic scattering problems," in *PIER 2: Finite Element and Finite Difference Methods in Electromagnetic Scattering*, M. A. Morgan, Ed. New York: Elsevier, 1990.

[8] J. G. Blaschak and G. A. Kriegsmann, "A comparative study of absorbing boundary conditions," *J. Comput. Phys.*, vol. 77, pp. 109–139, July 1988.

[9] D. S. Katz, E. T. Thiele, and A. Taflove, "Validation and extension to three dimensions of the Berenger PML absorbing boundary condition for FTTD Meshes," *IEEE Microwave Guide Wave Lett.*, vol. 4, pp. 268–270, Aug. 1994.

[10] G. Dural and M. I. Aksun "Closed-form Green's functions for general sources and stratified media," *IEE Trans. Microwave Theory Tech.*, vol. 43, pp. 1545–1552, July 1995.

[11] J. Berenger, "A perfectly matched layer for the absorption of electromagnetic waves," *J. Computat. Phys.*, vol. 114, pp. 185–200, Oct. 1994.

[12] W. C. Chew, *Waves and Fields in Inhomogeneous Media*. New York: Van Nostrand Reinhold, 1990.

[13] Y. Hua and T. Sarkar, "Generalized pencil-of-function method for extracting poles of an EM system from its transient response," *IEEE Trans. Antennas Propagat.*, vol. 37, pp. 229–234, May 1989.

[14] J. R. Mosig and F. Gardiol, "A dynamical radiation model for microstrip structures," *Adv. Electron. Electron Phys.*, vol. 59, pp. 139–233, 1982.

[15] M. I. Aksun and R. Mittra, "Derivation of closed-form Green's functions for general microstrip geometries," *IEEE Trans. Microwave Theory Tech.*, vol. 40, pp. 2055–2062, Nov. 1992.

M. I. Aksun (M'92) received the B.S. and M.S. degrees in electrical and electronics engineering from the Middle East Technical University, Ankara, Turkey, in 1981 and 1983, respectively, and the Ph.D. degree in electrical and computer engineering from the University of Illinois at Urbana-Champaign, in 1990.

From 1990–1992, he was a Post Doctoral Fellow at the Electromagnetic Communication Laboratory, University of Illinois at Urbana-Champaign. Since 1992, he has been on the faculty of the department of electrical and electronics engineering at Bilkent University, Ankara, Turkey, where he is currently an Associate Professor. His research interests include the numerical methods for electromagnetics, microstrip antennas and microwave, and millimeter-wave integrated circuits.

Gülbin Dural (S'85-M'88) received the B.S. and M.S. degrees in electrical and electronics engineering from the Middle East Technical University, Ankara, Turkey, in 1981 and 1983, respectively, and the Ph.D. degree in electrical engineering from The Ohio State University, Columbus, in 1988.

From 1981–1983, she was with the Middle East Technical University as a Graduate Assistant, and from 1984–1988, she was with The Ohio State University ElectroScience Laboratory as a Graduate Research Associate. Since 1989, she has been on the faculty of the Department of Electrical and Electronics Engineering at the Middle East Technical University, where she is currently an Associate Professor. Her research interests include the numerical methods for electromagnetics, microstrip antennas, microwave and millimeter-wave integrated circuits, and SAR and ISAR imaging techniques.

DESIGN OF AN ACTIVE MICROSTRIP ARRAY USING A MICROWAVE CIRCUIT SIMULATOR

Şimşek Demir, Canan Toker, Altunkan Hızal
Electrical and Electronics Eng. Dept.,
Middle East Technical University,
Ankara, Turkey

Abstract

ve antenna array design and simulation of this vith a microwave circuit simulator are presented. ive antenna array is a TV receive only (TVRO) operating at 10 GHz. It is a 8x4 array of ılar microstrip patch antennas. Eight low noise 's are placed in the antenna. Passive antenna ristics are usually obtained by analytical ıes or using special softwares for this purpose. The al representation as well as the nonreciprocal of the active device necessitates the use of a circuit or. In this work, both the antenna and the active characteristics are obtained in the same medium, microwave circuit simulator LIBRA. The array e is simulated with LIBRA for gain, noise ıture, radiation pattern, directivity and bandwidth.

Microstrip Patch Antenna

ive antenna array will work at a single polarization. ore, the microstrip patch antenna is designed as a ular patch rather than a square patch. This ed the degree of freedom in the patch design. The of the patch is chosen considering its input ınce and patch length is dictated by the resonance on at 10 GHz. The substrate of the microstrip re is RT Duroid 5880. Parameters of this substrate en in Table I.

h	Loss tangent	Cladding
0.787 mm	0.0009	70 µm gold plated copper

Table I. Substrate parameters (RT Duroid 5880)

strip patch is modeled using Pues and Van de e model [1]. The element values of this model have ncy dependence. It is observed that this dependence ear in the vicinity of center frequency. The wave circuit simulator LIBRA allows defining the nt values as simple functions. Using this property of nulator, frequency dependence of the patch model is ed in the simulations as first order polynomial ons of the frequency.

Antenna Array

The microstrip antenna array is a parallel fed structure. Four parallel fed patch antennas are taken as a sub array and called as B array. Overall antenna array is consisted of eight parallel fed B arrays, and called as A array. Antenna structure and related dimensions are given in figure 1. Quarter wave impedance transformers are used between the patch antennas in order to make amplitude tapering and also, to decrease the loading of antennas with preceeding elements .

The planar antenna array structure is designed for narrow beam and low side lobe level in H-plane. To maintain this criteria, the antenna structure in this dimension is not altered, whereas dimensions and structure of the feedline in the perpendicular dimension are kept as variables of design for active circuit integration.

Active Circuit

G/T ratio of the active antenna is intended to be kept high. An important way to reach this goal is to use low noise active devices. NEC 32484A pHEMTs are the low noise transistors used in the design. Scattering and noise parameters of this transistor at the frequency of interest, 10 GHz, are given in Table II. This transistor has a noise figure as low as 0.51 dB at 10 GHz when input impedance is selected as the optimum noise impedance. The active circuit is placed between each B array and the feedline, thus 8 low noise transistors are used in total. NEC 32484A is a packaged transistor, therefore, it is possible to make a hybrid design.

The transistors are self biased at V_{DS}=2V and I_D=10mA for low noise operation. This is achieved by connecting a capacitor in one of the two source terminals of the pHEMT, and a resistor in the other one. Drain terminals of all the transistors are connected to the feedline. Therefore drain voltage is given from a single point and RF output is DC blocked using a coaxial capacitor. With this configuration total DC power consumption will be about 0.16 W.

03-3318-7/97/$5.00 © 1997 IEEE

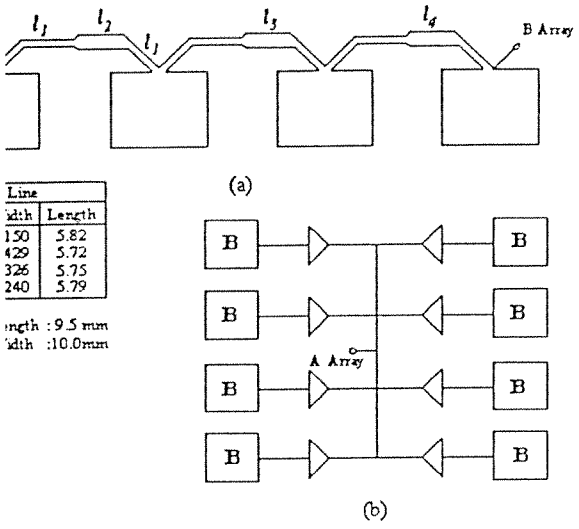

Line	
idth	Length
150	5.82
429	5.72
326	5.75
240	5.79

ngth : 9.5 mm
idth :10.0mm

gure 1. Structure and dimensions of microstrip patch na array. (a) Microstrip patch and B array (b) Structure of A array.

uency	NF_{opt}	Γ_{opt}	r_n
GHz	0.51 dB	0.40 131°	0.09

(a)

S_{11}	S_{12}	S_{21}	S_{22}
-142°	0.096 14°	3.03 40°	0.485 -95°

(b)

ble II. (a) Noise and (b) scattering parameters of NEC 32484A.

temperature of the passive antenna is about 25 K space noise is not counted for. Optimum noise of the active device is given as 0.51dB. This figure ponds approximately to 36 K. Comparison of um noise figure of the active device and the passive na noise temperature shows that noise contribution the active device is an important quantity in ining the noise temperature of the active antenna. forth, active device should be operated at or close to timum noise figure.

strip transmission lines and open circuited stubs are for impedance transforming and will simply be ed as matching sections. Line width and lengths of elements are the design variables. Transistor and the ing sections should fit onto the area between a B and the feedline. Also none of the microstrip lines l be close to each other because otherwise parasitic ng will occur. These considerations limited the er and physical sizes of elements used for matching. fier topology is given in figure 2.

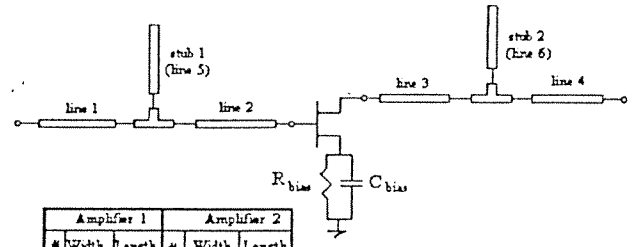

	Amplifier 1			Amplifier 2	
#	Width	Length	#	Width	Length
1	0.181	1.280	1	0.171	1.276
2	0.486	2.306	2	0.455	2.321
3	0.796	2.128	3	0.797	2.145
4	0.540	7.108	4	0.515	7.368
5	0.150	4.724	5	0.151	4.704
6	0.592	3.949	6	0.600	3.875

Figure 2. Amplifier topology and dimensions of matching elements

Short circuit stubs are not used because no accurate characterization of the production process exists for short circuits. Thus, open circuited stubs are preferred and the open circuit end-effects which are easier to characterize are included in the simulations [2].

In the active array design input impedance of the amplifier is the input impedance of B array and the output impedance is the impedance seen looking towards the feedline at the point of junction. Because of feedline structure and the loading effects, the output impedance as defined above is different for amplifiers at different positions. Observing the symmetry of the feedline structure it is easily seen that there are two different output impedances, consequently there should be two similiar but different output matching circuits. One amplifier is effective in determining the load of other amplifier. Therefore an iterative optimization procedure is followed.

Noise figure of an amplifier is strongly dependent on its input impedance. Therefore the input impedance of the B array should be transformed to the optimum noise impedance of the active device in order to reach its optimum noise figure. It should be noted that the matching microstrip elements are lossy. Henceforth, noise figure of the active circuit is greater than the optimum noise figure of the active device.

Moreover, in order to be able to take the available power from a source, input impedance of the amplifier should be conjugately matched to the input impedance of the source. The input power to the amplifier from B array is related to antenna efficiency, that is, efficiency of the B array is less than one if the delivered power from B array is less than the available power of the B array. Therefore, input matching circuit should not only transform the input impedance of the B array to the optimum noise impedance of the active device but also transform the input impedance of the active device to the conjugate impedance of the input impedance of B array. On the otherhand,

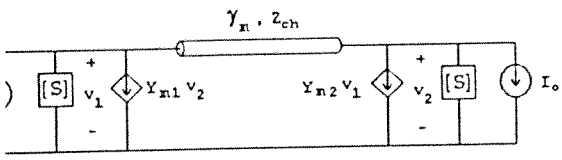

igure 3. Microstrip patch model in receive mode.

impedance of the amplifier should be adjusted to maximum gain from the amplifier. In practice, onstraints may not be satisfied simultaneously.

mpedance of the B array is real and about 105Ω at z. The input impedance of the amplifier is matched input impedance of the B array and under above erations matching circuits are optimized to yield a igure of 0.58 dB and about 8 dB gain at 10 Ghz. r point to be considered is the frequency bandwidth antenna. In order not to limit this bandwidth, both nd gain performance of the amplifiers should have nough frequency bandwidths.

Active Antenna Simulation Results

mulate the array in receive mode, hypothetical t sources are connected to the patch antennas to nt received electromagnetic wave. The patch a element receives electromagnetic power from two herefore two current sources equal in amplitude and ut of phase are connected to each antenna element. nagnitudes of the current sources for antenna nts in different positions are taken to be the same se a uniform illumination of the array is assumed e antenna elements are identical. The absolute value currents depends on effective length of the slots and ntensity of the incident field. The receive mode entation of the patch antenna is given in figure 3.

simulations, a load impedance of 50Ω is connected output of the A array. Output power of the active n is defined as the power delivered to this load lance. Input power is the sum of the power delivered each antenna element when all current sources, fiers etc. are present in the system. Amplification of tive system is defined as the ratio of output power to put power. The amplification term takes the place of fficiency term in the gain definition of an antenna n is, for a passive antenna, directivity times the ency of the antenna. With this definition, fication is 15.2dB at 10 GHz.

temperature of the active system is calculated by the ator using the noise correlation matrices. Current es representing the received power are disconnected, he noise current delivered to the load impedance from ne-port A array is calculated. The noise power due to this noise current is converted to noise temperature using the well-known relation:

$$P_n = \overline{i}_n^2 R_L = kTB \qquad (1)$$

The resultant noise at the load impedance is due to the losses in the active system and the noise generated by the active device. Noise temperature calculated in this manner is about 29.2 dB-K at 10 GHz. The ratio of amplification of the active system to the noise temperature is -14 dB. In order to find the antenna gain to noise temperature ratio, G/T, effect of directivity should be included. Simulation results for amplification, noise temperature and output power when 10 μA current sources are connected, are given in figure 4. Since amplification is defined as the ratio of output power to the input power, frequency dependence of output power is also important; i.e.; although amplification remains constant, output power may decrease.

In order to obtain the radiation pattern, progressive phase shift is introduced to the hypothetical current sources. The magnitude of the phase shift is a function of element spacing, free space wavelength, physical position of the element in the array and angle of incidence. Output power as a function of angle of incidence gives the radiation pattern of the array which does not include the dependence of effective length of the microstrip patch on angle of incidence. Magnitude of the hypothetical current sources can be set as a function of angle of incidence which will count for the dependence of effective length on angle of incidence. Array factor which is much more rapidly changing than this dependence dominates in determining the radiation pattern in low angles of incidence. Therefore dependence of effective length on angle of incidence is neglected. H-plane radiation pattern which is obtained by this way is given in figure 5. Side lobe level is below 19 dB in H-plane. E-plane radiation pattern is also obtained and directivity is calculated using the approximate formula of Krauss for directivity. Directivity of the active array is about 22 dB at 10 GHz.

The frequency dependence of the array characteristics is also investigated. Frequency bandwidth for output power is about 600 MHz. However, the dependence of radiation pattern on frequency is much more higher. As frequency deviates from the center frequency in either direction, side-lobe level increases rapidly. Therefore, frequency bandwidth of the antenna is mainly determined with radiation pattern bandwidth.

Stability of both the amplifiers and the active system are investigated. All over the simulation frequency range, real part of amplifier ouput impedances and the A array output impedance are positive. Therefore, for any passive load, this one port system is stable.

Conclusion

: array simulation method using a microwave ıulator is described. The designed active array is : antenna and since there are nonreciprocal ı the system, the array cannot be analysed as a ng antenna which is the usual case for passive ırays. To simulate the array in receive mode, cal current sources are connected to the patch to represent the induced short circuit currents.

ıod described here is applicable not only to the ;ays but to the passive arrays as well. By this ɔf simulation, efficiency (amplification), noise ıre, radiation pattern, directivity, gain and frequency bandwidth of antenna arrays can be obtained in the same computational environment.

Acknowledgement

The partial support provided by TUBITAK (Turkish Scientific and Technological Research Council) and ASELSAN (Military Electronics Industry Inc.) under the project COST 245 are gratefully acknowledged.

Reference:

[1] Pues, H., Van de Capelle, A., "Accurate transmission line model for the rectangular microstrip antenna", IEE Proceedings, vol. 131, Pt. H, No. 6, Dec. 1984.

[2] J.R. James, P.S. Hall (Ed.), *Handbook of Microstrip Antennas*, Peter Peregrinus Ltd., London, 1989.

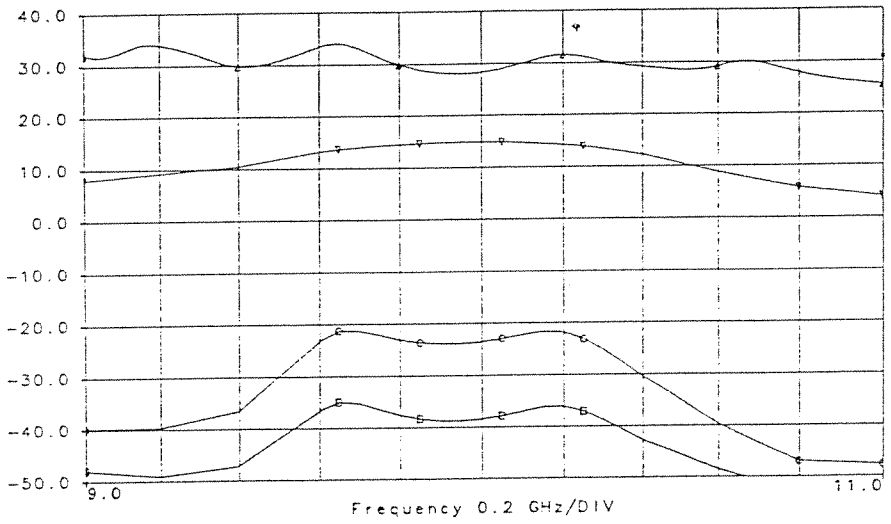

Figure 4. Amplification, noise and output power responses of the active system. □ :Input power, o: Output power, ▽:Amplification(dB), △:Noise temperature (dB-K)

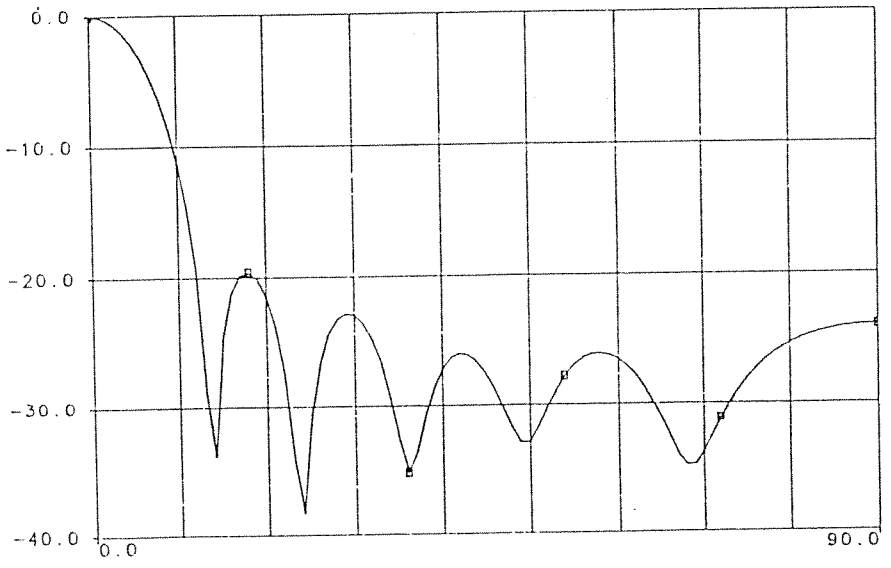

Figure 5. H-plane radiation pattern of the active array.

A NOVEL LOW NOISE ACTIVE CIRCUIT REPLACEMENT CRITERIA FOR PARALLEL FED LARGE SCALE ACTIVE ANTENNA ARRAYS

SIMSEK DEMIR, CANAN TOKER, ALTUNKAN HIZAL

Middle East Technical University, Electrical and Electronics Eng. Dept.

06531, Ankara, TURKEY

Abstract: In this work noise analysis of parallel feed structures for active antenna arrays are presented. Signal and noise behaviour of the feed structures are signified by the newly introduced concepts of "coherent" and "incoherent" impedance match of power combining structures. It is also shown that a feed structure can be re-designed for low noise operation without affecting its radiation characteristics. Optimum design of parallel feed structures for low noise operation is explained. Also an optimum use of active elements in such structures is investigated to have a low overall noise temperature of the antenna array with minimum number of active elements. In the analysis a new method is introduced where a "noise equivalent line length" is defined. This definition which unifies the contribution of noise from different array elements, is used in the design of a parallel feed structure and as an active circuit replacement criteria in passive arrays.

I. INTRODUCTION

An important figure of merit for receive antennas is noise performance. Since 1960's antenna arrays have been investigated for better signal-to-noise ratios, Lo et al. (1), including the recent active antenna structures, Grabherr and Menzel (2). However, in these analysis, feed lines are not studied for their noise performance. Moreover, explicit methods for low noise design of feed structures do not appear in the literature.

Receive antenna array design for certain radiation characteristics is related to the case where all elements receive coherent signal. Feed structure designs that are appearing in the literature are mainly concerned with impedance matching for coherent excitation. However, impedance matching for coherent excitation does not imply the incoherent impedance matching which is the case where the signal that are combined in the structure are incoherent. The response of a feed structure to excitations from incoherent sources such as internal noise of the antenna array, is totally different and such a concept is not considered previously. In our work, incoherent matching of the feed structures is accounted for the first time. Moreover, a novel concept, 'noise equivalent line length', is introduced and utilized for noise analysis of feed structures. Without loss of generality, feed structures that are constructed by transmission lines are investigated.

Using analysis above a low noise large scale antenna array design guide is presented where the critical point to insert a low noise gain element for improved noise performance is identified. In our analysis, it is also shown that insertion of low noise active elements in an antenna array improves the noise performance, however where to insert the active elements is a design problem from point of view of labor, cost and improvement in performance. We defined node, branch, virtual node, virtual branch, and level concepts for parallel feed structures. A weighted equivalent line length function is introduced. This novel function which carefully combines the analysis results of the previous works, stands for the noise contribution of a line segment in a parallel feed structure to the output noise power and utilized for comparing different feed network structures of large scale antenna arrays.

II. PARALLEL FEED STRUCTURE NOISE ANALYSIS

The noise analysis of feed structures is based on the noise analysis of a low loss transmission line, Collin (3). Characteristic impedance, Z_{ch}, attenuation per unit length, α, and length of the line, l, and the ambient temperature, T, determine the generated noise power. The attenuation factor of the line introduces an imaginary part to the Z_{ch} but it is assumed that line is low loss and therefore, Z_{ch} remains, practically, real. The source and load reflection coefficients are defined with respect to the characteristic impedance of the line. Available noise power of a low loss transmission line is obtained for $Z_L = Z_{out}^*$, where $L = e^{2\alpha l}$:

$$P_{n,available} = kT\Delta f \frac{L - |\Gamma_g|^2/L - 1 + |\Gamma_g|^2}{(1 - |\Gamma_g/L|^2)L} \tag{1}$$

Available noise power of a low loss transmission line is a function of source mismatch and loss factor. This power increases with increasing magnitude of source reflection coefficient. The upper limit of this available power is:

$$P_{n,available,max} = kT\Delta f \tag{2}$$

This means that in the limit of mismatch, a low loss transmission line introduces an available noise power equal to the available noise power of a resistor. Therefore matching is of ultimate importance from point of view of noise

ented. Signal and

generation which corresponds to incoherent impedance matching of the feed structure of the antenna array.

Above noise analysis is used towards the definition of a noise equivalent line length which simplifies the noise performance evaluation of the feed structures considerably. In doing so, the noise contributions from different elements of a feed structure to the output noise power is expressed in terms of a single parameter which puts explicitly the strength of the contribution relative to the theoretical minimum. Simple addition of these equivalent line lengths is a good comparison criteria for the overall noise performance of the feed structure. Moreover, this uncomplicated parameter, is used as a replacement criteria of active circuits in an antenna array for the optimum noise performance.

Let L be the loss factor of the line under investigation which has a source reflection coefficient, Γ_g, and loss coefficient, α, then its available noise power, P_{line}, is given by (1). Let L_{neqv} be the loss factor of a line which has a line length l_{eqv} and has the same loss coefficient, α. Furthermore let this line be impedance matched at its source side, then its available noise power is given by:

$$P_{eqv} = k\,T\,\Delta f \frac{L_{neqv} - 1}{L_{neqv}} \tag{3}$$

For the line under investigation, let us define an equivalent line which is matched and therefore has the available noise power in (3). If L_{neqv} is obtained such that $P_{eqv} = P_{line}$, then L_{neqv} turns out to be:

$$L_{neqv} \triangleq \frac{L^2 - |\Gamma_g|^2}{(L^2 - |\Gamma_g|^2) - (L-1)(L + |\Gamma_g|^2)} \tag{4}$$

Consequently, noise equivalent line length, l_{neqv}, of the *line* turns out to be:

$$l_{neqv} = \frac{1}{2\alpha} \ln\left(\frac{L^2 - |\Gamma_g|^2}{(L^2 - |\Gamma_g|^2) - (L-1)(L + |\Gamma_g|^2)}\right) \tag{5}$$

Using the equivalent line length, output noise temperature can be obtained through (3). Noise equivalent length of a mismatched line is longer than its physical length where minimum noise equivalent length which corresponds to matched case is equal to its physical length. Without comparing the actual noise temperatures, one can deduce the effect of mismatch on noise generation by comparing the noise equivalent and physical lengths. In Fig. 1, noise equivalent line length normalized with its physical line length is given as a function of the source reflection coefficient.

Noise contributions of different segments can be superposed in terms of their noise equivalent line lengths to give an approximate value for the total noise equivalent length. Let us consider two line segments with noise equivalent line length, loss factor and noise power which are represented with l_1, L_1 and P_1 and l_2, L_2 and P_2, respectively. Noise power of the first line section will be attenuated in the second one and the resultant noise power of cascaded connection is given by:

$$\begin{aligned} P_{total} &= kT\Delta f \frac{L_1 - 1}{L_1 \cdot L_2} + kT\Delta f \frac{L_2 - 1}{L_2} \\ &= kT\Delta f \frac{L_{eqv} - 1}{L_{eqv}} \end{aligned} \tag{6}$$

That is:

$$\begin{aligned} L_{eqv} &= L_1 \cdot L_2 \\ l_{eqv} &= l_1 + l_2 \end{aligned} \tag{7}$$

A parallel feed structure is composed of a number of transmission line sections which sometimes function as impedance transformers, and junction points of line sections which function as power combiners. Noise equivalent line lengths of these individual structures can be added to find the overall noise equivalent line length of the feed structure. For a $1 : q^2$ double section quarter wave impedance transformer, noise equivalent line length is obtained through the generated noise power by the line segments:

$$P_{n_1} = kT\Delta f \left(1 - \frac{L((Z_g - Z_1)^2 - (Z_g + Z_1)^2)}{(Z_g - Z_1)^2 - L^2(Z_g + Z_1)^2}\right)$$

$$P_{n_2} = kT\Delta f\left(1 - \frac{L((Z_g - qZ_1)^2 - (Z_g + qZ_1)^2)}{(Z_g - qZ_1)^2 - L^2(Z_g + qZ_1)^2}\right) \quad (8)$$

The total noise power at the output is:

$$P_{Total} = \frac{P_{n_1}}{L_2} + P_{n_2} \quad (9)$$

and noise equivalent line length of the impedance transformer is given by:

$$l_{nequ,tr} = \frac{1}{2\alpha}\ln\left(\frac{1}{1 - P_{Total}/kT\Delta f}\right) \quad (10)$$

For a $1 : p^2$ power combiner structure, the equivalent line length is calculated based on the noise power at the output port. For a transmission line power combiner, the output power is the sum of the available power at the input ports if the input signals are coherent and have the proper power ratio Parad and Moynihan (4). Otherwise, if the signals are incoherent, the output power is the weighted summation of the input powers where the weights are the power combination ratios. The following is the noise equivalent line length of the power combiner where port 1 is the output arm, and port 2 and 3 are the input arms:

$$l_{nequ,comb} = l_{nequ,1} + \frac{1}{1+p^2}l_{nequ,2} + \frac{p^2}{1+p^2}l_{nequ,3} \quad (11)$$

For the case, where the thermal noise powers of the two arms are equal, the noise equivalent line length is given by:

$$l_{nequ,comb} = l_{nequ,1} + l_{arm} \quad (12)$$

These individual structures are used to construct a parallel feed structure. The main frame of a parallel feed structure is a parallel arm where sub arrays are connected to form an array. The sub arrays might be antenna elements and the formed array might be a sub array to be used in the succesive level of the parallel feed network. The line segment between the sub array and the parallel arm is named as a *Branch* (Br). The junction point of a branch and the parallel arm is the *Connection Point* (CP) of the sub array and a *Virtual Connection Point* (VCP) of the parallel arm. The sections of the parallel arm between consecutive VCPs are named as *Virtual Branches* (VBr). A parallel arm array has a single branch and a single connection point at its ouput side, but, have more than one VCP and VBr depending on the number of antenna elements connected to the arm. In a parallel feed structure, all the antenna elements are virtually connected to the same point, output of the array, with complex weights to create the required radiation pattern. The Br's are used to obtain the necessary complex weight of the antenna element (sub array) and VBr are usually of $n\lambda/2$ length and used to supply the connectivity of the antenna elements. VBrs can be used to create a tapered feed by means of quarter-wave-length impedance transformers.

Contribution of available noise power of a lossy line segment, P_{line}, to the output noise power depends on signal power contribution weight factor of the line, w, to the output signal power. Hence, the noise contribution of a line to the noise power at the output is:

$$P_{out,line} = w \times P_{line} \quad (13)$$

For this noise power at the output, a weighted noise equivalent line length ${}^{w}L_{nequ}$, is defined similiar to the noise equivalent line length definition as:

$${}^{w}l_{nequ} = \frac{1}{2\alpha}\ln\left(\frac{L^2 - |\Gamma_g|^2}{(L^2 - |\Gamma_g|^2) - w(L-1)(L+|\Gamma_g|^2)}\right) \quad (14)$$

By this definition weighted equivalent length of each line segment in a structure can be calculated. These weighted equivalent lengths explicitly give the strength of each noise source in the structure, which enables the designer to see the relatively noisy parts of the feed structure. Summation of noise temperatures corresponding to these noise equivalent line lengths will give the overall noise temperature. On the otherhand, the sum of the individual noise equivalent lengths yields the noise equivalent line length of the feed structure.

The impedance at the output of the array decreases rapidly with the increasing number of parallel connected antenna elements, which makes it difficult to match for coherent and incoherent operation. This situation is prevented by

(8)

implementing impedance transformers at the connection points of sub arrays. In a corporate feed the number of these connection points is a maximum. Therefore, coherent and incoherent matching is solved with less problem in a corporate feed structure. Weighted noise equivalent line length formulation is applied to a $N = 2^n$ element uniform corporate fed microstrip rectangular patch antenna array which is incoherent impedance matched. The following is the noise equivalent line length for this structure based on (7):

$$\begin{aligned} l_{total,n\ even} &= \sum_{k=1}^{n/2} \lambda \cdot 2^{k-1} - \lambda/4 \\ &= \lambda \cdot 2^{n/2} - \frac{5}{4}\lambda \\ l_{total,n\ odd} &= l_{total,n-1} + \frac{1}{2}\lambda \cdot 2^{(n-1)/2} \end{aligned} \tag{15}$$

Because of spurious radiation losses and conductor losses, realizable microstrip transmission lines widths are limited. Consequently, characteristic impedances required for incoherent impedance match in parallel arm structures are impractical and incoherent mismatch is unavoidable. Such a structure may be coherent impedance matched but because of incoherent impedance mismatch its noise equivalent line length will be much worse than minimum attainable length. Weighted noise equivalent line length of a $2 \times p$ element uniform fed parallel arm structure has the following approximate noise equivalent line length, including the incoherent mismatch:

$$l_{total} = \sum_{k=1}^{p/2-1} \frac{1}{2\alpha} \ln\left(\frac{L^2 - |\Gamma_{g,k}|^2}{L^2 - |\Gamma_{g,k}|^2 - w(L-1)(L + |\Gamma_{g,k}|^2)}\right) \tag{16}$$

where,

$$\begin{aligned} w &= \frac{2k}{p} \\ \Gamma_{g,k} &= \frac{Z_{ant}/2k - Z_{ch,k}}{Z_{ant}/2k + Z_{ch,k}} \end{aligned} \tag{17}$$

A two level parallel arm structure has the shortest physical line length but because of the incoherent mismatch, the noise equivalent line length might be several times longer than the physical line length. For a corporate feed structure, the total physical line length is a maximum, but because of easy integration of impedance transformers, incoherent impedance can be attained, and noise equivalent line length can be made a minimum. The noise equivalent line length is a measure to decide the structure of the array for low noise operation from this point of view.

III. ACTIVE ANTENNA ARRAY DESIGN

For the line segments in the structure, line lengths are determined with phasing requirements and characteristic impedances should be chosen for the incoherent impedance match. However, in the cases where incoherent impedance match is not attained, noise performance will be degraded. For a large antenna array, active circuit integration might be a solution for low noise operation. In that case l_{neqi} will be a design guide to determine the insertion level of the active devices in the feed structure. This level will depend on the noise figure and gain of the active circuit and the loss of the line segments. Fig. 2 shows schematically, levels in a corporate feed structure where active elements are placed at one of them. Replacing active devices at level 1 is the best for lowest noise performance at the expense of large number of active circuits, i.e., 2^n. However, there will be a level in the structure where noise improvement is just achieved with decreased number of active elements compared to a passive antenna array.

In order to see this fact let us consider the two cases given in Fig. 3. In this figure the connection point, A, of two successive levels, k and $k+1$ are shown with noise equivalent length l_{neq1} corresponding to levels 1 to k of the structure shown in Fig. 2, and noise equivalent length l_{neq2} corresponding to levels $k+1$ to n. A feed structure with noise temperature, T_f and efficiency, η_f, can be partitioned into two consecutive sections with noise temperatures and efficiencies, T_1, η_1 and T_2, η_2, respectively, where $T_f = T_1 \times \eta_2 + T_2$ and $\eta_f = \eta_1 \times \eta_2$, and to improve the performance, an LNA can be placed between these two partitions as shown in the Fig. 3.b. Depending on η_2 and T_2 distributed amplification may yield even a better G/T compared to $(G/T)_{passive}$. Notice that, when comparing noise powers of these two systems, active system's noise power should be normalized since signal power of active system is G times more than the passive system's. Distributed amplification yields a better G/T than the passive case when the following equation yields a result greater than zero :

$$P_{out,passive} - \frac{P_{out,dist}}{G} = T_J - \eta_2(T_{LNA} + T_1) - \frac{T_2}{G}$$
$$= T_2(1 - \frac{1}{G}) - \eta_2 T_{LNA} \quad (18)$$

To satisfy this condition, high G and low T_{LNA} are required. This equation also implies that active circuit integration is necessary for low efficiency systems. Using this calculation maximum length of noise equivalent line of the second partition of the feed structure can be determined, where an active circuit with a certain G and T_{LNA} should be inserted for better noise performance. This point will be the optimum point where the number of required LNAs is a minimum and the noise performance of the passive array is improved.

IV. ACTIVE ARRAY

A 16 x 16 corporate fed microstrip antenna array on a RT-DUROID 5880 substrate is designed. Quarter-wave-line impedance transformers are placed acording to the results of section III, to the feed structure to decrease the noise generation by the lossy feed lines. The rectangular patch antennas are resonant at 10 GHz having a 276 Ω resistive input impedance. The uniform fed antennas are equi-separated by a distance, d, which is determined by radiation pattern considerations. The total weighted equivalent line length of this 16 x 16 patch array is calculated to be about 14.8 λ which corresponds to $T = 101°K$ for $T_{amb} = 290°K$. Using microstrip matching elements and an ultra low noise pHEMT, NEC 32484A, a low noise amplifier is designed. The noise figure of the amplifier is 0.6dB and gain is 14dB. It is assumed, and shown that appropriate matching circuits whose total physical length will be about $\lambda/2$ can be designed independent of wherever the amplifier is inserted in the feed structure, Demir et al. (5). In case, this amplifier is connected to the output of the 16 x 16 passive array, noise temperature at the output of the amplifier turns out to be $T = 35.6dB\text{-}K$. Using weighted equivalent line length method and the results of section V, the noise temperatures corresponding to different amplifier placement levels are calculated and presented in Table 1. The improvement of noise performance with the added number of amplifiers is clearly seen from this table.

Using Table 1, above equations yield that active antenna has a better G/T than the passive antenna for connection level 7 which is also implied by (18). It can be said that for this structure and the amplifiers concerned, the level where the improvement is just achieved is level 7 where four active elements are required. Further improvements can be achieved using more active elements at the different levels as can be seen from Table 1.

Level	1	2	3	4	5	6	7	8	output
# of amp.	256	128	64	32	16	8	4	2	1
T_{level} (dB-K)	30.7	30.9	31.1	31.7	32.1	32.9	33.6	34.7	35.6

Table 1: Number of amplifiers and the output noise temperature for different levels as connection points of amplifiers.

V. CONCLUSION

Noise analysis of feed structures of antenna arrays are not considered in detail, previously. In this work, noise analysis of low loss transmission lines are given and a new concept named as "noise equivalent line length" is introduced. Through the signification of coherent and incoherent impedance matching concepts, noise sources in a parallel feed antenna array are identified and strength of these sources are expressed in terms of their noise equivalent line lengths. This provided the means to apply the noise equivalent line length as a low noise parallel feed structure design guide. Coherent impedance matching which is important for efficient radiation characteristics does not imply incoherent impedance matching which is important for noise generation of the feed structure. Moreover, noise equivalent line length is also utilized as an active circuit replacement critéria in antenna arrays which showed that G/T performance of a passive antenna array may be improved by inserting active circuits to certain levels in the feed structure.

References

[1] Y. T. Lo, S. W. Lee and Q.H. Lee, 'Optimization of directivity and signal-to-noise ratio of an arbitrary antenna array', Aug. 1966, Proc. IEEE, vol. 54, pp 1033-1045.

[2] W. Grabherr and W. Menzel, 'Broadband, low loise active receiving microstrip antenna', in Proc. 24th European Microwave Conf., Sep. 1994, pp 1785-1790.

[3] R. E. Collin, Antennas and Radiowave Propagation, New York, McGraw Hill Int. Ed., 1985.

[4] L. I. Parad and R. L. Moynihan, 'Split-Tee power divider', Jan. 1965, IEEE Trans. Microwave Theory Tech., vol. MTT-13, no. 1, pp 91-95.

[5] S. Demir, C. Toker and A. Hizal, 'Design of an active microstrip array using a microwave circuit simulator', in Proc. IEEE MTT-S Top. Symp. on Tech. for Wireless Appl., Vancouver, Canada, Feb. 1997, pp 103-106.

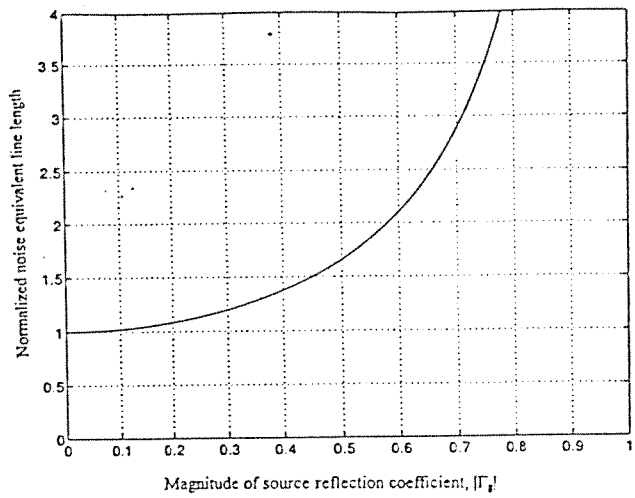

Fig. 1. Variation of noise equivalent line length with the source reflection coefficient, normalized with its physical line length.

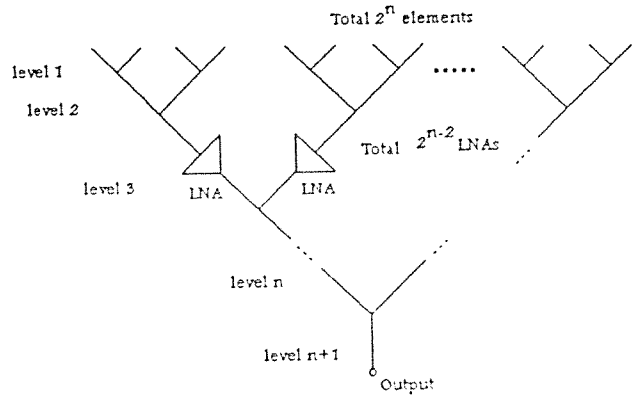

Fig. 2. Schematic representation of a $N=2^n$ element corporate feed structure.

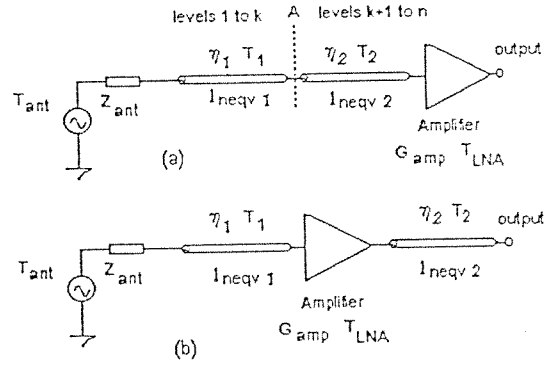

Fig. 3. Active circuit integration with antenna arrays: (a) LNA connected to level n+1 (b) LNAs connected to level k+1.

USE OF COMPUTATIONALLY EFFICIENT SPATIAL-DOMAIN METHOD OF MOMENTS IN CAD OF MICROSTRIP ANTENNAS

L. Alatan[1]

M.I. Aksun[2]

M.T. Birand[1]

1 Middle East Technical University Dept. of Electrical & Electronics Eng. Ankara 06531 TURKEY
2 Bilkent University Dept. of Electrical & Electronics Eng. Ankara 06533 TURKEY

Abstract

An efficient and rigorous technique, based on the spatial-domain MoM in conjunction with the closed-form Green's functions, is presented for the analysis and the design of printed geometries in a multilayer environment. The derivation of the closed-form Green's functions and the analytical evaluation of the MoM matrix entries have alleviated the most of the computational burden of the spatial-domain MoM. By performing non-uniform meshing, fine adjustment of the dimensions of the analyzed geometry is made possible without increasing the number of unknowns. In addition, with the use of the order-recursive Gaussian elimination in the solution of the MoM matrix equation when the original geometry is modified, the computational efficiency of the spatial-domain MoM is further improved. The assessment of this improvement is demonstrated here in the optimization of the dimensions of an inset-fed patch antenna.

1 Introduction

Since printed geometries in layered media are widely used in the applications of microstrip antennas and monolithic milimeterwave and microwave integrated circuits, efficient and accurate modeling of such structures has gained a lot of interest. There are basically two approaches for the modeling of printed geometries; i) using a simple equivalent model such as transmission line model, cavity model in the analysis of microstrip antennas, and quasi-TEM, quasi-static approaches for the characterization of interconnects, transmission line discontinuities, ii)using a full-wave method like the method of moments, the finite difference time domain method and finite element method. Since the equivalent models are numerically efficient, they might be prefered in the computer-aided-design procedures involving optimization, but they often lack accuracy and are valid for specific geometries. In the case of microstrip antennas, for example, when stubs, parasitic elements or discontinuities are introduced, a full-wave analysis method has to be employed. Therefore, one need to improve the numerical efficiency of these rigorous techniques without sacrificing the accuracy. After a series of studies, the spatial-domain MoM has become a computationally efficient method which can be used in CAD applications. These studies involve casting the spatial-domain Green's functions into closed forms[1, 2] and analytically evaluating the MoM matrix elements[3]. The analytical evaluation of the integrals are performed by using the Taylor series expansion of the integrands. Consequently, the elimination of the numerical integrals, involved in the traditional spatial-domain MoM, results in a significant improvement in the matrix fill-time.

When the analyzed geometry is large, most of the computation time is dedicated for the solution of the matrix equation. However, in interactive design or optimization, the whole geometry is not changed at each iteration but some part of it is deleted or added, so at each step some few rows and columns are added to or deleted from the previous matrix. For this type of applications, order recursive Gaussian elimination (ORGE) method[4], developed to improve the computational efficiency of solving matrix equations for modified geometries, can be utilized very efficiently. This method provides the solution of the modified matrix with the use of the solution in the previous iteration, hence eliminates the repeated solution of the whole matrix equation. Since the computation time is reduced significantly, the real time assessment of the results, due to small changes in the geometry, becomes possible.

The improvements in the matrix fill-time and in the matrix solution time, make the MoM an efficient numerical method which can be used in conjunction with an optimization procedure. However, when the method is performed with equal subintervals, very small cell sizes, which lead to a large number of unknowns, should be prefered in order to be able to optimize the dimensions of the desired geometry. Hence, instead of uniform meshing, the dimensions of one or two subintervals are made variable, and they are optimized to obtain the desired specifications.

Supported in part by TÜBİTAK (The Scientific and Technical Research Council of Turkey) within the scope of COST 245 project.

The numerically efficient procedure presented in this paper is employed to optimize the dimensions of an inset-fed patch antenna and the results are presented in Section 2.

2 Results and Discussions

In this section, an inset-fed patch antenna shown in Fig.1 is analyzed. The permittivity and the thickness of the substrate are 2.2 and 0.7874 mm, respectively and the operation frequency is 10GHz. The dimensions of the patch antenna are 0.9488cm×0.9488cm. This geometry is analyzed by using the Galerkin's MoM and the basis and testing functions are chosen to be the rooftop functions which are triangular functions in the longitudinal direction and uniform in the transverse direction. The input impedance of the antenna which is normalized with respect to the impedance of the feed line is calculated to be 3.39 Ω.

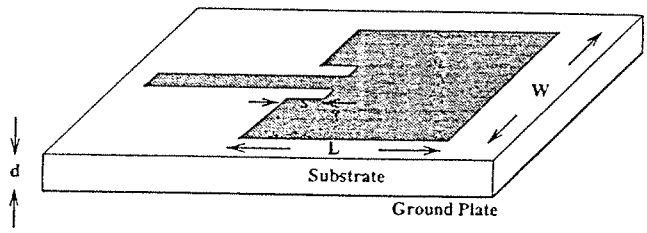

Figure 1: Inset-fed patch antenna configuration

For typical patch widths ($\approx \lambda/2$), the input impedance of the antenna is so high that it is required to feed the antenna with a very narrow transmission line to decrease the mismatch between the antenna and the feed network. To eliminate this problem, the antenna feed point should be shifted towards the center of the patch by inserting notches.

The depth of the notch changes both the real and imaginary parts of the input impedance and this variation is given in Table 1. During the analysis, the unknowns are ordered in such a way that the matrix entries corresponding to the notch region are placed at the end of the MoM matrix, so the effect of the changes in the notch depth can be observed immediately by applying the ORGE method. In obtaining the results, the width of the notch is chosen to be equal to the width of the feed line which is 0.10542cm. The input impedances are

depth of the notch	input impedance of the antenna
0. cm	3.39+j0.0
0.06325 cm	3.36+j0.46
0.12650 cm	2.70+j1.53
0.18975 cm	2.11+j1.94
0.25300 cm	1.75+j2.17

Table 1: Variation of the input impedance with the notch depth

From the table it can be seen that, when the inset-fed configuration is used, it is desired to re-tune the antenna. This tuning can be achieved either by changing the length of the patch or by adding stubs to proper locations. In this study changing the length of the patch is prefered and the results are given in Table 2. To this end, the method is performed by using uniform meshing, at this point, a vertical division with variable width (Section 1 shown in Fig.2) is added in order to be able to tune the length of the patch.

length of the patch	depth of the notch	input impedance of the antenna
0.96600	0.18975 cm	2.81+j0.0
0.97075	0.25300 cm	2.31+j0.0

Table 2: Input impedance of tuned antennas for different notch depths

If it is desired to obtain a specific input impedance level, the width of the Section 2 shown in Fig.3, should also be made variable and the width of the two sections (1 and 2) should be optimized. In this case, the shaded region

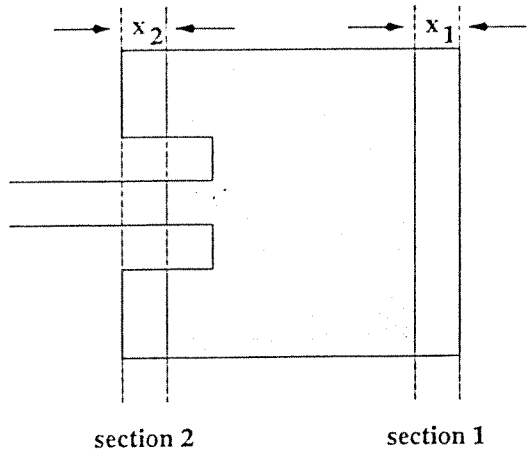

Figure 2: Non-uniform meshing with variable widths x1 and x2

shown in Fig.2, is analyzed first and the other sections are added to this region in order to apply the ORGE method efficiently. The width of the two regions are optimized to obtain input impedance of 1.8 and 1.6, the results are given in Table 3.

input impedance of the antenna	length of the patch	depth of the notch
1.8+j0.0	0.9755 cm	0.283 cm
1.6+j0.0	0.9775 cm	0.291 cm

Table 3: The depth of the notch and the length of the patch for the desired input impedance levels

These results show that the input impedance of the patch antenna can be decreased and adjusted to a desired value by increasing the depth of the notch. However, the depth of the notch can not be chosen arbitrarily large since it degrades the radiation pattern[5].

3 Conclusion

An efficient and accurate numerical modeling of printed structures is presented and employed in the characterization of an inset-fed microstrip antenna. It is observed that the use of the order recursive Gaussian elimination in addition to the closed-form Green's functions has improved the computational efficiency of the spatial-domain MoM. When non-uniform meshing is used, the width of the variable section can be utilized as a parameter of the optimization procedure and the design of the printed geometry with specific properties can be efficiently performed.

References

[1] Y. L. Chow, J. J. Yang, and D. F. Fang and G. E. Howard, "Closed form spatial Green's function for the thick substrate," *IEEE Trans. Microwave Theory Tech.*, vol. MTT-39, pp. 588-592, Mar. 1991.

[2] M. I. Aksun, " A robust approach for the derivation of the closed-form Green's functions," *IEEE Trans. Microwave Theory Tech.*, in press.

[3] L. Alatan, M. I. Aksun, K. Mahadevan, and M. T. Birand, " Analytical evaluation of the MoM matrix elements," *IEEE Trans. Microwave Theory Tech.*, in press.

[4] K. Naishadham, and P. Misra, " Order recursive Gaussian elimination and efficient CAD of microwave circuits, " *Proceedings of IEEE MTT-S International Microwave Symposium*, vol. 3, pp. 1435-1438, Orlando, May 16-20, 1995.

[5] S. C. Wu, M. G. Alexopoulos, and O. Fordham, " Feeding Structure contribution to radiation by patch antennas with rectangular boundaries, " *IEEE Trans. Antennas and Prop.*, vol. APS-40, pp. 1245-1249, Oct. 1992.

PERFORMANCE OF A 10 GHz 32 ELEMENTS RECEIVING PLANAR MICROSTRIP ANTENNA ARRAY

A. Hızal[(1)] , Ş. Demir[(1)] , L. Alatan[(1)] , C. Bulutay[(1)] , and H. Yıldız [(2)]

[(1)] Department of Electrical and Electronics Engineering,
Middle East Technical University,
06531- Ankara, TURKEY.
[(2)] ASELSAN, Macunköy, Ankara, TURKEY

ABSTRACT

4 by 8 planar receiving arrays are designed for the operating frequency of 10 GHz, having rectangular microstrip patch elements. For a low sidelobe level, amplitude tapering is implemented by using double-section transmission-line transformers. The losses of these feed lines are also used beneficially which leads to a very low noise temperature for the total array. An appreciable amount of the generated thermal noise is radiated to outer space which is further responsible for the low noise temperature. Sensitivity analyses are performed against several manufacturing tolerances. The input return loss, gain, and the pattern of the array are measured and compared with our theoretical predictions. To reduce the stray radiation from feeder lines and to improve the matching of patch radiators, the design is also repeated with narrow microstrip feed lines.

1. INTRODUCTION

Planar microstrip antenna arrays are in current demand due to their low profiles and costs together with their compatibility with electronic circuits. This is especially the case for *receiving* array's where power requirements are moderate. From the engineering point of view, the design of receiving planar microstrip antenna arrays with a large number of elements is a challenging task. Inaccuracies in the radiating and feeder element models together with manufacturing tolerances can accumulate leading to poor performance of the array at the initial design frequency.
In this work we present the design and the performance of a 32 element microstrip receiving antenna array for the 10 GHz centre frequency. For a satisfactory result, we followed a systematic study in both theoretical and experimental aspects. The details of the procedure and the results are explained in the next sections.

2. DESIGN OF THE ARRAY

2.1 Models

The success of the array design relies predominantly on an accurate modeling of the radiating elements and feeder lines. For the former we use the improved transmission-line model due to Pues and Van de Capelle (Ref. 1) that takes into account the mutual coupling of radiating slots and with accurate slot admittance expressions. The microstrip transmission-lines are modeled using planar waveguide model (Ref. 2). This approach favors the computer-aided design (CAD) procedure in contrast to full-wave treatments which are at the moment not very suitable to CAD. To assess the accuracy of our models we first designed two single patches for 3 GHz and 10 GHz frequencies and compared with our measurements. It is observed that centre frequency can be attained to an accuracy of 20 MHz at 10 GHz. This is repeated for a 4-element linear array that actually forms the sub-array of the full (4x8) array and a very good agreement with measurement is obtained.

2.2 Array

To reduce the side lobe levels a Gaussian amplitude tapering is used along both orthogonal directions. This is achieved using double-section microstrip transformers between the elements. With the advantage of the centre fed topology, the losses of the feed lines are used beneficially, aiding the amplitude tapering and this, in turn, resulted in a high efficiency of the array. The layout of the design is given in Fig. 1. In the implementation RT-Duroid 5880 substrate is used having the parameters: $\varepsilon_r = 2.2 \pm 0.015$, h=0.7874 mm , t=0.035mm , $\tan\delta =$ 0.0009.

The thermal noise analysis of the array is performed and resulted in a low noise temperature: T≅26°K at 10 GHz. This is mainly due to the fact that generated noise contributions from lossy transmission-lines and patches are radiated before reaching the load at the output.

3. THEORETICAL SENSITIVITY ANALYSIS

The uncertainties in the models used and manufacturing tolerances need to be systematically accounted for to identify the critical parts in the design. To investigate the sensitivity to patch slot admittances we introduced an additional ±10% slot susceptance but the effect was seen to be marginal. For the geometrical dimensions we introduced ±30μm deterministic errors and this only slightly affected the input matching of the antenna. Furthermore, the inclusion of step discontinuity capacitances yielded minor changes and can be neglected in the design. Finally the substrate permittivity is changed within the specifications of the manufacturer (ε=2.185-2.215). It is seen that the centre frequency deviates ±40 MHz around 10 GHz. We further identified that permittivity change primarily affects the patches rather than microstrip feed lines.

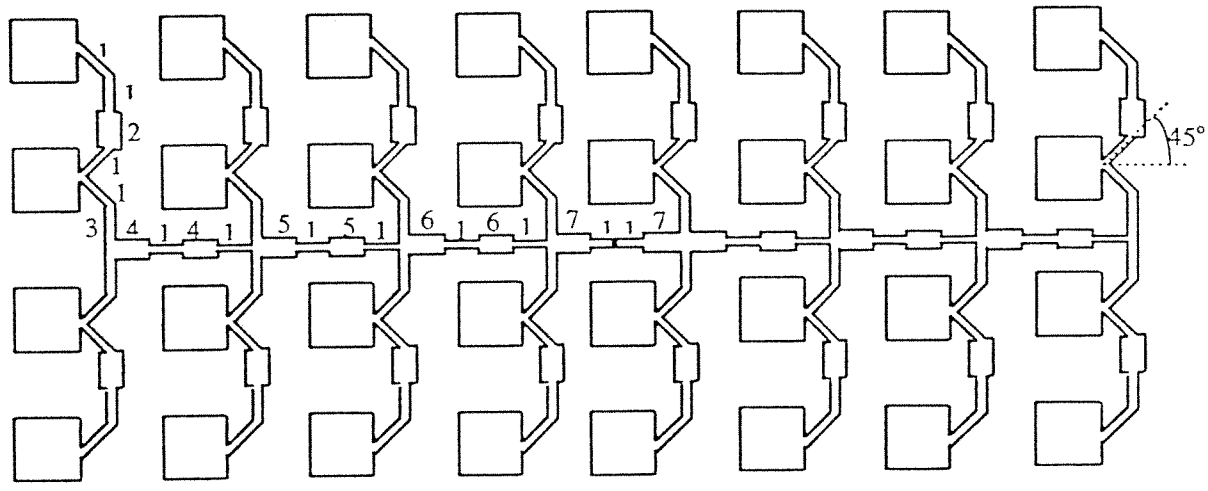

Fig. 1 Schematic layout of the 32 element microstrip array.

4. MEASUREMENTS

Against manufacturing tolerances, three separate arrays with square patch elements (of size 9.488 × 9.488 mm^2) were manufactured having slightly different dimensions. Their measured centre frequencies were slightly shifted (10.14 GHz to 10.2 GHz). However, the exact centre frequency (10 GHz) is obtained easily by means of very thin dielectric coating. This also proves that the array design is sensitive to the permittivity of the substrate and the superstrate. It should be mentioned that this method of tuning must be marginal in frequency as the radiation pattern can deteriorate due to mis-phasing of the elements.

Line No.	Width (μm)	Length (mm)	
1	150.0	5.787	
2	748.0	5.626	**Length of Patch:** 9.451 mm
3	99.0	5.818	
4	266.0	5.741	**Width of Patch:** 10 mm
5	224.1	5.755	
6	186.3	5.771	**Width of Patch Feeder Line (W_f):**
7	551.0	5.666	$\sqrt{2}$ 150 = 212 μm

Table I: Geometrical dimensions of the narrow strip array design; see also Fig. 1.

5. NARROW STRIP DESIGN AND MEASUREMENT RESULTS

The 4 × 8 element array is also realized with rectangular patches and narrow microstrip lines having 150 μm width. Geometrical dimensions of the design are given in Table I. The narrow feed lines have higher characteristic impedances (Z_{ch}≅159 Ω) and the impedance contrast between a patch radiator (Z_{patch}=275 Ω) and the feed line is reduced, enabling an easier match. Furthermore, the stray radiation from the feed lines is reduced. Unfortunately, the performance of thin lines are more vulnerable to manufacturing tolerances. The resulting small deviations in the centre frequency can be tuned by dielectric coating, however, as mentioned previously, this can also deteriorate the radiation characteristics of the antenna. In Figs. 2-5 the measured input VSWR, E-plane, H-plane and cross polarization patterns of the narrow strip design are presented. Gain is measured with respect to a *standard* X-Band horn antenna as 20.2±1 dB, which compares well with our theoretically expected value of 21.84 dB.

ACKNOWLEDGMENT

Antennas are manufactured in ASELSAN Military Electronics Industries. The partial support of TUBITAK (Turkish Scientific and Technical Council) is acknowledged.

6. REFERENCES

1. Pues H. & Van de Capelle 1984, Accurate transmission-line model for the rectangular microstrip antenna, IEE Proc. H, 131, 6, 334-339.
2. Collin R. E. 1992, *Foundations for Microwave Engineering*, Second Ed., McGraw Hill, New York.

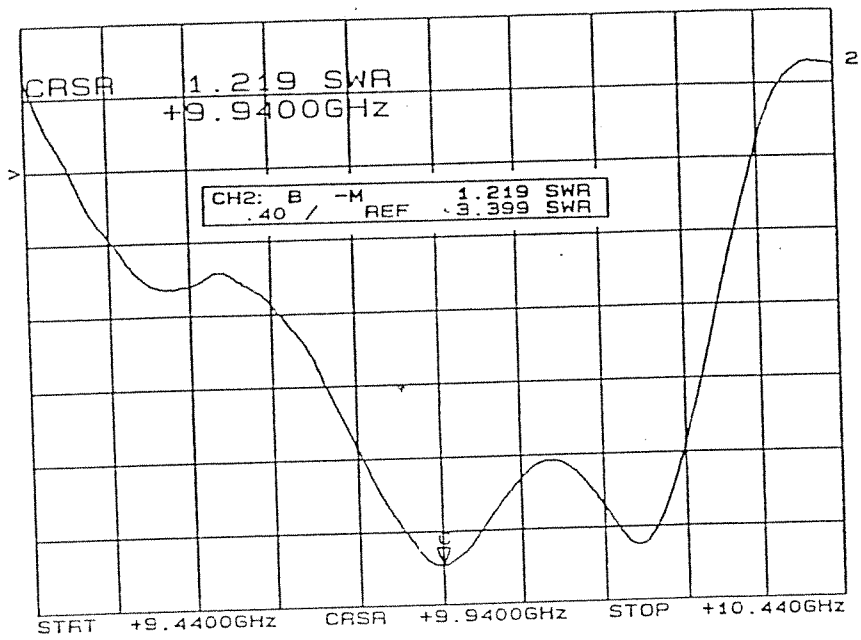

Fig. 2: Input VSWR of the narrow strip array.

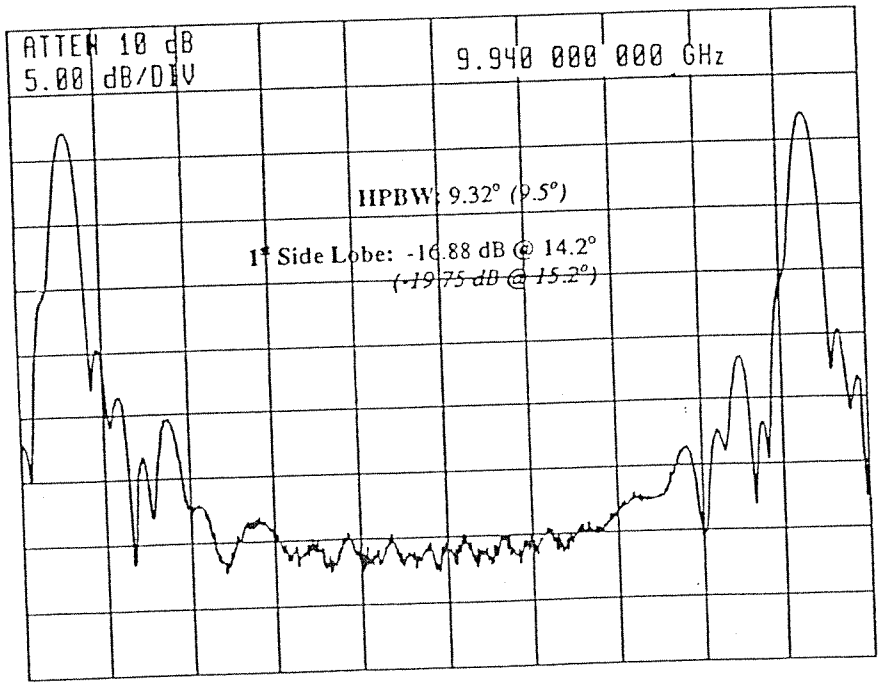

Fig. 3: E-Plane power radiation pattern. The distance between two main peaks corresponds to 360°. Half power beam width and first side lobe level are indicated; theoretical predictions are given in parentheses.

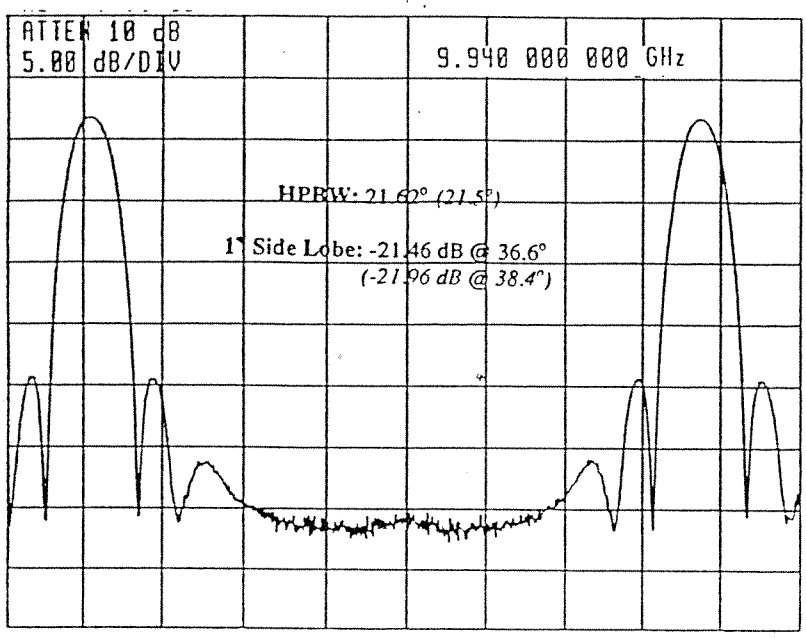

Fig. 4: H-Plane power radiation pattern. The distance between two main peaks corresponds to 360°. Half power beam width and first side lobe level are indicated; theoretical predictions are given in parentheses.

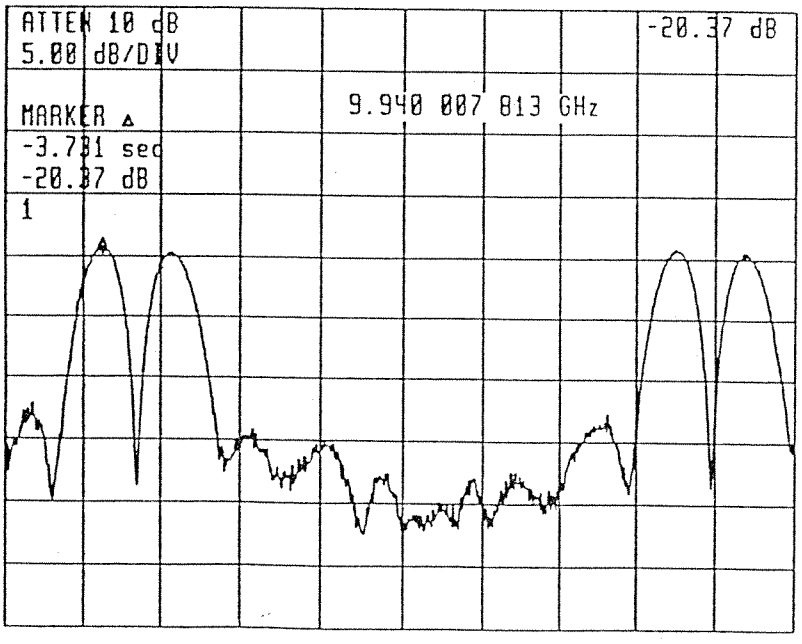

Fig. 5: Cross polarization pattern in the H-plane. The interval corresponding to 360° can be identified from periodic pattern.

L. Alatan*[1] M.I. Aksun[2] M.T. Birand[1]
1 Middle East Technical University Dept. of Electrical & Electronics Eng.
Ankara 06531 TURKEY
2 Bilkent University Dept. of Electrical & Electronics Eng. Ankara 06533 TURKEY

Abstract

An efficient and rigorous technique, based on the spatial-domain MoM in conjunction with the closed-form Green's functions, is presented for the analysis and the design of printed geometries in a multilayer environment. The derivation of the closed-form Green's functions and the analytical evaluation of the MoM matrix entries have alleviated the most of the computational burden of the spatial-domain MoM. In addition, with the use of the order recursive Gaussian elimination in the solution of the MoM matrix equation, when the original geometry is modified, the computational efficiency of the spatial-domain MoM is further improved. The assessment of this improvement is demonstrated here, in the characterization of a series-fed microstrip array and an inset-fed microstrip antenna.

1 Introduction

Since printed geometries in layered media are widely used in the applications of microstrip antennas and monolithic milimeterwave and microwave integrated circuits, efficient and accurate modeling of such structures has gained a lot of interest. There are basically two approaches for the modeling of printed geometries; i) using a simple equivalent model such as transmission line model, cavity model in the analysis of microstrip antennas, and quasi-TEM, quasi-static approaches for the characterization of interconnects, transmission line discontinuities, ii)using a full-wave method like the method of moments, the finite difference time domain method and finite element method. Since the equivalent models are numerically efficient, they might be prefered in the computer-aided-design procedures involving optimization, but they often lack accuracy and are valid for specific geometries. In the case of microstrip antennas, for example, when stubs, parasitic elements or discontinuities are introduced, a full-wave analysis method has to be employed. Therefore, one need to improve the numerical efficiency of these rigorous techniques without sacrificing the accuracy. After a series of studies, the spatial-domain MoM has become a computationally efficient method which can be used in CAD applications. These studies involve casting the spatial-domain Green's functions into closed forms[1, 2] and analytically evaluating the MoM matrix elements[3]. Consequently, the elimination of the numerical integrals, involved in the traditional spatial-domain MoM, results in a significant improvement in the matrix fill-time.

Supported in part by TÜBİTAK (The Scientific and Technical Research Council of Turkey) within the scope of COST 245 and EEEAG 132 projects.

0-7803-3216-4/96$5.00 © 1996 IEEE

printed onto this region and the corresponding matrix entries are selected from the stored matrix. As a result, the analysis of any structure printed on this region requires only a solution of a matrix equation whose computation time increases with the dimension of the matrix (usually $O(N^3)$). In interactive design or optimization, the whole geometry is not changed at each iteration but some part of it is deleted or added, so at each step some few rows and columns are added to or deleted from the previous matrix. For this type of applications, order recursive Gaussian elimination method[5], developed to improve the computational efficiency of solving matrix equations for modified geometries, can be utilized very efficiently. This method provides the solution of the modified matrix with the use of the solution in the previous iteration, hence eliminates the repeated solution of the whole matrix equation. Since the computation time is reduced significantly, the real time assessment of the results, due to small changes in the geometry, becomes possible. The numerically efficient procedure presented in this paper is employed to analyze two different geometries and their results are presented in Section 2.

2 Results and Discussions

In this section, two rectangular patch antennas connected in series as shown in Fig.1a are analyzed. The permittivity and the thickness of the substrate are 2.55 and 1.59 mm, respectively and the operation frequency is 2.275GHz. A region of 17.688cm × 4.02cm, which is chosen to be large enough to incorporate the largest possible circuit that we would like to investigate, is divided into subregions and the corresponding MoM matrix is obtained. Out of this area, a square patch antenna with dimensions 4.02cm × 4.02cm is chosen and its normalized (with respect to 50Ω) input impedance is calculated as 6.78+j0.0. Since the main goal is to investigate the characteristics of a series-fed array of two elements, the second antenna can easily be printed on the original area for which the corresponding MoM matrix elements have already been calculated. As series-fed antennas are generally used for broadside operation, the length of the transmission line connecting the two patches is adjusted to $\lambda/2$(4.623cm) by inserting or deleting some cells between the antennas. The current distribution of the geometry shown in Fig.1a, is given in Fig.2a and the input impedances of antenna # 1 and # 2 in this configuration are given in Table 1. These results show that the mutual coupling between the antennas shifts the resonant frequencies of the patches. Moreover, the input impedance of the patch #1 is changed due to the loading of the patch #2. The coupling and loading effects are observed for different transmission line lengths and the results are also given in Table 1. It is observed that the mutual coupling decreases with increasing the length of the transmission line and the input impedance of the antenna #2 approaches to that of the resonance condition. On the other hand, when the length of the transmission line is different from $\lambda/2$, antenna #1 is loaded by different complex loads, consequently the resonance condition of the array can be achieved by readjusting the length of the first antenna. This behavior should be taken into

Table 1: Variation of the input impedances with the length of the transmission line

An other geometry, analyzed by using the method proposed in this paper, is the inset-fed patch antenna shown in Fig.1b. For typical patch widths ($\approx \lambda/2$), the input impedance of the antenna is so high that it is required to feed the antenna with a very narrow transmission line to decrease the mismatch between the antenna and the feed network. To eliminate this problem, the antenna feed point should be shifted towards the center of the patch by inserting notches. The depth of the notch changes both the real and imaginary parts of the input impedance and this variation is given in Table 2. In obtaining the results, the width of the notch is chosen to be equal to the width of the 50Ω feed line which is 0.4467cm. When the

depth of the notch	input impedance of the antenna
0. cm	6.78+j0.0
0.201 cm	1.36+j2.73
0.402 cm	0.42+j1.61

Table 2: Variation of the input impedance with the notch depth

inset-fed configuration is used, it is desired to retune the antenna. This tuning can be achieved either by changing the length of the patch or by adding stubs to proper locations. In this study changing the length of the patch is prefered and the results are given in Table 3. The current distribution corresponding to the antenna with a notch depth of 0.8388cm is shown in Fig.2b. These results show that the input

length of the patch	depth of the notch	input impedance of the antenna
4.132cm	0.4132 cm	5.57+j0.0
4.194cm	0.8388 cm	3.49+j0.0

Table 3: Input impedance of tuned antennas for different notch depths

impedance of the patch antenna can be decreased and adjusted to a desired value by increasing the depth of the notch. However, the depth of the notch can not be chosen arbitrarily large since it degrades the radiation pattern[4].

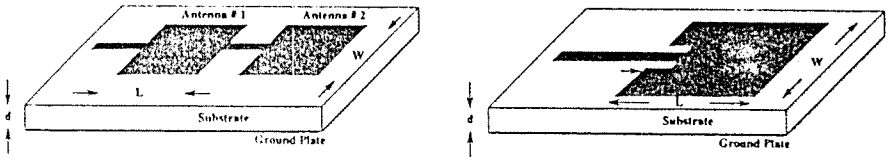

(a) (b)

Figure 1: (a) Series-fed antenna array; (b) Inset-fed patch antenna

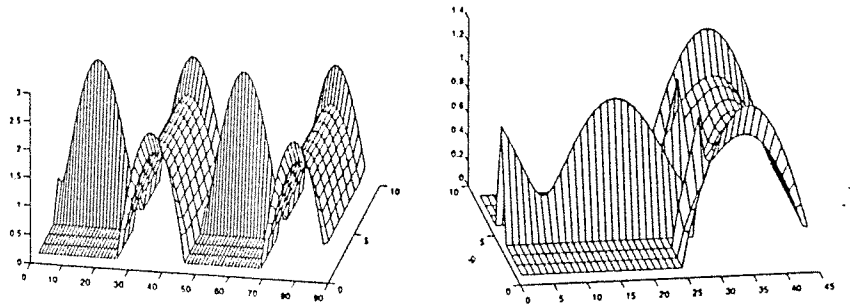

(a) (b)

Figure 2: Current distributions for (a) series-fed array; (b) inset-fed patch

References

[1] Y. L. Chow, J. J. Yang, and D. F. Fang and G. E. Howard, "Closed form spatial Green's function for the thick substrate," *IEEE Trans. Microwave Theory Tech.*, vol. MTT-39, pp. 588-592, Mar. 1991.

[2] M. I. Aksun, " A robust approach for the derivation of the closed-form Green's functions,"*IEEE Trans. Microwave Theory Tech.*, in press.

[3] L. Alatan, M. I. Aksun, K. Mahadevan, and M. T. Birand, " Analytical evaluation of the MoM matrix elements," *IEEE Trans. Microwave Theory Tech.*, in press.

[4] S. C. Wu, M. G. Alexopoulos, and O. Fordham, " Feeding Structure contribution to radiation by patch antennas with rectangular boundaries, " *IEEE Trans. Antennas and Prop.*, vol. APS-40, pp. 1245-1249, Oct. 1992.

[5] K. Naishadham, and P. Misra, " Order recursive Gaussian elimination and efficient CAD of microwave circuits, " *Proceedings of IEEE MTT-S International Microwave Symposium*, vol. 3, pp. 1435-1438, Orlando, May 16-20, 1995.

RADIATION OF DIPOLES IN MULTILAYERED CYLINDER WITH FERRITE LAYER

Özlem AYDIN, Altunkan HIZAL
Middle East Technical University, Department of Electrical and Electronics Engineering
Ankara, TURKEY
e-mail:ozlem@rorqual.cc.metu.edu.tr

ABSTRACT: Radiation characteristics of infinitesimal dipole in multilayered circular cylindrical structure including gyromagnetic media are investigated. Transversal field equations in spectral domain are obtained for gyromagnetic medium in cylindrical coordinates. These expressions are formed into a set of linear differential equations. The solution at each layer is expressed in terms of state transition matrices. Fields are matched at the interfaces. Far fields are evaluated asymptotically. The effects of changing the bias field, the thickness of the layers, the frequency, and the medium parameters are examined.

INTRODUCTION: In recent years, there is a considerable interest in the interaction of electromagnetic waves with anisotropic media. Scattering from anisotropic circular cylinder has been analyzed in detail by many authors. However, radiation of sources from cylindrically layered structures with anisotropic layers has not been considered in all aspects yet. In [1], fields have been assumed not vary in axial direction, hence nonuniform transmission line expressions have been used. In [2], cylindrical wave functions have been used to analyze radiation from infinite longitudinal slot on an anisotropic dielectric coated conducting cylinder. In both of these papers, sources are infinite in axial direction resulting in no axial variation. The extension to the three dimensions greatly increases the complexity of the problem.

In this paper, far fields of an arbitrarily oriented source in multilayered cylindrical structure with ferrite are found using state-transition matrix approach, [3]. Source can be placed in any layer. All media are assumed linear and homogeneous. Since ferrite as a gyromagnetic material possesses dyadic permeability, more parameters which can affect the far fields, will be introduced. This provides additional degree of freedom to the design of the antenna. exp(jωt) time dependence is assumed and suppressed throughout the formulation.

FORMULATION: Geometry of the problem is shown in Fig.1. The inner layer is a perfect conductor with radius d_o, the outermost region $\rho>d_N$ is free space. In general, the i'th layer ($d_{i-1}<\rho<d_i$) is homogeneous gyromagnetic material. Gyromagnetic material can be characterized by dyadic permeability and scalar permittivity.

0-7803-3216-4/96$5.00 © 1996 IEEE

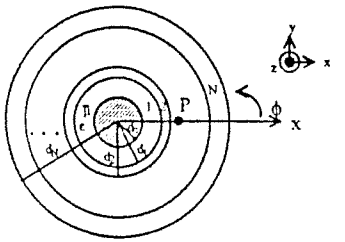

Figure 1. Geometry of the problem

For axially magnetized ferrite, the permeability tensor is given by

$$\overleftrightarrow{\mu} = \mu_o \begin{bmatrix} 1+\chi & j\kappa & 0 \\ -j\kappa & 1+\chi & 0 \\ 0 & 0 & 1 \end{bmatrix}, \chi = \frac{\omega_o \omega_m}{\omega_o^2 - \omega^2}, \kappa = \frac{\omega \omega_m}{\omega_o^2 - \omega^2}, \quad \omega_m = \gamma \mu_o M_s, \ \omega_o = \gamma B_o, \quad (1)$$

where $\mu_o M_s$ is the saturation magnetization constant of ferrite, ω is the angular operating frequency, γ is the gyromagnetic ratio, B_o is the applied magnetic field.

Maxwell's curl equations in gyromagnetic medium are decomposed into longitudinal (ρ) and transversal (transverse to ρ) components. In dielectric coating case, fields can be expressed as a superposition of TE and TM waves. However, in anisotropic coating, field components are coupled. The cylindrical transformation given by

$$\bar{E}(n, k_z) = \frac{1}{2\pi} \int_0^{2\pi} d\phi \int_{-\infty}^{\infty} dz \, \bar{E}(\rho, \phi, z) e^{-jn\phi} e^{-jk_z z},$$

$$\bar{E}(\rho, \phi, z) = \sum_{n=-\infty}^{\infty} e^{jn\phi} \frac{1}{2\pi} \int_{-\infty}^{\infty} \bar{E}(n, k_z) e^{jk_z z} dk_z, \quad (2)$$

is used to transform transversal field components. Transformed field components are formed into a set of linear differential equations

$$\frac{d}{d\rho}\psi(\rho) = A(\rho)\psi(\rho) + S, \quad (3)$$

where $\psi = \left[\bar{E}_z \ \ \bar{E}_\phi \ \ \bar{H}_z \ \ \bar{H}_\phi\right]^T$ and S is 4x1 source vector. Entries of 4x4 matrix A depend on the variable ρ. The general solution of this differential equation set can be expressed as, [3],

$$\psi_f(\rho) = \Phi(\rho, \rho_o)\psi_f(\rho_o) + \int_{\rho_o}^{\rho} \Phi(\rho, \lambda) S(\lambda) d\lambda, \quad (4)$$

where $\Phi(\rho, \rho_o)$ is the state transition matrix of the source free system. State transition matrix relates the tangential electric and magnetic fields at one interface to the other. Due to the ρ dependence, the state transition matrices are evaluated numerically. Fields in the free space are expressed as a series of Hankel functions of the second kind. Using the boundary conditions at the conductor, and at the interfaces between the layers, fields in free space are found. The inverse Fourier transforms can be evaluated using the Method of Steepest Descents to find far fields, asymptotically.

NUMERICAL RESULTS: The radiation patterns of an infinitesimal dipole in a multilayered cylindrical structure are presented in this section. In the given examples one of the layer is magnetized ferrite and the others are isotropic dielectrics. Radiation patterns for both axially and circumferentially magnetized ferrite layer have been obtained. In Fig.2, the radiation patterns of a half-wave narrow axial slot on a conducting cylinder coated by circumferentially magnetized ferrite are shown. It is observed that shape of the pattern changes and directivity increases when cylinder is coated by ferrite. Also, main beam direction changes with the strength of the magnetization field.

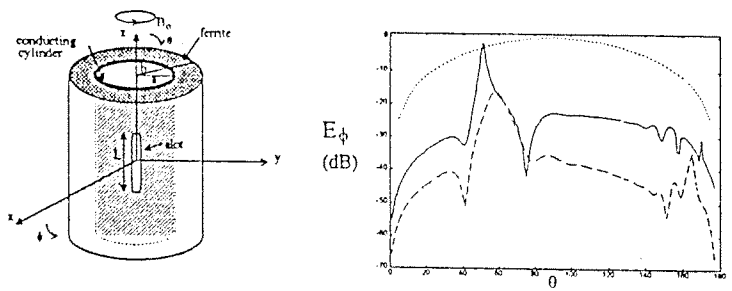

Figure 2. Geometry and radiation patterns of slot on ferrite coated conducting cylinder, f=18GHz, $\mu_o M_s$=0.3T, d_o=2λ, d_1-d_o=1.2mm, ε_f=14, solid line: ω_o/ω=0.75, dashed line: ω_o/ω=0.78, dotted line: without ferrite

In Fig.3 and Fig.4 the radiation patterns of infinitesimal dipole in the two layer cylindrical structure are shown. First layer is a magnetized ferrite and the second layer is a isotropic dielectric. The dipole is assumed to be placed at the point where $\rho = d_1$ and $\phi = 0$ at the interface of ferrite and dielectric. The orientation of the dipole can be $\hat{x}$, $\hat{y}$, $\hat{z}$ direction. In Fig.3, ferrite is magnetized circumferentially, whereas ferrite is magnetized axially in Fig.4. In circumferentially magnetized case, there is no cross polarized component. However there exits significant cross polarized component in axially magnetized case.

Radiation characteristics as a function of other parameters, such as thickness of layers, saturation magnetization value of ferrite, dielectric constants, have also been examined and will be presented in the symposium.

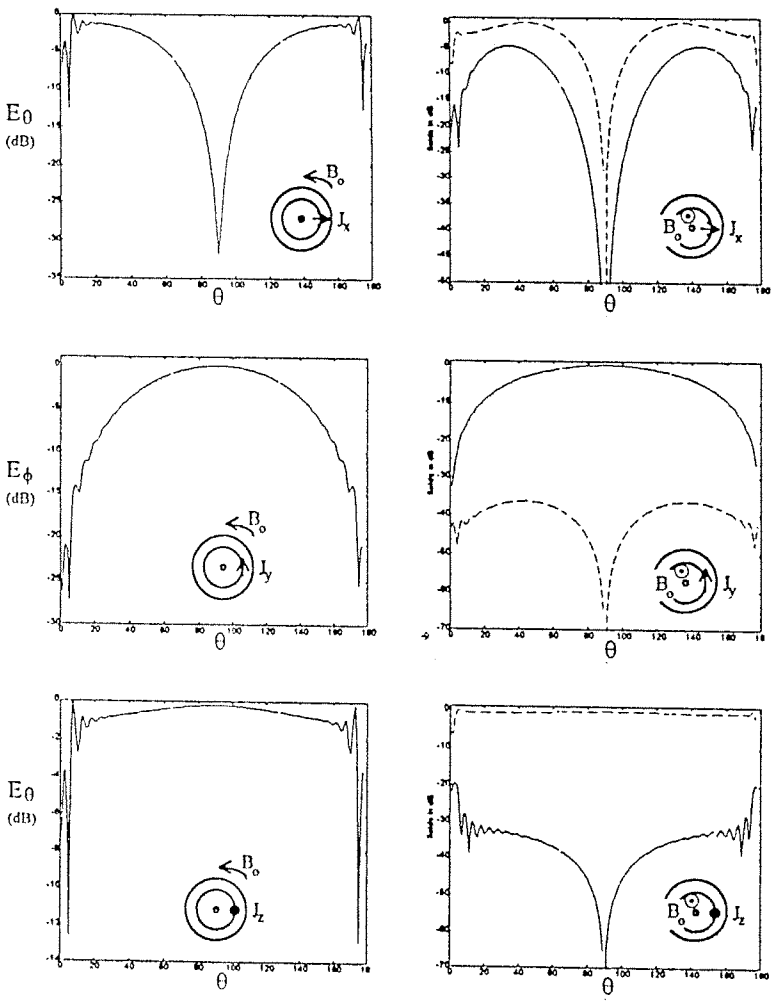

Fig.3. Far fields for circumferentially mag. ferrite Fig.4. Far fields for axially mag. ferrite
f=20GHz, $\mu_o M_s$=0.3T, d_o=2λ, d_1-d_o=1.2mm, d_2-d_1=1.2mm, ε_f=14, ε_d=12, ω_o/ω=0.07
(in Fig.4. solid line: E_ϕ component, dashed line: E_θ component)

REFERENCES:
[1] J.R. Wait, 'Transverse propagation of waveguide modes in a cylindrically stratified magnetoplasma', *Electromagnetic Waves in Stratified Media*, p.529-544, Pergamon Press.
[2] X.B. Wu and W. Ren, 'Axial slot antenna on an anisotropic dielectric-coated circular cylinder', *IEE Proc., Microwaves, Antennas, Propagation*, vol.141, no.6, p.527-530, Dec. 1994.
[3] P.M. Derusso, R.J. Roy and C.M. Close, *State Variables for Engineers*, Ch.6, John Wiley, 1967.

AN IMPROVED DESIGN OF 2-18 GHz VIVALDI ANTENNA AND A NEW DESIGN OF 6-18 GHz ANTENNA ARRAY

Erdal SAYGINER*, Hayrullah YILDIZ*, Altunkan HIZAL**

(*) ASELSAN Inc.Microwave and System Technologies Division Ankara, Turkey
(**) Middle East Technical University (M.E.T.U) Ankara, Turkey

The recent researches on microwave and millimeter wave technologies demand antennas those are compact, low cost, reproducible, planar and can be easily integrated with front end circuits on the same substrate. Vivaldi antenna is a member of the class of aperiodic continuously scaled traveling wave antenna structures and theoretically has an infinite instantaneous frequency bandwidth (1:20). It has a significant gain, low side lobe level, and symmetric end fire beam [1]. It is a planar, compact, low profile, low cost antenna. It is an exponentially tapered slotline antenna. The slotline is double sided and balanced [2]. At the input of the antenna a balun exists for transition from microstrip to balanced slotline.

Vivaldi antenna belongs to the class of slow traveling wave antenna and for that kind of structures radiation occurs only at nonuniformities, curvatures, and discontinuities. Discontinuities, can be distributed or discrete, interrupt a bound wave on the surface of the antenna and cause radiation. For Vivaldi antenna the radiation takes place when the slot width equals to the half of the free space wavelength of the radiation frequency. At that point phase velocity of the traveling wave is equal to the free space wave velocity. Vivaldi antenna is in principal a frequency independent antenna, for it has a scaled geometry, with frequency. However, since it should be truncated physically at a certain point, a lower cut off frequency for the antenna exists.

The feed structure of the antenna consists of an unbalanced microstip line, then followed by a suspended microstrip tapered balun, and ends with an equal width balanced line. All of them have a 50 Ohm characteristic impedance. Then double sided slotline radiating section follows (Figure1).

The design is the continuation of an earlier work [3] on a single Vivaldi antenna operating in 1-18 GHz frequency band. In this work, first a single antenna which operates on 2-18 GHz frequency band is re-designed. The antenna has a double sided slotline radiating part fed by a microstripline. There is a balun between the microstripline and double sided slotline. The balun has been also re-designed using a finite element program [7,8]. Afterwards the geometric structure is printed on a RT/duroid substrate. The input return loss (Figure2) and radiation characteristics of the antenna has been measured. Secondly a Vivaldi antenna that operates on 6-18 GHz frequency band has been designed using a similar feeding and radiating structure but this time the length of the balun has been decreased. The designed antenna is manufactured on a RT/duroid substrate. The return loss of the antenna is measured (Figure 3). It was observed that the results were not as good as expected. So, some experiments on the structure have been done and it is redesigned having a longer radiating part. The new design is realized in the form of an array by rearranging eight of these elements in a circular geometry. The array is manufactured on a single RT/duroid substrate. The input return loss of the of

the elements of the array has been measured and it is seen that it has better return loss characteristics than the previously designed single 6-18 GHz Vivaldi antenna (Figure 4). Also the radiation pattern and gain of some of the elements of the array have been measured (Figure 5,6,7).

The results of return loss and radiation characteristics measurements are found satisfactory. The designed and manufactured circular array can be used in monopulse amplitude or phase comparison DF systems. Another possible application is pattern configurable antenna. The idea is that a number of the elements of the array are used at a time to form a beam which can be steered by changing the elements of the beam forming array by means of electronic switching. The array design should include the antenna element spacings (antennas and radius) as a design parameter.

References

[1] Gibson, P.J., " The Vivaldi Aerial ".
9 th European Microwave Conference Proceedings,1979,pp.101-105.

[2] Gazit, E., " Improved Design of The Vivaldi Antenna".
IEE Proceedings Vol.-135, 1988 pp.89-92.

[3] Günalp N., Birand T., Hızal A., "Design of Tapered Slot Antennas with Broadband Feeds".
Contribution by the Turkish COST-223 Working Group METU (Turkey): Cost 223 Final Report.

[4] Birant T., et al., "Antennas in 1990`s: Active Antenna Array for Future Satellite and Terrestrial Communication".
Project Final Report for TUBITAK within the Frame Work of the COST-223 Project. January 1993 Ankara.

[5] Gvozdev, V.I., "Use of The Unbalanced Slotted Line in SHF Microcircuits".
Radio Eng. & Electron Phys., Vol.-27, 1982, pp. 42-47.

[6] Schiek, B., Köhler, J., " An Improved Microstrip-to-Microslot Transition."
IEEE Trans. Vol. MTT-24, 1976, pp. 231-233.

[7] Kuzuoğlu, M., " A New Finite Element Method for Electromagnetic Boundary Value Problems in Combined Exterior and Interior Regions".
Ph. D. Thesis in Elec. and Electron. Eng. METU., 1986.

[8] Akdeniz, T. " Analysis of Microstrip and Microstrip-like Structures by the Finite Element Method ".
A Master's Thesis in Elec. and Electron. Eng. METU., 1989.

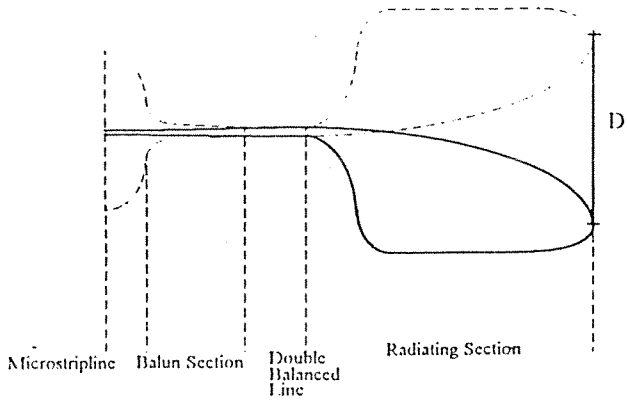

Figure 1 Improved Vivaldi Antenna

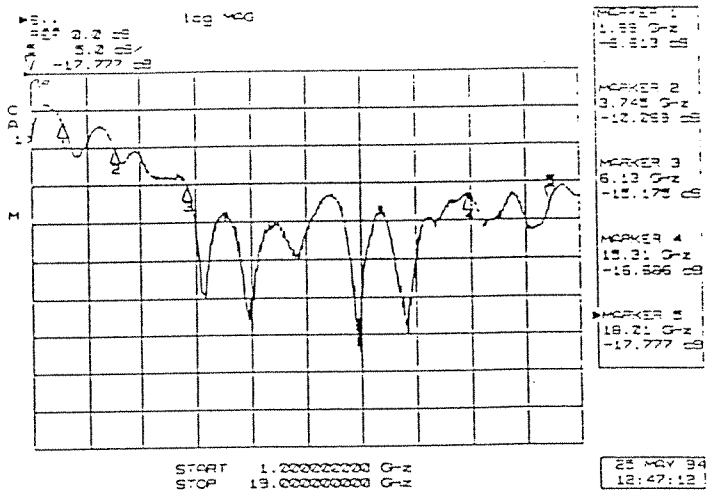

Figure 2 Return Loss Characteristics of 2-18 GHz Vivaldi Antenna

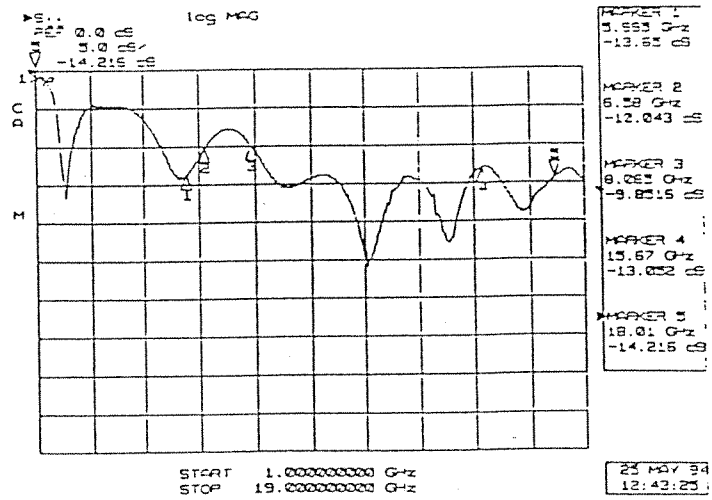

Figure 3 Return Loss Characteristics of 6-18 GHz Vivaldi Antenna

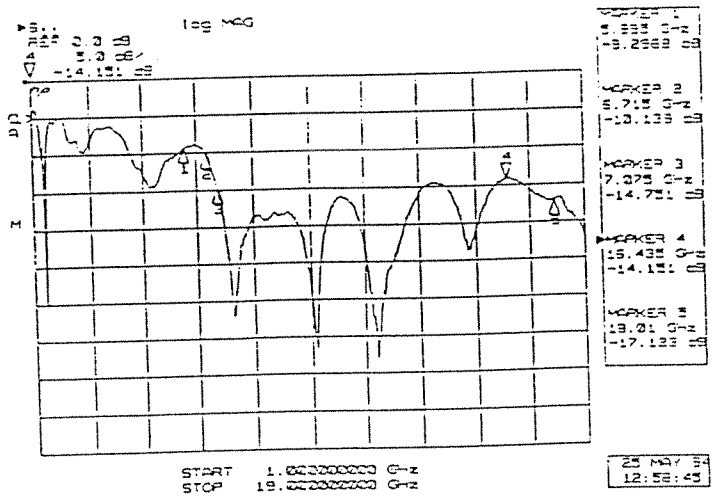

Figure 4 Return Loss Characteristics of an Array Element

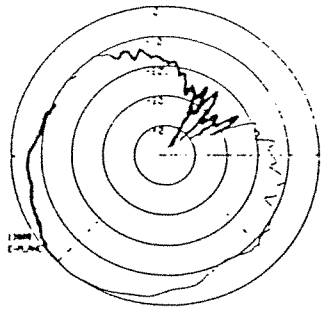

Figure 5 Radiation Pattern of an Array Element at 13 GHz.

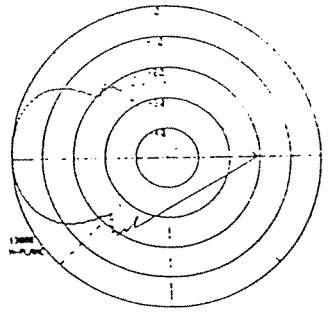

Figure 6 Radiation Pattern of an Array Element at 13 GHz.

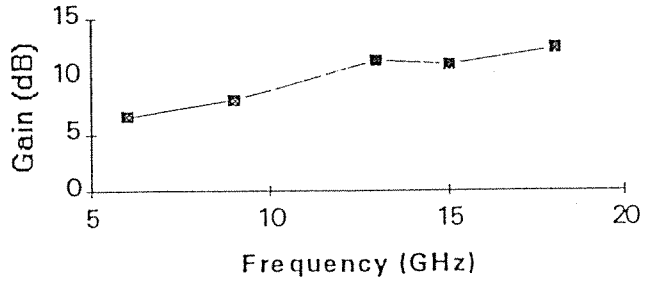

Figure 7 Gain Characteristics of an Array Element

MUTUAL COUPLING EFFECTS of FINITE RECTANGULAR PHASED ARRAYS

Hüseyin Yavuz and O. Merih Büyükdura
Middle East Technical University
Electrical & Electronics Engineering Department
06531 Ankara-Türkiye
Phone:90-312-210 1000(Ext.2362), Fax:90-312-210 1261
E-Mail: boran@vm.cc.metu.edu.tr

Abstract — A rigorous integral equation formulation for the analysis of a phased array of flange-mounted waveguide apertures is given for a finite number of elements and nonuniform spacings. The resulting set of integral equations is reduced to a matrix equation called the coupling matrix which relates the coefficients of all the modes in all the waveguides to one another. The solution then yields the dominant mode reflection coefficient, coefficients of scattered modes and hence the field in each waveguide. The block-Toeplitz symmetry property for the uniformly spaced linear and rectangular grid arrays is utilized in the solution of the system of equations.

Introduction

Flange mounted rectangular waveguides are the basic radiating elements of many microwave antennas. They find many applications in aeronautics, phased array systems as well as in diathermy and hyperthermia. They have been investigated both as single radiators and as coupled radiators.

The radiating aperture of the waveguide establishes a discontinuity for the incident dominant waveguide mode TE_{10}. The reflection coefficient of the dominant mode due to the aperture discontinuity depends upon the aperture admittance, which changes with the change in dimensions of the radiating aperture. The dominant mode is also coupled to higher order modes by this discontinuity, which have quite an important effect on the aperture field distribution especially near the edges. Coefficients of these higher order modes are also directly related to the aperture dimensions.

In phased arrays with a large number of elements, almost all of the elements have nearly the same active reflection coefficient. But the reflection coefficients of the elements near the edges are quite different from those of central elements. Infinite array approximations are valid for the large arrays. However, this approximation becomes less accurate for the smaller arrays. This is because of the mutual coupling characteristics of the elements. In a practical finite sized array, aperture admittance and hence the active reflection coefficient of elements strongly depend on the element location.

In this paper mutual coupling and evanescent mode effects on the performance of the flange-mounted finite rectangular waveguide arrays is presented.

Formulation

Consider the $M \times N$ element array of apertures backed by rectangular waveguides flange-mounted on an infinite, conducting ground plane. For the sake of simplicity the elements are spaced in a rectangular grid as shown in Figure 1 and each waveguide is assumed to be fed by the dominant TE_{10} mode phased accordingly with the desired scan angle.

The problem is divided into $M \times N + 1$ regions using the equivalence principle, that is the apertures are covered by a perfect electric conductor. Appropriate dyadic Green's functions are used to represent the fields in both waveguide and half-space regions. Then the solution is achieved by expanding the electric field at the apertures in terms of a linear combination of waveguide modes weighted by unknown coefficients. The continuity of transverse component of the magnetic field is then enforced. After inner multiplying the resulting equation with suitable testing functions (again waveguide mode distributions - essentially Galerkin's Method) a set of algebraic equations are obtained, which are reduced to a matrix equation. The matrix is called coupling matrix and it relates the coefficients of all the modes in all the waveguides to one another. The solution then yields the reflection coefficient for the dominant mode and through it the

0-7803-1772-6/94/$3.00

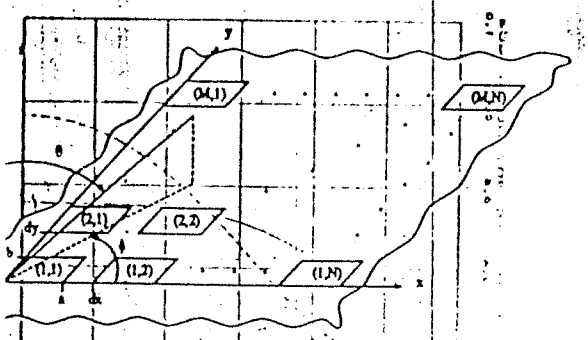

igure 1: $M \times N$ rectangular grid phased array.

ture admittance and the coefficients of the higher r modes excited by the aperture discontinuity of y elements. The detailed derivation of this analy- given in [1] and [2].

Computed Results

n earlier variational study [3] and in [2] the use of inant mode as the aperture distribution has been rn to be adequate for predicting the input admit- e of a single radiating waveguide. However, this is he case for the aperture field distribution.

flange-mounted single rectangular waveguide $a = 0.7\lambda$ and $\frac{a}{b} = 2.25$ is solved using differ- number of expansions for the electric field at the ture to examine the effect of evanescent modes ie equivalent magnetic current $\vec{M} = 2\vec{E} \times \hat{z}$ over perture. The coefficients of the 1 (TE_{10}) and 6 :10,12,30,32; TM:12,32) mode solutions are used otain $\vec{M}$ over the aperture as shown in Figures 2 3 respectively. It is seen that the magnitude of $\vec{M}$ ially near the edges of the waveguide is strongly ndent on the number of the expansion functions in the solution. This is due to the edge singular- aving a behaviour of $r^{-\frac{1}{2}}$ where r is the distance the edge of the aperture. It is expected that the tion pattern of flange mounted waveguide should be effected by higher order modes excited by the ure discontinuity.

he scattered mode coefficients (mode voltages) of ange termination of the same geometry are also lated and compared with those obtained by Bau- l et.al. [4] and McPhie et.al. [5] in Table 1 where greement is very good. As expected, the dom- TE_{10} reflected mode amplitude dominates the s. All the quantities in Table 1 are calculated 15 modes of expansion for the electric field in aveguide. The same geometry is solved using

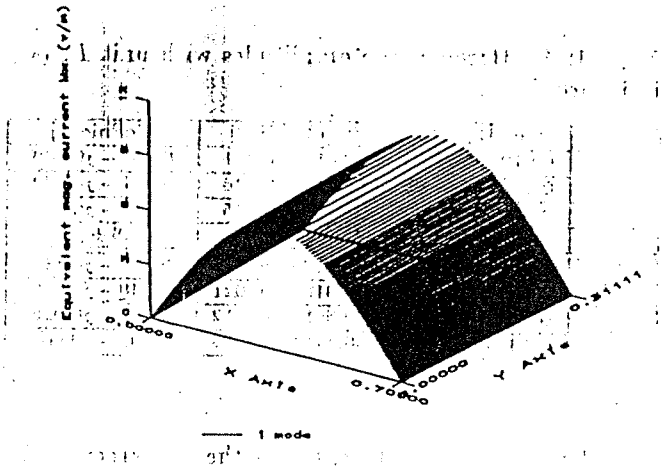

Figure 2: Aperture field distribution of flange mounted rectangular waveguide with 1 mode of expansion.

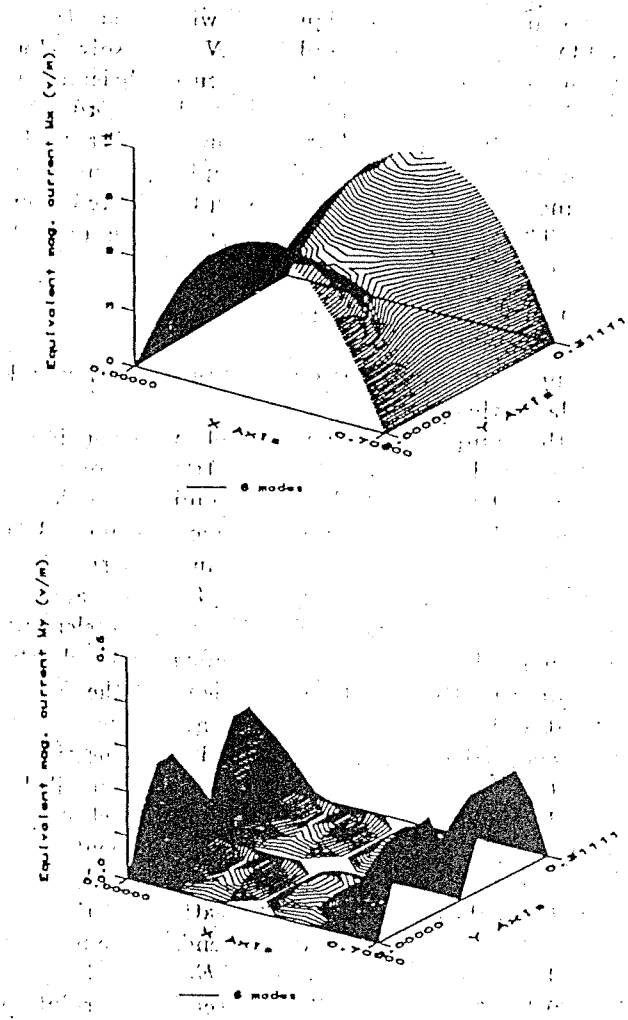

Figure 3: Aperture field distribution of flange mounted rectangular waveguide with 6 modes of expansion.

ble 1: Scattered mode amplitudes with unit TE_{10} idence

ode	Our Results	Baudrand [4]	McPhie [5]
E_{10}	$0.079 - j0.237$	$0.066 - j0.271$	$0.063 - j0.240$
E_{30}	$0.026 - j0.049$	$0.022 - j0.046$	$0.027 - j0.049$
E_{50}	$0.018 - j0.017$	$0.012 - j0.015$	$0.015 - j0.018$
E_{12}	$0.035 - j0.011$	$0.031 - j0.011$	$-0.033 + j0.032$
M_{12}	$0.194 - j0.108$	$-0.182 + j0.134$	$0.156 - j0.112$
M_{32}	$0.008 - j0.021$	$-0.010 + j0.021$	$0.048 - j0.020$
M_{52}	$0.007 - j0.011$	$-0.008 + j0.012$	$0.052 - j0.026$
M_{14}	$0.135 - j0.063$	$-0.128 + j0.069$	$0.101 - j0.063$

nodes of expansion to examine the convergence of e formulation. TE_{10} mode amplitude is found as $078 - j0.239$) which differs from the 15 modes solu- n by only about 0.6%.

The array given in Figure 1 with $a = dx = 714\lambda$, $b = dy = 0.254\lambda$ and $M = N = 5$ is solved for e dominant mode element reflection coefficients for th the E-plane and H-plane scans. The coordinate stem and variables used are also shown in Figure 1. ch waveguide is fed by a unit amplitude dominant E_{10} mode phased accordingly with the desired scan gle. The (m, n)'th element of the array is phased the scan angle (θ, ϕ) by

$$e^{jk(n-1)dx \sin\theta\cos\phi} e^{jk(m-1)dy \sin\theta\cos\phi}$$

anning is done in the H-plane when $\theta = 0$ or π and E-plane when $\theta = \pm\frac{\pi}{2}$.

In the computations 6 modes of expansion func- ns are used to represent the electric field over the ertures. The magnitude of the dominant mode re- ction coefficients of the center element (element 3,3) d corner elements (elements 1,1 and 5,5) are given Figures 4 and 5 as a function of E-plane and H- ane scan angle, respectively. The effect of element cation and hence the mutual coupling is seen clearly comparing the reflection coefficients of the center ement and corner elements both in E-plane and H- ane scans given in Figures 4 and 5, respectively. nus, the radiation pattern of the array also will be ected by the mutual coupling of the array elements.

The tangential electric field in the element aper- res is determined for 0° scan angle for the pur- se of calculating the radiation pattern. The accu- cy of this representation will depend on the number modes used. Again 1 mode (TE_{10}) and 6 modes (E:10,12,30,32; TM:12,32) are used for the solution the electric field in the apertures in which the mu- al coupling between all the modes in all the waveg- des is taken into account to examine the effect of gher order modes excited by the aperture discontinu-

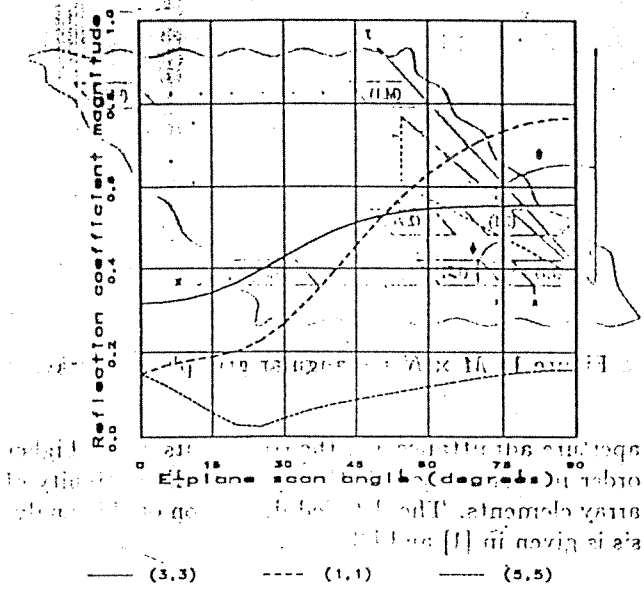

Figure 4: Dominant mode reflection coefficients of elements (1,1), (3,3) and (5,5) of the 5 × 5 array as a function of E-plane scan angle.

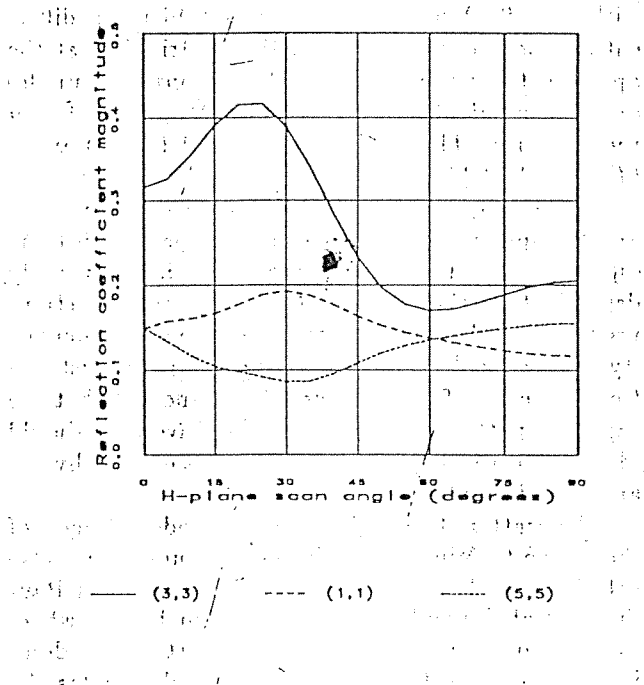

Figure 5: Dominant mode reflection coefficients of elements (1,1), (3,3) and (5,5) of the 5 × 5 array as a function of H-plane scan angle.

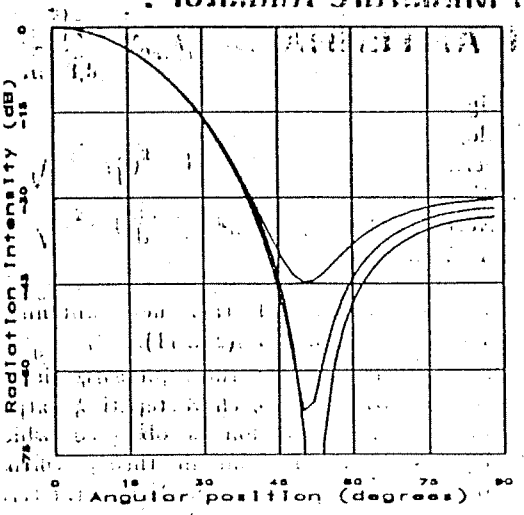

ure 6: Radiation intensity as a function of angular ition θ, $\phi = 90°$ where solid : 1 mode without tual coupling, dotted : 1 mode and dashed : 6 des solutions.

to the radiation pattern of the array. In addition to se two types of electric field distribution, dominant de (TE_{10}) electric field distribution is assumed to st over the apertures ignoring the mutual coupling ween the array elements to show the effect of mu- l coupling on the radiation pattern.

Far field radiation intensity $| H_\theta(\theta,\phi) |^2 + | (\theta,\phi) |^2$ is calculated for the above three types of rture field distributions as a function of angular ition θ for $\phi = \frac{\pi}{2}$ and presented in Figure 6. In figure, the solid and dotted lines are obtained us- dominant mode aperture field distribution without l with the effect of mutual coupling, respectively, ile the dashed line is obtained using 6 modes of ex- nsion for each aperture field distribution. As shown Figure 6 a notch is seen when mutual coupling be- en the array elements is ignored while the other two utions have no such behaviour. This is because of mutual coupling effects. The effect of evanescent des is also important as shown in Figure 6 where a node solution (dashed line) is about 20 dB below the node solution (dotted line) around $\theta = 52°$. This erence is too large to ignore.

Conclusion

e most expensive part of the solution is the calcula- n of the matrix elements via numerical integration. wever, if an equally spaced linear or a rectangu- grid array is of interest the resulting coupling ma- x is block-Toeplitz and each Toeplitz block has also ne symmetry. The cpu time and the storage area required for the solution of the problem are highly reduced when these symmetry properties are used. No matrix inversion is carried out to reduce the numerical errors incurred in the calculations for rectangular grid arrays but a recursive algorithm is used to solve the block-Toeplitz system.

Another important feature of the formulation is that the coupling matrix is independent of excitation of array elements, so it is calculated and inverted only once for the specified geometry of the array. Then the response of the array for any kind of excitation is found using the same matrix.

References

[1] H. Yavuz and O. M. Büyükdura, 'Rigorous analysis of finite rectangular arrays with simultaneous integral equations', Proc. of IEEE APS international symposium, 3, 1262, Ann Arbor MI, (June, 1993).

[2] H. Yavuz 'Analysis of flange-mounted finite rectangular waveguide arrays', Ph.D Dissertation, Middle East Technical University, December 1993.

[3] M. H. Cohen et al., 'The aperture admittance of a rectangular waveguide radiating into half-space', Antenna Lab., Ohio State Univ. Res. Foundations, Rep. No. 339-22, Contract USAF W33-038-ac-21114 (November, 1951).

[4] H. Baudrand et al., 'Study of radiating properties of open-ended rectangular waveguides', IEEE Trans. AP, 36, 1071 (August, 1988).

[5] R. H. MacPhie and A. I. Zaghloul, 'Radiation from a rectangular waveguide with infinite flange-exact solution by the correlation matrix method', IEEE Trans. AP, 28, 497 (July, 1980).

MMIC TEKNOLOJİSİ KULLANILARAK TASARIMLANMIŞ VOLTAJ KONTROLLÜ OSİLATÖR

S.Cüneyt BİRDİR
ASELSAN AŞ.. MST GRUBU. P.K. 101.
Yenimahalle. 06172 ANKARA

Nilgün GÜNALP
ORTA DOĞU TEKNİK ÜNİVERSİTESİ. Elektrik-Elektronik Müh. Bölümü. 06531 ANKARA

ÖZET: Bir mikrodalga voltaj kontrollü osilatör (VCO) devresi. devre elemanlarının tek bir taban üzerine inşa edilerek gerçekleştirildiği monolitik mikrodalga entegre devre teknolojisi (MMIC) kullanılarak tasarımlanmış ve GEC Marconi firmasının F20 tasarım kurallarına uygun olarak bu firmaya imal ettirilmiştir /1/. Kontrol voltajı 1V ile -8V arasında değişen VCO. 9.295GHz-11.028GHz bandında osilasyon göstermektedir.

I.GİRİŞ

MMIC teknolojisi hızla gelişen bir teknoloji olup. askeri ve ticari alanlardaki mikrodalga sistemlerde önemli ölçüde kullanılmaya başlanmıştır. Bu teknolojide GaAs MESFET'ler ve diğer devre elemanları tek bir GaAs taban üzerinde üretilmektedir. Düşük fiyatlarla çok sayıda üretimlerin yapılabilmesi, yüksek performans, tekrar edilebilir üretim, küçük hacim ve güvenilirlik gibi özellikler MMIC devrelerine büyük avantajlar sağlamaktadır. Bu avantajlar yüzünden çeşitli şoklara, ısı değişimlerine ve sert sarsıntılara dayanabilen MMIC devreleri. uzay bilimleri ve askeri teknolojilerde pek çok uygulama alanı bulabilmektedir /2/.

Bu çalışma bir MMIC voltaj kontrollü osilatörün tasarımını anlatmakta, simülasyon sonuçları ile ölçüm sonuçlarını karşılaştırmaktadır. Osilatör tasarımı negatif direnç teorisine dayanmakta olup, aktif eleman olarak GaAs MESFET transistör seçilmiştir. Tasarımdaki optimizasyon ve analizlerde doğrusal olmayan simülasyon sonuçları önem taşıdığı için LIBRA simülasyon programının harmonik balans analiz yöntemi kullanılmıştır. Devre elemanlarının taban üzerine yerleşimi (layout) için ise CADENCE (Artist) yazılım programından yararlanılmıştır.

II.VCO TASARIMI

GEC Marconi firmasının elemanlarıyla tasarımı yapılan /3,4/ VCO'nun şematik gösterimi Şekil 1'de. layout gösterimi ise Şekil 2'de verilmiştir. Layout için kullanılan alanın sınırlı olması nedeniyle devre bir MMIC LNA'nın iki toprak via'sını kullanmaktadır. Bu negatif direnç osilatöründe toplam 300 µm gate genişliği olan 4 parmaklı (4×75) MESFET aktif eleman olarak kullanılmıştır. Gate girişinde görülen negatif direnç, FET'in source bacağından yapılan kapasitif geri besleme ile elde edilmiştir. Osilasyon frekansını belirleyen değişken kapasite (varaktör) yine Marconi'nin 4×75'lik MESFET'i ile oluşturulmuştur.

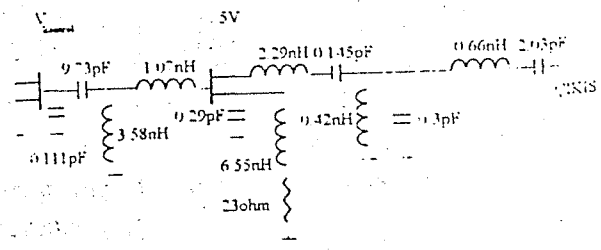

Şekil 1. VCO'nun Şematik Gösterimi

Drain ve source çıkışları birleştirilerek toprağa çekilen transistör, gate girişindeki besleme voltajı ile değişen gate - source.

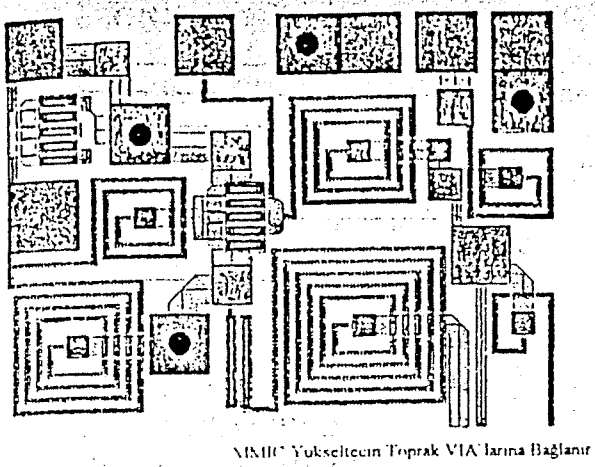

Şekil 2. VCO'nun Layout Gösterimi

kapasitesi ve eklenen paralel bir kapasite yardımı ile istenen değerlerde değişebilen voltaj kontrollü bir kapasite olarak kullanılmıştır. Gate girişi negatif beslenen MESFET, seri bir direnç R ve kapasite C kombinasyonu ile modellenebilir. Eklenen paralel kapasite C' (Şekil 3) ise girişte görünen empedansı şu şekilde etkilemektedir:

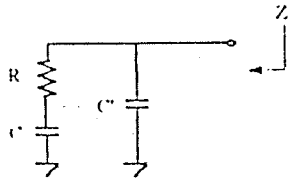

Şekil 3. Varaktör Eşdeğer Devresi

$$Re\{Z\} = \frac{RC^2}{\omega^2 C^2 C'^2 R^2 + (C+C')^2} \qquad (1)$$

$$Im\{Z\} = \frac{-\omega^2 C^2 C' R^2 - (C+C')}{\omega^3 C^2 C'^2 R^2 + \omega(C+C')^2} \qquad (2)$$

Bu empedans yine frekansa bağımlı bir direnç R_v ve ona seri bir kapasite C_v olarak ifade edildiğinde R_v ve C_v değerleri aşağıdaki gibi olur:

$$R_v = \frac{RC^2}{\omega^2 C^2 C'^2 R^2 + (C+C')^2} \qquad (3)$$

$$C_v = \frac{\omega^2 C^2 C'^2 R^2 + (C+C')^2}{\omega^2 C^2 C' R^2 + (C+C')}. \qquad (4)$$

10GHz'deki simülasyon sonuçlarına göre, varaktör devresinin girişinde görülen direnç ve kapasite değerleri Tablo 1'de kontrol voltajının bir fonksiyonu olarak verilmiştir.

Tablo 1. Varaktör Eşdeğer Devresi

V_{gate} (V)	R_v (Ω)	C_v (pF)
0.5	4.59	1.268
0.0	3.49	0.857
-1.0	2.94	0.633
-2.5	2.60	0.532
-10	2.35	0.416

Rezonatör devresi varaktör ile birlikte osilasyon frekansını tayin eder. Besleme devresi, drain akımı $I_{dss}/2$ olacak biçimde ayarlanmıştır. Geri besleme devresindeki kapasite iki adet polyimide kapasitenin paralellenmesiyle oluşturulmuş, böylelikle parazitik etkiler azaltılmış ve layout alanı daha etkin bir şekilde kullanılmıştır. Çıkıştaki bant geçiren filtre, harmonik frekansları önlemek amacıyla eklenmiştir. LIBRA'da devre simülasyonu yapabilmek için, pasif Marconi elemanlarının parazitik etkilerini de içeren elektriksel modelleri kullanılmıştır. Bu yüzden spiral bobinler, silikon nitrat ve poliyimide kapasiteler, ideal elemanlardan oluşan küçük alt devreler halinde simülasyona sokulmuşlardır. MESFET'ler için ise LIBRA'ya uygun, lineer olmayan Curtice-Cubic transistör modeli kullanılmıştır /5/. Tasarımı LIBRA'da incelemek için, programın OSCTEST /6/ adlı elemanı ana eleman olarak kullanılmıştır. Bu eleman kullanıcıya bir AC sinyalin asıl bileşenini geri besleme döngüsüne verme imkanı sağlayarak, osilasyon frekansı ve çıkış gücünü bulmaya yarar. Elemanın tasarımı, devrenin doğal durumunu bozmayacak şekilde yapılmıştır.

Yapılan büyük işaret teknikli simülasyon sonuçlarına göre başlangıç (çok küçük bir AC sinyal uygulamasıyla yapılan lineer olmayan simülasyon tekniği ile bulunmuştur) ve kalıcı durum osilasyonları Tablo 2'de görülmektedir.

Tablo 2. VCO'nun Osilasyon Durumu

$V_{kontrol}$ (V)	$f_{başlangıç}$ (GHz)	$f_{osilasyon}$ (GHz)	Çıkış Gücü (dBm)
0.5	9.46	8.79	12.54
0	9.62	9.27	13.14
-0.5	9.72	9.60	12.70
-1	9.80	9.71	12.45
-1.5	9.83	9.82	12.18
-2	9.88	9.88	12.06
-2.5	9.90	9.92	11.90
-10	10.15	10.15	10.95

Üretimi tamamlandıktan sonra gelen devre üzerinde BİLKENT Üniversitesi'nde yapılan ölçüm sonuçları Tablo 3'de verilmiştir. Bu ölçüm sonuçlarına kablo ve konnektör kayıpları da dahil olduğu için değerlendirme yapılırken çıkış gücüne bu kayıp kadar daha güç eklemek gerekir. Şekil 4 ve 5 kontrol voltajının 0.25V adımlarla 1V ile -10V arasında taratılmasıyla elde edilmiştir. Şekil 6 spektrum analizörde "hold maksimum" modunda kaydedilmiştir. Besleme hatlarında şok bobinler olmadığı için besleme kablolarının etrafına yüksek permeability (μ) 'si olan maddeler konulmuştur.

Tablo 3. VCO'nun Osilasyon Frekansları, Çıkış Güçleri ve Besleme Akımları (Drain Besleme Voltajı 5V)

$V_{kontrol}$ (V)	f_{osc} (GHz)	$P_{çıkış}$ (dBm)	$I_{besleme}$ (mA)
1.0	9.295	6.33	32.7
0.5	9.592	7.67	31.3
0.0	10.040	7.67	29.3
-0.5	10.311	8.00	27.7
-1.0	10.488	8.00	26.6
-1.5	10.674	7.50	25.9
-2.0	10.928	5.50	25.9
-3.0	11.010	5.17	25.9
-4.0	11.016	4.83	25.9
-5.0	11.019	4.50	25.9
-6.0	11.022	4.33	25.85
-8.0	11.028	3.67	25.8

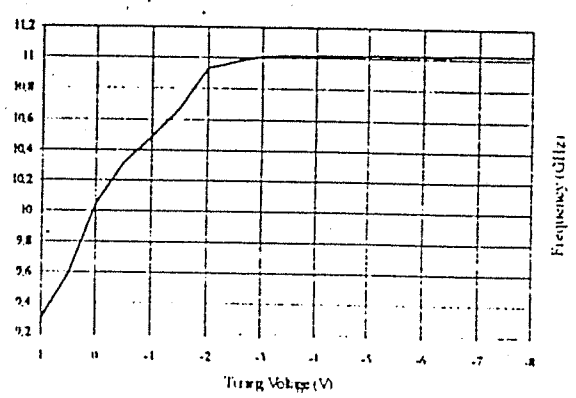

Şekil 4. Kontrol Voltajına Karşılık Osilasyon Frekansı

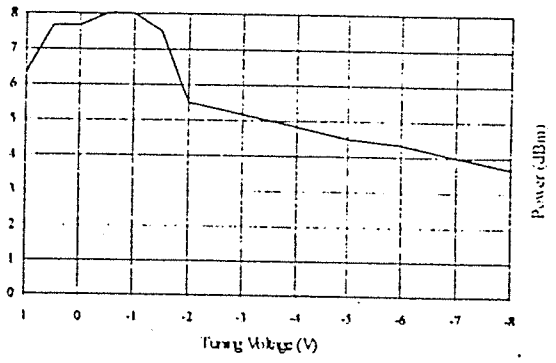

Şekil 5. Kontrol Voltajına Karşılık Çıkış Gücü

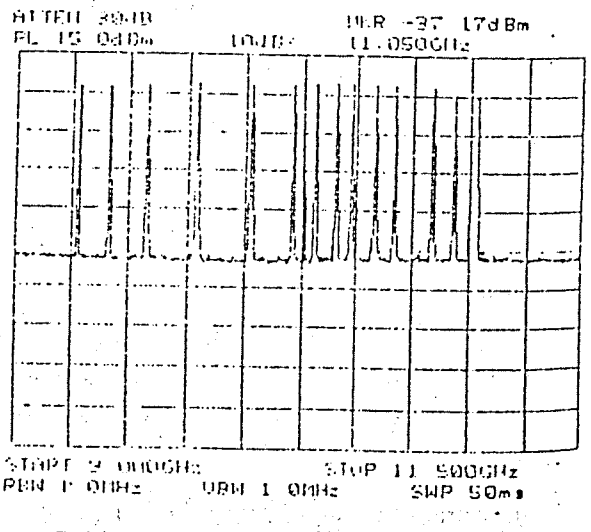

Şekil 6. Hold Maksimum Modunda Spektrum Analizör Çıktısı (Kontrol Voltajı 0.25V Adımlarla 1V ile -10V Arasında Taratıldı)

III.SONUÇ

Bir MMIC VCO tasarlanıp imal edilmiştir. 9.295GHz ile 11.028GHz arasında osilasyon gösteren VCO, 1V ile -8V arasında değişen DC voltaj ile kontrol edilmektedir.

REFERANSLAR:

1/ S. C. Birdir, Design of Microwave Voltage Controlled Oscillators Using MMIC Technology, Ms. Thesis, (1994).

2/ A. Sweet, MIC & MMIC Amplifier and Oscillator Design, Artech House, Boston, (1990).

3/ K. Kurokawa, "Some Basic Characteristics of Broadband Negative Resistance Oscillator Circuits", The Bell System Technical Journal, 1937, (July-August, 1969).

4/ GaAs IC Foundry Design Guide Process F20/F14, GEC Marconi, (1993).

5/ S. A. Maas, Nonlinear Microwave Circuits, Artech House, Boston, (1988).

6/ EESOF Element Catalog, Version 3.5, (November, 1982).

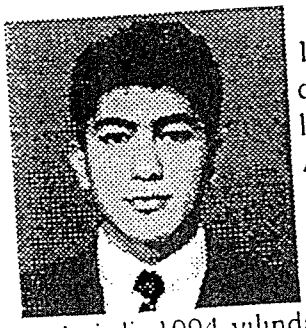

S.Cüneyt BİRDİR 1970 yılında Ankara' da doğdu. İlk, orta ve lise öğrenimini Ankara'da tamamladı. 1992 yılında ODTÜ Elektrik-Elektronik Mühendisliği Bölümü' nü bitirdi. 1994 yılında MMIC VCO konulu tezi ile yüksek lisans derecesi aldı. 1992-1994 yıllarında ODTÜ' de mikrodalga sistemleri grubunda araştırma görevlisi olarak çalıştı. Halen Aselsan A.Ş.'de elektronik yüksek mühendisi olarak görev yapıyor.

MMIC TEKNOLOJİSİYLE DÜŞÜK GÜRÜLTÜLÜ YÜKSELTEÇ VE ANTEN ANAHTARI TASARIMI

Fatih ÜSTÜNER*, Nilgün GÜNALP**
* TÜBİTAK Marmara Araştırma Merkezi, Gebze, KOCAELİ
e-mail: ustuner@ yunus.mam.gov.tr
**ODTÜ Elektrik-Elektronik Mühendisliği, ANKARA
e-mail:nilgun-gunalp@metu.edu.tr

STRACT

this work, a low noise amplifier and an antenna T/R tch are designed for a 1.9 GHz wireless nmunication system in monolithic microwave grated circuit (MMIC) form. The designed circuits e manufactured abroad. The active matching is d in the design of the LNA. Moreover an mmetric circuit topology is proposed for the T/R tch. The minimum usage of the wafer area without rificing from electrical performance is one of the in purposes. The similarity between the simulation measurement results shows that this purpose can realizable.

GİRİŞ

MMIC teknolojisi köken olarak öncelikle X-nd ve yukarı frekanslar için GaAs yarı-iletkeninin sek frekanstaki üstün özelliklerinden yararlanılarak iştirilmiştir. Başlangıçta MMIC devreler sadece keri sistemler için geliştirilmiş, yüksek maliyeti sivil temlerde kullanılmasını engellemiştir. Bununla ikte 90'lı yıllarda gittikçe yaygınlaşmaya başlayan siz hücresel iletişim sistemlerinin (GSM, PCN, CT gibi) tümleşik devreler için büyük pazar adetmesi, MMIC teknolojisinin sivil sistemlere de nelmesini sağlamıştır. Bu sistemlerde, silikon yarı-keni kullanılarak yapılması oldukça zor olan RF vrelerin (düşük gürültülü yükselteçler, anten ahtarları, güç yükselticileri, karıştırıcılar, osilatörler) MIC formunda gerçekleştirilmesi hedeflenmiştir. Bu ışmada bu yönelimin etkisinde yola çıkılarak 1.9 z'de çalışan bir telsiz iletişim sistemi için LNA ve ten anahtarı iki ayrı MMIC devre olarak arımlanmıştır.

DÜŞÜK GÜRÜLTÜLÜ YÜKSELTEÇ TASARIMI

Amaç

Amaç istenen elektriksel özelliklere en düşük nga alanında ulaşmaktır. Kazancın 13 dB civarında, rültü faktörünün ise 3 dB'den az olması deflenmiştir. Ayrıca giriş ve çıkış dönüş kayıplarının dB'den iyi olması istenmiştir. İşletim frekansı 1.9 z 'dir. Devrenin 400 Mhz' lik (%20) bir band genişliğinde en fazla 1 dB'lik bir değişimle belirlenen kazancı vermesi istenmiştir.

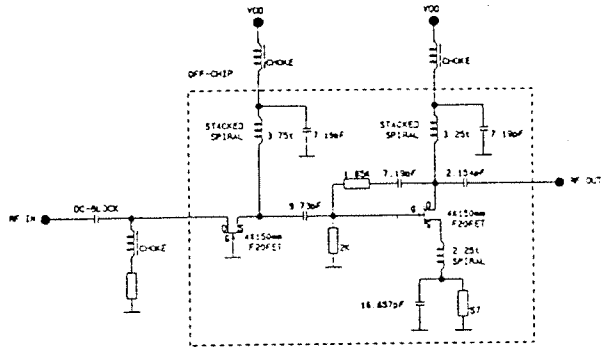

Şekil: 1 Düşük Gürültülü Yükselteç Devre Şeması

b) Tasarım

Devrenin giriş tarafında aktif uyumlama kullanılmıştır. Aktif uyumlama ortak-kapı konfigürasyonundaki FET'in düşük giriş yansıma katsayısı özelliğinin kullanılmasıyla ortaya çıkan bir uyumlama metodudur[1]. GaAs MESFET ortak-kaynak konfigürasyonunda yüksek kazançlı ve düşük gürültülü çalışırken, ortak-kapı konfigürasyonunda iyi bir giriş uyumlama özelliği gösterir.

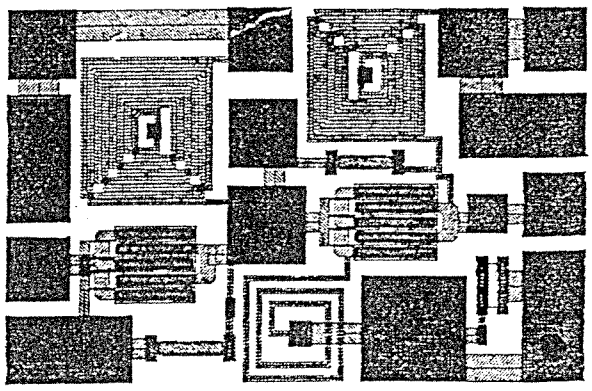

Şekil: 2 LNA Devre Yerleşim Planı

Tasarımlanan yükseltici (Şekil 1) iki kattan ışur: Birinci kat sonraki katın girişini uyumlamak ıacıyla kullanılan bir ortak-kapı yapısındadır. İkinci bir ortak-kaynak FET şeklindedir ve LNA'nın esas kseltici kısmını oluşturur. Optimum gürültü uyum ıpedansını eşlenik giriş uyum empedans seviyesine tirmek için ortak-kaynak FET'in kaynağında seri düktif geri besleme kullanılmıştır[2]. Ayrıca, ortak-pı FET, savakına bağlanan bir dirençle kararlı hale tirilmiştir. Bir bobin kullanımı yoluyla ortak-kapı tının eşlenik uyumlu çıkış empedansı ortak-kaynak tının eşlenik uyum giriş empedansına getirilmiştir. tak-kaynak FET katının çıkışı bir L-tipi yüksek çirgen yapı kullanılarak sistem empedansına umlandırılmıştır. Daha sonraki aşamada, gerçek MIC elemanlar modellenerek devredeki yerlerine onulmuş ve devre belirlenen hedefler çerçevesinde otimize edilmiştir.

Devrenin yerleşim planı Şekil 2'de örülmektedir. İşletim frekansı düşük olduğundan rim alana düşen eleman yoğunluğu yüksek ıtulmuştur. Yonganın boyutları 1.18X0.74 mm (0.9 mm^2) 'dir.

) Simülasyon ve Ölçüm Sonuçları

Devre simülasyonu Libra ortamında erçekleştirilmiştir. Devre tepkeleri HP8510C devre nalizörü kullanılarak Bilkent Üniversitesi'nde lçülmüştür. Simülasyon ve ölçüm sonuçları Şekil 'de verilmiştir.

Simülasyon sonuçlarına göre kazancın 0.5 dB eviyesinde değişiklikler gösterdiği band genişliği 600 Mhz'dir. Bandın ortasında elde edilen kazanç 14 dB, iriş ve çıkış dönüş kayıpları 14 dB'den daha iyidir. Gürültü seviyesi 3 dB'den iyidir. Kararlılık analizleri onucu yükselticinin 20 Ghz'e kadar kararlı olduğu örülmüştür.

Ölçüm sonuçlarına göre kazanç yaklaşık 1.5 Ghz'lik bir bandda 12.5 dB civarındadır. Prob kayıplarını göz önüne alırsak, öngörülen kazanç değerinin 0.5 db altına düşüldüğü, bununla birlikte band genişliğinin 600 Mhz'i aşıp 1.5 Ghz olduğu tesbit edilmiştir. S_{11} parametresinin simülasyon sonucunu aynen takip ettiği görülmüş, ayrıca öngörülenden çok daha iyi bir sonuca ulaşıldığı tesbit edilmiştir. S_{22} parametresi için de benzer yorum yapılabilir.

III. ANTEN ANAHTARI

a) Amaç

Anten anahtarını tasarımlarken gözetilen amaç yine maliyet etkin yani elektriksel performansdan fazla ödün vermeksizin en küçük yonga alanının kullanılması olmuştur.

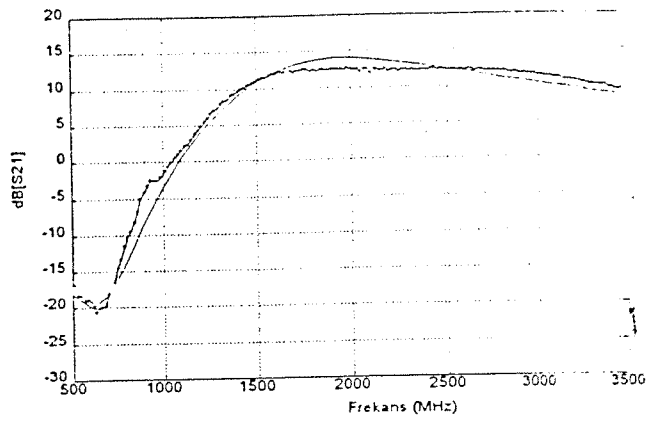

(a)

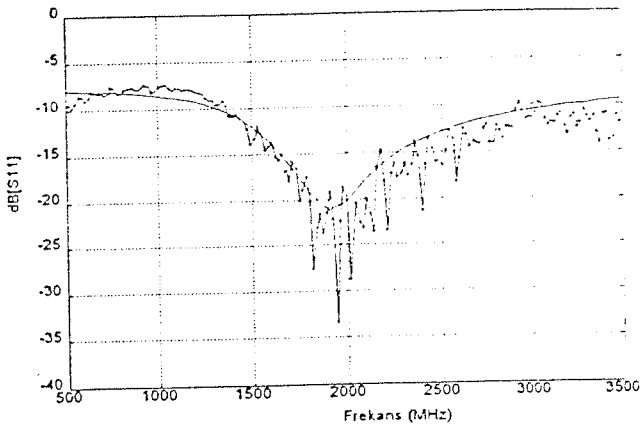

(b)

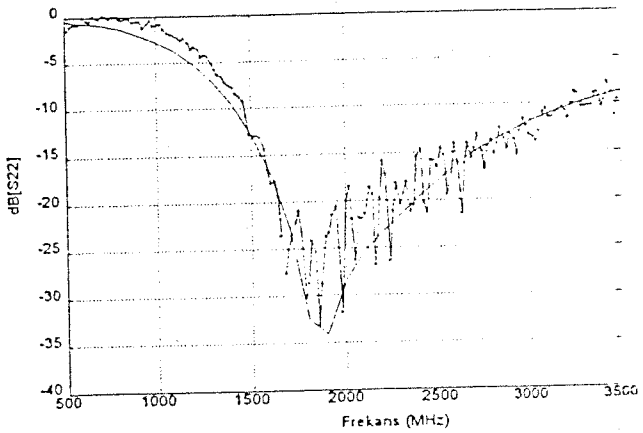

(c)

Şekil: 3 Ölçüm (—o—) ve Simülasyon (——) sonuçları

(a) Kazanç (S_{21})
(b) Giriş Dönüş Kaybı (S_{11})
(c) Çıkış Dönüş Kaybı (S_{22})

Bu çalışmamızda, TX-ANT araya giriş ının 0.3 dB'den düşük olmasını, ANT-RX araya kaybının 1 dB'den düşük olmasını, TX-RX ndaki izolasyonun 20 dB'den iyi olmasını ve n anahtarının 400 mW gücü üzerinden ebilmesi hedeflenmiştir (TX gönderici giriş inalini, ANT anten terminalini, RX alıcı çıkış inalini belirtir.)

asarım

Telsiz sistemi anten anahtarı aslında tek plu çift yönlü (SPDT) bir anahtar olarak tasnif bilir. SPDT olarak yapılan genel amaçlı MMIC n anahtarları ise hem TX hattında hem de RX nda aynı devre topolojisini (Şekil 4.a) kullanırlar. iz uygulamalarında, TX-ANT hattındaki araya giriş ının azaltılması ANT-RX hattındaki araya giriş ının azaltılmasından daha önemlidir. Bu nedenle l 4.b'de verilen asimetrik devre topolojisi ilmiştir.

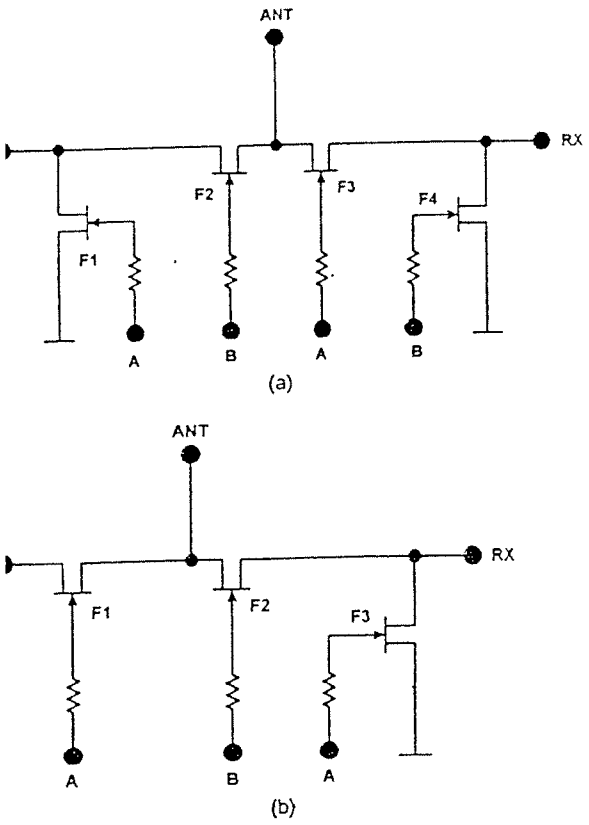

il: 4 (a) Genel Amaçlı SPDT RF Anahtarı Yapısı
(b) Önerilen Anten Anahtarı Yapısı

Devre topolojisinin belirlenmesinden sonraki ma, kullanılacak FET'lerin eşdeğer devrelerinin n açık hem de kapalı konumda) tesbiti ve devre nanlarının FET'in kapı genişliğine oranlı değerlerini nak oldu. Anahtarlama elemanı olarak, FET'lerin n açık hem de kapalı konumları birbirinin benzeri ok eşdeğer devre ile modellenmiştir[3,4,5]. Açık konumda devreyi belirleyen en önemli eleman R_{ON} direncidir. Kapalı konumdaki önemli eleman ise savak ile kaynak arasında oluşan kapasiteyi modelleyen C_{ds}'tir. Her ne kadar bu iki eleman devrenin elektriksel performansına egemen ise de modellerdeki diğer elemanlarında bulunması devre performansının daha kesin doğrulukta tahmin edilmesini sağlayacağından eldeki FET bilgileri[6] çerçevesinde diğer elemanlarda bulunmuştur. Amaçlar çerçevesinde üç FET'in kapı genişlikleri optimize edilmiştir. Bir diğer amaç olan anahtarın 400 mW gücü kaldırabilme yeteneği ise FET'lerin bu güç seviyesinde devredeki akım ve gerilime dayanıklı olmalarıyla ilgilidir. Seçilen ve optimize edilen FET'lerin istenen güç seviyesinin üstünde bir seviyeye dayanıklı oldukları tesbit edilmiştir.

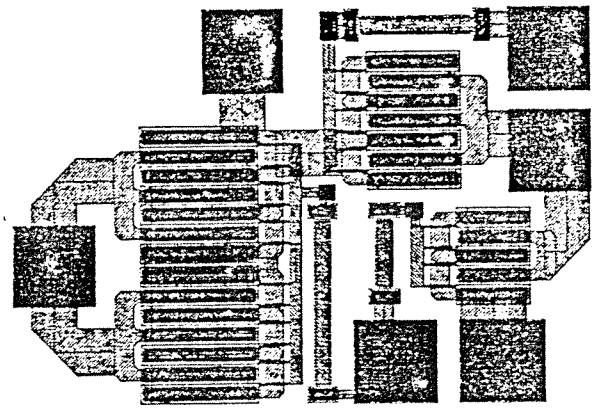

Şekil: 5 Anten Anahtarı Yerleşim Planı

Devre yerleşim planı (Şekil 5) 0.86X0.585 mm bir diğer deyişle 0.5 mm^2'lik alan kaplamaktadır. 3 numaralı FET'in kaynağı toprağa çekilmemiş böylece devrenin pozitif gerilimle çalışabilmesi mümkün olmuştur.

c) Simülasyon ve Ölçüm Sonuçları

5 adet numune devrenin ölçümü devreleri üreten firmanın laboratuvarlarında yapılmıştır. 5 devrede de elde edilen sonuçlar benzerdir. Devrenin TX-ANT araya giriş kaybı simülasyon ve ölçüm sonuçları (Şekil 6) birbirini son derece yakından izlemektedir. Sadece işletim frekansı civarında ölçüm sonucunun beklenenden biraz daha kötü olduğu görülmektedir. AT-RX araya giriş kaybı ise beklenenden biraz daha iyi çıkmıştır. TX-RX arasındaki izolasyonun simülasyon sonuçları 30 dB'den daha iyi bir dereceye sahip gözükmektedir. Karşılaştırılabilecek doğrudan bir ölçüm sonucu mevcut değildir. Bununla beraber dolaylı yoldan fikir edinebileceğimiz TX konumunda ANT-RX izolasyonu ölçüm sonucu mevcuttur. TX konumunda TX ve ANT terminallerinin birbirine çok yakın seviyelerde olduğu gözönüne alınırsa karşılaştırmanın gerçekçi olacağı

şüphesizdir. Ölçüm sonucuna göre izolasyon 30 db civarındadır.

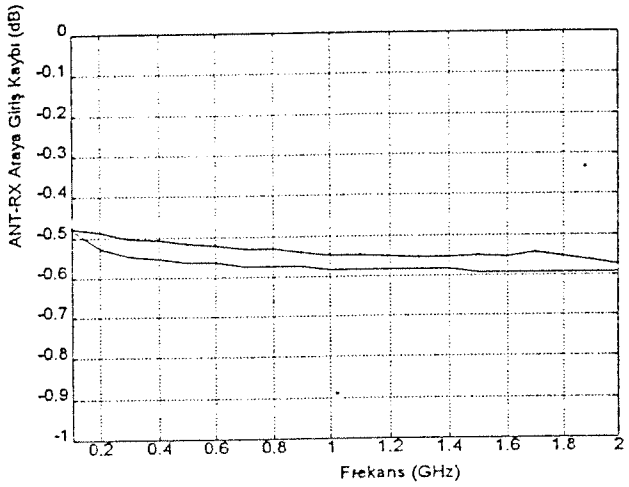

(a)

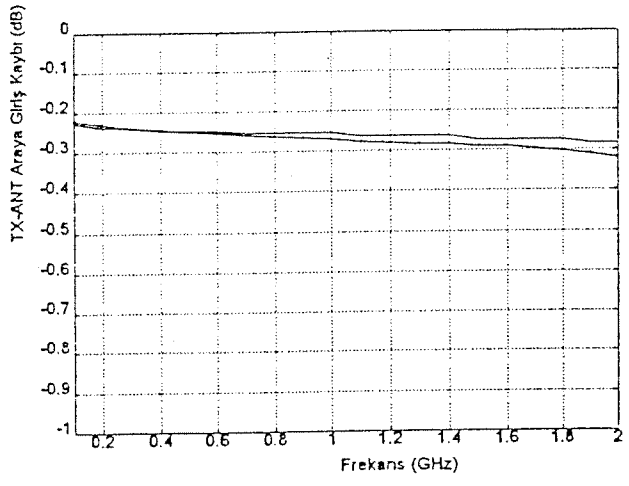

(b)

Şekil: 7 Ölçüm (—o—) ve Simülasyon (——) sonuçları

(a) ANT-RX Araya Giriş Kaybı
(b) TX-ANT Araya Giriş Kaybı

IV. SONUÇ

Elde edilen sonuçlar simülasyonda kullanılan eşdeğer devre modellerinin ve eleman değerlerinin gerçekçi olduğunu göstermiştir. MMIC tasarımında, bilgisayar destekli mühendislik ve tasarım araçları yoğun olarak kullanılır. Ayrıca kullanılan modellerin güvenilirliği büyük önem arzeder. Devrenin üretiminden sonra hibrit veya ayrık RF devrelerde mümkün olan elektriksel performansa müdahale imkanı MMIC'te tektaş yapıdan dolayı imkansızdır. Bununla birlikte bu çalışmada yapılan tasarımların kanıtladığı gibi, eğer devre elemanlarından ve iletim hatlarından kaynaklanabilecek parazitikler eşdeğer devre elemanlarıyla simülasyon ortamına yansıtılabilirse oldukça tatmin edici sonuçlar alınabilir.

Bu çalışmada elde edilen bir diğer sonuçta aktif uyumlamanın tektaş devre tasarımında başarıyla uygulanabilmesidir. Anten anahtarı için önerilen asimetrik devre yapısı kısıtlı enerjiye sahip telsiz uygulamaları açısından önemlidir.

KAYNAKÇA:

[1]. Niclas, " Active Matching with Common-gate MESFETs" IEEE MTT-33, no. 6, June 1985, pp.492-499.
[2]. Engberg, " Simultaneous Input Power Match and Noise Optimization Using Feedback" IV. Euro. Mw. Conf. 1974 pp.385-389.
[3]. Ayasli, "Microwave Switching with GaAs FETs", Microwave Journal, vol.25, no: 11, pp.61-74, 1982.
[4]. Jain, Gutmann, "Modeling and design of GaAs MESFET control devices for broad-band applications" IEEE T-MTT-38, pp.109-117, February 1990.
[5]. Gopinath, Rankin, "GaAs FET RF Switches", IEEE T-ED-32, pp.1272-1278, July 1985.
[6]. GEC-MARCONI "GaAs Foundry Design Rule Guide F14/F20 Process", 1991

ÇOK KATMANLI SİLİNDİRİK YAPILARDAKİ GENEL AKIM KAYNAKLARI İÇİN GERÇEK UZAYDA KAPALI FORMDA GREEN FONKSİYONLARININ ÇIKARILMASI

Çağatay TOKGÖZ, Gülbin DURAL
Orta Doğu Teknik Üniversitesi
Elektrik ve Elektronik Mühendisliği Bölümü
06531 - Ankara

TRACT

o-level approximation technique is employed to in the closed-form spatial domain Green's tions of the electric and magnetic fields due to ric and magnetic sources of z and ϕ-oriented es located in an arbitrary layer of a cylindrical, ified medium. First, the electric and magnetic field ponents representing the coupled TM and TE es are derived recursively in the spectral domain an arbitrary observation layer. Then, the field essions are decoupled between the TM and TE es for the purpose of obtaining the spectral ain Green's functions which are approximated by plex exponentials in two consecutive steps by g the Generalized Pencil of Function (GPOF) iod. For the Green's functions approximated in the step, the large argument behaviour of zero order kel functions is used for the transformation into the ial domain by the Sommerfeld identity. In the ond step, the remaining portion of the Green's tions are approximated and transformed into the ial domain, analytically.

İRİŞ

tromagnetik teorinin birçok uygulamasında, enerji tli kompozisyonlara sahip katmanlı yapıların içinde endirilmektedir. Bu nedenle, çok katmanlı bir yapı sine yerleştirilmiş noktasal bir akım kaynağına ait imler geniş uygulama alanlarına sahiptir. Bu tür ılamaların bazılarında çok katmanlı yapı veya kı devre, katmanlar arasından geçirilen bir akımla enmekte, bazılarında ise yapı, katmanların dışında ınan bir kaynağın oluşturduğu yayılımdan enmektedir. Çok katmanlı yapıların bilhassa ınma elektroniğinde ve optikte geniş kullanım ıları vardır.

katmanlı düzlemsel yapılar için gerçek uzayda alı formda elde edilen ifadeler daha önce nlanmıştır [1], [2]. Ancak, çok katmanlı silindirik ve sel yapılar için henüz böyle bir çalışma nlanmamıştır. Bu çalışmada, çok katmanlı dirik yapılara ait Green fonksiyonlarının gerçek yda ve kapalı formda çıkarılması için geliştirilen iki malı bir yöntem anlatılmaktadır.

2. FORMÜLASYON

Bu çalışmada, içiçe silindirik katmanlardan oluşan bir yapının herhangi bir katmanında ve (ρ',ϕ',z') koordinatlarında bulunan z ya da ϕ yönündeki elektrik ya da magnetik noktasal bir akım kaynağının, herhangi bir katmanda bulunan ve (ρ,ϕ,z) koordinatlarına sahip olan bir gözlem noktasında oluşturduğu elektrik ve magnetik alanların Green fonksiyonları, gerçek uzayda ve kapalı formda elde edilmiştir. Bu katmanların sayısında herhangi bir sınırlama olmayıp, herbir katmanın ayrı bir elektrik veya magnetik özelliği olabileceği gibi, katmanlar mükemmel elektrik veya magnetik iletkenlerden de oluşabilmektedir. Formülasyonda $e^{j\omega t}$ zaman bağımlılığı kabul edilmiştir. Silindirik ve çok katmanlı genel bir yapı Şekil 1'de gösterilmiştir.

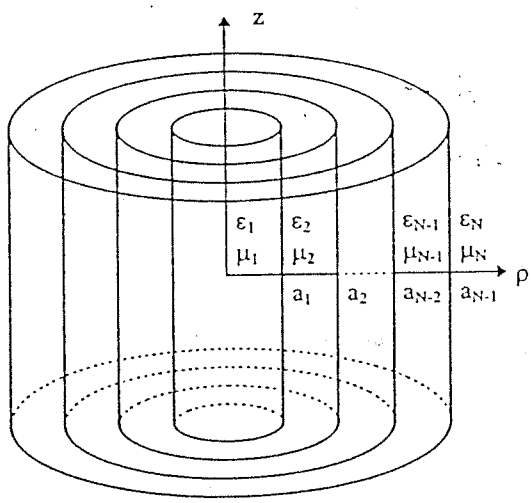

ŞEKİL:1 N katmanlı silindirik yapı modeli

2.1. Green Fonksiyonlarının Spektral Uzayda Hesaplanması:

Düz ve küresel çok katmanlı yapılardan farklı olarak ve ϕ veya z bağımlılığının olmadığı durumlar hariç, silindirik yapılarda TM ve TE modlardan herhangi biri tek başına katmanlar arasındaki sınır koşullarını sağlayamadığı için, bu modlar kaynak katmanında aynı anda çözülerek bu katmandaki elektrik ve magnetik alan ifadeleri bulunur. Gözlem noktası,

aynak katmanından farklı bir katmanda bulunduğu aman, kaynak ve gözlem katmanlarındaki dalgalar rasındaki genlik faktörü iteratif bir yöntemle ulunmalı [3] ve kaynak katmanındaki alan ifadeleri bu aktör ile çarpılarak gözlem katmanına ait alan adeleri şekline dönüştürülmelidir. TM ve TE modların ynı anda çözülmesinden dolayı katmanlar arasındaki ansıma ve iletimi temsil eden terimler 2x2 matrisler larak elde edilmektedir. Bulunan ifadelerdeki TM ve E modlara ait terimler birbirinden ayrılarak gözlem atmanına ait Green fonksiyonları kolaylıkla esaplanabilir. Spektral uzayda, z ve ϕ yönündeki oktasal elektrik akım kaynaklarının gözlem atmanında oluşturduğu Green fonksiyonları aşağıda erilmiştir:

$$\widetilde{G}^{E}_{zz} = -\frac{1}{4w}\sum_{n=-\infty}^{\infty} e^{jn(\phi-\phi')}\frac{k_{\rho_j}^2}{\varepsilon_j} f_{11}$$

$$\widetilde{G}^{H}_{zz} = -\frac{1}{4w}\sum_{n=-\infty}^{\infty} e^{jn(\phi-\phi')}\frac{k_{\rho_j}^2}{\varepsilon_j} f_{21}$$

$$\widetilde{G}^{E}_{\phi z} = -\frac{1}{4w}\sum_{n=-\infty}^{\infty} e^{jn(\phi-\phi')}\frac{k_{\rho_j}^2}{\varepsilon_j}\left[\frac{nk_z}{k_{\rho_i}^2\rho} f_{11} + \frac{jw\mu_i}{k_{\rho_i}}\frac{df_{21}}{d(k_{\rho_i}\rho)}\right]$$

$$\widetilde{G}^{H}_{\phi z} = -\frac{1}{4w}\sum_{n=-\infty}^{\infty} e^{jn(\phi-\phi')}\frac{k_{\rho_j}^2}{\varepsilon_j}\left[-\frac{jw\varepsilon_i}{k_{\rho_i}}\frac{df_{11}}{d(k_{\rho_i}\rho)} + \frac{nk_z}{k_{\rho_i}^2\rho} f_{21}\right]$$

$$\widetilde{G}^{E}_{z\phi} = -\frac{1}{4w}\sum_{n=-\infty}^{\infty} e^{jn(\phi-\phi')}\left[\frac{nk_z}{\varepsilon_j\rho'} f_{11} - jwk_{\rho_j}\frac{df_{21}}{d(k_{\rho_j}\rho')}\right]$$

$$\widetilde{G}^{H}_{z\phi} = -\frac{1}{4w}\sum_{n=-\infty}^{\infty} e^{jn(\phi-\phi')}\left[\frac{nk_z}{\varepsilon_j\rho'} f_{21} - jwk_{\rho_i}\frac{df_{22}}{d(k_{\rho_j}\rho')}\right]$$

$$\widetilde{G}^{E}_{\phi\phi} = -\frac{1}{4w}\sum_{n=-\infty}^{\infty} e^{jn(\phi-\phi')}\left\{\frac{nk_z}{\varepsilon_j\rho'}\left[\frac{nk_z}{k_{\rho_i}^2\rho} f_{11} + \frac{jw\mu_i}{k_{\rho_i}}\frac{df_{21}}{d(k_{\rho_i}\rho)}\right]\right.$$

$$\left. -jwk_{\rho_j}\frac{df_{22}}{d(k_{\rho_j}\rho')}\left[\frac{nk_z}{k_{\rho_i}^2\rho} f_{12} + \frac{jw\mu_i}{k_{\rho_i}}\frac{df_{22}}{d(k_{\rho_i}\rho)}\right]\right\}$$

$$\widetilde{G}^{H}_{\phi\phi} = -\frac{1}{4w}\sum_{n=-\infty}^{\infty} e^{jn(\phi-\phi')}\left\{\frac{nk_z}{\varepsilon_j\rho'}\left[-\frac{jw\varepsilon_i}{k_{\rho_i}}\frac{df_{11}}{d(k_{\rho_i}\rho)} + \frac{nk_z}{k_{\rho_i}^2\rho} f_{21}\right]\right.$$

$$\left. -jwk_{\rho_j}\frac{df_{22}}{d(k_{\rho_j}\rho')}\left[-\frac{jw\varepsilon_i}{k_{\rho_i}}\frac{df_{12}}{d(k_{\rho_i}\rho)} + \frac{nk_z}{k_{\rho_i}^2\rho} f_{22}\right]\right\} \qquad (1)$$

Yukarıdaki ifadelerde,

$$\bar{F}_n(\rho,\rho') = \begin{bmatrix} f_{11} & f_{12} \\ f_{21} & f_{22} \end{bmatrix}$$

$$= \begin{cases} \left[J_n(k_{\rho_i}\rho)\bar{I} + H_n^{(2)}(k_{\rho_i}\rho)\bar{\bar{R}}_{i,i-1}\right]\cdot\bar{A}_{n_i}, & \rho < \rho', \\ \left[H_n^{(2)}(k_{\rho_i}\rho)\bar{I} + J_n(k_{\rho_i}\rho)\bar{\bar{R}}_{i,i+1}\right]\cdot\bar{A}_{n_i}, & \rho > \rho', \end{cases} \qquad (2)$$

matrisinin elemanları kullanılmıştır. Burada, birinci tür Bessel ve ikinci tür Hankel fonksiyonları, gözlem katmanında sırasıyla silindirin içine ve dışına doğru ilerleyen dalgaları temsil etmektedir. Yukarıdaki ifadelerde kaynak ve gözlem katmanlarına ait olan terimlerin belirtilmesinde sırasıyla j ve i alt indeksleri kullanılmış olup, k_j ve k_i, sırasıyla, kaynak ve gözlem katmanlarındaki yayılma katsayıları olmak üzere $k_j^2 = k_{\rho_j}^2 + k_z^2$ ve $k_i^2 = k_{\rho_i}^2 + k_z^2$ bağıntıları geçerlidir. Bütün katmanlar için k_z sabit olup, k_ρ değişkendir. Ayrıca, $\bar{\bar{R}}_{i,i-1}$ ve $\bar{\bar{R}}_{i,i+1}$, gözlem katmanından, sırasıyla, alt ve üst katmanlara doğru ilerleyen dalgalara ait genelleştirilmiş yansıma matrisleridir. $\bar{A}_{n_i}$ ise yine bu katmandaki dalgaların genliklerini temsil eden, kaynak ile gözlem katmanları arasındaki genelleştirilmiş iletim matrisini ve kaynak katmanına ait bilgileri içeren bir matristir.

2.2. Green Fonksiyonlarının Gerçek Uzayda Kapalı Formda İfade Edilmesi:

Gerçek uzaydaki Green fonksiyonları, spektral uzaydaki Green fonksiyonları cinsinden aşağıdaki integral dönüşümü ile ifade edilmektedir:

$$G(z) = \frac{1}{2\pi}\int_{-\infty}^{\infty} dk_z e^{-jk_z(z-z')}\widetilde{G}(k_z) \qquad (3)$$

Bu ifadede G ve $\widetilde{G}$, sırasıyla, gerçek ve spektral uzaydaki Green fonksiyonlarını temsil etmektedirler.

Yukarıdaki integralde k_z değişkeninin izlediği yolun eksi sonsuzdan artı sonsuza kadar gitmesi, integralin hesaplanmasını güçleştirmektedir [4]. Bunun yanında, k_z değişkeninin bu yol üzerinde herhangi bir katmanın yayılma katsayısına eşit olduğu noktalarda, o katmana ait k_ρ değişkeni ve dolayısıyla o katmandaki dalgaları temsil eden Hankel fonksiyonlarının argümanları sıfıra gitmektedir. Bu durumda, argümanı sıfır olan Hankel fonksiyonlarının değerleri sonsuza gitmekte ve integralin bu yol üzerinde alınması mümkün olmamaktadır. İntegralin izlediği yolun bu noktalardan geçmeyecek ve aynı zamanda da hataya yolaçmayacak şekilde deforme edilmesi, integralin kolayca alınmasını sağlayacaktır.

Bu çalışmada, integralin sayısal olarak hesaplanmasını kolaylaştırmak amacıyla iki aşamalı bir yöntem önerilmektedir. Her iki aşamada da, spektral uzaydan gerçek uzaya dönüşümü analitik olarak yapabilmek ve gerçek uzayda kapalı formda ifadeler bulabilmek amacıyla, spektral uzaydaki Green fonksiyonları Generalized Pencil of Function (GPOF)

ıtemi kullanılarak [5] kompleks üstel terimlerle ıklaştırılmıştır. Bu aşamalar şu şekilde açıklanabilir:

aşamada, spektral uzayda k_z değişkeninin büyük ğerlerine karşılık gelen Green fonksiyonlarının k_ρ ğişkeninin fonksiyonu olan kompleks üstellerle ıklaştırılması amacıyla, Green fonksiyonları bu ğişkenin izlediği yol üzerinde eşit aralıklarla ağıdaki gibi örneklenir;

$$= -jk_z t \qquad T_2 \le t < T_3 \tag{4}$$

een fonksiyonlarının örneklenen herbir değeri, k_ρ ğişkeninin o örnekleme noktasındaki değerinin ekökü ile çarpılarak aşağıda gösterildiği gibi N_3 e kompleks üstel terimle yaklaştırılır;

$$\widetilde{G}_{k_\rho} \cong \sum_{k=1}^{N_3} a_k e^{k_\rho b_k} \tag{5}$$

rada, $\widetilde{G}_{k_\rho}$ spektral uzaydaki Green fonksiyonlarının ıarıda verilen yol üzerinde örneklenen bölümünü ısil etmektedir.

ndiği gibi, argümanlarının genliği büyük olduğu nan Hankel fonksiyonları kompleks üstel ksiyonlar gibi davranmaktadırlar;

$$H_0^{(2)}(x) \cong \sqrt{\frac{j2}{\pi}} \frac{e^{-jx}}{\sqrt{x}} \tag{6}$$

ıarıda tanımlanan örnekleme yolundaki k_ρ ğerlerine karşılık gelen Hankel fonksiyonu ümanlarının genlikleri yeterince büyük olacak ilde T_2 değeri seçilmelidir. Bu sayede, yukarıda npleks üstel terimlerle yaklaştırılmış olan Green ksiyonları Hankel fonksiyonları cinsinden de ifade lebilmektedir:

$$\cong \sum_{k=1}^{N_3} a_k \frac{e^{k_\rho b_k}}{\sqrt{k_\rho}} \cong \sum_{k=1}^{N_3} c_k H_0^{(2)}(k_\rho d_k) \tag{7}$$

şekilde yaklaştırılan spektral uzaydaki Green ksiyonlarının analitik olarak gerçek uzaya ınabilmesi için aşağıdaki eşitliğin integral ıüşümüne benzerliğinden yararlanılmaktadır.

$$\frac{e^{jk_z|\vec{r}-\vec{r}'|}}{|\vec{r}-\vec{r}'|} = \frac{-j}{2}\int_{-\infty}^{\infty} dk_z e^{-jk_z(z-z')} H_0^{(2)}(k_\rho |\vec{\rho}-\vec{\rho}'|) \tag{8}$$

Yukarıdaki integral eşitliği kullanıldığında, spektral uzayda Hankel fonksiyonları ile yaklaştırılan Green fonksiyonları kapalı formda gerçek uzaya aktarılabilirler.

Spektral uzayda, yukarıda tanımlanan yolda yaklaştırılan Green fonksiyonları spektral uzayın tümünde tanımlanan Green fonksiyonlarından çıkarılarak bu yolun dışında kalan bölge ile sınırlanmış Green fonksiyonları elde edilir.

$$\widetilde{G}_{k_z} = \widetilde{G} - \widetilde{G}_{k_\rho} \tag{9}$$

Bu aşamada dikkat edilmesi gereken, k_z değişkeninin yukarıda tanımlanan yol üzerinde bütün katmanların yayılma katsayılarından büyük olmasını sağlayacak bir T_2 değerinin seçilmesidir.

Bu aşamada, k_z değişkeni reel değerlere sahip olacak şekilde örnekleme yapılması durumunda, izlenen yol daha önce bahsedilen ve integralin tanımsız olduğu noktalar üzerinden geçecektir. Bu durumu engellemek ve aynı zamanda k_z değişkenini eşit aralıklarla örnekleyebilmek amacıyla, bu değişkenin izlediği yol deforme edilerek iki kısıma bölünmüştür. İlk aşamada Hankel fonksiyonları ile yaklaştırılan Green fonksiyonlarının orijinallerinden çıkarılması ile elde edilen Green fonksiyonları, $\widetilde{G}_{k_z}$, her iki kısımda sırasıyla aşağıdaki gibi örneklenir:

$$k_z = k_j\left[jt + \frac{t}{T_1}\right] \qquad 0 \le t < T_1 \tag{10}$$

$$k_z = k_j\left[\sqrt{1+T_2^2} + (1 + jT_1 - \sqrt{1+T_2^2})\left(\frac{T_2 - t}{T_2 - T_1}\right)\right] \qquad T_1 \le t < T_2 \tag{11}$$

Örneklenen Green fonksiyonları, her iki bölümde k_z değişkeninin fonksiyonu olan, sırasıyla, N_1 ve N_2 tane kompleks üstel terimle yaklaştırılabilirler;

$$\widetilde{G}_{k_z} \cong \sum_{l=1}^{N_1} a_l e^{k_z b_l} + \sum_{m=1}^{N_2} a_m e^{k_z b_m} \tag{12}$$

Bu şekilde yaklaştırılan spektral uzaydaki Green fonksiyonları dönüşüm integraline konulduğunda, bu integral kompleks üstel fonksiyonların sınırlı integrali halini alır ve gerçek uzaydaki Green fonksiyonları analitik olarak kolayca hesaplanabilir. Son olarak, her iki aşamada hesaplanan gerçek uzaydaki Green fonksiyonları toplanarak kapalı formda Green fonksiyonları elde edilmiş olur.

3. UYGULAMALAR

Gerçek uzayda kapalı formda elde edilen yaklaşık sonuçlar, dönüşüm integralinin sayısal hesaplanması ile bulunan kesin sonuçlarla karşılaştırılmış ve sonuçların uyum içinde oldukları gözlenmiştir.

Örnek olarak, mükemmel elektrik iletkenliğine sahip, yarıçapı 20 mm. olan, dış yüzeyinde 1 mm. kalınlığında dielektrik bir katman ($\varepsilon_r = 2.3$) bulunan ve hava boşluğu içerisine yerleştirilmiş bir yapı 4.7 GHz'te incelenmiştir. Hava ile dielektrik arasındaki arayüze yerleştirilmiş $(\rho' = 21\ \text{mm.}, \phi' = 0, z' = 0)$ z ve ϕ yönündeki noktasal elektrik akım kaynaklarının, hava boşluğundaki bir gözlem noktasında $(\rho = 40\ \text{mm.}, \phi = 30°, z)$ oluşturdukları elektrik alanlara ait Green fonksiyonları gerçek uzayda kapalı formda bulunmuş ve genlik grafikleri Şekil 2 ve 3'te gösterilmiştir.

4. SONUÇ

Bu çalışmada, çok katmanlı silindirik bir yapının herhangi bir katmanına yerleştirilen elektrik ya da magnetik noktasal akım kaynaklarının oluşturduğu elektrik ve magnetik alanlara ait Green fonksiyonları gerçek uzayda ve kapalı formda elde edilmiştir. Önerilen yöntem dönüşüm integralinin sayısal olarak hesaplanması güçlüğünü ortadan kaldırmakta ve hesaplama süresini önemli ölçüde azaltmaktadır.

KAYNAKÇA

[1] Gülbin Dural ve M. I. Aksun, "Closed-form Green's functions for general sources and stratified media", *IEEE Trans. Microwave Theory and Tech.* Vol. MTT-43, No.7, pp. 1545-1552, Temmuz 1995

[2] M. I. Aksun, "A robust approach for the derivation of closed-form Green's functions", *IEEE Trans. Microwave Theory and Tech.* Vol. MTT-44, No.5, pp. 651-658, Mayıs 1996

[3] W. C. Chew, *Waves and Fields in Inhomogeneous Media*. Piscataway, NJ: IEEE Press, 1995

[4] W. C. Chew, "The singularities of a Fourier-type integral in a multicylindrical layer problem", *IEEE Trans. Antennas and Prop.* Vol. AP-31, No.4, pp. 653-655, Temmuz 1983

[5] Y. Hua ve T. K. Sarkar, "Generalized pencil-of-function method for extracting poles of an EM system from its transient response", *IEEE Trans. Antennas and Prop.* Vol. AP-37, No.2, pp. 239-234, Şubat 1989

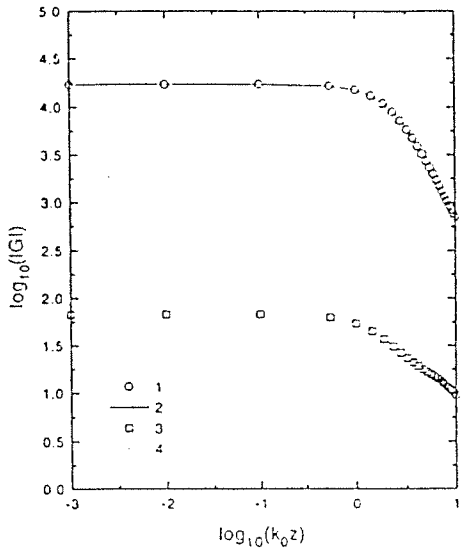

ŞEKİL:2 G sembolü, z yönündeki noktasal bir elektrik akım kaynağının oluşturduğu G^E_{zz} ve $\int G^E_{\phi z}\, dz$ Green fonsiyonlarının, 1 ve 3 nolu grafiklerde kesin, 2 ve 4 nolu grafiklerde ise yaklaşık değerlerini temsil etmektedir. Katman-0: toprak, katman-1: $\varepsilon_r = 2.3$, katman-2: boşluk, $a_1 = 20\ \text{mm.}$, $a_2 = \rho' = 21\ \text{mm.}$, $\rho = 40\ \text{mm.}$, $\phi = 30°$, $\phi' = z' = 0$, f=4.7 GHz.

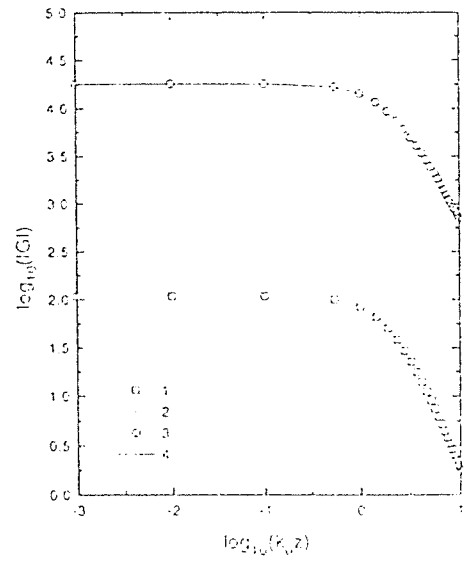

ŞEKİL:3 G sembolü, ϕ yönündeki noktasal bir elektrik akım kaynağının oluşturduğu $\int G^E_{z\phi}\, dz$ ve $G^E_{\phi\phi}$ Green fonsiyonlarının, 1 ve 3 nolu grafiklerde kesin, 2 ve 4 nolu grafiklerde ise yaklaşık değerlerini temsil etmektedir. Katman-0: toprak, katman-1: $\varepsilon_r = 2.3$, katman-2: boşluk, $a_1 = 20\ \text{mm.}$, $a_2 = \rho' = 21\ \text{mm.}$, $\rho = 40\ \text{mm.}$, $\phi = 30°$, $\phi' = z' = 0$, f=4.7 GHz.

Özgün Düşük Gürültülü Aktif Anten Dizisi Analiz ve Tasarım Yöntemi

Ş.DEMİR, Ç. TOKER, A. HIZAL
Orta Doğu Teknik Üniversitesi
Elektrik ve Elektronik Mühendisliği Bölümü
06531 ANKARA

ABSTRACT

In this work, noise analysis of active receive antenna systems are given. Noise analysis of low loss transmission lines is given and a new concept, 'noise equivalent line length' is introduced. Importance of incoherent impedance match is shown and based on the noise equivalent line length, noise performance of different antenna array feed structures are also studied. It is shown that an antenna array feed structure can be re-designed without affecting the radiation performance for a lower noise temperature. It is also shown that active antenna arrays may have superior noise performance compared to passive antenna arrays. Application of noise equivalent line length as an active circuit replacement criteria in antenna arrays is given.

1. GİRİŞ

Gürültü, alıcı anten sistemleri için önemli bir tasarım kriteridir. 1960'lardan beri alıcı anten sistemlerinde gürültü faktörlerinin belirlenmesi, hesaplanması konularında çalışmalar yapılmaktadır [1]. Son yıllarda aktif anten yapıları kullanılmaya başlanmıştır. Aktif anten yapıları için de gürültü analizi ve ölçümleri konularında çalışmalar sürmektedir [2]. Ancak, bu çalışmaların hiçbirinde anten besleme yapısının kendi gürültü sıcaklığı hesaba katılmamış, tasarımlarda bu sıcaklığı azaltma konusu dikkate alınmamıştır. Alıcı antenlerde gürültü sıcaklığının ölçülmesi çok zor olduğu için güvenilir bir analiz yöntemi son derece önemlidir. Besleme yapılarında kullanılan iletim hatlarının kayıplı olması gürültü faktörünün hesaba katılmasını gerekli kılmaktadır. Özellikle büyük ölçekli anten dizilerinde besleme yapılarında oluşan kayıplar anten verimliliğini %70'ler seviyesine indirmektedir [3]. Aynı nedenle, kayıp faktörü ile doğrudan ilişkili olan gürültü faktörü de önemli derecede artmaktadır.

Anten dizilerinin gürültü sıcaklığının belirlenmesi ve düşük gürültülü bir besleme yapısının tasarımı ve analizi çalışmaları sürmektedir. Bu çalışmada, aktif anten dizisi tasarımına uygulanması sunulmaktadır. Anten besleme yapıları seri ve paralel tipte olmak üzere iki ayrı grupta incelenebilir. Bu çalışmada daha yaygın kullanıma sahip olan paralel besleme yapıları esas alınmıştır.

Paralel besleme yapıları temel olarak güç birleştirici yapılardır. Işınım örüntüsüne bağlı olarak antenlerden faz ilintili (coherent) gelen işaretler, besleme yapısı üzerinde birleştirilerek anten çıkışına aktarılırlar. Anten dizisi, dışarıdan alınan işaret ve gürültü için aynı biçimde davrandığından, bu biçimdeki çalışma, işaret-gürültü oranı (SNR) analizi çalışmalarına temel oluşturmuştur [4]. Ancak, kayıplı elemanlardan oluşan besleme yapısı kendi başına ısıl (thermal) gürültü oluşturduğu için, hem dışardan alınan gürültü ile hem yapı içindeki diğer elemanların yarattığı gürültü ile faz ilintili değildir (incoherent). Bu nedenle şimdiye kadar yapılan çalışmalardan tamamen farklı bir çalışmayı gerektirmektedir.

2.KAYIPLI İLETİM HATTI GÜRÜLTÜ HESABI

Anten dizisi besleme yapıları bir çok uygulamada iletim hatları ile oluşturulur. Bu nedenle, kayıplı iletim hatlarının gürültü analizi, besleme yapılarının gürültü analizinde temel oluşturmaktadır. Yaptığımız analizde, iletim hattı kaybının, iletim hattı karakteristik empedansını, Z_{line}, gerçel sayı olarak kabul etmemizi engellemeyecek kadar düşük olduğunu kabul ettik. Kaynak ve yük yansıma katsayıları bu empedansa göre tanımladığında:

$$\Gamma_g = \frac{Z_g - Z_{line}}{Z_g + Z_{line}} \tag{1}$$

ve

$$\Gamma_L = \frac{Z_L - Z_{line}}{Z_L + Z_{line}} \tag{2}$$

olmaktadır. α iletim hattının zayıflatma faktörünü göstermek üzere, kayıp faktörü, L:

$$L = e^{2\alpha l} \tag{3}$$

olarak tanımlanmıştır. Bu durumda, bu iletim hattının, Z_L yüküne aktaracağı gürültü gücü şöyledir:

$$P_n = kT\Delta f \frac{1-|\Gamma_L|^2}{|1-\Gamma_L\Gamma_g/L|^2 L}\left(L - |\Gamma_g|^2/L - 1 + |\Gamma_g|^2\right) \tag{4}$$

Yük empedansı, çıkış empedansının eşleniği olduğu durumda aktarılan güç, en fazla aktarılabilecek güce eşit olduğundan, kayıplı bir iletim hattının aktarabileceği en fazla gürültü gücü şöyledir:

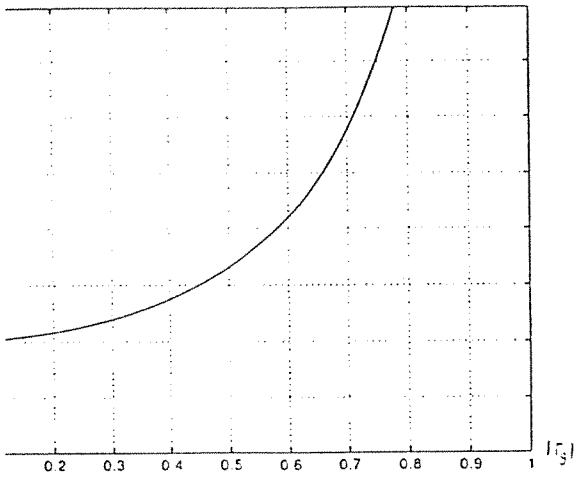

. 1. Eşdeğer hat uzunluğunun kaynak yansıma yısı ile değişimi

$$_{ix} = kT\Delta f \frac{L - |\Gamma_g|^2 / L - 1 + |\Gamma_g|^2}{\left(1 - |\Gamma_g / L|^2\right)L} \quad (5)$$

ik incelendiğinde görülen odur ki, gürültü gücü yansıma katsayısının mutlak büyüklüğü ile a ve yansıma en yüksek değerine ulaştığında:

$$P_{n,\max} = kT\Delta f \quad (6)$$

adır. Bu gürültü, bir direncin aktarabileceği en üce karşılık geldiğinden, uygun tasarlanmamış n hattının ne kadar çok gürültü yaratabileceği ektedir.

aliz, besleme yapılarındaki farklı elemanların katkılarını veren, besleme yapısının genel değerlendirmesinde kullanılacak olan, bir er hat uzunluğu' tanımında kullanılmıştır. Bu etrenin kullanıldığı uygulamalar ileriki erde verilmektedir.

nluğu ℓ, kaynak yansıma katsayısı Γ_g olan ıen iletim hattının kayıp faktörü olsun. Bu da aktarabileceği gürültü gücü (5)'de verildiği L_{neqv} aynı kayıp özeliklerine sahip, ℓ_{neqv} ğunda, kaynak yansıma katsayısı sıfır olan bir ıattı olsun. Bu hattın aktarabileceği gürültü:

$$P_{eqv} = kT\Delta f \frac{L_{neqv} - 1}{L_{neqv}} \quad (7)$$

tır. İncelenen hattın, gürültü özelliklerini bu er hat ile gösterelim. L_{neqv}, $P_{line}=P_{eqv}$ olacak le seçildiğinde her iki hat da aynı gürültü ü yaratacaktır. Bu durumda:

$$_{qv} = \frac{L^2 - |\Gamma_g|^2}{\left(L^2 - |\Gamma_g|^2\right) - (L-1)\left(L + |\Gamma_g|^2\right)} \quad (8)$$

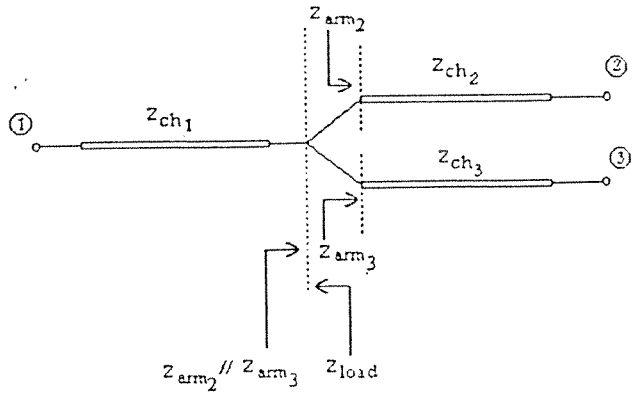

ŞEKİL 2. Güç birleştiricinin şematik gösterimi

$$l_{neqv} = \frac{1}{2\alpha} \ln\left(\frac{L^2 - |\Gamma_g|^2}{\left(L^2 - |\Gamma_g|^2\right) - (L-1)\left(L + |\Gamma_g|^2\right)}\right) \quad (9)$$

olacaktır. Bu 'eşdeğer hat uzunluğu' gürültü sıcaklığının bulunmasında doğrudan kullanılmaktadır. Eşdeğer hat uzunluğu fiziksel uzunluk birimi ile ifade edilmekte ve en az değeri hattın fiziksel uzunluğuna eşit olmaktadır. Bu biçimde gürültü sıcaklığını hesaplamadan gürültünün yansıma katsayısından kaynaklanan artışı belirlenebilir, farklı özellikteki iletim hatları gürültü bakımından karşılaştırılabilir. Şekil 1'de fiziksel uzunluk ile normalize edilmiş olarak, gürültü eşdeğer uzunluğunun yansıma katsayısı ile değişimi verilmiştir.

Bir anten dizisi besleme yapısı güç birleştiriciler, Şekil 2, kullanılarak tanımlanabileceğinden, bu yapıların analizi; anten dizisi besleme yapılarının gürültü analizine temel oluşturmaktadır. Güç birleştirici yapıların analizinden görülebileceği gibi faz ilintili gelen işaretler yansımaya uğramadan eklenmekte, bu nedenle giriş kapılarından alınan toplam güç çıkış kapısına aktarılabilmektedir. Sadece faz ilintili durum için uyumlanmış olan bu yapılar, aralarında faz ilintisi olmadan gelen işaretler için, giriş empedans uyumu olmadığından, yansıma yaratmakta ve gelen güç ancak güç birleştirici kollarının birleştirme oranı kadar çıkışa aktarılabilmektedir. $\ell_{eqv,1}$ ve $\ell_{eqv,2}$ eşdeğer uzunluğunda iki kolu olan bir birleştirici, kollar arasındaki birleştirme oranı $1:p^2$ olduğunda:

$$\ell_{comb} = \frac{1}{1+p^2}\ell_{eqv,1} + \frac{p^2}{1+p^2}\ell_{eqv,2} \quad (10)$$

eşdeğer hat uzunluğuna sahip olacaktır. Kollar aynı özelliklere sahipse, yani $\ell_{eqv} = \ell_{eqv,1} = \ell_{eqv,2}$ ise:

$$\ell_{comb} = \ell_{eqv} \quad (11)$$

olacaktır. Anten dizisi besleme yapısı içinde arka arkaya bağlanmış olan güç birleştiricilerin birleştirme oranları çarpılarak bulunacak olan bir ağırlık katsayısı, w, bu birleştiricilerin önüne bağlanmış olan

bir yapının ya da anten elemanının, çıkışa aktarabileceği gürültü gücünün bulunmasında çarpan olarak kullanılacaktır. Gürültü gücünün takip eden kayıplı yapılarda belli bir kayıp faktörü ile, L_{pro}, zayıflayacağı da dikkate alındığında, çıkışa aktarılan güç:

$$P_{out,line} = w \times \frac{1}{L_{pro}} \times P_{line} \qquad (11)$$

olacaktır. Buna ilişkin olarak tanımlanacak bir ağırlıklı eşdeğer hat uzunluğu, ${}^{w}\ell_{neqv}$:

$${}^{w}l_{neqv} = \frac{1}{2\alpha} \ln \left(\frac{L^2 - |\Gamma_g|^2}{\left(L^2 - |\Gamma_g|^2\right) - \frac{w}{L_{pro}}(L-1)\left(L + |\Gamma_g|^2\right)} \right) \qquad (12)$$

olacaktır.

3. ANTEN BESLEME DİZİSİ GÜRÜLTÜ SICAKLIĞI

Anten besleme dizisinin gürültü sıcaklığının bulunmasında ağırlıklı eşdeğer hat uzunluğu tanımı kullanılmıştır. 2x*p* elemanlı bir paralel anten dizisinin eşdeğer hat uzunluğu, $w = \frac{2k}{p}$, $\Gamma_{g,k} = \frac{Z_{ant}/2k - Z_{line,k}}{Z_{ant}/2k + Z_{line,k}}$ ve $L_{pro,k} = L^{p/2-1-k}$ olmak üzere:

$$l_p = \frac{1}{2\alpha} \sum_{k=1}^{p/2-1} \ln \left(\frac{L^2 - |\Gamma_{g,k}|^2}{L^2 - |\Gamma_{g,k}|^2 - \frac{w}{L_{pro,k}}(L-1)\left(L + |\Gamma_{g,k}|^2\right)} \right) \qquad (13)$$

olarak bulunmaktadır. Bu tip yapılarda besleme katsayılarını değiştirmemek için, anten elemanları arasına empedans dönüştürücüler bağlanamamakta, bunun sonucunda paralel bağlanan anten empedansları uyumlaması oldukça güç empedans seviyeleri yaratmaktadır. Eleman sayısı arttıkça artan bu empedans uyumsuzluğu oldukça hızlı artan bir gürültü sıcaklığı yaratmaktadır. *Corporate* besleme yapılarında böyle bir sorun olmadığından, fiziksel hat uzunluğu daha fazla da olsa, eşdeğer hat uzunluğu daha kısa çıkabilmektedir. Faz ilintili ve ilintisiz durumlar için empedans uyumlu olan $N=2^n$ elemanlı bir *corporate* besleme yapısının eşdeğer hat uzunluğu:

$$\begin{aligned} l_{n,even} &\approx \sum_{k=1}^{n/2} \lambda \cdot 2^{k-1} - \lambda/4 \\ &\approx \lambda \cdot 2^{n/2} - 5/4 \cdot \lambda \\ l_{n,odd} &\approx l_{n-1} + 1/2 \cdot \lambda \cdot 2^{(n-1)/2} \end{aligned} \qquad (14)$$

olarak bulunmaktadır.

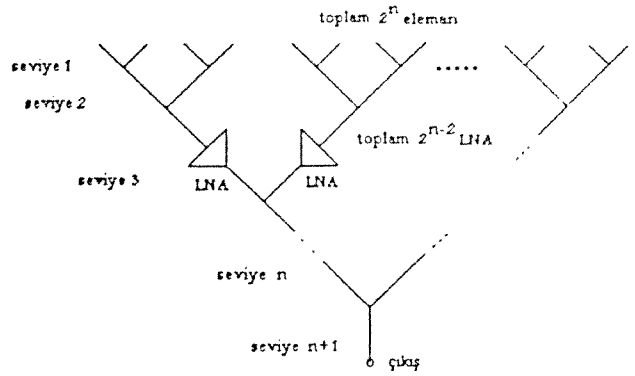

ŞEKİL 3. *corporate* besleme yapısı şematik gösterimi

4. AKTİF ANTEN DİZİLERİNDE GÜRÜLTÜ

Alıcı antenlerde gürültü performansı kazanç gürültü sıcaklığı oranı (G/T) ile ölçülmektedir. Alıcı anten dizilerinin yüksek kazançlı ve düşük gürültülü olması için aktif eleman kullanılarak aktif anten dizisi haline getirilmesi başarılı sonuçlar vermektedir [5]. Alıcı sistemlerde pasif bir anten dizisinin çıkışına düşük gürültülü yükselteç (LNA) bağlanması gereklidir. Ancak, anten dizisine LNA bağlanması, gürültü faktörüne bağlı olmadan, anten sisteminin gürültü sıcaklığını artırır. Çıkışına LNA bağlanmış bir anten dizisini, anten dizisi içerisine dağınık olarak yükselteç bağlanarak aktif hale getirilmiş bir anten dizisi ile karşılaştırdığımızda ise görürüz ki, yükselteçler anten elemanlarına ne kadar yakın konulursa gürültü faktöründeki iyileşme o kadar artar. Hatta, bazı durumlarda pasif antenin G/T oranından daha yüksek oranlar elde edilebilir.

Şekil 3'teki gibi bir *corporate* besleme yapısını göz önüne alalım. η besleme yapısının verimliliğini, T_A anten elemanının gürültü sıcaklığını, T_{LNA} yükseltecin gürültü sıcaklığını, T_f besleme yapısının gürültü sıcaklığını, G yükseltecin kazancını göstermek üzere, sadece çıkışa yükselteç bağlandığında, gürültü gücü:

$$P_{tek} = k\Delta f\left(\left(\eta T_A + T_{LNA}\right) + T_f\right) \cdot G \qquad (15)$$

olacaktır. Yükselteçler çıkıştan önceki bir seviyeye bağlandığında ise, $T_f = T_1 x \eta_2 + T_2$ ve $\eta = \eta_1 x \eta_2$ olmak üzere, η_1 ve T_1 yükselteç öncesindeki, η_2 ve T_2 yükselteç sonrasındaki besleme yapısının verimlilik ve gürültü sıcaklığını gösterdiğinde gürültü gücü:

$$P_{dağınık} = k\Delta f\left(G\eta_2\left(\eta_1 T_A + T_1 + T_{LNA}\right) + T_2\right) \qquad (16)$$

olacaktır. (15) ve (16)'nın karşılaştırmasından, yükselteçlerin anten dizisi besleme yapısında dağınık olarak yerleştirildiğinde daha yüksek bir G/T oranına ulaşıldığı görülmektedir. (16), pasif anten dizisi gürültü sıcaklığı ile karşılaştırıldığında ise:

$$T_2\left(1 - \frac{1}{G}\right) - \eta_2 T_{LNA} \rangle 0 \qquad (17)$$

olduğu durumda yükselteçlerin dağınık olarak besleme yapısına yerleştirilmesi, pasif anten

den daha yüksek bir G/T oranı oluşturur. düğü gibi, anten besleme yapısında kullanılan hatlarının kayıp faktörü arttığında ya da ılan anten elemanı sayısı artması sonucunda hattı uzunluğu arttığında, düşük gürültü faktörlü k kazançlı yükselteçler kullanmak anten ıin gürültü performansını iyileştirecektir.

SARIM ÖRNEĞİ

alışmada güsterilmiş olduğu gibi anten dizisi me yapısının faz ilintili işaretler için empedans ılu tasarlandığı gibi yapı içinden kaynaklanan tü gibi faz ilintisi olmayan işaretler için de edans uyumlu tasarlanması gerekmektedir. Böyle asarım çalışmasında 4x8 *corporate* beslenmiş bir anten dizisinde sadece besleme dizisinde nılan iletim hatlarının karakteristik empedansları ştirilerek gürültü sıcaklığı yarıya indirilmiştir. ıidaki örnekte 16x16 bir pasif anten dizisi lanmış ve farklı seviyelere yükselteçler anarak gürültü sıcaklıkları hesaplanmıştır.

DUROID 5880 substrat üzerinde mikroşerit örtgen yama anten tasarlanmıştır. Antenlerin giriş edansı 10 GHz'te 276Ω dur. 256 anten *corporate* eme yapısında düzgün dağılımlı olarak enerek alıcı bir anten dizisi haline getirilmiştir. en elemanları arasındaki fiziksel mesafe ışınım ıtüsü özelliklerine göre seçilmiştir. Çeyrek dalga u iletim hatları kullanılarak empedans dönüşümleri ılmış ve besleme yapısı hem faz ilintili hem de faz ili olmayan işaretler için empedans uyumlu hale rilmiştir. Bu besleme yapısının toplam eşdeğer nluğu. çevre sıcaklığı 290°K olduğu durumda 101°K karşılık gelmek üzere 14.8 λ olarak aplanmıştır.

roşerit empedans uyumlama elemanları ve ultra ük gürültü faktörlü bir pHEMT, NEC 32484A, lanılarak bir yükselteç tasarlanmıştır. Yükseltecin GHz'teki gürültü faktörü 0.6dB, kazancı ise 14dB rak hesaplanmıştır. Uyumlamada kullanılan vrelerin antenler arasındaki fiziksel alana dırılabildiği daha önceki bir çalışmada sterilmıştır [5]. Bu yükselteç anten dizisinin çıkışına ğlandığında T=35.6dB-K gürültü sıcaklığı ışmuştur. Ağırlıklı eşdeğer hat uzunluğu ve aktif ten dizisi gürültü analiz yöntemleri kullanılarak kselteçler besleme yapısı üzerinde farklı seviyelere ğlandığında elde edilen gürültü sıcaklıkları saplanmış ve Tablo 1'de verilmiştir. Bu tablodan ıkça görülmektedir ki yükselteçler anten emanlarına yaklaştıkça aktif antenin gürültü caklığı düşmektedir. Ayrıca, (17)'nin sağlanma şulu dikkate alındığında görülmektedir ki bu tasarım neğinde. 7. ya da daha önceki seviyelere yükselteç ağlandığında aktif anten dizisi pasif antenden daha iksek bir G/T oranında çalışacaktır.

TABLO 1. 16x16 aktif anten dizisinde yükselteç yerleştirme seviyesine bağlı gürültü sıcaklığı

Seviye	1	2	3	4	5
Yüks. Sayısı	256	128	64	32	16
T (dB-K)	30.7	30.9	31.1	31.7	32.1

Seviye	6	7	8	çıkış
Yüks. Sayısı	8	4	2	1
T (dB-K)	32.9	33.6	34.7	35.6

6. SONUÇ

Bu çalışmada, düşük kayıplı iletim hatlarının kullanıldığı anten dizisi besleme yapılarının analizi verilmiş ve 'eşdeğer hat uzunluğu' kavramı tanıtılmıştır. Besleme yapıları için faz ilintisi olmayan işaretler için de empedans uyumlamanın önemli olduğu gösterilmiştir.

'Eşdeğer hat uzunluğu' kavramı aktif anten dizilerinin analiz ve tasarımında kullanılmış ve anten dizilerinde yükselteç yerleştirilecek noktaların belirlenmesinde bir tasarım kriteri olarak kullanımı gösterilmiştir. Çok düşük gürültü seviyeli aktif elemanların kullanılmaya başlanması ile birlikte, aktif anten dizilerinin alıcı anten yapılarında kullanılma alanları daha da yaygınlaşacaktır.

KAYNAKÇA:

[1] Y. T. Lo, S. W. Lee and Q.H. Lee, 'Optimization of directivity and signal-to-noise ratio of an arbitrary antenna array', Proc. IEEE, vol. 54, pp. 1033-1045, Aug. 1966.

[2] H. An, B. Nauwelaers, A. van de Capelle, 'Noise figure measurement of receiving active microstrip antennas', Electron. Lett., vol. 29, no. 18, pp. 1594-1596, Sep. 1993.

[3] M. A. Weiss, 'Microstrip antennas for millimeter waves', IEEE Trans. Antennas Propagat., vol AP-29, pp. 171-176, Jan. 1981.

[4] L.P.Winkler and M. Schwartz, 'A fast numerical method for determinig the optimum SNR of an array subject to a Q factor constraint', IEEE Trans. Antennas Propogat., vol. AP-20, pp. 503-505, July 1972.

[5] Ş. Demir, C. Toker and A. Hızal, 'Design of an active microstrip array using a microwave circuit simulator', in Proc. IEEE MTT-S Top. Symp. on Tech. for Wireless Appl., Vancouver, Canada, Feb. 1997. pp. 103-106.

EK II:

COST-245 PROJESİNİN

ULUSLARARASI ORGANİZASYONU

A SHORT DESCRIPTION OF THE PROJECT

COST 245

ACTIVE ARRAYS AND ARRAY FED REFLECTOR ANTENNAS

1993 - 1997

prepared by Juan R. Mosig, EPF-Lausanne, Switzerland

GOAL

To design, analyze, build and demonstrate new type of ANTENNAS for mobile communications and broadcasting via satellite

MOTIVATION

- ❒ **Increasing communications traffic via satellite**

  leads to:

- ❒ **Increasing technical requirements for antennas**

  (in satellites, at ground stations, on mobiles)

  - ✔ **High efficiency**
  - ✔ **Multibeam (fixed and mobile)**
  - ✔ **Reconfigurable**
  - ✔ **Frequency agility and re-use**
  - ✔ **Geographical coverage and footprints**
  - ✔ **Tracking capabilities**

A GOOD CANDIDATE

- ❒ Active or semiactive integrated antennas and phased arrays of these antennas

  - ⇨ Also good for cellular base stations and other commercial applications

PROBLEMS TO BE SOLVED

1. Find good basic designs for these antennas and their associated BeamForming Networks

2. Model and analyze these structures and develop CAD packages

3. Combine with microwave electronics and waveguides to arrive at the active antenna

COST 245 Project

❒ A well conceived working team

➪ Multidisciplinary

✔ Antenna theory

✔ Microwave electronics

✔ Numerical electromagnetics

✔ Satellite/Mobile Telecoms

➪ Multiprofile

✔ Universities (B, CH, CR, D, DK, F, GR, I, I, N, NL, PL, P, S, TR)

✔ Telecom companies (Saab-Ericsson, Alcatel Espace, Alenia Spazio, GEC-Marconi, DASA-Dornier, Siemens, CASA, ERA, Ericsson M. S., Dassault)

✔ R&D Institutes (CNET-F, VTT-SF, SINTEF-N, DETyCOM-E, FT2-D, TNO-NL, FOA-S)

✔ European Space Agency

COST 245 Project

- 17 European Countries + ESA

- 3 Working Groups
  - ✔ WG1 : Antenna modeling and CAD Tools
  - ✔ WG2 : Radiating elements and arrays
  - ✔ WG3 : Active Antenna architectures

- 3 Workshops
  - ✔ CAD for antennas
    StGallen, CH, Feb. 1994 hosted by EPFL
  - ✔ MMIC technologies for active antennas
    Friedrichshafen, D, Sep. 95
    hosted by Siemens-Dornier
  - ✔ Active Antennas

    (Noordwijk, NL, June 96, hosted by ESA-ESTEC, open to a worldwide audience of 200 attendees

COST 245: Key Achievements

- ❒ Working Group 1
  - ✔ Development of two complementary CAD tools, intended for industrial use, able to deal with technologically relevant printed antennas
  - ✔ Presently developed as stand alone versions, their integration into a general Antenna Design Framework (ADF) is underway.
- ❒ Working Group 2
  - ✔ Development of dual polarized antennas for satellite communications and broadcasting.
  - ✔ Design and study of radiating elements with generation of very low passive intermodulation
- ❒ Working Group 3
  - ✔ development and consolidation of the new transmit antenna concept of semi-active multi-matrix antennas, originally introduced in COST Project 223 for multibeam mobile communications satellites

THE NEAR FUTURE:
The COST 260 Project

"Smart antennas: computer aided design & technology"

- ⇨ MoU approved on January 1997
- ⇨ At least, 15 signatory countries expected
- ⇨ Logical follow-up of COST-245
  - ✔ Develop and validate CAD tools
  - ✔ Speed up the demonstration of new antenna concepts in close collaboration with TSUNAMI
  - ✔ Continue to provide an European Forum for exchange and cooperation

The COST 245 Project in Switzerland

- Swiss representative: EPF-Lausanne

  (Co-leader of Working Group 1)

- Swiss experts
  - ✔ Huber+Suhner, Herisau
  - ✔ Ascom-Tech, Maegenwil

- Spin-offs
  - ✔ EPFL: partner in several european projects
  - ✔ CAD softwares for ESA-ESTEC
  - ✔ Know-how and technology transfert to swiss industries : H+S, Ascom-Tech, Asulab...

  (antenna designs for commercial applications)

ANNEX III. COST 245 Mailing list

Date: 25 November 1995

B
Prof. G Vandenbosch
K.U. Leuven, Div. ESAT-TELEMIC
Kardinaal Mercierlaan 94
B-3001 Leuven
Belgium
TEL.: +32 16 321110
TELEX:
TELEFAX: +32 16 321986
EMAIL: guy.vandenbosch@esat.kuleuven.ac.be
NCOST: 245
ROLE: Member
W.G.: 1

BG
Prof. HD Hristov
Tech. Univ. of Varna (VMEI), Dept. of Radiotechnics
Ul. Studentska 1
BU-9010 Varna
Bulgaria
TEL.: +359 52 886308
TELEX:
TELEFAX: +359 52 871910
EMAIL: hristov@radio.tu-varna.bg or h.hristov@ieee.org
NCOST: 245
ROLE:
W.G.: 2

CEC
Ms. K Coenen
COST Telecom Secretariat, BU-9, 2/76
200 rue de la Loi
B-1049 Brussels
Belgium
TEL.: +32 2 295 6950
TELEX:
TELEFAX: +32 2 296 2981
EMAIL: kco@postman.dg13.cec.be
NCOST:
ROLE:
W.G.:

CEC
Mr. A Galetsas
COST Telecom Secretariat, BU-9, 2/76
200 rue de la Loi
B-1049 Brussels
Belgium
TEL.: +32 2 299 0450
TELEX:
TELEFAX: +32 2 296 2981
EMAIL: aga@postman.dg13.cec.be
NCOST:
ROLE:
W.G.:

CH
Mr. P Gay-Balmaz
LEMA, EPFL
Ecublens
CH-1015 Lausanne
Switzerland
TEL.: +41 21 693 2669
TELEX:
TELEFAX: +41 21 693 2673
EMAIL: mosig@lema.de.epfl.ch
NCOST: 245
ROLE: Expert
W.G.: 1

CH
Prof. JR Mosig
LEMA, EPFL
Ecublens
CH-1015 Lausanne
Switzerland
TEL.: +41 21 693 4628
TELEX:
TELEFAX: +41 21 693 2673
EMAIL: mosig@lema.de.epfl.ch
NCOST: 245
ROLE: Member
W.G.: 1

CH
Ms. A Skrivervik
LEMA, EPFL
Ecublens
CH-1015 Lausanne
Switzerland
TEL.: +41 21 693 2669
TELEX:
TELEFAX: +41 21 693 2673
EMAIL: anja@lema.de.epfl.ch
NCOST: 245
ROLE: Member
W.G.: 1

CRO
Prof. J Bartolic
Univ. of Zagreb, Faculty of Electr. Eng. and Computing
Unska 3
CRO-41000 Zagreb
Croatia
TEL.: +385 1 612 9663
TELEX:
TELEFAX: +385 1 612 1396
EMAIL: jbartol@zea.cc.fer.hr or juraj.bartolic@fer.hr
NCOST: 245
ROLE: Member
W.G.: 1,3

CRO
Mr. Z Sipus
Univ. of Zagreb, Faculty of Electr. Eng. and Computing
Unska 3
CRO-41000 Zagreb
Croatia
TEL.: +385 1 612 9663
TELEX:
TELEFAX: +385 1 611 1396
EMAIL: zsipus@zea.cc.fer.hr
NCOST: 245
ROLE: Expert
W.G.: 1

D
Dr. G Braun
Daimler Benz Aerospace, Dept.: RSY41
P.O.B. 80 11 69
D-81663 München
Germany
TEL.: +49 89 607 27382
TELEX:
TELEFAX: +49 89 607 21059
EMAIL:
NCOST: 245
ROLE: Expert
W.G.: 3

D
Mr. F Dobias
Univ. of Paderborn
D-33098 Paderborn
Germany
TEL.: +49 5251 60 2221
TELEX:
TELEFAX: +49 5251 60 3238
EMAIL: dobias@ntws1.uni-paderborn.de
NCOST: 245
ROLE: Expert
W.G.: 3

D
Mr. G Fischer
Univ. of Paderborn
D-33098 Paderborn
Germany
TEL.: +49 5251 60 3861
TELEX:
TELEFAX: +49 5251 60 3238
EMAIL: fischer@ntws1.uni-paderborn.de
NCOST: 245
ROLE: Expert
W.G.: 3

D
Dr. W Bornemann
Daimler Benz Aerospace
P.O.B. 80 11 69
D-81663 München
Germany
TEL.: +49 89 607 24303
TELEX:
TELEFAX: +49 89 607 23384
EMAIL:
NCOST: 245
ROLE: Expert
W.G.: 3

D
Mr. A Brunner
Siemens AG, Antenna Development
Landshuterstrasse 26
D-85716 Unterschleissheim
Germany
TEL.: +49 89 3179 2665
TELEX:
TELEFAX: +49 89 3179 2682
EMAIL:
NCOST: 245
ROLE: Expert
W.G.: 2,3

D
Dr. K-P Dombek
FTZ der Deutschen Telekom
Am Kavalleriesand 3, FZ 235a
D-64295 Darmstadt
Germany
TEL.: +49 6151 832525
TELEX: 419511 ftz d
TELEFAX: +49 6151 834948
EMAIL:
NCOST: 245
ROLE: Member
W.G.: 1

D
Dr.-Ing. G Gottwald
Univ. of Karlsruhe, Inst. für Höchstfrequenztechnik und Elektronik
Kaiserstrasse 12
D-76128 Karlsruhe
Germany
TEL.: +49 721 608 2525
TELEX:
TELEFAX: +49 721 691865
EMAIL: gerd@ihewap.etec.uni-karlsruhe.de
NCOST: 245
ROLE: Expert
W.G.: 1,2

D
Dr.-Ing. E Heidrich
I&S Hochfrequenztechnik
D-77839 Lichtenau-Ulm
Germany
TEL.: +49 7227 8981
TELEX:
TELEFAX: +49 7227 8982
EMAIL:
NCOST: 245
ROLE: Expert
W.G.: 1,2

D
Dr. B Marx
FTZ der Deutschen Telekom
Am Kavalleriesand 3, FZ 235e
D-64295 Darmstadt
Germany
TEL.: +49 6151 833851
TELEX: 419511 ftz d
TELEFAX: +49 6151 834948
EMAIL:
NCOST: 245
ROLE: Member
W.G.: 2

D
Mr. G Schindler
Siemens AG, Antenna Development
Landshuterstrasse 26
D-85716 Unterschleissheim
Germany
TEL.: +49 89 3179 2676
TELEX:
TELEFAX: +49 89 3179 2682
EMAIL:
NCOST: 245
ROLE: Expert
W.G.: 2,3

D
Dr. R Zahn
Dornier/Daimler Benz Aerospace
Dept. RSX 25
D-88039 Friedrichshafen
Germany
TEL.: +49 7545 84959
TELEX:
TELEFAX: +49 7545 8 4177
EMAIL: zahn@spacediv.dofn.de
NCOST: 245
ROLE: Expert
W.G.: 3

D
Dr. D Leistner
Daimler Benz Aerospace, Dept.: RST 26
P.O.B. 80 11 69
D-81663 München
Germany
TEL.: +49 89 607 22296
TELEX:
TELEFAX: +49 89 607 27206
EMAIL:
NCOST: 245
ROLE: Expert
W.G.: 3

D
Mr. F Rostan
Univ. of Karlsruhe, Inst. für Höchstfrequenztechnik und Elektronik
Kaiserstrasse 12
D-76128 Karlsruhe
Germany
TEL.: +49 721 608 2525
TELEX:
TELEFAX: +49 721 691865
EMAIL: rostan@ihewap.etec.uni-karlsruhe.de
NCOST: 245
ROLE: Expert
W.G.: 1,2

D
Mr. P Shutie
Dornier/Daimler Benz Aerospace
Dept. RSX 25
D-88039 Friedrichshafen
Germany
TEL.: +49 7545 84959
TELEX:
TELEFAX: +49 7545 8 4177
EMAIL:
NCOST: 245
ROLE: Expert
W.G.:

DK
Dr. P Balling
ASC, Antenna Systems Consultant, ApS
Søndertoften 107
DK-2630 Tåstrup
Denmark
TEL.: +45 42 52 1952
TELEX: 16600 fotex attn: ansycon taastrup
TELEFAX: +45 42 52 0172
EMAIL: pballing@inet.uni-c.dk & pballing@unidhp.uni-c.dk
NCOST: 245
ROLE: External Secretary
W.G.: 1,3

DK
Prof. JE Hansen
Electromagnetics Institute, DTU
Bld. 348
DK-2800 Lyngby
Denmark
TEL.: +45 45 881444
TELEX: 3752 dthdia dk
TELEFAX: +45 45 93 1634
EMAIL: jh@emi.dtu.dk
NCOST: 245
ROLE: Member
W.G.: 1

DK
Dr. A Ostergaard
Electromagnetics Institute, DTU
Bld. 348
DK-2800 Lyngby
Denmark
TEL.: +45 45 881444
TELEX: 3752 dthdia dk
TELEFAX: +45 45 93 1634
EMAIL: allan@emi.dtu.dk
NCOST: 245
ROLE: Expert
W.G.: 1

DK
Dr. HH Viskum
TICRA
Kronprinsensgade 13
DK-1114 Copenhagen K
Denmark
TEL.: +45 33 124572
TELEX:
TELEFAX: +45 33 120880
EMAIL:
NCOST:
ROLE:
W.G.:

E
Mr. C Martin-Pascual
DETyCOM, A.I.E.
Laguna, 7
E-28220 Majadahonda (Madrid)
Spain
TEL.: +34 1 638 6213
TELEX:
TELEFAX: +34 1 638 6099
EMAIL: tdc@cc.csic.es
NCOST: 245
ROLE: Member
W.G.: 2

E
Mr. C Montesano
CASA
Avda Aragon 404
E-28022 Madrid
Spain
TEL.: +34 1 585 7831
TELEX: 48540 casa e
TELEFAX: +34 1 747 4799
EMAIL:
NCOST:
ROLE:
W.G.: 2

E
Ms. J Redoli Granados
E.T.S.I.T.
Ciudad Universitaria
E-28040 Madrid
Spain
TEL.: +34 1 549 5700/ 336 7360
TELEX: 47430 etsit e
TELEFAX: +34 1 543 2002
EMAIL: judith@gr.ssr.upm.es
NCOST: 245
ROLE: Expert
W.G.: 2

E
Prof. M Sierra
E.T.S.I.T
Ciudad Universitaria
E-28040 Madrid
Spain
TEL.: +34 1 549 5700/ 336 7360
TELEX: 47430 etsit e
TELEFAX: +34 1 543 2002
EMAIL: manolo@gr.ssr.upm.es
NCOST: 245
ROLE: Member
W.G.: 2,3

ESA
Dr. A Roederer
ESA/ESTEC - XE
PB 299
NL-2200 AG Noordwijk
Netherlands
TEL.: +31 71565 3935
TELEX: 39098 nl
TELEFAX: +31 71565 4999
EMAIL: aroedere@vmprofs.estec.esa.nl
NCOST: 245
ROLE: Vice Chairman and Member
W.G.: 1,2,3

F
Mr. J-P Daniel
Univ. of Rennes
avenue du General Leclerc
F-35042 Rennes
France
TEL.: +33 99 28 62 19
TELEX:
TELEFAX: +33 99 286969
EMAIL: jean-pierre.daniel@univ-rennes1.fr
NCOST: 245
ROLE: Member
W.G.: 1

F
Mr. J-F Dreyfuss
France Telecom, CNET - Paris B/RSH/HYS
38-40, rue du General Leclerc
F-92131 Issy-les-Moulineaux, Cedex
France
TEL.: +33 1 4529 6574
TELEX:
TELEFAX: +33 1 4529 4534
EMAIL: dreyfusj@issy.cnet.fr
NCOST: 245
ROLE: Member
W.G.: 3

F
Mr. P-L Ouvrard
Dassault Electronique
55, quai Marcel Dassault
F-92214 Saint-Cloud, Cedex, Paris
France
TEL.: +33 1 49118025
TELEX: 633 299 f
TELEFAX: +33 1 4602 5778
EMAIL:
NCOST: 245
ROLE: Expert
W.G.: 3

F
Prof. A Papiernik
Univ. de Nice, Lab. d'Electronique
CNRS Bat4, rue Albert Einstein
F-06560 Valbonne
France
TEL.: +33 92 942801
TELEX: 970006 f
TELEFAX: +33 92 942812
EMAIL: papi@mimosa.unice.fr
NCOST: 245
ROLE: Expert
W.G.: 1,2,3

F
Mr. P Voisin
Alcatel Espace
26, avenue S.F. Champollion, BP 1187
F-31037 Toulouse
France
TEL.: +33 61 195990
TELEX: atesp 521 355 f
TELEFAX: +33 61 195205
EMAIL:
NCOST: 245
ROLE: Expert
W.G.: 3

GR
Prof. JG Fikioris
Nat. Tech. Univ. of Athens
42 Patission Ave.
GR-10682 Athens
Greece
TEL.: +30 1 3816 934
TELEX: 221682 ntua gr
TELEFAX: +30 1 3826 792
EMAIL: gfikio@naxos.esd.ece.ntua.gr
NCOST: 245
ROLE: Member
W.G.: 1

GR
Prof. JD Kanellopoulos
Nat. Tech. Univ. of Athens
42 Patission Ave.
GR-10682 Athens
Greece
TEL.: +30 1 0
TELEX: 221682 ntua gr
TELEFAX: +30 1 3826 792
EMAIL:
NCOST: 245
ROLE: Member
W.G.: 1

GR
Mr. JD Vazouras
Nat. Tech. Univ. of Athens
42 Patission Ave.
GR-10682 Athens
Greece
TEL.: +30 1 0
TELEX: 221682 ntua gr
TELEFAX: +30 1 3826 792
EMAIL:
NCOST: 245
ROLE: Expert
W.G.: 1

I
Dr. B Casali
IDS
Via Roma 50
I-56126 Pisa
Italy
TEL.: +39 0 505 02769
TELEX:
TELEFAX: +39 0 505 02470
EMAIL: ids@vm.cnvce.cnr.it
NCOST: 245
ROLE: Expert
W.G.: 1

I
Dr. G Doro
Alenia Spazio
Via Saccomuro, 24
I-00131 Roma
Italy
TEL.: +39 6 4151 2230
TELEX: 614337 sesrom i
TELEFAX: +39 6 4151 2389
EMAIL:
NCOST:
ROLE: Member
W.G.: 3

I
Dr. M Lisi
Alenia Spazio
Via Saccomuro, 24
I-00131 Roma
Italy
TEL.: +39 6 4151 2230
TELEX: 614337 sesrom i
TELEFAX: +39 6 4151 2389
EMAIL:
NCOST:
ROLE: Expert
W.G.: 3

I
Mr. V Santachiara
Alenia Spazio
Via Saccomuro, 24
I-00131 Roma
Italy
TEL.: +39 6 4151 2346
TELEX: 614337 sesrom i
TELEFAX: +39 6 4151 2389
EMAIL:
NCOST:
ROLE: Expert
W.G.: 1,3

I
Dr. A Toscano
Dipartimento di Ingegneria Elettronica, Terza Università di Roma
Via C. Segre 2
I-00146 Roma
Italy
TEL.: +39 6 556 2305
TELEX:
TELEFAX: +39 6 556 1373
EMAIL:
NCOST: 245
ROLE: Expert
W.G.: 1

I
Prof. L Vegni
Dipartimento di Ingegneria Elettronica, Terza Università di Roma
Via C. Segre 2
I-00146 Roma
Italy
TEL.: +39 6 556 2305
TELEX:
TELEFAX: +39 6 556 1373
EMAIL:
NCOST: 245
ROLE: Member
W.G.: 1

N
Mr. F Bekkadal
Sintef - Delab
Norwegian Institute of Technology
N-7034 Trondheim
Norway
TEL.: +47 73 59 43 12
TELEX: 55 552 delab n
TELEFAX: +47 73 59 1099
EMAIL: fritz.bekkadal@delab.sintef.no
NCOST: 245
ROLE: Member
W.G.: 1,2,3

N
Mr. BA Brynjarsson
Sintef - Delab
Norwegian Institute of Technology
N-7034 Trondheim
Norway
TEL.: +47 73 59 24 46
TELEX: 55 552 delab n
TELEFAX: +47 73 59 1099
EMAIL: bjarki.brynjarsson@delab.sintef.no
NCOST: 245
ROLE: Member
W.G.: 1,2,3

N
Ms. I Jensen
Sintef - Delab
Norwegian Institute of Technology
N-7034 Trondheim
Norway
TEL.: +47 73 50 27 40
TELEX: 55 552 delab n
TELEFAX: +47 73 59 10 99
EMAIL: irene.jensen@delab.sintef.no
NCOST: 245
ROLE: Expert
W.G.: 1,2,3

N
Mr. SA Skyttemyr
Telenor Research
P.O. Box 83
N-2007 Kjeller
Norway
TEL.: +47 63 80 92 95
TELEX:
TELEFAX: +47 63 81 00 76
EMAIL: svein.skyttemyr@tf.telenor.no
NCOST: 245
ROLE: Expert
W.G.: 2,3

N
Mr. JA Aas
The Norwegian Institute of Technology
N-7034 Trondheim
Norway
TEL.: +47 73 59 43 07
TELEX: 55 552 delab n
TELEFAX: +47 73 50 73 22
EMAIL: aas@tele.unit.no
NCOST: 245
ROLE: Member
W.G.: 1,2,3

NL
Ir. PFM Giesselink
Hollandse Signallapparaten B.V.
P.O.Box 42
NL-7550 GD Hengelo
Netherlands
TEL.: +31 74 483069
TELEX: 38151 bhthd nl
TELEFAX: +31 74 484009
EMAIL: giesselink@hgf.signaal.nl
NCOST: 245
ROLE: Expert
W.G.: 3

NL
Ir. M Hajian
Technische Universiteit Delft
Mekelweg 4, PO Box 5031
NL-2628 CD Delft
Netherlands
TEL.: +31 15 78 62 56
TELEX: 38151 bhthd nl
TELEFAX: +31 15 78 40 46
EMAIL: m.hajian@et.tudelft.nl
NCOST: 245
ROLE: Member
W.G.: 2,3

NL
Dr. WPMN Keizer
FEL TNO
Oude Waalsdorperweg 63
NL-2597 AK The Haque
Netherlands
TEL.: +31 70 326 4221
TELEX:
TELEFAX: +31 70 328 0961
EMAIL: keizer@fel.tno.nl
NCOST: 245
ROLE: Member
W.G.: 3

NL
Prof. LP Ligthart
Delft Univ. of Techn.
Mekelweg 4, PO Box 5031
NL-2628 CD Delft
Netherlands
TEL.: +31 15 786230
TELEX: 38151 bhthd nl
TELEFAX: +31 15 784046
EMAIL:
NCOST: 245
ROLE: Expert
W.G.: 2

NL
Mr. JR Schmidt
PTT Research Neher Laboratory
St Paulusstraat, 4
NL-2260 AK Leidschendam
Netherlands
TEL.: +31 70 332 5227
TELEX: 31236 dul nl
TELEFAX: +31 70 322 6477
EMAIL:
NCOST:
ROLE:
W.G.:

P
Prof. AM Barbosa
DEEC/IT, Instituto Superior Técnico
Av Rovisco Pais
P-1096 Lisboa Codex
Portugal
TEL.: +351 1 8417358
TELEX:
TELEFAX: +351 1 8482987
EMAIL: d781@beta.ist.utl.pt
NCOST: 245
ROLE: Member
W.G.: 1,2

P
Prof. JF da Rocha Pereira
Univ. de Aveiro
Aveiro
Portugal
TEL.: +351 34 370327
TELEX:
TELEFAX: +351 34 381128
EMAIL: jrp@ua.pt
NCOST: 245
ROLE: Member
W.G.: 2

P
Prof. CA Fernandes
Instituto Superior Tecnico
Av Rovisco Pais
P-1096 Lisboa Codex
Portugal
TEL.: +351 1 8417736
TELEX:
TELEFAX: +351 1 8472001
EMAIL: d1916@beta.ist.utl.pt
NCOST: 245
ROLE: Expert
W.G.: 2

P
Mr. J Fernandes
Univ. de Aveiro
Aveiro
Portugal
TEL.: +351 34 383090
TELEX:
TELEFAX: +351 34 383091
EMAIL: jf@ua.pt
NCOST: 245
ROLE: Expert
W.G.: 2

P
Prof. J Pedro
Dept. Electrónica, Univ. de Aveiro
Aveiro
Portugal
TEL.: +351 34 383090
TELEX:
TELEFAX: +351 34 383091
EMAIL: jf@ua.pt
NCOST: 245
ROLE: Expert
W.G.: 3

P
Prof. C Peixeiro
Instituto Superior Técnico
Av Rovisco Pais
P-1096 Lisboa Codex
Portugal
TEL.: +351 1 8417736
TELEX:
TELEFAX: +351 1 8482987
EMAIL: ecpeixe@beta.ist.utl.pt
NCOST: 245
ROLE: Expert
W.G.: 1,2

PL
Prof. DJ Bem
Tech. Univ. of Wroclaw, Inst. of Telecom and Acoustics
Wybrzeze Wyspianskiego 27
PL-50-370 Wroclaw
Poland
TEL.: +48 71 223 473
TELEX: 712559 pwr pl
TELEFAX: +48 71 223 473
EMAIL: bem@zr.ita.pwr.wroc.pl
NCOST: 245
ROLE: Member
W.G.: 2,3

PL
Mr. P Kabacik
Tech. Univ. of Wroclaw, Inst. of Telecom and Acoustics
Wybrzeze Wyspianskiego 27
PL-50-370 Wroclaw
Poland
TEL.: +48 71 203 083
TELEX: 712559 pwr pl
TELEFAX: +48 71 223 473
EMAIL: pawel@zr.ita.pwr.wroc.pl
NCOST: 245
ROLE: Expert
W.G.: 2,3

S
Prof. EF Bolinder
Chalmers Univ. of Techn.
S-41296 Gothenburg
Sweden
TEL.: +46 31 772 1739
TELEX: 2369 chalbib s
TELEFAX: +46 31 16 45 13
EMAIL: piotr@nt.chalmers.se
NCOST: 245
ROLE: Chairman and Member
W.G.: 3

S
Dr. O Dahlsjö
Ericsson Microwave Systems
Bergfotsgatan 2
S-43184 Mölndal
Sweden
TEL.: +46 31 671241
TELEX: 20905 ericsmw s
TELEFAX: +46 31 671551
EMAIL:
NCOST: 245
ROLE: Expert
W.G.:

S
Dr. A Derneryd
Ericsson Microwave Systems
Mobile Communications
S-43184 Mölndal
Sweden
TEL.: +46 31 671042
TELEX: 20905 ericsmw s
TELEFAX: +46 31 673321
EMAIL: emwadd@emw.ericsson.se
NCOST: 245
ROLE: Expert
W.G.: 1, 2

S
Mr. S Hagelin
FOA, Div. Microwave Technology
Box 1165
S-58111 Linköping
Sweden
TEL.: +46 13 118409
TELEX:
TELEFAX: +46 13 131665
EMAIL: svehag@lin.foa.se
NCOST: 245
ROLE: Expert
W.G.: 3

S
Dr. P Ingvarson
Saab Ericsson Space AB
S-40515 Gothenburg
Sweden
TEL.: +46 31 671095
TELEX:
TELEFAX: +46 31 673866
EMAIL: per.ingvarson@space.se
NCOST: 245
ROLE: Expert
W.G.: 1,2

S
Prof. P-S Kildal
Chalmers Univ. of Techn.
S-41296 Gothenburg
Sweden
TEL.: +46 31 772 1718
TELEX: 2369 chalbib s
TELEFAX: +46 31 772 1740
EMAIL: simon@nt.chalmers.se
NCOST: 245
ROLE: Member
W.G.: 1,2

S
Mr. A Molker
Ericsson Microwave Systems
Bergfotsgatan 2
S-43184 Mölndal
Sweden
TEL.: +46 31 672016
TELEX: 20905 ericsmw s
TELEFAX: +46 31 671551
EMAIL:
NCOST: 245
ROLE: Expert
W.G.:

S
Dr. P Starski
Chalmers Univ. of Techn.
Div. of Microwave Tech.
S-41296 Gothenburg
Sweden
TEL.: +46 31 772 1734
TELEX:
TELEFAX: +46 31 16 45 13
EMAIL: piotr@nt.chalmers.se
NCOST: 245
ROLE: Expert
W.G.: 3

FIN
Mr. A Hujanen
VTT Information Technology
P.O. Box 1202
FIN-02044 VTT
Finland
TEL.: +0 0 0
TELEX: 123704 vttte sf
TELEFAX: +358 0 456 7013
EMAIL: arto.hujanen@vtt.fi
NCOST: 245
ROLE: Expert
W.G.:

FIN
Mr. K Markus
VTT Information Technology
P.O. Box 1202
FIN-02044 VTT
Finland
TEL.: +358 0 456 5625
TELEX: 123704 vttte sf
TELEFAX: +358 0 456 7013
EMAIL: kari.markus@vtt.fi
NCOST: 245
ROLE: Member
W.G.: 2,3

TR
Prof. N Günalp
Dept. EE, METU
İnönü Bulvari, ODTU-BALGAT
TR-06531 Ankara
Turkey
TEL.: +90 312 210 1000
TELEX: 060744462 ttee tr
TELEFAX: +90 312 210 1261
EMAIL: gunalp@rorqual.cc.metu.edu.tr
NCOST: 245
ROLE: Member
W.G.: 1,2

TR
Mr. H Yildiz
Aselsan, A.S., Microwave and Systems Tech. Div.
PK. 101, Yenimahalle
TR-06172 Ankara
Turkey
TEL.: +90 312 385 19 00
TELEX: 42638
TELEFAX: +90 312 354 52 05
EMAIL:
NCOST: 245
ROLE: Expert
W.G.: 2

FIN
Mr. K Laukkanen
VTT Information Technology
P.O. Box 1202
FIN-02044 VTT
Finland
TEL.: +358 0 45 66576
TELEX: 123704 vttte sf
TELEFAX: +358 0 456 7013
EMAIL: kalevi.laukkanen@vtt.fi
NCOST: 245
ROLE: Member
W.G.: 1,3

TR
Prof. T Birand
Dept. EE, METU
İnönü Bulvari, ODTU-BALGAT
TR-06531 Ankara
Turkey
TEL.: +90 312 210 1258
TELEX: 060744462 ttee tr
TELEFAX: +90 312 210 1110
EMAIL:
NCOST: 245
ROLE: Member
W.G.: 1,2

TR
Prof. A Hizal
Dept. EE, METU
İnönü Bulvari, ODTU-BALGAT
TR-06531 Ankara
Turkey
TEL.: +90 312 210 1000
TELEX: 060744462 ttee tr
TELEFAX: +90 312 210 1261
EMAIL: altunkan@vm.cc.metu.edu.tr
NCOST: 245
ROLE: Expert
W.G.: 2

UK
Dr. G Cox
Matra Marconi Space
Anchorage Road
Portsmouth PO3 5PU
U.K.
TEL.: +44 1705 664966
TELEX: 86666
TELEFAX: +44 1705 675 496
EMAIL:
NCOST:
ROLE: Expert
W.G.:

UK
Mr. JM Griffin
GEC Marconi Research Centre
West Hanningfield Road
Chelmsford, Essex CM2 8HN
U.K.
TEL.: +44 1245 473331
TELEX:
TELEFAX: +44 1245 475010
EMAIL:
NCOST: 245
ROLE: Expert
W.G.: 2,3

UK
Dr. RS Orton
GEC Marconi Research Centre
West Hanningfield Road
Chelmsford, Essex CM2 8HN
U.K.
TEL.: +44 1245 473331
TELEX:
TELEFAX: +44 1245 475010
EMAIL:
NCOST: 245
ROLE: Member
W.G.: 2,3

UK
Mr. D Sanchez-Hernandez
Communications Research Group, Electronic & Electrical Eng. Dept.
King's College, Univ. of London
Strand, London WC2R 2LS
U.K.
TEL.: +44 171 873 2889
TELEX:
TELEFAX: +44 171 836 4781
EMAIL: david@orion.eee.kcl.ac.uk
NCOST: 245
ROLE: Expert
W.G.: 3

UK
Mr. MW Shelley
ERA Technology Ltd.
Cleeve Road
Leatherhead, Surrey KT22 7SA
U.K.
TEL.: +44 1372 367000
TELEX: 264045 eralhd g
TELEFAX: +44 1372 367099
EMAIL: info@era.co.uk
NCOST:
ROLE: Expert
W.G.: 2,3

UK
Prof. B Westcott
Univ. of Southampton
Southampton
U.K.
TEL.: +44 1703 593647
TELEX:
TELEFAX: +44 1703 595147
EMAIL:
NCOST: 245
ROLE: Expert
W.G.: 3

BİBLİYOGRAFİK BİLGİ FORMU	
1- Proje No: COST 245	2- Rapor Tarihi: 31.10.1997
3- Projenin Başlangıç ve Bitiş Tarihleri: 1.1.1994 - 1.7.1997	
4- Projenin Adı: Aktif Faz Taramalı Diziler ve Dizi Beslemeli Antenler (Active Phased Arrays and Array Fed Antennas)	
5- Proje Yürütücüsü ve Yardımcı Araştırıcılar: Proje Yürütücüsü: Prof. Dr. T. Birand. Araştırıcılar: Prof. Dr. C. Toker, Prof. Dr. A. Hızal, Prof. Dr. N. Günalp, Prof. Dr. M. Büyükdura, Doç. Dr. G. Dural, Öğr. Gör. Dr. C. Bulutay, Öğr. Gör. Dr. Ö. Çivi, Öğr. Gör. Dr. L. Alatan, Öğr. Gör. Ş. Demir.	
6- Projenin Yürütüldüğü Kuruluş ve Adresi: ODTÜ Elektrik ve Elektronik Mühendisliği Bölümü	
7- Destekleyen Kuruluş(ların) Adı ve Adresi:	

8- Öz (Abstract):

Bu projede faz taramalı anten dizileri, aktif diziler, akıllı antenler, monolitik mikrodalga entegre devreler (MMIC), geniş bantlı antenler ve bu tür yapıların nümerik metotlarla analizi konularında çalışmalar yapılmıştır. Bu çalışmalar, AET üye ülkeleriyle işbirliği ve koordinasyon içerisinde yürütülmüştür.

Within the framework of this project, research has been carried out on phased array antennas, active arrays, smart antennas, monolithic microwave integrated circuits (MMIC), wide band antennas and numerical methods for the analysis of these structures. These studies have been conducted in cooperation with the member countries of European Community.

Anahtar Kelimeler: Faz taramalı diziler, aktif anten dizileri, mikroşerit antenler,monolitik mikrodalga entegre devreler, moment metodu.

9- Proje ile ilgili Yayın/Tebliğlerle ilgili Bilgiler

Proje kapsamında ortaya çıkan 16 adet yurt dışı ve yurt içi yayın raporun ekinde sunulmuştur.

10- Bilim Dalı: Elektromanyetik Alanlar ve Mikrodalga Tekniği
Doçentlik B. Dalı Kodu: ISIC Kodu:
Uzmanlık Alanı Kodu:

11- Dağıtım (*) : ☐ Sınırlı ☒ Sınırsız

12- Raporun Gizlilik Durumu : ☐ Gizli ☒ Gizli Değil

(*) Projenizin Sonuç Raporunun ulaştırılmasını istediğiniz kurum ve kuruluşları ayrıca belirtiniz